CHALLENGES FOR RADIATION TRANSPORT MODELLING: MONTE CARLO AND BEYOND

EDITED BY: Miguel Antonio Cortés-Giraldo, Francis A. Cucinotta, Susanna Guatelli and Vasilis Vlachoudis

PUBLISHED IN: Frontiers in Physics

frontiers Research Topics

ISSN 1664-8714
ISBN 978-2-88976-105-0
DOI 10.3389/978-2-88976-105-0

About Frontiers

Frontiers is more than just an open-access publisher of scholarly articles: it is a pioneering approach to the world of academia, radically improving the way scholarly research is managed. The grand vision of Frontiers is a world where all people have an equal opportunity to seek, share and generate knowledge. Frontiers provides immediate and permanent online open access to all its publications, but this alone is not enough to realize our grand goals.

Frontiers Journal Series

The Frontiers Journal Series is a multi-tier and interdisciplinary set of open-access, online journals, promising a paradigm shift from the current review, selection and dissemination processes in academic publishing. All Frontiers journals are driven by researchers for researchers; therefore, they constitute a service to the scholarly community. At the same time, the Frontiers Journal Series operates on a revolutionary invention, the tiered publishing system, initially addressing specific communities of scholars, and gradually climbing up to broader public understanding, thus serving the interests of the lay society, too.

Dedication to Quality

Each Frontiers article is a landmark of the highest quality, thanks to genuinely collaborative interactions between authors and review editors, who include some of the world's best academicians. Research must be certified by peers before entering a stream of knowledge that may eventually reach the public - and shape society; therefore, Frontiers only applies the most rigorous and unbiased reviews.
Frontiers revolutionizes research publishing by freely delivering the most outstanding research, evaluated with no bias from both the academic and social point of view. By applying the most advanced information technologies, Frontiers is catapulting scholarly publishing into a new generation.

What are Frontiers Research Topics?

Frontiers Research Topics are very popular trademarks of the Frontiers Journals Series: they are collections of at least ten articles, all centered on a particular subject. With their unique mix of varied contributions from Original Research to Review Articles, Frontiers Research Topics unify the most influential researchers, the latest key findings and historical advances in a hot research area! Find out more on how to host your own Frontiers Research Topic or contribute to one as an author by contacting the Frontiers Editorial Office: frontiersin.org/about/contact

CHALLENGES FOR RADIATION TRANSPORT MODELLING: MONTE CARLO AND BEYOND

Topic Editors:
Miguel Antonio Cortés-Giraldo, Sevilla University, Spain
Francis A. Cucinotta, University of Nevada, Las Vegas, United States
Susanna Guatelli, University of Wollongong, Australia
Vasilis Vlachoudis, European Organization for Nuclear Research (CERN), Switzerland

Citation: Cortés-Giraldo, M., A., Cucinotta, F., A., Guatelli, S., Vlachoudis, V., eds. (2022). Challenges for Radiation Transport Modelling: Monte Carlo and Beyond. Lausanne: Frontiers Media SA. doi: 10.3389/978-2-88976-105-0

Table of Contents

frontiers | Frontiers in Physics

EDITORIAL
published: 14 April 2022
doi: 10.3389/fphy.2022.884140

Editorial: Challenges for Radiation Transport Modelling: Monte Carlo and Beyond

M. A. Cortés-Giraldo[1]*, *F. A. Cucinotta*[2], *S. Guatelli*[3] and *V. Vlachoudis*[4]

[1]Department of Atomic, Molecular and Nuclear Physics, Universidad de Sevilla, Seville, Spain, [2]School of Integrated Health Science, University of Nevada Las Vegas, Las Vegas, NV, United States, [3]Center for Medical Radiation Physics, University of Wollongong, Wollongong, NSW, Australia, [4]Accelerator Systems Department, European Organization for Nuclear Research (CERN), Geneva, Switzerland

Keywords: radiation transport calculations, Monte Carlo simulation, microdosimetry, nuclear and particle physics, computing efficiency

Editorial on the Research Topic

Challenges for Radiation Transport Modelling: Monte Carlo and Beyond

Radiation transport codes have become a key tool in many fields of research, from high energy physics to medical applications, passing through detector design optimization, radiation protection on Earth and in space, and other fields of applications. Over the last decades, many codes with different approaches and specific purposes have been developed. Also, general-purpose Monte Carlo codes are being continuously developed in order to expand their domains of applicability and/or improve their computational efficiency.

A total of twelve (12) papers have been published in this research topic, of which nine (9) present original research works. Approximately two thirds of the papers included correspond to the application of Monte Carlo codes in medical physics, especially in dosimetry and microdosimetry, whereas the others present latest developments and/or adaptations of general-purpose radiation transport codes, such as FLUKA, Penelope/PENH or Geant4.

As for the papers with general-purpose perspective, the work by Asai et al. presents a translation to C++ of the Penelope physics subroutines originally written in FORTRAN, so that transport of electrons and positrons with the class-II algorithm implemented in Penelope is now possible with the Geant4 toolkit. The mean features of the resulting code, named PenG4, are also described and verified using as benchmark calculations obtained with Penelope. The paper by Ahdida et al. describes the physics processes currently implemented in the code distributed by the FLUKA.CERN Collaboration. The code has reached a high level of maturity, as shown by its applications in research fields such as transport of high energy hadron beams in crystal devices, evaluation of radiobiological effects, and description of effects induced by ionizing radiation in microelectronic devices. Future development plans under object-oriented programming paradigm are also described. In another general-purpose work, Salvat and Quesada have calculated databases of proton-impact elastic collisions and ionizations for neutral atoms, from hydrogen (Z = 1) to einsteinium (Z = 99), using the relativistic plane-wave Born approximation including binding and Coulomb-deflection corrections. These databases were incorporated into PENH code with the aim of incorporating the transport of neutrons and include their effect on simulated dose distributions of interest in proton therapy. García-Pareja et al. present a review of the variance-reduction techniques available for radiation transport Monte Carlo codes, including combinations of several ones, as it occurs with the ant-colony method; they concluded that the ant-colony method is proved to be effective in focusing the radiation flux towards small volumes of interest, whereas interaction forcing was useful in simulations involving small probabilities for key processes in the volume of interest. Finally, Sarrut

OPEN ACCESS

Edited and reviewed by:
Cinzia Da Via,
The University of Manchester, United Kingdom

***Correspondence:**
M. A. Cortés-Giraldo
miancortes@us.es

Specialty section:
This article was submitted to Radiation Detectors and Imaging, a section of the journal Frontiers in Physics

Received: *25 February 2022*
Accepted: *09 March 2022*
Published: *14 April 2022*

Citation:
Cortés-Giraldo MA, Cucinotta FA, Guatelli S and Vlachoudis V (2022) Editorial: Challenges for Radiation Transport Modelling: Monte Carlo and Beyond. Front. Phys. 10:884140. doi: 10.3389/fphy.2022.884140

et al. presented a perspective work on the use of artificial intelligence methods for Monte Carlo simulation in medical physics and their main associated challenges; they covered the use of neural networks in various situations, such as dose estimation, dose denoising from low statistic calculations, detector modelling, and source and phase-space modeling, among others. Further, they discuss the current challenges still open in this promising field.

Microdosimetry and track-structure simulations of charged particles is the main topic of various papers, given its relevance in the radiation quality assessment in radiation therapy and radiation protection. In this context, Kyriakou et al. present the latest advances in their theoretical work on the dielectric models included in Geant4-DNA for application to electron transport, improving its capabilities from 10 eV to 1 MeV, with work in progress to extend the validity range up to 10 MeV. In another work, Baratto-Roldán et al. show the main capabilities of a code developed to calculate with Geant4-DNA various microdosimetry quantities for track segment of protons in liquid water, including the energy imparted to the site per electronic collision of the proton, a quantity needed to relate dose-average linear energy transfer (LET) with dose-mean lineal energy; due to the effect of secondary electrons, the analysis suggested the possibility of using an effective mean chord length for the relation mentioned above. The work by Kundrát et al. addresses the incorporation of track-structure calculations in macroscopic simulations, a key issue in multi-scale simulation. In this work, the authors produced with PARTRAC a database of DNA damage induced by protons and light ions up to neon below 500 MeV/u, and discussed the capabilities of the analytical formulas derived in terms of energy and LET to incorporate the biological effect into macroscopic simulations. Finally, Bianchi et al. verified the repeatability and reproducibility of a miniaturized tissue-equivalent proportional counter (mini-TEPC) by simulating the experimental conditions at the CATANA facility (Catania, Italy) with the *hadrontherapy* example of the Geant4 toolkit.

Finally, in other works Monte Carlo simulations were the cornerstone in the development of dose calculation systems in radiation therapy with protons and light ions. Grevillot et al. developed an independent dose calculation system called IDEAL, based on GATE-RTion, with the purpose of improving quality assurance of light ion beam therapy in MedAustron Ion Therapy Center (Wiener Neustadt, Austria); the benchmark against treatment planning system (TPS) calculations showed limitations arising from the pencil beam algorithm implemented in the TPS in presence of air cavities. Another Monte Carlo dose calculation engine, MonteRay, has been developed by Lysakovski et al. aiming at supporting clinical activity in proton therapy and MRI-guided therapy at the Heidelberg Ion Beam Therapy Center (HIT, Heidelberg, Germany); the engine was benchmarked against calculations with FLUKA with a remarkable agreement in various case scenarios. At the same institution, Besuglow et al. compared calculations "carried out with FLUKA" with various lateral beam profiles measured for helium ion beams with a 2D-array of liquid-filled ionization chambers with the aim of building a database for the first clinical TPS supporting raster-scanned helium ion therapy.

AUTHOR CONTRIBUTIONS

This Editorial was prepared jointly by MC-G, FC, SG and VV.

Conflict of Interest: The authors declare that the research was conducted in the absence of any commercial or financial relationships that could be construed as a potential conflict of interest.

frontiers in Physics

ORIGINAL RESEARCH
published: 11 August 2021
doi: 10.3389/fphy.2021.704760

The GATE-RTion/IDEAL Independent Dose Calculation System for Light Ion Beam Therapy

L. Grevillot[1]†, D. J. Boersma[1,2]†, H. Fuchs[1,3], M. Bolsa-Ferruz[1,3], L. Scheuchenpflug[1,4], D. Georg[3], G. Kronreif[2] and M. Stock[1]*

[1]MedAustron Ion Therapy Center, Wiener Neustadt, Austria, [2]ACMIT Gmbh, Wiener Neustadt, Austria, [3]Department of Radiation Oncology, Medical University of Vienna, Vienna, Austria, [4]Isotope Physics, Faculty of Physics, University of Vienna, Vienna, Austria

Patient specific quality assurance can be improved using an independent dose calculation system. In addition, the implementation of such a system may support light ion beam therapy facilities in reducing the needs for beam time, by substituting some of the experimental patient-specific quality assurance procedures by independent dose calculation. The GATE-RTion-based IDEAL system for light ion beam therapy was developed for this purpose. It was built in a DICOM-in, DICOM-out fashion, for easy integration into a state-of-the-art technology-based workflow for scanned ion beam therapy. This article describes the IDEAL system, followed by its clinical implementation at MedAustron for proton and carbon ion beams. Medical physics acceptance and commissioning steps are presented together with key results: for 3D proton and carbon ion reference boxes, 97% of the points agreed within 5% from the measurements. Experimental validation of stopping powers using real pig samples were between 1.8% and 3.8% for soft tissues. Finally, five clinical cases are described, i.e. two proton and three carbon ion treatments. Dosimetric benchmarking against TPS calculations are presented and discussed in details. As expected, the IDEAL software evidenced limitations arising from the pencil beam algorithm available in the TPS for carbon ions, especially in the presence of air cavities. The IDEAL system was found to satisfy the clinical requirements for independent dose calculation of scanned ion beam delivery systems and is being clinically implemented at MedAustron. The open-source code as well as the documentation was released on the OpenGATE collaboration website, thus allowing for long term maintenance and future upgrades based on a more widespread utilization.

Keywords: GATE, GEANT4, independent dose caculation, proton, carbon ion, light ion beam therapy, IDEAL, GATE-RTion

OPEN ACCESS

Edited by:
Miguel Antonio Cortés-Giraldo, Sevilla University, Spain

Reviewed by:
Daniel Sanchez-Parcerisa, Complutense University of Madrid, Spain
Stanislav Pospíšil, Czech Technical University in Prague, Czechia

***Correspondence:**
L. Grevillot
loic.grevillot@medaustron.at

†*These authors have contributed equally to this work and share first authorship*

Specialty section:
This article was submitted to Radiation Detectors and Imaging, a section of the journal Frontiers in Physics

Received: *03 May 2021*
Accepted: *14 July 2021*
Published: *11 August 2021*

Citation:
Grevillot L, Boersma DJ, Fuchs H, Bolsa-Ferruz M, Scheuchenpflug L, Georg D, Kronreif G and Stock M (2021) The GATE-RTion/IDEAL Independent Dose Calculation System for Light Ion Beam Therapy. Front. Phys. 9:704760. doi: 10.3389/fphy.2021.704760

INTRODUCTION

Light Ion Beam Therapy (LIBT) is an advanced form of radiation therapy. While proton therapy is a more widespread technology, dual particle facilities equipped with both protons and carbon ions, such as MedAustron, are only six worldwide[1]. Clinically other types of ions may be of interest, however this article focuses on the particles and technology currently available at MedAustron, which are scanned proton and carbon ion beams [1]. Scanned ion beam therapy consists in scanning

[1]https://www.ptcog.ch/index.php/facilities-in-operation.

a small pencil beam laterally in the Planning Target Volume (PTV), while sparing the surrounding Organs At Risks (OARs) as much as possible. The distal conformation of the tumor is ensured by adjusting the beam energy and hence its range into the patient for each pencil beam delivered. Treatment planning is the key process to prepare the treatment. It necessitates a 3D CT scan of the patient anatomy acquired in the treatment position. PTVs, OARs and any other necessary Region Of Interest (ROI) are then delineated in the CT images and then the treatment plan is prepared. This article addresses the specific issue of the Patient-specific Quality Assurance (PSQA) process, after the treatment planning is completed.

PSQA can either be performed via measurements or *via* Independent Dose Calculation (IDC) system. The main advantage of the measurements is to include the verification of the beam delivery workflow. However, experimental PSQA suffers several limitations: 1) measurements are usually performed in a homogeneous phantom, which is not representative of the patient anatomy, therefore potential limitations of dose computation algorithms in patient anatomy cannot be verified; 2) QA is limited to a few measurement positions; 3) the set-up is fixed in the room and does not allow to check the patient positioning workflow; 4) it requires beam time for each plan to be irradiated, thus limiting the patient throughput and treatment planning adaptation. The main draw-back of IDC-based PSQA, is to exclude the treatment delivery and patient positioning workflow verification in the room. However, in contrast to the points 1, 2, 3, and 4 mentioned previously, the IDC is performed virtually in the full 3D patient geometry, simulating the beam delivery and patient positioning independently of the Treatment Planning System (TPS) at no beam time cost. Assuming LIBT centers implement comprehensive beam delivery and in-room equipment (patient positioning and verification systems) QA programs, IDC-based PSQA is a valid measure to complement or even substitute part of the experimental PSQA. According to ICRP112 [2], on the prevention of accidental exposure from new external beam radiation therapy technology, the "Calculation of the number of MUs for each patient independently from the TPS would have avoided most of the major accidental exposures resulting from the misuse of a TPS." (where MU stands for Monitor Units). Over the last decade, several groups have been working on the development and implementation of IDC systems, mostly for scanned proton beams. Different home-made implementations have been proposed and developments were usually tailored by facility specificities [3–6]. The implementation of a Monte Carlo (MC) algorithm in an IDC system was shown to illuminate dose computation issues from analytical algorithms implemented in TPS, which would not otherwise be detected using traditional experimental PSQA [7]. However, it is generally recognized that IDC as such, i.e. the recomputation of a plan exported by the TPS using an IDC system, only allows to check TPS dose computation errors, but cannot detect beam delivery failures or data transfer corruption. For this reason, several groups have worked on the combination of IDC systems with machine steering files and/or treatment log-files [7–11]. With respect to LIBT, for ions heavier than protons, much less literature is available. Some dedicated codes are under development, either analytical [12] or MC-based [13]. An easy-to-use particle therapy platform based on FLUKA and supporting IDC functionality, biological dose calculation as well as dose-averaged LET distributions prediction for scanned proton and carbon ion beams was presented in [14]. Alternatively, GATE-RTion: a GATE/Geant4 release for clinical applications in scanned ion beam therapy [15] is available. It was validated for protons and carbon ions [5, 6, 16–19] and developed to make the bridge between researchers and clinical users in facilities equipped with scanned ion beam delivery systems. Fragmentation spectra of both FLUKA and Geant4 have been validated in the past [20] and found compatible for clinical use. More recently, it was shown that FLUKA vs. Geant4-based particle spectra resulted in RBE-weighted dose deviation of less than 1% in average in the entrance up to the end of the target region, with larger deviations in the distal fall-off and the tail of up to 3% and 5%, respectively [21].

This paper presents the GATE-RTion-based Independent DosE cAlculation system for LIBT (IDEAL). It was developed in a collaboration between the Medical University of Vienna, the Austrian Center for Medical Innovation and Technology and the MedAustron ion therapy center. First, the software architecture and implementation details are described. Second, the clinical implementation strategy as performed at MedAustron for scanned proton and carbon ion beams is presented. The result section includes a brief review of the installation, configuration and acceptance testing, followed by key medical commissioning results (beam modeling and CT calibration). Finally, five patient treatments (2 protons and 3 carbon ions) are retrospectively evaluated using IDEAL for typical indications treated at MedAustron.

MATERIALS AND METHODS

IDEAL System Description

IDEAL V1.0 was released[2] on March, 23rd, 2021, using GATE-RTion V1.0 [15] as dose engine. IDEAL was built as a wrapper around GATE-RTion, in a DICOM-in/DICOM-out fashion. The aim was that IDEAL should be easy to integrate into state-of-the-art technology, but in a vendor independent fashion, for scanned ion beam therapy facilities (**Figure 1**). TPS DICOM files are exported to IDEAL to run an IDC. IDEAL output DICOM dose files together with the TPS DICOM dose files can then be imported into any other clinical software for dose review and/or comparison.

In the following sections, the description of the most relevant features and implementation details of IDEAL are provided, however the full documentation of IDEAL is available online[3]. GATE/Geant4 [22, 23] specific features will also be briefly presented, however for full details the reader is invited to read the GATE documentation, as well as the corresponding papers cited in the upcoming sections.

Synopsis

IDEAL is designed to run on a GNU/Linux cluster in order to provide simulation results within a reasonable time (e.g. less

[2]https://github.com/OpenGATE/IDEAL.

[3]https://pyidc.readthedocs.io/en/1.0.

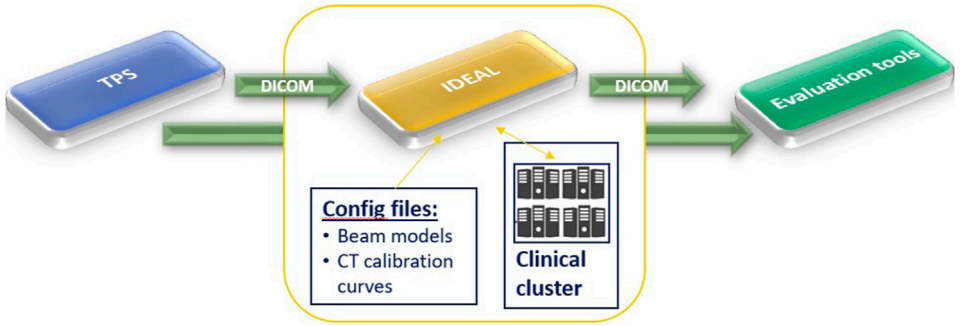

FIGURE 1 | High level workflow of IDEAL. It shows that IDEAL was conceived in a DICOM-in/DICOM-out fashion, to ease the use of GATE-RTion for IDC in LIBT.

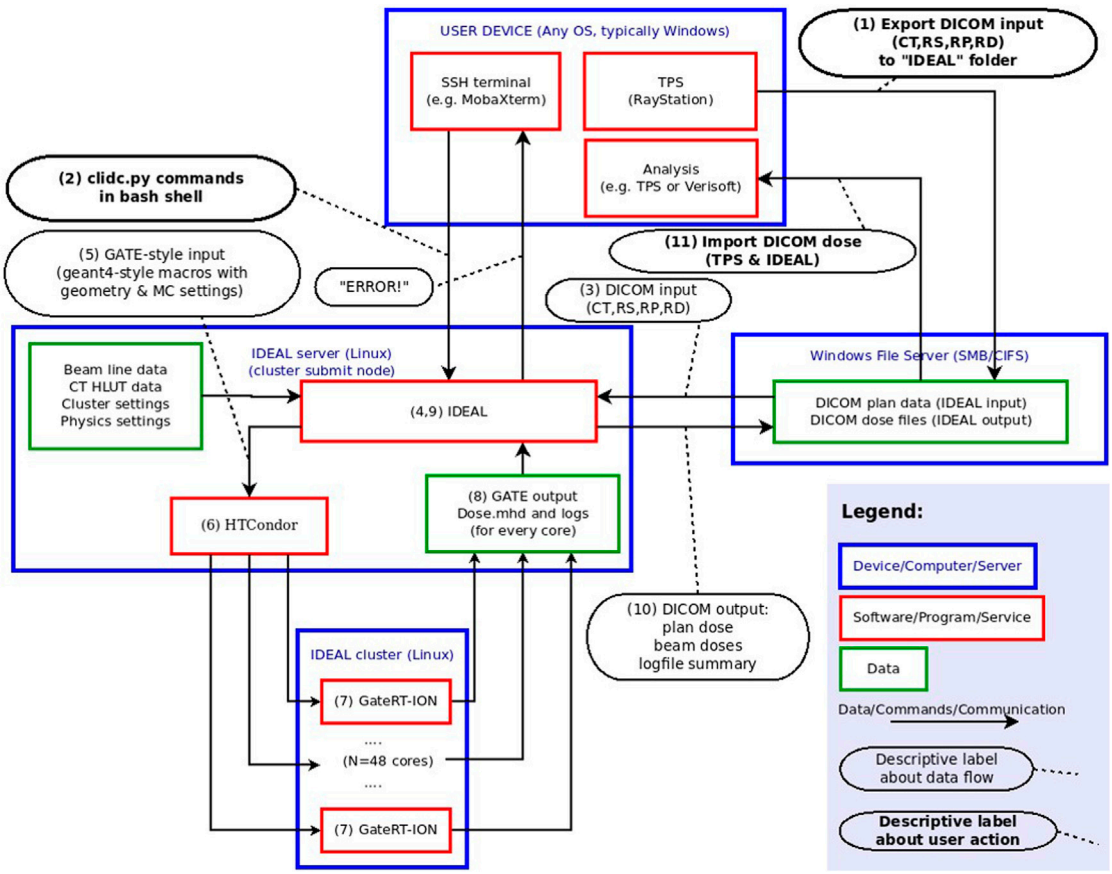

FIGURE 2 | Device-oriented workflow of IDEAL. This figure describes from a technical view-point the different modules implemented in the IDEAL software to allow for GATE-RTion-based IDC in LIBT. The numbers in parentheses are used in the text to describe the workflow in more detail.

than 2 h). IDEAL is implemented as a set of python modules and scripts, which convert the information from the input TPS DICOM files (*PLAN, DOSE, STRUCT* and *CT*) into a set of files and scripts that can be used to run GATE-RTion. Beam models, nozzle geometry and CT calibration curves must be configured during installation and commissioning. Two interfaces are available: a graphical user interface (*socrates.py*) and a command line interface (*clidc.py*). The dose grid is by default the same as used by the TPS, but a different spatial resolution can be defined by overriding the

number of voxels per dimension. Each of the beam dose distributions as well as the plan dose distributions can be stored as DICOM dose file.

Device-Oriented Workflow

A device oriented workflow is shown in **Figure 2**. In the following, the enumeration refers to the parenthesized numbers in the figure.

1) The DICOM treatment files from the TPS are exported to a shared file system, which is also mounted on the submission node of the cluster.
2) After logging into the submission node (typically with a generic secure shell utility) the user starts the independent dose calculation: the treatment plan file must be selected and a goal set (number of primaries, average uncertainty or a fixed calculation time).
3) IDEAL retrieves the plan file and all referred data (structure set, CT and TPS dose files).
4) A GATE simulation folder is populated with macros, input data, and configuration data, based on the treatment plan data and the clinic-specific configuration data (which are provided by the user during installation and commissioning). The beam model, CT calibration curve and output dose resolution are selected based on the input data, but can be overridden in the user interface.
5) Scripts are created to run an instance of GateRTion on each core of the cluster. Each beam in the input plan will be run using the HTCondor[4] job management system. E.g. for a plan with two beams and a cluster with 48 nodes, 96 jobs will run. Additional scripts are generated to perform the pre- and post-processing steps (described below).
6) The "Directed Acyclic Graph manager" (DAGman) is a meta-scheduler for HTCondor, which is used to sequentially run first the preprocessing script, then (concurrently) the simulation jobs, and finally the post-processing script. After submitting the DAGman job, a job control daemon (a daemon is a computer program that runs as a background process) is started on the submission node.
7) The simulation is configured in such a way that most of the time all cores are simulating the same beam.
8) Each job saves the intermediate dose distribution and the simulation statistics (including the number of simulated primaries). The job control daemon periodically reads the intermediate results and checks whether the goal has been reached. Once this is the case, a semaphore file is created that will cause the *StopOnScript* actor from GATE to terminate the simulation.
9) The post-processing script accumulates the results and converts them to DICOM.
10) The results are copied to the shared folder.
11) The user imports the results back into a third party system for further analysis.

[4]https://research.cs.wisc.edu/htcondor/htc.html.

Pre-processing

The external ROI of the CT (i.e. the contour describing the external contour of the "patient anatomy", including potentially boluses and contention mask, if any) is padded with a 10 mm thickness of air ("air box margin") on all six sides. This air-padding aims at improving the correctness of the skin dose calculation. The bounding box is enclosing both the padded external ROI of the CT and the TPS dose distribution. The CT image is then cropped to fit the bounding box. Any voxel whose central point is not within the external ROI is overridden with air (*G4_AIR*). Hounsfield Unit (HU) values are truncated to the maximum HU value specified in the relevant CT protocol. ROI overrides specified by the user are applied to each voxel whose central point lies within the specified ROI. The material overrides are implemented by extending a copy of the interpolated CT calibration curve: in the extension, HU values larger than the initial maximum HU value are generated and associated with the override materials. A dose mask file is created with the same geometry as the output dose files, with value 1 (or 0) for all voxels with the central point inside (or outside) the external ROI, in order to limit the dose output to within the external ROI, if specified by the user.

GATE-RTion Simulation

By convention a Gate work directory has 3 subfolders: *mac* (Gate/Geant4 macro), *data* (any input files that are not macro files) and *output* (simulation outputs). As IDEAL simulates each beam separately, there is a main macro file for each beam. Assuming a treatment plan with 3 beams running on a cluster with 50 physical cores, 150 output directories would be created. The corresponding output directories are suffixed with the job number.

Geometry: CT or Phantom

The geometry for the simulation is defined in such a way that the isocenter coincides with the origin in the Geant4 coordinate system. A *patientbox* volume is defined as the smallest rectangular box that is centered on the isocenter and contains the bounding box described earlier. The material for the *world* and *patientbox* volumes is *G4_AIR*. The cropped CT image is imported into Gate using the *ImageNestedParametrisedVolume* geometry element defined by GATE/Geant4 as a daughter volume of the *patientbox*. Using the *TranslateTheImageAtThisIsoCenter* command with the isocenter coordinates taken from the DICOM plan data, the CT image is translated with respect to the origin of the *patientbox*. The couch rotation is performed on the *patientbox*. For commissioning purposes, it can be useful to run the simulation on a geometrically defined phantom instead of a CT image. To this end, phantoms can be defined during commissioning. The planned couch angle has no effect on the positioning of such phantoms.

HU to Material Definition

For each CT protocol, 2 calibration curves are required: *HU to density* and *HU to composition*. GATE provides a *HounsfieldMaterialGenerator* tool to interpolate these 2 curves using the density tolerance parameter ([22] for more details) and generate the CT calibration input files needed for GATE. While

the initial implementation for GATE was based on the well-established Schneider method [23]; alternative calibration files could be defined. IDEAL automatically selects the CT protocol based on some criteria, which are configurable. If a CT protocol is used for the first time, the CT calibration input files are generated and saved in the *cached folder* in order to be re-used in future. Any change to the input density and composition calibration files, as well as on the density parameter, will trigger a new generation of CT calibration input files in the *cached folder*.

Beam Delivery Description

For each treatment machine (beam line), GATE macro files describing the available passive elements (range shifters, ripple filters, etc.) for that beamline are required [19]. A physical description of the nozzle geometry (beam monitors, vacuum windows, exit window, etc.) may be optionally provided. The DICOM treatment plan is converted into a *treatment plan file*, which together with the *source description file*, are used as the 2 key inputs for the *GateSourceTPSPencilBeam* to simulate the beam delivery ([24] for more details). Beam optics and energy properties from all spots in the beam are randomly sampled, with probabilities proportional to the number of planned particles per spot, and Gaussian distributions given by the *source description file*.

Physics Settings and Dose Computation

Different physics builders can be configured for protons and carbon ions. In addition, typical simulation settings (e.g.: cut, step size) can be set-up as a compromise between speed and accuracy [5]. The dose scoring is handled by the so-called *DoseActor* attached to the cropped CT image, using the *mass weighting algorithm*, which is the most accurate method available in GATE for scoring the dose [25]. Depending on the settings, the *dose to medium* or the *dose to water* are scored using the resolution of the CT [26]. Intermediate results are saved periodically during the simulation (default every 300 s) as *mhd* files. The job control daemon and post-processing script monitor and resample the intermediate dose outputs to the specified final dose output resolution.

Uncertainty Goal

The job control daemon computes an estimate of the Type A uncertainty in each resampled voxel when resampling the intermediate dose distributions. A *mean maximum* value of dose-per-primary is estimated by computing the mean of the *Ntop* (default = 100) highest values in the distribution. A threshold value is defined as a fraction *P* (default 50%) of this *mean maximum*. The *average uncertainty* is computed as the average of the relative uncertainties of those voxels having a dose-per-primary higher than this threshold.

Post-processing

IDEAL accumulates the dose distributions and total number of primaries from all simulated beams on all cluster cores and scale the dose with the ratio of the planned and simulated number of primary particles. A *dose scaling factor* can also be applied, if configured. The dose scaling factor allows for correcting systematic dose deviations observed between simulations and measurements. Finally, IDEAL resamples the beam doses to the specified resolution. For protons, the *effective dose* is computed by scaling the physical dose by a constant factor (typically 1.1). If configured, the system will also compute the plan doses (*physical* and *effective* for protons, *physical* only for carbon ions). The *user log summary* text file with settings and performance data is updated. Outputs (*beam* and *plan dose* files, *user log summary*) are copied on a Windows shared folder (if configured). The outputs from all Gate-RTion simulations are compressed and temporary copies removed.

Acceptance and Commissioning

Acceptance Testing

The clinical implementation of IDEAL was divided into several steps. An acceptance testing protocol was carried out in order to verify that the system complies with all requirements and to validate the system installation and configuration at the MedAustron ion therapy facility.

Beam Modeling

Beam modeling was carried out by modeling the full MedAustron nozzle [1], in order to have the most accurate beam models, including nuclear secondaries produced in the nozzle. The validation of the proton horizontal fixed beam line was presented in [16]. Beam modeling of the subsequent proton and carbon ion beamlines was automated using the tools and procedures described in [27]. The beam models were used as input to calibrate the MedAustron beam delivery monitors (so called Dose Delivery System) in absolute number of particles per monitor unit in reference conditions [28]. Therefore, the beam models are intrinsically calibrated in number of particles per monitor unit in reference conditions. However, due to various sources of uncertainties, calibration in reference conditions does not necessarily mean that the beam model output in 3D generated SOBP has the same accuracy. Therefore, the beam models were subsequently validated in 3D and scaling factors for proton and carbon ion beam models were defined.

Dosimetric Commissioning in Water

The beam modeling validation followed a similar procedure as for TPS commissioning in water [29], using the so called 3D-block (PTW, Freiburg, Germany), equipped with 24 PinPoint ionization chambers type 31015 (PTW, Freiburg, Germany). Dose deviations were always normalized to the maximum predicted dose. Simulation pass rates against the PinPoint measurements taken as reference were evaluated considering the 3%, 5% and 7% dose difference criteria (normalized to the maximum predicted dose). In addition, signed and unsigned mean dose deviations (again normalized to the maximum predicted dose and considering all measurement points for the corresponding treatment plan) were provided.

The proton horizontal beam model was validated in details: target of different shapes and complexity were considered (square, cylinder, H-shape etc.), using different air gaps

(at isocenter (ISD0) or at a non-isocentric reference point 50 cm upstream isocenter (ISD50) for horizontal beam lines), with or without range shifter. These treatment plans included field sizes from 3 to 20 cm, from 0.03 to 2-liter volumes and more, centered between 3 and 31 cm depth.

Based on the proton horizontal beam model validation experience, a similar procedure was applied to the carbon ion horizontal beam model, but for a restricted subset of four key reference targets: Box6_ISD0 (0.2 L), Box8_ISD0 (0.5 L) and Box10_ISD0 (1 L) at isocenter, as well Box6_ISD50_RS (0.2 L) with range shifter at non-isocentric reference position ISD50. The reference boxes 6/8/10/6_RS were centered at 6/15/25/5 cm and 6/13/21.8/5 cm, for protons and carbon ions, respectively.

Vertical beam models were only tested during acceptance testing. Except otherwise specified, simulations were run using a 2 mm scoring grid and a 1% statistical uncertainty goal. The Toolkit for the Evaluation of Dicom Doses (TEDD) developed to support the dosimetric commissioning process was described in [30].

CT Calibration and Validation

Six CT protocols are used clinically for patient treatment: three for adults and three for pediatric cases. The CT calibration was performed using slabs of tissue-equivalent materials from CIRS. The lightest tissue-like material was lung-like starting with a density of 0.195 g/cm^3 and the densest bone-like material was 2.7 g/cm^3. The exact same measurements initially used for the commissioning of the TPS were used to commission the CT curves in IDEAL. A total of eight different tissue-like materials were used. All protocols were calibrated following the stoichiometric calibration from Schneider [23]. The CT validation was performed by comparison of Water Equivalent Thickness (WET) measurements of pig tissues [31] against IDEAL and TPS simulations, using a 160-MeV proton beam. A total of 10 tissue samples (lung, adipose, brain, kidney, heart, blood, spleen, liver, muscle, bone) were inserted in an 8-cm thick phantom (in the beam direction). A CT scan of the tissue phantom was performed using 2 CT protocols (adult-abdominal and adult-head). The median HU value of each ROI for the different tissues was calculated and converted into density. For simplicity, two main ROIs were afterwards created: a cylinder of 6 cm diameter and 8 cm length in front of a 50-cm cubic box. In the TPS, the cylinder was overridden with the tissue densities and the corresponding ICRU material that are provided to represent real tissues [32]. In IDEAL, the cylinder was overridden with the Schneider material whose HU range included the calculated median HU. The densities of the chosen Schneider materials differed by 0.1% in average from the real tissue densities. The box was overridden with water.

Clinical Examples

Five clinical treatment plans were selected to evaluate the capabilities of IDEAL (**Table 1**). Two treatments with protons (patients P1 and P2) and three treatments with carbon ions (patients C1, C2, C3). The TPS used was RayStation 8B (RaySearch Laboratories, Stockholm, Sweden). Proton treatment plans were computed using the MC algorithm version 4.2, using a statistical uncertainty of 0.5%. Carbon ion treatment plans were computed using the pencil beam algorithm version 3.0. Proton treatments were always planned without ripple filters (RiFis) in non-isocentric conditions (i.e. the patient is shifted towards the nozzle), as explained in [28]. Carbon ion treatment beams were always planned with RiFis, which are a necessary accessories for carbon ion therapy [19] in isocentric condition, except when the range shifter (RS) was used in addition, in which case the patient was shifted towards the nozzle as for proton treatments. Different target volumes were simulated, from 71cc up to 1.1 L. Different treatment locations were evaluated, such as para-nasal cavities, abdomen and pelvic regions. Typically, the CT protocol for head has a slice thickness of 2 mm and the abdomen/pelvic protocols have a slice thickness of 3 mm. A combination of horizontal beams (HBL) and vertical beams (VBL) were used. All treatment plans used the so called Multiple Field Optimization Technique (MFO) as defined in Ref. [33], i.e. each beam delivered a non-homogeneous dose to the target. Different doses per fraction were applied: from 1.8 Gy per fraction up to 7.5 Gy per fraction. Treatments reporting more than one PTV indicated the usage of a so called Simultaneously Integrated Boost (SIB) technique [34], i.e. a different dose per fraction applied to the different PTVs in the same treatment plan (e.g. P1 and P2). All selected treatment plans were evaluated retrospectively. The TPS DICOM treatment plan files (Plan, Structure, CT, Physical and Effective Doses of the Plan and Beams) were exported without anonymizing the data. IDEAL was run on a cluster using a single command line (clidc.py -l “username” -u “uncertainty goal” “MyPlan.dcm”) for each patient specifying the uncertainty goal to 1% for each beam, while the CT protocol and beam models were automatically selected. After the simulations finished, the IDEAL DICOM doses were automatically saved to the Windows share folder. To prevent confusion in the clinical TPS, the treatment plan files including the IDEAL doses were imported into a test TPS for evaluation. Proton doses were evaluated in RBE-weighted dose (using a constant 1.1 RBE factor). For carbon ions, doses were evaluated in physical dose. Key clinical quantities for the target volumes ($D_{98\%}$, Mean dose, $D_{2\%}$) and organs at risks (Mean dose, $D_{2\%}$) were considered: the $D_{98\%}$ is the minimum dose received by 98% of the volume (also called near minimum dose) and the $D_{2\%}$ is the maximum dose received by 2% of the volume (also called near maximum dose). Dose Volume Histograms (DVH) were also evaluated between the TPS and IDEAL, as they represent the dose distributions as a function of the organ volumes and allow extracting clinical indicators such as $D_{98\%}$, Mean dose and $D_{2\%}$.

The IDEAL and TPS doses were also imported into VeriSoft version 7.2 (PTW, Freiburg, Germany) for computation of the gamma index in 3D. Gamma analysis was performed considering 3%/3mm and 3%/2 mm parameters, using dose difference normalized to the maximum dose and restricted to voxels

TABLE 1 | Description of the clinical treatment plans verified with IDEAL. The columns RS and RiFi indicate the presence (y)/absence (n) of range shifter and ripple filters for each of the 2 beams used for each treatment. In the column Beams, HBL and VBL indicate usage of Horizontal and Vertical Beam Lines.

Patient	Particle type	Number of beams	Resolution (mm3)	RS	RiFi	Tumor type	Location	Beams	Treatment technique	Target	Volume (cc)	Dose per fraction (Gy)	Total dose (Gy)
P1	p	2	2 × 2 × 2	n/n	n/n	Pancreas	Abdomen	HBL + VBL	MFO	PTV1	204	5	25
										PTV2	71	7.5	37.5
P2	p	2	3 × 3 × 3	y/n	n/n	Ewing sarcoma	Para-nasal	HBL + VBL	MFO	PTV1	1,135.7	1.8	50.4
										PTV2	447.3	1.93	54.04
C1	c	2	2 × 2 × 2	n/y	y/y	Angiosarcoma	Para-nasal	HBL + VBL	MFO	PTV1	465.4	4.8	43.2
C2	c	2	2 × 2 × 2	y/n	y/y	Chordoma	Sacral region	HBL + VBL	MFO	PTV1	1,047.07	4.6	41.4
C3	c	2	3 × 3 × 3	n/n	y/y	Prostate	Pelvic	HBL + VBL	MFO	PTV2	247.03	4.8	14.4

TABLE 2 | GATE-RTion/Geant4 physics settings as configured in the IDEAL implementation used at MedAustron.

—	Cut (mm)	Tracking cut (mm)	Step limiter (mm)
—	(e–/e+)	(e–/e+)	(Proton, deuteron, triton, alpha, generic ion)
World	1,000	10	1,000
Patient box	1	1	1
Patient	0.5	0.5	0.5

having a dose larger than 10% of the maximum dose. Simulation times were also recorded.

RESULTS

IDEAL Installation, Configuration and Acceptance

IDEAL was set-up on a cluster made of 1 submit node and 2 computing nodes of 24 physical cores each (48 cores in total). During acceptance, more than 60 tests were successfully conducted, on the functionalities, performances and accuracy of the system. The most relevant IDEAL configuration parameters were presented earlier and the selected settings for the implementation at MedAustron are briefly listed here: the same scoring resolution as the input TPS dose files was used and the dose outside the external ROI was removed. The CT protocol was automatically selected based on the *SeriesDescription* DICOM tag and the *density tolerance* was set to 0.01 g cm^{-3}. A full geometrical description of the nozzle was provided for each beam line, together with beam models (*source description file*) for proton and carbon ion beams. The options *dose to water*, *effective dose* using a 1.1 RBE factor (for protons only) and *plan dose* were selected. The default N_{top} (100) and p (50%) values were used. Dose scaling factors were defined during commissioning and configured. The GATE-RTion recommended proton and carbon ion physics-builder were used [15], namely QGSP_BIC_HP_EMZ and Shielding_EMZ. *Cut*, *tracking cut* and *step-limiter* values were set as presented in **Table 2**, following recommendations from the literature [5, 35], as a compromise between speed and accuracy. Further relevant details on the CT calibration and beam modeling details are provided in the following sections.

Commissioning Results

Beam Modeling Accuracy in 1D/2D

Beam ranges for protons and carbon ions simulated using GATE-RTion/IDEAL agreed very well with measured ranges in water with differences of less than 0.2 mm. Bragg peak width estimated at the 80% dose level were within 0.3 mm. Simulated beam sizes in air agreed nicely with measured data, with maximum deviation of less than 0.3 mm (in FWHM) at all measured positions in the beam path from nozzle exit until 20 cm after the treatment isocenter. At isocenter deviations were even lower, with maximum deviations of 0.2 mm. Overall agreement in range and beam optics were found to be close to the measurement uncertainties.

Beam Modeling Validation in 3D

In total for 3D validation, more than 34 proton treatment plans and 4.000 measurement points were evaluated. For carbon ions, the 4 key reference plans and more than 565 measurement points were considered. Scaling factors of 0.97 and 1.03 were applied to the proton and carbon ion beam models based on the review of the four reference boxes. The need for scaling factors may be due to a combination of dosimetric uncertainties and nuclear model uncertainties. All results presented in this section consider these two scaling factors. The overview of all 3D commissioning results is summarized in **Table 3**. The lower agreement considering the 3% dose difference criteria for carbon ions, as compared to protons, can be understood when looking at the results for the reference boxes in **Table 4**. One can see a dose output variation with energy as a function of the measurement depth for carbon ions, with an under-

TABLE 3 | 3D validation overview for protons and carbon ions in terms of pass-rates (considering dose difference criteria of 3%, 5% and 7%) and average dose deviations.

Particle type	Measurement points	Pass-rate(%)			Averaged dose deviation(%)	
		3%	5%	7%	Signed	Unsigned
p	4,079	96.5	99.4	99.8	0.5	1.0
c	565	90.5	98.8	99.4	−0.5	1.3

TABLE 4 | 3D validation results for the reference boxes in terms of pass-rates (considering dose difference criteria of 3%, 5% and 7%) and average dose deviations.

Reference plan	Particle type	Measurement points	Pass-rate(%)			Averaged dose deviation(%)	
			3%	5%	7%	Signed	Unsigned
Box6_ISD0	c	134	97.8	100.0	100.0	0.8	1.1
Box8_ISD0	c	181	97.8	98.9	100.0	−0.7	0.9
Box10_ISD0	c	132	69.7	97.0	98.5	−2.1	2.3
Box6_ISD50_RS	c	118	96.6	99.2	99.2	0.2	0.9
Box6_ISD0	p	196	99.0	100.0	100.0	0.3	0.8
Box8_ISD0	p	484	96.7	99.6	100.0	0.7	1.0
Box10_ISD0	p	268	100.0	100.0	100.0	0.2	0.8
Box6_ISD50_RS	p	132	99.2	100.0	100.0	0.9	1.0

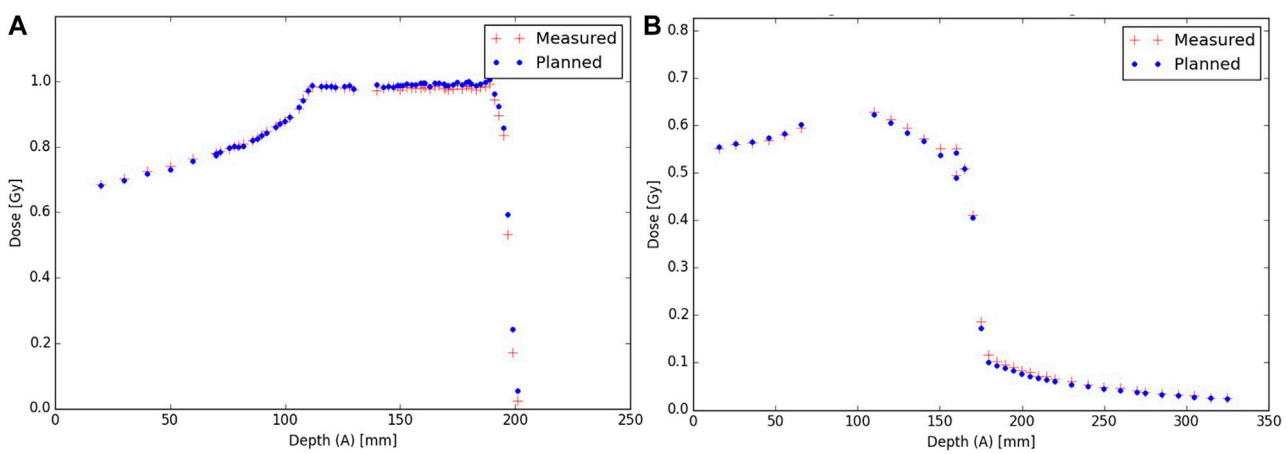

FIGURE 3 | Evaluation of IDEAL Box8 for protons **(A)** and carbon ions **(B)** against measurements.

estimation of the dose in average of −2.1% for the deep seated box10, while the shallow box6 presents an overestimation of the dose by 0.8%. Overall, for both protons and carbon ions, the use of range shifter and different air gaps (ISD0 and ISD50) did not indicate any systematic deviation in the beam modeling results. The results presented are within clinical tolerances. The evaluation of the SOBP for the Box8 for both protons and carbon ions is illustrated in **Figure 3**.

CT Calibration and Validation

The differences between the measured WET and each of the two simulated WET (using TPS and GATE-RTion/IDEAL) as a function of the tissue density is presented in **Figure 4**. For densities between 0.93 and 1.08 g cm^{-3}, IDEAL overestimates the WET up to 3.8%. The WET calculated in the TPS presented a 1.2% better agreement with the measured WET in average. For low and high density materials, this tendency is not observed. A larger difference was found for both tissue groups with a maximum difference of 11% (bones/TPS) and 8.7% (bones/IDEAL). A difference up to 9.5% and 8.7% was found for lung/TPS and lung/IDEAL, respectively.

Evaluation of Clinical Cases With IDEAL

The evaluation of the 5 clinical treatment plans is summarized in **Table 5**. Gamma pass rate was higher than 97% for all plans considering the 3%/3 mm gamma parameters. Considering the 3%/2 mm gamma parameters, pass rate was higher than 95% for 3 patients and only slightly

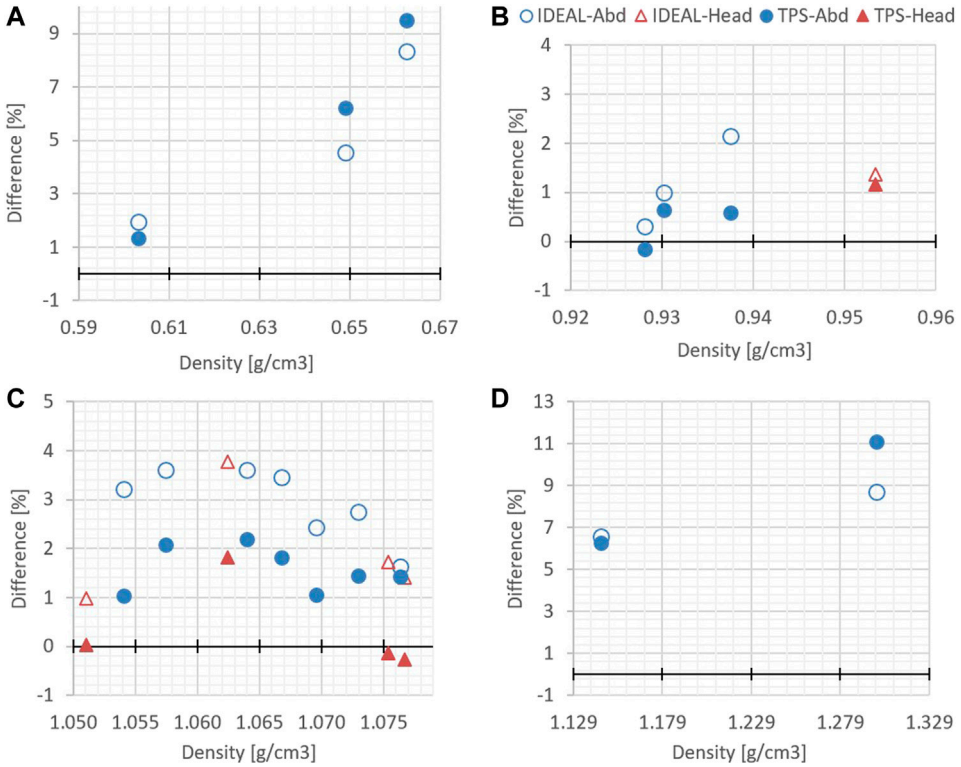

FIGURE 4 | Differences between simulated WET (TPS and GATE-RTion/IDEAL) and measured WET, as a function of the tissue density. **(A)** corresponds to the lung region, **(B)** and **(C)** to the soft tissues regions and **(D)** to the bone region.

lower for P2 and C1. With respect to PTVs and OARs, mean doses and near maximum doses ($D_{2\%}$) parameter were in excellent agreement, within a few tenths of Gy. The near minimum doses ($D_{98\%}$) to the PTVs were also in excellent agreement for most plans, except for P2 which presented differences of 1.3 and 2 Gy for PTV2 and PTV1, respectively. This can be explained by the fact that a non-negligible part of the PTV overlaps with the lung, where the dose uncertainty is larger. An illustration of dose differences and dose profiles in that patient are presented in **Figure 5**. With respect to patient C1, differences were mostly related to the air cavities and the interface with dense bone. As the TPS features a pencil beam algorithm, one can expect MC to better perform in such a case. This fact is illustrated in **Figure 6**, where large differences in dose were observed in an air cavity, followed by a large range difference of up to 4 mm (yellow dose profile, **Figure 6**). In contrast, not going through any air cavity depicts an excellent agreement between the two dose engines (blue dose profile, **Figure 6**). To complete the evaluation, patient P1, for which gamma analysis was larger than 99% is presented in **Figure 7**. Dose differences within the target and plateau region were low. However, differences occur around the target, due to range differences between GATE-RTion/IDEAL and the TPS, where the horizontal and the vertical beams stop (**Figure 7**, bottom right). Agreement in terms of DVH was excellent (**Figure 7**, top right). Simulation times were varying significantly between protons and carbon ions and are discussed in the next section.

DISCUSSION

Simulation times were presented in **Table 5**. Patient P2 and C2, both have a tumor volume slightly larger than 1 L. While the proton simulation result was obtained in 1.3 h, the carbon ion simulation took 32.7 h using the current cluster capacity of 48 cores. The reasons for larger computation times with carbon ions are partly due to the production and tracking of nuclear secondaries, which stop after the primary carbon ion range and produce the dose tail after the carbon ion Bragg peak. In addition, simulation speed may be significantly influenced by the nuclear models selected in Geant4. The QMD model selected in this study is assumed to be the most accurate, however it was shown that its computation speed can be at least a factor 2 to 3 slower, than other standard models such as BIC [36]. For daily clinical use, simulation times of the order of 1–2 h maximum are desirable. In the context of this study, we recomputed patient C2, using a scoring grid of 3 mm (which for the pelvic region is clinically acceptable) and considered a statistical uncertainty of 2%, which reduced the computation time to 4.3 h. The gamma pass rates at 3%/3mm and 2%/2 mm were 97.8 and 94.4%,

TABLE 5 | Comparison of IDEAL simulations with TPS. Key clinical quantities for the target volumes ($D_{98\%}$, Mean dose, $D_{2\%}$) and organs at risks (Mean dose, $D_{2\%}$) are considered, as well as simulation times and gamma index pass-rates.

Patient	Dose engine	Target				OARs			Simulation		Gamma index pass-rate	
		Name	$D_{98\%}$	Mean	$D_{2\%}$	Name	Mean (Gy)	D2 (Gy)	Primaries	Time (hrs)	3%/3 mm (%)	3%/2 mm (%)
P1	IDEAL	PTV1	15.3	29.2	40.0	Liver	1.7	14.7	1.9E + 07	0.9	99.8	99
	TPS		15.7	29.3	39.7		1.7	14.8	—	—	—	—
	IDEAL	PTV2	28.9	36.7	41.0		—	—				
	TPS		29.2	36.8	40.8							
P2	IDEAL	PTV1	34.8	50.2	56.3	Spinal cord	16.5	50.3	3.4E + 07	1.3	98.3	94.7
	TPS		36.8	50.5	56.0		16.2	49.7	—	—	—	—
	IDEAL	PTV2	46.9	53.6	57.0	Lungs	7.8	50.9				
	TPS		48.2	53.8	56.7		8.0	51.7				
C1	IDEAL	PTV1	2.3	9.1	10.9	Optics nerve right	8.1	9.6	4.5E + 07	29.4	97.4	94.3
	TPS		2.2	9.2	10.9		8.1	9.7	—	—	—	—
	IDEAL		—	—	—	Cochlea right	4.3	5.9				
	TPS						4.2	5.6				
	IDEAL					Bulbus right	5.6	8.4				
	TPS						5.5	8.2				
C2	IDEAL	PTV1	13.0	16.4	18.3	Rectum	4.0	12.1	4.6E + 07	32.7	98.9	96.6
	TPS		13.3	16.7	18.6		4.2	12.3	—	—	—	—
	IDEAL		—	—	—	Nerve roots	11.5	16.7				
	TPS						11.6	17.0				
	IDEAL					Cauda equina	11.1	17.2				
	TPS						11.1	17.5				
C3	IDEAL	PTV2	3.4	4.9	5.3	Rectum	0.5	3.2	9.2E + 06	17.7	98.8	97.5
	TPS		3.5	5.0	5.4		0.5	3.4	—	—	—	—
	IDEAL		—	—	—	Bladder	0.8	4.9				
	TPS						0.8	5.0				
	IDEAL					Urethra	3.3	4.7				
	TPS						3.4	4.9				

respectively, which is logically lower than the 98.8 and 96.6% pass rates from the reference simulation (with 2 mm scoring grid and 1% statistical uncertainty). Increasing the gamma criteria (for the 3 mm resolution and 2% uncertainty simulation) to 4%/3 mm and 4%/2 mm provided gamma pass rates of 99.1 and 97.5%, respectively. It seems therefore clinically acceptable to adapt the dose grid and simulation uncertainty requirement, if needed, in order to reduce computation time to clinically acceptable values. Increasing the cluster capacity by a factor 2, would bring the computation time down to the order of 2 h in such a case. In addition and as mentioned earlier, using alternative and faster nuclear models such as BIC could be an option, but commissioning should be repeated.

The IDC concept was already recommended and implemented as a routine QA tool in conventional radiotherapy in the last century. Unfortunately, the traditional empirical dose calculation models were of very limited applicability for advanced treatment techniques, such as Intensity Modulated Radiation Therapy (IMRT). Experimental methods were therefore implemented for PSQA, thus substituting IDC for complex treatment techniques. As the number of patients treated with advanced radiotherapy techniques steadily increased over the years, experimental PSQA resulted in a significantly increased workload. In 2010, ESTRO published a booklet on "Independent Dose Calculations Concepts and Models" [37]. At that time, one key limitation of both types of QA (experimental and IDC), was that verification was performed in a homogeneous phantom and not in the patient geometry. Nevertheless, it was already suggested that IDC could be used to replace experimental PSQA [38, 39]. Development of dose calculation algorithms over the years made IDC the only possibility to perform QA in the patient geometry. Nowadays, it seems that the radiation therapy community in general (including both conventional and LIBT), is moving back to the roots of PSQA using IDC, rather than experimental PSQA [40]. In the framework of the Imaging and Radiation Oncology Core (IROC) [41], it was demonstrated that IDC was 12 times more sensitive at detecting treatment failures for IMRT than experimental PSQA. The commissioning of the first commercial IDC system for CyberKnife and based on a MC algorithm was reported in [42]. The main conclusion stated that this IDC system will replace all routine experimental PSQA. One motivation from the authors is related to the complexity of the measurements and as for the previous study, a lack of sensitivity of the experimental PSQA, which is limited to the beam delivery and therefore could be replaced by an appropriate machine QA program. For protons, the first commercial and MC-based IDC system, called myQA iON (IBA-dosimetry, Schwarzenbruck, Germany), was recently commissioned

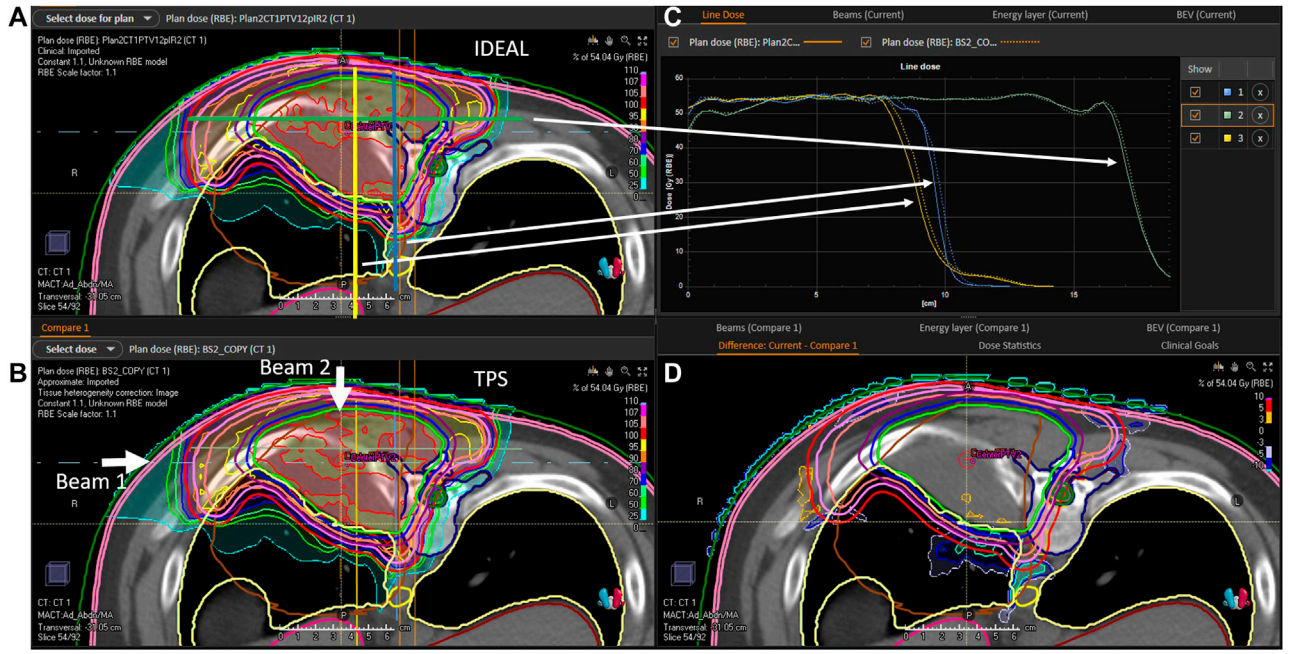

FIGURE 5 | P2 evaluation. **(A)**: 2D IDEAL dose distribution in a CT slice (transversal view), **(B)**: 2D TPS dose distribution in a CT slice (transversal view), **(C)**: 1D dose profiles extracted from the 2D IDEAL and TPS dose distributions presented on the **(A,B)** (full line = IDEAL, dotted line = TPS), **(D)**: 2D dose difference in a CT slice extracted from the 2D IDEAL and TPS dose distributions presented on the **(A,B)** (IDEAL—TPS). Beam directions are represented on the **(B)** picture. On the **(A)** blue yellow and green lines represent the dose profiles presented on the **(C)**.

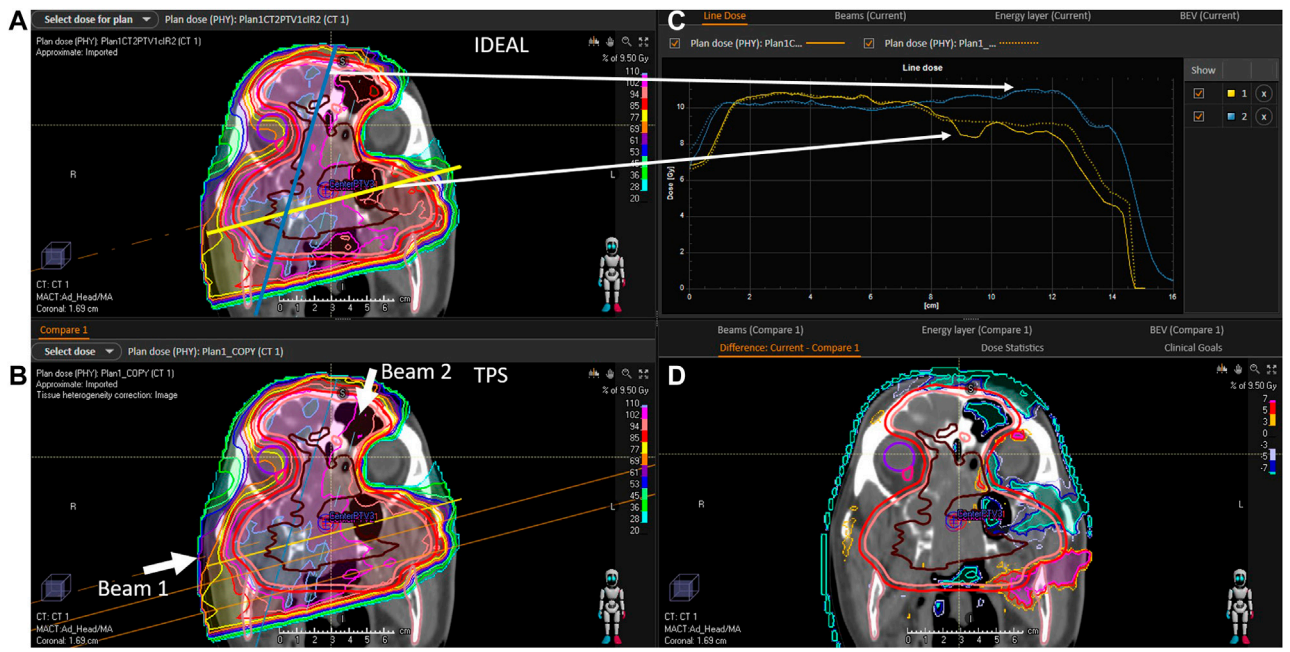

FIGURE 6 | C1 evaluation **(A)**: 2D IDEAL dose distribution in a CT slice (coronal view), **(B)**: 2D TPS dose distribution in a CT slice (coronal view), **(C)**: 1D dose profiles extracted from the 2D IDEAL and TPS dose distributions presented on the **(A,B)** (full line = IDEAL, dotted line = TPS), **(D)**: 2D dose difference in a CT slice extracted from the 2D IDEAL and TPS dose distributions presented on the **(A,B)** (IDEAL—TPS). Beam directions are represented on the **(B)** picture. On the **(A)** blue and yellow lines represent the dose profiles presented on the **(C)**.

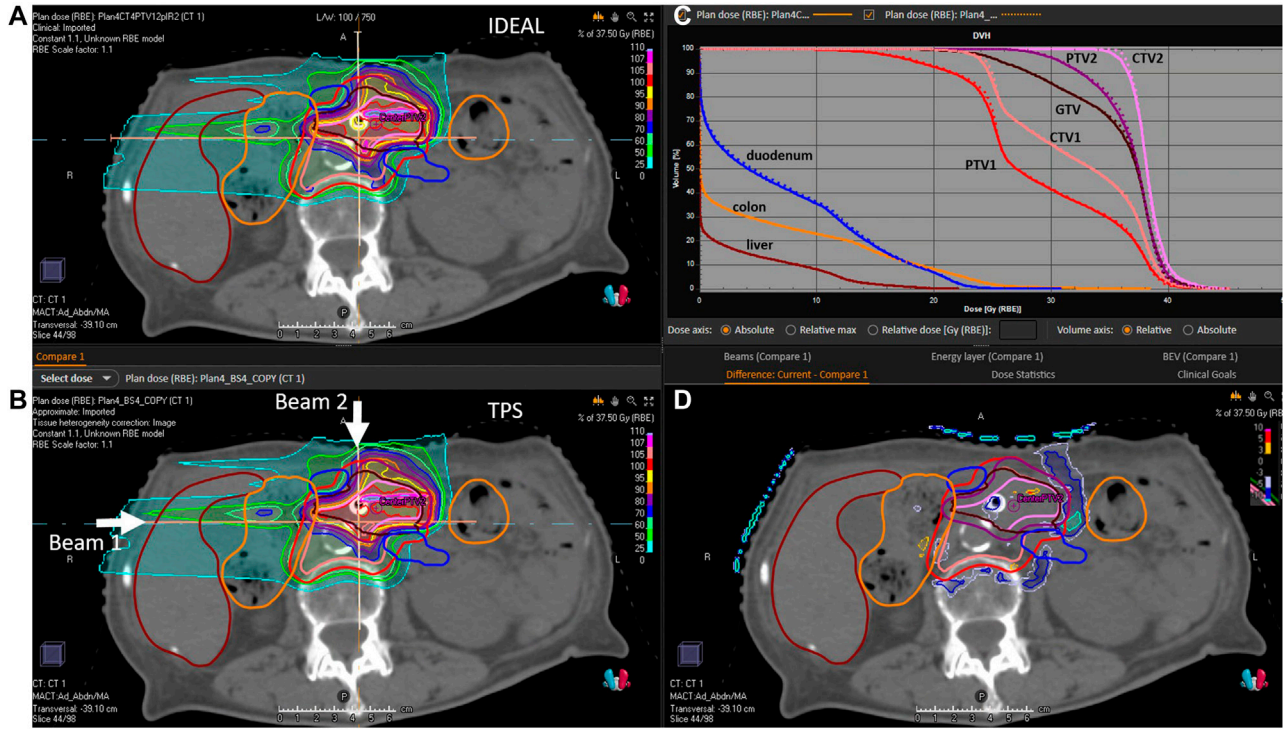

FIGURE 7 | P1 evaluation. **(A)**: 2D IDEAL dose distribution in a CT slice (transversal view), **(B)**: 2D TPS dose distribution in a CT slice (transversal view), **(C)**: 1D dose volume histograms extracted from the 3D IDEAL and TPS dose distributions (full line = IDEAL, dotted line = TPS), **(D)**: 2D dose difference in a CT slice extracted from the 2D IDEAL and TPS dose distributions presented on the **(A,B)** (IDEAL−TPS). Beam directions are represented on the **(B)** picture.

and implemented clinically at the MedAustron ion therapy facility. Experimental PSQA was reduced by 25% and it will increase step-wise up to 50% on average by the end of 2021.

The substitution of experimental PSQA by IDC allows for further improvements of the QA process, for instance by combining IDC with treatment log-files. The use of treatment log files allows in theory verifying machine delivery parameters for any treatment fraction, thus overcoming the capabilities of experimental PSQA, which is limited to a single fraction delivered to a QA phantom prior treatment. Integrating log-files as inputs to an IDC system was shown to be much more sensitive in detecting proton delivery errors, than experimental PSQA. Indeed, out of 21 error scenarios tested, 11 were detected by IDC and only 1 by PSQA [9]. Log-file-based QA is suggested as a potential improvement to bridge the gap between machine QA, PSQA and daily patient treatment [7, 42]. Artifical Intelligence may also play a role in future to support, for instance, the prediction of possible PSQA failures [43].

In the context of adaptive radiotherapy, the aim is to shorten the cycle between image generation, contouring, plan adaptation and treatment. Hence, it is very important to be able to quickly recompute the dose into the daily patient anatomy. The development of fast IDC systems and further optimized QA is a necessity for such applications. IDC tolerance levels should be related to Tumor Control Probability (TCP) and Normal Tissue Complication Probability (NTCP) [37]. A first attempt in this direction was provided in [11], but with another initial purpose in the framework of Model-Based approaches, to confirm the decision-making process for patient selection, when NTCP models are used as a basis. If NTCP models are not available (or not calibrated for the clinics), the review of DVHs and clinical goals is actually a practical alternative to evaluate IDC-based PSQA outcome in a more clinically relevant manner.

In the context of LIBT, including particles others than protons (e.g. carbon ions), no commercial system is currently available. Currently, the only commercial TPS available is RayStation (RaySearch Laboratories, Stockholm, Sweden). For carbon ions, the pencil beam algorithm developments of RayStation were largely based on pre-calculations performed using the FLUKA MC code. In this respect, IDEAL represents an interesting solution for MC-based IDC, as it is based on GATE-RTion and the Geant4 [15, 44, 45] physics models. For the purpose of replacing experimental PSQA by IDC-based PSQA, evaluating the physical dose distribution in the patient may be sufficient. For protons, a fixed 1.1 RBE value may be used. However, variable proton RBE values were suggested, as there is evidence of increased RBE towards the end of the Bragg peak [46]. For carbon ions, several RBE models are available, but the uncertainties of these models are rather large [47, 48]. The implementation of various RBE models for the purpose of proton and carbon ion IDC may support research projects. For the clinical purpose of independently evaluating the TPS dose computation, very similar RBE models should be implemented in the IDC tool and in the TPS, otherwise large discrepancies between

the two dose engines would be observed due to the RBE models uncertainty, thus making the clinical evaluation very difficult.

In this work, the GATE-RTion/IDEAL software version 1.0 was presented and the clinical implementation methodology was described in detail. IDEAL was applied retrospectively for 5 clinical treatments and was found to successfully perform IDC in the field of LIBT for scanned proton and carbon ion beams. Thanks to its DICOM-in/DICOM-out design fashion, IDEAL was easily compatible with state-of-the-art technology, thus allowing for dose review and comparison in different medical Software. IDEAL is provided open-source and is maintained by the OpenGATE community. It will therefore benefit of further upgrades tailored by medical and research needs in future.

DATA AVAILABILITY STATEMENT

The raw data supporting the conclusion of this article will be made available by the authors, without undue reservation.

AUTHOR CONTRIBUTIONS

LG is the lead author. He coordinated the project work and was in charge of the carbon ion commissioning and clinical examples. DB is the second lead author in equal contribution with LG, as he was the main developer of IDEAL. HF was in charge of acceptance testing and beam modelling. MB-F was in charge of the commissioning the HU curves. LS was in charge of proton commissioning. DG was the project coordinator from MUW. GK was the project coordinator from ACMIT. MS was the project coordinator from MedAustron.

FUNDING

The financial support from ACMIT Gmbh, Medical University of Vienna and MedAustron is gratefully acknowledged. The competence center ACMIT is funded within the scope of the COMET program (Competence Centers for Excellent Technologies) by Austrian ministries BMK and BMDW, and by the governments of Lower Austria and Tyrol. The competence center program COMET is managed by the Austrian Funding Agency FFG.

ACKNOWLEDGMENTS

Joanna Gora and Antonio Carlino from MedAustron are gratefully acknowledged for providing support in IDEAL CT calibration validation and dosimetric commissioning, respectively. Alessio Elia is gratefully acknowledged for fruitful discussions on GATE Monte Carlo simulations and proton IDC. Ruben Gonzalo Gleyzes is deeply acknowledged for his continuous support on the development of the TEDD toolkit.

REFERENCES

1. Stock M, Georg D, Ableitinger A, Zechner A, Utz A, Mumot M, et al. The Technological Basis for Adaptive Ion Beam Therapy at MedAustron: Status and Outlook. *Z für Medizinische Physik* (2018) 28(3):196–210. doi:10.1016/j.zemedi.2017.09.007
2. Ortiz López P, Cosset JM, Dunscombe P, Holmberg O, Rosenwald JC, Pinillos Ashton L, et al. ICRP Publication 112. A Report of Preventing Accidental Exposures from New External Beam Radiation Therapy Technologies. *Ann ICRP 112* (2009) 39(4):1–86. doi:10.1016/j.icrp.2010.02.002
3. Mackin D, Li Y, Taylor MB, Kerr M, Holmes C, Sahoo N, et al. Improving Spot-Scanning Proton Therapy Patient Specific Quality Assurance with HPlusQA, a Second-Check Dose Calculation Engine. *Med Phys* (2013) 40(12):121708. doi:10.1118/1.4828775 Available from: http://www.ncbi.nlm.nih.gov/pubmed/24320494.
4. Fracchiolla F, Lorentini S, Widesott L, and Schwarz M. Characterization and Validation of a Monte Carlo Code for Independent Dose Calculation in Proton Therapy Treatments with Pencil Beam Scanning. *Phys Med Biol* (2015) 60(21):8601–19. doi:10.1088/0031-9155/60/21/8601
5. Winterhalter C, Taylor M, Boersma D, Elia A, Guatelli S, Mackay R, et al. Evaluation of GATE-RTion (GATE/Geant4) Monte Carlo Simulation Settings for Proton Pencil Beam Scanning Quality Assurance. *Med Phys* (2020) 47(11):5817–5828. doi:10.1002/mp.14481
6. Aitkenhead A, Sitch P, Jenny R, Winterhalter C, Patel I, and Ranald M. Automated Monte-Carlo Re-calculation of Proton Therapy Plans Using Geant4/Gate: Implementation and Comparison to Plan-specific Quality Assurance Measurements. *Br J Radiol* (2020) 93(1114):20200228. doi:10.1259/bjr.20200228
7. Johnson JE, Beltran C, Wan Chan Tseung H, Mundy DW, Kruse JJ, Whitaker TJ, et al. Highly Efficient and Sensitive Patient-specific Quality Assurance for Spot-Scanned Proton Therapy. *PLoS One* (2019) 14(2):e0212412. doi:10.1371/journal.pone.0212412
8. Meier G, Besson R, Nanz A, Safai S, and Lomax AJ. Independent Dose Calculations for Commissioning, Quality Assurance and Dose Reconstruction of PBS Proton Therapy. *Phys Med Biol* (2015) 60(7):2819–36. Available from. doi:10.1088/0031-9155/60/7/2819
9. Matter M, Nenoff L, Meier G, Weber DC, Lomax AJ, and Albertini F. Alternatives to Patient Specific Verification Measurements in Proton Therapy: a Comparative Experimental Study with Intentional Errors. *Phys Med Biol* (2018) 63(20):205014. doi:10.1088/1361-6560/aae2f4
10. Guterres Marmitt G, Pin A, Ng Wei Siang K, Janssens G, Souris K, Cohilis M, et al. Platform for Automatic Patient Quality Assurance via Monte Carlo Simulations in Proton Therapy. *Physica Med* (2020) 70 (September):49–57. Available from. doi:10.1016/j.ejmp.2019.12.018
11. Meijers A, Guterres Marmitt G, Ng Wei Siang K, van der Schaaf A, Knopf AC, Langendijk JA, et al. Feasibility of Patient Specific Quality Assurance for Proton Therapy Based on Independent Dose Calculation and Predicted Outcomes. *Radiother Oncol* (2020) 150:136–41. Available from:. doi:10.1016/j.radonc.2020.06.027
12. Mein S, Choi K, Kopp B, Tessonnier T, Bauer J, Ferrari A, et al. Fast Robust Dose Calculation on GPU for High-Precision 1H, 4He, 12C and 16O Ion Therapy: the FRoG Platform. *Sci Rep* (2018) 8(1):1–12. doi:10.1038/s41598-018-33194-4
13. Schiavi A, Senzacqua M, Pioli S, Mairani A, Magro G, Molinelli S, et al. Fred: A GPU-Accelerated Fast-Monte Carlo Code for Rapid Treatment Plan Recalculation in Ion Beam Therapy. *Phys Med Biol* (2017) 62(18):7482–504. doi:10.1088/1361-6560/aa8134
14. Kozłowska WS, Böhlen TT, Cuccagna C, Ferrari A, Fracchiolla F, Magro G, et al. FLUKA Particle Therapy Tool for Monte Carlo Independent Calculation of Scanned Proton and Carbon Ion Beam Therapy. *Phys Med Biol* (2019) 64(7):075012. doi:10.1088/1361-6560/ab02cb
15. Grevillot L, Boersma DJ, Fuchs H, Aitkenhead A, Elia A, Bolsa M, et al. Technical Note: GATE-RTion: a GATE/Geant4 Release for Clinical Applications in Scanned Ion Beam Therapy. *Med Phys* (2020) 47(8):3675–81. doi:10.1002/mp.14242

16. Elia A, Resch AF, Carlino A, Böhlen TT, Fuchs H, Palmans H, et al. A GATE/Geant4 Beam Model for the MedAustron Non-isocentric Proton Treatment Plans Quality Assurance. *Physica Med* (2020) 71:115–23. Available from. doi:10.1016/j.ejmp.2020.02.006–
17. Grevillot L, Boersma D, Gleyzes RG, Scheuchenpflug L, Carlino A, Elia A, et al. OC-0217: Commissioning of IDEAL/GATE-RTion for Proton and Carbon Ion Independent Dose Calculation (IDC). In: ESTRO 2020 (2020). [Internet]. Available from: https://www.estro.org/Congresses/ESTRO-2020/197/profferedpapers11-dosecalculationforadvancedtechni/160/commissioningofideal-gate-rtionforprotonandcarboni
18. Fuchs H, Vatnitsky S, Stock M, Georg D, and Grevillot L. Evaluation of GATE/Geant4 Multiple Coulomb Scattering Algorithms for a 160 MeV Proton Beam. *Nucl Instr Methods Phys Res Sect B Beam Interact Mater Atoms* (2017) 410:122–126. doi:10.1016/j.nimb.2017.08.006
19. Grevillot L, Stock M, and Vatnitsky S Evaluation of Beam Delivery and Ripple Filter Design for Non-isocentric Proton and Carbon Ion Therapy. *Phys Med Biol* (2015) 60(20):7985–8005. Available from: http://www.ncbi.nlm.nih.gov/pubmed/26418366. doi:10.1088/0031-9155/60/20/7985
20. Böhlen TT, Cerutti F, Dosanjh M, Ferrari A, Gudowska I, Mairani A, et al. Benchmarking Nuclear Models of FLUKA and GEANT4 for Carbon Ion Therapy. *Phys Med Biol* (2010) 55(19):5833–47. Available from. doi:10.1088/0031-9155/55/19/014
21. Resch A, Lackner N, Niessen T, Engdahl S, Elia A, Boersma D, et al. Impact of Beamline-specific Particle Energy Spectra on Clinical Plans in Carbon Ion Beam Therapy. In: ESTRO Conference, 39 (2020). p. OC-0577.
22. Grevillot L, Bertrand D, Dessy F, Freud N, and Sarrut D GATE as a GEANT4-Based Monte Carlo Platform for the Evaluation of Proton Pencil Beam Scanning Treatment Plans. *Phys Med Biol* (2012) 57(13):4223–44. Available from: http://www.ncbi.nlm.nih.gov/pubmed/22684098. doi:10.1088/0031-9155/57/13/4223
23. Schneider W, Bortfeld T, and Schlegel W. Correlation between CT Numbers and Tissue Parameters Needed for Monte Carlo Simulations of Clinical Dose Distributions. *Phys Med Biol* (2000) 45(2):459–78. doi:10.1088/0031-9155/45/2/314
24. Grevillot L, Bertrand D, Dessy F, Freud N, and Sarrut D. A Monte Carlo Pencil Beam Scanning Model for Proton Treatment Plan Simulation Using GATE/GEANT4. *Phys Med Biol* (2011) 56(16):5203–19. doi:10.1088/0031-9155/56/16/008 Available from: http://www.ncbi.nlm.nih.gov/pubmed/21791731.
25. Deschler T, Arbor N, Carbillet F, and Nourreddine A. Dose Calculations in Heterogeneous Volumes with the GATE Monte Carlo Software for Radiological protection. *Radioprotection* (2019) 54(2):125–32. doi:10.1051/radiopro/2019014
26. Paganetti H. Dose to Water versus Dose to Medium in Proton Beam Therapy. *Phys Med Biol* (2009) 54(14):4399–421. Available from:. doi:10.1088/0031-9155/54/14/004
27. Fuchs H, Elia A, Resch AF, Kuess P, Lühr A, Vidal M, et al. Computer-assisted Beam Modeling for Particle Therapy. *Med Phys* (2020) 48(2):841–51. doi:10.1002/mp.14647
28. Grevillot L, Osorio Moreno J, Letellier V, Dreindl R, Elia A, Fuchs H, et al. Clinical Implementation and Commissioning of the MedAustron Particle Therapy Accelerator for Non-isocentric Scanned Proton Beam Treatments. *Med Phys* (2019) 1–13. doi:10.1002/mp.13928
29. Carlino A, Böhlen T, Vatnitsky S, Grevillot L, Osorio J, Dreindl R, et al. Commissioning of Pencil Beam and Monte Carlo Dose Engines for Non-isocentric Treatments in Scanned Proton Beam Therapy. *Phys Med Biol* (2019) 64(17):17NT01. doi:10.1088/1361-6560/ab3557
30. Scheuchenpflug L "*Development of a Commissioning Tool for the Independent Dose Calculation Software IDEAL for the Patient Specific Quality Assurance at MedAustron.* "Vienna: University of Vienna (2020). MASTER'S THESIS.
31. Góra J, Kragl G, Vatnitsky S, Böhlen TT, Teichmeister M, and Stock M. Validation of the CT Number to Mass Density Conversion Curve for Proton Dose Calculation: Proton Range Measurements in Animal Tissues. In: ESTRO Conference 36. Vienna, Austria (2017).
32. White DR, Booz J, Griffith RV, Spokas JJ, and Wilson IJ *ICRU Report 44, the Composition of Body Tissues*. [Internet]. Reports Int Comm Radiat Units Meas (1989). Available from: https://academic.oup.com/jicru/issue/16/1-2.
33. Das IJ, and Paganetti H. *Principles and Practice of Proton Beam Therapy*. Colorado Springs: AAPM Monograph, 2015 Summer School (2015).
34. Zhu XR, Poenisch F, Li H, Zhang X, Sahoo N, Wu RY, et al. A Single-Field Integrated Boost Treatment Planning Technique for Spot Scanning Proton Therapy. *Radiat Oncol* (2014) 9(1):1–12. doi:10.1186/1748-717x-9-202
35. Grevillot L, Frisson T, Zahra N, Bertrand D, Stichelbaut F, Freud N, et al. Optimization of GEANT4 Settings for Proton Pencil Beam Scanning Simulations Using GATE. *Nucl Instr Methods Phys Res Sect B: Beam Interact Mater Atoms* (2010) 268(20):3295–305. doi:10.1016/j.nimb.2010.07.011
36. Bolst D, Cirrone GAP, Cuttone G, Folger G, Incerti S, Ivanchenko V, et al. Validation of Geant4 Fragmentation for Heavy Ion Therapy. [Internet]. *Nucl Instr Methods Phys Res Sect A* (2017) 869:68–75. doi:10.1016/j.nima.2017.06.046
37. Karlsson M, Ahnesjö A, Georg D, Nyholm T, and Olofsson J. Independent Dose Calculations Concepts and Models. In: *ESTRO Booklet N°10*. Brussels: ESTRO (2010).
38. Georg D, Nyholm T, Olofsson J, Kjær-Kristoffersen F, Schnekenburger B, Winkler P, et al. Clinical Evaluation of Monitor Unit Software and the Application of Action Levels. *Radiother Oncol* (2007) 85(2):306–15. doi:10.1016/j.radonc.2007.04.035
39. Georg D, Stock M, Kroupa B, Olofsson J, Nyholm T, Ahnesjö A, et al. Patient-specific IMRT Verification Using Independent Fluence-Based Dose Calculation Software: Experimental Benchmarking and Initial Clinical Experience. *Phys Med Biol* (2007) 52(16):4981–92. doi:10.1088/0031-9155/52/16/018
40. Zhu TC, Stathakis S, Clark JR, Feng W, Georg D, Holmes SN, et al. Report of AAPM Task Group 219 on Independent Calculation-Based Dose/MU Verification for IMRT. *Med Phy* (2021) doi:10.1002/mp.15069
41. Kry SF, Glenn MC, Peterson CB, Branco D, Mehrens H, Steinmann A, et al. Independent Recalculation Outperforms Traditional Measurement-based IMRT QA Methods in Detecting Unacceptable Plans. *Med Phys* (2019) 46(8):3700–8. doi:10.1002/mp.13638
42. Milder MTW, Alber M, Söhn M, and Hoogeman MS. Commissioning and Clinical Implementation of the First Commercial Independent Monte Carlo 3D Dose Calculation to Replace CyberKnife M6 Patient-specific QA Measurements. *J Appl Clin Med Phys* (2020) 21(11):304–11. doi:10.1002/acm2.13046
43. Valdes G, Adamson J, and Cai J. Artificial Intelligence for Prediction of Measurement-based Patient-specific Quality Assurance Is Ready for Prime Time. *Med Phys* (2021) 48:2701–4. doi:10.1002/mp.14870
44. Jan S, Benoit D, Becheva E, Carlier T, Cassol F, Descourt P, et al. GATE V6: a Major Enhancement of the GATE Simulation Platform Enabling Modelling of CT and Radiotherapy. *Phys Med Biol* (2011) 56(4):881–901. Available from: http://iopscience.iop.org/article/10.1088/0031-9155/56/4/001/pdf. doi:10.1088/0031-9155/56/4/001
45. Allison J, Amako K, Apostolakis J, Arce P, Asai M, Aso T, et al. Recent Developments in GEANT4. *Nucl Instr Methods Phys Res Sect A* (2016) 835(July):186–225. Available from. doi:10.1016/j.nima.2016.06.125
46. Paganetti H, Blakely E, Carabe-Fernandez A, Carlson DJ, Das IJ, Dong L, et al. Report of the AAPM TG-256 on the Relative Biological Effectiveness of Proton Beams in Radiation Therapy. *Med Phys* (2019) 46(3):e53–e78. doi:10.1002/mp.13390
47. Schardt D, Elsässer T, and Schulz-Ertner D. Heavy-ion Tumor Therapy: Physical and Radiobiological Benefits. *Rev Mod Phys* (2010) 82:383–425. doi:10.1103/revmodphys.82.383
48. Fossati P, Matsufuji N, Kamada T, and Karger CP. Radiobiological Issues in Prospective Carbon Ion Therapy Trials. *Med Phys* (2018) 45(11):e1096–110. doi:10.1002/mp.12506

Conflict of Interest: DB and GK were employed by the company ACMIT Gmbh.

The remaining authors declare that the research was conducted in the absence of any commercial or financial relationships that could be construed as a potential conflict of interest.

Publisher's Note: All claims expressed in this article are solely those of the authors and do not necessarily represent those of their affiliated organizations, or those of the publisher, the editors and the reviewers. Any product that may be evaluated in this article, or claim that may be made by its manufacturer, is not guaranteed or endorsed by the publisher.

frontiers in Physics

ORIGINAL RESEARCH
published: 13 August 2021
doi: 10.3389/fphy.2021.727816

Repeatability and Reproducibility of Microdosimetry With a Mini-TEPC

A. Bianchi[1,2,3], *A. Selva*[3], *P. Colautti*[3], *G. Petringa*[4], *P. Cirrone*[4], *B. Reniers*[2], *A. Parisi*[1], *F. Vanhavere*[1] *and V. Conte*[3]*

[1]Belgian Nuclear Research Centre, SCK•CEN, Mol, Belgium, [2]UHasselt, Faculty of Engineering Technology, Centre for Environmental Sciences, Nuclear Technology Center, Hasselt, Belgium, [3]INFN Laboratori Nazionali di Legnaro, Legnaro, Italy, [4]INFN Laboratori Nazionali Del Sud, Catania, Italy

Experimental microdosimetry measures the energy deposited in a microscopic sensitive volume (*SV*) by single ionizing particles traversing the *SV* or passing by. The fundamental advantage of experimental microdosimetry over the computational approach is that the first allows to determine distributions of energy deposition when information on the energy and nature of the charged particles at the point of interest is incomplete or fragmentary. This is almost always the case in radiation protection applications, but discrepancies between the modelled and the actual scenarios should be considered also in radiation therapy. Models for physical reality are always imperfect and rely both on basic input data and on assumptions and simplifications that are necessarily implemented. Furthermore, unintended events due to human errors or machine/system failures can be minimized but cannot be completely avoided.

Though in proton radiation therapy (PRT) a constant relative biological effectiveness (RBE) of 1.1 is assumed, there is evidence of an increasing RBE towards the end of the proton penetration depth. Treatment Planning Systems (TPS) that take into account a variable linear energy transfer (LET) or RBE are already available and could be implemented in PRT in the near future. However, while the calculated dose distributions produced by the TPS are routinely verified with ionization chambers as part of the quality assurance program of every radiotherapy center, there is no commercial detector currently available to perform routine verification of the radiation quality, calculated by the TPS through LET or RBE distributions. Verification of calculated LET is required to make sure that a complex robustly optimized plan will be delivered as planned. The scientific community is coming to conclusion that a new domain of Quality Assurance additionally to the physical dose verification is required, and microdosimetry can be the right approach to address that. A first important prerequisite is the repeatability and reproducibility of microdosimetric measurements. This work aims at studying experimentally the repeatability and reproducibility of microdosimetric measurements performed with a miniaturized Tissue Equivalent Proportional Counter (mini-TEPC) in a 62 MeV proton beam. Experiments were carried out within 1 year and without propane gas recharging and by different operators. RBE was also calculated by applying the Loncol's weighting function *r(y)* to microdosimetric distributions. Demonstration of reproducibility of measured microdosimetric quantities $\overline{y}_F$, $\overline{y}_D$ and RBE_{10} in 62 MeV proton beam makes this TEPC

OPEN ACCESS

Edited by:
Francis A. Cucinotta, University of Nevada, Las Vegas, United States

Reviewed by:
Anatoly Rosenfeld, University of Wollongong, Australia
Geetika Jain, University of Delhi, India

***Correspondence:**
V. Conte
conte@lnl.infn.it

Specialty section:
This article was submitted to Radiation Detectors and Imaging, a section of the journal Frontiers in Physics

Received: *19 June 2021*
Accepted: *31 July 2021*
Published: *13 August 2021*

Citation:
Bianchi A, Selva A, Colautti P, Petringa G, Cirrone P, Reniers B, Parisi A, Vanhavere F and Conte V (2021) Repeatability and Reproducibility of Microdosimetry With a Mini-TEPC. Front. Phys. 9:727816. doi: 10.3389/fphy.2021.727816

a possible metrological tool for LET verification in proton therapy. Future characterization will be performed in higher energy proton beams.

Keywords: microdosimetry, microdosimeters, proton theraphy, RBE = relative biological effectiveness, hadron therapy, reproducibility, repeatibility, radiation quality assessment

INTRODUCTION

In current proton therapy a fixed RBE equal to 1.1 is used to weight the physical dose for all depths of the primary proton range [1]. However, an increase in RBE has been observed in several biological assays, in correspondence to the LET increase in the last few millimeters of the primary particle range [2–5]. In spite of this radiobiological evidence, there is no quantitative and widely accepted procedure for radiation quality specification in current proton therapy practice. Assuming a constant RBE of 1.1 can lead to an underestimation of the RBE-weighted dose to surrounding healthy tissues, which is thought to be one of the sources of unintended normal tissue toxicity [6].

The introduction of improved treatment planning that takes into account the variations of LET and RBE with depth could result in a higher therapeutic gain by restraining the dose delivered to surrounding healthy tissues and critical organs [7]. Treatment Planning Systems (TPS) that consider a variable LET or RBE as an optimization strategy are already available and could be implemented in PRT to improve the treatment outcome in the near future. In this context, experimental microdosimetry [8] can be used to validate simulated physical quantities that are descriptive of the radiation quality, in an analogous way as ionization chambers are used to validate the accuracy of Monte Carlo dose calculations, as part of the quality assurance program of every radiotherapy center [9]. Standard detectors should be made available to perform routine verification of the radiation quality calculated by the TPS through LET or RBE distributions.

The introduction of microdosimetric measurements as a verification of radiation quality in a clinical environment requires some important prerequisites. One important prerequisite is the reproducibility of the measurements.

The reference device in experimental microdosimetry is the Tissue Equivalent Proportional Counter (TEPC), which registers event by event the energy deposited in macroscopic volumes of gas with an inner pressure that allows to mimic the interaction in a micrometric volume of biological tissue. At the Legnaro National Laboratories of the Italian Institute for Nuclear Physics (LNL-INFN) miniaturized TEPCs have been developed and designed to cope with high intensity beams of clinical facilities. With respect to the commercial Farwest LET-½ counter, which has a cross sectional area of 127 mm^2, the smallest mini-TEPC has a cylindrical sensitive volume with an active cross-sectional area of only 0.8 mm^2. The original prototype of the mini-TEPC was designed to work with continuous gas flow to guarantee a constant refresh of the counting gas inside the sensitive volume [10]. However, safety and security regulations in radiotherapy centers generally prohibit access to clinical rooms with propane gas bottles. For this reason, a new prototype has been developed, to work without gas flow [11]. The microdosimetric characterization of the 62 MeV modulated proton beam line of CATANA (Centro di AdroTerapia ed Applicazioni Nucleari Avanzate), the Italian Eye Proton Therapy Facility in Catania, Italy [12] has been performed with this detector in different measurement runs. The measurements were repeated four times in separate measurement runs, at a distance of 4 months from each other, so that the last was carried out 1 year after the first without changing the gas in this period of time.

The detector response has been characterized both in terms of repeatability, the short term variation in measurements taken by a single person under the same experimental conditions, and in terms of reproducibility, the variation of the response in different measurement runs.

Bearing in mind the clinical potential of microdosimetry, the main aim of this paper is to study the repeatability and reproducibility of measurements carried out during four measurement runs at the 62 MeV therapeutic proton beam of CATANA with a miniaturized Tissue Equivalent Proportional Counter (mini-TEPC) used in sealed mode without flowing the filling gas and without changing it for 1 year.

Frequency and dose mean values of lineal energy were derived from microdosimetric distributions and compared with the track and dose–mean LET calculated by means of Geant4 simulations. RBE was also assessed by microdosimetric measurements, using a biological weighting function, and then it was compared with biological measurements performed by other authors in the same radiation field. The standard deviation of repeated measurements is evaluated.

MATERIALS AND METHODS

The Detector

The new mini-TEPC is based on the design of an existing prototype described in [10]. Only the gas ducts have been enlarged to improve the vacuum cleaning and the gas filling procedures. More attention has been paid in the machining of the external case to guarantee the vacuum tightness [11]. The scheme of the detector is reported in **Figure 1**. The sensitive volume is a right cylinder of 0.9 mm in diameter and height, and it is indicated in pink in **Figure 1**. The anode is a 10 μm gold-plated tungsten wire and the cathode is a 0.35 mm thick cylindrical shell made of conductive A150 plastic. The sensor is embedded in an additional insulating cylindrical shell, made of Rexolite®, of 0.35 mm of thickness. The detector is inserted in a 0.2 mm thick titanium sleeve which serves for vacuum sealing and electromagnetic shielding.

After 3–4 days of vacuum and as many days of continuous flow with propane gas, the detector was sealed at a pressure of

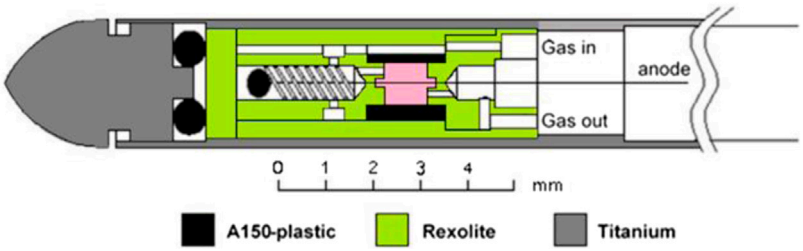

FIGURE 1 | Simplified scheme of the detector.

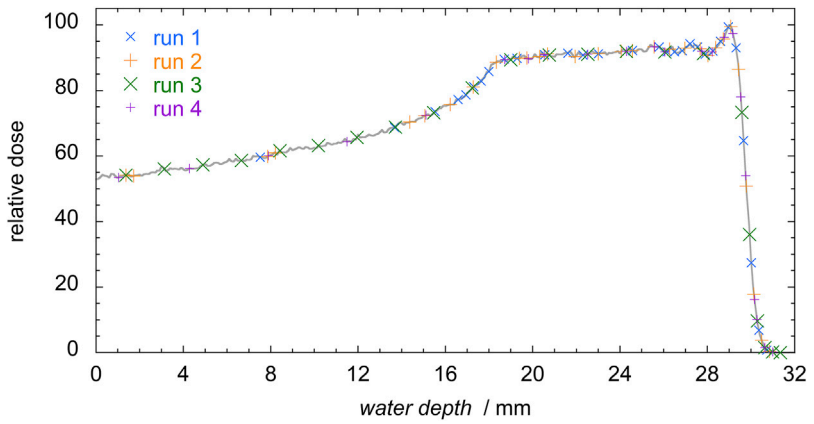

FIGURE 2 | Simulated depth-dose profile (grey) and measurements positions in the four measurement runs. A total of 130 distributions were measured.

454.0 mbar corresponding to a diameter of 75 μg/cm^2 in propane. The pressure was monitored in the various measurement runs, and after 1 year the registered pressure inside the mini-TEPC was 453.7 mbar. More details on the mini-TEPC are given in [11].

The CATANA Spread out Bragg Peak and Monte Carlo Simulations

The 62 MeV proton spread out Bragg peak (SOBP) of the LNS-INFN has a total range in water of 29.5 mm and a width of 11 mm. The energy modulation is obtained passively with a rotating wheel [12]. The detector was placed at several positions across the SOBP; **Figure 2** shows the relative depth-dose profile in water, and the measuring positions at the different runs. Different depths were obtained interposing between the collimator and the mini-TEPC several layers of polymethyl methacrylate (PMMA), 0.35 mm in thickness. A total of about 25 positions were analyzed for each measurement run. The equivalent depth in water was obtained by multiplying the PMMA total thickness by a constant factor 1.16, which corresponds to the average ratio of the stopping powers of protons in PMMA and water in the energy range 0–62 MeV. The water-equivalent thickness of the detector, evaluated as 1.4 mm, was added to the phantom thickness. By comparing the microdosimetric distributions measured at several specific depths obtained with stacks of different (but nominally equal) PMMA layers, a maximum uncertainty of 0.2 mm was observed in the corresponding water depth. Conservatively, the uncertainty in positioning has been assessed as ± 0.2 mm at all depths.

The CATANA beam line has been simulated with the HADRONTHERAPY [13] application of the Geant4 Monte Carlo code [14] to obtain the unrestricted total track-averaged LET, $\overline{L}_T^{tot}$, and the total dose-averaged LET, $\overline{L}_D^{tot}$, which include the contribution by both primary and secondary particles originating from nuclear interactions, as a function of the penetration depth in water, z. The calculation was performed on the basis of the implementation reported in [15], improved and updated to reduce the dependence on the transport parameters such as voxel size, production cut and step length [16, 17]. The formulation adopted to perform the calculation in a region is the following:

$$\overline{L}_T^{tot}(z) = \frac{\sum_{j=1}^{n}\left(\sum_{i=1}^{N} L_i l_i\right)_j}{\sum_{j=1}^{n}\left(\sum_{i=1}^{N} l_i\right)_j} \quad (1)$$

$$\overline{L}_D^{tot}(z) = \frac{\sum_{j=1}^{n}\left(\sum_{i=1}^{N} L_i \varepsilon_i\right)_j}{\sum_{j=1}^{n}\left(\sum_{i=1}^{N} \varepsilon_i\right)_j} \quad (2)$$

At each particle step i, the electronic stopping power, L_i, extracted from the Geant4 look-up tables, is weighted with the particle track length l_i and the energy loss ε_i, respectively. The

index j is referred to all n ions generated by the primary beam in hadronic interactions. This approach allows for a precise and simultaneous evaluation of absorbed dose and average LETs, for a voxel size of arbitrary dimensions, with negligible dependence with the cut variations [18]. Electromagnetic and hadronic interactions were simulated with the G4EmStandardPhysics-option4 and the QGSP-BIC-HP physics list, respectively [19, 20]. More details on the Monte Carlo simulations of absorbed dose and LET are given in [17].

The simulated $\overline{L}_T^{tot}(z)$ and $\overline{L}_D^{tot}(z)$ distributions are compared to the measured frequency-mean and dose-mean lineal energies.

Measurements and Data Analysis

Four measurement runs were carried out, at a time interval of about 4 months from each other, the last one exactly 1 year after the first. The mini-TEPC was kept sealed, without changing the filling gas, and the same operating conditions were used: the anode was kept grounded through the preamplifier and the cathode was biased at −700 V. A total of about $2{\cdot}10^6$ events were counted at each position. The signal of the detector was processed by a low-noise custom-made preamplifier, whose output was then fed in parallel to two spectroscopy amplifiers set at different gains, but with the same shaping time constant of 0.5 μs. Each output signal was then digitized separately by peak-sensing analog-to-digital converters (ADC) and then histogrammed. In the first three runs a data acquisition system (DAQ) based on CAMAC (computer-automated measurement and control) standard was used, with a 14 bit ADC module (model AD114 by EG and G ORTEC) for the high gain sub-spectrum, and a 13 bit ADC (model AD413 by EG and G ORTEC) for the low gain part. During the fourth measurement run a compact Multi Channel Analyzer (MCA) module (model ASPEC-MCA-927 by EG and G ORTEC) was used in place of the CAMAC system; data were also acquired in parallel with a digital FPGA (field-programmable gate array) based DAQ (model DT5780 by CAEN), which digitizes the complete waveforms directly from the preamplifier by means of flash-ADCs and then implements a trapezoidal filter for the pulse height analysis. Differences with the data acquired with the two systems are also discussed in this paper as a reproducibility test. Microdosimetric distributions from the different measurement runs have been analyzed with the same methodology by different operators.

Data from the four measurement runs were calibrated in lineal energy using the spectrum acquired beyond the Bragg peak, where the dose decreased by around 80% (in purple in **Figure 4**). The value of 143 keV/μm was assigned to the flex of the proton edge and the same factor was used for all the data of the same measurement run [21].

A detection threshold of about 0.4 keV/μm was registered due to environmental noise conditions, but all the frequency distributions of the lineal energy, $f(y)$, have been linearly extrapolated down to 0.01 keV/μm.

The microdosimetric lineal energy distributions $f(y)$ were processed to calculate the dose weighted distribution $d(y)$, and then the frequency and dose-mean lineal energy, $\overline{y}_F$ and $\overline{y}_D$, according to the following equations:

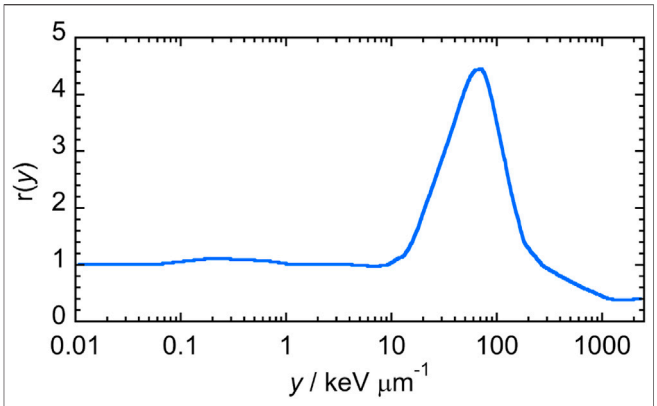

FIGURE 3 | Loncol's biological weighting function. Figure adapted from [22].

$$d(y) = \frac{yf(y)}{\int_0^\infty yf(y)\mathrm{d}y} \tag{3}$$

$$\overline{y}_F = \int_0^\infty yf(y)\mathrm{d}y \; and \; \overline{y}_D = \int_0^\infty yd(y)\mathrm{d}y \tag{4}$$

The RBE was assessed from the dose distributions of the lineal energy $d(y)$, through the application of the Loncol's biological weighting function $r(y)$, shown in **Figure 3** [22],

$$RBE_\mu = \int_0^\infty r(y)d(y)\mathrm{d}y \tag{5}$$

The microdosimetric RBE_μ calculated with **Equation 5** was compared to the RBE_{10} of human glioblastoma U87 cells that had been exposed to the same radiation field [3].

The repeatability of the measurements acquired with the mini-TEPC was studied by repeating nine times the same measurement at a water depth z = 23 mm, in the first measurement run; operating conditions and data analysis procedure were kept the same.

The reproducibility of the response of the detector is analyzed in terms of shape of the microdosimetric distributions in four positions of the SOBP (P1 at entrance, P3 at mid-SOBP, P4 at Bragg Peak and P5 at fall-off) measured 1 year apart. For all the other positions the reproducibility has been studied in terms of mean values of lineal energy, $\overline{y}_F$ and $\overline{y}_D$, calculating for each position the standard deviation of the five values with respect to the average. The same procedure was applied to evaluate the reproducibility of the microdosimetric RBE assessment, RBE_μ

RESULTS AND DISCUSSION

As an example of the measured microdosimetric distributions, a subset of $yd(y)$ distributions measured at five specific positions across the SOBP is shown in **Figure 4**. As protons slowdown in the phantom, their LET increases and also the stochastic

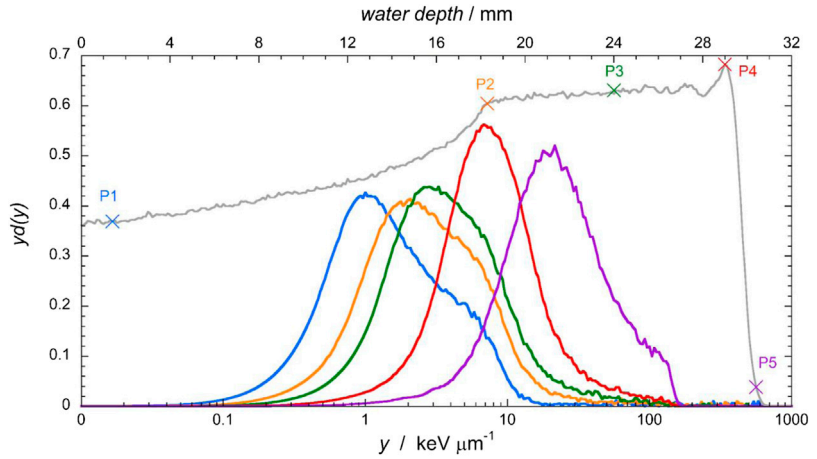

FIGURE 4 | Microdosimetric *yd(y)* distributions measured at five different positions across the SOBP, indicated as P1, P2, P3 P4, and P5 in the depth-dose profile.

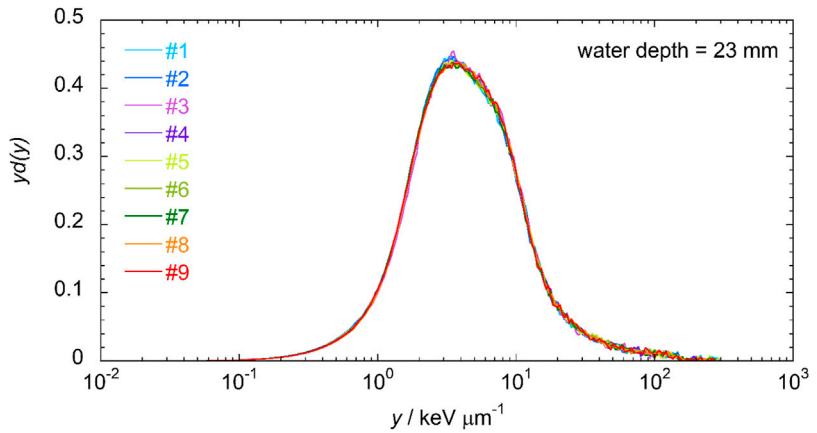

FIGURE 5 | Nine microdosimetric distributions gathered in the same measurement run at a depth of 23 mm.

probability of large lineal energy events. In consequence, the *yd(y)* distributions shift to larger *y* values as the depth increases. The p-edge region is clearly recognizable in the last spectrum, beyond the Bragg peak.

Repeatability

Repeatability tests (or test-retest reliability studies) aim to evaluate the precision of successive measurements of the same quantity, under the same experimental conditions, i.e., with the same method, the same radiation field, the same operator, and using the same equipment within short intervals of time.

To test this feature of the mini-TEPC, repeated measurements in the same position of the SOBP were performed in one measurement run. The chosen position is at around 23 mm in water equivalent depth that corresponds to the mid-SOBP position obtained with a calibrated PMMA range shifter. Nine microdosimetric distributions were consecutively gathered without changing any operational condition or parameters of the detector and acquisition set-up. **Figure 5** shows the results of

TABLE 1 | Individual and average values of the frequency and dose mean lineal energies of the nine microdosimetric distributions reported in **Figure 5**, and the standard deviation of the measurements.

	$\bar{y}_F$	$\bar{y}_D$
#1	2.56	7.4
#2	2.53	7.2
#3	2.57	7.3
#4	2.56	7.5
#5	2.56	7.5
#6	2.56	7.4
#7	2.55	7.6
#8	2.60	7.5
#9	2.58	7.4
Mean	2.56	7.4
Std Deviation	0.02 (0.8%)	0.1 (1.4%)

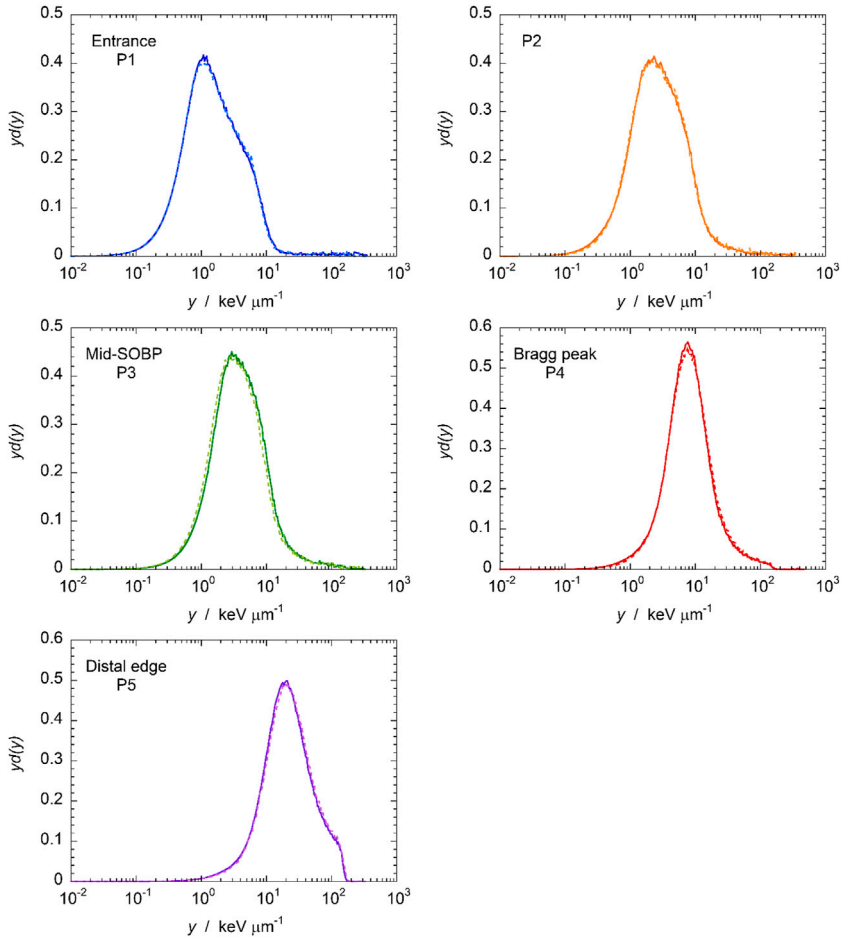

FIGURE 6 | Microdosimetric distributions measured at five positions along the SOBP (see **Figure 4**). The solid line indicates the distribution acquired with shaping amplifier and peak sensing ADC, the dash line the one gathered with the digital solution.

the nine consecutive measurements. The microdosimetric *yd(y)* distributions are very similar to each other, and to quantify the reproducibility it is more convenient to look at the frequency-mean and dose-mean values of the lineal energy, $\overline{y}_F$ and $\overline{y}_D$, which are summarized in **Table 1**.

The $\overline{y}_F$ values are distributed with a relative standard deviation from the average of 0.8%, while the standard deviation of $\overline{y}_D$ values from the average is 1.4%. Differences in $\overline{y}_D$ values are larger due to the contribution of rare large sized events, which only give a small contribution to $\overline{y}_F$. The observed differences are acceptable within the total uncertainties, which are 7% for the frequency-mean lineal energy and 5% for the dose-mean lineal energy [23].

Reproducibility

Reproducibility is the major principle of the scientific method. It means that to have a scientific result, what is produced as an outcome in one study should be obtained in an independent study when the same methodology is applied. In the case of the study of the reproducibility of the mini-TEPC response, four measurement runs covering 1 year of time were performed and considered as independent studies in which the conditions of measurement (electronic noise, environmental conditions, cabling, stack of PMMA layers, etc.) were changed together with the operators that gathered and analyzed the data, though using the same analysis methodology.

In the fourth measurement run, data were also acquired with a different data acquisition system. A fully digital DAQ that registers signals directly from the preamplifier performing a digital pulse processing (DPP) for the peak height was used, in parallel to the analog DAQ where the signal is processed through a Gaussian shaping amplifier and then the peak amplitude is converted into a digit by means of a peak sensing ADC. The post-processing of the peak-heights histograms was the same for both data sets. Ideally, the microdosimetric distributions and derived quantities should be independent of the DAQ, however small differences are expected due to the different processing of the raw signal at the output of the preamplifier: shaping amplifier and peak sensing ADC or digital solution. The microdosimetric distributions measured with the two DAQs in the five positions of **Figure 4**, are shown as a representative example in **Figure 6**. The results obtained in other positions are

TABLE 2 | The frequency and dose mean lineal energies obtained during the fourth measurement run at different positions, with the two DAQs: pulse shaping plus peak sensing ADC (analog) or fully digital (digital). See text for more details.

Depth/mm	$\overline{y}_F$-Analog	$\overline{y}_F$-Digital	$\overline{y}_D$-Analog	$\overline{y}_D$-Digital
1.4	0.850	0.848	3.23	3.36
4.3	0.882	0.893	3.30	3.68
7.9	1.02	0.967	3.86	3.89
11.5	1.13	1.06	3.92	3.52
15.1	1.26	1.18	3.94	3.76
18.7	1.49	1.56	5.28	5.14
19.8	1.57	1.63	5.16	5.42
20.5	1.62	1.69	5.50	5.48
22.5	1.98	1.84	5.96	5.71
24.3	2.23	2.07	6.52	6.30
25.6	2.34	2.43	6.92	6.95
26.1	2.70	2.48	7.45	6.99
27.7	3.07	3.26	7.87	8.36
28.2	3.28	3.75	8.07	8.95
28.8	3.93	4.23	9.47	10.1
29.2	4.80	5.17	11.5	12.1
29.5	6.99	7.45	16.5	17.2
29.8	8.39	9.15	20.3	21.4
30.2	10.6	11.2	25.2	27.3

summarized in **Table 2**, through the frequency and dose mean lineal energy values, $\overline{y}_F$ and $\overline{y}_D$ obtained from the distributions.

In order to check the reproducibility of data gathered with the mini-TEPC, the first comparison that is worth doing regards the shape of the microdosimetric distributions in the same positions 1 year apart. The microdosimetric distributions measured at the five positions of **Figure 4** are shown in **Figure 7**, using the same colors: the line represents the spectrum of the first measurement run while the circles stand for the spectrum of the last measurement run 1 year apart both gathered with the same analog DAQ. Microdosimetric distributions measured in four positions are presented: entrance, mid-SOBP, Bragg peak and distal edge.

From **Figure 7** it is possible to observe that the shape of the microdosimetric distributions is consistent in all the shown positions 1 year apart indicating that the response of the detector is stable.

The frequency-mean lineal energy values, as a function of the water depth, were multiplied by a constant factor 1.5, because a systematic reduction the experimental values of $\overline{y}_F(z)$ was observed, as compared to the $\overline{L}_T^{tot}(z)$ [11]. The five sets of experimental $1.5\,\overline{y}_F(z)$ values and the simulated $\overline{L}_T^{tot}(z)$ are shown in **Figure 8**, as a function of the water depth z. The average value of the five sets of measurements is also shown in **Figure 8** as a green line, while the light green band represents 1 standard deviation. It can be easily noticed that the dispersion of values obtained at different runs is small, and that the agreement between the experimental values of $1.5\,\overline{y}_F(z)$ and the simulated $\overline{L}_T^{tot}(z)$ is very good, at all depths.

The differences in the frequency-mean lineal energy values for the five significant positions indicated in **Figure 4**, are reported in **Table 3**.

The standard deviation of the data is always less than 5%, except from the regions where the $\overline{y}_F(z)$ and the $\overline{L}_T^{tot}(z)$ vary more rapidly, at the beginning and above all, at the end of the SOBP. In these regions small shifts in the water depth result in large variations in the value. In the reported measurements we considered an uncertainty of 0.2 mm in the position of the detector, due to the fact that different sets of PMMA layers were used, which produces larger standard deviations in the $\overline{y}_F$ values measured beyond the Bragg peak. Apart from the last 1.5 mm of the proton depth, the standard deviations of the data seem to be independent of the depth. To confirm that the dispersion of measured $\overline{y}_F$ values is approximately the same at any position across the SOBP, the relative standard deviation values (RSD) are histogrammed in **Figure 9**. It can be noted that the values of the relative standard deviation of the frequency-mean lineal energies are approximately Gaussian, as expected for the probability distribution of a random error. The centroid of the Gaussian fit is at a relative standard deviation of 5% with a variance of 2%, meaning that, according to the Gaussian distribution confidence levels, 68% of the data are assessed with a standard deviation of 5 ± 2%. This means that for approximately the 84% of the data the standard deviation is smaller than the usual uncertainty of 7% assigned to $\overline{y}_F$, and about 98% of the data have a standard deviation smaller than 9%.

The analysis of the reproducibility was repeated for the dose mean lineal energy $\overline{y}_D$, whose measured values are shown in **Figure 10**. The computed total dose-average LET, $\overline{L}_D^{tot}$, is also shown for comparison (black line). It is clear from the figure that the dispersion of $\overline{y}_D$ values derived in different measurement run is small, and that the correspondence to simulated $\overline{L}_D^{tot}$ is very good, even if in the entrance region the lineal energy is generally smaller than the LET, and beyond the Bragg peak it is generally larger. These small differences are to be expected.

When comparing the mean values of the lineal energy and the corresponding average LET values, it is important to notice that LET and the lineal energy are analogous but different quantities. One of the relevant differences is that the LET describes the mean energy loss by a particle in a thin matter layer of infinite extension, therefore it is always centered on the core of the charged particle track. In contrast, the lineal energy is determined by the energy imparted to a volume of finite dimensions, arbitrarily positioned in the irradiated matter. When a large volume is irradiated with heavy ions, energy will be deposited by both the primary particle and the secondary electrons emerging from the primary track. If the volume is small, it is sometimes crossed by the core of the ion track but more often by the delta electrons. The energy deposited in the sensitive volume *SV* by delta electrons initiated outside *SV* produces small size events that contribute to the microdosimetric distributions, whereas they are not counted as independent events in LET calculations. In general, the size of the volume has a large impact on the overall microdosimetric spectrum, and the frequency and dose mean values of the lineal energy can be smaller or greater than the corresponding track- and dose-averaged LET [24].

Another factor that has to be taken into account is that measurements are performed in propane while simulations in

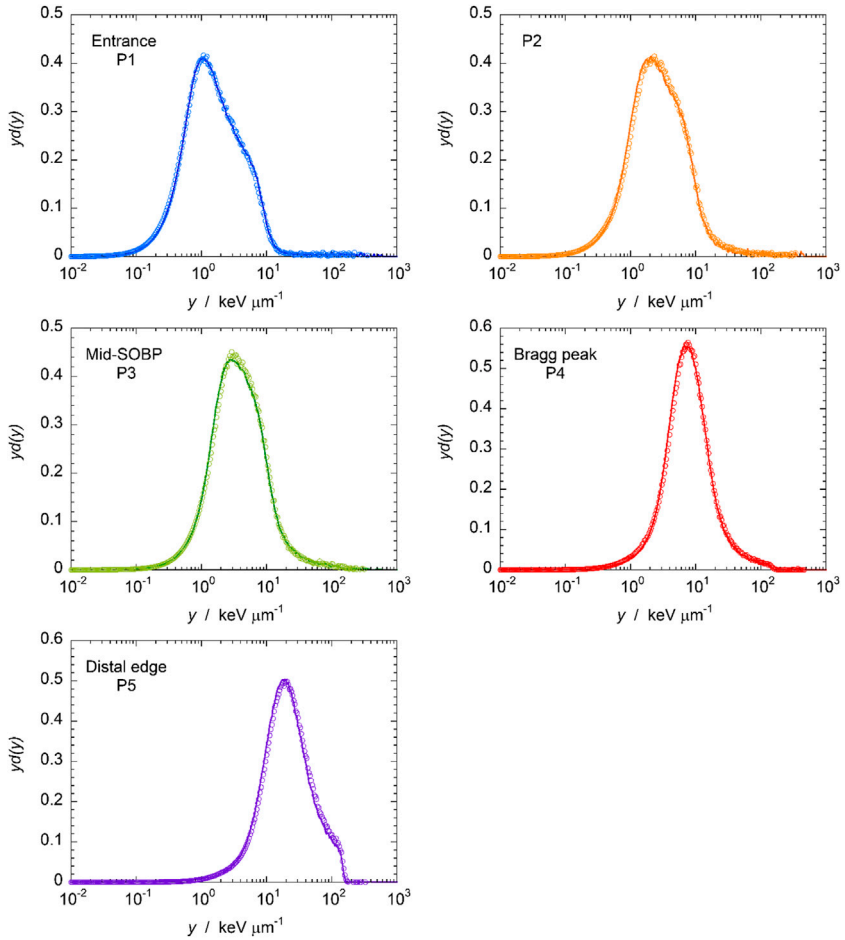

FIGURE 7 | Five microdosimetric distributions measured at five positions along the SOBP (see **Figure 4**). The solid line indicates the spectrum of the first run, circles the one gathered in the fourth run.

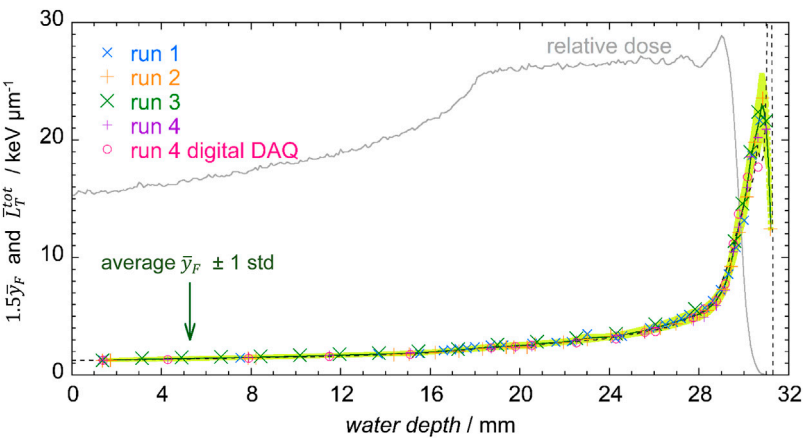

FIGURE 8 | MC simulated $\bar{L}_T^{tot}(z)$ (dashed black line) and experimental $\bar{y}_F(z)$ (symbols) as a function of the water depth. The average values of five different experimental data are also represented (green line) with 1 standard deviation (light green band). The MC simulated depth-dose profile is also shown.

TABLE 3 | Average values and standard deviation of $1.5\overline{y}_F$ from microdosimetric distributions measured in five SOBP positions, as shown in **Figure 4**. Numbers in parenthesis indicate the corresponding measurement runs.

	$\overline{y}_F$ – P1	$\overline{y}_F$ – P2	$\overline{y}_F$ – P3	$\overline{y}_F$ – P4	$\overline{y}_F$ – P5
Minimum	1.23 (#2)	2.2 (#4)	3.1 (#4 digital)	7.0 (#3)	18 (#4 digital)
Maximum	1.32 (#1)	2.5 (#1)	3.5 (#3)	7.8 (#1)	22 (#4)
Mean	1.27	2.3	3.3	7.4	20
Std deviation	0.03 (2.6%)	0.1 (5.2%)	0.2 (4.8%)	0.3 (4.6%)	1 (6.6%)

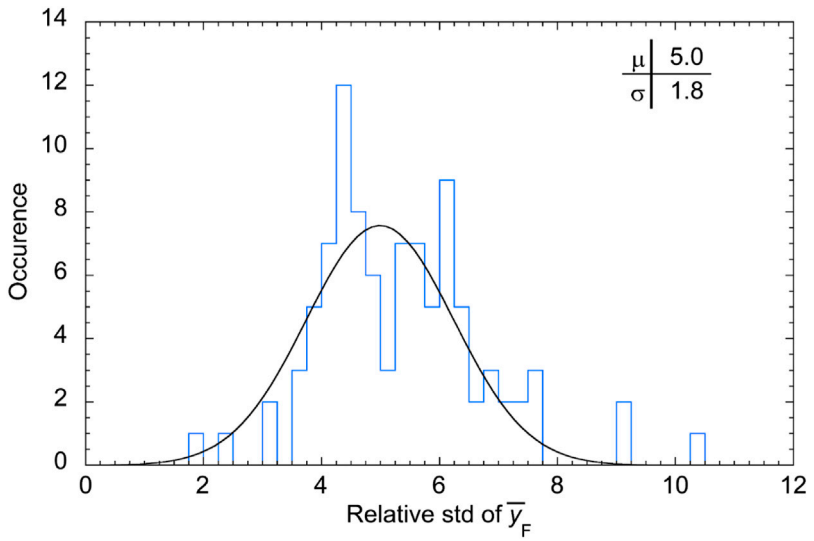

FIGURE 9 | Occurrence of the relative standard deviation values for the frequency-mean lineal energy.

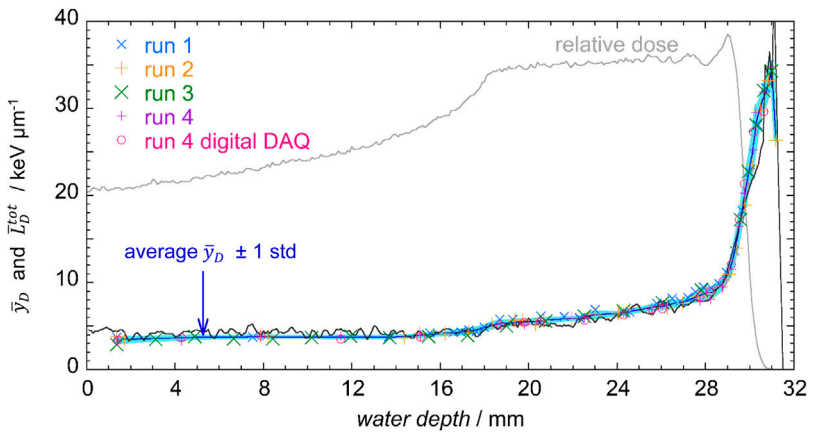

FIGURE 10 | Total MC simulated $\overline{L}_D^{tot}$ (black line) and measured $\overline{y}_D$ (symbols), as a function of the water depth. The average $\overline{y}_D$ value of five measurements is also shown with 1 standard deviation (blue line with light blue band). The MC simulated depth-dose profile is also shown.

water, which could results in some differences between the measured microdosimetric distributions and those that would be measured in water, in particular in the distal edge, where the ratio of the stopping powers in propane and water increases with respect to the average value [25].

In **Table 4**, data from five microdosimetric distributions for each of the five positions shown in **Figure 4**, are reported together with the corresponding standard deviation.

The relative standard deviation is 11% at P1, and in the entrance region of the SOBP before the dose plateau, where

TABLE 4 | Average values and standard deviation of $\overline{y}_D$ obtained in five five positions along the SOBP, as indicated in **Figure 4**. Numbers in parenthesis indicate the corresponding measurement runs.

	$\overline{y}_D$ – P1	$\overline{y}_D$ – P2	$\overline{y}_D$ – P3	$\overline{y}_D$– P4	$\overline{y}_D$– P5
Minimum	2.9 (#3)	4.6 (#3)	6.3 (#4 digital)	10.6 (#2)	28 (#2)
Maximum	3.9 (#2)	5.3 (#1)	6.7 (#3)	11.4 (#1)	31 (#4)
Mean	3.4	5.6	6.6	11.0	29
Std deviation	0.4 (11%)	0.3 (5.6%)	0.2 (2.6%)	0.4 (3.8%)	1 (3.5%)

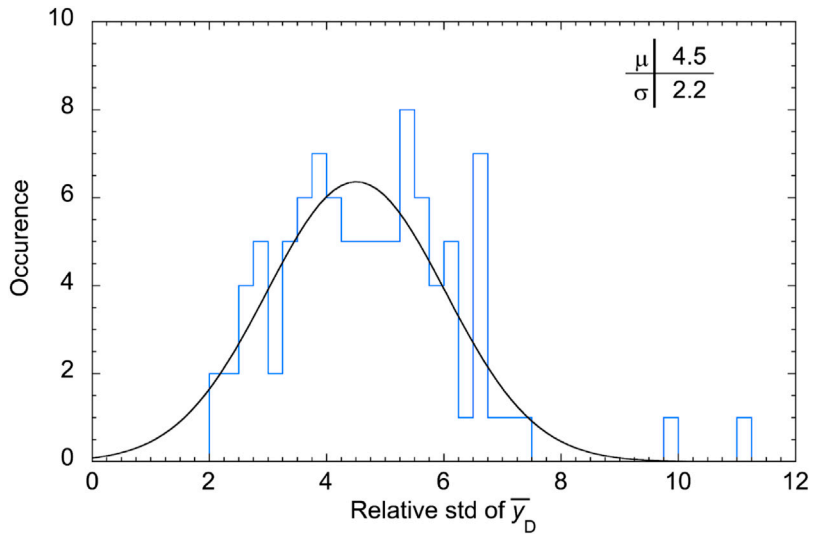

FIGURE 11 | Occurrence of the relative standard deviation values for the dose-mean lineal energy $\overline{y}_D$.

rare large-size events are most influential on the dose-mean lineal energy [11], while it is almost independent of the measuring position in the other regions of the SOBP. being randomly distributed about a mean value of 4.5%. The complete distribution of the relative standard deviation of the dose-mean lineal energy values is reported as a histogram in **Figure 11**.

The distribution of the relative std is approximately a Gaussian function, as the probability distribution of a random error. The mean value is 4.5% and the variance 2.2%. This means that about 84% of the data have a standard deviation smaller than 7% and about 98% of the data have a relative standard deviation smaller than 9%.

The largest deviations are reached in the entrance part of the SOBP, where rare large y events caused by high LET target fragments produced in nuclear reactions contribute significantly to $\overline{y}_D$. All microdosimetric distributions have been acquired with a total number of $2{\cdot}10^6$ events, for a measuring time of about 3 min. With this statistics, there is a small number of large y events (only about 20 events above 100 keV/μm, and less than 10 events above 250 keV/μm), which have therefore large statistical uncertainties, up to 100% if only one event has been counted. In **Figure 12**, two *yd(y)* distributions are shown, measured in the first position P1 during the second and the third measuring runs. The double logarithmic representation emphasizes the contribution of rare large y events to the dose-weighted distribution. The two distributions are very similar, and mainly differ for a few large size events at $y > 260$ keV/μm that are present in the first measurement run but not in the second one. It is this small fraction of events in the rightmost part of the first spectrum that increases the corresponding $\overline{y}_D$ value from 2.95 to 3.87 keV/μm, and this is mostly responsible for the high $\overline{y}_D$ standard deviation, up to 11%, in entrance region of the SOBP. However, the statistical uncertainty of this contribution is very large, close to 100%. The $\overline{y}_D$variation excluding events above 260 keV/μm is about 1% for these two microdosimetric distributions. In general, to reduce the statistical uncertainty a larger number of events should be measured, in particular in the entrance region, where the impact of rare large y events is maximum.

Finally, the dose distributions of the lineal energy can be weighted on empirical biological weighting functions, to assess the RBE variability as a function of the depth. The uncertainty on the evaluated microdosimetric RBEμ values derived from application of the Loncol's function has been also studied.

The RBE_μ has been calculated for the whole set of data from the four measurement runs, using **Equation 5**. The results are shown in **Figure 13**, together with the average values.

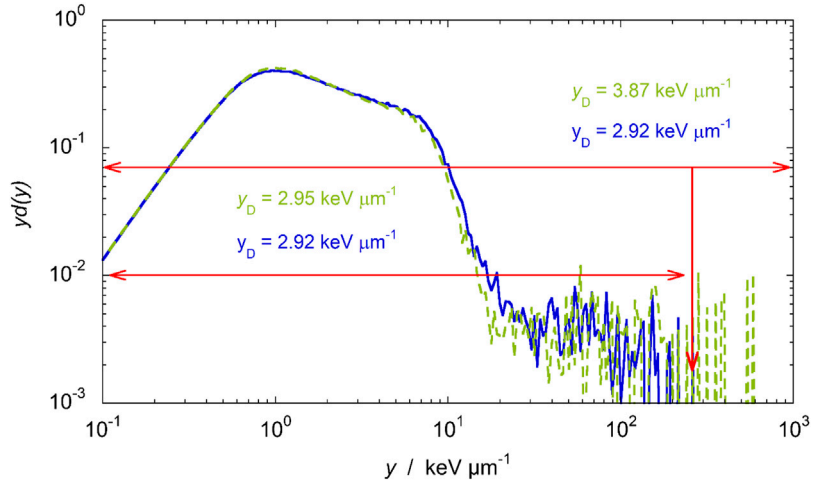

FIGURE 12 | *yd(y)* distributions measured in two different measurement runs at water-depth = 1.4 mm. The double logarithmic scale points out the influence of rare high *y* events.

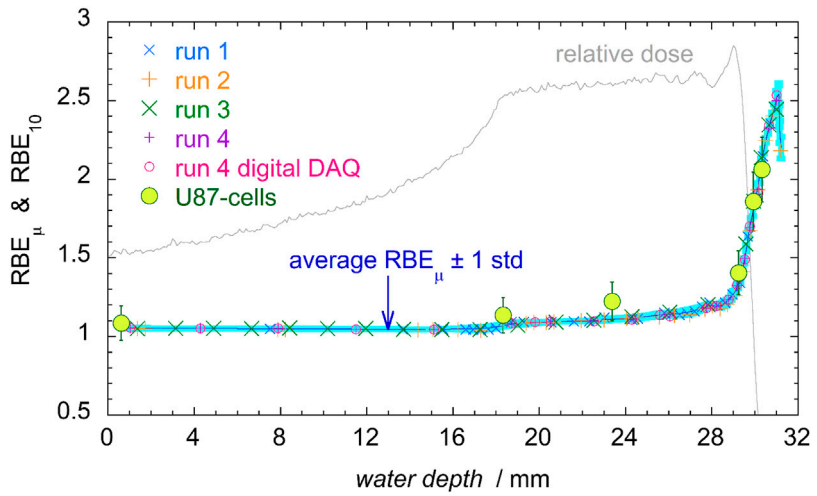

FIGURE 13 | RBE$_\mu$ of the four measurement runs (see legend), with the average values (blue line) and its standard deviation (light blue band). The large green circles represent radiobiological data from *in vitro* cell survival experiment for glioblastoma U87 cells, with a 10% uncertainty [3].

The RBE$_{10}$ values for human glioblastoma U87 cells irradiated in the same radiation field [3] are also shown in **Figure 13**. At a first glance, it is noticeable that at all depths the RBE$_\mu$ values are all concentrated close to the mean, exhibiting little spread.

The distribution of the relative standard deviation is histogrammed in **Figure 14**. Two population groups can be individuated: a first group of samples with very small standard deviations from the mean (below 0.3%), on the left side of the plot, and a wider distribution of events with approximately Gaussian shape and mean value of 0.88. The first group is populated by measurements performed at the entrance region of the SOBP, in which most part of the *d(y)* distribution is in the range of *y* values less than 10 keV/µm, where the Loncol's weighting function *r(y)* is approximately equal to 1 (see **Figure 3**). Following **Eq. 5**, the RBE$_\mu$ is then almost the same as the integral of *d(y)* which is equal to one by definition of *d(y)*, independently of the spectral shape. Consequently, RBEµ values in the entrance region dominated by small *y* events are also almost equal to 1 with only small deviations.

Finally, it can also be observed that RBE$_\mu$ values are the same as the RBE$_{10}$ radiobiological data, within a 10% estimated uncertainty on RBE$_{10}$. This result encourages the use of microdosimetry as a tool for a fast and cheap assessment of the relative biological effectiveness.

To summarize the results, **Figure 15** shows the relative standard deviations of repeated measurements of $\overline{y}_F$, $\overline{y}_D$ and RBE$_\mu$ as a function of the measuring depth *z* across the SOBP. These relative standard deviations can be interpreted as the type

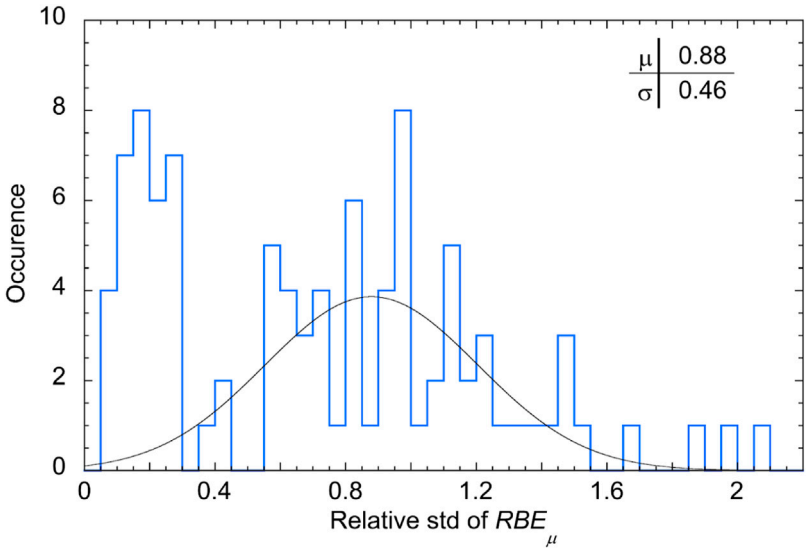

FIGURE 14 | Occurrence of the relative standard deviation values for the microdosimetric RBE_m.

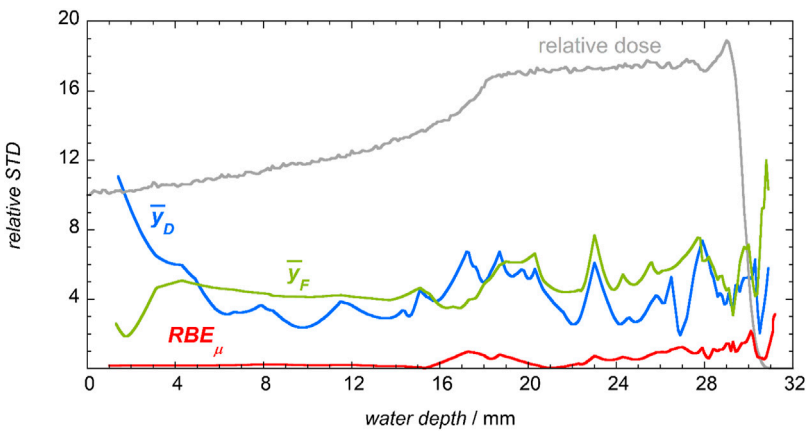

FIGURE 15 | The relative standard deviation values for $\bar{y}_F$, $\bar{y}_D$ and RBE_μ as a function of the water depth.

A standard uncertainties, according to GUM definitions [26]. Based on the analysis of our results, the uncertainties in the entrance region at small depths can be reduced increasing the statistics of recorded events, while the uncertainties in the distal part of the SOBP, where the radiation quality changes rapidly, can be reduced increasing the precision in the detector positioning.

CONCLUSION

Four consecutive measurement runs have been performed at the 62 MeV proton beam line of CATANA, which is used to treat ocular melanoma, with a mini-TEPC working without gas flow. The analysis of the results allowed to evaluate the repeatability and the reproducibility of microdosimetric measurements with this detector, with particular focus on the frequency-mean and dose mean values of the lineal energy, and on the microdosimetric assessment of the RBE with the Loncol's weighting function. The response of this new mini-TEPC is repeatable when it measures in a short time span the same spectrum, showing only small fluctuations below 2% both in $\bar{y}_F$ and $\bar{y}_D$. Furthermore, measurements are reproducible and stable over 1 year within approximately a 5% uncertainty on $\bar{y}_F$ and $\bar{y}_D$. The differences are higher in the entrance part of the dose profile, due to the contribution of rare large events that are subject to large uncertainties, and in the distal part, where the sharp change in radiation quality makes the positioning uncertainties more influential.

Experimental $\bar{y}_F$ values have been compared to unrestricted total track-averaged LET values obtained by means of Monte

Carlo simulations. The agreement is good within one standard deviation when a factor 1.5 is applied to experimental data.

Experimental $\overline{y}_D$ values have been compared to unrestricted total dose-averaged LET values obtained by means of Monte Carlo simulations. The two quantities are in good agreement, though small differences are observable, which are consistent with the different nature of lineal energy *y* and LET. The observed stability and reproducibility over time encourages the use of experimental microdosimetry as a tool for radiation quality assurance purposes. In addition, microdosimetric quantities could be included in new treatment planning systems meant to optimize innovative irradiation modalities that lead to higher therapeutic gains.

Finally, it has been shown that microdosimetric distributions can be used to assess the biological effectiveness using the Loncol's biological weighting function (RBE_{μ}). The RBE_{μ} has been calculated for the five sets of microdosimetric distributions, and the resulting data show only minor fluctuations around the average, with a standard deviation that is less than 1% in most of the SOBP profile. This result suggests that experimental microdosimetry can provide a fast and cheap biological effectiveness assessment with high reproducibility and stability over time.

DATA AVAILABILITY STATEMENT

The raw data supporting the conclusions of this article will be made available by the authors, without undue reservation.

AUTHOR CONTRIBUTIONS

AB: performed the measurements, analyzed and discussed the results, and wrote the first draft of the paper. AS: performed the measurements, and analyzed and discussed the results. PCo: took part in the measurements and discussion. GP and PCi: performed the simulations and assisted the group during the measurement campaigns. BR, AP, and FV revised the manuscript. VC: coordinated the work, performed the measurements, analyzed the data, and wrote the final version of the manuscript.

FUNDING

The research is funded by the fifth commission of INFN.

REFERENCES

1. Paganetti H, Niemierko A, Ancukiewicz M, Gerweck LE, Goitein M, Loeffler JS, et al. Relative Biological Effectiveness (RBE) Values for Proton Beam Therapy. *Int J Radiat Oncology*Biology*Physics* (2002) 53:407–21. doi:10.1016/s0360-3016(02)02754-2
2. Britten RA, Nazaryan V, Davis LK, Klein SB, Nichiporov D, Mendonca MS, et al. Variations in the RBE for Cell Killing along the Depth-Dose Profile of a Modulated Proton Therapy Beam. *Radiat Res* (2013) 179:21–8. doi:10.1667/rr2737.1
3. Chaudhary P, Marshall TI, Perozziello FM, Manti L, Currell FJ, Hanton F, et al. Relative Biological Effectiveness Variation along Monoenergetic and Modulated Bragg Peaks of a 62-MeV Therapeutic Proton Beam: a Preclinical Assessment. *Int J Radiat Oncology*Biology*Physics* (2014) 90:27–35. doi:10.1016/j.ijrobp.2014.05.010
4. Paganetti H. Relative Biological Effectiveness (RBE) Values for Proton Beam Therapy. Variations as a Function of Biological Endpoint, Dose, and Linear Energy Transfer. *Phys Med Biol* (2014) 59:R419–R472. doi:10.1088/0031-9155/59/22/r419
5. Paganetti H, Blakely E, Carabe-Fernandez A, Carlson DJ, Das IJ, Dong L, et al. Report of the AAPM TG-256 on the Relative Biological Effectiveness of Proton Beams in Radiation Therapy. *Med Phys* (2019) 46(3):e53–e78. doi:10.1002/mp.13390
6. Lühr A, von Neubeck C, Krause M, and Troost EGC. Relative Biological Effectiveness in Proton Beam Therapy - Current Knowledge and Future Challenges. *Clin translational Radiat Oncol* (2018) 9:35–41. doi:10.1016/j.ctro.2018.01.006
7. Unkelbach J, and Paganetti H. Robust Proton Treatment Planning: Physical and Biological Optimization. *Semin Radiat Oncol* (2018) 28(2):88–96. doi:10.1016/j.semradonc.2017.11.005
8. International Commission on Radiation Units and Measurements (ICRU). Microdosimetry. Report 36 (1983).
9. Wagenaar D, Tran LT, Meijers A, Marmitt GG, Souris K, Bolst D, et al. Validation of Linear Energy Transfer Computed in a Monte Carlo Dose Engine of a Commercial Treatment Planning System. *Phys Med Biol* (2020) 65:025006. doi:10.1088/1361-6560/ab5e97
10. De Nardo L, Cesari V, Donà G, Magrin G, Colautti P, Conte V, et al. Mini-TEPCs for Radiation Therapy. *Radiat Prot Dosimetry* (2004) 108(4):345–52. doi:10.1093/rpd/nch023
11. Conte V, Bianchi A, Selva A, Petringa G, Cirrone GAP, Parisi A, et al. Microdosimetry at the CATANA 62 MeV Proton Beam with a Sealed Miniaturized TEPC. *Physica Med* (2019) 64:114–22. doi:10.1016/j.ejmp.2019.06.011
12. Cirrone GAP, Cuttone G, Lojacono PA, Lo Nigro S, Mongelli V, Patti IV, et al. A 62-MeV proton beam for the treatment of ocular melanoma at Laboratori Nazionali del Sud-INFN. *IEEE Trans Nucl Sci* (2004) 51(3):860–5. doi:10.1109/tns.2004.829535
13. Cirrone GAP, Cuttone G, Di Rosa F, Raffaele L, Russo G, Guatelli S, et al. The Geant4 Toolkit Capability in the Hadron Therapy Field: Simulation of a Transport Beam Line. *Nucl Phys B* (2005) 150:54–7. doi:10.1016/j.nuclphysbps.2005.04.061
14. Allison J, Amako K, Apostolakis J, Arce P, Asai M, Aso T, et al. Recent Developments in GEANT4. *Nucl Instrum Meth A* (2016) 835:186–225. doi:10.1016/j.nima.2016.06.125
15. Romano F, Cirrone GAP, Cuttone G, Rosa FD, Mazzaglia SE, Petrovic I, et al. A Monte Carlo Study for the Calculation of the Average Linear Energy Transfer (LET) Distributions for a Clinical Proton Beam Line and a Radiobiological Carbon Ion Beam Line. *Phys Med Biol* (2014) 59:2863–82. doi:10.1088/0031-9155/59/12/2863
16. Petringa G, Cirrone GAP, Cuttone G, Pandola L, Milluzzo GG, Pisciotta P, et al. Development and Analysis of the Track-, Dose-LET and RBE Calculations with a Therapeutical Proton and Ion Beams Using Geant4 Monte Carlo Code. *Physica Med* (2017) 42(1):9. doi:10.1016/j.ejmp.2017.09.023
17. Petringa G, Pandola L, Agosteo S, Catalano R, Colautti P, Conte V, et al. Monte Carlo Implementation of New Algorithms for the Evaluation of Averaged-Dose and -track Linear Energy Transfers in 62 MeV Clinical Proton Beams. *Phys Med Biol* (2020) 65(23):235043. doi:10.1088/1361-6560/abaeb9
18. Zhu H, Chen Y, Sung W, McNamara AL, Tran LT, Burigo LN, et al. The Microdosimetric Extension in TOPAS: Development and Comparison with Published Data. *Phys Med Biol* (2019) 64:145004. doi:10.1088/1361-6560/ab23a3
19. Geant4. Geant4 Physics List Guide (2009). Available from: http://geant4-userdoc.web.cern.ch/geant4-userdoc/UsersGuides/PhysicsListGuide/html/index.html.
20. Ivanchenko VN, Apostolakis J, Bagulya A, Bogdanov A, Grichine V, Incerti S, et al. Geant4 Electromagnetic Physics for LHC Upgrade. *J Phys Conf Ser* (2014) 513:022015. doi:10.1088/1742-6596/513/2/022015

21. Bianchi A, Mazzucconi D, Selva A, Colautti P, Parisi A, Vanhavere F, et al. Lineal Energy Calibration of a Mini-TEPC via the Proton-Edge Technique. *Radiat Measurements* (2021) 141:106526. doi:10.1016/j.radmeas.2021.106526
22. Loncol T, Cosgrove V, Denis JM, Gueulette J, Mazal A, Menzel HG, et al. Radiobiological Effectiveness of Radiation Beams with Broad LET Spectra: Microdosimetric Analysis Using Biological Weighting Functions. *Rad Prot Dosim* (1994) 52:347–52. doi:10.1093/oxfordjournals.rpd.a082212
23. Moro D, Seravalli E, and Colautti P. Statistical and Overall Uncertainties in Proton Therapy Microdosimetric Measurements. LNL Report 200/2003 (2003).
24. Lindborg L, Hultqvist M, Carlsson Tedgren Å, and Nikjoo H. Lineal Energy and Radiation Quality in Radiation Therapy: Model Calculations and Comparison with experiment. *Phys Med Biol* (2013) 58(10):3089–105. doi:10.1088/0031-9155/58/10/3089
25. PSTAR (2021). Htmlpping Power and Range Tables for Protons. Available from: https://physics.nist.gov/PhysRefData/Star/Text/PSTAR.html.
26. BIPM. Guide to the Expression of Uncertainty in Measurement. JCGM 100: 2008 (2008).

Conflict of Interest: The authors declare that the research was conducted in the absence of any commercial or financial relationships that could be construed as a potential conflict of interest.

The handling editor declared a past co-authorship with the authors PCo, GP, PCi, and VC.

frontiers in Physics

ORIGINAL RESEARCH
published: 08 September 2021
doi: 10.3389/fphy.2021.719682

Coupling Radiation Transport and Track-Structure Simulations: Strategy Based on Analytical Formulas Representing DNA Damage Yields

Pavel Kundrát[1,2]*, *Werner Friedland*[2], *Andrea Ottolenghi*[3] and *Giorgio Baiocco*[3]*

[1]Department of Radiation Dosimetry, Nuclear Physics Institute, Czech Academy of Sciences, Prague, Czechia, [2]Institute of Radiation Medicine, Helmholtz Zentrum München—German Research Center for Environmental Health (GmbH), Neuherberg, Germany, [3]Radiation Biophysics and Radiobiology Group, Physics Department, University of Pavia, Pavia, Italy

OPEN ACCESS

Edited by:
Susanna Guatelli,
University of Wollongong, Australia

Reviewed by:
Tuba Conka Yildiz,
Türkisch-Deutsche Universität, Turkey
Mario A. Bernal,
State University of Campinas, Brazil
Ngoc Hoang Tran,
Centre d'Etudes Nucleaires de Bordeaux Gradignan (CENBG), France

***Correspondence:**
Pavel Kundrát
kundrat@ujf.cas.cz
Giorgio Baiocco
giorgio.baiocco@unipv.it

Specialty section:
This article was submitted to Radiation Detectors and Imaging, a section of the journal Frontiers in Physics

Received: 02 June 2021
Accepted: 25 August 2021
Published: 08 September 2021

Citation:
Kundrát P, Friedland W, Ottolenghi A and Baiocco G (2021) Coupling Radiation Transport and Track-Structure Simulations: Strategy Based on Analytical Formulas Representing DNA Damage Yields. Front. Phys. 9:719682. doi: 10.3389/fphy.2021.719682

Existing radiation codes for biomedical applications face the challenge of dealing with largely different spatial scales, from nanometer scales governing individual energy deposits to macroscopic scales of dose distributions in organs and tissues in radiotherapy. Event-by-event track-structure codes are needed to model energy deposition patterns at cellular and subcellular levels. In conjunction with DNA and chromatin models, they predict radiation-induced DNA damage and subsequent biological effects. Describing larger-scale effects is the realm of radiation transport codes and dose calculation algorithms. A coupling approach with a great potential consists in implementing into radiation transport codes the results of track-structure simulations captured by analytical formulas. This strategy allows extending existing transport codes to biologically relevant endpoints, without the need of developing dedicated modules and running new computationally expensive simulations. Depending on the codes used and questions addressed, alternative strategies can be adopted, reproducing DNA damage in dependence on different parameters extracted from the transport code, e.g., microdosimetric quantities, average linear energy transfer (LET), or particle energy. Recently, a comprehensive database on DNA damage induced by ions from hydrogen to neon, at energies from 0.5 GeV/u down to their stopping, has been created with PARTRAC biophysical simulations. The results have been captured as a function of average LET in the cell nucleus. However, the formulas are not applicable to slow particles beyond the Bragg peak, since these can have the same LET as faster particles but in narrower tracks, thus inducing different DNA damage patterns. Particle energy distinguishes these two cases. It is also more readily available than LET from some transport codes. Therefore, a set of new analytical functions are provided, describing how DNA damage depends on particle energy. The results complement the analysis of the PARTRAC database, widening its potential of application and use for implementation in transport codes.

Keywords: ionizing radiation, track structure, DNA damage, double strand breaks, clustered damage, light ions, radiation transport codes

INTRODUCTION

Radiation transport codes are a key tool for many research and practical applications dealing with radiation-matter interactions. Many codes exist, including FLUKA, Geant4, MCNP, PHITS or TOPAS [1–5]; recent reviews focused on radiotherapy applications can be found in [6, 7]. In most cases a common issue has to be faced: The radiation field and the resulting dose distribution have to be captured at a rather large spatial scale, e.g., in a human body, in a high-energy physics detector, or in a shielding layer in a space habitat. At the same time, however, radiation action proceeds through energy deposition events (mainly ionizations and excitations of target atoms) that are spatially distributed with a ~nm spacing. Coupling these spatial scales and dealing with them in a common simulation framework is, without a doubt, a challenge. Two main approaches exist, namely the condensed-history approach, suitable for macroscopic simulations, and event-by-event track-structure approach, dedicated to microscopic and nanoscopic simulations. In the condensed-history approach, the radiation transport simulation algorithm deals with the cumulative effects of multiple particle collisions, approximated in a single "step." The step is modelled as a path free of interactions, and an overall change in particle energy (using stopping power functions) and direction of motion is considered at its end. The actual free path length, energy lost and deflection are sampled stochastically. Nuclear reactions, leading to the production of different particles after the interaction has taken place, can also be simulated. Codes using such an approach are widely and successfully applied and allow accurate calculation of, e.g., radiation dose in targets of different sizes. On the contrary, track-structure codes [8, 9] are developed to simulate all single collisions with atomic electrons in the target in an event-by-event manner. The outcome of the simulation is the set of spatial coordinates of ionizations and excitations induced by the primary particle and its secondary electrons, and energy depositions in each event, forming the particle track. Concerning different target materials, radiation transport with a condensed-history approach mainly requires the knowledge of particle stopping power (as well as cross-section data for nuclear reactions), while an event-by-event simulation requires accurate knowledge of all interaction cross sections with atomic electrons [10]. Track-structure calculations are therefore mostly performed in water only.

For medical applications of ionizing radiation, but also in radiation protection, the macroscopic scale of interest is that of the whole radiation field impacting on the person. Accurate calculations of physical absorbed dose are needed in the organs and tissues of the exposed person, even for radiotherapy applications not only in the treatment volume but also in surrounding regions [11, 12]. Different elemental compositions and tissue inhomogeneities must be considered. At the same time, radiation effects in terms, e.g., of cancer cell killing or inducing genomic aberrations or mutations can be traced back to radiation interactions taking place at the scale of sensitive subcellular targets such as nuclear DNA or chromosomal domains. The description and, as far as possible, prediction of these effects requires simulation tools with a track-structure approach, coupled to a software replica of the target genomic content. Also, in addition to interactions with the DNA molecule (direct damage), it is necessary to consider that energy depositions in water in the cell can lead to water radiolysis, with the production of free radicals that can diffuse, chemically react with one another and damage DNA (indirect damage). Advanced track-structure codes such as PARTRAC [8] have been developed in this sense, currently allowing the full simulation of the chain of events from radiation traversal of a single-cell model (using liquid water as a surrogate material) to the induction of initial DNA damage (as well as, to some extent, damage evolution and repair).

Within this general context, efforts are currently ongoing to develop biophysical simulation tools that can provide at the same time a macroscopic description of the radiation field and its consequences in terms of damage at the cellular/subcellular level, e.g., the Geant4/Geant4-DNA project [13]. However, different strategies can be pursued to couple existing radiation transport codes using the condensed-history approach with track-structure codes. This would lead to a better exploitation of available tools, extending the applicability of transport codes towards biological endpoints, and of track-structure codes towards larger volumes and inclusion of secondary particles produced by nuclear reactions. A simple coupling approach with a great potential consists in the implementation in radiation transport codes of analytical formulas or look-up tables that capture the results of track-structure simulations on the induced DNA damage. Proceeding in this way brings a number of important advantages: Existing radiation transport codes either already provide the information needed for the coupling, or can be easily developed to do so; The coupling can also be performed off-line by the users, requiring no real development of the transport code; Implementation of formulas or tables in the transport code also leads to a significant saving of computational time with respect to running new simulations.

The question then arises as to which information is best suited to make the bridge between the output of the radiation transport and the track-structure code. A radiation transport code should be able to describe the characteristics of the radiation field with a wide choice of observables (particle types, energy distribution, LET distribution, direction of motion, etc.) in targets of varying sizes, ideally down to the step length used for calculations in the condensed-history approach. Of course, a full characterization of the field at a spatial scale that corresponds to the volume of a single cell is neither practical nor reasonable to achieve in terms of computational time when considering a macroscopic target. For instance, in the scenario of a voxelized target, the typical size of the cubic voxel is of the order of ~1 mm, and averaging procedures can be used to extract parameters that describe the radiation field in the voxel. Interestingly, analytical formulas have been implemented, e.g., in the code PHITS, which allow calculation of the distribution of microdosimetric quantities in macroscopic target regions [5]. By definition, microdosimetric quantities as the lineal energy are built considering the stochasticity of energy depositions by radiation in sensitive sites of micrometric size. As such, it could be argued that they are ideal to characterize the radiation field in a single cell nucleus

that can be assumed as a quasi-spherical volume with a linear dimension of ~10 μm. These considerations are at the basis of our previous works, in which we proposed a full coupling between PHITS and PARTRAC to derive the RBE of neutrons of different energy [14, 15], as well as a full set of analytical functions [16] reproducing PARTRAC results on different types of DNA damage as a function of an LET estimate, when the cell nucleus is irradiated with a variety of light ions at radiotherapy-relevant energies down to stopping. Such LET estimate, obtained by dividing the dose delivered to the cell nucleus by particle fluence (with appropriate conversion of units), is indeed analogous to the concept of the dose-mean lineal energy in microdosimetry. However, some limitations exist for this coupling approach using LET-based functions: The dose-mean lineal energy (or a definition of LET that is coherent with that adopted in PARTRAC calculations) might not be readily available for all transport codes. Furthermore, the same LET value is crossed twice as the particle slows down, in its distal and proximal parts of the Bragg peak, but the track characteristics, including its biological effectiveness, are different. Consequently, when plotting DNA damage as a function of LET, hooks appear, and single-valued mathematical functions cannot reproduce the full set of results including the lowest particle energies. A representation of DNA damage as a function of particle energy can instead be proposed to solve this issue. It also has the advantage that particle energy distributions can be easily extracted from transport codes.

Starting from these considerations, we provide in this work a set of new analytical functions exploring how PARTRAC results on DNA damage depend on particle energy, for light ions up to Ne, with energies per nucleon (specific energies, hereafter termed just energies) from 0.5 GeV/u down to stopping. The new formulas reproduce DNA damage yields per unit dose or per particle track, and complement previous results for damage yields as a function of particle LET. Overall, different choices are thus made possible for transport code users who want to implement such formulas in a radiation transport code. We further discuss how the availability of these formulas sets the basis of an efficient strategy to perform the coupling between radiation transport and track-structure codes. We discuss the limitations of such a strategy and how these can be addressed, in particular in relation to the issue of electronic equilibrium. Results of the full coupling between transport and track-structure codes for specific case studies shall be presented elsewhere, this work widening the potential of application of PARTRAC results and their use for an extension of existing transport codes to derive DNA-damage-based estimates of biological effectiveness.

MATERIALS AND METHODS

PARTRAC Track-Structure Simulations

PARTRAC [8, 17–21] is a family of biophysical simulation tools for modelling the biological effects of ionizing radiation at subcellular and cellular scales. It possesses a modular structure that reflects the underpinning mechanisms and processes. Individual modules integrate knowledge from radiation physics, chemistry, biophysics of DNA and its radiation damage, and radiation biology. The modular structure of the tool facilitates model refinements, integration of novel features, as well as extensions to further endpoints.

The simulations start with a module that describes physical processes of radiation interaction with the traversed matter. The code is capable of handling photons, electrons, protons and light ions over a wide energy range as relevant for natural, medical and technical applications. Typically, liquid water is used as a surrogate for biological material. For photons, the user may specify a homogeneous medium with an arbitrary atomic composition. For each particle type, established cross-section data are implemented. The respective dataset is stochastically sampled to generate an *in silico* representation of the interaction pattern, in an event-by-event mode, i.e., simulating individual ionizations, excitations and further processes (except nuclear reactions). The primary particle is followed until stopping or until leaving the given volume of interest, which typically surrounds a cell. Also, all secondary electrons liberated by the primary particles are tracked, as well as all higher-order particles. Each such generated track is different, but they share some global features, e.g., dense core regions in ion tracks surrounded by penumbras with sparse secondary electron tracks.

In a subsequent module that represents pre-chemical and chemical processes of track development, individual ionization and excitation events are converted to reactive species or relaxed to water molecules. Branching ratios, yields of diverse species, and their diffusive properties are implemented. Diffusion of species is followed together with their mutual reactions, in a step-by-step mode. In addition to mutual reactions, the species are removed upon attacking cellular DNA, histones, or in non-specific reactions governed by their lifetimes.

Multi-scale DNA and chromatin models are implemented. They range from an atomic model of DNA double-helix, over its binding to nucleosomes, formation of ~30 nm chromatin fiber, its loops and domains to chromosome territories within cell nuclei. Two such multi-scale models are available in PARTRAC at present, a spherical one for human lymphocytes and an elliptical one for human fibroblasts.

By overlaying these DNA and chromatin models with radiation tracks in terms of energy deposition patterns (so-called direct radiation effects) and attacks of reactive species (indirect effects), DNA damage is scored. Energy deposits within the sugar-phosphate backbone as well as attacks of hydroxyl radicals are in a stochastic manner converted to DNA strand breaks. Breaks on both strands within a genomic distance of 10 base pairs (bp) are scored as double-strand breaks (DSBs). Even DSBs may cluster, especially for high-LET particles. DSB clusters are scored whenever two or more DSBs appear within 25 bp. DSB clusters are an example of clustered lesions (locally multiply damaged sites) that likely pose critical challenges to cellular repair systems, and may represent initial damage finally leading to chromosome aberrations and cell killing. The term DSB sites includes both isolated DSBs and their clusters: an isolated DSB forms a DSB site, and a cluster of, e.g., three DSBs separated by less than 25 bp from each other is scored as a single DSB site as well. Beyond this simple classification

scheme, PARTRAC includes another module that allows the user to score DNA fractionation patterns on numerous scales ranging from very short fragments (tens of bp) up to fragments of chromosomes (hundreds of Mbp).

Finally, much attention has been devoted in the last decade to the development of the repair module in PARTRAC [17, 18, 22–25]. It represents the non-homologous end-joining pathway of DSB repair, the dominant DSB repair in human cells in G0 and G1 cell-cycle phases. The module explicitly accounts for the action of repair enzymes as well as for the mobility of chromatin breaks. It has been extended to chromosome aberrations too. Promising preliminary results have been obtained for the endpoint of cell killing as well.

PARTRAC results have been validated against available large experimental datasets within radiation physics, chemistry, and biology, cf. [8] and Refs. therein. The tool has served as a benchmark for other codes. Its recent applications included a model that provided mechanistic interpretation for the biological effectiveness of neutrons [14, 15], a model of radiation-induced bystander effects [26–30], or a study on radiation effects on mitochondrial DNA [31].

In this work, we have analyzed the previously published comprehensive database of PARTRAC simulations on DNA damage induced by light ions [20, 21]. Model cell nuclei were irradiated by ^{1}H, ^{4}He, ^{7}Li, ^{9}Be, ^{11}B, ^{12}C, ^{14}N, ^{16}O or ^{20}Ne ions at starting energies of 0.25, 0.5, 1, 2, 4, 8, 16, 32, 64, 128, 256 or 512 MeV/u. The ions were started fully stripped of electrons. The ion source was an 80 μm^2 circle, placed tangentially to a model lymphocyte nucleus (sphere with 10 μm diameter, containing 6.6 Gbp DNA in 23 chromosome pairs). Interactions were scored in a spherical "world" region of interest with the diameter of 14.22 μm, concentric with the nucleus model. Per ion type and energy, at least 1,280 particles were simulated (up to 3.2 million high-energy protons). The simulations were divided into 256–8,192 runs with 5–3,200 particles per run. Statistical uncertainties are reported as ± 1.96 times the standard deviation, hence covering 95% confidence intervals on the simulated DNA damage yields, calculated based on Poisson distributions.

DSBs, DSB clusters and DSB sites were scored. From absolute numbers of the lesions and the deposited dose, damage yields per Gy per Gbp were calculated. In this work, this is referred to as a dose-based approach. Alternatively, damage yields were considered per track per Gbp, which may serve as a basis for a fluence-based approach. These two approaches can both be used to couple radiation transport to track-structure simulations using different strategies. It is up to the transport code user to select the appropriate one, depending on the availability of radiation transport results and on the specific case under study. This is addressed later in the discussion.

Analytical Representation of DNA Damage Yields

To enable the conversion from the dose-based approach to the fluence-based one, the simulation results on the dose deposited in the nucleus per track D_{track} (in Gy) were fitted as a function of the ion starting energy E (in MeV/u) by:

$$D_{track} = \frac{p_1 E^{p_2}}{\left(1 + \exp\left(p_3\right) E^{p_4}\right)^{p_5}}. \tag{1}$$

The selection of this functional form was motivated by the shape of the simulation results in a log-log scale (cf. the *Results* section). This function combines two power-law terms, E^{p_2} and $E^{p_2-p_4p_5}$, with a smooth, logistic-like transition in-between them. Parameters p_3 (used in an exponential form to guarantee positivity of the resulting power-law coefficients) and p_5 affect the transition region, and p_1 scales the magnitude of the function.

The yields Y of DSBs, DSB clusters and DSB sites (expressed per Gy per Gbp) were fitted as a function of the ion starting energy E (expressed in MeV/u) by:

$$Y = p_0 + p_1 \frac{1}{1 + \left(E \exp\left(p_2\right)\right)^{p_3}} \left(1 - \frac{1}{1 + \left(E \exp\left(p_4\right)\right)^{p_5}}\right) + p_6 \frac{1}{1 + \left(E \exp\left(p_7\right)\right)^{p_8}}. \tag{2}$$

These functions combine three power-law terms with logistic-like transitions in-between. For parameters $p > 0$, the first and the last term decrease, while the second one increases with increasing energy. Parameters p_2, p_4 and p_7 govern the position of these logistic power-law functions; p_3, p_5 and p_8 their slopes; p_1 and p_6 the magnitude of the effects; and p_0 depicts the high-energy asymptotic behavior. The high-energy (i.e., low-LET) behavior was taken from Ref. 16, using the following values: p_0 = 6.8 DSB, 0.07 DSB clusters, and 6.8 DSB sites per Gy per Gbp.

Parameters of these test functions were fitted to the results of track-structure simulations using non-linear model fitting in Matlab (The MathWorks Inc., United States). This was done for each damage type and each ion separately, and for per-track doses as well. Some terms or parameters were not needed in some cases, and were thus not included (cf. *Results*). A few parameter values were fixed manually (in particular the parameter p_8 for DSBs and their sites, cf. *Results*) in order to help avoid overfitting, especially to avoid local minima or maxima that otherwise might occur as mere artifacts of the fitting procedure, with no support by the simulation results. Damage yields per track per Gbp were then obtained by the product of **formula (2)** for the yields per Gy per Gbp and **formula (1)** for the dose per track.

Amorphous Track-Structure Calculations

With the given setup of PARTRAC track-structure simulations, only ions were considered whose track core regions hit the nucleus. Ions passing nearby and hitting the nucleus only by their penumbra regions were neglected. This approach was selected to limit the computational costs of track-structure simulations for high-energy ions that produce very wide but low-density penumbra regions, e.g., 512MeV/u protons liberating secondary electrons with ranges in water and hence track radius of a few millimetres but total LET (including the track core) of about 0.2 keV/μm only. To assess the limitations of this approach, additional calculations were performed using an amorphous track structure model [32] which assumes a radial dose distribution:

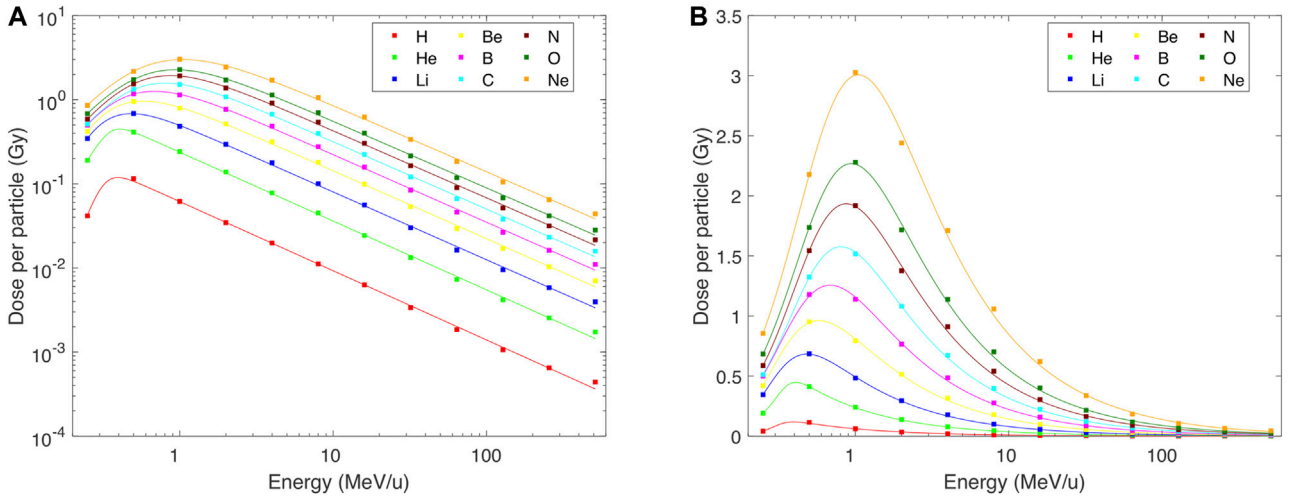

FIGURE 1 | Mean dose deposited to the lymphocyte nucleus per single track of H–Ne ions with starting energies from 0.25 to 512 MeV/u, as simulated with PARTRAC event-by-event track-structure simulations (symbols) and fitted by analytical formulas **Eq. 1** (lines) with parameters listed in **Table 1**. Panel **(A)** in logarithmic scale to highlight the wide range of values and the quality of fits; panel **(B)** in linear scale.

$$D(r) = \begin{cases} \lambda/r_c^2 & \text{for} \quad r < r_c = 0.3\,\text{nm}\,(\text{track core}), \\ \lambda/r^2 & \text{for} \quad r_c <= r <= r_{tr}\,(\text{penumbra}), \\ 0 & \text{for} \quad r > r_{tr}, \end{cases} \tag{3}$$

where the track radius r_{tr} (in μm) is given by $r_{tr} = 0.062\,E^{1.7}$, with E (MeV/u) denoting the ion energy [32, 33], and λ is an integration constant proportional to the LET of the track. The fraction of LET deposited in the inner part of the track (up to a specific distance R from the track axis, e.g., the radius of cell nucleus) was then calculated by:

$$f(R) = \frac{\ln(r_{tr}/R)}{0.5 + \ln(r_{tr}/r_c)} \quad \text{for} \quad r_{tr} > R, \qquad f(R) = 1 \text{ otherwise}, \tag{4}$$

where ln denotes natural logarithm. The average LET fraction deposited to the spherical cell nucleus by tracks that hit the nucleus by their core regions (and alternatively by nearby tracks) was calculated in Matlab (The MathWorks Inc., United States) by numerically integrating the radial dose distribution overlapping with the cell nucleus and averaging over the impact parameters (i.e., the distance of the track core from the cell nucleus centre).

RESULTS

Mean doses deposited per track to the spherical cell nucleus are presented vs particle starting energy in **Figure 1**. The results in **Figure 1** do not include tracks whose cores do not intersect the nucleus but whose penumbra may still deposit energy there. The results of PARTRAC event-by-event track-structure simulations are depicted by symbols. Lines show their fits using **formula (1)**, with parameters listed in **Table 1**. As the doses deposited per particle cover a very wide range, from 0.44 mGy for 512 MeV protons (H ions) to 3.03 Gy for 1 MeV/u Ne ions, we show the plot in both logarithmic and linear scales. Except for 512 MeV/u,

TABLE 1 | Parameters of analytical functions (**Eq. 1**) describing the dose deposited to the cell nucleus (in Gy) per single started particle as a function of its starting energy (in MeV/u).

Ion	p_1	p_2	p_3	p_4	p_5
H	46.99	5[a]	9.684	8.493	0.6855
He	12.37	3[a]	9.657	9.327	0.4093
Li	4,926	5.725	4.053	2.887	2.262
Be	25,010	6.094	3.209	2.169	3.182
B	83.77	3.169	2.171	2.114	1.879
C	20.19	2.438	1.594	2.234	1.45
N	23.89	2.444	1.407	2.087	1.553
O	21.74	2.275	1.174	1.958	1.567
Ne	32.44	2.329	1.003	1.723	1.809

[a]*Parameter value fixed manually.*

the analytical formulas nicely reproduce the simulation results. In particular, they capture the overall power-law increase of deposited dose with decreasing energy, down to about 0.5–1 MeV/u. Also the decrease of deposited dose with further decreasing energy is reproduced. Note that the plotted doses are mean values over all simulated tracks. The actual energy deposit by a track depends on its path length within the nucleus, and hence hugely differs from tracks whose cores hit the nucleus centrally to those hitting it only peripherally. Even larger variations would be obtained if also tracks were considered that overlap with the nucleus by their penumbras only (cf. *Discussion*). The stochastic nature of individual interactions plays a minor role only, due to the high numbers of events per track.

DNA damage patterns largely but not fully follow the pattern of the dose per track. Indeed, when the yields of DSBs, DSB clusters or DSB sites are plotted per track (**Figures 2–4** panels A and B), the overall patterns resemble those in **Figure 1**: The induction of each of these damage classes increases with decreasing energy, approximately according to a power law

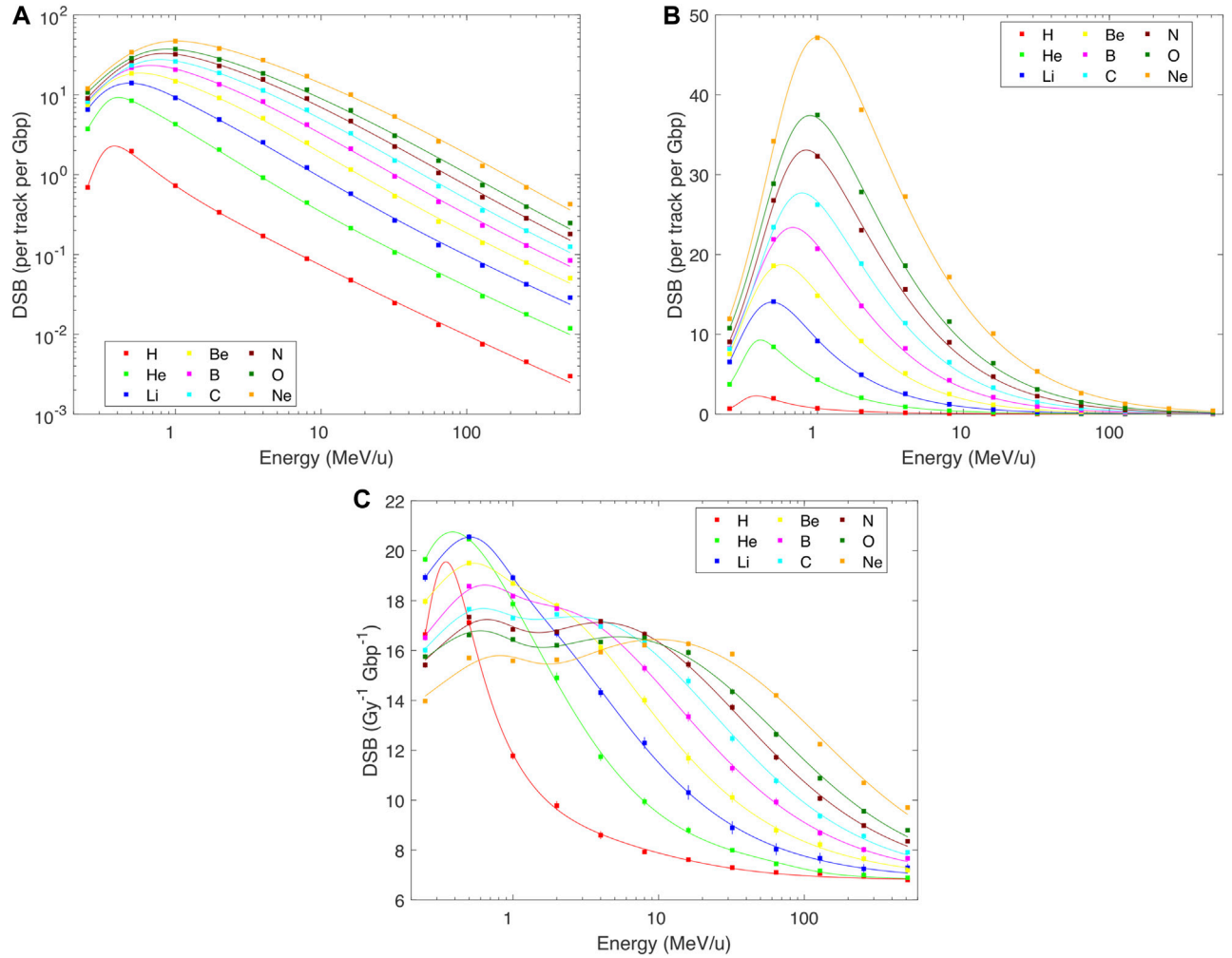

FIGURE 2 | PARTRAC simulations of the yields of DNA double-strand breaks (DSBs) in human lymphocytes by H–Ne ions with starting energies from 0.25 to 512 MeV/u (symbols), fitted by analytical formulas (lines). Error bars depict estimated 95% confidence intervals of the simulated results. Where error bars are not visible, they are smaller than the symbols. Panels **(A,B)**: yields per track per Gbp, in logarithmic and linear scales, calculated as a product of **Eqs 1** and **2**, details in the text; panel **C:** yield per Gy per Gbp, in linear scale, fitted by **Eq. 2** with parameters in **Table 2**.

down to about 0.5–1 MeV/u, and then decreases. However, a finer structure is revealed when damage yields are analyzed per unit dose: Total DSB yields (**Figure 2C**) increase from about 6.8 DSB per Gy per Gbp at high energies to about three times higher values at around 1 MeV/u for light ions, and saturate at around 16 DSB per Gy per Gbp for B–Ne ions below about 10 MeV/u. There is a systematic indication for a wavy behavior at these low energies for relatively heavy ions. Much more pronounced variations are seen for DSB clusters: Their yields (**Figures 3C,D**) increase from values as low as 0.07 per Gy per Gbp at high energies to about 1 for H, 2.6 for He, and 1.9–2.8 per Gy per Gbp for heavier ions at energies of 1–10 MeV/u. Similarly to DSBs, also for clusters the simulations predict a wavy behavior with local minima around 1 MeV/u for ions from C to Ne. The yields of DSB sites (**Figure 4C**) at high energies are about equal to total DSBs, as the vast majority of DSBs are formed as isolated ones. At low energies, however, the yields of DSB sites drop down, for the heaviest studied ions getting close to or even below the high-energy values. This happens as an increasing fraction of DSBs form clusters, which are counted as single sites only but as multiple DSBs. The simulations suggest that cluster yields may further increase at energies <0.5 MeV/u. For all damage classes, the results of track-structure simulations are nicely reproduced by the present analytical formulas. This holds not only for the damage yields per Gy (panels C) that were fitted by the formulas, but also for the yields per track (panels A and B) which were not fitted directly. Even the wide ranges of DSB cluster yields are represented properly (cf. the log-log plot in **Figure 3D**).

Estimates of the deposited energy that are not reflected by the present track-structure simulations are shown in **Figure 5**, using the amorphous track-structure model. At high energies, only a part of the ion LET is actually deposited to the traversed nucleus (black circles). For instance, for 512 MeV/u ions this fraction

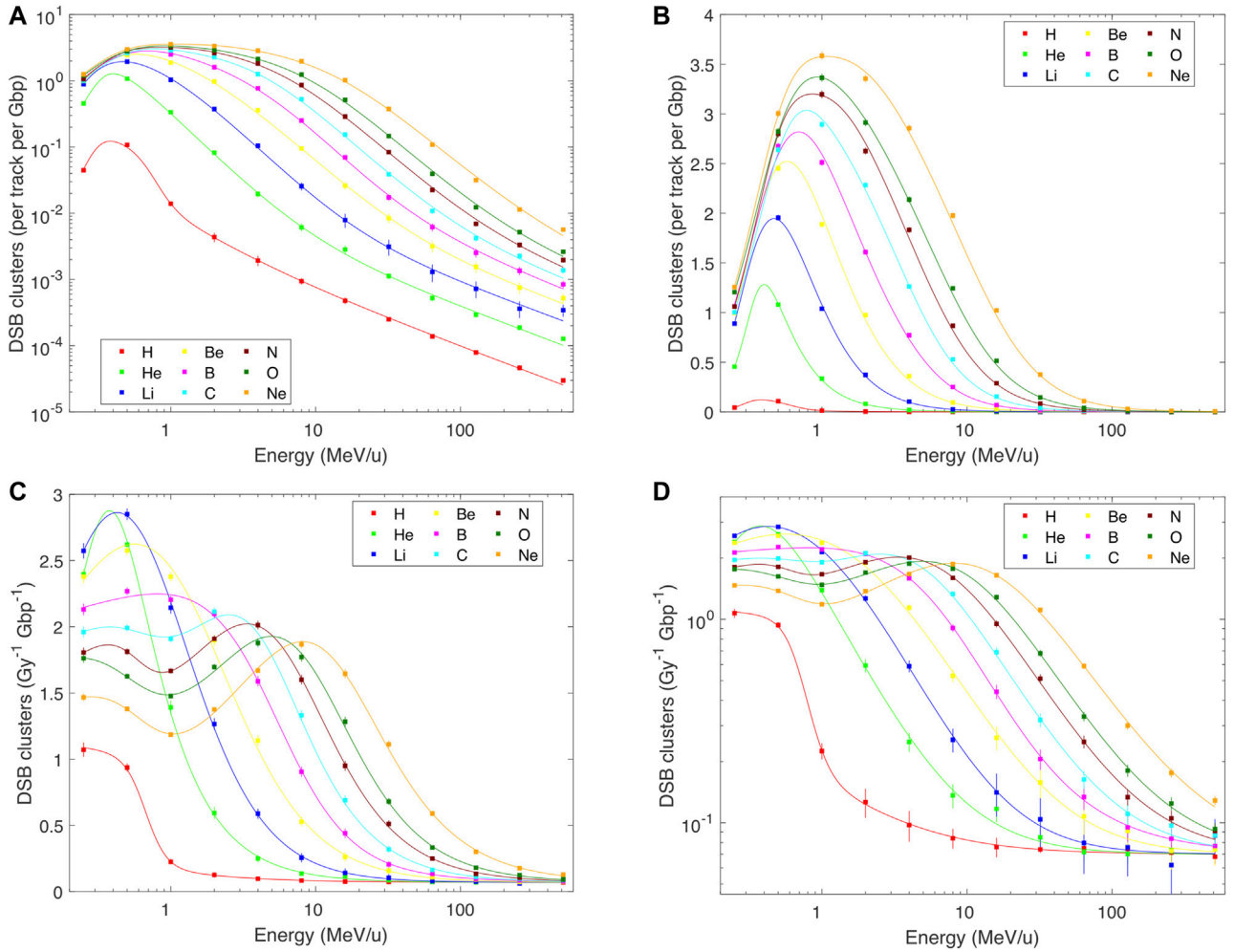

FIGURE 3 | PARTRAC simulations (symbols) and their fits by analytical formulas (lines) for the yields of DNA double-strand break clusters (DSB clusters) in human lymphocytes by H–Ne ions with starting energies from 0.25 to 512 MeV/u. Error bars depict estimated 95% confidence intervals of the simulated results. Where error bars are not visible, they are smaller than the symbols. Panels **(A,B)**: yields per track per Gbp, in logarithmic and linear scales, calculated as a product of **Eqs 1** and **2**, details in the text; panels **(C,D)**: yield per Gy per Gbp, in linear and logarithmic scales, fitted by **Eq. 2** with parameters in **Table 2**.

drops to about 60%, so that the reported PARTRAC simulations can be expected to miss almost 40% of the total energy deposited by the track. However, this missing fraction rapidly decreases with decreasing ion energy, e.g., to 23% for 64 MeV/u tracks, and further diminishes (down to almost a zero fraction) for tracks narrower than the cell nucleus (energies below about 14 MeV/u). To reduce the missing fraction at a given energy, tracks passing in the vicinity of the nucleus would have to be included (coloured circles). However, the source and the simulation region would have to be largely increased, up to mm-sized regions for high-energy ions, with high computational costs of the track-structure simulations. Fortunately, the results of a simple formula, **Eq. 4**, for dose in the inner track part (black stars) provide a useful approximation of the fraction of energy deposited to the nucleus and hence also for the fraction that is missing in the track-structure simulations of high-energy ions, and can be used in conjunction with **Eqs 1** and **2** in a fluence-based coupling strategy (cf. *Discussion*).

DISCUSSION

Analytical formulas have been provided, which represent the total yields of DNA double-strand breaks, their clusters, and DSB sites as a function of particle starting energy. It has to be made clear that the aim of this work was neither to provide a theoretical model of DNA damage by ion beams, nor to develop an optimal model to reproduce simulation data in terms of using a strictly limited number of parameters. The aim was solely to reproduce the simulation data in a phenomenological way, but with a high degree of accuracy, to facilitate their use within the framework of a radiation transport code.

Three classes of DNA damage were analyzed, in all cases considering the total damage, i.e., resulting from DNA lesions induced both directly (*via* direct energy deposition to DNA) and indirectly (mediated by free radicals). We have chosen to include in this study only selected classes of DNA damage, as justified in

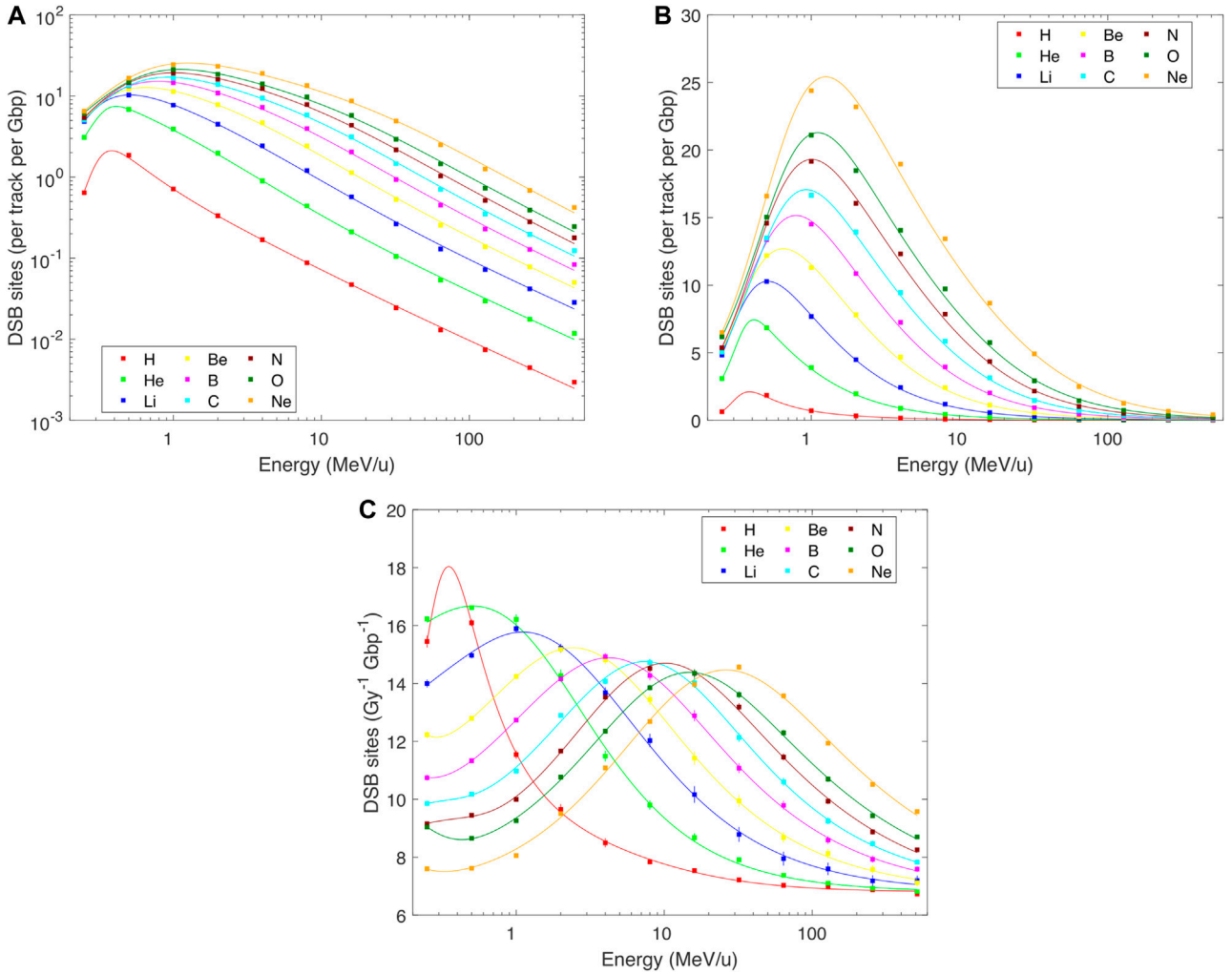

FIGURE 4 | PARTRAC simulations on DNA double-strand break sites (DSB sites) induced in human lymphocytes by H–Ne ions with starting energies from 0.25 to 512 MeV/u (symbols), fitted by analytical formulas (lines). Error bars depict estimated 95% confidence intervals of the simulated results. Where error bars are not visible, they are smaller than the symbols. Panels **(A,B)**: yields per track per Gbp, in logarithmic and linear scales, calculated as a product of **Eqs 1** and **2**, details in the text; panels **(C)**: yield per Gy per Gbp, in linear scale, fitted by **Eq. 2** with parameters in **Table 2**.

the following: DSBs are commonly considered as key initial lesions related to biological effects of ionizing radiation. However, even the majority of DSBs can be repaired. Clustered DNA lesions, in particular DSB clusters, likely pose critical challenges to the cellular repair system, and may typically lead to lethal events [34]. When patterns obtained for diverse classes of DNA damage are compared to those observed for cell killing in dependence on particle LET, a remarkably close match is seen for DSB sites [20], suggesting this endpoint is a good indicator of the outcome of the exposure in terms of inactivating cell replication.

The basic mechanistic assumption that underpins the present coupling strategy is that the analyzed DNA damage is additive, i.e., that the yields of the studied damage classes upon a mixed-field irradiation are given by a sum of yields from individual tracks. Due to the local nature of DSBs, their clusters and sites, this assumption is fulfilled up to doses of the order of several hundred Gy [16, 35]: The probability that, e.g., two DSBs induced by different primary particles would combine into a DSB cluster is negligible, since the two DSBs would have to occur within 25 bp. The same argument holds even stronger for a combination of two strand breaks into a DSB, which would have to take place within 10 bp. Note that deviations from additivity (and linearity) appear at much lower doses for larger-scale effects such as fragmentation on Mbp scales or chromosome aberrations, which typically happen over micrometer distances.

It is important to note that the setup used in the track-structure simulations that were performed to obtain the results fitted in this work does not provide electronic equilibrium conditions, both longitudinally and laterally. This is because the ions were started from a source directly adjacent to the cell nucleus and with an area as large as the nucleus section. This setup differs from the typical simulation with a transport code, where, except for the initial build-up region, the equilibrium

TABLE 2 | Parameters of analytical functions (**Eq. 2**) describing the yields of DSBs, DSB clusters or DSB sites (expressed per Gy per Gbp) as a function of the particle starting energy (in MeV/u).

Damage class	Ion	p_0	p_1	p_2	p_3	p_4	p_5	p_6	p_7	p_8
DSBs	H	6.8	2,225	4.383	1.496	1.229	5[a]	2.117	−2.157	1[a]
	He	6.8	20.34	−0.1394	0.9576	1.836	2.494	0.3958	−4.489	3[a]
	Li	6.8	24.72	−0.4768	0.7773	0.5978	1.275	7.005	0.2697	3[a]
	Be	6.8	27.11	−0.7543	0.7285	0.2434	1.284	7.271	0.3267	3[a]
	B	6.8	16.6	−2.223	0.765	0.5143	1.331	6.26	0.222	3[a]
	C	6.8	15.3	−2.886	0.7945	0.4991	1.074	5.31	0.2156	3[a]
	N	6.8	14.35	−3.385	0.7939	0.2434	1.119	5.882	0.0947	3[a]
	O	6.8	13[a]	−4.001	0.8346	0.6792	0.7566	4.227	0.118	3[a]
	Ne	6.8	12.25	−4.733	0.8575	0.2528	0.7971	3.903	−0.124	3[a]
DSB clusters	H	0.07	0.2727	0.7528	N.A.[b]	N.A.[b]	N.A.[b]	0.842	0.4005	6[a]
	He	0.07	7,397	6.215	1.387	1.032	3.036	N.A.[b]	N.A.[b]	N.A.[b]
	Li	0.07	4.78	0.04548	1.478	1.655	1.446	N.A.[b]	N.A.[b]	N.A.[b]
	Be	0.07	4.807	−0.5186	1.354	1.446	0.7224	N.A.[b]	N.A.[b]	N.A.[b]
	B	0.07	27.87	−1.602	1.717	−30.49	0.07955	0.04258	−4.197	0.9484
	C	0.07	14,050	−1.436	1.892	−15.45	0.5891	1.322	0.3845	2.319
	N	0.07	9,846	−1.878	1.699	−20.92	0.4185	0.9001	0.5209	3.879
	O	0.07	16,580	−2.193	1.717	−20.58	0.4632	1.229	0.5935	2.352
	Ne	0.07	19,920	−2.63	1.65	−20.55	0.4852	0.9957	0.4774	2.837
DSB sites	H	6.8	1,534	4.445	1.407	1.238	5[a]	2.132	−1.892	1[a]
	He	6.8	2,471	−0.2154	1.186	−16.29	0.3077	N.A.[b]	N.A.[b]	N.A.[b]
	Li	6.8	619.8	−0.8108	1.061	−12.27	0.3134	−0.5969	0.3384	3[a]
	Be	6.8	1,130	−1.12	1.2	−9.143	0.5235	107	2.909	3[a]
	B	6.8	1,106	−1.594	1.177	−9.346	0.5437	2.789	1.681	3[a]
	C	6.8	11,550	−2.058	1.258	−12.88	0.6085	1.429	0.9488	3[a]
	N	6.8	1,226	−2.093	1.268	−8.002	0.736	1.319	0.7188	3[a]
	O	6.8	1,473	−2.476	1.229	−8.963	0.7052	2.987	1.494	3[a]
	Ne	6.8	74.89	−0.7502	0.5977	−3.04	1.118	3,773	4.454	3[a]

[a]*Parameter value fixed manually.*

[b]*N.A.: not applicable; the corresponding term not needed and hence not included in the fit formula for the given damage type and ion species.*

conditions are fulfilled throughout the volume of interest. Fortunately, the longitudinal difference does not impose a serious limitation on the applicability of the present coupling strategy, at least in the dose-based scheme, as shown by pilot track-structure simulations with gradually increased source-to-nucleus distances [21]: Both the deposited dose and damage yields (as absolute numbers of lesions) are underestimated by present simulations compared with the case of electronic equilibrium, with differences that can reach 20% for high-energy ions. However, these effects almost cancel out in the yields of DSB classes per unit dose, which differ between the two setups by a few percent only. Similarly, also the lateral difference hardly affects the applicability of the dose-based scheme, since considerable fractions of energy deposited by a track are not reflected by the present setup only for high-energy, low-density tracks. The present setup with an ion source not larger than the cross section of a cell nucleus ignores energy deposited to the nucleus by tracks passing not directly through the nucleus but only in its vicinity (up to a few millimeters at the highest energies), i.e., tracks that overlap with the nucleus by their penumbras only. When the per-track dose and yields of DSB classes (fluence-based scheme) are considered, for high-energy ions one should add the contribution from electrons not included in the results reported here but present under the equilibrium conditions. Both longitudinally and laterally, this may correspond to spatial scales of a few millimeters. Laterally, although even high-energy tracks contain a core region with energy deposition density much higher than in the penumbra region (where it drops with the inverse square of the distance from track axis), notable fractions of energy may be deposited in large outer regions of the track. Importantly, energy depositions in the outer region are very sparse, and the resulting DNA damage corresponds to the low-LET limit of the present approach, i.e., to the yields of $p_0 = 6.8$ DSB, 0.07 DSB clusters, and 6.8 DSB sites per Gy per Gbp. Yet the doses and damage yields should be added when using the fluence-based approach for the highest particle energies. **Equation 4** used in conjunction with our p_0 parameter values provides a first quick means for doing so. Further studies including the full simulation of tracks with PARTRAC, the inclusion of larger track-to-nucleus distances and the derivation of radial dose distribution profiles would offer the possibility of a test of validity and further refinement of this correction using the same approach.

The results presented in this work set the basis of a strategy to couple radiation transport and track-structure simulations, as discussed hereafter. The coupling could be performed in a dose-based or a fluence-based scheme, with the limitation just discussed. The main piece of information that needs to be extracted from the radiation transport code is the particle type and energy distributions at the site of interest. This means characterizing particle types and their energies at the entrance

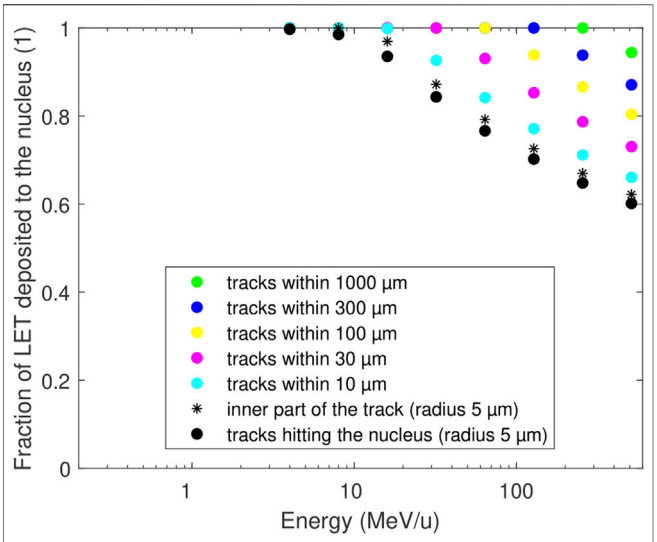

FIGURE 5 | Energy deposited to a cell nucleus when only tracks are considered that directly hit the nucleus with their cores (black circles) as in the present track-structure simulations, or including the contribution from all tracks within a larger region (coloured symbols) at a given fluence. The deposited energy is expressed as the fraction of the particle LET (linear energy transfer). The mean deposit per track directly hitting the nucleus (black circles) can be approximated by the energy deposit by the inner part of the track with the same size, **Eq. 4** (black stars). Calculations based on the amorphous track structure model.

plane tangential to the cell nucleus. In most applications, the radiation field characteristics will hardly vary over several neighbouring cells, so that using a voxel size of ~10 µm containing a single cell only would be unnecessarily detailed. However, typical voxel sizes in radiation transport codes of ~1 mm may be too coarse. Finer voxelization may be needed in the regions of spatially highly varying field characteristics, such as narrow Bragg peak regions in active scanning techniques in hadron radiotherapy, or when dealing with short-range alpha particles from internal emitters or boron capture therapies. Compared with simulations of (physical) dose deposition only, this may involve some additional interpolation (or even extrapolation) steps or averaging procedures.

A strategy to couple transport codes with track-structure simulations based on the use of a dose-based formalism would require the explicit calculation of the dose delivered to the target site per particle type with the radiation transport code. Ideally, one should then calculate the dose-weighted distribution of particle energies in the same site, and sum all damage yields corresponding to the different energy bins as calculated with the analytical formula of **Eq. 2**, to finally obtain the total damage. Another possibility would be to evaluate the first moment of the dose-weighted distribution of particle energy (basically, the energy value at which, on average, a given kind of particle is delivering dose) and apply **Eq. 2** to this single energy value. This approximation is conceptually similar to the coupling performed with the application of LET-based formulas using the dose-average LET in the target site as a single LET value for a given species, as done in our previous work [14]. Its validity would have to be tested by dedicated simulations.

Within a fluence-based approach, both the dose to target nuclei (**Eq. 1**) and DNA damage induced per particle track (**Eq. 1** multiplied by **Eq. 2**) are made available. A strategy based on the use of such an approach would then require the calculation of particle fluence (distribution in energy bins) for all particle species at the entrance of the target site. As discussed above, the full distribution of particle energies could possibly be replaced by a single average value, but also in this case the use of the dose-weighted average seems more suited than the fluence-weighted one. The extent to which the use of average energy values represents a good approximation should be investigated in the specific case. Generally speaking, the use of look-up tables with fluence-to-dose conversion factors is a common solution proposed by, e.g., ICRP publications for radiation protection applications. The fluence-based approach with analytical functions proposed in this work represents an analogous solution. It complements the fluence-to-dose conversion factors with fluence-to-damage ones that can eventually be used to apply a biological "weight" on top of the (physical) absorbed dose.

The present work complements the analysis of our previous study [16], where DNA damage yields were parameterized as a function of particle LET in the cell nucleus. Parameterizing DNA damage in terms of particle energy rather than LET has several advantages: First, particle energy is more readily available from transport codes than LET in the restricted sense as obtained from PARTRAC track-structure simulations, i.e., as energy deposited to the cell nucleus per unit track length. This LET estimate bears a large similarity to the microdosimetric lineal energy, but the availability of microdosimetric quantities is limited to a few transport codes such as PHITS. Second, the use of energy circumvents the issue of the same LET value that appears at two different energies during the particle slowing down. Thus the energy-based parameterization enables using a single mathematical function to describe the particle effectiveness in inducing DNA damage from fast down to stopping particles. Third, not only the most stable isotopes considered in this work but also other ones such as ^{2}H, ^{3}He or ^{11}C are present in mixed fields generated when irradiating, e.g., with a ^{12}C beam. DNA damage induction by diverse isotopes of the same species has not been explicitly addressed by PARTRAC simulations so far. However, one may foresee that, perhaps except for the Bragg peak region (energies below a few MeV/u), electronic interactions are very similar for isotopes with the same atomic number and charge at the same velocity, i.e., at the same energy per nucleon (specific energy). Their LET values, however, differ due to the differing masses. While a dedicated LET-based function depicting the effectiveness in inducing DNA damage would thus have to be used for each isotope, the energy parameterizations presented in this work should be largely generally applicable. Simulations directed at testing this hypothesis shall be performed in the future.

In conclusion, the present results provide a basis for coupling radiation transport codes to PARTRAC track-structure simulations. Such a coupling combines the strengths of both approaches. Transport codes bring the ability to deal with macroscopic scales, and track-structure simulations provide detailed representation of the underpinning mechanisms from energy deposition by radiation to the induction of DNA damage. The selection of the actual

coupling strategy *via* a dose- or fluence-based approach and characterizing the radiation field by energy or LET distributions or weighted mean values depends on the particular transport code and specific situation studied. The provided analytical formulas represent a rather simple solution that opens the way to many future applications, including but not limited to modelling the biological effects of ion beam radiotherapy, proton boron capture therapy and boron neutron capture therapy.

DATA AVAILABILITY STATEMENT

The original contributions presented in the study are included in the article/Supplementary Material, further inquiries can be directed to the corresponding authors.

AUTHOR CONTRIBUTIONS

PK, WF, AO, and GB designed the research. WF, PK, and GB performed PARTRAC simulations. PK proposed the analytical formulas and performed the fits. PK, WF, and GB interpreted the results. PK and GB drafted the manuscript. All authors critically read and reviewed the manuscript.

FUNDING

The research leading to these results was supported by institutional funding of the Nuclear Physics Institute CAS, Helmholtz Zentrum München and University of Pavia, and partially by the Czech Science Foundation (project number 21-06451S).

REFERENCES

1. Battistoni G, Bauer J, Boehlen TT, Cerutti F, Chin MPW, and Dos Santos Augusto R, et al. The FLUKA Code: an Accurate Simulation Tool for Particle Therapy. *Front Oncol* (2016) 6:116. doi:10.3389/fonc.2016.00116
2. Allison J, Amako K, Apostolakis J, Arce P, Asai M, and Aso T, et al. Recent Developments in Geant4. *Nucl Instr Methods Phys Res Section A: Acc Spectrometers, Detectors Associated Equipment* (2016) 835:186–225. doi:10.1016/j.nima.2016.06.125
3. Werner CJ, Bull JS, Solomon CJ, Brown FB, McKinney GW, and Rising ME, et al. MCNP Version 6.2 Release Notes. In: *MCNP6.2 Release Notes*. Los Alamos: Los Alamos National Laboratory, report LA-UR-18-20808 (2018). doi:10.2172/1419730
4. Faddegon B, Ramos-Méndez J, Schuemann J, McNamara A, Shin J, and Perl J, et al. The TOPAS Tool for Particle Simulation, a Monte Carlo Simulation Tool for Physics, Biology and Clinical Research. *Physica Med* (2020) 72:114–21. doi:10.1016/j.ejmp.2020.03.019
5. Sato T, Iwamoto Y, Hashimoto S, Ogawa T, Furuta T, and Abe S-i, et al. Features of Particle and Heavy Ion Transport Code System (PHITS) Version 3.02. *J Nucl Sci Technol* (2018) 55:684–90. doi:10.1080/00223131.2017.1419890
6. Brualla L, Rodriguez M, and Lallena AM. Monte Carlo Systems Used for Treatment Planning and Dose Verification. *Strahlenther Onkol* (2017) 193:243–59. doi:10.1007/s00066-016-1075-8
7. Muraro S, Battistoni G, and Kraan AC. Challenges in Monte Carlo Simulations as Clinical and Research Tool in Particle Therapy: a Review. *Front Phys* (2020) 8:567800. doi:10.3389/fphy.2020.567800
8. Friedland W, Dingfelder M, Kundrát P, and Jacob P. Track Structures, DNA Targets and Radiation Effects in the Biophysical Monte Carlo Simulation Code PARTRAC. *Mutat Research/Fundamental Mol Mech Mutagenesis* (2011) 711:28–40. doi:10.1016/j.mrfmmm.2011.01.003
9. Nikjoo H, Emfietzoglou D, Liamsuwan T, Taleei R, Liljequist D, and Uehara S. Radiation Track, DNA Damage and Response-A Review. *Rep Prog Phys* (2016) 79:116601. doi:10.1088/0034-4885/79/11/116601
10. Dingfelder M. Track-structure Simulations for Charged Particles. *Health Phys* (2012) 103:590–5. doi:10.1097/HP.0b013e3182621292
11. Hall EJ, and Giaccia AJ. *Radiobiology for the Radiologist*. 8th ed. 9781496335418. Philadelphia: Wolters Kluwer (2019).
12. Friedland W, and Kundrát P. Modeling of Radiation Effects in Cells and Tissues. In: Brahme A, editor. *Comprehensive Biomedical Physics*, Vol. 9. Amsterdam: Elsevier (2014). p. 105–42. doi:10.1016/b978-0-444-53632-7.00906-0
13. Geant4-DNA. Geant4-DNA: Extending the Geant4 Monte Carlo Simulation Toolkit for Radiobiology (2021). Available from: http://geant4-dna.org/ (Accessed May 20, 2021).
14. Baiocco G, Barbieri S, Babini G, Morini J, Alloni D, and Friedland W, et al. The Origin of Neutron Biological Effectiveness as a Function of Energy. *Sci Rep* (2016) 6:34033. doi:10.1038/srep34033
15. Baiocco G, Barbieri S, Babini G, Morini J, Friedland W, and Kundrát P, et al. At the Physics-Biology Interface: the Neutron Affair. *Radiat Prot Dosimetry* (2018) 180:278–81. doi:10.1093/rpd/ncx222
16. Kundrát P, Friedland W, Becker J, Eidemüller M, Ottolenghi A, and Baiocco G. Analytical Formulas Representing Track-Structure Simulations on DNA Damage Induced by Protons and Light Ions at Radiotherapy-Relevant Energies. *Sci Rep* (2020) 10:15775. doi:10.1038/s41598-020-72857-z
17. Friedland W, Jacob P, and Kundrát P. Stochastic Simulation of DNA Double-Strand Break Repair by Non-homologous End Joining Based on Track Structure Calculations. *Radiat Res* (2010) 173:677–88. doi:10.1667/RR1965.1
18. Friedland W, and Kundrát P. Track Structure Based Modelling of Chromosome Aberrations after Photon and Alpha-Particle Irradiation. *Mutat Res* (2013) 756:213–23. doi:10.1016/j.mrgentox.2013.06.013
19. Schmitt E, Friedland W, Kundrát P, Dingfelder M, and Ottolenghi A. Cross-section Scaling for Track Structure Simulations of Low-Energy Ions in Liquid Water. *Radiat Prot Dosimetry* (2015) 166:15–8. doi:10.1093/rpd/ncv302
20. Friedland W, Schmitt E, Kundrát P, Dingfelder M, Baiocco G, and Barbieri S, et al. Comprehensive Track-Structure Based Evaluation of DNA Damage by Light Ions from Radiotherapy-Relevant Energies Down to Stopping. *Sci Rep* (2017) 7:45161. doi:10.1038/srep45161
21. Friedland W, Kundrát P, Schmitt E, Becker J, and Li W. Modeling DNA Damage by Photons and Light Ions over Energy Ranges Used in Medical Applications. *Radiat Prot Dosimetry* (2019) 183:84–8. doi:10.1093/rpd/ncy245
22. Friedland W, Kundrát P, and Schmitt E. Modelling Proton Bunches Focussed to Submicrometre Scales: Low-LET Radiation Damage in High-LET-like Spatial Structure. *Radiat Prot Dosimetry* (2015) 166:34–7. doi:10.1093/rpd/ncv146
23. Friedland W, and Kundrát P. Chromosome Aberration Model Combining Radiation Tracks, Chromatin Structure, DSB Repair and Chromatin Mobility. *Radiat Prot Dosimetry* (2015) 166:71–4. doi:10.1093/rpd/ncv174
24. Schmid TE, Friedland W, Greubel C, Girst S, Reindl J, and Siebenwirth C, et al. Sub-micrometer 20MeV Protons or 45MeV Lithium Spot Irradiation Enhances Yields of Dicentric Chromosomes Due to Clustering of DNA Double-Strand Breaks. *Mutat Res Genet Toxicol Environ Mutagen* (2015) 793:30–40. doi:10.1016/j.mrgentox.2015.07.015
25. Friedland W, Kundrát P, Schmitt E, Becker J, Ilicic K, and Greubel C, et al. Modeling Studies on Dicentrics Induction after Sub-micrometer Focused Ion Beam Grid Irradiation. *Radiat Prot Dosimetry* (2019) 183:40–4. doi:10.1093/rpd/ncy266
26. Friedland W, Kundrát P, and Jacob P. Track Structure Calculations on Hypothetical Subcellular Targets for the Release of Cell-Killing Signals in Bystander Experiments with Medium Transfer. *Radiat Prot Dosimetry* (2011) 143:325–9. doi:10.1093/rpd/ncq401

27. Kundrát P, and Friedland W. Track Structure Calculations on Intracellular Targets Responsible for Signal Release in Bystander Experiments with Transfer of Irradiated Cell-Conditioned Medium. *Int J Radiat Biol* (2012) 88:98–102. doi:10.3109/09553002.2011.595874
28. Kundrát P, and Friedland W. Non-linear Response of Cells to Signals Leads to Revised Characteristics of Bystander Effects Inferred from Their Modelling. *Int J Radiat Biol* (2012) 88:743–50. doi:10.3109/09553002.2012.698029
29. Kundrát P, and Friedland W. Mechanistic Modelling of Radiation-Induced Bystander Effects. *Radiat Prot Dosimetry* (2015) 166:148–51. doi:10.1093/rpd/ncv170
30. Kundrát P, and Friedland W. Enhanced Release of Primary Signals May Render Intercellular Signalling Ineffective Due to Spatial Aspects. *Sci Rep* (2016) 6:33214. doi:10.1038/srep33214
31. Friedland W, Schmitt E, Kundrát P, Baiocco G, and Ottolenghi A. Track-structure Simulations of Energy Deposition Patterns to Mitochondria and Damage to Their DNA. *Int J Radiat Biol* (2019) 95:3–11. doi:10.1080/09553002.2018.1450532
32. Elsässer T, Cunrath R, Krämer M, and Scholz M. Impact of Track Structure Calculations on Biological Treatment Planning in Ion Radiotherapy. *New J Phys* (2008) 10:075005. doi:10.1088/1367-2630/10/7/075005
33. Kiefer J, and Straaten H. A Model of Ion Track Structure Based on Classical Collision Dynamics (Radiobiology Application). *Phys Med Biol* (1986) 31:1201–9. doi:10.1088/0031-9155/31/11/002
34. Nickoloff JA, Sharma N, and Taylor L. Clustered DNA Double-Strand Breaks: Biological Effects and Relevance to Cancer Radiotherapy. *Genes* (2020) 11:99. doi:10.3390/genes11010099
35. Kreipl MS, Friedland W, and Paretzke HG. Interaction of Ion Tracks in Spatial and Temporal Proximity. *Radiat Environ Biophys* (2009) 48:349–59. doi:10.1007/s00411-009-0234-z

Conflict of Interest: The authors declare that the research was conducted in the absence of any commercial or financial relationships that could be construed as a potential conflict of interest.

Publisher's Note: All claims expressed in this article are solely those of the authors and do not necessarily represent those of their affiliated organizations, or those of the publisher, the editors and the reviewers. Any product that may be evaluated in this article, or claim that may be made by its manufacturer, is not guaranteed or endorsed by the publisher.

frontiers in Physics

REVIEW
published: 27 October 2021
doi: 10.3389/fphy.2021.718873

Variance-Reduction Methods for Monte Carlo Simulation of Radiation Transport

Salvador García-Pareja[1]*, *Antonio M. Lallena*[2] *and Francesc Salvat*[3]

[1]Unidad de Gestión Clínica de Radiofísica Hospitalaria, Hospital Regional Universitario de Málaga, Málaga, Spain, [2]Departamento de Física Atómica, Molecular y Nuclear, Universidad de Granada, Granada, Spain, [3]Facultat de Física (FQA and ICC), Universitat de Barcelona, Barcelona, Spain

After a brief description of the essentials of Monte Carlo simulation methods and the definition of simulation efficiency, the rationale for variance-reduction techniques is presented. Popular variance-reduction techniques applicable to Monte Carlo simulations of radiation transport are described and motivated. The focus is on those techniques that can be used with any transport code, irrespective of the strategies used to track charged particles; they operate by manipulating either the number and weights of the transported particles or the mean free paths of the various interaction mechanisms. The considered techniques are 1) splitting and Russian roulette, with the ant colony method as builder of importance maps, 2) exponential transform and interaction-forcing biasing, 3) Woodcock or delta-scattering method, 4) interaction forcing, and 5) proper use of symmetries and combinations of different techniques. Illustrative results from analog simulations (without recourse to variance-reduction) and from variance-reduced simulations of various transport problems are presented.

Keywords: Monte Carlo simulation, statistical uncertainties, variance-reduction methods, splitting and Russian roulette, ant colony algorithms, interaction forcing, delta scattering

OPEN ACCESS

Edited by:
Susanna Guatelli,
University of Wollongong, Australia

Reviewed by:
Cindy Le Loirec,
CEA Cadarache, France
Mauro Menichelli,
Istituto Nazionale di Fisica Nucleare di Perugia, Italy
Marc Verderi,
UMR7638 Laboratoire Leprince-Ringuet (LLR), France

***Correspondence:**
Salvador García-Pareja
salvador.garcia.sspa@juntadeandalucia.es

Specialty section:
This article was submitted to Radiation Detectors and Imaging, a section of the journal Frontiers in Physics

Received: *01 June 2021*
Accepted: *06 October 2021*
Published: *27 October 2021*

Citation:
García-Pareja S, Lallena AM and Salvat F (2021) Variance-Reduction Methods for Monte Carlo Simulation of Radiation Transport. Front. Phys. 9:718873. doi: 10.3389/fphy.2021.718873

1 INTRODUCTION

Monte Carlo simulation has become the tool of choice for solving the Boltzmann linear transport equation for high-energy radiation (particles) in complex material structures. As compared with alternative deterministic finite-difference methods, Monte Carlo simulation has several distinct advantages. Firstly, it can describe arbitrary interaction processes, including those with cross sections that are rapidly varying functions of the physical variables (e.g., the atomic photoelectric effect, whose total cross section presents sharp absorption edges). Secondly, Monte Carlo simulation can easily follow particles through material systems with complex geometries, where deterministic methods would find great difficulties even to define the appropriate boundary conditions. Finally, the stochastic nature of Monte Carlo methods permits a straightforward evaluation of statistical (class A) uncertainties of simulation results, while finite-difference methods allow only rough estimations of accumulated numerical errors. Although Monte Carlo codes have reached a high degree of sophistication, simulation suffers from the drawback of requiring very large computation times, particularly for fast charged particles and neutrons, which experience a very large number of interactions before being brought to rest.

Generally, a Monte Carlo simulation involves a radiation source with specified characteristics, which emits primary particles in various initial states. The state variables of a particle are the

particle's kind k (defined by its mass and charge), the kinetic energy E (energy in the case of photons), position $\mathbf{r}$ and direction of motion $\hat{\mathbf{d}}$. Primary particles propagate through a material system consisting of homogeneous bodies limited by passive surfaces. The materials in the system are assumed to be homogeneous and isotropic; usually they are pure elements or compounds with well defined stoichiometric composition and with $\mathcal{N}$ atoms or molecules per unit volume. Particles undergo discrete interactions with the material, in which they lose energy, change their direction of motion, and occasionally, may release secondary particles with lower energies[1]. Some interactions cause excitations of the material, which decay with the emission of other secondary particles. The result of the interaction cascade is that each primary particle induces a "shower" of particles that evolves by progressively increasing the number of particles and reducing their average energy, until the energies of all involved particles fall below the corresponding cutoff or absorption energies, at which particles are assumed to be effectively absorbed in the material.

For a given material, each interaction mechanism (int) of particles of kind k and energy E is characterized by a molecular differential cross section (DCS). Because of the assumed isotropy of the material, the DCSs depend only on the polar angle of scattering, θ, and the energy transfer W. The DCSs are conveniently expressed as

$$\frac{\mathrm{d}^2\sigma_{k,\mathrm{int}}}{\mathrm{d}W\,\mathrm{d}\cos\theta} = \sigma_{k,\mathrm{int}}(E)\,p_{k,\mathrm{int}}(E;W,\cos\theta), \tag{1}$$

where $\sigma_{k,\mathrm{int}}(E)$ is the total (integrated) cross section and $p_{k,\mathrm{int}}(E;W,\cos\theta)$ is the joint probability distribution function (PDF) of the energy loss and the angular deflection $\cos\theta$. In the case of polarized particles, the DCS may also depend on the azimuthal scattering angle ϕ [1], although polarization does not affect the total cross section. The product $\mu_{k,\mathrm{int}}(E) = \mathcal{N}\,\sigma_{k,\mathrm{int}}(E)$ is the interaction probability per unit path length, and its inverse $\lambda_{\mathrm{int}} = \mu^{-1}_{k,\mathrm{int}}(E)$ is the mean free path between interactions.

The length s of the free flight of a particle to its next interaction is a random variable with PDF

$$p(s) = \lambda^{-1}\,\exp\left(-\lambda^{-1}s\right), \tag{2}$$

where

$$\lambda^{-1} = \sum_{\mathrm{int}} \mu_{k,\mathrm{int}}(E) \tag{3}$$

is the total inverse mean free path. The kind of interaction that occurs at the end of a free flight, and the angular deflection and the energy transfer in the interaction are random variables with PDFs determined by the total cross sections and the DCSs of the active interaction mechanisms.

A simulation code generates the trajectory of a particle as a sequence of free flights, each ending with an interaction where the particle changes its direction of flight, loses energy, and may induce the emission of secondary particles. A Monte Carlo calculation consists of the generation of a large number N of showers by numerical random sampling from the relevant PDFs (see e.g., Ref. [1] and references therein). The sought numerical information on the transport process is obtained as an average over the simulated showers.

A number of general-purpose Monte Carlo codes for simulation of the coupled transport of photons and charged particles are available (e.g., PENELOPE [1], MCNP [2], GEANT4 [3], FLUKA [4], EGSnrc [5], EGS5 [6], TRIPOLI-4 [7], and PHITS [8]). They perform detailed event-by-event simulation for photons, while charged particles are simulated by means of a combination of class I and class II schemes (see Ref. [9]). In class I or "condensed" simulation schemes, the trajectory of a charged particle is split into segments of predefined length and the cumulative energy loss and angular deflection resulting from the interactions along each segment are sampled from approximate multiple scattering theories. Class II, or "mixed", schemes simulate individual hard interactions (i.e., interactions with energy loss or polar angular deflection larger than certain cut-offs W_c and θ_c) from their restricted DCSs, and the effect of the soft interactions (with W or θ less than the corresponding cut-offs) between each pair of hard interactions is described by means of multiple-scattering approximations. Class II schemes describe hard interactions accurately (i.e., according to the adopted DCSs) and also provide a better description of soft events (because multiple scattering approximations are more accurate when applied to soft collisions only).

The present article deals with strategies to speed up transport simulations, generally known as *variance-reduction techniques* (VRTs). Some Monte Carlo codes allow applying various of these techniques automatically, while other codes may require some extra coding by the user. Our aim here is to offer a general perspective of the VRTs and of their capabilities. For the sake of simplicity, we consider analog Monte Carlo simulations, in which the transport process retains its Markovian character. In these simulations, when a particle reaches an interface separating two different materials, we stop the particle at the interface, and proceed with the simulation in the next material by using the appropriate interaction DCSs. In addition, we only consider VRTs that are independent of the geometry, unless otherwise indicated.

In **Section 2** we summarize the essentials of Monte Carlo simulation. The basic ideas leading to the formulation of VRTs for transport simulations are presented in **Section 3**, followed by the description of various VRTs that are applicable to any Monte Carlo transport algorithm. Results from illustrative simulation examples are presented in **Section 4**. These were generated by using the Monte Carlo code system PENELOPE [1, 10], which simulates the coupled transport of electrons/positrons and photons.

2 STATISTICAL UNCERTAINTY, EFFICIENCY, AND VARIANCE REDUCTION

Formally, any Monte Carlo simulation is equivalent to the evaluation of one or several integrals. This equivalence permits a formal foundation for Monte Carlo techniques, which is best illustrated by considering the calculation of the one-dimensional integral of a function $F(x)$ over an interval (a, b),

[1]We use the term secondary to qualify particles emitted as a result of interactions

$$I = \int_a^b F(x)\,\mathrm{d}x. \tag{4}$$

To introduce randomness into this deterministic problem, we consider an arbitrary PDF, $p(x)$, such that.

$$p(x)\begin{cases} \geq 0, & \text{if } x \in (a,b) \text{ and } F(x) \neq 0, \\ = 0, & \text{otherwise,} \end{cases} \tag{5a}$$

and

$$\int_a^b p(x)\,\mathrm{d}x = 1, \tag{5b}$$

and we express the integral in the form of an expectation value:

$$I = \int_a^b f(x)\,p(x)\,\mathrm{d}x = \langle f \rangle \tag{6a}$$

with

$$f(x) = \frac{F(x)}{p(x)}. \tag{6b}$$

Then, the integral can be evaluated by generating a large number N of random values x_i from $p(x)$ and, by virtue of the law of large numbers, we have

$$\langle f \rangle = \lim_{N\to\infty} \frac{1}{N} \sum_{i=1}^{N} f(x_i). \tag{7}$$

The integral that defines the variance of f,

$$\mathrm{var}(f) = \int_a^b f^2(x)\,p(x)\,\mathrm{d}x - \langle f \rangle^2, \tag{8}$$

can be evaluated in a similar way:

$$\mathrm{var}(f) = \lim_{N\to\infty} \left\{ \frac{1}{N} \sum_{i=1}^{N} f^2(x_i) - \left[\frac{1}{N} \sum_{i=1}^{N} f(x_i) \right]^2 \right\}. \tag{9}$$

Actually, in a Monte Carlo simulation run, the number N of random values generated is finite and, if we repeat the calculation a number of times (with "independent" seeds of the random number generator) we get different values of the estimator

$$\bar{f} = \frac{1}{N} \sum_{i=1}^{N} f(x_i), \tag{10}$$

which fluctuate about the mean

$$\langle \bar{f} \rangle = \langle \frac{1}{N} \sum_{i=1}^{N} f(x_i) \rangle = \frac{1}{N} \sum_{i=1}^{N} \langle f \rangle = \langle f \rangle \tag{11}$$

with variance

$$\mathrm{var}(\bar{f}) = \mathrm{var}\left[\frac{1}{N} \sum_{i=1}^{N} f(x_i) \right] = \frac{1}{N^2} \sum_{i=1}^{N} \mathrm{var}(f) = \frac{1}{N}\,\mathrm{var}(f). \tag{12}$$

Here the properties of the expectation and the variance have been used. The central limit theorem then implies that, for sufficiently large N, the probability distribution of $\bar{f}$ is the normal distribution with variance var(f)/N. In the limit $N \to \infty$, the quantity

$$\sigma^2(\bar{f}) = \frac{1}{N} \left\{ \frac{1}{N} \sum_{i=1}^{N} f^2(x_i) - \bar{f}^2 \right\} \tag{13}$$

is an unbiased estimator for var($\bar{f}$). The results of the Monte Carlo simulation should always be given in the form $\bar{f} \pm k\sigma(\bar{f})$. With the coverage factor $k = 3$, the uncertainty bar contains the true value $\langle f \rangle$ of the integral with a probability of 0.997 (3σ rule).

It is worth noticing that the PDF $p(x)$ can be selected arbitrarily, with the proviso that it complies with **Eq. 5a**. It is to be expected that Monte Carlo calculations with different PDFs would yield estimates $\bar{f}$ with different statistical uncertainties $\sigma(\bar{f})$. As a figure of merit to evaluate the effectiveness of a Monte Carlo calculation, it is common to use the efficiency ϵ defined as

$$\epsilon = \frac{\bar{f}^2}{\sigma^2(\bar{f})}\,\frac{1}{T}, \tag{14}$$

where T is the computer (CPU) time spent in the calculation. Although during the calculation the value of ϵ fluctuates randomly, the amplitude of its fluctuations decreases when N increases and ϵ tends to a constant value when $N \to \infty$, because $\sigma^2(\bar{f})$ and T are proportional to N^{-1} and N, respectively.

The variance-reduction techniques (VRTs) are strategies aimed at increasing the efficiency of the calculation of the integral without modifying its expectation, i.e., aimed at reducing the relative statistical uncertainty attained after a given CPU time. They normally operate by modifying the PDF $p(x)$ to lessen the variance. It is worth pointing out that a reduction of the variance implies an increase in efficiency only when the sampling process remains simple enough not to outweigh the reduction of variance.

3 VRTS IN TRANSPORT SIMULATIONS

A Monte Carlo simulation of radiation transport can be regarded as the simultaneous evaluation of a number of integrals of the type

$$Q = \int q(x)\,p(x)\,\mathrm{d}x \tag{15}$$

where Q is the quantity of interest, $q(x)$ is the contribution of an individual shower, the random variable x (usually an array of random variables) characterizes each individual shower, and $p(x)$ is the PDF for the occurrence of that particular shower. For example, Q may be the average energy deposited into a certain volume $\mathcal{V}$ of the geometry, in which case $q(x)$ is the energy deposited by the set of particles in a shower (not only the primary particle). The simulation of each individual shower provides a random value of $q(x)$ distributed according to $p(x)$. Notice that the PDF $p(x)$ is ultimately determined by the interaction DCSs of the transported particles, and does not need to be specified.

The Monte Carlo estimator of the quantity Q is obtained by generating a sufficiently large number N of showers and setting.

$$\bar{Q} = \frac{1}{N}\sum_{i=1}^{N} q_i, \tag{16a}$$

and

$$\sigma^2(\bar{Q}) = \frac{1}{N}\left\{\frac{1}{N}\sum_{i=1}^{N} q_i^2 - \bar{Q}^2\right\}, \tag{16b}$$

where q_i is the contribution (deposited energy in the above example) of the i-th shower. Generally, a shower consists of a number n of particles, and each of these particles may contribute to the score, that is

$$q_i = \sum_{j=1}^{n} q_{ij}, \tag{17}$$

where q_{ij} stands for the contribution of the j-th particle of the shower.

In radiation transport simulations, VRTs are implemented by assigning each particle a weight w, which is a factor, usually real and non-negative, that multiplies all the contributions of that particle to the scored quantities. Primary particles emitted from unbiased sources are usually assigned a weight equal to unity. Biased sources can also be considered by assigning appropriate weights to the emitted particles. Generally, secondary particles inherit the weight of the parent particle that induced their emission.

In a very general way (see e. g., Ref. [11]), VRTs can be classified as sppliting-based and importance-sampling-based techniques. The latter modify the interaction PDFs, $p(s)$ and $p_{k,\mathrm{int}}(E;\, W,\, \cos\theta)$, while the former manipulate the numbers and weights of transported particles without altering the interaction PDFs. Most VRTs are based on the following considerations.

Let $\bar{Q}$ denote the result of an analog simulation (without applying any VRT, with all weights equal to unity) and $\bar{Q}_{\mathrm{VRT}}$ the result of simulating the same arrangement with some sort of VRT (with certain particle weights w_j), i.e.,

$$\bar{Q} = \frac{1}{N}\sum_{i=1}^{N}\left(\sum_{j} q_{ij}\right) \tag{18a}$$

and

$$\bar{Q}_{\mathrm{VRT}} = \frac{1}{N}\sum_{i=1}^{N}\left(\sum_{k} w_k q_{ik}\right), \tag{18b}$$

with the respective associated variances.

$$\sigma^2(\bar{Q}) = \frac{1}{N}\left\{\frac{1}{N}\sum_{i=1}^{N}\left(\sum_{j} q_{ij}\right)^2 - \bar{Q}^2\right\} \tag{19a}$$

and

$$\sigma^2(\bar{Q}_{\mathrm{VRT}}) = \frac{1}{N}\left\{\frac{1}{N}\sum_{i=1}^{N}\left(\sum_{k} w_k q_{ik}\right)^2 - \bar{Q}_{\mathrm{VRT}}^2\right\}. \tag{19b}$$

It is then possible that with a proper selection of weights w_k, and the associated contributions q_{ik}, we can keep the result unbiased, i.e., such that $\bar{Q}_{\mathrm{VRT}} = \bar{Q}$, within statistical uncertainties and, at the same time, have an increased efficiency. Generally the efficiencies of quantities other than Q may decrease, but their expectation values should remain unaltered. As a rule of thumb, the variance $\sigma^2(\bar{Q}_{\mathrm{VRT}})$ is reduced when the number of contributions to the score increases and their weights become more uniform.

Unfortunately, VRTs are extremely problem-dependent, and general recipes to optimize efficiency cannot be given. We limit our considerations to simple VRTs that can be readily implemented in a generic transport code, with no specific requirements about the simulation geometry, to reduce the variance of a given quantity Q, keeping the estimators of other quantities, of lesser interest, unbiased. More elaborate VRTs, such as the DXTRAN method implemented in MCNP [2, 12], which rely on partially-deterministic methods, will not be considered.

3.1 Splitting and Russian Roulette

These two techniques, which are normally used in conjunction, are effective in problems where interest is focused on a limited volume in the space of state variables $(\mathbf{r}, E, \hat{\mathbf{d}})$, the "region of interest" (RoI). The basic idea of splitting and Russian roulette is to favour the flux of radiation towards the RoI and inhibit the radiation that moves away from that region, thus saving part of the numerical work that would be wasted tracking particles that are not likely to contribute to the scores. Situations in which these VRTs are utilized include the calculation of dose functions in deep regions of irradiated objects, the evaluation of radial doses from collimated beams at positions far from the beam axis, and studies of backscattering of particle beams. Splitting is also useful, e.g., in simulations where primary particles are read from pre-calculated phase-space files [13]; since these files are limited in size, splitting the primary particles allows reducing the statistical uncertainty, at the cost of increasing the simulation time.[2]

Splitting consists of transforming a particle, with weight w_0 and in a certain state, into a number $\mathcal{S} > 1$ of copies with weights $w = w_0/\mathcal{S}$ in the same state. Splitting should be applied when the particle "approaches" the RoI. The Russian roulette technique is, in a way, the reverse process: when a particle tends to move away from the RoI it is "killed" with a certain probability $\mathcal{K}$ $(0 < \mathcal{K} < 1)$ and, if it survives, its weight is increased by a factor $1/(1-\mathcal{K})$. Here, killing means that the particle is just discarded (and does not contribute to the scores anymore). Evidently, splitting and killing leave the simulation unbiased.

Splitting reduces the variance, but one should avoid using splitting factors that are too large, because the extra work needed for tracking the various split particles may reduce the simulation efficiency and increases the computation time. By contrast, Russian roulette increases the variance (because it produces fewer contributions with higher weights) and reduces the CPU time. Russian roulette can be used for avoiding the simulation of low-weight particles, which would spend the same CPU time as

[2]It is worth noticing that the finite size of the phase-space files implies a "latent" uncertainty, which sets a lower limit to the uncertainty attainable by splitting [14].

for particles with large weights to produce very small contributions to the scores.

The effectiveness of these VRTs relies on the adopted values of the parameters $\mathcal{S}$ and $\mathcal{K}$, and on the strategy used to decide when splitting and killing are to be applied. To take care of these questions, most Monte Carlo codes make use of the so-called *weight-windows*, which serve to homogenize the weight values of the particles reaching certain RoIs, avoiding the occurrence of "variance bombs" (particles with huge weights) that would produce large increases of the variance. Usually, *weight-window methods* split the relevant portion of the particle-state space $(k, \mathbf{r}, E, \hat{\mathbf{d}})$ into cells and assign to each cell a weight window (w_l, w_u). When a particle reaches a cell with a weight outside the window, it is split or killed with probability such that the weight of the resulting particles is within the cell window. The cell structure and corresponding weight windows are usually defined from knowledge of partial simulation results.

3.1.1 Consistent Adjoint Driven Importance Sampling Method

Elaborate VR schemes (see, e.g., Ref. [15]) combine source biasing and weight-window strategies, by considering an *importance function* that measures the likelihood of particles in that cell to contribute to the score. Approximate importance functions can be inferred from previous simulations, or from a deterministic discrete-ordinate transport calculation.

Global strategies for automatically determining importance functions have been developed, mostly for photon and neutron transport because these particles have relatively large mean free paths. Thus, the Consistent Adjoint Driven Importance Sampling (CADIS) method, determines the importance function from a deterministic adjoint calculation [16]. The FW-CADIS method [17] uses a similar strategy starting from a deterministic forward calculation. These are hybrid methods, in the sense that they combine Monte Carlo simulation with a deterministic (discrete-ordinate) calculation. They have been implemented in various codes (e.g., MCNP and TRIPOLI-4) for coupled neutron-gamma simulations and shielding calculations [18, 19].

3.1.2 Ant Colony Method

A simpler, and easier to implement, procedure to progressively build an importance function from information acquired from the simulation itself is provided by the *ant colony method* [20]. Ant colony algorithms were first proposed by Dorigo et al. [21] and are based on the collective behavior of ant colonies in their searching for food: ants that find food sources return to the nest laying down trails of pheromone. Paths to abundant sources are followed by a greater number of ants and the pheromone level increases, guiding other ants to these sources.

The ant colony method is applied to particles within a limited volume of the particle-state space $(k, \mathbf{r}, E, \hat{\mathbf{d}})$, which is split into cells. In the absence of symmetries, we may use Cartesian space coordinates, $\mathbf{r} = (x, y, z)$ and represent direction vectors by means of the polar angle θ and the azimuthal angle ϕ, $\hat{\mathbf{d}} = (\sin\theta\cos\phi, \sin\theta\sin\phi, \cos\theta)$. We can then define cells consisting of finite intervals of the continuous variables x, y, z, E, θ, and ϕ, for the various kinds k of particles. If the problem under consideration has some symmetry, it may be advantageous to adapt the cell structure to that symmetry. From now on, the application volume and its cell partition are assumed to be defined; to simplify the formulas, each cell is denoted by a single index i and, accordingly, the value of the importance of a cell is written as I_i. We say that a particle passes the cell i when it begins a step of his trajectory within that cell.

The ant colony algorithm described here is consistent as long as all particles that enter the cell structure from outside, or that start their trajectories from within the structure, have weights equal to a power of 2. If this is not the case, i.e., if a particle enters or starts its journey in the cell structure with a weight w such that $2^{n-1} < w < 2^n$, Russian roulette with killing probability $\mathcal{K} = 1 - w/2^n$ is played. Evidently, this protection is unnecessary when the only VRT applied is the ant colony method in a single cell structure.

The importance map is determined from information gathered either from preliminary simulations or in the course of the simulation run. Let $N_i^{(P)}$ denote the total weight of particles that passed the cell i, and let $N_i^{(C)}$ be the total weight of particles that passed that cell *and*, subsequently, they or any of their descendants reached the RoI. The fraction

$$P_i = N_i^{(C)}/N_i^{(P)} \tag{20}$$

characterizes the relevance of the cell. Evidently, P_i ranges between 0 (none of the particles that pass cell i, nor its descendants, reach the RoI) and 1 (all particles passing the cell i arrive, themselves or their descendants, to the RoI). The importance of cell i is defined as

$$I_i = 2^{[\kappa_i]}, \tag{21}$$

where $[\kappa_i]$ denotes the closest integer to κ_i, and

$$\kappa_i \equiv \begin{cases} 5\,\dfrac{P_i - P_0}{P_0}, & \text{if } P_i \le P_0, \\ 12\,\dfrac{P_i - P_0}{1 - P_0}, & \text{if } P_i > P_0. \end{cases} \tag{22}$$

The quantity P_0 is the probability that a primary particle, or one of its descendants, arrives in the RoI. Notice that the importance defined in **Eq. (21)** is positive and increases with the likelihood that particles passing the i-th cell contribute to the scores. As a matter of fact, the definition of κ_i is somewhat arbitrary; other increasing functions of P_i and such that $\kappa_i(P_0) = 0$ would do the job. The numerical coefficients in the definition of **Eq. (22)** yield values of the exponent $[\kappa_i]$ between −5 and 12. Practical experience indicates that moderate variations of those coefficients do not produce significant improvements of the effectiveness of the method.

Once a suitable importance map is acquired, splitting and Russian roulette are activated as follows. When a transported particle having weight w moves from the cell i to the cell f,

- if $w\,I_f > 1$, the particle is split into $\mathcal{S} = w\,I_f$ particles, each one with weight $w' = w/\mathcal{S} = I_f^{-1}$;

- if $w\,I_f < 1$, Russian roulette is applied with killing probability $\mathcal{K} = 1 - w\,I_f$; when the particle survives, it is assigned the weight $w' = w(1-\mathcal{K})^{-1} = I_f^{-1}$, and
- if $w\,I_f = 1$, no action is taken.

The definition of I_i as a power of 2, **Eq. (21)**, combined with this strategy, implies that particles that passed a given cell have the same weight, $w = I_i^{-1}$, irrespective of their previous evolution. We recall that more uniform weights normally have associated a smaller variance.

The ant colony method has been proven to be effective in simulations of clinical linear electron accelerators [22, 23], in a study of the response of MOSFET dosimeters [24], in dosimetry calculations of radiosurgery treatments [25], in the optimization of certain radiotherapy procedures [26], and in calculations of specific absorption fractions in Nuclear Medicine [20].

3.2 Path-Length Biasing

As mentioned above, the path length s to the next interaction is a random variable whose PDF is given by **Eq. (2)**. The VRTs described in this Subsection operate by sampling s from a modified PDF, $p'(s)$, and, to keep the simulation results unbiased, they replace the weight w of the particle with a new value w' such that [15].

$$w'\,p'(s)\,\mathrm{d}s = w\,p(s)\,\mathrm{d}s,$$

that is

$$w' = w\,\frac{p(s)}{p'(s)}. \tag{23}$$

3.2.1 Exponential Transform

There are situations in which one is mostly interested on the transport properties in localized spatial regions. For instance, in shielding calculations we wish to evaluate the dose in deep volumes of irradiated objects, while in backscattering studies our interest is focused on the surface region where the local dose varies quite abruptly (build-up effect). In those situations, the VRT of *exponential transform* [27] allows concentrating the simulated interactions near or within the RoI. This technique consists of modifying the value of the mean free path λ, which is replaced with

$$\lambda' = \frac{\lambda}{a}, \tag{24}$$

where a is a positive constant. That is, the PDF of the free-flight length to the next interaction is replaced with

$$p'(s) = \frac{1}{\lambda'}\,\exp(-s/\lambda'), \tag{25}$$

and random values of the path length s are sampled by the inverse-transform method, which gives the familiar sampling formula

$$s = -\lambda'\,\ln(1-\xi). \tag{26}$$

Here ξ is a random number distributed uniformly between 0 and 1. The modified weight

$$w' = w\,\frac{p(s)}{p'(s)} = \frac{w}{a}\,\exp\left[-\frac{s}{\lambda}(1-a)\right] \tag{27}$$

must be used in all subsequent contributions to the scores.

When $a > 1$ the interactions occur at smaller path lengths, if $a = 1$ the simulation is analog, and when $0 < a < 1$ the path lengths between interactions are stretched. In the case of photon beams impinging on thick material blocks, the exponential transform with $a < 1$ is useful in shielding calculations, while with $a > 1$ helps in determining the dose in the build-up zone, near the entrance surface of the beam. Naturally, the "constant" a can be made direction-dependent (see, e.g., Ref. [2])

In principle the exponential transform is only valid when particles move in a homogeneous body surrounded with vacuum. It may not be applicable in complex geometries, where the transported particle may enter a different material before reaching the position of the next interaction, except when specific interface crossing strategies are adopted.

3.2.2 Forced-Interaction Biasing

Calculations of the dose in low-density gas volumes, or of the emission of secondary particles from thin material bodies use to have low efficiencies in analog simulations because the probability of having an interaction in those volumes and bodies is exceedingly small. A simple VRT that is very effective in these cases consists in forcing an interaction in a restricted path length interval, say between 0 and a given maximum length L. This is accomplished by sampling the path length s to the next interaction from the PDF [2].

$$p'(s) = \left[\lambda^{-1}\int_0^L \exp(-s'/\lambda)\,\mathrm{d}s'\right]^{-1}\lambda^{-1}\exp(-s/\lambda), \tag{28}$$

limited to the interval $(0, L)$. The path length s can then be sampled by the inverse transform method, which leads to the sampling formula

$$s = -\lambda\,\ln[1-\xi(1-\exp(-L/\lambda)]. \tag{29}$$

Notice that when $L \to \infty$, this formula reduces to the familiar form of **Eq. (26)**. To compensate for the effect of forcing the interaction, the weight w of the particle is replaced with the new weight

$$w' = w\,\frac{p(s)}{p'(s)} = w[1-\exp(-L/\lambda)]. \tag{30}$$

Since both the exponential transform and the forced-interaction biasing modify the particle weight, they may produce particles with very large or very small weights. It is then convenient to combine these VRTs with splitting and Russian roulette so as to keep the weights between reasonable limits.

3.3 Woodcock Method

This VRT, also known as the delta scattering method [28–30], is helpful in simulations of photon beams. It takes advantage of the

high penetration of photons to simplify their tracking through material systems with complex geometries. This is made possible by assuming that, in addition to the physical interactions, the transported photons may undergo delta interactions, i.e., fake interactions that do not modify the state variables of the particle. Photons are transported freely across the system using an augmented inverse mean free path, Λ^{-1}, which is required to be larger than the actual total inverse mean free paths in all the materials crossed by a trajectory ray. The event at the end of each free flight is assumed to be either a real interaction or a delta interaction (which does nothing). Delta interactions occur with probability $1 - \lambda^{-1}/\Lambda^{-1}$, where λ^{-1} is the actual total inverse mean free path in the current material. Thus, the probability of real interactions per unit path length, which is equal to λ^{-1}, remains unaltered.

This procedure avoids the need for computing intersections of particle rays with interfaces at the expense of having to determine which material is at the end of each free flight. Hence delta scattering will improve the efficiency for geometries where locating a particle (i.e., finding the material at its current position) is faster than normal tracking. It is particularly effective in calculations of dose distributions from photon beams in voxelized structures such as those obtained from computerized tomography. The Woodcock method is also applicable to fast neutrons, and to any kind of particles that have relatively large mean free paths. Unfortunately, the efficiency gain from this method is small when secondary charged particles are also tracked.

3.4 Interaction Forcing

Sometimes, a high variance results from an extremely low interaction probability. Consider, for instance, the simulation of the energy spectrum of bremsstrahlung photons emitted by medium energy (~ 100 keV) electrons in a thin foil of a certain material. As radiative events are much less probable than elastic and inelastic scattering, the uncertainty of the simulated photon spectrum will be relatively large. Another difficult situation is found in the calculation of dose from photon beams on thin foils, where the interaction probability is very small. In such cases, an efficient VRT is to artificially increase the interaction probability of the process A of interest, i.e., to force interactions of type A to occur more frequently than for the real process. Our practical implementation of interaction forcing consists of replacing the mean free path λ_A of the real process by a shorter one, $\lambda_{A,f} = \lambda_A/\mathcal{F}$ with $\mathcal{F} > 1$. This implies that between each pair of "real" A interactions we will have, on average, $\mathcal{F} - 1$ "forced" A interactions. We consider that the PDFs for the energy loss and the angular deflections (and the directions of emitted secondary particles, if any) in the forced interactions are the same as for real interactions, i.e., the VRT does not affect the interaction PDFs.

For the sake of programming simplicity, the length of the free jump to the next A interaction (real or forced) of the transported particle is sampled from the exponential distribution with the reduced mean free path $\lambda_{A,f}$. To keep the simulation unbiased, we must manipulate the weights of the particles. Let w be the weight of the transported particle. We correct for the introduced distortion of the mean free path as follows:

- A weight $w_f = w/\mathcal{F}$ is assigned to the deposited energy, the released secondary particles, and to any other alteration of the medium (such as, e.g., charge deposition) that result from A interactions (real and forced) of the transported particle. For non-forced interactions of types other than A, the particle weight w is used.
- Interactions of type A (real and forced) are simulated to determine the energy loss and the possible emission of secondary particles, but the state variables of the transported particle are altered only when the interaction is real. As the probability of having a real A interaction is $1/\mathcal{F}$, the energy E and direction of movement $\hat{\mathbf{d}}$ of the projectile are varied only when the value ξ of a random number falls below $1/\mathcal{F}$, otherwise E and $\hat{\mathbf{d}}$ are kept unchanged (forced A interactions do not alter the state variables of the transported particle).

Of course, interaction forcing should be applied only to interactions that are dynamically allowed, i.e., for particles with energy above the corresponding "reaction" threshold. Evidently, quantities directly related to forced interactions will have a reduced statistical uncertainty due to the increase in number of these interactions. However, for a given simulation time, other quantities may exhibit standard deviations larger than those of the analog simulation because of the time spent in simulating the forced interactions. It is worth noticing that our implementation of interaction forcing introduces forced interactions randomly along the particle trajectory, independently of the geometry, and it keeps the weight of the transported particle unaltered. This is at odds with the VRT of forced-interaction biasing (frequently referred to also with the name of interaction forcing), where forced events alter the weight of the transported particle and occur with probabilities that need to be specified in accordance with the local geometry.

Interaction forcing can be activated locally, at any stage of the trajectory of a particle. Evidently, repeated application of interaction forcing may produce particles with very small weights. In practice this may be avoided by using this VRT only for particles within a given weight window (w_l, w_u). For instance, if interaction forcing is the only VRT applied and if primary particles are assigned unit weights, a window (0.5,1.5) ensures that interaction forcing with $\mathcal{F} > 2$ will be applied only to the primary particles. This weight-window control is more effective than, e.g., combining interaction forcing with Russian roulette.

Interaction forcing has been efficiently used in simulations of electron-probe microanalysis [31, 32], photon beams from medical electron accelerators [33], the response of ionization chambers [34], and the calculation of doses absorbed in small organs in Nuclear Medicine treatments [20].

Although this VRT effectively reduces the statistical uncertainties of results involving the emission of secondary particles and the energy deposition in very thin volumes, it violates energy conservation (because the sum of energies

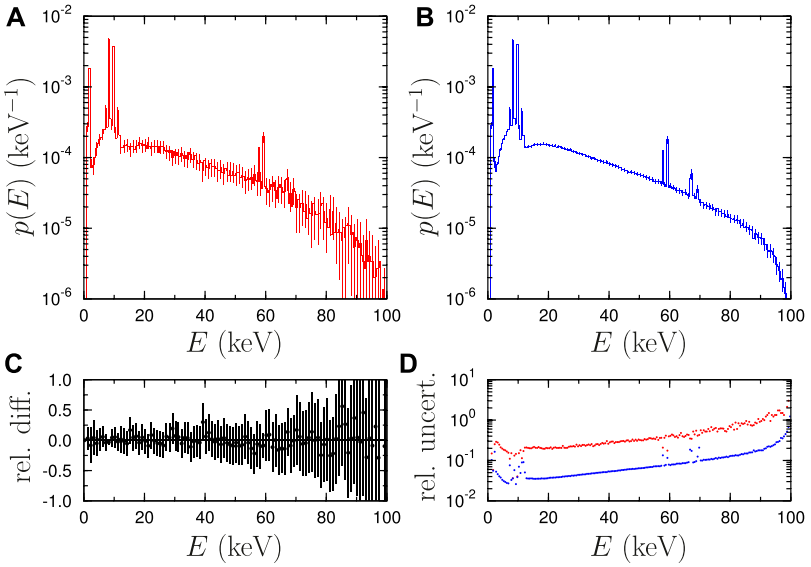

FIGURE 1 | X-ray emission spectra from a tungsten target bombarded by 100 keV electrons at normal incidence. Error bars represent statistical uncertainties with a coverage factor $k = 3$. The upper left plot **(A)** is the result from a 30 min analog simulation. The upper right plot **(B)** was generated in a run of 15 min of the same code by using the VRTs of interaction forcing and emission splitting of bremsstrahlung photons and x-rays, as described in the text. The lower plots display the relative difference between these results **(C)** and a comparison of the relative uncertainties of each simulation **(D)**.

deposited along a track differs from the energy lost by the projectile) and, therefore, yields energy deposition spectra that are biased. Consequently, it cannot be used, e.g., in simulations of energy spectra from scintillation or semiconductor detectors, which require computing the distribution of total energy deposited *by all particles in a shower* into the sensitive volume of the detector. Because it is very difficult to avoid this kind of bias, many simulations of energy-deposition spectra are purely analog.

3.5 Other Methods

Exploitation of local symmetries present in the simulation is often very useful in reducing the variance [33]. For instance, when the radiation beam and the geometry are locally symmetric under rotations about an axis, splitting can be made more effective if the position *and* the direction of each of the $\mathcal{S}$ split particles are rotated around the symmetry axis by a random angle $\varphi = 2\pi\xi$. Thus, the $\mathcal{S}$ split particles are assigned different positions and directions, and this gives a net information gain and an increase in efficiency [35].

Splitting is also useful to favor the emission of secondary particles by taking advantage of the emission symmetries of these particles. The method can be applied, e.g., in simulations of x-ray emission spectra from targets irradiated by electrons with energies of the order of 100 keV and smaller. These electrons emit bremsstrahlung photons and x rays with quite small probabilities. The energy of bremsstrahlung photons depends basically of the polar emission angle and it is quite costly to sample. It is then practical to split each emitted bremsstrahlung photon by assigning to the split ones random values of the azimuthal emission angle, in order to increase the likelihood that one of these photons reaches the detector. Similarly, the number of x rays released in the relaxation of ionized atoms may be increased by splitting them and assigning to the split x rays independent random directions. These VRTs are frequently referred to as *directional bremsstrahlung or x-ray splitting*; they have been employed, e.g., in simulations of microanalysis measurements [32] and clinical linear accelerators [36], and in dosimetry calculations of radiosurgery [25], usually accompanied with Russian roulette to reduce the number of photons not moving towards the RoI [37]. It is also worth noticing that directional splitting can be applied in combination with interaction forcing.

As a last example, we quote the so-called "range rejection" method, which simply consists of absorbing a particle when it (and its possible descendants) cannot leave (or reach) the RoIs. Range rejection is useful, e.g., when computing the total energy deposition of charged particles in a given spatial RoI. When the residual range of a particle (and its possible descendants) is less than the distance to the nearest limiting surface of the RoI, the particle will deposit all its energy either inside or outside the considered RoI (depending on its current position) and simulation of the track can be stopped. Range rejection is not adequate for photon transport simulation because the concept of photon range is not well defined (or, to be more precise, because photon path length fluctuations are very large). Care must also be exercised when applying range rejection to high-energy electrons or positrons because of the possibility that bremsstrahlung photons emitted by these particles leave or reach the RoI. It is worth mentioning that this technique does not modify the weights of the particles involved.

As a final comment, we would like pointing out that wery frequently, an effective increase of efficiency may be obtained by simply avoiding unnecessary calculations. This is usually true for

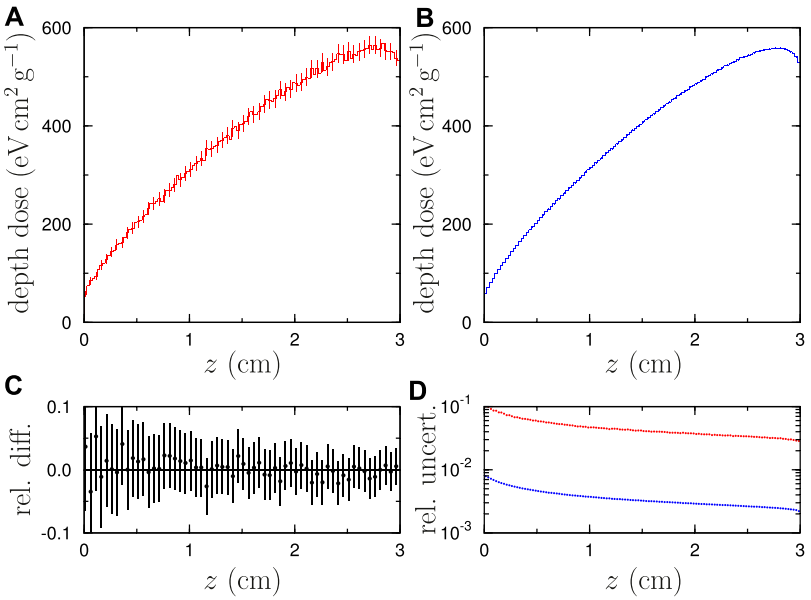

FIGURE 2 | Depth-dose distribution (energy deposited per unit mass thickness) in a 3 cm air layer irradiated by 1.25 MeV photons at normal incidence. **(A)** Result from an analog simulation, after 83 min of CPU time. **(B)** Result from the variance-reduced simulation (interaction forcing with $\mathcal{F} = 5,000$), 10 min CPU time. Other details are the same as in **Figure 1**.

simulation codes that incorporate general-purpose geometry packages. In the case of simple (e.g., planar, spherical, cylindrical) geometries the program may be substantially simplified and this may speed up the simulation appreciably. In general, the clever use of possible symmetries of the problem under consideration may lead to spectacular variance reductions. For example, when both the source and the material system are symmetric under rotations about an axis, the dose distribution also has that symmetry and it can be tallied by using cylindrical bins. This amounts to removing one spatial coordinate (the azimuthal angle) and leads to an effective reduction of the variance of the calculated local dose.

4 SIMULATION EXAMPLES AND PRACTICAL ASPECTS

We present here examples of simulations that have low efficiencies when formulated in analog form and where VRTs prove to be effective. As already mentioned, using a VRT allows increasing the efficiency of the calculation of a certain quantity or a set of related quantities, at the expense of worsening the efficiencies of other quantities. Once a quantity of interest is identified, the user selects the VRTs to be applied among those offered by the simulation code, or those that can be coded additionally, and sets the values of the parameters that define the adopted VRTs. In principle, the optimal parameter values (i.e., those giving the highest efficiency) can only be determined from trial simulations. In many cases, knowledge of the energy-dependent mean free paths, and the CSDA ranges of charged particles, allows estimating appropriate values of the VRT parameters, avoiding the burden of performing trial simulations.

It is not obvious how to quantify the efficiency of calculated continuous distributions (such as energy spectra or dose distributions), which are delivered in the form of histograms with multiple bins. In such cases, the effectiveness of VRTs is best appreciated from a plot of the simulated histogram with statistical uncertainties displayed as error bars.

The simulations reported here were all performed by using the PENELOPE code running on an Intel Core i7-8550U computer at 1.99 GHz. The parameters of the adopted VRTs were fixed beforehand, guided by previous experience. They may not be optimal, i.e., the efficiency could be improved further by varying those parameter values. The following examples show that even a blind setting of the VRT parameters may save quite a fraction of the computer time.

4.1 Electron-Induced Photon Emission

High-energy electrons emit bremsstrahlung photons and induce the emission of x-rays from atoms ionized by electron impact. These are the photons released, e.g., from x-ray generators and from the target in electron-probe microanalysis measurements [32]. The difficulty of simulations of photon emission by electrons with energies of the order of, or lower than 100 keV is the low probability with which these electrons induce the emission of photons. The VRT of interaction forcing has been proven to be effective to cope with this problem. **Figure 1** displays results from simulations of 100 keV electrons impinging normally on a foil of tungsten with a thickness equal to the CSDA range of the electrons ($R = 1.526 \times 10^{-3}$ cm). The displayed histograms are energy distributions of photons emitted from the

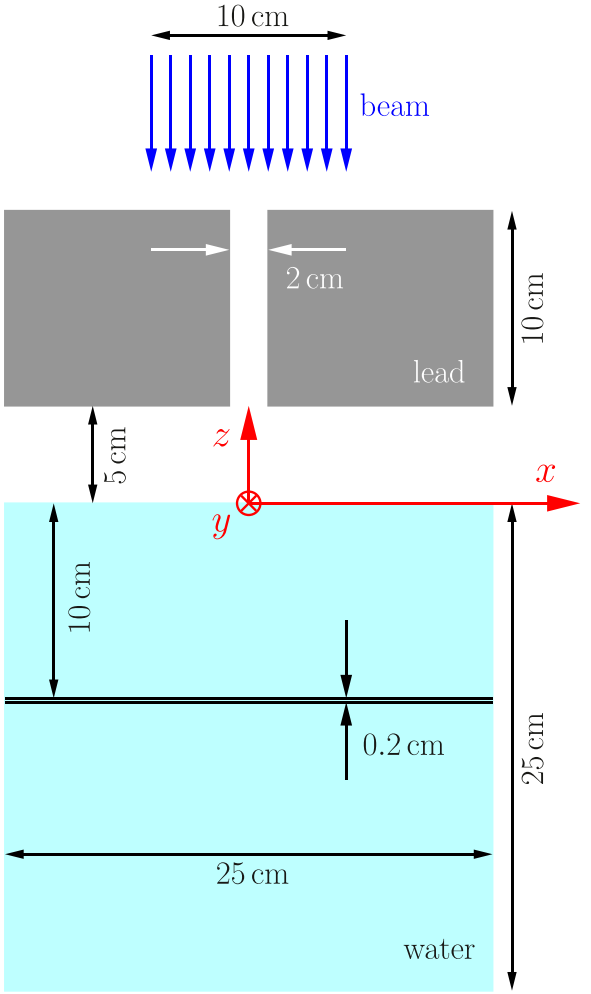

FIGURE 3 | Geometrical setup adopted in the simulation of dose profiles from photon beams in water.

irradiated surface of the foil obtained from 1) an analog simulation (without any VRT applied) run for half an hour (left plot), and 2) a 15-min simulation using interaction forcing of inner-shell ionization with $\mathcal{F} = 7.5$ and of bremsstrahlung emission with $\mathcal{F} = 300$, combined with emission splitting of x-rays and bremsstrahlung photons with $\mathcal{S} = 3$ (right plot). The VRT was applied only to primary electrons by defining a narrow weight window, which excluded all secondary particles.

The forcing factors were determined by setting the mean free paths $\lambda_{A,f}$ of the forced interactions of primary electrons ($E = 100$ keV) equal to a fraction of the CSDA range. With forcing factors determined in this way, we ensure that each primary electron undergoes on average a certain number of forced interactions along its trajectory. In the present simulations we took $\lambda_{A,f} = R/25$ for both bremsstrahlung and x-ray emission. Splitting proves to be useful when the photon detector covers a small solid angle [32]; in our case, all photons that leave the irradiated surface are counted and, consequently, using a larger splitting factor would not improve the efficiency appreciably.

The lower left plot in **Figure 1** displays the relative differences between the analog and variance-reduced simulations, which average to zero within statistical uncertainties as expected. The lower right plot shows the relative uncertainties of the two simulation results. Notice that, because of the different forcing factors for bremsstrahlung emission and inner-shell ionization, the relative uncertainties of the x-ray lines differ from the continuous trend of the bremsstrahlung background. The combined use of interaction forcing and photon-emission splitting is seen to effectively increase the efficiency of simulations of photon spectra, without altering the reliability of the results.

4.2 Dose in Thin Material Bodies

Another difficult calculation is that of the deposited energy in bodies having thicknesses much less than the total mean free paths of the transported particles. This situation is encountered, e.g., in simulations of the response to photon beams of ionization chambers, where the active gas is almost completely transparent to photons. Again, interaction forcing provides an effective practical solution in this case.

Results from analog and variance-reduced simulations of the spatial dose distribution from a 1.25 MeV photon beam in a 3 cm-thick air layer at normal incidence are displayed in **Figure 2**. The analog simulation lasted for 83 min and involved the generation of 2×10^9 showers (a part of them involving no interactions at all). In the variance-reduced simulation, we applied interaction forcing to the interactions of photoabsorption, Compton scattering and pair production, all them with $\mathcal{F} = 5,000$. We used a weight window with end points equal to 0.95 and 1.05, so that interaction forcing is activated only for primary photons; the plotted distribution was generated in a 10-min run. It is seen that the application of a single VRT leads to an spectacular increase in efficiency. It is worth noticing that the variation of the dose with depth in **Figure 2** is due to the transport of secondary particles; if electrons and positrons were not followed, the depth-dose would be essentially constant within the air layer.

4.3 Energy Deposition in Complex Geometries

The application of VRTs in cases with complex geometries and small RoIs may require careful planing and even modifications of the simulation code. It is in these cases where the ant colony method proves to be effective, mostly when combined with interaction forcing. As an example, we consider the situation described in **Figure 3**: a 10 cm by 10 cm parallel beam of 6 MeV photons impinges normally on a collimator followed by a cubic water phantom. The collimator is a 10 cm thick lead block with a cylindrical hole in the direction of the beam and 1 cm radius. The simulation is designed to determine the lateral dose profile (in the direction of the x axis) at a depth of 10 cm in the water phantom by scoring the energy deposited in a 0.2 cm thick layer split into bins of 0.1 and 0.2 cm in the directions of the x and y axes, respectively. The analog simulation is slow partially because of the

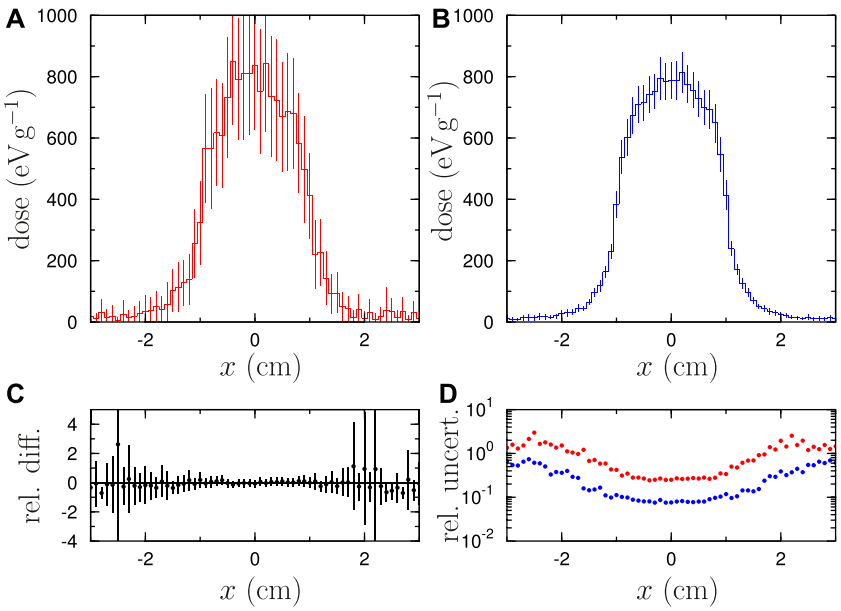

FIGURE 4 | Dose profile of a collimated 6 MeV photon beam in water using the geometry shown in **Figure 3**. **(A)** Result from an analog simulation, after 720 min of CPU time. **(B)** Result from the variance-reduced simulation (ant colony method, as described in the text), generated after 72 min CPU time. Other details are the same as in **Figure 1**.

work spent in following secondary radiation that is generated and absorbed within the lead collimator.

In the variance-reduced simulation we applied the ant colony method. The geometry volume was partitioned by means of a uniform ortogonal mesh of planes into cubic cells of 0.5 cm side, each one identified by the three indexes (k_x, k_y, k_z). An additional index, k_p, designated the particle kind (= 1 for electrons and positrons, and = 2 for photons). Finally, a fifth index, k_E, indicated the energy bin: the energy range covered by the simulation, from 0 to 6 MeV, was split into 3 cells of 2 MeV width. That is, the adopted importance map was defined as a five-dimensional matrix $I(k_x, k_y, k_z, k_p, k_E)$.

The RoI has been defined as the set of cells where the lateral dose profile is tallied (i.e., a row of cells parallel to the x axis). Initially, no variance reduction technique is applied, and the importance map is built from the progressing analog simulation until the gathered information is sufficient to switch on the VRT. It has been considered that after 1,000 showers have contributed to the RoI scores, the information in the importance map is detailed anough to activate splitting and Russian roulette guided by the ant colony algorithm described in Section 3.1.2. As the building of the importance map continues during all the simulation, its "quality" improves progressively. Of course, the importance map can be stored and reused in subsequent runs.

Figure 4 displays transverse dose profiles resulting from the analog (upper left panel) and the variance-reduced simulation (upper right panel) runs. Notice that the analog run was ten times longer than the variance-reduced one. The difference between the magnitude of the respective uncertainties is evident. While the profile obtained from the variance-reduced simulation is nearly symmetric, as expected, the result from analog simulation still shows a slight asymmetry. The lower left panel displays the relative differences between both calculations, which average to zero within statistical uncertainties. Finally, the lower right panel shows the relative uncertainties of the two simulation results. Although there is not much difference between the relative uncertainties, consideration of CPU times shows that the use of the ant colony method increases the efficiency by a factor of about 100.

5 CONCLUDING COMMENTS

We have described a set of relatively simple VRTs that operate either by manipulating the numbers and weights of the transported particles or by modifying the mean free paths for the relevant interaction processes. The ant-colony method (Section 3.1.2), in spite of its conceptual simplicity, has proven to be effective in focusing the radiation flux towards small RoIs in complex geometries. The VRT of interaction forcing (Section 3.4), has been shown to be useful in simulations with PENELOPE of processes with intrinsic small probabilities, such as calculations of absorbed doses in thin material bodies and the emission of photons from samples irradiated by electron beams.

The examples in the last Section evidence the usefulness of VRTs to speed up simulations of radiation transport in difficult situations. The effectiveness of these techniques is mostly determined by the edequacy of the adopted VRTs and their defining parameters. Although optimal parameters may be determined from trial simulations, a great deal of exploratory work can be saved by considering the dimensions of the material

system relative to the mean free paths of the relevant interaction processes, and to the CSDA ranges of charged particles. General-purpose Monte Carlo codes should provide tables of these quantities, as functions of the energy of the particles, calculated from the DCSs adopted in the code. The auxiliary program *tables.f* of the PENELOPE code system can be used to generate such tables for electrons, positrons and photons in arbitrary materials.

AUTHOR CONTRIBUTIONS

All authors listed have made a substantial, direct, and intellectual contribution to the work and approved it for publication.

FUNDING

Financial support from the Spanish Ministerio de Ciencia, Innovación y Universidades/Agencia Estatal de Investigación/ European Regional Development Fund (ERDF) of European Union (projects nos. RTI2018-098117-B-C22 and PID2019-104888GB-I00) and the Junta de Andalucía (projects nos. FQM387 and P18-RT-3237) is gratefully acknowledged.

ACKNOWLEDGMENTS

We are thankful to the reviewers for their thorough analysis of the original manuscript and for many comments and suggestions.

REFERENCES

1. Salvat F. *PENELOPE-2018: A Code System for Monte Carlo Simulation of Electron and Photon Transport. Document NEA/MBDAV/R(2019)1*. Boulogne-Billancourt: OECD Nuclear Energy Agency (2019).
2. X-5 Monte Carlo Team. *MCNP–A General Monte Carlo N-Particle Transport Code, Version 5. Report LA-UR-03-1987*. Los Alamos: Los Alamos National Laboratory (2003).
3. Allison J, Amakoca K, Apostolakisd J, Arce P, Asaif M, Asog T, et al. Recent Developments in Geant4. *Nucl Instrum Meth A* (2016) 835:186–225. doi:10.1016/j.nima.2016.06.125
4. Ferrari A, Sala PR, Fassò A, and Ranft J. Fluka: a Multi-Particle Transport Code. In: *Tech. Rep. CERN-2005-00X, INFN TC 05/11, SLAC-R-773*. Geneva: CERN (2005). doi:10.2172/877507
5. Kawrakow I, and Rogers DWO. The EGSnrc Code System: Monte Carlo Simulation of Electron and Photon Transport. In: *Tech. Rep. PIRS-701*. Ottawa: National Research Council of Canada (2001).
6. Hirayama H, Namito Y, Bielajew AF, Wilderman SJ, and Nelson WR. The EGS5 Code System. In: *Tech. Rep. SLAC-R-730 (KEK 2005-8)*. Menlo Park: Stanford Linear Accelerator Center (2006).
7. Brun E, Damian F, Diop CM, Dumonteil E, Hugot FX, Jouanne C, et al. TRIPOLI-4, CEA, EDF and AREVA Reference Monte Carlo Code. *Ann Nucl Energ* (2015) 82:151–60. doi:10.1016/j.anucene.2014.07.053
8. Sato T, Iwamoto Y, Hashimoto S, Ogawa T, Furuta T, Abe S-I, et al. Features of Particle and Heavy Ion Transport Code System (PHITS) Version 3.02. *J Nucl Sci Technol* (2018) 55:684–90. doi:10.1080/00223131.2017.1419890
9. Berger MJ. Monte Carlo Calculation of the Penetration and Diffusion of Fast Charged Particles. In: B Alder, S Fernbach, and M Rotenberg, editors. *Methods in Computational Physics*, Vol. 1. New York: Academic Press (1963). p. 135–215.
10. Baró J, Sempau J, Fernández-Varea JM, and Salvat F. PENELOPE: An Algorithm for Monte Carlo Simulation of the Penetration and Energy Loss of Electrons and Positrons in Matter. *Nucl Instr Methods Phys Res Section B: Beam Interactions Mater Atoms* (1995) 100:31–46. doi:10.1016/0168-583x(95)00349-5
11. Rubino G, and Tuffin B. *Rare Event Simulation Using Monte Carlo Methods*. Hoboken, NJ: John Wiley & Sons (2009).
12. Booth TE. *Monte Carlo Variance Reduction Approaches for Non-boltzmann Tallies. Report LA-12433*. Los Alamos: Los Alamos National Laboratory (1992).
13. Capote R, Jeraj R, Ma CM, Rogers DW, Sánchez-Doblado F, Sempau J, et al. Phase-space Database for External Beam Radiotherapy. Summary Report of a Consultants' Meeting. In: *Tech. Rep. INDC (NDS)-0484*. Vienna: International Atomic Energy Agency (2006).
14. Sempau J, Sánchez-Reyes A, Salvat F, Tahar HOb., Jiang SB, and Fernández-Varea JM. Monte Carlo Simulation of Electron Beams from an Accelerator Head Using PENELOPE. *Phys Med Biol* (2001) 46:1163–86. doi:10.1088/0031-9155/46/4/318
15. Haghighat A. *Monte Carlo Methods for Particle Transport*. 2nd ed. Boca Raton: CRC Press (2021).
16. Wagner JC, and Haghighat A. Automated Variance Reduction of Monte Carlo Shielding Calculations Using the Discrete Ordinates Adjoint Function. *Nucl Sci Eng* (1998) 128:186–208. doi:10.13182/nse98-2
17. Wagner JC, Peplow DE, and Mosher SW. FW-CADIS Method for Global and Regional Variance Reduction of Monte Carlo Radiation Transport Calculations. *Nucl Sci Eng* (2014) 176:37–57. doi:10.13182/nse12-33
18. Petit O, Lee Y-K, and Diop CM. Variance Reduction Adjustment in Monte Carlo TRIPOLI-4 Neutron Gamma Coupled Calculations. *Prog Nucl Sci Tech* (2014) 4:408–12. doi:10.15669/pnst.4.408
19. Nowak M, Mancusi D, Sciannandrone D, Masiello E, Louvin H, and Dumonteil E. Accelerating Monte Carlo Shielding Calculations in TRIPOLI-4 with a Deterministic Adjoint Flux. *Nucl Sci Eng* (2019) 193:966–81. doi:10.1080/00295639.2019.1578568
20. Díaz-Londoño G, García-Pareja S, Salvat F, and Lallena AM. Monte Carlo Calculation of Specific Absorbed Fractions: Variance Reduction Techniques. *Phys Med Biol* (2015) 60:2625–44. doi:10.1088/0031-9155/60/7/2625
21. Dorigo M, Maniezzo V, and Colorni A. Ant System: Optimization by a colony of Cooperating Agents. *IEEE Trans Syst Man Cybern B* (1996) 26:29–41. doi:10.1109/3477.484436
22. García-Pareja S, Vilches M, and Lallena AM. Ant colony Method to Control Variance Reduction Techniques in the Monte Carlo Simulation of Clinical Electron Linear Accelerators. *Nucl Instr Methods Phys Res Section A: Acc Spectrometers, Detectors Associated Equipment* (2007) 580:510–3. doi:10.1016/j.nima.2007.05.217
23. García-Pareja S, Vilches M, and Lallena AM. Ant colony Method to Control Variance Reduction Techniques in the Monte Carlo Simulation of Clinical Electron Linear Accelerators of Use in Cancer Therapy. *J Comput Appl Maths* (2010) 233:1534–41. doi:10.1016/j.cam.2008.03.052
24. Carvajal MA, García-Pareja S, Guirado D, Vilches M, Anguiano M, Palma AJ, et al. Monte Carlo Simulation Using the PENELOPE Code with an Ant colony Algorithm to Study MOSFET Detectors. *Phys Med Biol* (2009) 54:6263–76. doi:10.1088/0031-9155/54/20/015
25. García-Pareja S, Galán P, Manzano F, Brualla L, and Lallena AM. Ant colony Algorithm Implementation in Electron and Photon Monte Carlo Transport: Application to the Commissioning of Radiosurgery Photon Beams. *Med Phys* (2010) 37:3782–90. doi:10.1118/1.3456108
26. Cenizo E, García-Pareja S, Galán P, Bodineau C, Caudepón F, and Casado FJ. A Jaw Calibration Method to Provide a Homogeneous Dose Distribution in the Matching Region when Using a Monoisocentric Beam Split Technique. *Med Phys* (2011) 38:2374–81. doi:10.1118/1.3581377
27. Clark FH. The Exponential Transform as an Importance-Sampling Device – A Review. In: *Document ORNL-RSIC-14*. Oak Ridge: Oak Ridge National Laboratory (1966).
28. Woodcock E, Murphy T, Hemmings P, and Longworth S. Techniques Used in the GEM Code for Monte Carlo Neutronics Calculations in Reactors and Other Systems of Complex Geometry. In: *Proc. Conf. On Applications of Computing Methods to Reactor Problems. Tech. Rep. ANL-7050*. Argonne: Argonne National Laboratories (1965).

29. Coleman WA. Mathematical Verification of a Certain Monte Carlo Sampling Technique and Applications of the Technique to Radiation Transport Problems. *Nucl Sci Eng* (1968) 32:76–81. doi:10.13182/nse68-1
30. Sempau J, Wilderman SJ, and Bielajew AF. DPM, a Fast, Accurate Monte Carlo Code Optimized for Photon and Electron Radiotherapy Treatment Planning Dose Calculations. *Phys Med Biol* (2000) 45:2263–91. doi:10.1088/0031-9155/45/8/315
31. Tian L, Zhu J, Liu M, and An Z. Bremsstrahlung Spectra Produced by Kilovolt Electron Impact on Thick Targets. *Nucl Instr Methods Phys Res Section B: Beam Interactions Mater Atoms* (2009) 267:3495–9. doi:10.1016/j.nimb.2009.08.009
32. Llovet X, and Salvat F. PENEPMA: A Monte Carlo Program for the Simulation of X-ray Emission in Electron Probe Microanalysis. *Microsc Microanal* (2017) 23:634–46. doi:10.1017/s1431927617000526
33. Brualla L, Salvat F, and Palanco-Zamora R. Efficient Monte Carlo Simulation of Multileaf Collimators Using Geometry-Related Variance-Reduction Techniques. *Phys Med Biol* (2009) 54:4131–49. doi:10.1088/0031-9155/54/13/011
34. Benmakhlouf H, Sempau J, and Andreo P. Output Correction Factors for Nine Small Field Detectors in 6 MV Radiation Therapy Photon Beams: A PENELOPE Monte Carlo Study. *Med Phys* (2014) 41:041711. doi:10.1118/1.4868695
35. Bush K, Zavgorodni SF, and Beckham WA. Azimuthal Particle Redistribution for the Reduction of Latent Phase-Space Variance in Monte Carlo Simulations. *Phys Med Biol* (2007) 52:4345–60. doi:10.1088/0031-9155/52/14/021
36. Rodriguez M, Sempau J, and Brualla L. A Combined Approach of Variance-Reduction Techniques for the Efficient Monte Carlo Simulation of Linacs. *Phys Med Biol* (2012) 57:3013–24. doi:10.1088/0031-9155/57/10/3013
37. Kawrakow I, Rogers DWO, and Walters BRB. Large Efficiency Improvements in BEAMnrc Using Directional Bremsstrahlung Splitting. *Med Phys* (2004) 31:2883–98. doi:10.1118/1.1788912

Conflict of Interest: The authors declare that the research was conducted in the absence of any commercial or financial relationships that could be construed as a potential conflict of interest.

Publisher's Note: All claims expressed in this article are solely those of the authors and do not necessarily represent those of their affiliated organizations, or those of the publisher, the editors and the reviewers. Any product that may be evaluated in this article, or claim that may be made by its manufacturer, is not guaranteed or endorsed by the publisher.

frontiers in Physics

ORIGINAL RESEARCH
published: 27 October 2021
doi: 10.3389/fphy.2021.726787

Microdosimetry and Dose-Averaged LET Calculations of Protons in Liquid Water: A Novel Geant4-DNA Application

Anna Baratto-Roldán[1,2], Alejandro Bertolet[3,4], Giorgio Baiocco[5], Alejandro Carabe[6] and Miguel Antonio Cortés-Giraldo[2]**

[1]Centro Nacional de Aceleradores, Seville, Spain, [2]Department of Atomic, Molecular and Nuclear Physics, Universidad de Sevilla, Seville, Spain, [3]Department of Radiation Oncology, Massachusetts General Hospital, Boston, MA, United States, [4]Harvard Medical School, Boston, MA, United States, [5]Radiation Biophysics and Radiobiology Group, Department of Physics, University of Pavia, Pavia, Italy, [6]Hampton University Proton Therapy Institute, Hampton University, Hampton, VA, United States

The spatial distribution of energy deposition events is an essential aspect in the determination of the radiobiological effects of ionizing radiation at the cellular level. Microdosimetry provides a theoretical framework for the description of these events, and has been used in several studies to address problems such as the characterization of Linear Energy Transfer (LET) and Relative Biological Effectiveness (RBE) of ion beams for proton therapy applications. Microdosimetry quantities and their distributions can be obtained by means of Monte Carlo simulations. In this work, we present a track structure Monte Carlo (MC) application, based on Geant4-DNA, for the computation of microdosimetric distributions of protons in liquid water. This application provides two sampling methods *uniform* and *weighted*, for the scoring of the quantities of interest in spherical sites, with diameters ranging from 1 to 10 μm. As an element of novelty, the work shows the approach followed to calculate, without resorting to dedicated simulations, the distribution of energy imparted to the site per electronic collision of the proton, which can be used to obtain the macroscopic dose-averaged LET as proposed by Kellerer. Furthermore, in this work the concept of *effective mean chord length* is proposed to take into account δ-ray influx and escape in the calculation of macroscopic dose-averaged LET for proton track segments and retrieve the agreement predicted by Kellerer's formula. Finally, the results obtained demonstrate that our MC application is reliable and computational-efficient to perform calculations of microdosimetric distributions and dose-averaged LET of proton track segments in liquid water.

Keywords: Geant4-DNA, dose-averaged LET, microdosimetry, lineal energy, site sampling method, proton therapy

OPEN ACCESS

Edited by:
Paul Sellin,
University of Surrey, United Kingdom

Reviewed by:
Giuseppe Schettino,
National Physical Laboratory, United Kingdom
Dimitris Emfietzoglou,
University of Ioannina, Greece

****Correspondence:***
Anna Baratto-Roldán
abaratto@us.es
Miguel Antonio Cortés-Giraldo
miancortes@us.es

Specialty section:
This article was submitted to Radiation Detectors and Imaging, a section of the journal Frontiers in Physics

Received: *17 June 2021*
Accepted: *05 October 2021*
Published: *27 October 2021*

Citation:
Baratto-Roldán A, Bertolet A, Baiocco G, Carabe A and Cortés-Giraldo MA (2021) Microdosimetry and Dose-Averaged LET Calculations of Protons in Liquid Water: A Novel Geant4-DNA Application. Front. Phys. 9:726787. doi: 10.3389/fphy.2021.726787

1 INTRODUCTION

The radiobiological effects of ionizing radiation can be traced back to the microscopic patterns of energy deposition in irradiated media, which can be described quantitatively with the formalism of microdosimetry [1–3]. In view of the growing awareness of the variations of proton Relative Biological Effectiveness (RBE) with increasing Linear Energy Transfer (LET) [4–6], several studies have turned to the framework of microdosimetry to approach problems such as the characterization of LET

distributions for proton therapy beams and the determination of their RBE [7–10]. Indeed, by obtaining the LET distributions it is possible to optimize treatment plans, taking into account the actual biological impact of radiation by working on LET objectives and constraints. Microdosimetry, on one hand, permits the calculation of RBE from a microscopic approach by means of the Microdosimetric-Kinetic Model (MKM) [11–13] for cell killing endpoint and, on the other hand, provides physical concepts and computational tools to calculate macroscopic dose-averaged LET ($\bar{L}_D$) distributions. These, in fact, being representative both of the amount of energy imparted and of its spatial concentration, are strictly related to the biological damage induced by radiation.

The microscopic analogue of the LET is called lineal energy (y), which is a stochastic quantity that accounts for the energy imparted per unit length to a certain sensitive volume, called *site*, by an incident particle and all its secondary products [14]. As for the macroscopic distribution of LET, the microscopic distribution of y can be biologically characterised by its dose-weighted average, $\bar{y}_D$ [15]. The difference between $\bar{L}_D$ and $\bar{y}_D$ is given by energy straggling, which can be accounted for by considering the weighted average δ_2 of the energy imparted to the site per individual collision ε_c of the incident particle. The mathematical description of this relation was given by Kellerer, and can be used to extract the macroscopic dose-averaged LET of a beam from its microdosimetric distributions [16–18].

The calculation of microdosimetric distributions and their moments can be carried out both analytically or by means of Monte Carlo (MC) simulations. In this work, we present the main features of a MC code developed with Geant4 [19–21] for the computation of microdosimetric distributions generated by proton track segments in liquid water *via* track-structure simulations done with the package Geant4-DNA [22–25]. Our code provides two sampling methods, called *uniform* and *weighted*, for the computation of the quantities of interest in spherical sites. We also highlight the description of the novel scoring method followed to compute of the energy imparted to the site per electronic collision of the primary proton, in order to connect the obtained $\bar{y}_D$ values to the macroscopic $\bar{L}_D$ ones avoiding resorting to dedicated calculations as discussed in our previous work [26]. Following the description of the geometry and the sampling algorithm implemented, the results obtained for microdosimetric distributions for different site sizes and energies are presented. Finally, the code is tested and benchmarked by comparing the $\bar{L}_D$ calculated with the formula proposed by Kellerer and the macroscopic one. As we found significant deviations from its prediction, probably due to the influence of secondary electrons, here we propose the usage of a quantity, named *effective mean chord length*, $\bar{l}_F$, with which we calculated *effective* frequency- and dose-averaged lineal energies, $\bar{y}_F^*$ and $\bar{y}_D^*$, respectively, so that we could recover the agreement predicted by Kellerer for protons between 10 and 90 MeV.

2 MATERIALS AND METHODS

2.1 Theoretical Framework

The use of the LET for the description of the biological effect of different radiation qualities at a small scale presents some limitations, the principal ones being that the concept of LET does not consider the random nature of energy loss along a particle track and that it does not take into account the length of the track relative to a finite target structure. The effects of these limitations, and the ranges of proton energies and site dimensions in which they are relevant to energy deposition, were extensively studied by Kellerer and Chmelevsky [27–30]. For large site dimensions (of the order of 1–10 μm) and small proton energies (below 1 MeV), the energy deposition is strongly influenced by the limited range of protons, since the LET may change significantly along the path through the site. On the other hand, as the energy of the proton increases, energy straggling and eventually δ-rays influx and escape start playing an important role, which becomes more relevant as site dimensions get smaller [14]. The interplay of the various factors affecting the energy deposition in cellular or sub-cellular regions and their contribution to the macroscopic dose-averaged LET is discussed in detail in the following paragraphs.

2.1.1 Basic Microdosimetric Concepts

The basic microdosimetric quantity is the *energy imparted* to a site by a single energy-deposition event, ϵ_s, where an *event* is defined as an energy deposition due to particles that are statistically correlated. The energy imparted is a random variable, and its value varies from event to event. Therefore, predictions can be only made on the basis of probability distributions.

The *single-event distribution* $f(\epsilon_s)$ of the energy imparted is defined as the distribution of energy deposited in the site by exactly one event. The expectation value of ϵ_s following $f(\epsilon_s)$ is called frequency-averaged imparted energy per event:

$$\bar{\epsilon}_{sF} = \int_0^\infty \epsilon_s f(\epsilon_s) d\epsilon_s. \tag{1}$$

For radiobiological considerations, it is also useful to consider the *weighted* or *dose distribution* $d(\epsilon_s)$ of the energy imparted per event, where the contribution of each event is weighted by the energy it deposits:

$$d(\epsilon_s) = \frac{\epsilon_s f(\epsilon_s)}{\bar{\epsilon}_{sF}}. \tag{2}$$

The expectation value of ϵ_s following $d(\epsilon_s)$ is called dose-averaged imparted energy per event $\bar{\epsilon}_{sD}$ and it is given by:

$$\bar{\epsilon}_{sD} = \int_0^\infty \epsilon_s d(\epsilon_s) d\epsilon_s = \frac{1}{\bar{\epsilon}_{sF}} \int_0^\infty \epsilon_s^2 f(\epsilon_s) d\epsilon_s = \frac{\overline{\epsilon_{sF}^2}}{\bar{\epsilon}_{sF}}. \tag{3}$$

From **Eq. 3** it is possible to relate both averages through:

$$\bar{\epsilon}_{sD} = \bar{\epsilon}_{sF} + \frac{\sigma_{\epsilon_s}^2}{\bar{\epsilon}_{sF}} = \bar{\epsilon}_{sF}\left(1 + V_{\epsilon_s}\right), \tag{4}$$

where $\sigma_{\epsilon_s}^2$ and V_{ϵ_s} are the variance and relative variance of ϵ_s, respectively. In general any continuous stochastic quantity x can be characterized trough its frequency and weighted probability density functions $f(x)$ and $d(x)$, the second being obtained by weighting each event by the value of the stochastic quantity.

Therefore, the following general relations can be obtained for the frequency- ($\bar{x}_F$) and weighted-averaged ($\bar{x}_D$) values of x:

$$\bar{x}_F = \int x f(x)\,dx,$$
$$\bar{x}_D = \int x d(x)\,dx = \frac{\int x^2 f(x)\,dx}{\int x f(x)\,dx}, \quad (5)$$
$$\bar{x}_D = \bar{x}_F + \frac{\sigma_x^2}{\bar{x}_F} = \bar{x}_F(1 + V_x),$$

where σ_x and V_x are the variance and the relative variance of x, respectively.

Another fundamental microdosimetric quantity is the *lineal energy*, y, defined as:

$$y = \frac{\epsilon_s}{\bar{l}}, \quad (6)$$

where $\bar{l}$ is the mean chord length of the site. The chord length l is itself a stochastic quantity and represents the length of a particle track (considered a straight line) within a site. It depends on the shape and dimensions of the site and, if the track is considered as a straight line, the determination of $\bar{l}$ is a purely geometrical problem [18, 31].

The frequency-averaged lineal energy $\bar{y}_F = \bar{\epsilon}_{sF}/\bar{l}_F$ is the microdosimetric analogue of the frequency- or track-averaged LET, $\bar{L}_T$. If the so called "short track segment condition" holds, i.e., the site dimension is considerably smaller than the proton range so that the LET can be considered constant along the track segment across the site, the frequency-averaged lineal energy and the track-averaged LET coincide: $\bar{y}_F = \bar{L}_T$. It must be noted that, in the specific situations considered in this work, the macroscopic LET values are to be considered as *restricted*, since the site dimension determines a maximum cut-off to the distance that secondary electrons can travel from the place they are set in motion and therefore, to their kinetic energy. This is especially relevant for clinical applications, where the interest is focused on the energy deposited "locally" by a particle and not on its total energy loss.

2.1.2 The Relative Variance Formula for the Derivation of Macroscopic LET From Microdosimetry

As already mentioned at the beginning of this section, if a medium is exposed to an absorbed dose D, the actual energy imparted to a specified site will depend on various factors [30]. Firstly, the number of independent charged particles traversing the region and their different LET values if a composite beam impinges on the site. Secondly, the chord length associated to each proton crossing the site. Finally, even particles with same LET and chord length can result in a different energy imparted, as both the number of collisions along the chord and the energy lost in each collision might vary. The impact of this last factor, called energy straggling, can be expressed as $\epsilon_s = L \times l \pm \delta$, where L and l are respectively the LET and chord length of a particle, and δ is the stochastic variability of the energy imparted with respect to the expected energy $\bar{\epsilon}_s = L \cdot l$ due to straggling. The influence of the different random factors on the single-event distribution, under the short track segment condition, can be considered in terms of the relative variance of the different quantities [17], i.e.:

$$V_{\epsilon_s} = V_{LET} + V_l + V_l \cdot V_{LET} + V_\delta, \quad (7)$$

where V_{LET}, V_l and V_δ are the relative variances of the distributions of LET, chord length and energy straggling, respectively. The computation of the straggling distribution is complicated by the fact that the escape and influx of δ-rays from and into the region of interest presents considerable theoretical difficulties, and the problem needs to be studied with Monte Carlo simulations of δ-ray tracks. The relative variance of the straggling distribution, in particular, is determined by the weighted average of the distribution of energy imparted per individual proton collision:

$$\delta_2 = \bar{\varepsilon}_c\left(1 + \frac{\sigma_{\varepsilon_c}^2}{\bar{\varepsilon}_c^2}\right), \quad (8)$$

where $\bar{\varepsilon}_c$ and σ_{ε_c} are the average and the standard deviation of the distribution of energy imparted per collision, respectively. The relative variance of the straggling distribution can be demonstrated to be equal to [16]:

$$V_\delta = \frac{\delta_2}{\bar{\epsilon}_{sF}}. \quad (9)$$

Consequently, from **Eq. 7** the following formula can be obtained:

$$\frac{\bar{\epsilon}_{sD}}{\bar{\epsilon}_{sF}} = \left(\frac{\bar{L}_D}{\bar{L}_T} - 1\right)\left(\frac{\bar{l}_D}{\bar{l}_F}\right) + \frac{\bar{l}_D}{\bar{l}_F} + \frac{\delta_2}{\bar{\epsilon}_{sF}}. \quad (10)$$

By using the previous relations, and considering that $\bar{y}_D = \bar{\epsilon}_{sD}/\bar{l}_F$, the derivation of the subsequent relation for the dose-averaged LET is straightforward:

$$\bar{L}_D = \bar{y}_D\frac{\bar{l}_F}{\bar{l}_D} - \frac{\delta_2}{\bar{l}_D}. \quad (11)$$

As emerges from **Eq. 11**, identified hereafter as Kellerer's formula, macroscopic and microscopic quantities are related to each other. Therefore, the calculation through MC track structure simulations of the microdosimetric quantities $\bar{y}_D$, δ_2 and the chord length distributions can be used to obtain the dose-averaged LET of a given composite beam.

2.2 MC Track Structure Simulations

In order to calculate the various microdosimetric quantities in **Eq. 11** through MC track structure simulations, a particle track needs to be simulated and sampled, placing a site in such a way that at least one energy deposit occurs inside it. There are different types of randomness for the interception of a convex body with straight lines; in the following, two types will be distinguished: *uniform* and *weighted* [31, 32]. The first type results when a body is exposed to a uniform isotropic fluence of infinite straight lines, while the second occurs when an uniformly distributed random point is chosen in a body and is traversed by straight lines with uniform random direction. From a computational point of view, uniform sampling consist in randomly selecting a position for the

center of the site within the region of interest, while weighted sampling consist in selecting an energy transfer point and then placing a site randomly around it. An immediate drawback of the first method is that it is highly inefficient, since the chances of selecting areas with no energy imparted to them are really high. On the other hand, the second method ensures the occurrence of at least one energy transfer within the site, and it is more suitable for MC track structure calculations. The term "weighted" in this context, refers to the fact that the probability of selecting a point centered at a certain elementary volume dV is not uniform but weighted by a factor that compensates for the non-uniform density of transfer points around the particle track [14, 33].

The chord length is a stochastic quantity that depends on the geometry of the site and the straight line associated to each proton in the site. Therefore, its distribution and average values are strictly connected to the sampling method chosen, affecting the shape of Kellerer's formula [31]. However, with the selection of the appropriate weighting factor, uniform and random sampling methods can be considered as equivalent and, in the case of spherical sites of diameter d, **Eq. 11** takes the form [18]:

$$\bar{L}_D = \frac{8}{9}\bar{y}_D - \frac{4\delta_2}{3d}. \quad (12)$$

Straggling, on its side, is an independent random factor from LET and chord length, as even particles with same LET traversing the site with the same chord length might result in a different energy imparted per event ϵ_s. Therefore, it is not affected by the sampling method considered. However, when simulating a beam composed by particles of different LET, attention must be put to not include the variance of the LET distribution into the straggling one for the computation of δ_2, as explained extensively by Bertolet et al. [26].

In the following paragraphs, the main features of the MC application developed for the computation of the various quantities involved in Kellerer's formula are presented. All simulations were carried out with the Geant4 toolkit (version 10.5), by using our computing cluster hosted at Centro Informático Científico de Andalucía (CICA, Seville, Spain), consisting of 24 computational nodes, each with 2 × 12C AMD Abu Dhabi 6344 (2.6 GHz/6 MB) L3. For every case considered, a number of 250,000 proton tracks was simulated, divided into 250 parallel jobs. The Geant4-DNA package, available within Geant4, was used for this purpose. Compared to Geant4, which provides various physics list options based on a condensed-history approach for the transport of charged particles, Geant4-DNA includes models developed for track structure simulations, which allows the reproduction of each single interaction of neutral and charged particles with liquid water [22–25]. This is especially key to carry out an accurate modeling of electron transport below 1 keV, which affects to energy deposition tallied at sub-micrometric targets (below ~100 nm) as pointed out by Kyriakou et al. [34]. Geant4-DNA provides various physics list options as well, which mostly differ on the electron transport models used below 255 keV or its algorithm speed [25]. In this work, intended to highlight the code capabilities and illustrate the accuracy with which the dose-averaged LET

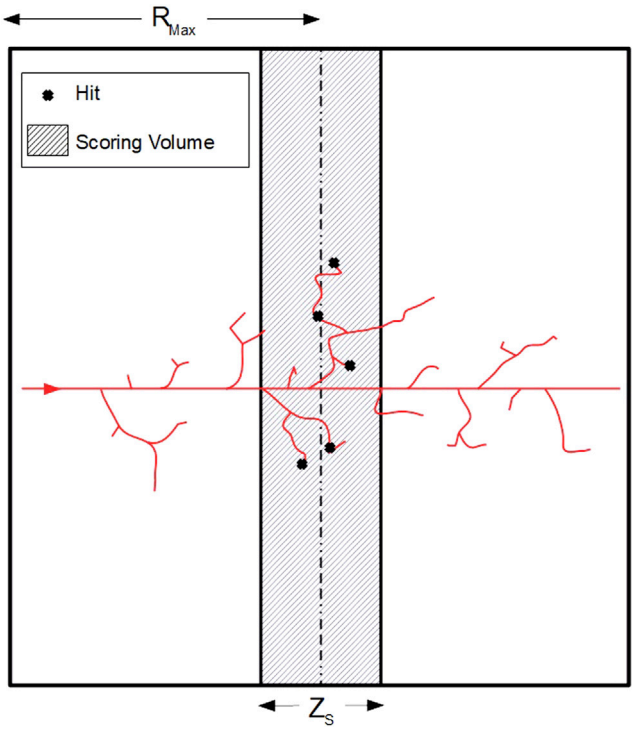

FIGURE 1 | Scheme of the geometry used for microdosimetry simulations (2D projection). The primary proton (red track) is generated at the surface (on the left) of a cubic water volume (world volume) and travels along the Z axis. The energy transfer points (hits) are then scored in the middle of the volume (shaded area), in a slab whose thickness (Z_S) varies depending on the dimension of the site. The spherical sites are not physically simulated, as they are virtually selected in the scoring volume with an algorithm that depends on the type of randomness considered. Finally, the half-dimension of the world volume (R_{max}) varies according to the maximum energy of the incident protons, and is slightly greater than the maximum range of the δ-rays emitted.

can be calculated from microdosimetry quantities, we used the "option 2" of the Geant4-DNA constructor, which is an accelerated version of Geant4-DNA default constructor. This package only allows calculations for proton energies below 100 MeV. Therefore, simulations were performed with mono-energetic proton beams in the range 10–90 MeV, choosing the lower limit to ensure the validity of the short track segment condition. Simulations carried out with *weighted* sampling ranged from 90 min (protons at 10–20 MeV) to 87 h (90 MeV) per 1,000 primary protons; as for simulations using *uniform* sampling of site position, they took from 170 min (20–40 MeV) to 87 h (90 MeV) including, to improve statistics, a loop of up to 1,000 tries which finished once at least one energy exchange point was found within the site.

For mono-energetic proton beams, the LET distribution approximates a delta function, centered at the LET of the particle for the specific energy considered. In this specific situation, therefore, the relation $\bar{L}_D = \bar{L}_T = \bar{y}_F$ (being $\bar{L}_D$ and $\bar{L}_T$ averages on restricted LET values, as stated previously) holds and can be used for the validation of the code [26]. Furthermore,

comparisons were also made with unrestricted macroscopic dose-averaged LET values, computed with the formula proposed by Cortés-Giraldo and Carabe [35]:

$$\bar{L}_{\mathrm{D}} = \frac{\sum_{n=1}^{N} \sum_{s=1}^{S_n} \omega_n L_{\mathrm{sn}} \varepsilon_{\mathrm{sn}}}{\sum_{n=1}^{N} \sum_{s=1}^{S_n} \omega_n \varepsilon_{\mathrm{sn}}}, \tag{13}$$

where n and s are the indexes for an event and a step, respectively, L_{sn} is the mean energy loss per unit path length in the material, $\varepsilon_{\mathrm{sn}}$ is the energy deposited by the primary particle along the step and ω_n its statistical weight. Further details of this calculation can be found in [35].

2.2.1 Geometry

Figure 1 shows the geometry of our microdosimetry code. The *world volume*, i.e., the volume that represents the experimental area and contains all the other components, consist of a water cubic box having half dimensions R_{max} slightly greater than the maximum range, $R_{\delta,\ \mathrm{max}}$, of δ-rays emitted by the incident protons. This range is calculated with the formula proposed by Tabata et al. [36], and the condition $R_{\mathrm{max}} \geq R_{\delta,\,\mathrm{max}}$ is necessary to ensure intra-track electronic equilibrium. The scoring volume, i.e., the volume in which the energy transfer points (*hits*) are detected and stored, is a water slab positioned in the center of the world volume with same transversal dimensions and thickness $Z_{\mathrm{S}} = 4d$, where d is the diameter of the site. The value of Z_{S} was set to ensure enough energy transfer points for each track within the scoring volume, being $4d$ a good compromise between its thickness and calculations carried out comparing the two site positioning methods explained below; more details can be found elsewhere [37]. Simulations were run with spherical sites of 1 and 10 μm diameter. In order to have the same proton kinetic energy distribution at the center of the world volume for both site diameters, the decision to set $R_{\mathrm{max}} = R_{\delta,\,\mathrm{max}} + Z_{\mathrm{S,\,max}}/2$ was taken, where $Z_{\mathrm{S,\,max}}$ is the thickness of the scoring volume corresponding to a site diameter of 10 μm.

In our simulations, the beam (red track in **Figure 1**) originates at the surface of the cubic volume located at $z = -R_{\mathrm{max}}$ and travels along the z-axis. The physical quantities of interest are scored in randomly placed spherical sites, that are virtually identified as regions of the scoring volume thanks to specific algorithms for the selection of their centers. For the site positioning, two sampling methods have been implemented, uniform and weighted random sampling, which are described in the next paragraph.

2.2.2 Scoring Algorithms

The most intuitive way of scoring energy deposition events in micrometric sites along a proton track would be to randomly select a point $\vec{P}_{\mathrm{C}}$ in the region of interest with a uniform probability, and to consider all the hit positions $\vec{P}_{\mathrm{h}_i}$ occurring at a distance $|\vec{P}_{\mathrm{h}_i} - \vec{P}_{\mathrm{C}}| \leq d/2$ from it. This sampling method, identified in this work as uniform, is very robust and it is not subject to any bias. The main drawback of this technique is that it is likely to be highly inefficient, as the probability of selecting volumes with no hits is really high and increases for smaller sites and higher energies.

To increase the sampling efficiency, weighted sampling can be used instead. In this case, an energy transfer point $\vec{P}_{\mathrm{H}}$ is randomly chosen with uniform probability among the hits of the simulated track. Then, the center of the site $\vec{P}_{\mathrm{C}}$ is sampled with uniform probability in a sphere of radius $d/2$ around $\vec{P}_{\mathrm{H}}$, i.e., at a distance $|\vec{P}_{\mathrm{C}} - \vec{P}_{\mathrm{H}}| \leq d/2$. Finally, all the energy transfer points $\vec{P}_{\mathrm{h}_i}$, within a distance $|\vec{P}_{\mathrm{h}_i} - \vec{P}_{\mathrm{C}}| \leq d/2$ are considered for the computation of the microdosimetric quantities in the site. In this way, the presence of at least one hit in the site is always ensured, and a sampling efficiency of 100% can be achieved. The downside of this method is that it is spatially biased towards regions of high density of hits, and a compensation factor must be introduced to "correct" the results and make them equivalent to uniform ones. As suggested by other studies [33, 38], this factor should be equal to the ratio of the number of hits that can be selected to the number of hits located in the randomly placed site.

The working principle of the two methods, and the way they were implemented in our code, is shown in **Figure 2**. In both cases, a hit selection region within the scoring volume, where $\vec{P}_{\mathrm{C}}$ and $\vec{P}_{\mathrm{H}}$ are sorted, can be identified. The dimensions of this region are chosen to ensure that all the randomly selected points are always fully included in the scoring volume, and depend on the scoring algorithm considered. In the case of weighted sampling, the compensation factor is set equal to $N_{\mathrm{sel}}/N_{\mathrm{int}}$ (see **Figure 3**), where N_{sel} is the number of hits (with energy different from zero) in the hit selection region that can be randomly selected and N_{int} is the number of hits in the intersection volume of the site and the hit selection region.

Once the position of the site is sorted, three main quantities are computed: the total energy deposited in the site per event, ϵ_{s}, the total energy deposited for each single proton collision, ε_{c}, and the *trajectory* length, s, of the proton traversing the site. In particular, for the computation of the energy imparted per individual proton collision, a *Sensitive Detector* class was specifically coded to identify uniquely the electronic showers generated by each collision. To this end, a distinctive tag is assigned to every primary electron set in motion by a proton collision. Then, taking advantage of the specific structure of the tracking algorithm of Geant4, all secondary electrons created by further collisions of the electron originating the shower are assigned the same tag, which becames an identifier of the shower. In this way, the energy deposited in the site by each δ-ray shower originating in the site or entering the site can be scored independently, as graphically represented in **Figure 4**.

3 RESULTS

Figure 5 shows the results obtained for the frequency-averaged energy imparted per event, $\bar{\epsilon}_{\mathrm{sF}}$, as a function of the energy and the site diameter, for the two sampling methods considered. Taking the uniform sapling method results as a reference, we obtained relative residuals below 5% for all the energies considered. Regarding the weighted-averaged energy deposited per individual proton collision, δ_2, an intermediate step is

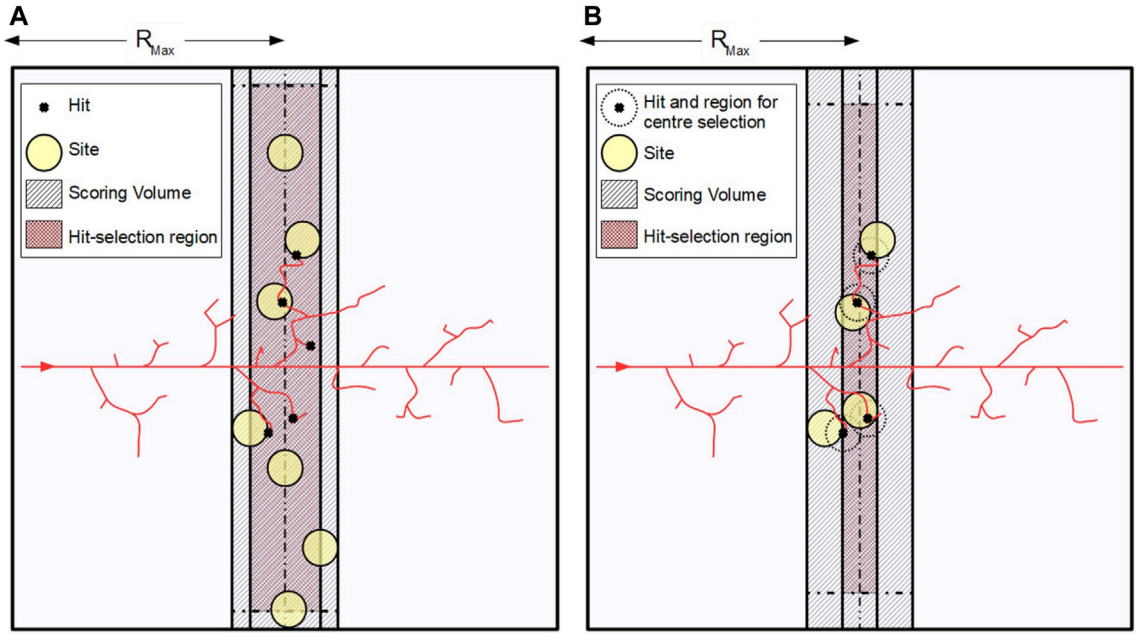

FIGURE 2 | Graphical representation of the working principle of the two sampling algorithms: **(A)** uniform sampling and **(B)** weighted sampling. In both cases, a hit selection region (maroon shaded area) is identified, where the centers of the sites (yellow circles) are sorted. The dimensions of this region depend on the sampling algorithm used and on the diameter of the site, as lateral margins must be left to ensure that the site is always fully included in the scoring volume. For uniform sampling this margin must be set equal to the site radius, while for weighted sampling the margin is equal to the site diameter.

necessary to extract its value from the simulations. This quantity is an independent random factor from LET and chord length, therefore their variances should not be included in the computation of δ_2 when calculating $\bar{L}_D$ with **Eq. 12**. This means that only the distribution of energy imparted per individual proton collision corresponding exactly to an energy imparted per event $\bar{\epsilon}_{sF}$ and a chord length $\bar{l}_F$ should be taken into account to calculate δ_2. In our previous work [26], this was done with a dedicated simulation, positioning the site in such a way that the particle traversed it with a path length equal to $\bar{l}_F$. In the work presented here, however, a new approach is proposed to extract δ_2 directly from the main MC simulation, by recording the two dimensional plot of the distribution $\epsilon_c^2 f(\epsilon_c)$ as a function of the primary proton trajectory length s within the site. By doing so, projections could be taken for intervals of s with size $0.1d$, to build a graph of δ_2 as a function of s. Examples of this graphs, for the weighted random sampling, are shown in **Figure 6**. For values of $s < d/2$, the main contribution to δ_2 is given by the δ-ray influx, whose influence decreases rapidly as s increases. For $s > d/2$, on the other hand, the value of δ_2 can be considered as constant. Therefore, since $\bar{l}_F = 2d/3 > d/2$ for a spherical site, the final values of δ_2 were extracted from the average of the points in the range $s > d/2$, weighted by their uncertainty. In **Figure 7** the values of δ_2 for the different sampling methods and site diameters considered are represented together as a function of the incident proton kinetic energy: again, taking the uniform sampling results as a reference, we obtained relative residuals below 6%.

The results obtained for the frequency-averaged lineal energy $\bar{y}_F$ with both sampling methods are presented in **Figure 8**. In this figure, $\bar{y}_F$ values and $\bar{L}_D$ values obtained with **Eq. 12** are compared, to verify the relation $\bar{y}_F = \bar{L}_D$, valid for mono-energetic beams. Constant LET condition was fulfilled for all scenarios, with the worst one being 10 MeV protons on 10-μm in-diameter sites, in which a change below 2% was observed. Taking the $\bar{y}_F$ values as a reference, the relative residuals of $\bar{L}_D$ for the different site diameters and sampling methods considered are represented in **Figure 9**. While for the 10 μm diameter site we find residuals approximately constant with energy and below 6%, for the 1 μm diameter site deviations increase with energy, reaching values of up to 30%. This effect is more evident looking at the weighted random sampling points, which are not subject to the lack of statistics that affects the uniform random sampling method, especially at higher energies. Moreover, this increasing difference between $\bar{L}_D$ and $\bar{y}_F$ for the 1 μm site, results in an anomalous behaviour of $\bar{L}_D$ if compared to the macroscopic dose-averaged LET obtained from **Eq. 13**, represented as a black shaded area in **Figure 8**. Indeed, this last value, being unrestricted, represents the maximum $\bar{L}_D$ achievable with Kellerer's formula and should never be crossed, a statement that is even stronger in the case of the 1 μm site against what happens in the figure.

To solve this problem, we proposed the use of new quantities named *effective mean chord length*, $\bar{l}_F^*$, and *effective frequency- and dose-averaged lineal energy*, $\bar{y}_{F,D}^*$, respectively. As done for the energy imparted per individual proton collision, a two dimensional plot of $\epsilon_s f(\epsilon_s)$ as a function of s was produced from the simulation, and

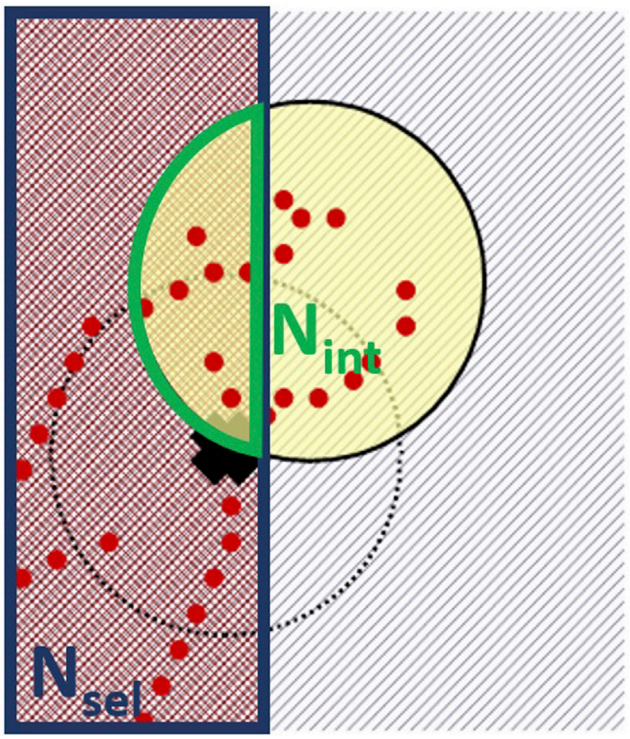

FIGURE 3 | Detail of the working principle of the weighted sampling method in **Figure 2B**. The compensation factor is computed as the ratio between the number of selectable hits (with deposited energy different from zero) in the hit selection region (N_{sel}) and the number of hits in the intersection volume of the site with the hit selection region (N_{int}).

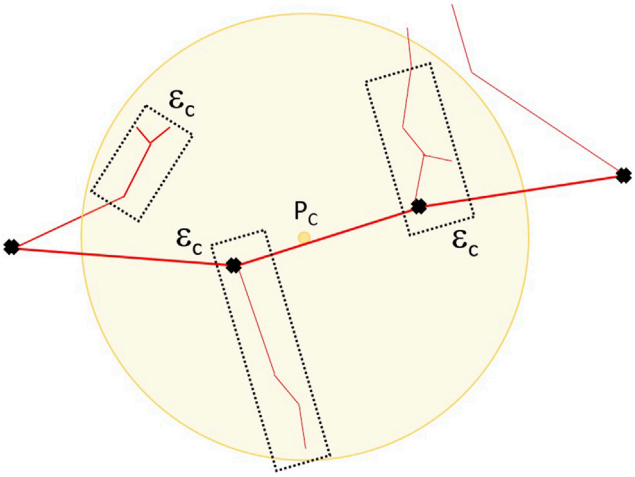

FIGURE 4 | Schematic representation of the scoring method for the evaluation of the energy deposited per single proton collision in the site, ε_c. The primary δ-ray generated by the proton collision is identified and assigned one distinctive tag, that is then inherited by all the secondary electrons in the shower. Only the energy deposition events happening within the site are accounted for in the calculation of ε_c, including δ-ray influx from outside the site.

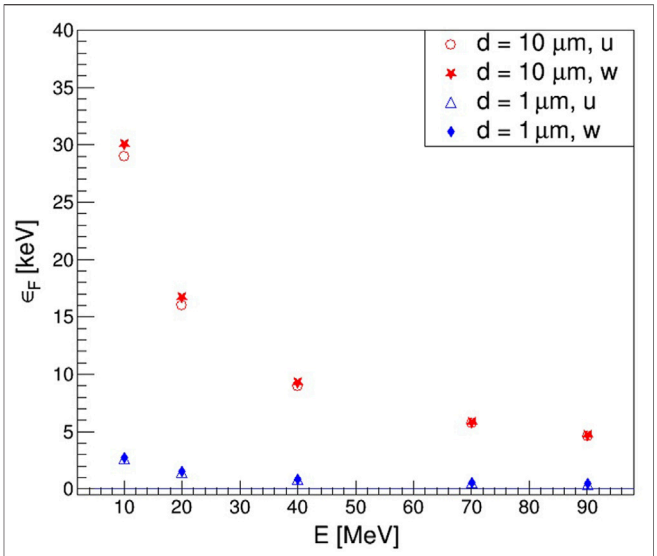

FIGURE 5 | Frequency-averaged energy imparted per event $\bar{\epsilon}_{sF}$ as a function of the proton energy. Uniform (open markers) and weighted (full markers) random sampling results are plot together and compared for sites of 1 (blue triangles and diamonds) and 10 µm (red circles and stars) diameter.

projections were extracted for intervals of s equal to $0.1d$. In this way, plots of the mean energy imparted per event ϵ_s as a function of the proton trajectory length could be built, as the ones shown in **Figure 10** for weighted random sampling. When proton tracks do not cross the site or pass tangent to it, i.e. $s \sim 0$, the only contribution to ϵ_s is given by δ-ray influx. Then, for higher s values, ϵ_s grows linearly with the trajectory length. Intersecting the frequency-averaged energies imparted per event obtained considering the full data set and the linear fits of ϵ_s as a function of s shown in **Figure 10**, the value of s corresponding exactly to an energy imparted per event equal to $\bar{\epsilon}_{sF}$ should be obtained. In principle, this value should correspond to the "geometrical" mean chord length $\bar{l}_F = 2d/3$, however, we found out that this was not the case as the mean chord lengths obtained, which we named *effective mean chord lengths* $\bar{l}_F^*$, were slightly different and varied with proton energy (see **Figure 11**).

Using the effective chord lengths for the computation of frequency and dose-averaged effective lineal energies, the results shown in **Figure 12** could be obtained, where all the values of $\bar{L}_D$ obtained with **Eq. 12** lay below the macroscopic unrestricted dose-averaged LET, as expected. In this figure, a general better agreement between uniform and weighted random sampling methods emerges, if compared to **Figure 8**. Relative residuals of our derived $\bar{L}_D$ values from $\bar{y}_F^*$ were found to be below 6% for both site dimensions and for all energies (see **Figure 13**) with the only exception of the points obtained for the two higher energies and the smallest site with uniform random sampling, which are strongly affected by the lack of statistics.

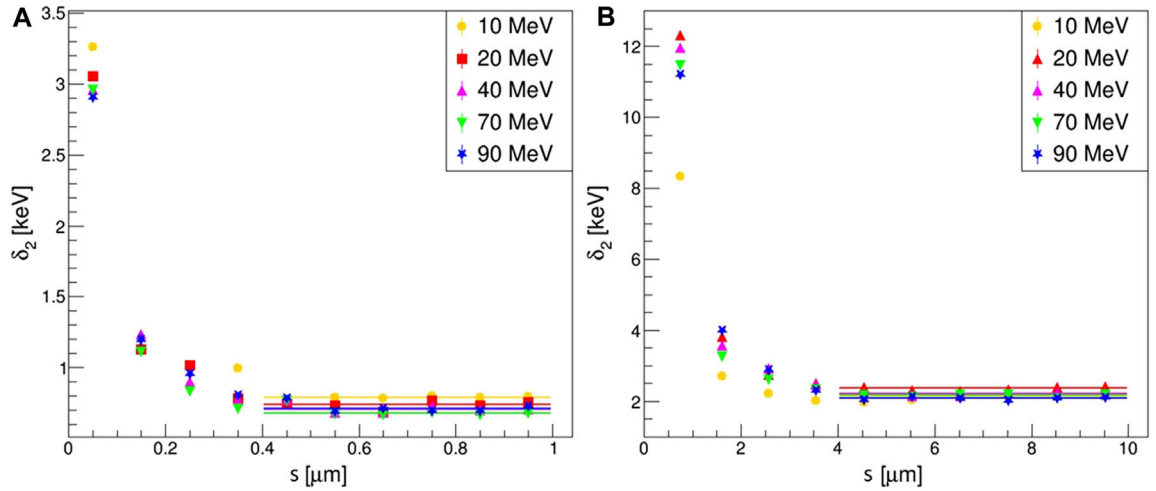

FIGURE 6 | Variation of δ_2 as a function of the proton trajectory length s within the site, obtained with weighted random sampling for the different energies. **(A)** sites of 1 μm diameter, **(B)** sites of 10 μm diameter. For the lower δ_2 values, the main contribution to δ_2 is given by the δ-ray influx, whose influence decreases quickly as s increases. For $s > d/2$, the value of δ_2 can be considered as constant. Since $\bar{l}_F > d/2$, the final values of δ_2 were extracted by averaging the points (weighted by their uncertainties) in the range $s > d/2$ (solid lines).

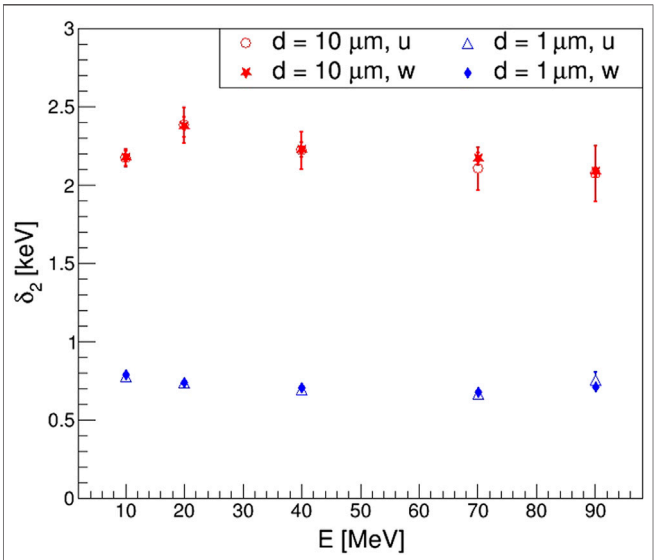

FIGURE 7 | Weighted average of the distribution of energy imparted per individual proton collision δ_2 as a function of the proton kinetic energy. Uniform (open markers) and weighted (full markers) random sampling results are compared for sites of 1 (blue triangles and diamonds) and 10 μm (red circles and stars) diameter sites.

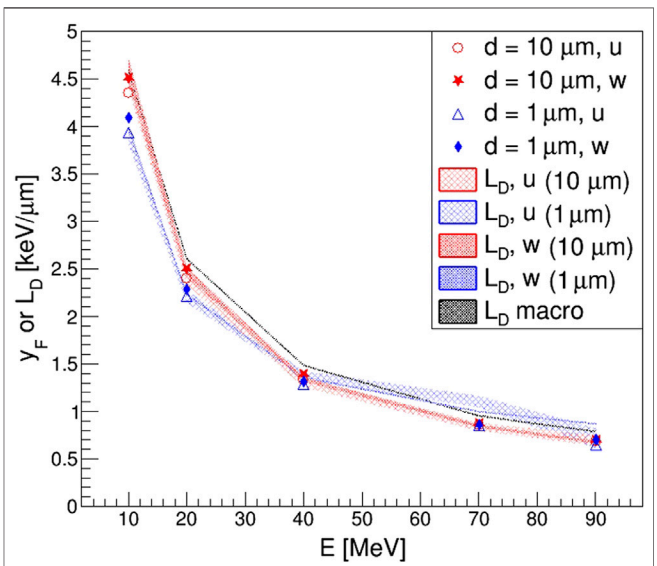

FIGURE 8 | Frequency-averaged lineal energy $\bar{y}_F$ as a function of the incident proton kinetic energy. Values obtained for uniform (open markers) and weighted (full markers) random sampling methods are compared for sites of 1 (blue triangles and diamonds) and 10 μm (red circles and stars) diameter. For mono-energetic proton beams the relation $\bar{L}_D = \bar{y}_F$ should hold, therefore $\bar{y}_F$ values are here superimposed to the respective $\bar{L}_D$ values derived from **Eq. 12**, represented as shaded areas whose thickness is given by the error associated to $\bar{L}_D$ for each diameter site. Finally, the macroscopic unrestricted $\bar{L}_D$ computed with **Eq. 13** is also reported as a reference.

4 DISCUSSION

In this work, a novel MC code for the computation of microdosimetric distributions generated by proton track segments in liquid water has been presented. Two different algorithms were implemented for the scoring of the quantities of interest: uniform and weighted random sampling for site positioning. While the first is ideally better as it is not subject to any bias, it is also very inefficient due to the high chances of selecting sites with no energy depositions within. On the contrary, weighted random sampling has a 100% efficiency, but might be

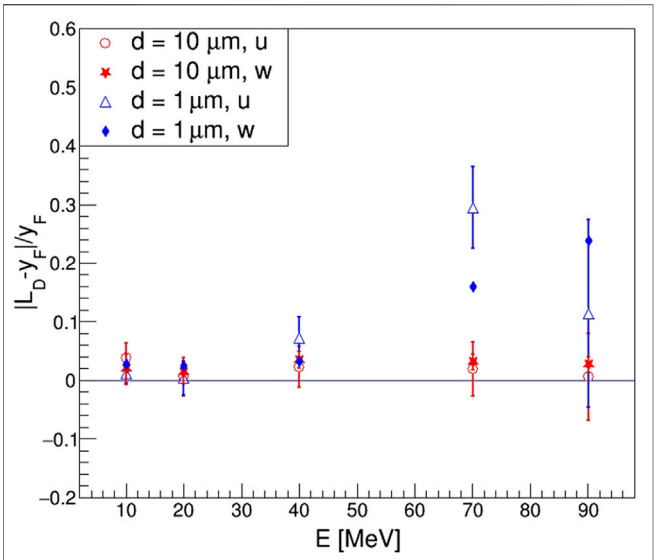

FIGURE 9 | Relative residuals of $\bar{L}_D$ from $\bar{y}_F$ for the different site diameters and sampling methods considered.

subject to biases related to the choice of the weighting factor. One of the main elements of novelty of our code is the inclusion of an algorithm for the computation of the distribution of energy imparted per individual proton collision. This distribution, which is impossible to measure experimentally, reflects the action of energy straggling and δ-ray influx and escape on the energy deposited in the site, and it is fundamental for the computation of dose-averaged LET from microdosimetric quantities with Kellerer's formula (**Eq. 11**).

In this study, our weighted random sampling algorithm was optimized so that the results obtained could be considered equivalent to uniform ones, with relative differences generally lower than 6%. Then, the code was used to run various simulations with mono-energetic proton beams, with energies in the range 10–90 MeV impinging on spherical sites of 1 and 10 µm diameter. Since for mono-energetic proton beams the relation $\bar{L}_D = \bar{y}_F$ holds, frequency-averaged lineal energy values obtained with both sampling methods were used as a reference for the validation of the code and the comparison with dose-averaged LET values obtained with **Eq. 12**. Furthermore, since the site dimensions considered were generally smaller than the maximum range of δ-rays emitted by the incident proton, the $\bar{L}_D$ values obtained in this way were expected to be restricted and always lower than the macroscopic unrestricted dose-averaged LET values, which were computed with **Eq. 13**.

While generally no evident problems emerged in the results obtained for the 10 µm diameter site, the 1 µm site arose questions about the validity of Kellerer's formula, as the $\bar{L}_D$ curve intersected the unrestricted one. This apparent contradiction was solved with our proposal of introducing the concept of *effective mean chord length* $\bar{l}_F^*$, defined as the trajectory length corresponding exactly to an energy imparted per event to the site equal to the $\bar{\epsilon}_{sF}$ obtained from the MC. Following this definition, $\bar{l}_F^*$ should be naturally equal to the "geometrical" mean chord length $\bar{l}_F = 2d/3$. However, this was proved to be wrong, as the effective value of the mean chord length not only differed slightly from the expected one, but varied also with the energy of the incident proton. This behaviour is probably related to the action of δ-ray influx, which affects the distribution of energy imparted to the site per event, increasing the actual value of $\bar{\epsilon}_{sF}$ with respect to what would be obtained by only considering direct

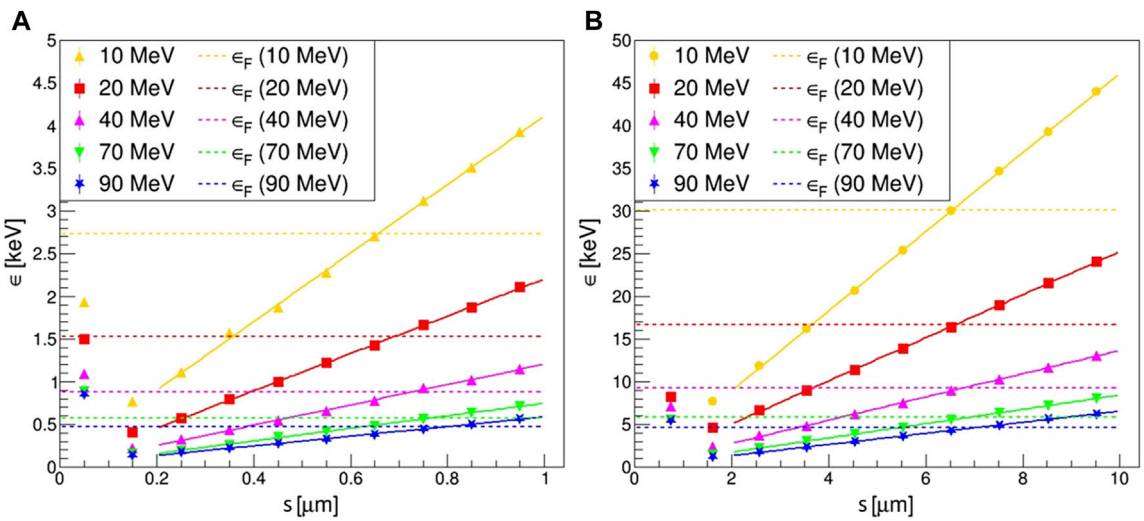

FIGURE 10 | Plot of the variation of the mean energy imparted per event, ϵ_s, as a function of the proton trajectory length s, described in the site, obtained with weighted random sampling for the different energies and sites: **(A)** 1 µm diameter; **(B)** 10 µm diameter. For $s \sim 0$, when proton tracks do not cross the site or pass tangent to it, the only contribution to ϵ_s is given by δ-ray influx. Then, for higher s, ϵ_s increases linearly with the trajectory length. The frequency-averaged energies imparted per event $\bar{\epsilon}_{sF}$ obtained considering the full data set are represented in this plot as horizontal dashed lines, each colour corresponding to one proton energy. The intersection point of the linear fit of ϵ_s as a function of s with $\bar{\epsilon}_{sF}$ corresponds to the effective mean chord length $\bar{l}_F^*$.

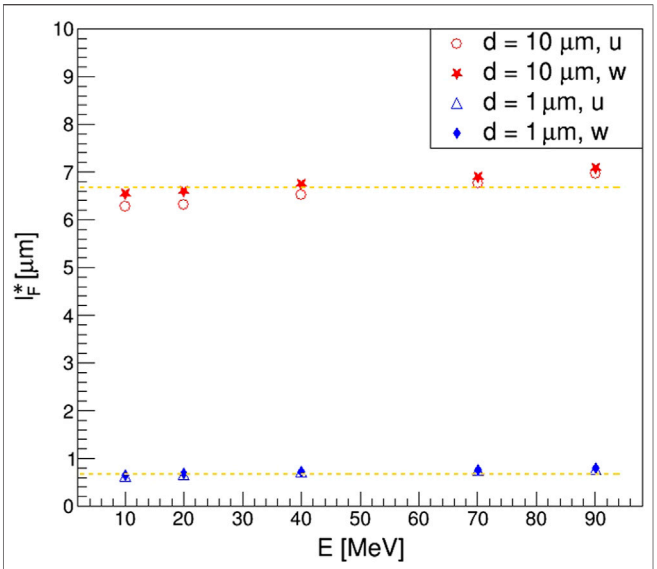

FIGURE 11 | Effective mean chord length $\bar{l}^*_F$ as a function of the proton energy obtained with uniform (open markers) and weighted (full markers) random sampling for sites of 1 µm (blue triangles and diamonds) and 10 µm (red circles and stars) diameter. The "geometrical" mean chord lengths $\bar{l}_F = 2d/3$ are reported for comparison as yellow horizontal dashed lines.

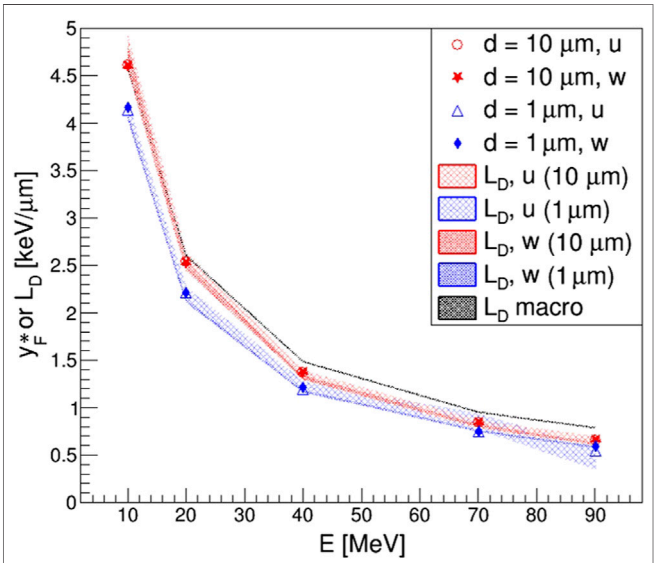

FIGURE 12 | Effective frequency-averaged lineal energy $\bar{y}^*_F$ as a function of the incident proton kinetic energy. Values obtained for uniform (open markers) and weighted (full markers) random sampling methods are compared for sites of 1 (blue triangles and diamonds) and 10 µm (red circles and stars) diameter. Values of $\bar{y}^*_F$ are superimposed to the respective $\bar{L}_D$ ones derived considering $\bar{y}^*_D$ instead of $\bar{y}_D$ in **Eq. 12**, represented as shaded areas whose thickness is given by the error associated to $\bar{L}_D$ for each diameter site. Finally, the macroscopic unrestricted $\bar{L}_D$ computed with **Eq. 13** is also reported as a reference.

traversals of proton tracks through the site, especially for the highest energies. By using the $\bar{l}^*_F$ values for the computation of frequency- and dose-averaged effective lineal energies, $\bar{y}^*_F$ and $\bar{l}^*_D$,

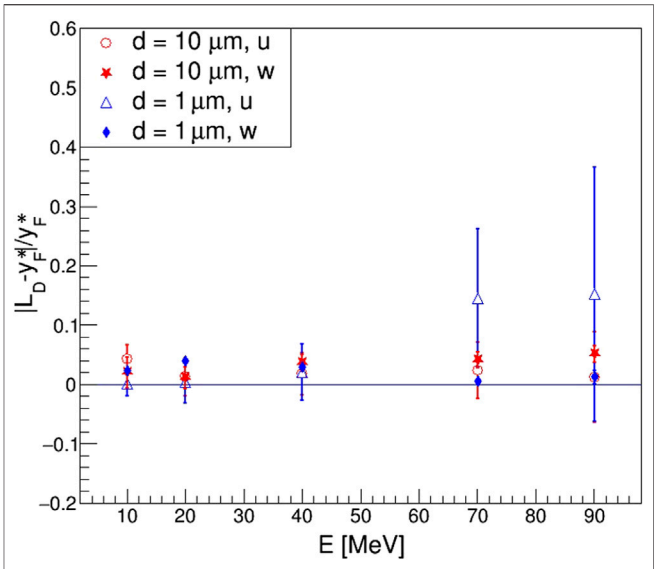

FIGURE 13 | Relative residuals of $\bar{L}_D$ from $\bar{y}^*_F$ for the different site diameters and sampling methods considered.

respectively, a better agreement was observed both between uniform and weighted random sampling results and between $\bar{L}_D$ and $\bar{y}^*_F$ curves. Furthermore, the nature of restricted LET emerged clearly in this case, being all the $\bar{L}_D$ values computed with Kellerer's formula below the macroscopic ones, and generally lower for the 1 µm diameter site. Indeed, the difference between restricted and unrestricted dose-averaged LET values decreases as the energy increases, especially expected for the 10 µm site, since the maximum range of δ-rays starts to be comparable to the site dimensions for proton energies below 20 MeV. Although the agreement found with our alternative approach looks promising, we must point out that this work only involved protons from 10 to 90 MeV (currently, Geant4-DNA simulates protons only up to 100 MeV). Thus, a dedicated analysis (beyond the scope of this work) extending the energy range and/or involving different ions and site shapes seems to be of interest to confirm our proposal, as well as cross-checking with other track-structure codes and experimental measurements. For the latter, it must be remarked that the beam energy spread and detector response introduce further variances in the distributions of microdosimetry quantities which must be carefully taken into account in such an analysis.

Concerning the δ_2-values, we observed deviations from previous works when comparing calculations with sites of 10 µm diameter. While the values obtained in this work were between 2.1 and 2.4 keV for protons from 10 to 90 MeV, lower values were reported previously using other approaches. With dedicated simulations, aiming at isolating its calculation from contributions due to the variance of single-event energy imparted variance as discussed in [26], we reported values of about 1.8 keV; previously, with a more approximated calculation with *G4EmPenelopePhysics* physics list [35], values of about 1.5 keV were reported for the same energy range. These deviations suggest

that the methodology followed to calculate δ_2 must be explained in detail, as it may impact the values of $\bar{L}_D$ calculated from microdosimetry quantities by means of **Eq. 12**. Moreover, different versions of the Geant4 toolkit were used across these works, thus the choice of transport models varied between them as well. This issue shows that a dedicated study to quantify the impact of different transport models on the calculated δ_2-value is of interest, but out of the scope of this article as Geant4 itself offers a wide variety of transport models combinations or physics list.

Using a weighted sampling approach in MC simulations to obtain microdosimetric quantities is undoubtedly advantageous in terms of computation time and efficiency. Indeed, the lower efficiency of uniform random sampling has emerged in our results numerous times, being its effects especially evident for sites of 1 μm diameter and proton kinetic energies above 70 MeV. For the same number of primary protons generated, a loss in statistic going from 60% to more than 90% in the worst case was observed, when comparing uniform sampling with weighted one. Therefore, the observed differences in the computational efficiencies clearly justifies the adoption of a weighted random sampling method for the computation of the microdosimetric quantities of interest, since equivalent results for $\bar{L}_D$ could be obtained by using the approach presented in this work. This method brings the advantage of permitting the calculation of RBE by means of models either based on microdosimetry, such as the MKM [11–13] or on LET [39–41] by means of calculating microdosimetry quantities only which, contrary to LET, can be measured. Thus, with the microdosimetry data provided by our code, one can derive analytical parameterisations to calculate the RBE by each approach, without having to derive a specific parameterisation for LET distributions [42–44]. Further, we expect the impact on the uncertainties found on our LET values retrieved from microdosimetry will be relatively small, and will not add up significantly to other more important sources of uncertainty, such as the (α/β) of the irradiated tissue.

The current version of the code, available upon request, is intended to be incorporated within the official examples of the Geant4 toolkit dealing with the extension Geant4-DNA, as it shows the main aspects of the calculation of microdosimetric quantities with track segments of protons and ions (such as He, Li, C, O or Si) using spherical sites, and illustrates how $\bar{L}_D$ can be retrieved from $\bar{y}_D$ calculated with protons. From a modelling perspective, spherical sites are good enough since sphere-based microdosimetry quantities correlate well with the yield of DSBs, as shown recently [45]. Thus, other shapes such as cylinders were not included in our study to avoid further complications in our analysis of the relations between macro- and microdosimetry distributions. However, they could be useful to benchmark our predictions against experimental results from microdosimetry with other shapes, as done previously in [46].

5 CONCLUSION

The use of a weighted random sampling approach in MC simulations for the calculation of microdosimetric quantities is widely supported in literature for its undeniable computational efficiency if compared to uniform random sampling. However, especially when considering segments of proton tracks traversing a *sensitive volume*, particular attention must be put in the computation of the weighting factors, to obtain unbiased results equivalent to uniform ones. In this work, we addressed this problem by developing a MC application for the computation of microdosimetric distributions generated by segments of proton tracks. A remarkable feature of our code, which would constitute a novelty as an official example of Geant4 toolkit, is the possibility of computing the distribution of energy imparted per single proton collision. This distribution, indeed, is strongly connected to the effect of energy straggling and δ-ray influx and escape on the energy deposited in a site per event, and represents the liaison between the microscopic dose-averaged lineal energy and the macroscopic dose-averaged LET, as theorised by Kellerer. To test and benchmark our code, we ran various simulations with mono-energetic proton beams, comparing frequency-averaged lineal energy results with dose-averaged LET ones obtained with Kellerer's formula. As predicted theoretically for proton beams of this kind in the short track segment condition, we obtained a very good agreement between the two quantities, with percentage differences always lower than 6%. In order to obtain this result, we resorted to a new quantity proposed in this work, the effective mean chord length $\vec{l}_F$, defined from the value of the primary proton trajectory length corresponding to the calculated frequency-averaged energy imparted to the site per single event. In fact, we observed that the action of δ-ray influx in the site strongly affected the distribution of energy imparted to the site per event, displacing its mean value with respect to what would be obtained by only considering direct traversals of proton tracks through the site. For this reason, further calculations at other proton energies and with other ions are of interest to assess the validity of our proposal beyond the limits of this work (protons from 10 to 90 MeV). Such a further study may suggest the introduction of minor corrections of the fitting parameters of our analytical microdosimetric models, described in [42, 43].

DATA AVAILABILITY STATEMENT

The raw data supporting the conclusions of this article will be made available by the authors, without undue reservation.

AUTHOR CONTRIBUTIONS

Conceptualization, AB-R, AB, AC, and MC-G; Methodology, AB-R, AB, AC and MC-G; Simulations, AB-R, AB, GB; Formal Analysis, AB-R, AB and MC-G; Resources, AC and MC-G; Writing-Original Draft Preparation, AB-R. and MC-G; Writing-Review and Editing, AB-R, AB, GB, AC, and MC-G; Project Administration, AC and MC-G; Funding Acquisition, MC-G.

FUNDING

This work was funded by Grant RTI2018-098117-B-C21 funded by MCIN/AEI/10.13039/501100011033 and by "ERDF A way of making Europe". The work also received funds from the European Union's Horizon 2020 research and innovation programme under the Marie Sklodowska-Curie Grant No. 675265, OMA–Optimization of Medical Accelerators, and from the Council for Economy, Industry, Knowledge and Universities of the Andalusian Government under Grant No. P18-RT-1900.

ACKNOWLEDGMENTS

All the Monte Carlo simulations presented in this work were carried out at the FIS-ATOM computing cluster hosted at CICA (Seville, Spain).

REFERENCES

1. Rossi HH. Spatial Distribution of Energy Deposition by Ionizing Radiation. *Radiat Res Suppl* (1960) 2:290–9. doi:10.2307/3583601
2. Rossi HH. Distribution of Radiation Energy in the Cell. *Radiology* (1962) 78: 530–5. doi:10.1148/78.4.530
3. Rossi HH. Correlation of Radiation Quality and Biological Effect. *Ann N Y Acad Sci* (1964) 114:4–15. doi:10.1111/j.1749-6632.1964.tb53559.x
4. Belli M, Cera F, Cherubini R, Vecchia MD, Haque AM, Lanzini F, et al. RBE-LET Relationships for Cell Inactivation and Mutation Induced by Low Energy Protons in V79 Cells: Further Results at the LNL Facility. *Int J Radiat Biol* (1998) 74:501–9. doi:10.1080/095530098141375
5. Peeler CR, Mirkovic D, Titt U, Blanchard P, Gunther JR, Mahajan A, et al. Clinical Evidence of Variable Proton Biological Effectiveness in Pediatric Patients Treated for Ependymoma. *Radiother Oncol* (2016) 121:395–401. doi:10.1016/j.radonc.2016.11.001
6. Grün R, Friedrich T, Traneus E, and Scholz M. Is the Dose-Averaged LET a Reliable Predictor for the Relative Biological Effectiveness? *Med Phys* (2019) 46:1064–74. doi:10.1002/mp.13347
7. Sanchez-Parcerisa D, Cortés-Giraldo MA, Dolney D, Kondrla M, Fager M, and Carabe A. Analytical Calculation of Proton Linear Energy Transfer in Voxelized Geometries Including Secondary Protons. *Phys Med Biol* (2016) 61:1705–21. doi:10.1088/0031-9155/61/4/1705
8. Marsolat F, De Marzi L, Pouzoulet F, and Mazal A. Analytical Linear Energy Transfer Model Including Secondary Particles: Calculations along the central axis of the Proton Pencil Beam. *Phys Med Biol* (2016) 61:740–57. doi:10.1088/0031-9155/61/2/740
9. Fager M, Toma-Dasu I, Kirk M, Dolney D, Diffenderfer ES, Vapiwala N, et al. Linear Energy Transfer Painting with Proton Therapy: a Means of Reducing Radiation Doses with Equivalent Clinical Effectiveness. *Int J Radiat Oncol Biol Phys* (2015) 91:1057–64. doi:10.1016/j.ijrobp.2014.12.049
10. Cao W, Khabazian A, Yepes PP, Lim G, Poenisch F, Grosshans DR, et al. Linear Energy Transfer Incorporated Intensity Modulated Proton Therapy Optimization. *Phys Med Biol* (2017) 63:015013. doi:10.1088/1361-6560/aa9a2e
11. Hawkins RB. A Microdosimetric-Kinetic Model of Cell Death from Exposure to Ionizing Radiation of Any LET, with Experimental and Clinical Applications. *Int J Radiat Biol* (1996) 69:739–55. doi:10.1080/095530096145481
12. Hawkins RB. A Microdosimetric-Kinetic Model for the Sensitization of V79 Cells to Radiation by Incorporation of Bromodeoxyuridine. *Radiat Res* (2001) 155:698–702. doi:10.1667/0033-7587(2001)155[0698:amkmft]2.0.co;2
13. Hawkins RB. A Microdosimetric-Kinetic Model for the Effect of Non-Poisson Distribution of Lethal Lesions on the Variation of RBE with LET. *Radiat Res* (2003) 160:61–9. doi:10.1667/rr3010
14. ICRU. Microdosimetry. Report 36. *J ICRU* (1983) 19:1–118. doi:10.1148/radiology.154.2.528
15. Lindborg L, and Nikjoo H. Microdosimetry and Radiation Quality Determinations in Radiation protection and Radiation Therapy. *Radiat Prot Dosimetry* (2011) 143:402–8. doi:10.1093/rpd/ncq390
16. Kellerer AM. Microdosimetry and the Theory of Straggling. In: *Biophysical Aspects of Radiation Quality*. Vienna: International Atomic Energy Agency (1968). p. 89–103. Second Panel Report.
17. Kellerer AM. Analysis of Patterns of Energy Deposition. In: H Ebert, editor. *Second Symposium on Microdosimetry*. Stresa (Italy): Euratom (1970). p. 107–36. doi:10.5282/ubm/epub.7951
18. Kellerer AM. Fundamentals of Microdosimetry. In: KR Kase, BE Bjärngard, and FH Attix, editors. *The Dosimetry of Ionizing Radiation*. Cambridge MA: Academic Press (1985). p. 77–162. doi:10.1016/b978-0-12-400401-6.50007-3
19. Agostinelli S, Allison J, Amako K, Apostolakis J, Araujo H, Arce P, et al. Geant4 – a Simulation Toolkit. *Nucl Instrum Meth Phys Res A* (2003) 506:250–303. doi:10.1016/S0168-9002(03)01368-8
20. Allison J, Amako K, Apostolakis J, Araujo H, Arce Dubois P, Asai M, et al. Geant4 Developments and Applications. *IEEE Trans Nucl Sci* (2006) 53:270–8. doi:10.1109/tns.2006.869826
21. Allison J, Amako K, Apostolakis J, Arce P, Asai M, Aso T, et al. Recent Developments in Geant4. *Nucl Instrum Meth Phys Res A* (2016) 835:186–225. doi:10.1016/j.nima.2016.06.125
22. Incerti S, Baldacchino G, Bernal M, Capra R, Champion C, Francis Z, et al. The Geant4-DNA Project. *Int J Model Simul Sci Comput* (2010) 01:157–78. doi:10.1142/S1793962310000122
23. Incerti S, Ivanchenko A, Karamitros M, Mantero A, Moretto P, Tran HN, et al. Comparison ofGEANT4very Low Energy Cross Section Models with Experimental Data in Water. *Med Phys* (2010) 37:4692–708. doi:10.1118/1.3476457
24. Bernal MA, Bordage MC, Brown JMC, Davídková M, Delage E, El Bitar Z, et al. Track Structure Modeling in Liquid Water: A Review of the Geant4-DNA Very Low Energy Extension of the Geant4 Monte Carlo Simulation Toolkit. *Physica Med* (2015) 31:861–74. doi:10.1016/j.ejmp.2015.10.087
25. Incerti S, Kyriakou I, Bernal MA, Bordage MC, Francis Z, Guatelli S, et al. Geant4-DNA Example Applications for Track Structure Simulations in Liquid Water: A Report from the Geant4-DNA Project. *Med Phys* (2018) 45: e722–2739. doi:10.1002/mp.13048
26. Bertolet A, Baratto-Roldán A, Barbieri S, Baiocco G, Carabe A, and Cortés-Giraldo MA. Dose-Averaged LET Calculation for Proton Track Segments Using Microdosimetric Monte Carlo Simulations. *Med Phys* (2019) 46: 4184–92. doi:10.1002/mp.13643
27. Kellerer AM, and Chmelevsky D. Concepts of Microdosimetry. I. Quantities. *Radiat Environ Biophys* (1975) 12:61–9. doi:10.1007/BF02339810
28. Kellerer AM, and Chmelevsky D. Concepts of Microdosimetry. II. Probability Distributions of the Microdosimetric Variables. *Radiat Environ Biophys* (1975) 12:205–16. doi:10.1007/BF01327348
29. Kellerer AM, and Chmelevsky D. Concepts of Microdosimetry. III. Mean Values of the Microdosimetric Distributions. *Radiat Environ Biophys* (1975) 12:321–35. doi:10.1007/BF01323420
30. Kellerer AM, and Chmelevsky D. Criteria for the Applicability of LET. *Radiat Res* (1975) 63:226–34. doi:10.2307/3574148
31. Kellerer AM. Chord-Length Distributions and Related Quantities for Spheroids. *Radiat Res* (1984) 98:425–37. doi:10.2307/3576477
32. Coleman R. Random Paths through Convex Bodies. *J Appl Probab* (1969) 6: 430–41. doi:10.1017/s0021900200032939
33. Kyriakou I, Emfietzoglou D, Ivanchenko V, Bordage MC, Guatelli S, Lazarakis P, et al. Microdosimetry of Electrons in Liquid Water Using the Low-Energy Models of Geant4. *J Appl Phys* (2017) 122:024303. doi:10.1063/1.4992076
34. Kyriakou I, Ivanchenko V, Sakata D, Bordage MC, Guatelli S, Incerti S, et al. Influence of Track Structure and Condensed History Physics Models of Geant4 to Nanoscale Electron Transport in Liquid Water. *Physica Med* (2019) 58: 149–54. doi:10.1016/j.ejmp.2019.01.001

35. Cortés-Giraldo MA, and Carabe A. A Critical Study of Different Monte Carlo Scoring Methods of Dose Average Linear-Energy-Transfer Maps Calculated in Voxelized Geometries Irradiated with Clinical Proton Beams. *Phys Med Biol* (2015) 60:2645–69. doi:10.1088/0031-9155/60/7/2645
36. Tabata T, Ito R, and Okabe S. Generalized Semiempirical Equations for the Extrapolated Range of Electrons. *Nucl Instr Methods* (1972) 103:85–91. doi:10.1016/0029-554x(72)90463-6
37. Baratto-Roldán A. *Development of an External Beam Line for Radiobiology Experiments and Microdosimetry Applications at the 18 MeV Proton Cyclotron Facility at CNA*. [Ph.D. Thesis]. Seville, Spain: Universidad de Sevilla (2020).
38. Famulari G, Pater P, and Enger SA. Microdosimetry Calculations for Monoenergetic Electrons Using Geant4-DNA Combined with a Weighted Track Sampling Algorithm. *Phys Med Biol* (2017) 62:5495–508. doi:10.1088/1361-6560/aa71f6
39. Carabe A, España S, Grassberger C, and Paganetti H. Clinical Consequences of Relative Biological Effectiveness Variations in Proton Radiotherapy of the Prostate, Brain and Liver. *Phys Med Biol* (2013) 58:2103–17. doi:10.1088/0031-9155/58/7/2103
40. Wedenberg M, Lind BK, and Hårdemark B. A Model for the Relative Biological Effectiveness of Protons: The Tissue Specific Parameter α/β of Photons Is a Predictor for the Sensitivity to LET Changes. *Acta Oncologica* (2013) 52:580–8. doi:10.3109/0284186X.2012.705892
41. McNamara AL, Schuemann J, and Paganetti H. A Phenomenological Relative Biological Effectiveness (RBE) Model for Proton Therapy Based on All Publishedin Vitrocell Survival Data. *Phys Med Biol* (2015) 60:8399–416. doi:10.1088/0031-9155/60/21/8399
42. Perales Á, Baratto-Roldán A, Kimstrand P, Cortés-Giraldo MA, and Carabe A. Parameterising Microdosimetric Distributions of Mono-Energetic Proton Beams for Fast Estimates of Y D and Y*. *Biomed Phys Eng Express* (2019) 5:045014. doi:10.1088/2057-1976/ab236a
43. Bertolet A, Baratto-Roldán A, Cortés-Giraldo MA, and Carabe-Fernandez A. Segment-Averaged LET Concept and Analytical Calculation from Microdosimetric Quantities in Proton Radiation Therapy. *Med Phys* (2019) 46:4204–14. doi:10.1002/mp.13673
44. Bertolet A, Cortés-Giraldo MA, Souris K, and Carabe A. A Kernel-Based Algorithm for the Spectral Fluence of Clinical Proton Beams to Calculate Dose-Averaged LET and Other Dosimetric Quantities of Interest. *Med Phys* (2020) 47:2495–505. doi:10.1002/mp.14108
45. Bertolet A, Ramos-Méndez J, Paganetti H, and Schuemann J. The Relation between Microdosimetry and Induction of Direct Damage to DNA by Alpha Particles. *Phys Med Biol* (2021) 66:155016. doi:10.1088/1361-6560/ac15a5
46. Bertolet A, Grilj V, Guardiola C, Harken AD, Cortés-Giraldo MA, Baratto-Roldán A, et al. Experimental Validation of an Analytical Microdosimetric Model Based on Geant4-DNA Simulations by Using a Silicon-Based Microdosimeter. *Radiat Phys Chem* (2020) 176:109060. doi:10.1016/j.radphyschem.2020.109060

Conflict of Interest: The authors declare that the research was conducted in the absence of any commercial or financial relationships that could be construed as a potential conflict of interest.

Publisher's Note: All claims expressed in this article are solely those of the authors and do not necessarily represent those of their affiliated organizations, or those of the publisher, the editors and the reviewers. Any product that may be evaluated in this article, or claim that may be made by its manufacturer, is not guaranteed or endorsed by the publisher.

frontiers in Physics

PERSPECTIVE
published: 28 October 2021
doi: 10.3389/fphy.2021.738112

Artificial Intelligence for Monte Carlo Simulation in Medical Physics

David Sarrut[1]*, *Ane Etxebeste*[1], *Enrique Muñoz*[2], *Nils Krah*[1,2] and *Jean Michel Létang*[1]

[1]University Lyon, INSA-Lyon, Université Claude Bernard Lyon 1, UJM-Saint Etienne, CNRS, Inserm, CREATIS UMR 5220, U1294, Lyon, France, [2]University of Lyon, Université Claude Bernard Lyon 1, CNRS/IN2P3, IP2I Lyon, Villeurbanne, France

Monte Carlo simulation of particle tracking in matter is the reference simulation method in the field of medical physics. It is heavily used in various applications such as 1) patient dose distribution estimation in different therapy modalities (radiotherapy, protontherapy or ion therapy) or for radio-protection investigations of ionizing radiation-based imaging systems (CT, nuclear imaging), 2) development of numerous imaging detectors, in X-ray imaging (conventional CT, dual-energy, multi-spectral, phase contrast . . .), nuclear imaging (PET, SPECT, Compton Camera) or even advanced specific imaging methods such as proton/ion imaging, or prompt-gamma emission distribution estimation in hadrontherapy monitoring. Monte Carlo simulation is a key tool both in academic research labs as well as industrial research and development services. Because of the very nature of the Monte Carlo method, involving iterative and stochastic estimation of numerous probability density functions, the computation time is high. Despite the continuous and significant progress on computer hardware and the (relative) easiness of using code parallelisms, the computation time is still an issue for highly demanding and complex simulations. Hence, since decades, Variance Reduction Techniques have been proposed to accelerate the processes in a specific configuration. In this article, we review the recent use of Artificial Intelligence methods for Monte Carlo simulation in medical physics and their main associated challenges. In the first section, the main principles of some neural networks architectures such as Convolutional Neural Networks or Generative Adversarial Network are briefly described together with a literature review of their applications in the domain of medical physics Monte Carlo simulations. In particular, we will focus on dose estimation with convolutional neural networks, dose denoising from low statistics Monte Carlo simulations, detector modelling and event selection with neural networks, generative networks for source and phase space modelling. The expected interests of those approaches are discussed. In the second section, we focus on the current challenges that still arise in this promising field.

Keywords: AI, Monte Carlo simulation, medical physics, GAN, deep learning

OPEN ACCESS

Edited by:
Susanna Guatelli,
University of Wollongong, Australia

Reviewed by:
Carlo Mancini,
Sapienza University of Rome, Italy
Olaf Nackenhorst,
Technical University Dortmund, Germany

***Correspondence:**
David Sarrut
david.sarrut@creatis.insa-lyon.fr

Specialty section:
This article was submitted to Radiation Detectors and Imaging, a section of the journal Frontiers in Physics

Received: *08 July 2021*
Accepted: *27 September 2021*
Published: *28 October 2021*

Citation:
Sarrut D, Etxebeste A, Muñoz E, Krah N and Létang JM (2021) Artificial Intelligence for Monte Carlo Simulation in Medical Physics. Front. Phys. 9:738112. doi: 10.3389/fphy.2021.738112

1 INTRODUCTION

Techniques based on Deep Learning have seen huge interest for several years showing, in particular, significant progress in computer vision. Many medical applications have adopted them (see Shen et al. [132] for a recent review) and a lot of research is currently underway. These recent developments around Machine Learning in medical physics have found applications in the field

of Monte Carlo simulations. In this work, we will review and discuss the use of artificial intelligence, or more specifically *machine Learning*, for Monte Carlo simulation for particle transport especially in the context of medical physics. Links to other fields such as particle physics, nuclear physics or solid state physics also exist, but they would be beyond the scope of this work.

The article is structured in the following three parts: **Sections 1.1 and 1.2** give a brief introduction of the principles of Monte Carlo simulation as well as deep learning, **Section 2** presents a literature review in the context of medical physics, and **Section 3** discusses on current challenges.

1.1 MONTE CARLO MODELLING IN MEDICAL PHYSICS

Monte Carlo codes in medical physics are similar to those used in high energy physics community (HEP). Specifically, the simulation engine simulates the transport of particles, mainly photons and light charged particles, across a set of geometrical objects made of well-defined materials, modeling the physical interactions between particles and matter. The transport is performed particle by particle in a step-by-step fashion. For all particles, at each step, stochastic models describing physical interactions (such as Compton scattering, photo-electric effect, ionisation, etc) are repeatedly evaluated based on databases of cross-sections. Thanks to this approach, the quantities determined via simulation, for example the absorbed dose distribution or the number of detected particles, are very accurately estimated even in complex geometries. Depending on the complexity of the simulated configuration, millions or even billions of particles should be tracked to reach an acceptable statistical convergence, making the whole process usually very long.

The use of Monte Carlo techniques for medical physics started to become increasingly popular in the late 1970s, in particular for the modelling of imaging systems in nuclear medicine, for the characterization of particle beam accelerators in radiotherapy, and for calculating the absorbed dose in patients for planning treatment [5, 14, 115, 130]. Since then, Monte Carlo simulations have become a widespread tool in research and development (R&D) for the design of nuclear imaging systems and dose calculation engines in treatment planning systems (TPS) [19, 41, 129, 139, 148].

An example of system development where Monte Carlo simulations are involved in the design, the control and test of the devices, and the tuning of reconstruction algorithms is the new generation of whole-body PET scanners. Prototypes currently under development include the EXPLORER [10] at UC Davis (United States), the PennPET [64] in Philadelphia (United States), the PET20.0 [146] in Ghent (Belgium) and J-PET [72] in Krakow (Poland). With regard to TPS, Monte Carlo simulations are often necessary to characterize the beam lines and the resulting particle phase spaces (photons or charged particles), to determine the dose point-kernels in analytical dose engines, or to directly calculate the absorbed dose in patients [129, 148]. The great accuracy of Monte Carlo calculations is particularly crucial for new radiotherapy protocols, such as hypo-fractionation [95], "flash" radiotherapy [74], and hadrontherapy (proton or ions [13, 50]) which involve very high dose rates and a high spatial conformation.

R&D activities in the field of Monte Carlo simulations have resulted in the development of generic computer codes, i.e. which allow the user to simulate a wide range of particles, energies, geometrical elements and physical interactions (EGSnrc [65], MCNPX [55], Penelope [120], Fluka [18], Geant4 [1, 4], Gate [57, 123, 124], etc.). The accuracy of the underlying physical models and cross-section databases has continuously been improved, also thanks to new experimental data. To counter the low efficiency of Monte Carlo simulation techniques, variance reduction techniques (VRT) [129, 139] have been developed and continue to be proposed to speed up computation times at a given precision.

The development of increasingly sophisticated acquisition systems and finer representations of patient data requires a complex modelling, costly in computer resources. Monte Carlo codes dedicated to a specific application also exist and usually offer a better computational performance than generic codes, but they are in general very restricted to the targeted applications. Most research teams rely on the latter for their work.

Monte Carlo simulation is inherently parallel because particle histories are treated as independent from each other. This is a major advantage for accelerating computations [148]. Powerful computing infrastructures (clusters) can thus be used by researchers to obtain Monte Carlo simulation results in an acceptable time. The recent enthusiasm for scientific computing on graphics cards (GPU) has also concerned several Monte Carlo developments [16, 45, 89, 118], but the codes ported to GPUs tend to be difficult to maintain and partly lose in generality by limiting themselves to well-defined applications.

1.2 Deep Learning Principles

Deep learning [17, 47, 76, 128] is a machine learning method performing supervised, non-supervised or semi-supervised learning tasks, in which the learning takes place across many different stages, as for example defined in [128]. It is most commonly accomplished using neural networks. A neural network is composed of connected neurons typically (but not necessarily) organized in layers. Connections between neurons have associated weights and a neuron is associated with an activation function which generates the neuron's output, e.g. a non-linear function mapping from an open into a closed real domain (e.g., values bounded between zero and one). The input to a neuron's activation function is the weighted sum over the outputs of all the connected neurons (belonging to the previous layer in a fully connected feedforward net), generating a complex mapping between the network's inputs and outputs. In **Eq. 1**, $x^{(i)}$, $W^{(i)}$ and $b^{(i)}$ represent respectively the output, the weights matrix and the bias for the layer i, whereas f stands for the activation function which is applied element-wisely. The number of neurons, the way they are connected (layers), the choice of activation functions and other parameters

are referred to as the "network architecture". The weights' values of the connections are parameters that will be determined during the training phase.

$$x^{(i+1)} = f\left(W^{(i)}x^{(i)} + b^{(i)}\right) \quad (1)$$

Indeed, training the model means optimizing a value for every weight in order to adapt the network to handle a task. This learning process uses a training dataset as input which, for supervised learning, groups pairs of input-output samples. Optimizing the network is typically performed by stochastic gradient descent where weights are updated using backpropagation (in a feedforward network) that computes the gradient of a loss function with respect to the weights of the network. The loss function is chosen depending on the problem at hand, for example to quantify how well the current model prediction matches the training dataset or, indirectly, to measure a distance between current and expected distribution.

Convolutional neural networks [73, 77, 156] is a famous approach to deal with high dimension input data such as images. They are regularized versions of (fully connected) networks based on convolution kernels that slide along input features and provide activation when some specific type of feature is detected at some spatial position in the input image. Hence, shared weights and local connections allow reducing the number of parameters and can thereby simplify the training process, improve generalisation, and reduce overfitting. A CNN architecture is composed of several building blocks (convolution layer, pooling layer, fuller connected layer, activation function, loss function, etc) that must be selected and put together into a network for each task.

Generative Adversarial Networks (GANs) are special deep neural network architectures recently reported [48] that, once trained, can be used to generate data with similar statistics as the training set. A GAN consists of two models that are simultaneously trained: a generative model G that aims to generate a targeted data distribution, and a discriminative model D that estimates the probability that a sample came from the training data rather than from the generative model. The *discriminator* D is trained to maximize the probability of correctly identifying samples from the training data as real and those generated by G as fake. The *generator* G is trained to produce data samples distributed similarly to the data distribution. Once trained, the resulting G model is able produce set of samples that are supposed to belong to the underlying probability distribution of the targeted data represented by the training dataset. A review can, for example, be found in [31]. This type of architecture is frequently used in multiple applications, in particular in the synthesis of photorealistic images or, for example in the medical physics field, to generate synthetic CT from MR images [80]. In the field of Monte Carlo particle tracking simulations in medical physics, several works have been proposed and will be discussed in the next sections.

2 LITERATURE REVIEW

Within the High Energy Physics (HEP) community, a lot of effort has already been made to improve and accelerate Monte Carlo simulation with the help of Machine Learning (including Deep learning) for various applications, in particular around the Geant4 code [44]. Among various examples: simulation of particle showers [108], modelling the response of detectors [144], pairs of jet simulation at LHC [39], nuclear interaction modelling [30], condensed matter physics [25, 133], etc. Interested readers may, for example, refer to several reviews [2, 3, 22, 51, 114] or to https://iml-wg.github.io/HEPML-LivingReview.

To our knowledge, no review has been proposed for the medical physics field. In the following sections, we thus review works which combine machine learning with Monte Carlo simulations in the medical physics field. Of course, particle transport simulation via Monte Carlo in HEP and medical physics share many similarities. Exchange among researchers working in these different fields would be desirable in order to share new knowledge and discoveries. Some of the works reviewed in the following deal with input data that are not an image, but are related to sets of particle properties. **Table 1** summarizes the type of input that is considered for each application. The motivation behind many of the presented works is to speed up the computation, e.g. dose calculations or image reconstructions, to the order of minutes rather than hours or days. Other motivation is to improve detector quality by better event selection or reconstruction.

TABLE 1 | AI-based applications related to Monte Carlo simulations and their corresponding input data type. The word "particles" as input type refers to a vector of particle properties such as energy, position, direction, weight, etc. CNN stands for convolutional neural networks and MLP stands for multi-layer perceptron.

Application	Input type	Refs (among others)	Main ML types
Dose computation	image	[49, 63, 79, 85, 90, 104, 116, 117, 147]	CNN, U-net
Dose denoising	image	[43, 59, 71, 101, 103, 111, 131, 153][1]	CNN, U-net
SPECT scan-time reduction	image	[82, 119, 121]	CNN, U-net
CBCT scatter modelling	image	[27, 58, 60, 75, 79, 84, 87, 88, 140, 145, 152, 155]	CNN, U-net
PET attenuation/scatter correction	image	[6, 97]	CNN, U-net
Detector response modelling	particles	[126, 144]	GAN, MLP
Source + phase space modelling	particles	[108, 125, 127]	GAN
Event selection	particles	[8, 12, 40, 46, 93, 98, 100, 102, 107, 157][2]	MLP, CNN
Interaction position in scintillators	various	[23, 33, 37, 99, 109, 110, 122, 150, 154]	MLP, CNN

[1] *http://hdl.handle.net/11603/19255*
[2] *http://hdl.handle.net/2078.1/thesis:14550*

2.1 AI-Based Dose Computation

Different studies have used Monte Carlo simulations and CNNs to estimate the dose distribution in imaging and radiotherapy. The general idea is to develop a fast neural network as an alternative to computationally intensive simulations. Typically, dose distributions computed with Monte Carlo simulations are used to generate large training and validation sets from CT images and treatment plans. For example, Lee et al. [79] proposed deep learning-based methods to estimate the absorbed dose distribution for internal radiation therapy treatments, i.e., where the radiation source is a radionuclide injected into the patient. A CNN was trained from PET and CT image patches associated with their corresponding dose distributions computed by GATE simulation [124] and considered as ground truth. The training database was composed of 10 patients with eight PET/CT timepoints after intravenous injection of 68Ga-NOTA-RGD, from 1 to 62 min post-injection. The network architecture was based on a U-net structure [116]. The first part of the network performed image downsampling operations (contracting path) and the second part, image upsampling (expansive path). The U-net considers both PET and CT as input data to predict the dose. It was operated on image patches rather than on full images because, in the studied scenario, the dose is mainly deposited locally (millimeters) around the source voxels, allowing memory and computation time gain. Note that local dose deposit would not be a valid assumption in case of radiation with larger range (high energy photons for example). The voxel dose rate errors between CNN-estimated and Monte Carlo-estimated dose were found to be less than 3% and was obtained within a few minutes compared to hours with Monte Carlo. Similarly, Götz [49] presented a hybrid method combining a U-net with empirical mode decomposition technique. The method takes as input CT images and corresponding absorbed dose maps estimated with the MIRD protocol (organ S-value [21]) from SPECT images for 177Lu internal radiation therapy treatment. Again, results seem very good, better than the fast Dose-Volume-Kernel (DVK) method [20] and faster than Monte Carlo.

Principles relatively similar to those developed in the previous examples related to internal radiation therapy have also been applied to external radiation therapy, i.e., where the radiation source is an external particle beam generated by an accelerator. Kalantzis et al. [63] performed a feasibility study of a multi-layer perceptron (MLP) to convert a 2D fluence map obtained from an electronic portal imaging device (EPID) to a dose map for IMRT, replicating conventional convolution kernel in TPS. Nguyen et al. [104] proposed to perform 3D radiotherapy dose prediction for head and neck cancer patients with a hierarchical densely connected U-net deep learning architecture, with prediction error lower than 10%. Liu et al. [85] developed a deep learning method for prediction of 3D dose distribution of helical tomotherapy for nasopharyngeal cancer leading to less than 5% prediction error.

Other developments for imaging dose and brachytherapy have been proposed. For example, Roser et al. [117] use a U-Net fed with first order fluence maps computed by fast ray-casting in order to estimate the total dose exposure including scattered radiation during image-guided x-ray procedures. The CNN was trained using smoothed results of MC simulations as output and ray-casting simulations of identical imaging settings and patient models as inputs. As a result, the proposed CNN estimated the skin dose with an error of below 10% for the majority of test cases. The authors conclude by stating that the combination of CNN and MC simulation has the potential to decrease the computational complexity of accurate skin dose estimation. As an example in brachytherapy, Mao et al. [90] investigated a CNN-based dose prediction models, using structure contours, prescription and delivered doses as training data, for prostate patients and cervical patients. Predictions were found to be very close to those from MC, with less than few percent differences for various dosimetry indexes (CTV).

At the current stage, it is unlikely that dose distributions predicted via DL will be used as the main dose computation method in clinical practice because the dose is expected to be estimated from physically plausible effects and modeling and not really by learning processes. Nevertheless, it may be useful for plan checking consistency, fast plan comparison or to guide plan optimization.

2.2 Deep Learning Based Monte Carlo Denoising

Instead of mapping from some kind of image data (e.g., patient CT, SPECT image) to a dose distribution, deep learning methods have also been developed as a post-processing step to Monte Carlo dose computations to reduce the noise in dose maps due to inherent statistical fluctuations in the deposited dose per voxel. Indeed, Monte Carlo denoising methods have been studied for a long time and have shown to be able to reduce computation time by smoothing statistical fluctuations [101]. The noise of the Monte Carlo computed dose is related to the variance on the deposited energy and decreases as the number of simulated particles, N, increases, specifically at a $1/\sqrt{N}$ rate. Hence, a large number of iterations is required to reach low fluctuation dose estimation, in particular in low dose regions where N is small. For simulation of detectors such as CT or PET/SPECT images, noise is generally considered as Poisson noise. Lowering the number of simulated particles translates into a net gain in computation speed. Several filtering methods [35, 36, 42, 66, 92] (among others) have been employed in denoising, such as 3D wavelet-based, advanced mean-median filtering, anisotropic diffusion and so on. In general, the methods manage to reduce dose fluctuations while preserving mean dose, but the effective acceleration depends significantly on the characteristics of the dose distribution [101].

The principle of CNN-based denoising is to feed a network with pairs of high-noise/low-noise dose distributions obtained from low and high statistics Monte Carlo simulations with the goal to generate low-noise dose maps from noisy ones. In many cases, the CNN architecture is derived from U-Net, but other architectures such as Dense-Net [54] or Conveying-Path Convolutional Encoder-decoder (CPCE [131]) were studied as well. CNN-based denoising has been applied to photon [43, 71, 103, 111] and proton dose [59][1] for various indications including

[1]http://hdl.handle.net/11603/19255

brain, head and neck, liver, lung, prostate, and to dose delocalization due to charged particles within MRI (in magnetic resonance-guided radiation therapy [29]). Evaluations were performed based on peak signal-to-noise ratio (PSNR), Dose Volume Histogram (DVH [53]) or gamma index ([81, 86]) as comparison metrics. Results were generally very encouraging. The CNN produced noise equivalent dose maps with approximately 10–100 times fewer particles than originally needed [11, 153]. Some difficulties remain: results depend on the size and complexity of the training datasets and it is to be seen how the method can be generalised to other datasets, e.g., how well does a network which was mainly trained on head and neck patients perform on prostate patients. Furthermore, denoised dose maps must preserve dose gradients and it is not yet fully clear how to guarantee this.

In SPECT and PET imaging, the image noise is (partly) related to the scan-time duration. Reducing the scan-time directly improves the clinical workflow and decreases involuntary motion during scanning on the one hand, but on the other hand increases image noise. Different denoising approaches based on DL have been proposed such as [32, 82, 121]. In particular, Ryden et al. [119] proposed an approach based on sparse projection data sampling where intermediate projections were interpolated using a deep CNN to avoid image degradation. DL-based denoising methods were also investigated for low dose CT imaging [111, 131, 151, 153]. More generally, deep learning image denoising methods may be a source of inspiration in this field [142].

2.3 AI for Modelling Scatter

DL-based methods have also been applied to cone-beam CT (CBCT) imaging. The main issues to be addressed in this modality are the poor image quality and the artefacts due to scatter. These arise because the imager panel, which is two-dimensional without anti-scatter grid, not only captures the attenuated primary photons from the x-ray source, but also those originating from coherent and incoherent scatter within the patient. For accurate image reconstruction, the scatter contribution would need to be known and subtracted from the raw projection images. In practice, this is impossible because the imager panel only provides a non-discriminative integrated intensity signal. A Monte Carlo simulation, on the other hand, can specifically tag scattered photons so that perfect scatter-free projections can be obtained via simulation. In fact, some earlier works on CBCT scatter correction rely on Monte Carlo simulation to estimate the scatter contribution in raw projection [58]. However, the direct Monte Carlo simulation of kV photons is too slow to be integrated into a clinical image reconstruction software, although heavy use of variance reduction techniques might improve this [88].

Recent works propose to use deep convolutional networks which learn from CBCT projections simulated via Monte Carlo. They generate estimated scatter images (projections) as output based on raw projections as input [75, 78, 87, 145]. Once trained, the network can replace the Monte Carlo simulation and be used as scatter estimator within the image reconstruction workflow. The technical details of the networks vary, but all report promising results with significant higher CNR (Contrast to Noise Ratio) compared to previous heuristic methods. It is worth mentioning that these methods rely on Monte Carlo simulations for training where primary photons can be distinguished from scattered ones and could not be easily trained on experimentally acquired projections which cannot directly provide explicit scatter images to learn from.

Other authors have reported CBCT scatter correction methods based on deep learning which operate in the image domain [27, 60, 84, 140, 152, 155]. More specifically, they take a CBCT image as input and generate a synthetic CT image as output, i.e. they estimate how a CT image of the patient anatomy described by the CBCT image would have looked like. These synthetic CT images seem to contain much fewer artefacts than the original CBCT images.

Attenuation and scatter correction in the image domain for PET imaging has also been proposed using deep convolutional neural networks [6, 97]. Datasets to train the networks consisted in experimentally acquired images, but in principle, these image-based scatter correction studies would also work on Monte Carlo generated data that may help to create large databases.

2.4 AI for Modelling Imaging Detector Response

The works presented so far rely on the output of Monte Carlo simulations, but they do not alter the simulation itself. The works in this section, on the other hand, replace part of a Monte Carlo simulation in an attempt to accelerate it. More specifically, the proposed works model the particle transport through part of the geometrical components implemented in the simulation. In contrast to the previous methods, the model's input and output are not necessarily images, but may be sets of particle properties (energy, position, etc).

To our knowledge, few works have been published on this topic in the medical physics field. One example was recently proposed to speed up simulation by modelling the response of a detector: instead of explicitly simulating the particle transport in the detector, this is emulated by the network. For example, one idea could be to speed-up simulations of SPECT imaging by modelling the collimator-detector response function (CDRF) that combines the cumulative effects of all interactions in the imaging head and may be approximated with Angular Response Functions (ARF) [38, 119, 126, 135]. In [126], the tabulated model of the CRDF has been replaced by a deep neural network trained to learn ARF of a collimator-detector system. The method has been shown to be efficient and to provide variance reduction that speeds up the simulation. Speed-up compared to pure Monte-Carlo was between 10 and 3,000: ARF methods are more efficient for low count areas (speed-up of 1,000–3,000) than for high count areas (speedup of 20–300) and more efficient for high energy radionuclides (such as 131I) that show large collimator penetration.

2.5 AI for Monte Carlo Source Modelling

Recent works in the medical physics field have explored the use of generative networks, GANs in particular, to model particle source

distributions and potentially speed up Monte Carlo simulations [125, 127]. In the proposed methods, the training data set is a phase space file generated by an analog MC simulation which contains properties (energy, position, direction) of all particles reaching a specific surface. Once the GAN is trained, the resulting network G acts as a compact and fast phase space generator for the MC simulations, replacing a large file of several gigabytes by a NN (G) of several megabytes. G has the ability to quickly generate a large number of particles which allows the user to speed-up the simulations significantly (up to a few orders of magnitude depending on the simulation configuration). In the first case [127], the GAN method was used to learn the distribution of particles exiting a the nozzle of a therapeutic linear electron accelerator (linac), and to model a brachytherapy treatment where the network learned the source distribution generated by seeds in the prostate region. Simulations performed with the GAN as a phase space generator showed a very good dosimetric accuracy compared to the real phase space. In the second case [125], the authors proposed to apply this approach to a more complex particle distribution, namely that of particles exiting a patient in a SPECT acquisition. Results showed that images of complex sources with low error compared to the reference image reconstructed from real phase space data were feasible.

It should be mentioned, although beyond the scope of this review, that several works in the HEP community have also shown how generative models may be very useful to model high-dimensional distributions. Among others, Paganini et al. [108] proposed a GAN model to simulate computer intensive electromagnetic showers in a multi-layer calorimeter, and de Oliveira et al. [34] also exploited GAN to produce jet images (2D representations of energy depositions from particles interacting with a calorimeter). Both methods reports large computational speedups compared to conventional Monte Carlo simulations.

2.6 Deep Learning in Nuclear Imaging

DL has also been explored in the context of nuclear imaging (PET, SPECT, Compton camera, etc.) - a field where Monte Carlo simulation plays a vital role in designing and validating imaging systems and reconstruction algorithms. Many of the proposed DL methods focus on post processing steps of raw data acquired by the imaging system which impact image quality.

In PET, for example, NNs have been investigated to identify random data points arising from annihilation events which lead to image noise [107] and for the correct sequence identification of PET events with multiple interactions of an annihilation photon in several detector elements, in which the first interaction position must be identified in order to recover the actual line of response [93, 102]. NNs have also been used to estimate the two-dimensional interaction position in the monolithic scintillator crystal in PET imagers, or a three-dimensional position when the depth of interaction (DoI) is estimated as well. The investigated NNs have yielded results with better spatial resolution [37, 122], higher uniformity across the crystal volume [98] or faster implementation [149] compared to other existing methods (e.g. maximum likelihood [112] or nearest neighbours [141], among many others).

In Compton imaging devices, ML has been investigated for sequence ordering of multiple-interaction events [157][2] and for signal and background discrimination of Compton camera data in the context of prompt gamma imaging [100]. It is also worth mentioning that DL-based methods have been studied for event selection in data measured by radiation detectors, in particular in HEP, as shown for example in [51]. Applications include detectors at the LHC [12], neutrino-dedicated detectors [8, 40] or measurement of gamma-rays in astrophysics [46]. We refer the reader to [2, 24, 51] for an overview in HEP field.

3 CURRENT CHALLENGES

Monte Carlo based particle transport codes are a central tool for many research questions and applications. This is certainly true for medical physics, the area we concentrate on here, as well as for other fields. We have shown in the previous sections that deep learning methods can be useful for various tasks during simulations, in particular to reduce the computation time (denoising, scatter modelling), but also to model complex systems (detector, source modelling) or perform advanced event selection. However, before those methods can replace conventional methods, especially in industrial or clinical settings, several challenges must be addressed.

Conventional methods in the context of Monte Carlo particle transport simulations are usually instructed by knowledge about the underlying physics processes. This results in specific mathematical or statistical models, usually containing parameters to be adjusted, e.g. based on a calibration or reference measurements. Neural networks, on the other hand, are effectively physics or model agnostic and simply learn properties from a given training dataset. Therefore, there is no *a priori* guarantee that a trained NN provides a plausible representation of the physics underlying the learned processes. At the same time, there are usually quantitative requirements associated with MC simulation tasks, e.g. accurate estimate of deposited energy or dose, accurate estimated particle properties, accurate phase space distributions. All of the following challenges are linked to the requirement that DL methods in MC simulations be reproducibly accurate and that accuracy can be evaluated.

Challenge 1: Quality of Data

One conventional challenge in DL is related to the limited database size, or its limited variability and adequacy to the learning process. There are several pitfalls such as: non homogeneous data, difficult data curation, insufficient representativity, etc. However, when learning from Monte Carlo data, the size of the training datase could, in principle, be only limited by the computation time. As the latter can quickly become prohibitive, data augmentation may be used anyway. When learning from MC data, the quality of the learnt process becomes strictly tightened to the quality of the simulation itself. If the modelled system contains error or bias, it will be present in the training dataset and learnt by the neural network. Simulation results

[2]http://hdl.handle.net/11603/19255

must therefore be properly validated to avoid bias (see next section) and comparison with experimental data, if feasible, is required.

Challenge 2: Performance Metric and Uncertainty

Evaluation of a trained neural network is conventionally performed by splitting the dataset into three separated parts for *training*, *validation*, and *test*. The model is first trained on the *training* dataset in order to optimize weights values according to the loss function. The *validation* dataset is successively used to provide unbiased validation of the final model during the training in order to tune hyperparameters (e.g., number of layers, number of epoch) and prevent overfitting (when the loss function still decreases in the training dataset, but starts to increase in the validation set). The *test* dataset provides final unbiased validation. The validation process in the context of Monte Carlo simulations may be different from traditional computer vision applications (photos, cinema, games etc) where visual perception is assessed. Here, quantitative validation of physical quantities is needed. The figures of merit to evaluate usually depend on the kind of application for which the network is developed. For example, for dose computation, standard criteria such as the "gamma index" [81, 86] or Dose Volume Histograms [53] could be used. It is to be explored how (clinically) relevant metrics and tolerance levels might be incorporated into the training and validation process. Ideally, final validation of a network should not only be performed against simulated data, but also against experimental data. Furthermore, collaborative open datasets [26] or challenges (such as [113]), yet specific to medical physics applications, may be useful.

One of the advantages of Monte Carlo simulations is that they are able to easily associate an (uncertainty) error with the simulated data. The MC statistical uncertainty (e.g. [28]) could hence be used to provide a target tolerance. In the context of medical physics, the uncertainty of data produced by generative networks needs to be carefully studied and understood, especially if those networks are to (partly) replace conventional MC simulations. In more practical terms, what are the noise properties of DL-generated images or dose distributions compared to their MC simulated counterparts? Two forms of uncertainty have been proposed which are referred to as *epistemic* and *aleatoric* [69, 91], where epistemic is the reducible (related to the lack of training data in certain areas of the input domain) and aleatoric the irreducible part of uncertainty (dealing with the potential intrinsic randomness of the real data generating process). As an example, approaches based on Bayesian neural networks [70, 106], by its ability to give an estimation of the uncertainty, may be an interesting lead.

Challenge 3: Neural Network Architecture and Hyperparameters

A challenge when working with deep neural networks is to select the appropriate network structure and capacity, i.e., number of neurons, number of layers, type of activation, etc., for a given problem and adjust the training process with appropriate hyperparameter values. Underfitting may occur if the model is too simple (not enough capacity) or too much regularized, so it tends to have poor predictive performance. Overfitting can be an issue which occurs e.g. when a too flexible network (too many parameters) learns structure in the data which merely derives from noise or other artefacts rather than true information. Several regularization methods, such as adding a penalty term on the weights (e.g., L1, L2) in the loss, or using dropout regularization [138], that randomly ignores some layer outputs, might help preventing overfitting issues and improving model generalization (capacity to perform on inputs not previously seen by the network).

When images are the input, convolution operations can be added in between network layers. Moreover, several architectures such as the well known UNet [116] or *pix2pix* conditional adversarial networks [56] (among others) have been proposed. When a network is used to bypass the Monte Carlo simulation and use as input an image, e.g. a patient CT or a PET image, conventional convolution filters can be applied. However, when particle properties are the input, the nature of each entry in the property vector may be different (position, energy, time, etc.). It remains to be studied how meaningful convolution operations can be defined on such an inhomogeneous input space, or if it may be applied only partly, e.g. on a single dimension such as energies. Furthermore, some particle properties such as charge or atomic weight are bound to be integer number rather than reals and may require specific processes, such as one-hot encoding as used for example in [126]. Finally, conservation laws or other physical principles might pose constraints which need to be built into the network optimisation, either by a specific architecture or an adapted loss function.

Challenge 4: Generative Models, Generative Adversarial Network

To simulate particle transport through a medium, a Monte Carlo code must generate particles according to some probability distribution. This can be the initial phase space distribution of the particle source, but also an intermediate step which creates new particles as a result of interactions with the target, e.g. inelastic nuclear scattering. In conventional Monte Carlo methods, this is done by sampling from a cumulative probability distribution and the accuracy with which the distribution is modelled and parametrized directly impacts the accuracy of the simulation results. Source particles can also be sampled explicitly from tabulated phase space files. In this context, generative models represent a new way to replace conventional particle generation methods in a Monte Carlo simulation. Understanding and mastering the technical aspects of such methods represents an important challenge.

Our review concentrated on GAN (**Section 2.5**) which have been explored for Monte Carlo simulation in medical physics. Many variants of GAN have been proposed to improve performance or to adapt to various applications (auxiliary GAN, bidirectional GAN, conditional GAN, Cycle GAN, InfoGAN, etc). Despite a large number of successful results, GAN have been shown to be notoriously difficult to train, suffering from several pitfalls: mode collapse, vanishing

gradient, instability. To tackle these issues, various formulations based on different metrics, such as the Wasserstein distance [7] and regularization methods [52, 61, 62, 94] have been proposed. An in-depth study of the most suitable variants for Monte Carlo simulations remains to be undertaken. For example, is it possible to obtain a precise and reliable modelling of all spatial characteristics of the dose distributions [67]? Can a GAN model a Linac gamma source precisely enough to include 511 keV peak [127]? Alternative generative learning processes, such as VAE (Variational AutoEncoders, see for example [68]) or, recently, Score-Based diffusion Generative Models [105, 136, 137, 143] may have a larger role to play in distribution modelling within Monte Carlo. In particular, VAE networks are designed to compress the input information into a constrained multivariate latent distribution (encoding) to reconstruct it as accurately as possible (decoding). Although VAEs seem generally less efficient than GAN in the field of photo-realistic image synthesis, it could be an interesting alternative to GAN in the medical physics field. Additionally, transfer learning may also be of interest where a model already trained on a given dataset may be adapted through training on another dataset.

The problem of reproducing a probability distribution by generative networks such as GAN arises far beyond the simple source modelling. In Monte Carlo simulations, certain interactions between particles, in particular nuclear processes, are based on very elaborate statistical distributions which require a lot of computing time, and generative networks would have a role to play. For instance, Bayesian neural networks have been proposed to improve mass predictions of nuclear models [106] and quantify the prediction uncertainty which becomes larger when the network is extrapolated away from the training region.

Finally, it is interesting to observe some subtle differences between GAN in computer vision and for tasks such as particle generation in a Monte Carlo simulation. In a computer vision application where a GAN generates images, it is mainly of interest that each image be as realistic as possible. In a Monte Carlo simulation, any generated particle with reasonable physical properties judged by itself is realistic. What really counts is whether the *distribution* of many generated particles is correct. The corresponding question in the computer vision application would be e.g., whether the GAN generates the correct proportion of long-haired brown dogs compared to short-haired black ones, albeit all of them individually might be realistic. In more technical terms, an image has a much higher dimension, i.e., number of pixels, than the vector of physical properties describing a particle. Out of the space of all images (including images with random noise), only a very small and sparse subspace contains realistic images, i.e., containing pixels which depict a desired kind of object. A particle distribution instead densely fills a relatively large portion of the full phase space. These differences likely impact the way GANs and other generative models perform in Monte Carlo simulations as opposed to computer vision tasks and will deserve more detailed attention.

Challenge 5: Explicability and Interpretability

Deep neural networks are sometimes criticized as being *black boxes*, or in other words for not providing direct insight into the way they link input and output. As an example: when modelling the response properties of a detector explicitly via a physics-motivated analytical model, the mathematical form of the model together with its parameters inform the user directly which kind of events will be detected in which fashion. In contrast, a deep neural network trained on Monte Carlo simulated data does not offer this transparency. The underlying reason is that a neural network is a highly flexible non-linear function whose parameters are the neuron weights optimized to best represent the training data. As the weights have no *a priori* meaning attached to them, they are difficult to interpret.

Monte Carlo simulation, on the other hand, is based on physics models with meaningful parameters and a thereby described quantitative relationship between input and output. Clearly, the randomized and iterative evaluation of a multitude of physics models make the final simulation output complex in certain cases, but the underlying mechanism remains explicitly defined. A challenge when using deep neural networks in the context of Monte Carlo simulations is therefore to gain insight in and control over the workings of the network. This leads to the concepts of *interpretation* and *explanation*.

Definitions of these terms can be found in [96], namely, an interpretation is the mapping of an abstract concept into a domain that the human can make sense of. An explanation is the collection of features of the interpretable domain that have contributed for a given example to produce an output. It is important to note that both terms apply to trained networks. Picking up the example of the detector response (**Section 2.4**), an interpretation links a specific detector response, e.g. the detection window in a SPECT imager, to the particle properties, i.e. its energy, direction etc. In this same example, the explanation is the collection of properties which have led a specific particle to be associated with a certain detector response? In this sense, explanation and interpretation are expected to aid with the validation of deep neural networks in terms of physical plausibility.

The difficulty of visualizing and studying explanation and interpretation of a network grows with the dimension of the input data. When the input is merely a vector with a particle's kinematic properties, i.e. with six or seven entries, the relevance of each of them for a given network decision can still be interpreted "manually". For high dimensional input such as CT images, other methods must be employed, e.g. activation maximization with an expert [15, 134]. For interpretation, gradient based methods such as deep Taylor expansion and backward propagation techniques such as layer-wise relevance propagation should be mentioned here [9].

A rich literature about machine learning interpretation methods exists [83], with a large part of the methods exploiting the gradient information flowing through the layers of the network in order to highlight their impact. Investigating and developing interpretation and explanation techniques in the context of Monte Carlo simulations to make DNN sufficiently "transparent" will be one of the challenges to address.

4 CONCLUDING REMARK

There may be a methodological change associated with the use of deep learning methods in medical physics simulation: to some extent, instead of mathematically mastering the phenomenon under

investigation, the modelling relies on a large amount of data to learn from heuristically. However, the Monte Carlo simulation which generates the training data needs to be skillfully set-up and evaluated in the first place. For the moment, even if it is envisioned that deep learning can improve simulations, it does not seem certain that it can always replace Monte Carlo. As the use of deep learning methods evolves, physics-driven dataset modelling, i.e., a mix between modelling based on large datasets and understanding of the underlying physics, will become increasingly important.

DATA AVAILABILITY STATEMENT

Publicly available datasets were analyzed in this study. This data can be found here: https://github.com/OpenGATE/Gate.

AUTHOR CONTRIBUTIONS

All authors listed have made a substantial, direct, and intellectual contribution to the work and approved it for publication.

FUNDING

This work was performed within the framework of the SIRIC LYriCAN Grant INCa-INSERM-DGOS-12563, the LABEX PRIMES (ANR-11-LABX-0063) of Université de Lyon, within the program "Investissements d'Avenir" (ANR-11-IDEX-0007), the MOCAMED project (ANR-20-CE45-0025) and the POPEYE ERA PerMed 2019 project (ANR-19-PERM-0007–04).

REFERENCES

1. Agostinelli S, Allison J, Amako K, Apostolakis J, Araujo H, Arce P, et al. Geant4 - a Simulation Toolkit. *Nucl Instr Methods Phys Res Section A: Acc Spectrometers, Detectors Associated Equipment* (2003) 506:250–303. doi:10.1016/S0168-9002(03)01368-8
2. Albertsson K, Altoe P, Anderson D, Anderson J, Andrews M, Espinosa JPA, et al. (2019). Machine Learning in High Energy Physics Community White Paper. *J Phys Conf Ser* 1085:022008.
3. Albrecht J, Alves AA, Amadio G, Andronico G, Anh-Ky N, Aphecetche L, et al. A Roadmap for HEP Software and Computing R&D for the 2020s. *Comput Softw Big Sci* (2019) 3:7. doi:10.1007/s41781-018-0018-8
4. Allison J, Amako K, Apostolakis J, Arce P, Asai M, Aso T, et al. Recent Developments in GEANT4. *Nucl Instr Methods Phys Res Section A: Acc Spectrometers, Detectors Associated Equipment* (2016) 835:186–225. doi:10.1002/hbm.25039
5. Andreo P. Monte Carlo Techniques in Medical Radiation Physics. *Phys Med Biol* (1991) 36:861–920. doi:10.1088/0031-9155/36/7/001
6. Arabi H, Bortolin K, Ginovart N, Garibotto V, and Zaidi H. Deep Learning-guided Joint Attenuation and Scatter Correction in Multitracer Neuroimaging Studies. *Hum Brain Mapp* (2020) 41:3667–79. doi:10.1002/hbm.25039
7. Arjovsky M, Chintala S, and Bottou L. Wasserstein Generative Adversarial Networks. Proceedings of the 34th International Conference on Machine Learning - Volume 70, ICML'17; Sydney, NSW (2017). p. 214–223.
8. Aurisano A, Radovic A, Rocco D, Himmel A, Messier MD, Niner E, et al. A Convolutional Neural Network Neutrino Event Classifier. *J Inst* (2016) 11: P09001. doi:10.1088/1748-0221/11/09/p09001
9. Bach S, Binder A, Montavon G, Klauschen F, Müller K-R, and Samek W. On Pixel-Wise Explanations for Non-linear Classifier Decisions by Layer-Wise Relevance Propagation. *PLOS ONE* (2015) 10:e0130140. doi:10.1371/journal.pone.0130140
10. Badawi RD, Shi H, Hu P, Chen S, Xu T, Price PM, et al. First Human Imaging Studies with the EXPLORER Total-Body PET Scanner*. *J Nucl Med* (2019) 60:299–303. doi:10.2967/jnumed.119.226498
11. Bai T, Wang B, Nguyen D, and Jiang S. Deep Dose Plugin: Towards Real-Time Monte Carlo Dose Calculation through a Deep Learning-Based Denoising Algorithm. *Mach Learn Sci Technol* (2021) 2:025033. doi:10.1088/2632-2153/abdbfe
12. Baldi P, Bauer K, Eng C, Sadowski P, and Whiteson D. Jet Substructure Classification in High-Energy Physics with Deep Neural Networks. *Phys Rev D* (2016) 93:094034. doi:10.1103/physrevd.93.094034
13. Battistoni G, Pinsky L, Santana M, Lechner A, Lari L, Smirnov G, et al. FLUKA Monte Carlo Calculations for Hadrontherapy Application (2012). Available at: https://cds.cern.ch/record/1537386.
14. Berger MJ, and Seltzer SM. Calculation of Energy and Charge Deposition and of the Electron Flux in a Water Medium Bombarded with 20-MeV Electrons. *Ann NY Acad Sci* (1969) 161:8–23. doi:10.1111/j.1749-6632.1969.tb34035.x
15. Berkes P, and Wiskott L. On the Analysis and Interpretation of Inhomogeneous Quadratic Forms as Receptive Fields. *Neural Comput* (2006) 18:1868–95. doi:10.1162/neco.2006.18.8.1868
16. Bert J, Perez-Ponce H, Bitar ZE, Jan S, Boursier Y, Vintache D, et al. Geant4-based Monte Carlo Simulations on GPU for Medical Applications. *Phys Med Biol* (2013) 58:5593–611. doi:10.1088/0031-9155/58/16/5593
17. Bishop C. *Pattern Recognition and Machine Learning*. Springer (2006).
18. Böhlen TT, Cerutti F, Chin MPW, Fassò A, Ferrari A, Ortega PG, et al. The FLUKA Code: Developments and Challenges for High Energy and Medical Applications. *Nucl Data Sheets* (2014) 120:211–4. doi:10.1016/j.nds.2014.07.049
19. Bolch WE. The Monte Carlo Method in Nuclear Medicine: Current Uses and Future Potential. *J Nucl Med* (2010) 51:337–9. doi:10.2967/jnumed.109.067835
20. Bolch WE, Bouchet LG, Robertson JS, Wessels BW, Siegel JA, Howell RW, et al. MIRD Pamphlet No. 17: the Dosimetry of Nonuniform Activity Distributions-Rradionuclide S Values at the Voxel Level. Medical Internal Radiation Dose Committee. *J Nucl Med* (1999) 40:11S–36S.
21. Bolch WE, Eckerman KF, Sgouros G, and Thomas SR. MIRD Pamphlet No. 21: A Generalized Schema for Radiopharmaceutical Dosimetry-Standardization of Nomenclature. *J Nucl Med* (2009) 50:477–84. doi:10.2967/jnumed.108.056036
22. Bourilkov D. Machine and Deep Learning Applications in Particle Physics. *Int J Mod Phys A* (2019) 34:1930019. doi:10.1142/s0217751x19300199
23. Bruyndonckx P, Leonard S, Tavernier S, Lemaitre C, Devroede O, Yibao Wu Y, et al. Neural Network-Based Position Estimators for PET Detectors Using Monolithic LSO Blocks. *IEEE Trans Nucl Sci* (2004) 51:2520–5. doi:10.1109/TNS.2004.835782
24. Carleo G, Cirac I, Cranmer K, Daudet L, Schuld M, Tishby N, et al. Machine Learning and the Physical Sciences. *Rev Mod Phys* (2019) 91:045002. doi:10.1103/RevModPhys.91.045002
25. Carrasquilla J, and Melko RG. Machine Learning Phases of Matter. *Nat Phys* (2017) 13:431–4. doi:10.1038/nphys4035
26. [Dataset] Cern. CERN Open Data Portal (2021). Available at: https://opendata.cern.ch/.
27. Chen L, Liang X, Shen C, Jiang S, and Wang J. Synthetic CT Generation from CBCT Images via Deep Learning. *Med Phys* (2020) 47:1115–25. doi:10.1002/mp.13978
28. Chetty IJ, Rosu M, Kessler ML, Fraass BA, Ten Haken RK, Kong F-M, et al. Reporting and Analyzing Statistical Uncertainties in Monte Carlo-Based Treatment Planning. *Int J Radiat Oncology*Biology*Physics* (2006) 65: 1249–59. doi:10.1016/j.ijrobp.2006.03.039
29. Chin S, Eccles CL, McWilliam A, Chuter R, Walker E, Whitehurst P, et al. Magnetic Resonance-guided Radiation Therapy: A Review. *J Med Imaging Radiat Oncol* (2020) 64:163–77. doi:10.1111/1754-9485.12968

30. Ciardiello A, Asai M, Caccia B, Cirrone Ga. P, Colonna M, Dotti A, et al. Preliminary Results in Using Deep Learning to Emulate BLOB, a Nuclear Interaction Model. *Physica Med* (2020) 73:65–72. doi:10.1016/j.ejmp.2020.04.005
31. Creswell A, White T, Dumoulin V, Arulkumaran K, Sengupta B, and Bharath AA. Generative Adversarial Networks: An Overview. *IEEE Signal Process Mag* (2018) 35:53–65. doi:10.1109/MSP.2017.2765202
32. Cui J, Gong K, Guo N, Wu C, Meng X, Kim K, et al. PET Image Denoising Using Unsupervised Deep Learning. *Eur J Nucl Med Mol Imaging* (2019) 46:2780–9. doi:10.1007/s00259-019-04468-4
33. Acilu PGd., Sarasola I, Canadas M, Cuerdo R, Mendes PR, Romero L, et al. Study and Optimization of Positioning Algorithms for Monolithic PET Detectors Blocks. *J Inst* (2012) 7:C06010. doi:10.1088/1748-0221/7/06/c06010
34. de Oliveira L, Paganini M, and Nachman B. Learning Particle Physics by Example: Location-Aware Generative Adversarial Networks for Physics Synthesis. *Comput Softw Big Sci* (2017) 1:4. doi:10.1007/s41781-017-0004-6
35. Deasy JO. Denoising of Electron Beam Monte Carlo Dose Distributions Using Digital Filtering Techniques. *Phys Med Biol* (2000) 45:1765–79. doi:10.1088/0031-9155/45/7/305
36. Deasy JO, Wickerhauser MV, and Picard M. Accelerating Monte Carlo Simulations of Radiation Therapy Dose Distributions Using Wavelet Threshold De-noising. *Med Phys* (2002) 29:2366–73. doi:10.1118/1.1508112
37. Decuyper M, Stockhoff M, Vandenberghe S, and Van Holen R. Artificial Neural Networks for Positioning of Gamma Interactions in Monolithic PET Detectors. *Phys Med Biol* (2021) 66:075001. doi:10.1088/1361-6560/abebfc
38. Descourt P, Carlier T, Du Y, Song X, Buvat I, Frey EC, et al. Implementation of Angular Response Function Modeling in SPECT Simulations with GATE. *Phys Med Biol* (2010) 55:N253–N266. doi:10.1088/0031-9155/55/9/n04
39. Di Sipio R, Giannelli MF, Haghighat SK, and Palazzo S. DijetGAN: A Generative-Adversarial Network Approach for the Simulation of QCD Dijet Events at the LHC. *J High Energ Phys* (2019) 2019:110. doi:10.1007/JHEP08(2019)110
40. DUNE CollaborationAbi B, Acciarri R, Acero MA, Adamov G, Adams D, et al. Neutrino Interaction Classification with a Convolutional Neural Network in the DUNE Far Detector. *Phys Rev D* (2020) 102:092003. doi:10.1016/j.jacr.2017.09.045
41. Fahey FH, Grogg K, and El Fakhri G. Use of Monte Carlo Techniques in Nuclear Medicine. *J Am Coll Radiol* (2018) 15:446–8. doi:10.1016/j.jacr.2017.09.045
42. Fippel M, and N sslin F. Smoothing Monte Carlo Calculated Dose Distributions by Iterative Reduction of Noise. *Phys Med Biol* (2003) 48:1289–304. doi:10.1088/0031-9155/48/10/304
43. Fornander H. *Denoising Monte Carlo Dose Calculations Using a Deep Neural Network*. Ph.D. thesis. KTH Royal Institute Of Technology School of Electrical Engineering and Computer Science (2019).
44. Foundation HS, Apostolakis J, Asai M, Banerjee S, Bianchi R, Canal P, et al. (2018). HEP Software Foundation Community White Paper Working Group - Detector Simulation. arXiv:1803.04165.
45. Garcia M-P, Bert J, Benoit D, Bardiès M, and Visvikis D. Accelerated GPU Based SPECT Monte Carlo Simulations. *Phys Med Biol* (2016) 61:4001–18. doi:10.1088/0031-9155/61/11/4001
46. Garnett RL, Hanu AR, Byun SH, and Hunter SD. Event Selection and Background Rejection in Time Projection chambers Using Convolutional Neural Networks and a Specific Application to the AdEPT Gamma-ray Polarimeter mission. *Nucl Instr Methods Phys Res Section A: Acc Spectrometers, Detectors Associated Equipment* (2021) 987:164860. doi:10.1016/j.nima.2020.164860
47. Goodfellow I, Bengio Y, and Courville A. *Deep Learning*, Vol. 1. MIT press Cambridge (2016).
48. Goodfellow I, Pouget-Abadie J, Mirza M, Xu B, Warde-Farley D, Ozair S, et al. *Advances in Neural Information Processing Systems*, 2 (2014). p. 2672–80.Generative Adversarial Nets.
49. Götz TI (2019). Technical Report: Time-Activity-Curve Integration in Lu-177 Therapies in Nuclear Medicine. arXiv:1907.06617 [physics].
50. Grevillot L, Boersma DJ, Fuchs H, Aitkenhead A, Elia A, Bolsa M, et al. Technical Note: GATE-RTion: a GATE/Geant4 Release for Clinical Applications in Scanned Ion Beam Therapy. *Med Phys* (2020) 47:3675–81. doi:10.1002/mp.14242
51. Guest D, Cranmer K, and Whiteson D. Deep Learning and its Application to LHC Physics. *Annu Rev Nucl Part Sci* (2018) 68:161–81. doi:10.1146/annurev-nucl-101917-021019
52. Gulrajani I, Ahmed F, Arjovsky M, Dumoulin V, and Courville A. (2017). Improved Training of Wasserstein GANs. In *Advances in Neural Information Processing Systems* Curran Associates, Inc., 30.
53. Speer TW, Knowlton CA, Mackay MK, Ma C, Wang L, Daugherty LC, et al. Dose Volume Histogram (DVH). In: LW Brady and TE Yaeger, editors. *Encyclopedia of Radiation Oncology*. Berlin, Heidelberg: Springer (2013). p. 166. doi:10.1007/978-3-540-85516-3_659
54. Huang G, Liu Z, van der Maaten L, and Weinberger KQ. Densely Connected Convolutional Networks. In: Proceedings of the IEEE Conference on Computer Vision and Pattern Recognition (2017). p. 4700–8. doi:10.1109/cvpr.2017.243
55. Hughes HG, Chadwick MB, Corzine RK, Egdorf HW, Gallmeier FX, Little RC, et al. Status of the MCNPX Transport Code. In: A Kling, FJC Barão, M Nakagawa, L Távora, and P Vaz, editors. *Advanced Monte Carlo for Radiation Physics, Particle Transport Simulation and Applications*. Berlin, Heidelberg: Springer (2001). p. 961–6. doi:10.1007/978-3-642-18211-2_154
56. Isola P, Zhu J-Y, Zhou T, and Efros AA. Image-to-Image Translation with Conditional Adversarial Networks. In: 2017 IEEE Conference on Computer Vision and Pattern Recognition (CVPR) (2017). p. 5967–76. doi:10.1109/cvpr.2017.632
57. Jan S, Benoit D, Becheva E, Carlier T, Cassol F, Descourt P, et al. GATE V6: A Major Enhancement of the GATE Simulation Platform Enabling Modelling of CT and Radiotherapy. *Phys Med Biol* (2011) 56:881–901. doi:10.1088/0031-9155/56/4/001
58. Jarry G, Graham SA, Moseley DJ, Jaffray DJ, Siewerdsen JH, and Verhaegen F. Characterization of Scattered Radiation in kV CBCT Images Using Monte Carlo Simulations. *Med Phys* (2006) 33:4320–9. doi:10.1118/1.2358324
59. Javaid U, Souris K, Dasnoy D, Huang S, and Lee JA. Mitigating Inherent Noise in Monte Carlo Dose Distributions Using Dilated U-Net. *Med Phys* (2019) 46:5790–8. doi:10.1002/mp.13856
60. Jiang Y, Yang C, Yang P, Hu X, Luo C, Xue Y, et al. Scatter Correction of Cone-Beam CT Using a Deep Residual Convolution Neural Network (DRCNN). *Phys Med Biol* (2019) 64:145003. doi:10.1088/1361-6560/ab23a6
61. Jolicoeur-Martineau A, and Mitliagkas I (2019). Connections between Support Vector Machines, Wasserstein Distance and Gradient-Penalty GANs. arXiv:1910.06922 [cs, stat]. October, 2019.
62. Jolicoeur-Martineau A, and Mitliagkas I (2020). Gradient Penalty from a Maximum Margin Perspective. arXiv:1910.06922 [cs, stat]. November 2020.
63. Kalantzis G, Vasquez-Quino LA, Zalman T, Pratx G, and Lei Y. Toward IMRT 2D Dose Modeling Using Artificial Neural Networks: A Feasibility Study. *Med Phys* (2011) 38:5807–17. doi:10.1118/1.3639998
64. Karp JS, Michael Geagan J, Muehllehner G, Matthew Werner E, McDermott T, Jeffrey Schmall P, et al. The PennPET Explorer Scanner for Total Body Applications. In: 2017 IEEE Nuclear Science Symposium and Medical Imaging Conference. NSS/MIC (2017). p. 1–4. doi:10.1109/nssmic.2017.8533068
65. Kawrakow I. *NRCC Report PIRS-701* (2001).The EGSnrc Code System, Monte Carlo Simulation of Electron and Photon Transport.
66. Kawrakow I. On the De-noising of Monte Carlo Calculated Dose Distributions. *Phys Med Biol* (2002) 47:3087–103. doi:10.1088/0031-9155/47/17/304
67. Kearney V, Chan JW, Wang T, Perry A, Descovich M, Morin O, et al. DoseGAN: A Generative Adversarial Network for Synthetic Dose Prediction Using Attention-Gated Discrimination and Generation. *Sci Rep* (2020) 10:11073. doi:10.1038/s41598-020-68062-7
68. Kingma DP, and Welling M. An Introduction to Variational Autoencoders. *FNT Machine Learn* (2019) 12:307–92. doi:10.1561/2200000056
69. Kiureghian AD, and Ditlevsen O. Aleatory or Epistemic? Does it Matter? *Struct Saf* (2009) 31:105–12. doi:10.1016/j.strusafe.2008.06.020
70. Kononenko I. Bayesian Neural Networks. *Biol Cybern* (1989) 61:361–70. doi:10.1007/BF00200801
71. Kontaxis C, Bol GH, Lagendijk JJW, and Raaymakers BW. DeepDose: Towards a Fast Dose Calculation Engine for Radiation Therapy Using

Deep Learning. *Phys Med Biol* (2020) 65:075013. doi:10.1088/1361-6560/ab7630
72. Kowalski P, Wiślicki W, Shopa RY, Raczyński L, Klimaszewski K, Curcenau C, et al. Estimating the NEMA Characteristics of the J-PET Tomograph Using the GATE Package. *Phys Med Biol* (2018) 63:165008. doi:10.1088/1361-6560/aad29b
73. Krizhevsky A, Sutskever I, and Hinton GE. *Advances in Neural Information Processing Systems*, 25. Curran Associates, Inc.) (2012). p. 1–9.ImageNet Classification with Deep Convolutional Neural Networks.
74. Lai Y, Jia X, and Chi Y. Modeling the Effect of Oxygen on the Chemical Stage of Water Radiolysis Using GPU-Based Microscopic Monte Carlo Simulations, with an Application in FLASH Radiotherapy. *Phys Med Biol* (2021) 66:025004. doi:10.1088/1361-6560/abc93b
75. Lalonde A, Winey B, Verburg J, Paganetti H, and Sharp GC. Evaluation of CBCT Scatter Correction Using Deep Convolutional Neural Networks for Head and Neck Adaptive Proton Therapy. *Phys Med Biol* (2020) 65:245022. doi:10.1088/1361-6560/ab9fcb
76. LeCun Y, Bengio Y, and Hinton G. Deep Learning. *Nature* (2015) 521: 436–44. doi:10.1038/nature14539
77. LeCun Y, Bengio Y, and Laboratories TB. *The Handbook of Brain Theory and Neural Networks*. MIT Press (1998). p. 255–8.Convolutional Networks for Images, Speech, and Time-Series.
78. Lee H, and Lee J. A Deep Learning-Based Scatter Correction of Simulated X-ray Images. *Electronics* (2019) 8:944. doi:10.3390/electronics8090944
79. Lee MS, Hwang D, Kim JH, and Lee JS. Deep-dose: A Voxel Dose Estimation Method Using Deep Convolutional Neural Network for Personalized Internal Dosimetry. *Sci Rep* (2019) 9:10308. doi:10.1038/s41598-019-46620-y
80. Lei Y, Harms J, Wang T, Liu Y, Shu HK, Jani AB, et al. MRI-only Based Synthetic CT Generation Using Dense Cycle Consistent Generative Adversarial Networks. *Med Phys* (2019) 46:3565–81. doi:10.1002/mp.13617
81. Li H, Dong L, Zhang L, Yang JN, Gillin MT, and Zhu XR. Toward a Better Understanding of the Gamma index: Investigation of Parameters with a Surface-Based Distance Methoda). *Med Phys* (2011) 38:6730–41. doi:10.1118/1.3659707
82. Lin C, Chang Y-C, Chiu H-Y, Cheng C-H, and Huang H-M. Reducing Scan Time of Paediatric 99mTc-DMSA SPECT via Deep Learning. *Clin Radiol* (2021) 76:315–e13. doi:10.1016/j.crad.2020.11.114
83. Linardatos P, Papastefanopoulos V, and Kotsiantis S. Explainable AI: A Review of Machine Learning Interpretability Methods. *Entropy* (2020) 23:18. doi:10.3390/e23010018
84. Liu Y, Lei Y, Wang T, Fu Y, Tang X, Curran WJ, et al. CBCT-based Synthetic CT Generation Using Deep-attention cycleGAN for Pancreatic Adaptive Radiotherapy. *Med Phys* (2020) 47:2472–83. doi:10.1002/mp.14121
85. Liu Z, Fan J, Li M, Yan H, Hu Z, Huang P, et al. A Deep Learning Method for Prediction of Three-dimensional Dose Distribution of Helical Tomotherapy. *Med Phys* (2019) 46:1972–83. doi:10.1002/mp.13490
86. Low DA, Harms WB, Mutic S, and Purdy JA. A Technique for the Quantitative Evaluation of Dose Distributions. *Med Phys* (1998) 25: 656–61. doi:10.1118/1.598248
87. Maier J, Eulig E, Vöth T, Knaup M, Kuntz J, Sawall S, et al. Real-time Scatter Estimation for Medical CT Using the Deep Scatter Estimation: Method and Robustness Analysis with Respect to Different Anatomies, Dose Levels, Tube Voltages, and Data Truncation. *Med Phys* (2019) 46:238–49. doi:10.1002/mp.13274
88. Mainegra-Hing E, and Kawrakow I. Fast Monte Carlo Calculation of Scatter Corrections for CBCT Images. *J Phys Conf Ser* (2008) 102:012017. doi:10.1088/1742-6596/102/1/012017
89. Maneval D, Ozell B, and Després P. pGPUMCD: An Efficient GPU-Based Monte Carlo Code for Accurate Proton Dose Calculations. *Phys Med Biol* (2019) 64:085018. doi:10.1088/1361-6560/ab0db5
90. Mao X, Pineau J, Keyes R, and Enger SA. RapidBrachyDL: Rapid Radiation Dose Calculations in Brachytherapy via Deep Learning. *Int J Radiat Oncology*Biology*Physics* (2020) 108:802–12. doi:10.1016/j.ijrobp.2020.04.045
91. Matthies HG. Quantifying Uncertainty: Modern Computational Representation of Probability and Applications. In: A Ibrahimbegovic and I Kozar, editors. *Extreme Man-Made and Natural Hazards in Dynamics of Structures*. Dordrecht: Springer Netherlands), NATO Security through Science Series (2007). p. 105–35. doi:10.1007/978-1-4020-5656-7_4
92. Miao B, Jeraj R, Bao S, and Mackie TR. Adaptive Anisotropic Diffusion Filtering of Monte Carlo Dose Distributions. *Phys Med Biol* (2003) 48: 2767–81. doi:10.1088/0031-9155/48/17/303
93. Michaud J-B, Tétrault M-A, Beaudoin J-F, Cadorette J, Leroux J-D, Brunet C-A, et al. Sensitivity Increase through a Neural Network Method for LOR Recovery of ICS Triple Coincidences in High-Resolution Pixelated- Detectors PET Scanners. *IEEE Trans Nucl Sci* (2015) 62:82–94. doi:10.1109/tns.2014.2372788
94. Miyato T, Kataoka T, Koyama M, and Yoshida Y. *International Conference on Learning Representations*, 1–26 (2018). Spectral Normalization for Generative Adversarial Networks.
95. Moiseenko V, Liu M, Bergman AM, Gill B, Kristensen S, Teke T, et al. Monte Carlo Calculation of Dose Distribution in Early Stage NSCLC Patients Planned for Accelerated Hypofractionated Radiation Therapy in the NCIC-BR25 Protocol. *Phys Med Biol* (2010) 55:723–33. doi:10.1088/0031-9155/55/3/012
96. Montavon G, Samek W, and Müller K-R. Methods for Interpreting and Understanding Deep Neural Networks. *Digital Signal Process.* (2018) 73: 1–15. doi:10.1016/j.dsp.2017.10.011
97. Mostafapour S, Gholamiankhah F, Dadgar H, Arabi H, and Zaidi H. Feasibility of Deep Learning-Guided Attenuation and Scatter Correction of Whole-Body 68Ga-PSMA PET Studies in the Image Domain. *Clin Nucl Med* (2021) 46(8):609–615. doi:10.1097/RLU.0000000000003585
98. Müller F, Schug D, Hallen P, Grahe J, and Schulz V. Gradient Tree Boosting-Based Positioning Method for Monolithic Scintillator Crystals in Positron Emission Tomography. *IEEE Trans Radiat Plasma Med Sci* (2018) 2:411–21. doi:10.1109/trpms.2018.2837738
99. Müller F, Schug D, Hallen P, Grahe J, and Schulz V. A Novel DOI Positioning Algorithm for Monolithic Scintillator Crystals in PET Based on Gradient Tree Boosting. *IEEE Trans Radiat Plasma Med Sci* (2019) 3:465–74. doi:10.1109/trpms.2018.2884320
100. Muñoz E, Ros A, Borja-Lloret M, Barrio J, Dendooven P, Oliver JF, et al. Proton Range Verification with MACACO II Compton Camera Enhanced by a Neural Network for Event Selection. *Sci Rep* (2021) 11:9325. doi:10.1038/s41598-021-88812-5
101. Naqa IE, Kawrakow I, Fippel M, Siebers JV, Lindsay PE, Wickerhauser MV, et al. A Comparison of Monte Carlo Dose Calculation Denoising Techniques. *Phys Med Biol* (2005) 50:909–22. doi:10.1088/0031-9155/50/5/014
102. Nasiri N, and Abbaszadeh S. *Medical Imaging 2021: Physics of Medical Imaging*, 11595. International Society for Optics and Photonics (2021). p. 115953W. doi:10.1117/12.2582063A Deep Learning Approach to Correctly Identify the Sequence of Coincidences in Cross-Strip CZT Detectors.
103. Neph R, Huang Y, Yang Y, and Sheng K. DeepMCDose: A Deep Learning Method for Efficient Monte Carlo Beamlet Dose Calculation by Predictive Denoising in MR-Guided Radiotherapy. In: D Nguyen, L Xing, and S Jiang, editors. *Artificial Intelligence in Radiation Therapy*, 11850. Cham: Springer International Publishing (2019). p. 137–45. doi:10.1007/978-3-030-32486-5_17
104. Nguyen D, Jia X, Sher D, Lin M-H, Iqbal Z, Liu H, et al. 3D Radiotherapy Dose Prediction on Head and Neck Cancer Patients with a Hierarchically Densely Connected U-Net Deep Learning Architecture. *Phys Med Biol* (2019) 64:065020. doi:10.1088/1361-6560/ab039b
105. Nichol A, and Dhariwal P. (2021). "Improved Denoising Diffusion Probabilistic Models," in *Proceedings of the 38th International Conference on Machine Learning*, 8162–8171.
106. Niu ZM, and Liang HZ. Nuclear Mass Predictions Based on Bayesian Neural Network Approach with Pairing and Shell Effects. *Phys Lett B* (2018) 778: 48–53. doi:10.1016/j.physletb.2018.01.002
107. Oliver JF, Fuster-Garcia E, Cabello J, Tortajada S, and Rafecas M. Application of Artificial Neural Network for Reducing Random Coincidences in PET. *IEEE Trans Nucl Sci* (2013) 60:3399–409. doi:10.1109/tns.2013.2274702
108. Paganini M, de Oliveira L, and Nachman B. CaloGAN: Simulating 3D High Energy Particle Showers in Multi-Layer Electromagnetic Calorimeters with Generative Adversarial Networks. *Phys Rev D* (2018) 97:014021. doi:10.1103/physrevd.97.014021
109. Pedemonte S, Pierce L, and Van Leemput K. A Machine Learning Method for Fast and Accurate Characterization of Depth-Of-Interaction Gamma Cameras. *Phys Med Biol* (2017) 62:8376–401. doi:10.1088/1361-6560/aa6ee5

110. Peng P, Judenhofer MS, Jones AQ, and Cherry SR. Compton PET: A Simulation Study for a PET Module with Novel Geometry and Machine Learning for Position Decoding. *Biomed Phys Eng Express* (2018) 5:015018. doi:10.1088/2057-1976/aaef03
111. Peng Z, Shan H, Liu T, Pei X, Zhou J, Wang G, et al. (2019). Deep Learning for Accelerating Monte Carlo Radiation Transport Simulation in Intensity-Modulated Radiation Therapy. arXiv:1910.07735 [physics], October 2019.
112. Pierce LA, Pedemonte S, DeWitt D, MacDonald L, Hunter WCJ, Van Leemput K, et al. Characterization of Highly Multiplexed Monolithic PET/Gamma Camera Detector Modules. *Phys Med Biol* (2018) 63:075017. doi:10.1088/1361-6560/aab380
113. Prevedello LM, Halabi SS, Shih G, Wu CC, Kohli MD, Chokshi FH, et al. Challenges Related to Artificial Intelligence Research in Medical Imaging and the Importance of Image Analysis Competitions. *Radiol Artif Intelligence* (2019) 1:e180031. doi:10.1148/ryai.2019180031
114. Radovic A, Williams M, Rousseau D, Kagan M, Bonacorsi D, Himmel A, et al. Machine Learning at the Energy and Intensity Frontiers of Particle Physics. *Nature* (2018) 560:41–8. doi:10.1038/s41586-018-0361-2
115. Rogers DWO. Low Energy Electron Transport with EGS. *Nucl Instr Methods Phys Res Section A: Acc Spectrometers, Detectors Associated Equipment* (1984) 227:535–48. doi:10.1016/0168-9002(84)90213-4
116. Ronneberger O, Fischer P, and Brox T. (2015). U-net: Convolutional Networks for Biomedical Image Segmentation. arXiv:1505.04597 [cs]. doi:10.1007/978-3-319-24574-4_28
117. Roser P, Zhong X, Birkhold A, Strobel N, Kowarschik M, Fahrig R, et al. Physics-driven Learning of X-ray Skin Dose Distribution in Interventional Procedures. *Med Phys* (2019) 46:4654–65. doi:10.1002/mp.13758
118. Rydén T, Heydorn Lagerlöf J, Hemmingsson J, Marin I, Svensson J, Båth M, et al. Fast GPU-Based Monte Carlo Code for SPECT/CT Reconstructions Generates Improved 177Lu Images. *EJNMMI Phys* (2018) 5:1. doi:10.1186/s40658-017-0201-8
119. Ryden T, van Essen M, Marin I, Svensson J, and Bernhardt P. Deep Learning Generation of Synthetic Intermediate Projections Improves 177Lu SPECT Images Reconstructed with Sparsely Acquired Projections. *J Nucl Med Official Publication, Soc Nucl Med* (2020) 62(4):528–535. doi:10.2967/jnumed.120.245548
120. Salvat F, Fernández-Varea J, and Sempau J. *Penelope. A Code System for Monte Carlo Simulation of Electron and Photon Transport*. Barcelona: NEA Data Bank, Workshop Proceeding (2007). p. 4–7.
121. Sanaat A, Shiri I, Arabi H, Mainta I, Nkoulou R, and Zaidi H. Deep Learning-Assisted Ultra-fast/low-dose Whole-Body PET/CT Imaging. *Eur J Nucl Med Mol Imaging* (2021). doi:10.1007/s00259-020-05167-1
122. Sanaat A, and Zaidi H. Depth of Interaction Estimation in a Preclinical PET Scanner Equipped with Monolithic Crystals Coupled to SiPMs Using a Deep Neural Network. *Appl Sci* (2020) 10:4753. doi:10.3390/app10144753
123. Sarrut D, Bała M, Bardiès M, Bert J, Chauvin M, Chatzipapas K, et al. Advanced Monte Carlo Simulations of Emission Tomography Imaging Systems with GATE. *Phys Med Biol* (2021) 66:10TR03. doi:10.1088/1361-6560/abf276
124. Sarrut D, Bardiès M, Boussion N, Freud N, Jan S, Létang J-M, et al. A Review of the Use and Potential of the GATE Monte Carlo Simulation Code for Radiation Therapy and Dosimetry Applications. *Med Phys* (2014) 41:064301. doi:10.1118/1.4871617
125. Sarrut D, Etxebeste A, Krah N, and Létang J. Modeling Complex Particles Phase Space with GAN for Monte Carlo SPECT Simulations: A Proof of Concept. *Phys Med Biol* (2021) 66:055014. doi:10.1088/1361-6560/abde9a
126. Sarrut D, Krah N, Badel JN, and Létang JM. Learning SPECT Detector Angular Response Function with Neural Network for Accelerating Monte-Carlo Simulations. *Phys Med Biol* (2018) 63:205013. doi:10.1088/1361-6560/aae331
127. Sarrut D, Krah N, and Létang JM. Generative Adversarial Networks (GAN) for Compact Beam Source Modelling in Monte Carlo Simulations. *Phys Med Biol* (2019) 64:215004. doi:10.1088/1361-6560/ab3fc1
128. Schmidhuber J. Deep Learning in Neural Networks: An Overview. *Neural Networks* (2015) 61:85–117. doi:10.1016/j.neunet.2014.09.003
129. J Seco and F Verhaegen, editors. *Monte Carlo Techniques in Radiation Therapy*. Boca Raton: CRC Press (2013). doi:10.1201/b13961
130. Seltzer SM. Electron-photon Monte Carlo Calculations: The ETRAN Code. *Int J Radiat Appl Instrumentation. A. Appl Radiat Isotopes* (1991) 42:917–41. doi:10.1016/0883-2889(91)90050-b
131. Shan H, Zhang Y, Yang Q, Kruger U, Kalra MK, Sun L, et al. 3-D Convolutional Encoder-Decoder Network for Low-Dose CT via Transfer Learning from a 2-D Trained Network. *IEEE Trans Med Imaging* (2018) 37:1522–34. doi:10.1109/tmi.2018.2832217
132. Shen C, Nguyen D, Zhou Z, Jiang SB, Dong B, and Jia X. An Introduction to Deep Learning in Medical Physics: Advantages, Potential, and Challenges. *Phys Med Biol* (2020) 65:05TR01. doi:10.1088/1361-6560/ab6f51
133. Shen H, Liu J, and Fu L. Self-learning Monte Carlo with Deep Neural Networks. *Phys Rev B* (2018) 97:205140. doi:10.1103/PhysRevB.97.205140
134. Simonyan K, Vedaldi A, and Zisserman A. Deep inside Convolutional Networks: Visualising Image Classification Models and Saliency Maps. In: Workshop at International Conference on Learning Representations (2014). p. 1–8.
135. Song X, Segars WP, Du Y, Tsui BMW, and Frey EC. Fast Modelling of the Collimator-Detector Response in Monte Carlo Simulation of SPECT Imaging Using the Angular Response Function. *Phys Med Biol* (2005) 50:1791–804. doi:10.1088/0031-9155/50/8/011
136. Song Y, and Ermon S. Generative Modeling by Estimating Gradients of the Data Distribution. *Adv Neural Inf Process Syst* (2019) 32.
137. Song Y, and Ermon S. (2020). "Improved Techniques for Training Score-Based Generative Models," In NIPS Workshop (*Neural Information Processing Systems*).
138. Srivastava N, Hinton G, Krizhevsky A, Sutskever I, and Salakhutdinov R. Dropout: A Simple Way to Prevent Neural Networks from Overfitting. *J Machine Learn Res* (2014) 15(1):1929–58.
139. Staelens S, and Buvat I. Monte Carlo Simulations in Nuclear Medicine Imaging. In: P Verdonck, editor. *Advances in Biomedical Engineering*. Amsterdam: Elsevier (2009). p. 177–209. doi:10.1016/B978-0-444-53075-2.00005-8
140. Stockhoff M, Van Holen R, and Vandenberghe S. Optical Simulation Study on the Spatial Resolution of a Thick Monolithic PET Detector. *Phys Med Biol* (2019) 64:195003. doi:10.1088/1361-6560/ab3b83
141. Taasti VT, Klages P, Parodi K, and Muren LP. Developments in Deep Learning Based Corrections of Cone Beam Computed Tomography to Enable Dose Calculations for Adaptive Radiotherapy. *Phys Imaging Radiat Oncol* (2020) 15:77–9. doi:10.1016/j.phro.2020.07.012
142. Tian C, Fei L, Zheng W, Xu Y, Zuo W, and Lin C-W. Deep Learning on Image Denoising: An Overview. *Neural Networks* (2020) 131:251–75. doi:10.1016/j.neunet.2020.07.025
143. Vahdat A, Kreis K, and Kautz J. (2021). Score-based Generative Modeling in Latent Space. *arxiv*.
144. Vallecorsa S. Generative Models for Fast Simulation. *J Phys Conf Ser* (2018) 1085:022005. doi:10.1088/1742-6596/1085/2/022005
145. van der Heyden B, Uray M, Fonseca GP, Huber P, Us D, Messner I, et al. A Monte Carlo Based Scatter Removal Method for Non-isocentric Cone-Beam CT Acquisitions Using a Deep Convolutional Autoencoder. *Phys Med Biol* (2020) 65:145002. doi:10.1088/1361-6560/ab8954
146. Vandenberghe S, Mikhaylova E, Brans B, Defrise M, Lahoutte T, Muylle K, et al. PET20.0: a Cost Efficient, 2mm Spatial Resolution Total Body PET with point Sensitivity up to 22% and Adaptive Axial FOV of Maximum 2.00m. In: Annual Congress of the European Association of Nuclear Medicine, Vol. 44 (2017). p. 305.
147. Vasudevan V, Huang C, Simiele E, Yu L, Xing L, and Schuler E. Combining Monte Carlo with Deep Learning: Predicting High-Resolution, Low-Noise Dose Distributions Using a Generative Adversarial Network for Fast and Precise Monte Carlo Simulations. *Int J Radiat Oncology*Biology*Physics* (2020) 108:S44–S45. doi:10.1016/j.ijrobp.2020.07.2157
148. Verhaegen F, and Seuntjens J. Monte Carlo Modelling of External Radiotherapy Photon Beams. *Phys Med Biol* (2003) 48:R107–R164. doi:10.1088/0031-9155/48/21/r01
149. Wang Y, Wang L, Li D, and Cheng X. A New Method of Depth-Of-Interaction Determination for Continuous crystal PET Detectors. In: 2014 IEEE Nuclear Science Symposium and Medical Imaging Conference. NSS/MIC (2014). p. 1–2. doi:10.1109/NSSMIC.2014.7430765

150. Wang Y, Zhu W, Cheng X, and Li D. 3D Position Estimation Using an Artificial Neural Network for a Continuous Scintillator PET Detector. *Phys Med Biol* (2013) 58:1375–90. doi:10.1088/0031-9155/58/5/1375
151. Wolterink JM, Leiner T, Viergever MA, and Isgum I. Generative Adversarial Networks for Noise Reduction in Low-Dose CT. *IEEE Trans Med Imaging* (2017) 36:2536–45. doi:10.1109/tmi.2017.2708987
152. Xie S, Yang C, Zhang Z, and Li H. Scatter Artifacts Removal Using Learning-Based Method for CBCT in IGRT System. *IEEE Access* (2018) 6:78031–7. doi:10.1109/ACCESS.2018.2884704
153. Yang Q, Yan P, Zhang Y, Yu H, Shi Y, Mou X, et al. Low-Dose CT Image Denoising Using a Generative Adversarial Network with Wasserstein Distance and Perceptual Loss. *IEEE Trans Med Imaging* (2018) 37:1348–57. doi:10.1109/tmi.2018.2827462
154. Zatcepin A, Pizzichemi M, Polesel A, Paganoni M, Auffray E, Ziegler SI, et al. Improving Depth-Of-Interaction Resolution in Pixellated PET Detectors Using Neural Networks. *Phys Med Biol* (2020) 65:175017. doi:10.1088/1361-6560/ab9efc
155. Zhang T, Chen Z, Zhou H, Bennett NR, Wang AS, and Gao H. An Analysis of Scatter Characteristics in X-ray CT Spectral Correction. *Phys Med Biol* (2021) 66:075003. doi:10.1088/1361-6560/abebab
156. Zhou D-X. Theory of Deep Convolutional Neural Networks: Downsampling. *Neural Networks* (2020) 124:319–27. doi:10.1016/j.neunet.2020.01.018
157. Zoglauer A, and Boggs SE. Application of Neural Networks to the Identification of the compton Interaction Sequence in compton Imagers. *2007 IEEE Nucl Sci Symp Conf Rec* (2007) 6:4436–41. doi:10.1109/nssmic.2007.4437096

Conflict of Interest: The authors declare that the research was conducted in the absence of any commercial or financial relationships that could be construed as a potential conflict of interest.

Publisher's Note: All claims expressed in this article are solely those of the authors and do not necessarily represent those of their affiliated organizations, or those of the publisher, the editors and the reviewers. Any product that may be evaluated in this article, or claim that may be made by its manufacturer, is not guaranteed or endorsed by the publisher.

frontiers in Physics

ORIGINAL RESEARCH
published: 03 November 2021
doi: 10.3389/fphy.2021.741453

Development and Benchmarking of a Monte Carlo Dose Engine for Proton Radiation Therapy

Peter Lysakovski[1,2], *Alfredo Ferrari*[1], *Thomas Tessonnier*[1], *Judith Besuglow*[1,2,3,4,5], *Benedikt Kopp*[1], *Stewart Mein*[1,3,4,5], *Thomas Haberer*[1], *Jürgen Debus*[1,5,6] *and Andrea Mairani*[1,7,3,8]*

[1]Department of Radiation Oncology, Heidelberg Ion Beam Therapy Center (HIT), Heidelberg University Hospital, Heidelberg, Germany, [2]Faculty of Physics and Astronomy, Heidelberg University, Heidelberg, Germany, [3]Clinical Cooperation Unit Translational Radiation Oncology, German Cancer Consortium (DKTK) Core-Center Heidelberg, National Center for Tumor Diseases (NCT), Heidelberg University Hospital (UKHD) and German Cancer Research Center (DKFZ), Heidelberg, Germany, [4]Division of Molecular and Translational Radiation Oncology, Heidelberg Faculty of Medicine (MFHD) and Heidelberg University Hospital (UKHD), Heidelberg, Germany, [5]Heidelberg Faculty of Medicine (MFHD) and German Cancer Research Center (DKFZ), Heidelberg Institute of Radiation Oncology (HIRO), National Center for Radiation Oncology (NCRO), Heidelberg University Hospital (UKHD), Heidelberg, Germany, [6]Clinical Cooperation Unit Radiation Oncology, German Cancer Consortium (DKTK) Core-Center Heidelberg, National Center for Tumor Diseases (NCT), Heidelberg University Hospital (UKHD) and German Cancer Research Center (DKFZ), Heidelberg, Germany, [7]Medical Physics, National Centre of Oncological Hadrontherapy (CNAO), Pavia, Italy, [8]Medical Faculty, Heidelberg University, Heidelberg, Germany

OPEN ACCESS

Edited by:
Miguel Antonio Cortés-Giraldo, Sevilla University, Spain

Reviewed by:
Adam Aitkenhead, The Christie National Health Service Foundation Trust, United Kingdom
Matteo Duranti, Istituto Nazionale di Fisica Nucleare di Perugia, Italy

***Correspondence:**
Andrea Mairani
Andrea.Mairani@med.uni-heidelberg.de

Specialty section:
This article was submitted to Radiation Detectors and Imaging, a section of the journal Frontiers in Physics

Received: *14 July 2021*
Accepted: *15 October 2021*
Published: *03 November 2021*

Citation:
Lysakovski P, Ferrari A, Tessonnier T, Besuglow J, Kopp B, Mein S, Haberer T, Debus J and Mairani A (2021) Development and Benchmarking of a Monte Carlo Dose Engine for Proton Radiation Therapy. Front. Phys. 9:741453. doi: 10.3389/fphy.2021.741453

Dose calculation algorithms based on Monte Carlo (MC) simulations play a crucial role in radiotherapy. Here, the development and benchmarking of a novel MC dose engine, MonteRay, is presented for proton therapy aiming to support clinical activity at the Heidelberg Ion Beam Therapy center (HIT) and the development of MRI (magnetic resonance imaging)-guided particle therapy. Comparisons against dosimetric data and gold standard MC FLUKA calculations at different levels of complexity, ranging from single pencil beams in water to patient plans, showed high levels of agreement, validating the physical approach implemented in the dose engine. Additionally, MonteRay has been found to match satisfactorily to FLUKA dose predictions in magnetic fields both in homogeneous and heterogeneous scenarios advocating its use for future MRI-guided proton therapy applications. Benchmarked on 150 MeV protons transported on a $2 \times 2 \times 2\,mm^3$ grid, MonteRay achieved a high computational throughput and was able to simulate the histories of more than 30,000 primary protons per second on a single CPU core.

Keywords: Monte Carlo (MC), dose calculation, radiotherapy, magnetic field, proton

INTRODUCTION

Image guided radiotherapy is at the forefront of innovative treatment delivery techniques. It has the potential to improve treatment efficacy via on-board imaging procedures such as adaptive planning and/or live monitoring, for instance via magnetic resonance (MR)-guided radiation therapy (MRgRT) [1, 2]. Over the last decade, clinical prototypes have combined low-field-strength MR and radioactive cobalt-60 sources for photon treatment, followed by linear accelerators and higher field-strength MR fields for improved image resolution [3–5].

Particle therapy (PT), a cancer treatment modality achieving superior dose conformity to solid tumours compared to conventional photon techniques [6, 7], would greatly benefit from on-board MR-guided treatment delivery [8]. For instance, at the Heidelberg Ion Beam Therapy Center (HIT) over 5,000 patients have been treated with proton and carbon ions since 2009 [9]. While ^{16}O ions have so far only been used for research purposes, HIT has treated the first patient with raster scanning ^{4}He ion beams in July 2021.

For all clinically administered ion beams, on-board MR-guided treatment delivery is currently not feasible. However, system developments for treatment planning and delivery of MR-guided particle therapy are underway at HIT. Here, we begin with considerations in dose calculation for MR-guided particle therapy. During MRgRT using photons, for example, the MR field (due to Lorentz forces) can impact the dose deposition of ionized electrons/delta-rays, with severity depending on patient anatomy and MR field strength [10, 11]. Hence, dose calculation corrections are introduced in clinical practice for improving accuracy [12]. Similarly, trajectories of fast charged particles like protons are altered by the MR field [13–15] and consequently, proper consideration must be given for accurate dose calculation.

With the aim of providing dose computations at various levels of accuracy and speed for current and future treatment in particle therapy with light and heavy ions, various systems have been introduced at HIT to support clinical deployment of PT. Initially, as a gold standard, a MC environment based on the MC code FLUKA [16, 17] has been developed and extensively benchmarked [18] for allowing database generation for clinical analytical treatment planning system (TPS) and patient recalculations. This framework required long computation times (hours to days depending on the number of CPUs available) which limited its usage in the analysis of large patient cohorts and for any adaptive/on-line planning.

In order to overcome these limitations, FRoG (Fast dose* Recalculation on GPU) has been introduced, an advanced analytical code capable of calculating dose, LET_d (dose-weighted Linear Energy Transfer) and biological dose for the four particle beams available at HIT [19–21] and which is in use at other PT facilities in Europe (Centro Nazionale di Adroterapia Oncologica [21], Danish Centre for Particle Therapy [22]. High levels of agreement within 1–2% [19, 21, 23] were found comparing FLUKA and FRoG recalculated dose-volume-histograms (DVH) of proton and other light ion patient plans even for complex cases such as lung irradiation [23]. However, analytical codes are usually designed for a specific task, making the introduction of new features such as MR-guidance [14, 24], positron emission tomography [25, 26] and prompt gammas [27] require large development effort and substantial changes in the physics engine. Fast MC engines have been introduced for proton beams [28–33] and helped streamline the development while reaching various levels of agreement when compared against gold standard MC codes such as FLUKA and TOPAS/Geant [34].

Several recent works have investigated the impact of MR-guidance on particle beam physics and modelling distortion due to the Lorentz force [13, 35–38]. Despite these characterizations however, no fast MC engine has been presented in literature which is able to perform clinically relevant particle therapy calculations in magnetic fields. In this work, a CPU-based fast MC dose engine for proton beams (MonteRay) was developed and benchmarked for supporting ongoing clinical activity and introducing novel treatment modalities, particularly within the MRI-guided particle therapy program at HIT.

MATERIALS AND METHODS

Programming Languages and Libraries

With performance and extensibility to GPUs in mind, the MonteRay MC engine was written in C++. Several external libraries were used either during development or execution of the MC code. The frameworks GoogleTest [39] and Benchmark [40] are used for testing and microbenchmarking the source code. The Boost library [41] is used for filesystem operations and parsing of configuration files. RapidXml [42] is used for reading of irradiation plans in XML format. ITK [43] and DCMTK [44] are used for reading CT images. FLUKA simulations were performed using FLUKA version 2020 0.6.

Geometry and Materials

Voxelized water phantom and patient geometries are implemented from computed tomography (CT) scans using the approach described in [45, 46], i.e. the Hounsfield Unit (HU) of each voxel is converted to a water equivalent path length, density and elemental composition. In total, 36 different materials, covering an HU range between -1000 HU and 3070 HU are used. HU values larger than 3070 are assumed to be metallic implants made from titanium. Each material is modeled as a combination of up to ten elements. Additionally, five extra materials (water, RW3, PMMA, air and carbon fiber) can be defined by the user for dosimetric studies. For the calculation of nuclear interactions, only the most abundant isotope of each element is considered: ^{1}H, ^{12}C, ^{14}N, ^{16}O, ^{23}Na, ^{24}Mg, ^{31}P, ^{32}S, ^{35}Cl,^{40}Ar, ^{39}K, ^{40}Ca and ^{48}Ti. However, just H, C, O and Ca already constitute more than 90% of a human's weight [47]. Including more materials in MonteRay is trivial if they consist only of the ten base elements already defined. Adding additional elements requires the generation of additional inelastic nuclear interaction databases (***Inelastic Nuclear Interactions***).

Handling the HIT-specific Beamline

The HIT beamline consists of various layers of different materials, including tungsten [48], with which the particle beam interacts before reaching the patient, resulting in a unique phase-space of particles. To avoid modelling and simulating the whole beamline in MonteRay, the approach described in [49] was used, i.e., sampling from a phase-space for each of the 255 quasi-monoenergetic proton beams available at the HIT facility. Each file contains the location, direction and energy of 10 million particles sampled on a plane perpendicular to the beam's direction before the patient's entrance. The phase space was generated using FLUKA and besides primary protons, secondary protons generated due to the primary particle's

interactions with the beamline are also considered. For now, however, all other secondary particles (deuterons, tritons, ^{3}He, ^{4}He and neutrons) are neglected. During simulation, our MC code randomly samples individual particles from these phase space files.

Transport

For the simulation of proton beams, MonteRay performs the transport of protons, deuterons, tritons, 3-Helium and 4-Helium. Of these particles, only protons undergo elastic and ***Inelastic Nuclear Interactions*** as described in ***Nuclear Interactions***. All transported particles experience energy loss and scattering through electromagnetic interactions as described in ***Electromagnetic Interactions***.

Energy is deposited either on a Cartesian or a cylindrical grid. Energy depositions from heavy nuclear recoils are recorded locally while energy lost through electromagnetic interactions are deposited along a track via the method described in [50]: given the particle's location at the beginning of the transport step $\vec{x_i}$ and its position at the end of the transport step $\vec{x_f}$, the point of energy deposition is chosen randomly *via*

$$\vec{x_{dep}} = \vec{x_i} \cdot (1 - \boldsymbol{U}) + \vec{x_f} \cdot \boldsymbol{U}, \tag{1}$$

where $\boldsymbol{U}$ is a random number uniformly distributed on the interval $[0, 1)$. This is an efficient method of avoiding aliasing effects due to floating-point inaccuracies at grid boundaries and mismatches between the CT and the scoring grid. To avoid discontinuities in the deposited dose, the particles are transported on a grid with spacing equal to or less than the requested scoring grids spacing. If a CT is loaded, this will be the CT grid. All simulations shown here, unless otherwise noted, were performed on a $1 \times 1 \times 1\,\mathrm{mm}^3$ Cartesian grid. At the beginning of each step, the distance to the next voxel's boundary $\boldsymbol{dx_{vox}}$ is calculated and the distance to the next nuclear interaction $\boldsymbol{dx_{nuc}}$ is sampled based on the total nuclear cross section introduced in ***Nuclear Interactions***. The smaller of these two values is chosen as the current iteration's step length $\boldsymbol{dx}$, i.e.

$$\boldsymbol{dx} = \boldsymbol{min}(\boldsymbol{dx_{vox}}, \boldsymbol{dx_{nuc}}). \tag{2}$$

The energy loss over the distance $\boldsymbol{dx}$ is calculated and the scattering angle is sampled after the approaches described in ***Electromagnetic Interactions***. In the presence of a magnetic field $\vec{\boldsymbol{B}}$, an additional deflection $\vec{\boldsymbol{\Delta u_m}}$ due to the Lorentz force is calculated after [51] using

$$\vec{\boldsymbol{\Delta u_m}} = \frac{\left(\vec{\boldsymbol{u}} \times \vec{\boldsymbol{B}}\right) \cdot \boldsymbol{z} \cdot \boldsymbol{c} \cdot \boldsymbol{dx}}{\boldsymbol{m} \cdot \boldsymbol{\gamma} \cdot \boldsymbol{\beta}}, \tag{3}$$

where $\boldsymbol{m}$ is the particle's rest mass, z is the particle's charge in units of the elementary charge, $\boldsymbol{\beta}$ is its velocity relative to the speed of light $\boldsymbol{c}$, $\vec{\boldsymbol{u}}$ is its normalized direction and $\boldsymbol{\gamma}$ is the Lorentz factor.

After updating the particle's position, energy and direction, if a nuclear interaction occurred, the type of nuclear interaction is determined, and the nuclear interaction performed as will be described in ***Nuclear Interactions***. The transport step is repeated until the particle's energy falls below a threshold of 1 MeV. The remaining energy is deposited in a single step. During transport, only protons undergo nuclear interactions. For all other particles, only electromagnetic energy losses are considered.

Angular deflections due to nuclear or electromagnetic interactions, expressed through a polar angle $\boldsymbol{\theta}$ and an azimuthal angle $\boldsymbol{\phi}$, are applied to the particle's initial direction $\vec{\boldsymbol{u}}$ to obtain the particle's final direction $\vec{\boldsymbol{u'}}$ *via*:

$$\vec{\boldsymbol{u'}} = \vec{\boldsymbol{v}} \cdot \boldsymbol{sin}(\boldsymbol{\theta}) \cdot \boldsymbol{cos}(\phi) + \vec{\boldsymbol{w}} \cdot \boldsymbol{sin}(\boldsymbol{\theta}) \cdot \boldsymbol{sin}(\phi) + \vec{\boldsymbol{u}} \cdot \boldsymbol{cos}(\boldsymbol{\theta}) \tag{4}$$

where the vectors $\vec{\boldsymbol{v}}$ and $\vec{\boldsymbol{w}}$ are chosen such that together with $\vec{\boldsymbol{u}}$, they form an orthonormal basis. Since all physical interactions considered in the simulation are independent of $\boldsymbol{\phi}$, any orthonormal basis can be used for this purpose. To find $\vec{\boldsymbol{v}}$, a run-time efficient algorithm described in [52] is used. The last constituent of the orthonormal basis is then computed using the cross product $\vec{\boldsymbol{w}} = \vec{\boldsymbol{u}} \times \vec{\boldsymbol{v}}$.

Electromagnetic Interactions

Interactions with electrons cause charged particles to continuously lose energy while travelling through matter. The mean energy loss per unit distance due to this process is called the stopping power $\boldsymbol{S}$, which is a function of energy and dependent on the projectile's mass and charge [53, 54]. FLUKA was used to tabulate the energy loss of the transported particles in water from 0.1 MeV/ u to 1,000 MeV/ u with 2000 linearly spaced intervals. To obtain the stopping power in materials other than water, the stopping power table for water was multiplied by a factor dependent on the materials HU value [45]. Since the step size $\boldsymbol{dx}$ is fixed at the beginning of each transport step, the mean energy loss $\overline{\boldsymbol{dE}}$ that the particle experiences during the step must be calculated. This problem is equivalent to solving the following equation:

$$\boldsymbol{E}(\boldsymbol{dx}) = \boldsymbol{E}_0 - \int_0^{\boldsymbol{dx}} \boldsymbol{S}(\boldsymbol{E}(\boldsymbol{y}))\boldsymbol{dy} \tag{5}$$

where $\boldsymbol{E}(\boldsymbol{x})$ is the particles energy after having travelled a distance $\boldsymbol{x}$ and $\boldsymbol{E}_0$ is the particle's energy at the beginning of the step. While this equation is in principle solvable under the assumption that $\boldsymbol{S}$ is linear along the step, a numerical approximation was used instead. This approximation is based on the following recurrence relation:

$$\overline{\mathbf{dE}_0} = \mathbf{dx} \cdot \mathbf{S}(\mathbf{E}_0) \tag{6}$$

$$\overline{\mathbf{dE}_\mathbf{n}} = \mathbf{dx} \cdot \mathbf{S}\left(\mathbf{E}_0 - \frac{\overline{\mathbf{dE}_{\mathbf{n}-1}}}{2}\right). \tag{7}$$

This recurrence relation is evaluated up to a depth of n = 3 to arrive at an accurate estimate of $\overline{\boldsymbol{dE}}$.

Scattering is a statistical process, so the stopping power only describes the mean energy loss per unit distance traveled. Theoretical treatments of this process have for example been done in [55, 56]. The distributions derived therein are complex and their sampling costly. But in the limit were **dx** is

large, the energy loss is approximately distributed normally around $\overline{dE}$. If dx is small on the other hand, the Gaussian approximation is inadequate and the distribution is skewed towards high energy losses [54]. Whether a Gaussian approximation is appropriate can be judged through the parameter κ given by

$$\kappa = \frac{\xi}{T_{max}}, \tag{8}$$

where ξ is given by

$$\xi = 2\pi \cdot N_a m_e r_e \rho \cdot dx \cdot \frac{q^2}{e^2}\frac{Z}{A} \cdot \frac{1}{\beta^2} \tag{9}$$

and T_{max} is given by

$$\mathrm{T_{max}} = \frac{2\mathrm{m_e}\beta^2\gamma^2}{1 + 2\gamma\frac{\mathrm{m_e}}{\mathrm{m}} + \frac{\mathrm{m_e^2}}{\mathrm{m^2}}}, \tag{10}$$

where N_a is Avogadro's number, m_e is the electron's mass, r_e is the classical electrons radius, q is the particles charge in Coulomb, Z is the target's atomic charge and A is the target's atomic number. Following [57], the energy loss distribution is approximated through a normal distribution if $\kappa \geq 10$ and a log-normal distribution if $\kappa < 10$. The normal distribution has mean $\overline{dE}$ and standard deviation σ as given for example in [53]:

$$\sigma = \sqrt{\xi \cdot T_{max}\left(1 - 0.5\beta^2\right)}. \tag{11}$$

The log-normal distribution's parameters are determined through a fit, matching the first four moments of the Vavilov distribution [57]. For very small $\kappa < 0.3$ [57], propose the use of a different distribution, but with step sizes of 1 mm it was found that adequate agreement can be achieved by sampling from a log-normal distribution even when $\kappa < 0.3$. During the simulations, care had to be taken here since occasionally, especially for very low-density materials like air, the energy loss sampled according to the log-normal approximation could become negative. In this case the approximation $dE = \overline{dE}$ was used.

Besides inelastic collisions with atomic electrons, charged particles also undergo elastic collisions with atomic nuclei. These interactions do not contribute to the particle's energy loss but deflect the particle. This too, is a statistical process. Commonly, MC simulations base their scattering model on Moliere's theoretical treatment [58]. The formula derived by Moliere is a series of functions

$$f(\vartheta) = \sum_n \frac{\vartheta f_n(\vartheta)}{B^n}, \tag{12}$$

where the reduced angle ϑ is related to the polar scattering angle θ used in **Eq. 1** *via*

$$\vartheta = \frac{\theta}{\chi_c\sqrt{B}} \tag{13}$$

and where χ_c and B are constants dependent on the target material, the incoming particle's energy and charge. These constants are defined in [58] together with an integral representation of the functions f_n. To clear up possible confusions, we note that in literature, frequently not the scattering angle ϑ is considered but instead the projected angle φ is used. This angle arises when one considers the projection of ϑ onto an axis perpendicular to the beam's direction. For a rigorous definition of ϑ and φ, we refer to [58, 59] and here we will only work with the angle ϑ.

Sampling from higher order terms of the Moliere distribution is computationally expensive, but approximations can be made. Perhaps the simplest is dropping higher order terms, i.e. terms where $n \geq 2$. Since B is a measure for the average number of single scattering events occurring along a step, when the step size dx is large the weight of the higher order terms decreases and the distribution can be approximated through a Rayleigh distribution in ϑ

$$\mathrm{f}(\vartheta) \approx \vartheta\exp\left(-\vartheta^2\right) \tag{14}$$

or a Gaussian distribution in φ

$$\mathrm{f}(\varphi) \approx \exp\left(-\varphi^2\right). \tag{15}$$

Single Gaussian approximations of the scattering angle have for example been introduced by Rossi [60] or Highland [61]. For the width σ of this Gaussian [60], provide the following empirical formula:

$$\sigma = \frac{E_s z}{\beta p}\sqrt{\frac{\rho dx}{\chi_0}}, \tag{16}$$

where z is the particle's charge in units of the elementary charge, ρ is the target's density, χ_0 is the target's radiation length and p is the particle's momentum in MeV/c. Originally, the value of E_s was given as 21 MeV but with the mixed Rayleigh-Rutherford approach that will be presented here, a value of 11.6 MeV was found to be better and was used throughout all simulations presented in ***Results***.

For small dx, the single Gaussian approximation does not adequately reproduce the large angle tails of Moliere's distribution. As a result, authors have proposed different modifications to the pure Gaussian probability distribution such as double or triple Gaussian parametrizations [62, 63] or parametrizations that use a Rutherford distribution to model the tail [31, 53, 64–66]. Generally, even when using fits of Gaussian mixture models, the large-angle tails of the Moliere distribution are not reproduced adequately. In this work, a parametrization similar to [64] was used, combining a Rutherford-like tail with a Rayleigh distribution at the center

$$P(\theta) = \begin{cases} \frac{\theta}{N\sigma^2}exp\left(-\frac{\theta}{2\sigma^2}\right), & \theta \leq \mathrm{k} \\ \frac{\alpha}{N\theta^3}, & \theta > \mathrm{k}. \end{cases} \tag{17}$$

For the simulations, the value $k = 3.5\sigma$ was used, the constant α was determined such that $P(\theta)$ is continuous at the boundary $\theta = \mathrm{k}$ and N was determined such that the probability density function is normalized, i.e.

$$\alpha = \frac{k^4}{\sigma^2} exp\left(-\frac{k^2}{2\sigma^2} \right) \text{and} \tag{18}$$

$$N = N_G + N_R. \tag{19}$$

Here, N_G and N_R are the integral of the Rayleigh and the Rutherford-like part respectively, given by

$$\mathrm{N_G} = 1 - \exp\left(-\frac{\mathrm{k}^2}{2\sigma^2} \right) \text{and} \tag{20}$$

$$\mathrm{N_R} = \frac{\mathrm{k}^2}{2\sigma^2} \exp\left(-\frac{\mathrm{k}^2}{2\sigma^2} \right). \tag{21}$$

Sampling of an angle θ is then done via inverse transform sampling using only a single uniformly distributed random number **U** after

$$\theta = \begin{cases} \sigma\sqrt{-2\,log\,(1 - U \cdot N)}, & U \le N_G \\ \dfrac{1}{\sqrt{\dfrac{1}{k^2} - \dfrac{2}{\alpha}\,(U \cdot N - N_G)}}, & U > N_G \cdot \end{cases} \tag{22}$$

Nuclear Interactions

Elastic Nuclear Interactions

The kinematics involved in elastic nuclear interactions are implemented fully relativistically. The total elastic cross section σ_{el} is calculated starting from the work of [67] and was tabulated in 500 evenly spaced bins ranging from 0.1 to 500.1 MeV for all 10 nuclei listed in ***Geometry and Materials***. The scattering angle in the center of mass frame is sampled according to a parametrization proposed in [68]. First, the momentum transfer t is sampled after

$$P(t) = A^{1.63}\, exp\left(14.5A^{0.66}t\right) + 1.4A^{0.33}\, exp\,(10t), \tag{23}$$

where, A is the target nucleus atomic number. Then, the center of mass scattering angle is calculated via

$$\cos\left(\theta_{\mathrm{CM}}\right) = 1 - \frac{\mathrm{t}}{2\mathrm{p_{CM}}}. \tag{24}$$

With p_{CM} being the center of mass momentum. From θ_{CM}, the laboratory frame polar scattering angles are computed and, together with a uniformly distributed azimuthal angle, applied to the resulting scattered particles.

Inelastic Nuclear Interactions

In particle therapy, inelastic nuclear scattering events generate the mixed radiation field, i.e. photons, protons, neutrons, deuterons, tritons, ^{3}He, ^{4}He and heavier fragments (nuclear recoils). In MonteRay, similarly to other works in literature [31, 32], photons and neutrons are assumed to be dosimetrically irrelevant and they are neither transported nor produced. The total inelastic cross section σ_{ine} for protons was calculated starting from the work of [69, 70]. To model the production of secondary particles, a database of nuclear event probabilities was generated based on nuclear models used internally by FLUKA. The database covers a primary proton energy T_{in} ranging from 10 to 300 MeV, in steps of 10 MeV. Tables were generated for each of the 10 elements defined in and for each of the five possible product particles considered: protons, tritons, deuterons, 3-Helium and 4-Helium. Each table (of the $30 \cdot 10 \cdot 5 = 1500$ tables) is divided into 100 bins in the kinetic energy T_{sec} and 100 bins in the solid angle Ω_{sec} of the secondaries. The 100 energy bins divide the range **0** to T_{in} into evenly spaced intervals and the 100 angular bins evenly divide the interval **0** to $4\,\pi$. If an inelastic nuclear event occurs during simulation, all possible products for the current target nucleus are created but assigned weights corresponding to their relative multiplicity (**Figure 1A**). Secondary particle energy (**Figure 1B**) and direction are chosen via a binary search on a cumulative probability distribution, generated at the beginning of the simulation by summing up the tables values. Additionally, the mean kinetic recoil energy is stored for each table and deposited on the spot following a nuclear event.

Benchmarking of the Developed Dose Engine

To benchmark MonteRay, its predictions were compared against experimental data acquired at HIT over the last years, published in [71, 72]. For scenarios where experimental data was not available, e.g. in presence of magnetic fields and for patient calculations, FLUKA predictions were used as a reference.

Comparison Metrics

To judge MonteRay's agreement with measurements or against other TPS, several common radiotherapy metrics were used. The relative error

$$\varepsilon_{\mathrm{rel}} = 200\,\frac{\mathrm{d_1} - \mathrm{d_2}}{(\mathrm{d_1} + \mathrm{d_2})}\,[\%] \tag{25}$$

was used to quantify the relative disagreement between two dose profiles, d_1 and d_2. Measured and calculated beam ranges were compared in terms of their R_{80} value which is defined as the depth distal to the Bragg peak (BP) where the dose falls to 80% of the BP value. The difference in range for two dose distributions was quantified through $\Delta R_{80} = |R^1_{80} - R^2_{80}|$. Agreement between lateral profiles was judged using the full width at half maximum (FWHM) value and the full width at 10% of the maximum (FW10%M) value. For the comparison of 3D dose distributions, the 3D local gamma pass rate was calculated. For this the python package pymedphys version 0.37.1 was used. For the calculation, similar to previous proton MC engines [28, 31, 73, 74], the dose percentage threshold was set to 2%, the distance threshold to 2 mm and the dose cutoff to 5% of the maximum dose. During the calculation of the gamma pass rate, dose outside the patient was not considered as it is clinically irrelevant. Another metric used to evaluate patient plans is the D_x value. For a given region of interest (ROI), it is defined as the minimum dose that x percent of the ROIs volume is exposed to.

To judge the deflection of a single beam in a magnetic field, we introduce the center of mass (COM) of the beam. Given a lateral profile scored in N bins at locations x_i with corresponding scored doses $d(x_i)$, we define it as

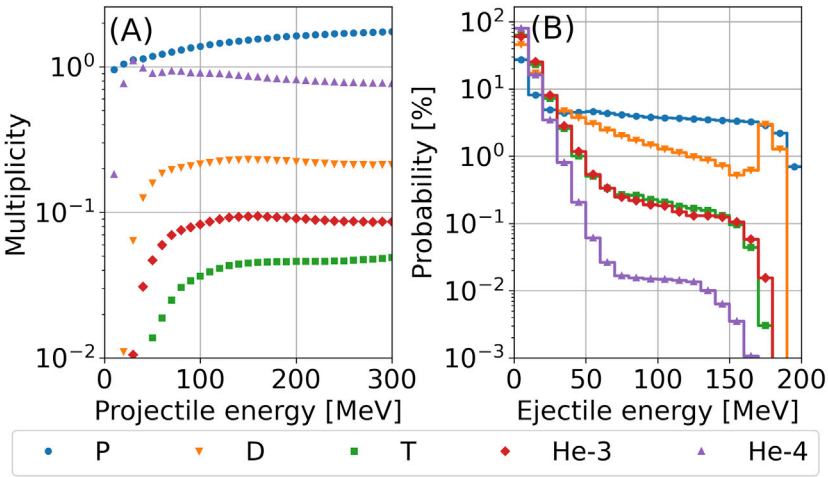

FIGURE 1 | (A) Average number of particles produced per p + ^{16}O collision as a function of the energy of the incoming proton. **(B)** For 200 MeV p + ^{16}O collisions, the angularly integrated probability (in %) of a secondary particle being produced in a certain energy bin (bin size: 10 MeV) is shown. Abbreviations stand for Protons (P), Deuterons (D), Tritons (T), Helium-3 (^{3}He) and Helium-4 (^{4}He).

$$COM = \frac{1}{N}\sum \boldsymbol{x_i} \cdot \boldsymbol{d}(\boldsymbol{x_i}). \tag{26}$$

Dosimetric Data

Various experimental data that was previously recorded at HIT was used to evaluate MonteRay's performance in terms of dosimetric accuracy. This data, included pencil-beam depth-dose distributions [71], lateral profiles of vertically scanned line profiles [75] and Spread-Out Bragg Peak (SOBP) plans [72]. Details on the measurement procedures were given in the mentioned references so only a quick overview will be given here.

Pencil beam depth-dose distributions in water were recorded using a PeakFinder water column (PTW, Freiburg) with a diameter of 8.16 cm. In total, 17 Bragg curves with beam energies spanning the entire energy range available at HIT (from 48.5 to 222.6 MeV) have been measured. The measurements took place in a clinical room at HIT. The resolution was 0.05 mm in the region of the BP.

Measurements of lateral profiles of vertically scanned irradiation lines in a water phantom were obtained at three energies (81.5, 158.5 and 222.6 MeV) using an array of 24 motorized pinpoint chambers (PTW, 0.03 cm^3) arranged in a block of six rows and four columns. The profiles were recorded perpendicularly to the direction of the vertically scanned line. Each scanned line consisted of 101 pencil beams ranging from -50 mm to +50 mm with a 1 mm spacing. The horizontal profiles were recorded starting from about 16 mm in water to 30 mm after the BP. For each energy, profiles at 42 depths were recorded. The distance between consecutive profiles was between 0.5 and 10 mm.

Three SOBP plans centered around 5 cm, 12.5 and 20 cm in water were created using a FLUKA-based treatment planning tool. The planned dose was 1 Gy within the 3 × 3 × 3 cm target region. Delivery of the plans happened in the experimental room at HIT with measurements being done with the same block of pinpoint ionization chambers used for acquiring the lateral profiles described earlier. The profiles were recorded starting at a depth of 16 mm to approximately 20 mm after the end of the SOBP. The step size between measurements in regions of high gradient and in regions of high dose was 1 mm.

FLUKA Calculations

Due to the lack of dosimetric data in magnetic fields, the transport in magnetic fields was benchmarked by comparing MonteRay against FLUKA. For this the effect of homogenous magnetic fields, applied perpendicular to the beam's direction, was studied for field strengths of 0.5, 1.0 and 2 T. In FLUKA, magnetic fields were enabled using the MGNFIELD card with default settings. The DEFAULTS card with value PRECISIO was enabled during FLUKA simulations to ensure high precision simulations.

Patient Planning

Patient planning was performed in the clinical TPS RayStation 10 A (RaySearch Laboraries, Stockholm, Sweden) on an anonymized DICOM patient data set representative of a meningioma treatment. A proton treatment plan using a single beam at 90° was optimized for evaluation of dose calculation accuracies in a patient anatomy. The initial spot positioning (hexagonal grid with spot spacing of 3.6 mm, energy spacing of 2.1 mm) and minimum number of particles (580.000 particles) settings follow clinical practice at HIT. Optimization was made on the planning target volume (PTV, ~112 cm^3) for 49.1 Gy/ 54 GyRBE in 30 fractions using a constant radiobiological effectiveness of 1.1. The resultant energy range spanned from ~78 to 151 MeV. The dose grid was set to 2 × 2 × 2 mm^3 in RayStation with a dose uncertainty of 0.5%. The treatment plan was exported in FLUKA and MonteRay for forward calculation with and without a magnetic field. The statistical uncertainty of the MonteRay and FLUKA runs was 1%. The dose uncertainty was estimated using the batch method. Dose cubes stemming

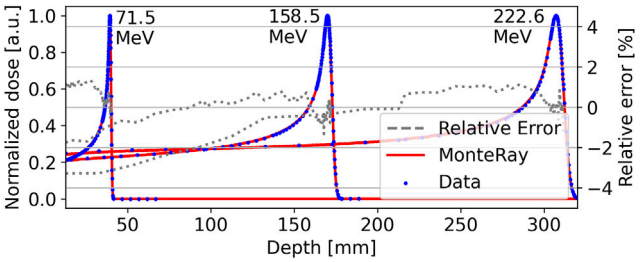

FIGURE 2 | Integrated depth-dose profiles of quasi-monoenergetic beams with energies of 71 MeV, 158.5, and 222.6 MeV are shown. Peakfinder measurements are indicated by blue points and MonteRay simulations as solid red lines. The relative error, after correcting for a lateral shift, between measurements and MonteRay simulations is shown with grey dotted lines after correcting for the lateral shift.

from FLUKA MC and MonteRay were ultimately imported in RayStation for dosimetric analysis (DVH and line profile evaluation). All doses were computed as dose-to-water and dose comparisons were made in Gy.

RESULTS

Pristine Bragg Peaks in Water

To evaluate the accuracy of MonteRay, we first compare the simulated dose in water $\boldsymbol{d_{MR}}$ to the dose measured at HIT $\boldsymbol{d_{HIT}}$ for 17 quasi-monoenergetic beams. The beam energies ranged from 71.5 to 222.6 MeV. **Figure 2** shows a comparison of the dose obtained with MonteRay with measured values for three exemplary energies of 71.5, 158.5 and 222.6 MeV. Due to the high resolution of the measured data (up to 0.05 mm in the BP region), the transport was performed on a Cartesian grid with $0.1 \times 0.1 \times 0.1\ \text{mm}^3$ resolution. Scoring likewise was done in 0.1 mm thick slices. To match the physical dimension of the detector, scoring was performed in a cylindrical volume with a radius of 4.08 cm. Both measurements and simulations were normalized to one at the BP. Across all the energies, the maximum, minimum and mean $\boldsymbol{\Delta R_{80}}$ values were 0.16, 0.06 and 0.10 mm, respectively. Once the MC calculations were shifted by $\Delta \boldsymbol{R_{80}}$, $\boldsymbol{d_{MC}}$ and $\boldsymbol{d_{HIT}}$ were quantitively compared using the relative error $\boldsymbol{\varepsilon_{rel}}$. The dose threshold for calculating $\boldsymbol{\varepsilon_{rel}}$ was set to 20% of maximum. The mean absolute $\boldsymbol{\varepsilon_{rel}}$ over all the investigated energies was 0.56 %.

For the verification of the lateral parametrization in water, measurements of vertically scanned proton beam lines, as described in ***Dosimetric Data***, were compared against MonteRay simulations. Lateral relative dose profiles at three energies, 81.5, 158.5 and 222.6 MeV, and at 40 different depths were compared. In **Figure 3** and for each energy, lateral profiles at three depths are visualized: at the entrance (top row), in the BP region (bottom row) and in the middle of these two (middle row). The depths are reported in each panel of **Figure 3**. The corresponding energy is given at the top of each column. After correcting for the error in FWHM already present at the entrance due to daily variations in the beam's shape, on average, the simulated FWHM matched the experimental data's FWHM within 0.1, 0.3 and 0.5 mm for the three energies, respectively. Likewise, the FW10%M values matched to within 0.1, 0.3 and 0.9 mm.

Spread Out Bragg Peaks in Water

Next, MonteRay's simulated dose was compared with dosimetric data from SOBP plans. The measurement process was described in ***Dosimetric Data***. The resulting depth-dose distributions are displayed in **Figure 4**, together with the measured values. The mean absolute relative error between measurements and predictions (excluding data in regions of high dose gradients, as performed in clinical routine) was (0.69%, 0.74%, 1.0%) with a standard deviation of (0.7%, 0.6%, 1.0%). The $\Delta \boldsymbol{R_{80}}$ values were 0.5, 0.3 and 0.3 mm, respectively. In the lower panels of **Figure 4**, lateral profiles at the entrance and at in the middle of the SOBP are shown. Here, the simulated SOBP widths matched the experimental ones on to within about 1 mm.

Magnetic Field Deflection in Homogenous Fields

To judge the accuracy of MonteRay when dealing with homogenous magnetic fields, MonteRay's simulations were first compared to FLUKA's for monoenergetic proton beams incident on water. The magnetic field was applied perpendicular to the beam's direction and four field strengths of 0 T, 0.5 T, 1 T and 2 T were compared. Planar profiles were scored with a resolution of $1 \times 1 \times 1\ \text{mm}^3$ but were afterwards integrated along 1 cm in the direction of the magnetic field axis to provide higher statistics. In **Figures 5A,B**, 2D dose distributions, perpendicular to the magnetic field, are shown for the case where the magnetic field strength was 2 T. In panel **(A)**, MonteRay's results are shown while FLUKA's results are displayed in panel **(B)**. For all tested field strengths, the gamma passing rate (as defined in ***Comparison Metrics***) was above 99.8%

In **Figure 5C**, lateral profiles at the BP position for the four field strengths are shown. From lateral profiles, COM, FWHM and FW%10M were computed at each depth up to the BP. The maximum differences in COMs (ΔCOM), FWHM (ΔFW_{50}) and FW10%M (ΔFW_{10}) between MonteRay and FLUKA are summarized in **Table 1**. For all tested field strengths and at all depths, the maximum distances between the COMs stayed below 0.15 mm, the maximum disagreements in the FWHM reached 0.21 mm while the maximum disagreements in the FW10%M reached 0.31 mm. Comparing integrated depth-dose profiles, the R_{80} values between MonteRay and FLUKA were found to agree to within 0.14, 0.18, 0.10 and 0.07 mm. The maximum relative errors in dose, after correcting for these shifts, was 1.2%.

Patient Case

In **Figure 6** panels **(A)** and **(B)**, the doses for a patient plan, calculated with FLUKA and MonteRay are shown in the axial plane. The gamma passing rate between MonteRay and FLUKA was computed to be 99.8%. In panel **(C)**, longitudinal profiles and in panel **(D)**, lateral profiles are shown. The profiles are shown for

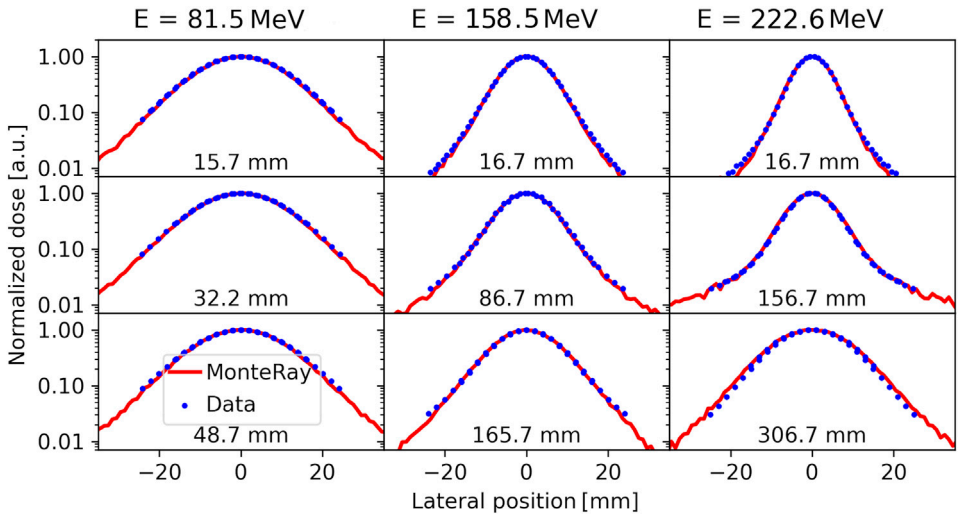

FIGURE 3 | Lateral dose profiles of vertically scanned proton lines at 81.5 MeV **(left column)**, 158.5 MeV (central column) and 222.6 MeV **(right column)** at different depths as reported in the panels. Measurements (blue points) are compared against MonteRay simulations (red lines).

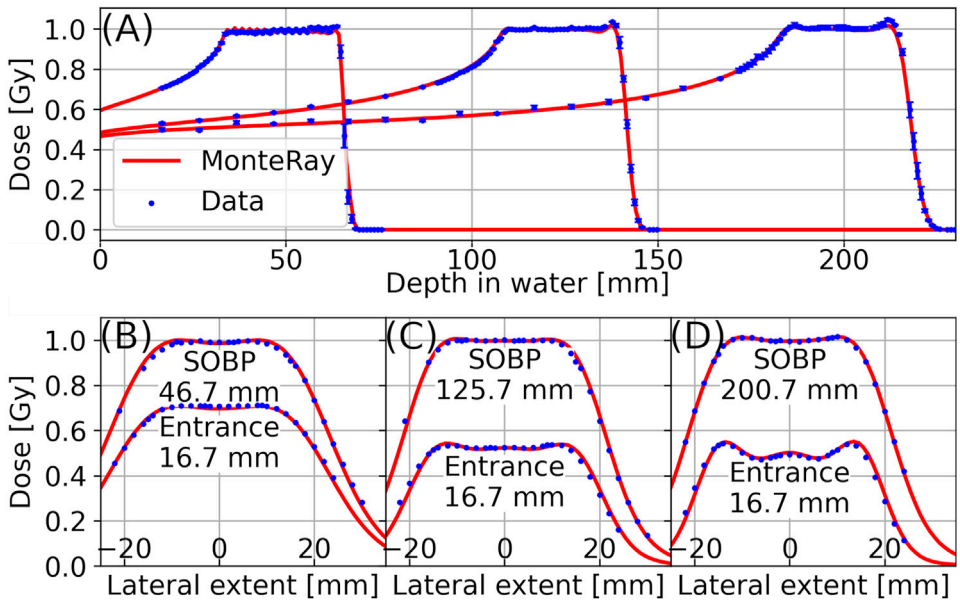

FIGURE 4 | In panel **(A)**, Longitudinal dose distributions of three proton SOBP plans in water with plateau depths of approximately 5 cm, 12.5, and 20 cm are shown. In panels **(B)**, **(C)**, and **(D)**, lateral profiles corresponding to the three SOBP plans are displayed. For each SOBP, one lateral profile at the entrance and one lateral profile in the middle of the SOBP is shown. Measurements (points) are compared against MonteRay's simulated values (lines).

simulated doses obtained from RayStation, FLUKA and MonteRay, and their locations are indicated in panel **(A)** through red horizontal (longitudinal) and vertical (lateral) lines. For RayStation, FLUKA and MonteRay, the lateral profile's FWHMs were 67.6, 68.1, and 68.3 mm. The widths at 10% of the maximum were 85.3, 86.1, and 85.9 mm. The differences in range between MonteRay/FLUKA and RayStation/FLUKA were calculated from the longitudinal profiles and found to be 0.4 and 0.6 mm, respectively. Both in terms of lateral and longitudinal profiles, MonteRay agrees well with FLUKA.

In **Figure 7A**, DVHs calculated for several regions of interest (ROI) are displayed: the CTV, the brain, the brainstem and the right optical nerve. The $\boldsymbol{D}_2$, $\boldsymbol{D}_{50}$ and $\boldsymbol{D}_{98}$ values were computed for the CTV and $\boldsymbol{D}_2$ values were computed for the organs at risk (OAR). To judge the quality of MonteRay, the relative difference in $\boldsymbol{D}_x$ values between MonteRay and FLUKA is compared to those between RayStation and FLUKA. Overall, the agreement

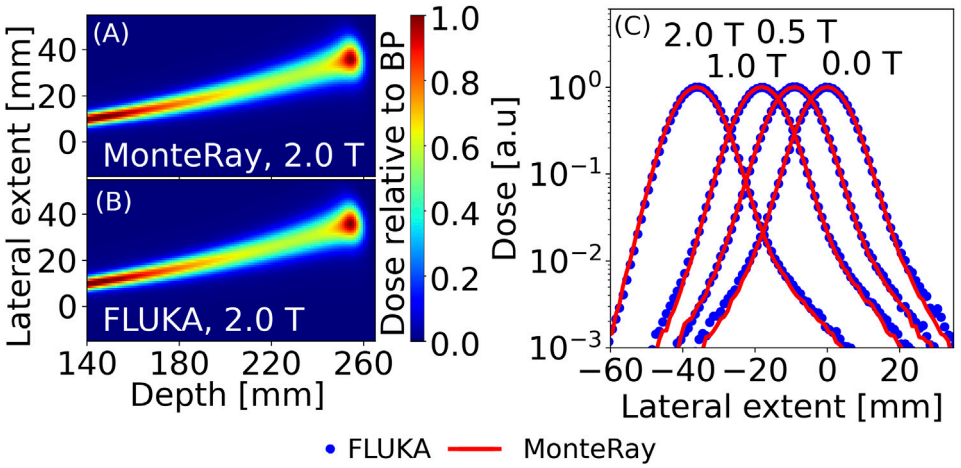

FIGURE 5 | For 200 MeV protons in water, 2D dose distributions calculated with MonteRay **(A)** and FLUKA **(B)** are shown in a plane perpendicular to the 2 T magnetic field. In **(C)**, Lateral profiles for 200 MeV protons in water and with magnetic field strengths of 0 T, 0.5 T, 1 T, and 2 T are displayed at the location of the BP. MonteRay's results are indicated by a red line while FLUKA's results are displayed as blue dots.

TABLE 1 | Comparison of MonteRay against Fluka for a 200 MeV proton beam incident on water with different homogenous magnetic fields applied perpendicular to the beam. The maximum differences in the COM (ΔCOM), FWHM (ΔFW_{50}) and FW10%M (ΔFW_{10}) across all depths up to the BP are reported.

Field strength [T]	ΔCOM [mm]	ΔFW_{50} [mm]	ΔFW_{10} [mm]
0	0.018	0.17	0.24
0.5	0.043	0.21	0.30
1.0	0.072	0.19	0.23
2.0	0.14	0.21	0.31

between MonteRay and FLUKA was of the same magnitude as the agreement between RayStation and FLUKA. For the CTV, good agreement in the D_2 value of 0.25%, the D_{50} value of 0.38% and the D_{98} value to within 0.58% was found. For the considered OARs the computed D_2 values matched within 0.50% for the brain, within 0.44% for the brainstem and to within 0.49% for the right optical nerve.

Patient Case With a Magnetic Field

To benchmark our magnetic field implementation, the previous patient plan was reused but for the dose calculation in MonteRay and FLUKA, a homogenous magnetic field of 1 T was applied throughout the CT volume. In **Figure 8**, the calculated doses in FLUKA (Panel **(A)**) and MonteRay (Panel **(B)**) are displayed. With the magnetic field enabled, the gamma passing rate between MonteRay and FLUKA was found to be 98.8%.

In panel **(C)**, longitudinal profiles and in panel **(D)**, lateral profiles are shown, and their locations are indicated in panel **(A)** through horizonal (longitudinal) and vertical (lateral) lines. Profiles are shown for simulated doses obtained with MonteRay and FLUKA. Additionally, in panel **(D)**, the lateral profile obtain d from RayStation without an applied magnetic field is shown. The deflection observed at the lateral profile's position was ~5 mm. Computed for FLUKA and MonteRay, the lateral profile's FWHMs were 67.4 mm, 67.5 mm. The widths at 10% of the maximum were 86.0 and 85.0 mm. The difference in range between MonteRay and FLUKA, calculated from the longitudinal profiles, was found to be 0.4 mm.

In **Figure 7B**, DVHs calculated on the same ROIs as in the previous section are shown. D_x values were computed for FLUKA and MonteRay. For the CTV we found agreement in the D_2 value of 2%, in the D_{50} value of 0.53% and in the D_{98} value of 1.2%. For the OARs, the computed D_2 values matched within 0.76% for the brain, within 2.1% for the brainstem and within 2.3% for the right optical nerve.

Runtime Benchmarks

The performance of MonteRay was evaluated for various test cases. All tests were performed on a six-core AMD Ryzen 5,3600 processor. The transport grid's resolution was set to $2 \times 2 \times 2$ mm^3. This resolution is used clinically at HIT and other fast MC codes have used this resolution for benchmarking [31]. For 150 MeV monoenergetic Protons in water with a FWHM of 1 cm, a throughput of 31 k primaries per second on a single core and 180 k primaries per second when using all six cores of the CPU, was measured. Under parallel load, the throughput therefore was 30 k primaries per second per core. In comparison, the computational throughput of FLUKA on the same problem on the same hardware was 1.1 k primaries per second.

For the patient plan, benchmarks were run on a $2 \times 2 \times 2$ mm^3 grid with 5,000 particles per pencil beam per core. In total, the plan consisted of 8313 pencil beams. On a single core, a throughput of 33 k particles per second was observed while the throughput on six core was measured to be 193 k primaries per second which corresponds to 32 k primaries per seconds per core.

DISCUSSION

The comparison of MonteRay predictions against dosimetric data and FLUKA simulations confirms that the implemented

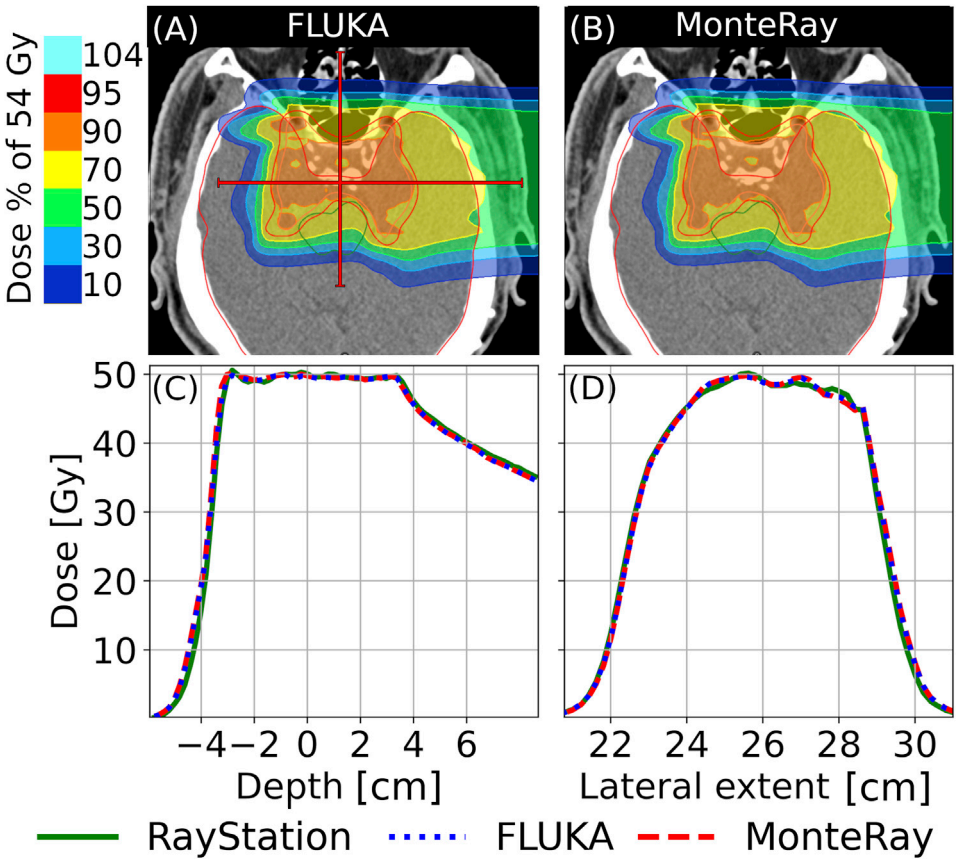

FIGURE 6 | Axial views of calculated doses for the plan described in Section 2.2.4 are shown for **(A)** FLUKA and **(B)** MonteRay. In panels **(C)** and **(D)**, longitudinal and lateral profiles are shown, respectively. The locations of the profiles relative to the 2D plots are indicated trough red lines in panel **(A)**. RayStation profiles are indicated by a solid green line, FLUKA profiles by a dotted blue line and MonteRay profiles by a dashed red line.

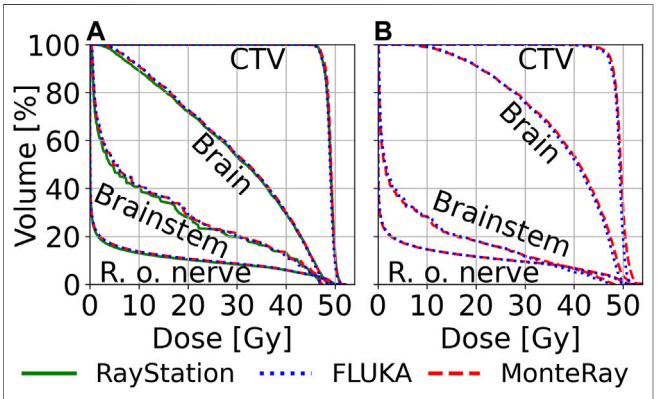

FIGURE 7 | Computed DVHs for the CTV, the brain, the brainstem and the right optical nerve (r. o. nerve) are shown. DVHs were computed for RayStation (green, solid line), FLUKA (blue, dotted line) and MonteRay (red, dashed line). In panel **(A)**, DVHs for the patient case without a magnetic field are shown while in panel **(B)** DVHs calculated for the case with an applied magnetic field are shown.

electromagnetic and nuclear models correctly reproduce the underlying physics. In terms of depth-dose distributions for pencil beams in water (***Pristine Bragg Peaks in Water***), the mean absolute relative error over all 17 compared energies was 0.56%, ranging from 0.33 to 0.60% for 102.6 and 222.6 MeV protons, respectively. The depth-dependent maximum absolute relative error varied from 0.95% (48.5 MeV) to 3.4% (222.6 MeV). The latter is located at the entrance channel of the highest energy (222.6 MeV) which is typically not used for clinical purpose. This underestimation could in part be explained through the fact that the current approach for sampling the initial particles neglects secondary d, t, ^{3}He and ^{4}He particles produced in the beamline. Our predictions are in line with other fast MC engines available in literature, for example [73], using FRED have found relative differences of up to about 3% for 200 MeV protons in water.

In terms of lateral evolution as function of depth, MonteRay matched satisfactorily the experimental data in terms of FWHM/FW10%M within on average 0.1, 0.3, and 0.9 mm for low, medium and high energies. The largest difference has been found in the Bragg peak region for 222.6 MeV protons with a maximum variation of the FW10%M of 2 mm. To evaluate possible shortcomings in the scattering model, we have compared FLUKA and MonteRay predictions for 200 MeV proton beams in water without the HIT beamline. The maximum FWHM(FW10%M) variation found was

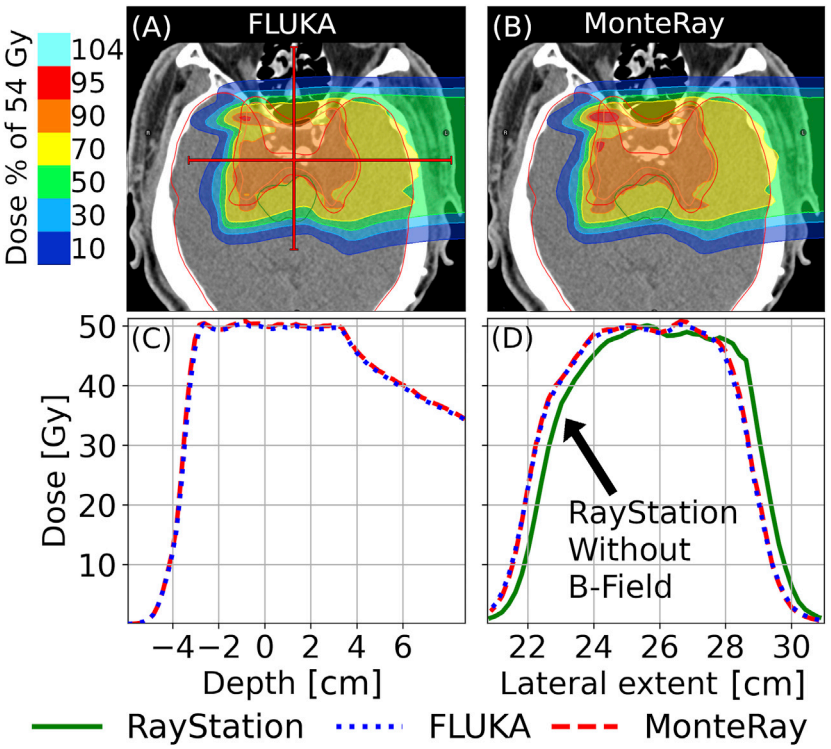

FIGURE 8 | Axial views of calculated doses for the plan described in Section 2.2.4 with an added perpendicular magnetic field of 1 T are shown for **(A)** FLUKA and **(B)** MonteRay. In panels **(C)** and **(D)**, longitudinal and lateral profiles are shown, respectively. Besides the lateral profiles obtained from FLUKA and MonteRay, we also show the lateral profile of the RayStation dose calculated without a magnetic field. The locations of the profiles relative to the 2D plots are indicated trough red lines in panel **(A)**. RayStation profiles are indicated by a solid green line, FLUKA profiles by a dotted blue line and MonteRay profiles by a dashed red line.

0.17 mm (0.24 mm) and the 3D gamma pass rate was 99.8% confirming the quality of the implemented model.

Prediction of SOBPs centered at different depths confirmed MonteRay's beam-model with an average agreement of 1% when compared against experimental data, well fulfilling clinical criteria. MonteRay's results have been found to be in line with FLUKA results for the same set of experimental SOBP data [71], with average FLUKA dose deviations of 0.9%.

Evaluation of MonteRay on a patient plan showed good agreement against simulations performed with FLUKA. In terms of D2, D50, and D98 we achieved similar agreement to FLUKA as RayStation did. The 3D gamma pass rate was calculated to be 99.8% showing that the implemented models and approximations for electromagnetic and nuclear interactions approximate the underlying physics well, also in a clinical setting. Computed 3D gamma pass rates were in line with those obtained by other fast MC engines [28, 33, 73].

Similarly, we evaluated the quality of our simulation when an additional magnetic field was applied to an irradiation plan. Compared to FLUKA, we found adequate agreement in terms of D2, D50, and D98 between 0.5 and 2.3%. The 3D gamma pass rate was 98.9%, showing that a simple approximation of the Lorentz force is adequate at describing the transport of charged particles in homogenous magnetic fields.

In terms of computational throughput, MonteRay was able to simulate 31 k primaries per second for a 150 MeV proton beam incident on water, transported on a $2 \times 2 \times 2$ mm^3 grid. Parallel execution on six cores was found to scale linearly, achieving a throughput of 180 k primaries per second. When benchmarked on a patient plan containing ~8300 pencil beams with energies ranging from ~78 to ~150 MeV, we measured a throughput of 33 k particles per seconds on a single core and 193 k particles on six cores. Again, linear scaling was observed which demonstrates that reading the phase space from disk is not a bottleneck, even when multiple cores are competing for random read access.

CONCLUSION AND OUTLOOK

In this work we have presented a novel MC engine, specialized for proton therapy calculations, currently under development at HIT. Good agreement with measured data and a full-fledged MC engine (FLUKA) has been found. MonteRay achieved fast tracking rates of more than 30 k proton primaries per second at 150 MeV on a $2 \times 2 \times 2$ mm^3 grid. In a next step, work will begin on porting our fast CPU engine onto GPUs. Following a heterogenous approach, i.e. using both CPUs and GPUs, we hope to achieve sub-minute runtimes even for large irradiation plans.

A custom Monte Carlo engine will also allow us to easily implement custom features such as computing the linear energy transfer or to add imaging capabilities by producing positrons or prompt gammas.

With helium beam treatment commencing at HIT, inclusion of helium beams in MonteRay is underway with inelastic nuclear databases having already been generated.

With the aim of MR guided ion therapy, we are the first fast MC engine to include magnetic field support. In the future we will expand our evaluation to inhomogeneous fields with a focus on simulating MRIs which are being installed at HIT for the purpose of MR guided ion therapy.

DATA AVAILABILITY STATEMENT

The raw data supporting the conclusions of this article will be made available by the authors, without undue reservation.

AUTHOR CONTRIBUTIONS

AM, AF, and PL were responsible for the conceptual design of the Monte Carlo engine. PL, BK, and AM developed the source code of the Monte Carlo engine. AM generated the materials database, including elastic and inelastic nuclear cross sections. AF developed the code for the generation of inelastic nuclear databases from FLUKA. JB generated the inelastic nuclear databases. PL, TT, and AM worked on the analysis of data. TT, AM, and SM collected and provided experimental data used in this work. TT computed and provided the patient plan and SOBP plans. JD and TH provided clinical direction during project development, manuscript writing and project administration and funding acquisition. All authors read and contributed to the preparation of the manuscript.

FUNDING

The authors acknowledge financial support through the German Federal Ministry of Education and Research (BMBF) within the project (Grant number: 13GW0436A).

ACKNOWLEDGMENTS

The authors would like to acknowledge Eric Heim's work on the initial setup of the C++ code base and unit testing framework. The authors would like to acknowledge Ahmad Neishabouri for his help with performing Fluka calculations and Eric Heim for his work on the initial setup of the C++ code base and the unit testing framework.

REFERENCES

1. Chandarana H, Wang H, Tijssen RHN, and Das IJ Emerging Role of MRI in Radiation Therapy. *J Magn Reson Imaging* (2018) 48:1468–78. doi:10.1002/jmri.26271
2. Pollard JM, Wen Z, Sadagopan R, Wang J, and Ibbott GS The Future of Image-Guided Radiotherapy Will Be MR Guided. *Bjr* (2017) 90:20160667. doi:10.1259/bjr.20160667
3. Mutic S, and Dempsey JF The ViewRay System: Magnetic Resonance-Guided and Controlled Radiotherapy. *Semin Radiat Oncol* (2014) 24:196–9. doi:10.1016/j.semradonc.2014.02.008
4. Liney GP, Whelan B, Oborn B, Barton M, and Keall P MRI-linear Accelerator Radiotherapy Systems. *Clin Oncol* (2018) 30:686–91. doi:10.1016/j.clon.2018.08.003
5. Acharya S, Fischer-Valuck BW, Kashani R, Parikh P, Yang D, Zhao T, et al. Online Magnetic Resonance Image Guided Adaptive Radiation Therapy: First Clinical Applications. *Int J Radiat Oncology*Biology*Physics* (2016) 94:394–403. doi:10.1016/j.ijrobp.2015.10.015
6. Durante M, and Loeffler JS Charged Particles in Radiation Oncology. *Nat Rev Clin Oncol* (2010) 7:37–43. doi:10.1038/nrclinonc.2009.183
7. Durante M, Orecchia R, and Loeffler JS Charged-particle Therapy in Cancer: Clinical Uses and Future Perspectives. *Nat Rev Clin Oncol* (2017) 14:483–95. doi:10.1038/nrclinonc.2017.30
8. Hoffmann A, Oborn B, Moteabbed M, Yan S, Bortfeld T, Knopf A, et al. MR-guided Proton Therapy: a Review and a Preview. *Radiat Oncol* (2020) 15:129. doi:10.1186/s13014-020-01571-x
9. Haberer T, Debus J, Eickhoff H, Jäkel O, Schulz-Ertner D, and Weber U The heidelberg Ion Therapy center. *Radiother Oncol* (2004) 73:S186–S190. doi:10.1016/s0167-8140(04)80046-x
10. Rankine LJ, Mein S, Cai B, Curcuru A, Juang T, Miles D, et al. Three-Dimensional Dosimetric Validation of a Magnetic Resonance Guided Intensity Modulated Radiation Therapy System. *Int J Radiat Oncol Biol Phys* (2017) 97:1095–104. doi:10.1016/j.ijrobp.2017.01.223
11. Klüter S Technical Design and Concept of a 0.35 T MR-Linac. *Clin Translational Radiat Oncol* (2019) 18:98–101. doi:10.1016/j.ctro.2019.04.007
12. Chamberlain M, Krayenbuehl J, van Timmeren JE, Wilke L, Andratschke N, Garcia Schüler H, et al. Head and Neck Radiotherapy on the MR Linac: a Multicenter Planning challenge Amongst MRIdian Platform Users. *Strahlenther Onkol* (2021) 1–11. doi:10.1007/s00066-021-01771-8
13. Raaijmakers AJE, Raaymakers BW, and Lagendijk JJW Magnetic-field-induced Dose Effects in MR-Guided Radiotherapy Systems: Dependence on the Magnetic Field Strength. *Phys Med Biol* (2008) 53:909–23. doi:10.1088/0031-9155/53/4/006
14. Wolf R, and Bortfeld T An Analytical Solution to Proton Bragg Peak Deflection in a Magnetic Field. *Phys Med Biol* (2012) 57:N329–N337. doi:10.1088/0031-9155/57/17/N329
15. Moteabbed M, Schuemann J, and Paganetti H Dosimetric Feasibility of Real-Time MRI-Guided Proton Therapy. *Med Phys* (2014) 41:111713. doi:10.1118/1.4897570
16. Ferrari A, Sala PR, Fasso A, and Ranft J *FLUKA: A Multi-Particle Transport Code*. Stanford: Stanford linear accelerator center (2005). doi:10.2172/877507
17. Böhlen TT, Cerutti F, Chin MPW, Fassò A, Ferrari A, Ortega PG, et al. The FLUKA Code: Developments and Challenges for High Energy and Medical Applications. *Nucl Data Sheets* (2014) 120:211–4. doi:10.1016/j.nds.2014.07.049
18. Bauer J, Sommerer F, Mairani A, Unholtz D, Farook R, Handrack J, et al. Integration and Evaluation of Automated Monte Carlo Simulations in the Clinical Practice of Scanned Proton and Carbon Ion Beam Therapy. *Phys Med Biol* (2014) 59:4635–59. doi:10.1088/0031-9155/59/16/4635
19. Mein S, Choi K, Kopp B, Tessonnier T, Bauer J, Ferrari A, et al. Fast Robust Dose Calculation on GPU for High-Precision 1H, 4He, 12C and 16O Ion Therapy: the FRoG Platform. *Sci Rep* (2018) 8:14829. doi:10.1038/s41598-018-33194-4
20. Mein S, Kopp B, Tessonnier T, Ackermann B, Ecker S, Bauer J, et al. Dosimetric Validation of Monte Carlo and Analytical Dose Engines with Raster-Scanning 1H, 4He, 12C, and 16O Ion-Beams Using an Anthropomorphic Phantom. *Physica Med* (2019) 64:123–31. doi:10.1016/j.ejmp.2019.07.001
21. Choi K, Mein S, Kopp B, Magro G, Molinelli S, Ciocca M, et al. FRoG-A New Calculation Engine for Clinical Investigations with Proton and Carbon Ion Beams at CNAO. *Cancers* (2018) 10:395. doi:10.3390/cancers10110395

22. Kopp B, Fuglsang Jensen M, Mein S, Hoffmann L, Nyström H, Falk M, et al. FRoG: An Independent Dose and LET D Prediction Tool for Proton Therapy at ProBeam Facilities. *Med Phys* (2020) 47:5274–86. doi:10.1002/mp.14417
23. Magro G, Mein S, Kopp B, Mastella E, Pella A, Ciocca M, et al. FRoG Dose Computation Meets Monte Carlo Accuracy for Proton Therapy Dose Calculation in Lung. *Physica Med* (2021) 86:66–74. doi:10.1016/j.ejmp.2021.05.021
24. Fuchs H, Moser P, Gröschl M, and Georg D Magnetic Field Effects on Particle Beams and Their Implications for Dose Calculation in MR-Guided Particle Therapy. *Med Phys* (2017) 44:1149–56. doi:10.1002/mp.12105
25. Parodi K Vision 20/20: Positron Emission Tomography in Radiation Therapy Planning, Delivery, and Monitoring. *Med Phys* (2015) 42:7153–68. doi:10.1118/1.4935869
26. Parodi K, Paganetti H, Shih HA, Michaud S, Loeffler JS, DeLaney TF, et al. Patient Study of *In Vivo* Verification of Beam Delivery and Range, Using Positron Emission Tomography and Computed Tomography Imaging after Proton Therapy. *Int J Radiat Oncol Biol Phys* (2007) 68:920–34. doi:10.1016/j.ijrobp.2007.01.063
27. Parodi K, and Polf JC *In Vivo* range Verification in Particle Therapy. *Med Phys* (2018) 45:e1036–e1050. doi:10.1002/mp.12960
28. Jia X, Schümann J, Paganetti H, and Jiang SB GPU-based Fast Monte Carlo Dose Calculation for Proton Therapy. *Phys Med Biol* (2012) 57:7783–97. doi:10.1088/0031-9155/57/23/7783
29. Jia X, Pawlicki T, Murphy KT, and Mundt AJ Proton Therapy Dose Calculations on GPU: Advances and Challenges. *Translational Cancer Res* (2012) 1:207–16. doi:10.3978/j.issn.2218-676X.2012.10.03
30. Giantsoudi D, Schuemann J, Jia X, Dowdell S, Jiang S, and Paganetti H Validation of a GPU-Based Monte Carlo Code (gPMC) for Proton Radiation Therapy: Clinical Cases Study. *Phys Med Biol* (2015) 60:2257–69. doi:10.1088/0031-9155/60/6/2257
31. Schiavi A, Senzacqua M, Pioli S, Mairani A, Magro G, Molinelli S, et al. Fred: a GPU-Accelerated Fast-Monte Carlo Code for Rapid Treatment Plan Recalculation in Ion Beam Therapy. *Phys Med Biol* (2017) 62:7482–504. doi:10.1088/1361-6560/aa8134
32. Deng W, Younkin JE, Souris K, Huang S, Augustine K, Fatyga M, et al. Technical Note: Integrating an Open Source Monte Carlo Code "MCsquare" for Clinical Use in Intensity-modulated Proton Therapy. *Med Phys* (2020) 47:2558–74. doi:10.1002/mp.14125
33. Tian Z, Shi F, Folkerts M, Qin N, Jiang SB, and Jia X A GPU Opencl Based Cross-Platform Monte Carlo Dose Calculation Engine (Gomc). *Phys Med Biol* (2015) 60:7419–35. doi:10.1088/0031-9155/60/19/7419
34. Faddegon B, Ramos-Méndez J, Schuemann J, McNamara A, Shin J, Perl J, et al. The TOPAS Tool for Particle Simulation, a Monte Carlo Simulation Tool for Physics, Biology and Clinical Research. *Physica Med* (2020) 72:114–21. doi:10.1016/j.ejmp.2020.03.019
35. Oborn BM, Dowdell S, Metcalfe PE, Crozier S, Mohan R, and Keall PJ Proton Beam Deflection in MRI fields: Implications for MRI-Guided Proton Therapy. *Med Phys* (2015) 42:2113–24. doi:10.1118/1.4916661
36. Padilla-Cabal F, Georg D, and Fuchs H A Pencil Beam Algorithm for Magnetic Resonance Image-Guided Proton Therapy. *Med Phys* (2018) 45:2195–204. doi:10.1002/mp.12854
37. Schellhammer SM, Hoffmann AL, Gantz S, Smeets J, van der Kraaij E, Quets S, et al. Integrating a Low-Field Open MR Scanner with a Static Proton Research Beam Line: Proof of Concept. *Phys Med Biol* (2018) 63:23LT01. doi:10.1088/1361-6560/aaece8
38. Schellhammer SM, and Hoffmann AL Prediction and Compensation of Magnetic Beam Deflection in MR-Integrated Proton Therapy: a Method Optimized Regarding Accuracy, Versatility and Speed. *Phys Med Biol* (2017) 62:1548–64. doi:10.1088/1361-6560/62/4/1548
39. GitHub, *Google/Googletest* (2021) Available from: https://github.com/google/googletest. (Accessed July 08, 2021).
40. GitHub, *Google/Benchmark* (2021) Available from: https://github.com/google/benchmark (Accessed July 08, 2021).
41. Boost C++ Libraries (2021) Available from: https://www.boost.org/ (Accessed July 09, 2021).
42. RapidXml (2009) Available from: http://rapidxml.sourceforge.net/ (Accessed July 08, 2021).
43. McCormick M, Liu X, Jomier J, Marion C, and Ibanez L ITK: Enabling Reproducible Research and Open Science. *Front Neuroinform* (2014) 8:13. doi:10.3389/fninf.2014.00013
44. Wilkens T dicom.offis.de - Home (2018). [cited 2021 Jul 10]. Available from: https://dcmtk.org/.
45. Schneider U, Pedroni E, and Lomax A The Calibration of CT Hounsfield Units for Radiotherapy Treatment Planning. *Phys Med Biol* (1996) 41:111–24. doi:10.1088/0031-9155/41/1/009
46. Parodi K, Ferrari A, Sommerer F, and Paganetti H Clinical CT-based Calculations of Dose and Positron Emitter Distributions in Proton Therapy Using the FLUKA Monte Carlo Code. *Phys Med Biol* (2007) 52:3369–87. doi:10.1088/0031-9155/52/12/004
47. Qin N, Pinto M, Tian Z, Dedes G, Pompos A, Jiang SB, et al. Initial Development of goCMC: a GPU-Oriented Fast Cross-Platform Monte Carlo Engine for Carbon Ion Therapy. *Phys Med Biol* (2017) 62:3682–99. doi:10.1088/1361-6560/aa5d43
48. Parodi K, Mairani A, and Sommerer F Monte Carlo-Based Parametrization of the Lateral Dose Spread for Clinical Treatment Planning of Scanned Proton and Carbon Ion Beams. *J Radiat Res* (2013) 54(1):i91–i96. doi:10.1093/jrr/rrt051
49. Tessonnier T, Marcelos T, Mairani A, Brons S, and Parodi K Phase Space Generation for Proton and Carbon Ion Beams for External Users' Applications at the Heidelberg Ion Therapy Center. *Front Oncol* (2015) 5:297. doi:10.3389/fonc.2015.00297
50. Seltzer SM An Overview of ETRAN Monte Carlo Methods. In: *Monte Carlo Transport of Electrons and Photons*. Boston, MA: Springer (1988). p. 153–81. doi:10.1007/978-1-4613-1059-4_7
51. Alex F Bielajew. "Electron Transport in E and B Fields. In: *Monte Carlo Transport of Electrons and Photons*. Boston, MA: Springer (1988). p. 421–34.
52. Duff T, Burgess J, Christensen P, Hery C, Kensler A, Liani M, et al. Building an Orthonormal Basis, Revisited. *J Comp Graphics Tech* (2017) 6:1–8.
53. Jackson JD *Classical Electrodynamics*. New York, NY: Wiley (1975).
54. Fano U Penetration of Protons, Alpha Particles, and Mesons. *Annu Rev Nucl Sci* (1963) 13:1–66. doi:10.1146/annurev.ns.13.120163.000245
55. Landau LD On the Energy Loss of Fast Particles by Ionization. *J Phys* (1944) 8:201–5.
56. Vavilov PV Ionization Losses of High-Energy Heavy Particles. *Soviet Phys JETP* (1957) 5:749–51.
57. Chibani O New Algorithms for the Vavilov Distribution Calculation and the Corresponding Energy Loss Sampling. *IEEE Trans Nucl Sci* (1998) 45:2288–92. doi:10.1109/23.725266
58. Moliere G Theorie der Streuung schneller geladener Teilchen II Mehrfach-und Vielfachstreuung. *Z für Naturforschung A* (1948) 3:78–97. doi:10.1515/zna-1948-0203
59. Scott WT The Theory of Small-Angle Multiple Scattering of Fast Charged Particles. *Rev Mod Phys* (1963) 35:231–313. doi:10.1103/RevModPhys.35.231
60. Rossi B, and Greisen K Cosmic-Ray Theory. *Rev Mod Phys* (1941) 13:240–309. doi:10.1103/RevModPhys.13.240
61. Highland VL Some Practical Remarks on Multiple Scattering. *Nucl Instr Methods* (1975) 129:497–9. doi:10.1016/0029-554x(75)90743-0
62. Frühwirth R, and Regler M On the Quantitative Modelling of Core and Tails of Multiple Scattering by Gaussian Mixtures. *Nucl Instr Methods Phys Res Section A: Acc Spectrometers, Detectors Associated Equipment* (2001) 456:369–89. doi:10.1016/s0168-9002(00)00589-1
63. Bellinzona VE, Ciocca M, Embriaco A, Fontana A, Mairani A, Mori M, et al. On the Parametrization of Lateral Dose Profiles in Proton Radiation Therapy. *Physica Med* (2015) 31:484–92. doi:10.1016/j.ejmp.2015.05.004
64. Kuhn SE, and Dodge GE A Fast Algorithm for Monte Carlo Simulations of Multiple Coulomb Scattering. *Nucl Instr Methods Phys Res Section A: Acc Spectrometers, Detectors Associated Equipment* (1992) 322:88–92. doi:10.1016/0168-9002(92)90361-7
65. Adelmann A, Calvo P, Frey M, Gsell A, Locans U, Metzger-Kraus C, et al. *OPAL a Versatile Tool for Charged Particle Accelerator Simulations*. arxiv: 1905.06654 (2019).
66. Bellinzona VE *A Non Gaussian Model for the Lateral Dose Evaluation in Hadrontherapy*. [PhD thesis]. Ludwig-Maximillians-University Munich (2017).

67. Tripathi RK, Wilson JW, and Cucinotta FA A Method for Calculating Proton-Nucleus Elastic Cross-Sections. *Nucl Instr Methods Phys Res Section B: Beam Interactions Mater Atoms* (2002) 194:229–36. doi:10.1016/s0168-583x(02)00690-0
68. Ranft J Estimation of Radiation Problems Around High-Energy Accelerators Using Calculations of the Hadronic cascade in Matter. *Part Accel* (1972) 3: 129–61.
69. Tripathi RK, Cucinotta FA, and Wilson JW Accurate Universal Parameterization of Absorption Cross Sections. *Nucl Instr Methods Phys Res Section B: Beam Interactions Mater Atoms* (1996) 117:347–9. doi:10.1016/0168-583X(96)00331-X
70. Tripathi RK, Cucinotta FA, and Wilson JW Accurate Universal Parameterization of Absorption Cross Sections III - Light Systems. *Nucl Instr Methods Phys Res Section B: Beam Interactions Mater Atoms* (1999) 155:349–56. doi:10.1016/s0168-583x(99)00479-6
71. Tessonnier T, Mairani A, Brons S, Haberer T, Debus J, and Parodi K Experimental Dosimetric Comparison of1H,4He,12C and16O Scanned Ion Beams. *Phys Med Biol* (2017) 62:3958–82. doi:10.1088/1361-6560/aa6516
72. Tessonnier T, Böhlen TT, Ceruti F, Ferrari A, Sala P, Brons S, et al. Dosimetric Verification in Water of a Monte Carlo Treatment Planning Tool for Proton, Helium, Carbon and Oxygen Ion Beams at the Heidelberg Ion Beam Therapy Center. *Phys Med Biol* (2017) 62:6579–94. doi:10.1088/1361-6560/aa7be4
73. Gajewski J, Garbacz M, Chang C-W, Czerska K, Durante M, Krah N, et al. Commissioning of GPU-Accelerated Monte Carlo Code FRED for Clinical Applications in Proton Therapy. *Front Phys* (2021) 8:403. doi:10.3389/fphy.2020.567300
74. Garbacz M, Battistoni G, Durante M, Gajewski J, Krah N, Patera V, et al. Proton Therapy Treatment Plan Verification in CCB Krakow Using Fred Monte Carlo TPS Tool. In: *World Congress on Medical Physics and Biomedical Engineering 2018*. Singapore: Springer (2019). p. 783–7. doi:10.1007/978-981-10-9035-6_144
75. Tessonnier T *Treatment of Low-Grade Meningiomas with Protons and Helium Ions*. [PhD thesis]. Ludwig-Maximillians-University Munich (2017).

Conflict of Interest: The authors declare that the research was conducted in the absence of any commercial or financial relationships that could be construed as a potential conflict of interest.

Publisher's Note: All claims expressed in this article are solely those of the authors and do not necessarily represent those of their affiliated organizations, or those of the publisher, the editors and the reviewers. Any product that may be evaluated in this article, or claim that may be made by its manufacturer, is not guaranteed or endorsed by the publisher.

frontiers in Physics

ORIGINAL RESEARCH
published: 13 December 2021
doi: 10.3389/fphy.2021.733949

Collisions of Nucleons with Atoms: Calculated Cross Sections and Monte Carlo Simulation

Francesc Salvat[1*†] *and José Manuel Quesada*[2†]

[1]*Facultat de Física (FQA and ICC), Universitat de Barcelona, Barcelona, Spain,* [2]*Departamento de Física Atómica, Molecular y Nuclear, Universidad de Sevilla, Sevilla, Spain*

After a summary description of the theory of elastic collisions of nucleons with atoms, we present the calculation of a generic database of differential and integrated cross sections for the simulation of multiple elastic collisions of protons and neutrons with kinetic energies larger than 100 keV. The relativistic plane-wave Born approximation, with binding and Coulomb-deflection corrections, has been used to calculate a database of proton-impact ionization of K-shell and L-, M-, and N-subshells of neutral atoms These databases cover the whole energy range of interest for all the elements in the periodic system, from hydrogen to einsteinium (Z = 1–99); they are provided as part of the PENH distribution package. The Monte Carlo code system PENH for the simulation of coupled electron-photon-proton transport is extended to account for the effect of the transport of neutrons (released in proton-induced nuclear reactions) in calculations of dose distributions from proton beams. A simplified description of neutron transport, in which neutron-induced nuclear reactions are described as a fractionally absorbing process, is shown to give simulated depth-dose distributions in good agreement with those generated by the GEANT4 code. The proton-impact ionization database, combined with the description of atomic relaxation data and electron transport in PENELOPE, allows the simulation of proton-induced x-ray emission spectra from targets with complex geometries.

Keywords: coupled electron-photon-proton transport, Monte Carlo simulation, PENELOPE-PENH code system, random-hinge method, neutron transport, proton-induced x-ray emission

OPEN ACCESS

Edited by:
Vasilis Vlachoudis, European Organization for Nuclear Research (CERN), Switzerland

Reviewed by:
Marco Incagli, Istituto Nazionale di Fisica Nucleare - sezione di Pisa, Italy
Tuba Conka Yildiz, Türkisch-Deutsche Universität, Turkey

****Correspondence:***
Francesc Salvat
francesc.salvat@ub.edu

†These authors have contributed equally to this work

Specialty section:
This article was submitted to Radiation Detectors and Imaging, a section of the journal Frontiers in Physics

Received: *30 June 2021*
Accepted: *01 November 2021*
Published: *13 December 2021*

Citation:
Salvat F and Quesada JM (2021) Collisions of Nucleons with Atoms: Calculated Cross Sections and Monte Carlo Simulation. Front. Phys. 9:733949. doi: 10.3389/fphy.2021.733949

1 INTRODUCTION

Motivated by the specific needs of protontherapy and proton-induced x-ray emission, we have recently extended the PENELOPE code system [1] to introduce the simulation of interactions and transport of protons [2, 3]. The resulting code, named PENH, performs class-II Monte Carlo simulation of coupled electron-photon-proton transport in material structures consisting of homogeneous bodies limited by quadric surfaces. In class II simulation schemes, hard interactions (that is, interactions involving scattering angles or energy losses larger than preselected cutoffs) are simulated by random sampling from their restricted differential cross sections (DCSs) while the cumulative effect of soft (sub-cutoff) interactions is described by means of a multiple-scattering approach. Class II simulation has distinct advantages in front of conventional condensed simulation (see, *e.g.*, Ref. [1]).

The PENH code accounts for elastic and inelastic collisions of protons with atoms, as well as for nuclear reactions induced by proton impact. Elastic collisions of protons with nuclei are described by

means of numerical DCSs obtained as the product of the DCS for scattering by the bare nucleus, which was computed by the method of partial-waves with the global optical-model potential of Koning and Delaroche [4], and a screening factor accounting for the effect of the screening of the Coulomb field of the nucleus by the atomic electrons, which was calculated from the eikonal approximation for the Dirac-Hartree-Fock-Slater potential of neutral atoms [2, 3, 5]. Proton-induced electronic excitations are simulated by means of DCSs obtained from the Born approximation with the Sternheimer-Liljequist model of the generalized oscillator strength (GOS) [1], which is modified by rescaling the relative contributions of the various electron subshells to give cross sections for the impact ionization of inner subshells equal to unpublished results obtained from accurate atomic GOSs [2]. Nuclear reactions induced by proton impact are simulated by using information from data files in ENDF-6 format [6], which provide cross sections, multiplicities, and angle-energy distributions of all reaction products: light ejectiles (up to alphas), gammas, as well as recoiling heavy residuals.

Although electromagnetic interactions are faithfully described for protons in the energy range from 100 keV up to 1 GeV, the unavailability of nuclear reaction data for energies higher than about 200 MeV, limit the possible applications of the code. Simulations with PENH are also limited by the fact that the code can only follow electrons/positrons, photons, and protons. To lessen the effect of this limitation, light charged ejectiles other than protons (deuterons, tritons, ^{3}He, and alphas) are tracked as weighted protons [3]. Neutrons and heavy products are not followed and their kinetic energies were assumed to be deposited at the reaction site. Comparison with results from other codes shows that, as one could predict, the calculated dose distributions from proton beams are generally accurate in the volume swept by the protons, but are generally too low outside that volume, mostly because of the neglect of neutron transport. In this respect, it is worth recalling that neutrons practically do not interact with electrons and, as a consequence, they have large mean free paths. In the energy range covered by the proton simulation code, nominally from 100 keV to 1 GeV, the mean free path of neutrons in water ranges from about 5 cm at 100 keV to ~ 66 cm at 1 GeV.

The aim of the present article is twofold. First, we present the theory and computational aspects of the calculation of the DCSs for elastic collisions of neutrons and protons, and of the cross sections for ionization of inner electron subshells of atoms by proton impact. We also describe the structure and contents of the associated numerical databases, which completely define the interaction models used in PENH for nucleons. Second, we present a simplified algorithm for the simulation of the effect of neutron transport in Monte Carlo calculations of dose distributions from proton beams, which only uses the information provided in the calculated elastic-scattering database, that is, the total and DCS for elastic collisions and the reaction cross section, which is one of the basic parameters used to set the nuclear optical-model potential. The main simplification is that neutron-induced nuclear reactions are described as purely absorptive, that is, when the transported neutron induces a reaction, the simulation of the neutron is discontinued and a fraction of its kinetic energy is assumed to be locally absorbed. It will be shown that, in spite of its crudeness, this transport algorithm accounts for the contribution of neutrons to the spatial dose distribution fairly accurately. Although random histories of neutrons with protontherapy energies (say, from 100 keV to ~ 300 MeV) may be simulated detailedly (*i.e.*, interaction by interaction) we adopt a class II tracking scheme, which is analogous to the ones used in PENELOPE-PENH for electrons/positrons and protons, because it allows speeding up simulations of high-energy neutrons.

The present article is organized as follows. In **Section 2** we describe the calculation of DCSs for elastic collisions of nucleons and protons with atoms (nuclei), the structure of the numerical database for elastic scattering of these particles, and the implementation of a class II algorithm for the simulation of multiple elastic scattering of neutrons. **Section 3** deals with the ionization of inner electron subshells of atoms by impact of protons, which is based on total cross sections calculated from the relativistic plane-wave Born approximation with corrections for binding/polarization and Coulomb deflection effects. After a brief presentation of the theory and sample results, the associated numerical database is described. The validation of the PENH calculation of dose distributions from proton beams is considered in **Section 4**. **Section 5** illustrates the simulation of proton-induced x-ray emission from solid targets. Finally, in **Section 6** we offer a few concluding remarks.

2 ELASTIC COLLISIONS

We consider elastic collisions of nucleons with atoms of the element of atomic number Z. In order to cover the range of kinetic energies of interest in proton therapy, up to about 300 MeV, we shall use relativistic collision kinematics. The simulation code transports particles in the laboratory (L) frame, where the material is at rest and the projectile moves with kinetic energy E before the collision. For simplicity, we consider that the z axis of the reference frame is parallel to the linear momentum of the projectile, which is given by

$$\mathbf{p} = c^{-1}\sqrt{E\,(E + 2\ mc^2)}\,\hat{\mathbf{z}}, \tag{1}$$

where c is the speed of light in vacuum and m is the projectile mass (= m_p for protons, and = m_n for neutrons). The total energy of the projectile is

$$\mathcal{W} = E + mc^2 = \sqrt{m^2c^4 + c^2p^2}. \tag{2}$$

We recall the general relations

$$p = \beta\gamma\, mc \qquad \text{and} \qquad E = (\gamma - 1)mc^2 \tag{3}$$

where

$$\beta = \frac{v}{c} = \frac{\sqrt{E\,(E + 2mc^2)}}{E + mc^2} \tag{4}$$

is the speed of the particle in units of c and

$$\gamma = \sqrt{\frac{1}{1-\beta^2}} = \frac{E + mc^2}{mc^2} \tag{5}$$

is the particle's total energy in units of its rest energy.

Elastic collisions involve a certain transfer of kinetic energy to the target atom, which is easily accounted for by sampling the collisions in the center-of-mass (CM) frame, which moves relative to the L frame with velocity

$$\mathbf{v}_{\rm CM} = \boldsymbol{\beta}_{\rm CM} c = \frac{c^2 \mathbf{p}}{E + mc^2 + M_{\rm A} c^2}, \tag{6}$$

where $M_{\rm A}$ is the mass of the atom. In the CM frame the linear momenta of the projectile and the atom before the collision are, respectively, $\mathbf{p}'_{\rm i} = \mathbf{p}'_0$ and $\mathbf{p}'_{\rm Ai} = -\mathbf{p}'_0$, with

$$\mathbf{p}'_0 = \frac{M_{\rm A} c^2}{\sqrt{(mc^2 + M_{\rm A} c^2)^2 + 2 M_{\rm A} c^2\, E}}\, \mathbf{p}. \tag{7}$$

Quantities in the CM frame are denoted by primes. After the elastic collision, in CM the projectile moves with momentum $p'_{\rm f} = p'_0$ in a direction defined by the polar scattering angle θ' and the azimuthal scattering angle ϕ', and the target atom recoils with equal momentum $p'_{\rm Af} = p'_0$ in the opposite direction. The final energies and directions of the projectile and the atom in the L frame are obtained by means of a Lorentz boost with velocity $-\mathbf{v}_{\rm CM}$. Thus, elastic collisions are completely determined by the DCS $d\sigma/d\Omega'$ in the CM frame.

We follow the approach described in our previous work on proton transport [3], *i.e.*, we assume that the interaction potential in the CM frame is central, because this is a prerequisite for applying the partial-wave expansion method to compute the DCS. Our approach can be qualified as semi-relativistic, because we are using strict relativistic kinematics but we do not account for the breaking of the central symmetry of the interaction when passing from the L to the CM frame.

2.1 Interaction Potential

The interaction of the incident nucleon with a bare nucleus of the isotope ${}^{A}Z$ having atomic number Z and mass number A can be described by a phenomenological complex optical-model potential

$$V_{\rm nuc}(r) = V_{\rm opt}(r) + {\rm i} W_{\rm opt}(r), \tag{8}$$

where the first term is a real potential, which in the case of projectile protons includes the Coulomb interaction, and the second term, ${\rm i}W_{\rm opt}(r)$, is an absorptive (negative) imaginary potential, which accounts for the loss of nucleons in the elastic channel caused by inelastic processes. Parameterizations of optical-model potentials are generally expressed as a combination of Woods–Saxon volume terms,

$$f(R,a;r) = \frac{1}{1 + \exp[(r-R)/a]}, \tag{9a}$$

and surface derivative (d) terms,

$$\begin{aligned} g(R,a;r) &= \frac{\rm d}{{\rm d}r} f(R,a;r) \\ &= \frac{1}{a} f(R,a;r)\big[f(R,a;r) - 1\big]. \end{aligned} \tag{9b}$$

The parameters in these functions are the radius R and the diffuseness a; typically, the radius is expressed as $R = r_0 A^{1/3}$. We consider global model potentials of the type

$$\begin{aligned} V_{\rm nuc}(r) = {} & V_{\rm v}(E;r) + V_{\rm d}(E;r) + V_{\rm c}(r) + V_{\rm so}(E;r)\, 2\,\mathbf{L}\cdot\mathbf{S} \\ & + {\rm i}[W_{\rm v}(E;r) + W_{\rm d}(E;r) + W_{\rm so}(E;r)\, 2\,\mathbf{L}\cdot\mathbf{S}] \end{aligned} \tag{10}$$

with the following terms:

1) Real volume potential:

$$V_{\rm v}(E;r) = V_{\rm v}(E)\, f(R_{\rm v}, a_{\rm v}; r). \tag{11a}$$

2) Real surface potential:

$$V_{\rm d}(E;r) = V_{\rm d}(E)\, 4a_{\rm d}\, g(R_{\rm d}, a_{\rm d}; r). \tag{11b}$$

3) Coulomb potential: approximated by the electrostatic potential of a uniformly charged sphere of radius $R_{\rm c}$,

$$V_{\rm c}(r) = \frac{z_0 Z e^2}{r} \begin{cases} \dfrac{r}{2R_{\rm c}}\left(3 - \dfrac{r^2}{R_{\rm c}^2}\right) & \text{if} r < R_{\rm c}, \\ 1 & \text{if} r \geq R_{\rm c}, \end{cases} \tag{11c}$$

where e is the elementary charge and $z_0 e$ the nucleon charge (z_0 = 1 for protons and = 0 for neutrons).

4) Real spin-orbit potential:

$$V_{\rm so}(E;r) = V_{\rm so}(E) \left(\frac{\hbar}{m_\pi c}\right)^2 \frac{1}{r}\, g(R_{\rm so}, a_{\rm so}; r), \tag{11d}$$

where the quantity in parentheses is the pion Compton wavelength, $\hbar/(m_\pi c) \simeq 1.429\,502$ fm.

5) Imaginary volume potential:

$$W_{\rm v}(E;r) = W_{\rm v}(E)\, f(R_{\rm w}, a_{\rm w}; r). \tag{11e}$$

6) Imaginary surface potential:

$$W_{\rm d}(E;r) = W_{\rm d}(E)\, 4a_{\rm wd}\, g(R_{\rm wd}, a_{\rm wd}; r). \tag{11f}$$

7) Imaginary spin-orbit potential:

$$W_{\rm so}(E;r) = W_{\rm so}(E) \left(\frac{\hbar}{m_\pi c}\right)^2 \frac{1}{r}\, g(R_{\rm wso}, a_{\rm wso}; r). \tag{11g}$$

The operators $\mathbf{L}$ and $\mathbf{S}$ are, respectively, the orbital and spin angular momenta (both in units of $\hbar$) of the projectile nucleon. We have indicated explicitly that the strengths of the potential terms are functions (usually expressed as polynomials) of the kinetic energy E of the projectile in the L frame. Except for the Coulomb term of protons, the potential is of finite-range, it vanishes when the distance r from the projectile to the nucleus

is larger than about twice the "nuclear radius", $R_{\rm nuc} \sim 1.2\,A^{1/3}$ fm. In the calculations we use the parameterization of the global optical-model potential of Koning and Delaroche [4].

2.2 Scattering Amplitudes and Cross Sections

The scattering of nucleons by nuclei in the CM frame is described by using the partial-wave expansion method. The underlying physical picture is that of a stationary process represented by a distorted plane wave, *i.e.*, by an exact solution of the time-independent relativistic Schrödinger equation for the potential $V_{\rm nuc}(r)$,

$$\left(-\frac{\hbar^2}{2\mu_{\rm r}}\,\nabla^2 + V_{\rm nuc}(r)\right)\psi(\mathbf{r}) = \frac{p_0'^2}{2\mu_{\rm r}}\,\psi(\mathbf{r}), \tag{12}$$

which asymptotically behaves as a plane wave with an outgoing spherical wave. The quantity $\mu_{\rm r}$ is the relativistic reduced mass of the projectile and the target atom, defined as

$$\mu_{\rm r} = c^{-2}\frac{\mathcal{W}_{\rm ni}'\mathcal{W}_{\rm Ai}'}{\mathcal{W}_{\rm ni}'+\mathcal{W}_{\rm Ai}'}, \tag{13}$$

where

$$\mathcal{W}_{\rm ni}' = \sqrt{m^2c^4 + c^2p_0'^2} \qquad \text{and} \qquad \mathcal{W}_{\rm Ai}' = \sqrt{M_{\rm A}^2c^4 + c^2p_0'^2} \tag{14}$$

are, respectively, the total energies of the projectile and the atom before the collision.

As the potential **(10)** contains spin-orbit terms, the wave function is a two-component spinor. Assuming that before the interaction the projectile moves in the direction of the z axis, the asymptotic, large-r behavior of the distorted plane wave is

$$\psi(\mathbf{r}) \underset{r\to\infty}{\sim} (2\pi)^{-3/2}\exp(\mathrm{i}kr\,\cos\theta')\chi + (2\pi)^{-3/2}\,\frac{\exp(\mathrm{i}kr)}{r}\,\mathcal{F}(\theta',\phi')\chi. \tag{15}$$

where χ is a spinor, which defines the spin state of the incident nucleon, $k = p_0'/\hbar$ is the projectile's wave number, and θ' and ϕ' are the polar and azimuthal scattering angles, *i.e.*, those of the direction $\hat{\mathbf{r}}$. The factor $\mathcal{F}(\theta',\phi')$ is a 2×2 matrix independent of r,

$$\mathcal{F}(\theta',\phi') = \begin{pmatrix} f(\theta') & -\exp(-\mathrm{i}\phi')\,g(\theta') \\ \exp(\mathrm{i}\phi')\,g(\theta') & f(\theta') \end{pmatrix}. \tag{16}$$

The functions $f(\theta')$ and $g(\theta')$ are called the "direct" and "splin-flip" scattering amplitudes, respectively. Evidently, these functions determine the final spin state of the scattered nucleon.

The scattering amplitudes can be calculated in terms of the phase shifts $\delta_{\ell j}$ of spherical waves with orbital and total angular momenta ℓ and j, respectively. Calculations are performed by using the Fortran subroutine package RADIAL of Salvat and Fernández-Varea [7], which implements a robust power series solution method that effectively avoids truncation errors and yields highly accurate radial functions. The calculation for protons is complicated by the fact that the atomic electrons screen the long-range Coulomb potential of the nucleus, resulting in an affective electrostatic potential that decreases in magnitude as the radial distance r increases. This screened atomic potential extends up to radial distances of the order of the atomic radius, $R_{\rm at} \sim 10^5 R_{\rm nuc}$ and, because of the small wavelengths of protons and heavier projectiles, the numerical calculation of phase-shifts for the screened nuclear potential is unfeasible. The DCSs for elastic scattering of protons can be calculated by combining a partial-wave calculation of the scattering by the bare nucleus with an electronic screening correction derived from the eikonal approximation [3]. Here we describe the calculation of the DCS for elastic collisions of neutrons, which is less demanding than for protons because, due to the absence of the Coulomb term, the interaction potential has a finite range.

The reduced radial functions, $P_{\ell j}(r)$ are the regular solutions of the radial wave equation

$$-\frac{\hbar^2}{2\mu}\,\frac{\mathrm{d}^2}{\mathrm{d}r^2}P_{\ell j}(r) + V_{\ell j}(r)\,P_{\ell j}(r) = \frac{p_0'^2}{2\mu}\,P_{\ell j}(r) \tag{17}$$

with the "radial" potential

$$V_{\ell j}(r) = V_{\rm v}(E;r) + V_{\rm d}(E;r) + \mathrm{i}[W_{\rm v}(E;r) + W_{\rm d}(E;r)] + [V_{\rm so}(E;r) + \mathrm{i}\,W_{\rm so}(E;r)]\left(j(j+1) - \ell(\ell+1) - \frac{3}{4}\right) + \frac{\hbar^2}{2\,\mu}\,\frac{\ell(\ell+1)}{r^2}. \tag{18}$$

The radial functions are normalized so that

$$P_{\ell j}(r) \underset{r\to\infty}{\sim} \sin\left(kr - \ell\frac{\pi}{2} + \delta_{\ell j}\right), \tag{19}$$

where $\delta_{\ell j}$ is the complex phase shift. The RADIAL subroutines determine each phase shift by integrating the corresponding radial equation from $r = 0$ outwards up to a radius $r_{\rm m}$ larger than the range of the nuclear interaction, and matching the numerical solution at $r_{\rm m}$ with a linear combination of the regular and irregular Bessel functions. It is worth mentioning that in the case of charged projectiles (protons and alphas), when electronic screening is ignored, the inner solution is matched to a combination of the regular and irregular Coulomb functions, and the phase shift is the sum of the calculated "inner" phase shift and the Coulomb phase shift (see, *e.g.*, Ref. [7]). All phase shifts with absolute values larger than 10^{-9} are calculated. In the following the phase shifts are denoted by the abridged notation $\delta_{\ell a}$ with $a = \text{sign}\,(j-\ell)$, *i.e.*, $\delta_{\ell+} \equiv \delta_{\ell,j=\ell+1/2}$ and $\delta_{\ell-} \equiv \delta_{\ell,j=\ell-1/2}$.

From the calculated phase shifts, the direct and spin-flip scattering amplitudes are evaluated from their partial-wave expansions

$$f(\theta') = \frac{1}{2\mathrm{i}k}\sum_{\ell}[(\ell+1)(S_{\ell+}-1) + \ell(S_{\ell-}-1)]\,P_\ell(\cos\theta') \tag{20a}$$

and

$$g(\theta') = \frac{1}{2\mathrm{i}k}\sum_{\ell}(S_{\ell-} - S_{\ell+})\,P_\ell^1(\cos\theta'), \tag{20b}$$

where $P_\ell(\cos\theta')$ and $P_\ell^1(\cos\theta')$ are Legendre polynomials and associated Legendre functions of the first kind [8], respectively, and

$$S_{\ell a} = \exp(2\mathrm{i}\delta_{\ell a}), \tag{21}$$

are the S-matrix elements.

For spin-unpolarized neutrons, the elastic DCS per unit solid angle in the CM frame is given by

$$\frac{\mathrm{d}\sigma_{\mathrm{el}}}{\mathrm{d}\Omega'} = \left|f(\theta')\right|^2 + \left|g(\theta')\right|^2. \tag{22}$$

Owing to the assumed spherical symmetry of the target nucleus, the angular distribution of scattered neutrons is axially symmetric about the direction of incidence, *i.e.*, independent of the azimuthal scattering angle in both the CM and L frames.

The total elastic cross section is obtained as the integral of the DCS,

$$\sigma_{\mathrm{el}} = \int \frac{\mathrm{d}\sigma_{\mathrm{el}}}{\mathrm{d}\Omega'}\, d\Omega' = 2\pi \int_{-1}^{1} \frac{\mathrm{d}\sigma_{\mathrm{el}}}{\mathrm{d}\Omega'}\, \mathrm{d}(\cos\theta'). \tag{23}$$

The grand total cross section σ_{T}, accounting for both elastic scattering and inelastic interactions or reactions, can be obtained from the optical theorem,

$$\sigma_{\mathrm{T}} = \sigma_{\mathrm{el}} + \sigma_{\mathrm{R}} = \frac{4\pi}{k}\,\mathrm{Im}\, f(0), \tag{24}$$

where σ_{R} denotes the reaction cross section, *i.e.*, the total cross section for inelastic interactions.

2.3 Elastic-Scattering Database

A Fortran program named PANELASTIC has been written to calculate differential and integrated cross sections for elastic collisions of protons, neutrons, and alphas with neutral atoms. It is assumed that the target atom is neutral and the calculated cross sections for each element are obtained as an average over those of the naturally occurring isotopes, weighted by their respective natural abundances [9]. Consistently, in the simulations we consider that the mass of a target atom is the average atomic mass of the element

$$M_{\mathrm{A}} = \frac{A_{\mathrm{w}}}{\mathrm{g/mol}}\,\mathrm{u} \tag{25}$$

where A_{w} is the molar mass of the element, and $\mathrm{u} = m(^{12}\mathrm{C})/12$ is the atomic mass unit. This simplification permits reducing the required information for each element to a single cross section table, irrespective of the number of isotopes of that element. PANELASTIC uses the nuclear optical model potentials of Koning and Delaroche [4] for protons and neutrons, and that of Su and Han [10] for alphas. The parameters of the global potential for nucleons are determined for $24 \le A \le 209$ and $E \le 200$ MeV. Owing to the lack of more accurate approximations, because the potential values vary smoothly with A, Z and E, we use those parameters for all isotopes and for energies up to 300 MeV, for higher energies the potential parameters at $E = 300$ MeV are employed.

In the case of protons (and also alphas) the screening of the Coulomb potential of the nucleus by the atomic electrons is described by means of the Dirac-Hartree-Fock-Slater analytical screening function [5], and the screening correction to the nuclear DCS is evaluated by means of the eikonal approximation [3]. Since scattering of charged particles is dominated by the long-range Coulomb interaction, the extrapolation of the nuclear optical-model potential to high energies has a small effect on proton transport calculations.

The program PANELASTIC calculates cross sections for elastic collisions of a projectile particle with a given isotope ^{A}Z for the kinetic energies of the projectile specified by the user. Alternatively, it can produce a complete database of DCSs and integrated cross sections for collisions of projectiles of a given type, with laboratory kinetic energies covering the range from 100 keV to 1 GeV for each element from hydrogen ($Z = 1$) to einsteinium ($Z = 99$). The database grid of energies is logarithmic, with 35 points per decade. For each energy the program calculates the DCS in CM, **Eq. 22**, for a grid of 1,000 polar angles θ'. In order to reduce the size of the database, and also to improve the accuracy of interpolation in energy, the DCS is considered as a function of the variable

$$Q \equiv 4\left(cp'_0\right)^2 \sin^2\left(\theta'/2\right), \tag{26}$$

c^2 times the square of the momentum transfer in CM. The original table is "cleaned", by removing points in regions where the DCS varies smoothly, to define a reduced grid that allows accurate cubic spline interpolation in Q. The DCS interpolated in this way is estimated to be accurate to four or more digits. For each projectile energy, the database includes the values of the total elastic cross section, **Eq. 23**, the reaction cross section obtained from **Eq. 24**, the first transport cross section (or momentum transfer cross section),

$$\sigma'_{\mathrm{tr},1} \equiv \int (1-\cos\theta')\,\frac{\mathrm{d}\sigma_{\mathrm{el}}}{\mathrm{d}\Omega'}\, d\Omega', \tag{27}$$

and the second transport cross section

$$\sigma'_{\mathrm{tr},2} \equiv \int \frac{3}{2}\,\left(1-\cos^2\theta'\right)\frac{\mathrm{d}\sigma_{\mathrm{el}}}{\mathrm{d}\Omega'}\, d\Omega'. \tag{28}$$

The values of these integrated cross sections serve to assess the accuracy of the DCS interpolation scheme adopted in the simulation. We recall that the total elastic cross section and the reaction cross section have the same values in the CM and the L frames.

2.4 Simulation of Neutron Elastic Collisions

The kinematics of elastic collisions of a neutron with laboratory energy E is completely determined by the polar scattering angle θ' in CM. In the CM frame, after an elastic collision the magnitudes of the linear momenta of the projectile and the target atom are the same as before the collision, and the scattering angles θ', ϕ' determine the directions of motion of the two particles in CM. As mentioned above, the final kinetic energy E_{nf} and the polar scattering angle θ of the projectile neutron in the L frame are obtained by a Lorentz boost with velocity $-\mathbf{v}_{\mathrm{CM}}$, which gives

$$E_{\mathrm{nf}} = \gamma_{\mathrm{CM}}\left(W'_{\mathrm{ni}} + \beta_{\mathrm{CM}}\, cp'_0\, \cos\theta'\right) - m_{\mathrm{n}}c^2 \tag{29}$$

and

$$\cos\theta = \frac{\tau + \cos\theta'}{\sqrt{\left(\tau + \cos\theta'\right)^2 + \gamma_{\rm CM}^{-2}\sin^2\theta'}}, \tag{30}$$

where

$$\gamma_{\rm CM} \equiv \sqrt{\frac{1}{1-\beta_{\rm CM}^2}} = \frac{E + m_{\rm n}c^2 + M_{\rm A}c^2}{(m_{\rm n}c^2 + M_{\rm A}c^2)^2 + 2M_{\rm A}c^2\,E} \tag{31}$$

and τ is the ratio of speeds of the CM and of the scattered neutron (in CM), $v_{\rm n}' = c^2 p_0'/\mathcal{W}_{\rm nf}'$,

$$\tau = \frac{v_{\rm CM}}{v_{\rm n}'} = \sqrt{\left(\frac{m_{\rm n}}{M_{\rm A}}\right)^2 \left(1-\beta_{\rm CM}\right)^2 + \beta_{\rm CM}}. \tag{32}$$

Notice that the azimuthal angle of the neutron direction in L is the same as in the CM frame. After the collision, in the L frame the target atom recoils with kinetic energy $E_{\rm A} = E - E_{\rm nf}$ and direction in the scattering plane with the polar angle

$$\cos\theta_{\rm A} = \frac{1-\cos\theta'}{\sqrt{\left(1-\cos\theta'\right)^2 + \gamma_{\rm CM}^{-2}\sin^2\theta'}}. \tag{33}$$

The DCS can also be expressed in terms of the scattering angles in the L frame by making use of the inverse of the relation (30),

$$\cos\theta' = \frac{-\tau\gamma_{\rm CM}^2\sin^2\theta \pm \cos\theta\sqrt{\cos^2\theta + \gamma_{\rm CM}^2\left(1-\tau^2\right)\sin^2\theta}}{\gamma_{\rm CM}^2\sin^2\theta + \cos^2\theta}. \tag{34}$$

If τ is less than unity only the plus sign before the square root has to be considered. For $\tau > 1$, there are two values of the CM deflection θ', given by **Eq. 34**, for each value of θ, which correspond to different final energies of the neutron in L. The DCS in the L frame is given by

$$\frac{{\rm d}\sigma_{\rm el}}{{\rm d}\Omega} = \left|\frac{{\rm d}\left(\cos\theta'\right)}{{\rm d}\left(\cos\theta\right)}\right| \frac{{\rm d}\sigma_{\rm el}}{{\rm d}\Omega'} \tag{35}$$

where the last factor is the DCS in the CM frame. Using the relation (34), we obtain

$$\frac{{\rm d}\sigma_{\rm el}}{{\rm d}\Omega} = \frac{\gamma_{\rm CM}^2\left[\tau\cos\theta \pm \sqrt{\cos^2\theta + \gamma_{\rm CM}^2\left(1-\tau^2\right)\sin^2\theta}\;\right]^2}{\left(\gamma_{\rm CM}^2\sin^2\theta + \cos^2\theta\right)^2\sqrt{\cos^2\theta + \gamma_{\rm CM}^2\left(1-\tau^2\right)\sin^2\theta}}\;\frac{{\rm d}\sigma_{\rm el}}{{\rm d}\Omega'}. \tag{36}$$

If $\tau < 1$ only the plus sign is valid and the scattering angle θ varies from 0 to π. When $\tau \geq 1$, the DCS vanishes for angles θ larger than

$$\theta_{\rm max} = \arctan\left(\sqrt{\frac{1}{\gamma_{\rm CM}^2\left(\tau^2-1\right)}}\right); \tag{37}$$

for angles $\theta < \theta_{\rm max}$, **Eq. 34** yields two values of θ' in $(0, \pi)$, the expression on the right-hand side of **Eq. 36** must then be evaluated for these two angles, and the resulting values added up to give the DCS in L. In class-II simulations **formula (36)** allows determining the contributions of soft elastic interactions to the first and second transport cross sections.

The elastic collision involves the transfer of energy $W = E_{\rm A}$ from the projectile to the target atom. The energy loss can be expressed in terms of the scattering angle in CM,

$$W = W_{\rm max}\,\frac{1-\cos\theta'}{2}, \tag{38}$$

where

$$W_{\rm max} = \frac{2M_{\rm A}c^2\,E\left(E + 2m_{\rm n}c^2\right)}{\left(M_{\rm A}c^2 + m_{\rm n}c^2\right)^2 + 2M_{\rm A}c^2E} \tag{39}$$

is the maximum energy loss in a collision, which occurs when $\theta' = \pi$. The energy-loss DCS is

$$\frac{{\rm d}\sigma_{\rm el}}{{\rm d}W} = 2\pi\left|\frac{dW}{d\left(\cos\theta'\right)}\right|^{-1}\frac{{\rm d}\sigma_{\rm el}}{{\rm d}\Omega'} = \frac{4\pi}{W_{\rm max}}\;\frac{{\rm d}\sigma_{\rm el}}{{\rm d}\Omega'}. \tag{40}$$

The nuclear stopping cross section is defined as

$$\begin{aligned}\sigma_{\rm st} &= \int_0^{W_{\rm max}} W\,\frac{{\rm d}\sigma_{\rm el}}{{\rm d}W}\,{\rm d}W \\ &= \frac{W_{\rm max}}{2}\left(2\pi\int_{-1}^{1}\left(1-\cos\theta'\right)\frac{{\rm d}\sigma_{\rm el}}{{\rm d}\Omega'}\,d\left(\cos\theta'\right)\right) = \frac{W_{\rm max}}{2}\,\sigma_{\rm tr,1}'.\end{aligned} \tag{41}$$

The code PENH simulates the transport of neutrons by using a class II tracking scheme that is analogous to the one employed for protons. The transport of neutrons is simplified by the fact that these particles only experience elastic collisions and nuclear reactions. The cross sections for these two processes are obtained from the partial-wave calculations of elastic scattering. The simulation of neutron-induced nuclear reactions is difficult because of the wide variety of open reaction channels, which are explicitly described in evaluated libraries for neutrons, although only for energies below 20 MeV. Since a detailed description of reactions induced by neutrons down to thermal energies is beyond the capabilities of a dose-calculation code, we consider nuclear reactions as a purely absorptive process that terminates the neutron trajectory and a fraction `FNABS` of the kinetic energy of the absorbed neutron is deposited locally. Comparison with simulation results from the codes FLUKA [11] and GEANT4 [12–14], which do include proper descriptions of neutron production and transport, shows that `FNABS` should be given a value less than unity, indicating that neutron reactions produce high-energy gammas that propagate to large distances from the reaction site. In spite of its crudeness, this procedure is found to provide a realistic correction to the simulated dose whenever the actual flux of neutrons is in "radiative equilibrium" (*i.e.*, when the number and average energy of neutrons that enter a small probe volume equal the number and average energy of those that leave that volume). Under these circumstances, a fraction `FNABS` of the energy absorbed through neutron-induced reactions remains on average at the reaction site.

3 IONIZATION OF INNER ELECTRON SHELLS BY PROTON IMPACT

The slowing down of fast protons in matter is mostly due to inelastic collisions, *i.e.*, collisions causing electronic excitations of the material. Protons also slow down due to elastic collisions with nuclei (the so-called *nuclear stopping*), an effect that is automatically accounted for by the simulation scheme adopted in PENH. The plane-wave Born approximation (PWBA) [15, 16] is suited for describing inelastic collisions of protons with velocities much larger than those of the active target electrons. We consider inelastic collisions of a proton with initial kinetic energy E and momentum $\mathbf{p}$ $[(cp)^2 = E\,(E + 2\,\mathrm{mc}^2)]$ with atoms of atomic number Z, characterized by the energy transfer $W = E - E'$ and the momentum transfer $\mathbf{q} = \mathbf{p} - \mathbf{p}'$, where E' and $\mathbf{p}'$ are, respectively, the energy and momentum of the projectile after the collision. The corresponding DCS is most conveniently considered as a function of the energy transfer W and the recoil energy Q, defined as the kinetic energy of an electron with linear momentum equal to the momentum transfer [15],

$$Q = \sqrt{(cp)^2 + (cp')^2 - 2cp\,cp'\,\cos\theta + \mathrm{m}_e^2c^4} - \mathrm{m}_e c^2. \tag{42}$$

The DCS obtained from the PWBA for ionizing collisions with electrons of a subshell a with binding energy E_a can be expressed as [17].

$$\frac{d^2\sigma_a}{dW\,dQ} = \frac{2\pi z_0^2 e^4}{\mathrm{m}_e v^2}\left[\frac{2\mathrm{m}_e c^2}{WQ\left(Q+2\mathrm{m}_e c^2\right)}\,\frac{df_a(Q,W)}{dW} + \frac{2\mathrm{m}_e c^2 W}{\left[Q\left(Q+2\mathrm{m}_e c^2\right)-W^2\right]^2}\left(\beta^2 - \frac{W^2}{Q\left(Q+2\mathrm{m}_e c^2\right)}\right)\frac{dg_a(Q,W)}{dW}\right] \tag{43}$$

where $z_0 = +1$ is the proton charge in units of e, and the functions $df\ (Q,\ W)/dW$ and $dg\ (Q,\ W)/dW$ are, respectively, the longitudinal and transverse generalized oscillator strengths (GOS). Bote and Salvat [17] have calculated these GOS for all electron shells of atoms with $Z = 1$ to 99 by using an independent-electron model with the Dirac-Hartree-Fock-Slater self-consistent potential of free atoms. The energy-loss DCS is obtained by integration over the kinematically allowed interval of recoil energies, (Q_-, Q_+), with endpoints given by **Eq. 42** with $\cos\theta = +1$ and -1,

$$\frac{\mathrm{d}\sigma_a}{\mathrm{d}W} = \int_{Q_-}^{Q_+} \frac{\mathrm{d}^2\sigma_a}{\mathrm{d}W\,dQ}\,\mathrm{d}Q. \tag{44}$$

In PENELOPE-PENH proton inelastic collisions are described by means of the PWBA with a simplified model of the GOS [1, 2], which is modulated so as to reproduce the cross sections for ionization of inner electron subshells read from the database. The main limitation of the PWBA is due to the neglect of the distortion of the projectile wave functions caused by the field of the target atom. For electrons and positrons, this distortion can be largely accounted for by using the distorted-wave Born approximation (DWBA), in which the projectile states are represented as distorted plane waves (see, *e.g.* [18], and references therein). Because of the slow convergence of the partial-wave series, this kind of calculation is only possible for projectile electrons and positrons with kinetic energies up to about $30E_a$. Bote and Salvat [17] used an optimized computation strategy, which combines the DWBA and the PWBA, to generate a database of electron-impact ionization cross sections for the K shell and the L and M subshells of all the elements from hydrogen to einsteinium ($Z = 1$–99) and for energies of the projectile from 50 eV up to 1 GeV. The results were found to agree well with available experimental data [19].

Unfortunately, the calculation of cross sections for inelastic collisions from the DWBA is not feasible for charged particles heavier than the electron, because the smallness of the de Broglie wavelength of the projectile renders the calculation of free spherical waves extremely difficult. Chen et al. [20], and Chen and Crasemann [21, 22] went beyond the PWBA by using the perturbed-stationary-state approximation of Brandt and Lapicki [23], which accounts for 1) alterations in the binding of the active electron due to the presence of the projectile near the nucleus of the target atom, and 2) the deflection of the projectile path caused by the Coulomb field of the nucleus. In our PWBA calculations of ionization cross sections for protons, these effects are introduced by means of semi-classical correcting factors, which are described in the following paragraphs.

- Binding effect

In collisions where the projectile proton penetrates deep into the target atom, the presence of the projectile modifies the binding energy of the active electron and, in the case of positively charged projectiles, leads to a reduction of the DCS. For the K shell and L subshells, Brandt and Lapicki [23] performed a first-order perturbation analysis, assuming that the projectile follows a straight trajectory and using hydrogenic wave functions. They obtained an ionization-energy shift of the active target electron given by

$$\Delta E_a = \frac{2z_0 E_a}{Z_a \Theta_a}\left[g_a(\xi) - h_a(\xi)\right], \tag{45}$$

where $Z_a = Z - \delta_a$ is the effective nuclear charge felt by the electrons in the unperturbed orbitals, with $\delta_\mathrm{K} = 0.3$ and $\delta_{\mathrm{L}i} = 4.15$. The quantity Θ_a is the reduced ionization energy,

$$\Theta_a = 2n_a^2 E_a/\left(Z_a^2 E_\mathrm{h}\right), \tag{46}$$

where $E_\mathrm{h} = \mathrm{m}_e e^4/\hbar^2 = 27.211$ eV is the Hartree energy. The last factor in **Eq. 45** is a function of the dimensionless parameter

$$\xi \equiv \frac{Z_a E_\mathrm{h}}{n_a E_a}\sqrt{\frac{\mathrm{m}_e}{M}\,\frac{2E}{E_\mathrm{h}}}. \tag{47}$$

In the calculations of ionization of K and L electrons we used the parameterization of the $g_a(\xi)$ and $h_a(\xi)$ functions given by Chen and Crasemann [21].

For M and outer shells, Chen et al. [20] considered that the effective ionization energy is the one of the "united" atom (*i.e.*, of the atom with atomic number $z_0 + Z$). We have adopted a similar

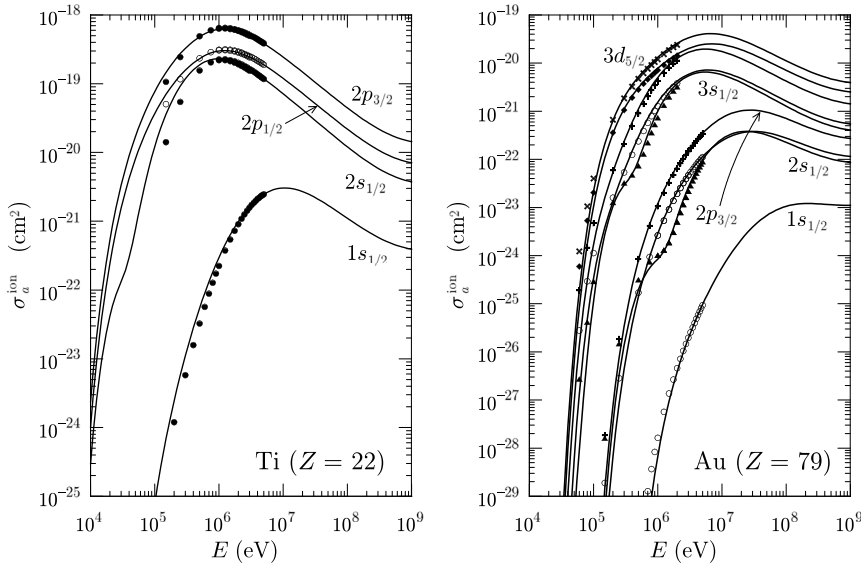

FIGURE 1 | Cross sections for ionization of the K, L and M subshells of titanium and gold by impact of protons as functions of the kinetic energy of the projectile. Solid curves represent the values in the PENH database. Symbols are results from equivalent PWBA calculations by Chen and Crasemann [21, 22], which also include the binding and Coulomb-deflection corrections.

approach, which avoids the need of considering ionization energies of other atomic species. Expressing the ionization energies of the unperturbed states as (screened hydrogenic levels)

$$E_a = \frac{\left(Z - \delta_a'\right)^2}{2n_a^2}\, E_{\rm h}, \tag{48a}$$

and noting that the screening constant δ_a' is nearly the same for neighbouring elements, we can approximate the effective ionization energy in the form

$$E_a' = \frac{\left(z_0 + Z - \delta_a'\right)^2}{2n_a^2}\, E_{\rm h}. \tag{48b}$$

This gives the following ionization-energy shift

$$\Delta E_a = E_a' - E_a = \frac{z_0^2 + 2z_0\left(Z - \delta_a'\right)}{2n_a^2}\, E_{\rm h}. \tag{49}$$

- Coulomb deflection

For projectiles with small speeds, the PWBA, and the equivalent straight-trajectory semi-classical approximation [see, *e.g.*, Ref. [24], and references therein], overestimate the ionization cross sections because they neglect the effect of the Coulomb field of the nucleus on the trajectory of the projectile. In the semi-classical treatment, the energy-loss DCS for a projectile following a classical hyperbolic orbit in the Coulomb potential of the bare target nucleus can be obtained by multiplying the energy-loss DCS, calculated by assuming that the projectile follows a straight trajectory, by a correction factor. This Coulomb-deflection factor was approximated as [23].

$$F_a^{\rm Coul}(E;W) = \left(1 - \frac{1}{3}x^{1/3} + \frac{5}{3}x^{2/3}\right)\exp\left(-2\pi x\right), \tag{50}$$

where

$$x = Z_0 Z \sqrt{\frac{M^3}{8m_e M_{\rm red}^2}\,\frac{E_{\rm h}}{E^3}}\, W. \tag{51}$$

The ionization cross section, including the binding and Coulomb-deflection corrections, is given by

$$\sigma_a^{\rm ion} = \int_{E_a+\Delta E_a}^{W_{\max}} F_a^{\rm Coul}(E;W)\,\frac{{\rm d}\sigma_a^{\rm cont}}{{\rm d}W}\,dW. \tag{52}$$

We have generated a database of proton-impact ionization cross sections for the K shell and the L, M and N subshells of the elements with Z = 1 to 99, by numerical integration of the energy-loss DCS obtained from the longitudinal and transverse GOSs calculated by Bote and Salvat [17]. **Figure 1** displays these ionization cross sections for electron subshells of the titanium and gold atoms. For comparison purposes, the plots include also values calculated by Chen and Crasemann [21, 22] for the DHFS potential but only with the longitudinal GOS. It is worth mentioning that our database includes relativistic effects in a more consistent way, and it covers the energy range up to 10^{11} eV for all elements from hydrogen (Z = 1) to einsteinium (Z = 99).

In the simulation code, the ionization cross sections are multiplied by an energy-dependent factor (deduced from the Sternheimer-Liljequist GOS model) that accounts for the reduction of the cross section caused by the density-effect correction [3].

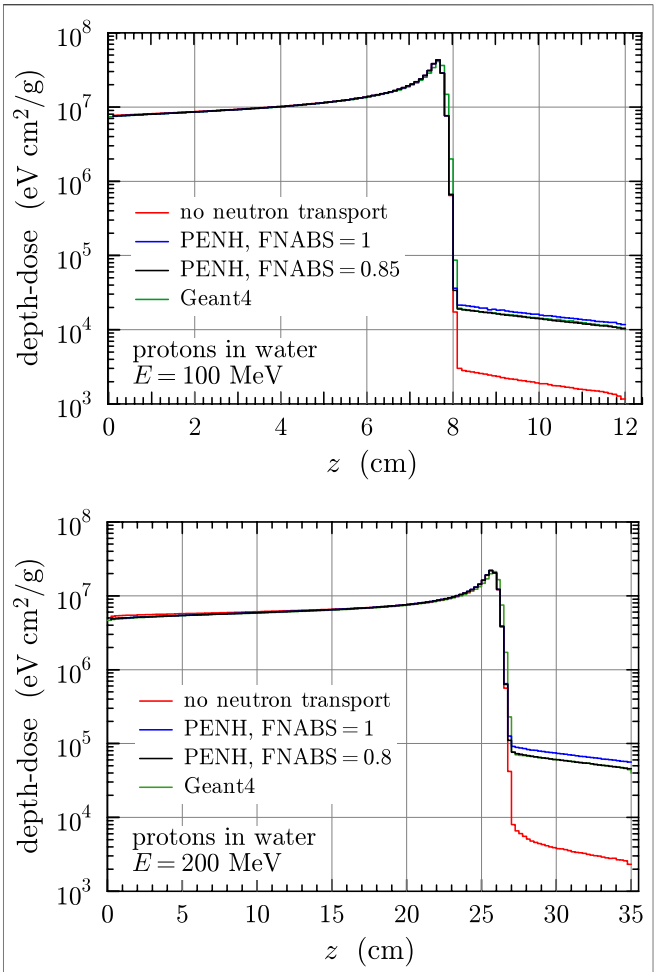

FIGURE 2 | Depth-dose functions of 100 and 200 MeV proton beams impinging normally on a water phantom. The green histograms are results from the GEANT4 code. Other histograms represent results from PENH with neutrons absorbed at the reaction site (red), and neutrons transported as explained in **Section 2.4** with the indicated values of FNABS (blue and black).

4 NEUTRON CONTRIBUTION TO THE DOSE DISTRIBUTION

The databases presented in the previous Sections for elastic collisions and impact ionization of protons provide realistic models for electromagnetic interactions of protons, and the class II simulation scheme avoids the use of multiple scattering approximations and their associated uncertainties.

As mentioned above, the original PENH code [3] gave a spatial dose distribution that was nearly correct near the proton beam axis, but the simulated dose was too small far from the beam axis. This was first noted by Verbeek et al. [25] and latter confirmed by the authors through comparison with results from the FLUKA and GEANT4 codes, which include neutron transport. The main cause of this underestimation of the distant dose was attributed to the neglect of neutron transport, and this motivated the inclusion of the present simple approach for neutrons. Preliminary simulations with the parameter FNABS = 1 gave depth-dose distributions from pencil beams of protons that were closer to, but slightly exceeded those from GEANT4. The discrepancy can be readily corrected by using a smaller value of FNABS.

Figure 2 compares depth-dose distributions of proton beams incident normally on a water phantom with energies of 100 and 200 MeV simulated with the PENH and GEANT4 codes. The red histograms were produced by assuming that neutrons resulting from proton-induced nuclear reactions are absorbed at the reaction site. The blue histograms resulted from assuming that neutrons are transported as described in **Section 2.4** with FNABS = 1. It is seen that the transport and absorption of neutrons increases the depth-dose beyond the Bragg peak by nearly a factor of 10, slightly exceeding the depth-dose generated by the GEANT4 code (green histograms). Reducing the value of FNABS to 0.85 and to 0.8 for 100 and 200 MeV protons gives depth-dose distributions nearly coincident with those from

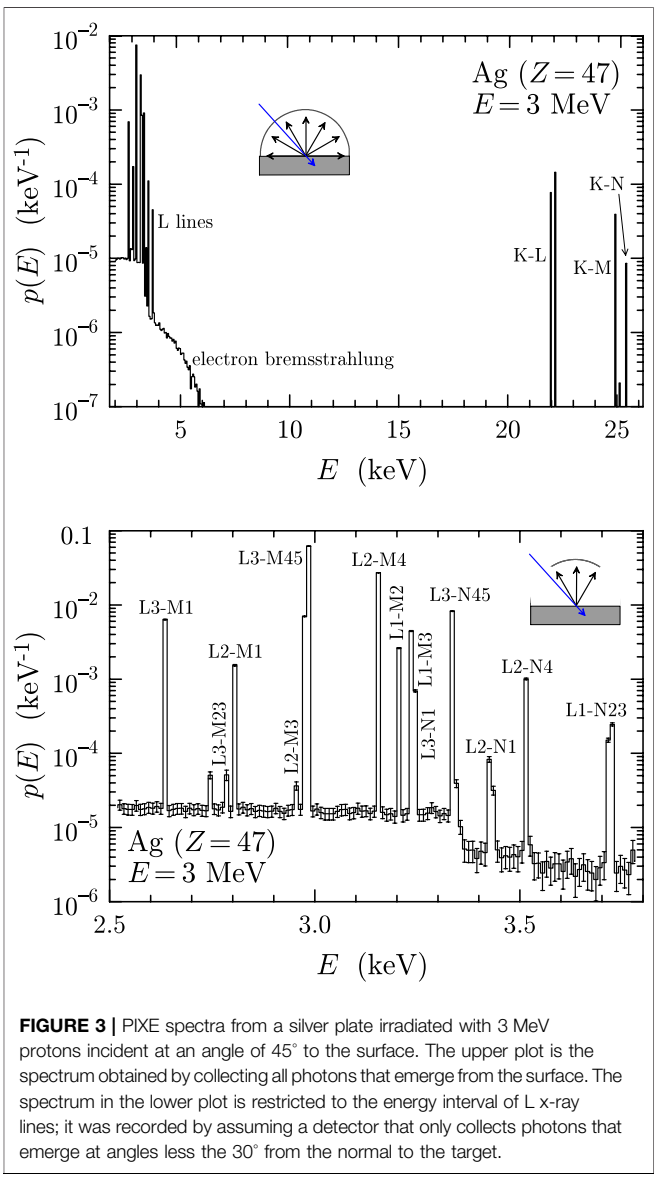

FIGURE 3 | PIXE spectra from a silver plate irradiated with 3 MeV protons incident at an angle of 45° to the surface. The upper plot is the spectrum obtained by collecting all photons that emerge from the surface. The spectrum in the lower plot is restricted to the energy interval of L x-ray lines; it was recorded by assuming a detector that only collects photons that emerge at angles less the 30° from the normal to the target.

GEANT4. The latter are seen to agree closely with the PENH result, except in the deep fall of the Bragg peak, probably because of differences in the proton transport physics of the two codes. Another relevant effect of neutron transport is a slight decrease of the depth-dose at shallow depths, which is visible in the plot for the 200 MeV beam; this effect is expected to increase in importance with the energy of incident protons because of the higher energies of the released neutrons.

5 SIMULATION OF PROTON-INDUCED X-RAY EMISSION

As PENH uses fairly reliable cross sections for proton impact ionization, together with a careful modeling of electromagnetic interactions, it may be used to simulate proton-induced x-ray emission (PIXE) spectra [26]. The code describes the relaxation of ionized atoms by means of the PENELOPE subroutines, which use transition probabilities from the Evaluated Atomic Data Library of Perkins et al. [27] and empirical values of the x-ray energies [1]. The simulation of PIXE spectra by PENH is analogous to that of electron induced x-ray emission by the PENELOPE code, which has been proved to be effective for quantification in electron-probe microanalysis [28]. It is worth noticing that PENH accounts for both the attenuation and the generation of x-ray fluorescence within the target. It also follows the bremsstrahlung emitted by secondary electrons, which produces a smooth background of in the simulated PIXE spectra. Primary protons also contribute to the background through the emission of atomic bremsstrahlung (see [29] and references therein), however, this mechanism is not accounted for in PENH. In its present form, our simulation code can be useful to determine the influence of the composition and local geometry of the irradiated target on the line intensities of the emitted x rays.

Figure 3 displays results from two simulations of x-ray spectra emitted from a silver target bombarded with 3 MeV protons impinging in a direction at an angle of 45° from the target surface. In those simulations neutrons were not followed, and the variance reduction techniques of interaction forcing and emission splitting of bremsstrahlung photons and x rays [1] were applied. The upper plot shows the energy spectrum of all photons that emerge from the target. The continuous background corresponds to bremsstrahlung emitted by secondary electrons. Since the maximum energy of secondary electrons released in inelastic collisions of 3 MeV photons is about 6.5 keV, the spectral background ends at this energy. A weak and noisy background component that extends to higher energies in the simulated spectrum (not shown in the upper plot of **Figure 3**) corresponds to gamma rays released in proton-induced nuclear reactions. The lower plot of **Figure 3** shows the energy spectrum of photons that emerge in directions forming angles less than 30° with the normal to the target, restricted to the energy interval of L lines. The most prominent x-ray lines can be readily identified from their numerical values in the PENELOPE database.

Simulated photon spectra correspond to an ideal detector with unit efficiency. They are output in the form of histograms with a fixed bin width, which implies a resolution in energy of the order of the bin width. To get results with an appearance closer to measurement data, the simulated spectrum should be convolved with the response function of the detector [28]. Comparison of spectra so obtained with measured spectra may help to identify features not evident from the experimental result.

6 CONCLUDING COMMENTS

In its present form, the PENH code provides a consistent description of electromagnetic interactions of electrons, positrons and protons with matter for projectiles with energies up to 1 GeV. The use of nuclear data from ENDF-formatted files allows accounting for proton-induced nuclear reactions, and the release of gammas and secondary particles resulting from these interactions, in the energy range covered by available libraries, which usually extends up to about 200 MeV. For protons with somewhat higher energies, the code can extrapolate the nuclear data, with the risk of distorting the results.

Since the interaction models implemented in PENH lose validity at low energies, the code should not be used for electrons, positrons and photons with $E \lesssim 1$ keV, and for protons and neutrons with $E < 100$ keV.

The method adopted for tracking neutrons is intended only to correct for the effect of neutron transport on the simulated dose distributions, of interest mostly in proton therapy. Processes where neutrons may have more relevance cannot be dealt with PENH.

DATA AVAILABILITY STATEMENT

The raw data supporting the conclusions of this article will be made available by the authors, without undue reservation.

AUTHOR CONTRIBUTIONS

All authors listed have made a substantial, direct, and intellectual contribution to the work and approved it for publication.

FUNDING

Financial support from the Spanish Ministerio de Ciencia, Innovación y Universidades /Agencia Estatal de Investigación /European Regional Development Fund, European Union, (projects nos. RTI2018-098117-B-C21 and RTI2018-098117-B-C22) is gratefully aknowledged.

REFERENCES

1. Salvat F. *PENELOPE 2018: A Code System for Monte Carlo Simulation of Electron and Photon Transport*. Boulogne-Billancourt, France: OECD Nuclear Energy Agency (2019). document NEA/MBDAV/R(2019)1. doi:10.1787/32da5043-en
2. Salvat F. A Generic Algorithm for Monte Carlo Simulation of Proton Transport. *Nucl Instr Methods Phys Res Section B: Beam Interactions Mater Atoms* (2013) 316:144–59. doi:10.1016/j.nimb.2013.08.035
3. Salvat F, Quesada JM. Nuclear Effects in Proton Transport and Dose Calculations. *Nucl Instr Methods Phys Res Section B: Beam Interactions Mater Atoms* (2020) 475:49–62. doi:10.1016/j.nimb.2020.03.017
4. Koning AJ, Delaroche JP. Local and Global Nucleon Optical Models from 1 keV to 200 MeV. *Nucl Phys A* (2003) 713:231–310. doi:10.1016/s0375-9474(02)01321-0
5. Salvat F, Martínez JD, Mayol R, Parellada J. Analytical Dirac-Hartree-Fock-Slater Screening Function for Atoms (Z=1-92). *Phys Rev A* (1987) 36:467–74. doi:10.1103/physreva.36.467
6. Trkov A, Herman M. ENDF-6 Formats Manual: Data Formats and Procedures for the Evaluated Nuclear Data Files. Technical Report CSEWG Document ENDF-102. Upton, NY: Brookhaven National Laboratory (2018). Report BNL-90365-2009 Rev. 2. doi:10.2172/1425114
7. Salvat F, Fernández-Varea JM. Radial: A Fortran Subroutine Package for the Solution of the Radial Schrödinger and Dirac Wave Equations. *Comput Phys Commun* (2019) 240:165–77. doi:10.1016/j.cpc.2019.02.011
8. Olver F, Lozier D, Boisvert R, Clark C. *NIST Handbook of Mathematical Functions*. New York: Cambridge University Press (2010). Available from: http://dlmf.nist.gov/ (Accessed December 1, 2021).
9. Coursey J. S., Schwab D. J., Tsai J. J., Dragoset R. A.. *Atomic Weights and Isotopic Compositions with Relative Atomic Masses*. [Dataset]. Gaithersburg, MD: National Institute of Standards and Technology (2015). Available from www.nist.gov/srd/chemistry (Accessed December 1, 2021).
10. Su X-W, Han Y-L. Global Optical Model Potential for Alpha Projectile. *Int J Mod Phys E* (2015) 24:1550092. doi:10.1142/s0218301315500925
11. Ferrari A, Sala PR, Fassò A, Ranft J. Fluka: a Multi-Particle Transport Code. Technical Report CERN-2005-00X. Geneva: CERN (2005). INFN TC 05/11, SLAC-R-773. doi:10.2172/877507
12. Agostinelli S, Allison J, Amako K, Apostolakis J, Araujo H, Arce P, et al. Geant4—a Simulation Toolkit. *Nucl Instrum Meth A* (2003) 506:250–303. doi:10.1016/S0168-9002(03)01368-8
13. Allison J, Amako K, Apostolakis J, Araujo HM, Arce Dubois P, Asai M, et al. Geant4 Developments and Applications. *IEEE Trans Nucl Sci* (2006) 53:270–8. doi:10.1109/TNS.2006.869826
14. Allison J, Amako K, Apostolakis J, Arce P, Asai M, Aso T, et al. Recent Developments in Geant4. *Nucl Instrum Meth A* (2016) 835:186–225. doi:10.1016/j.nima.2016.06.125
15. Fano U. Penetration of Protons, Alpha Particles, and Mesons. *Annu Rev Nucl Sci* (1963) 13:1–66. doi:10.1146/annurev.ns.13.120163.000245
16. Inokuti M. Inelastic Collisions of Fast Charged Particles with Atoms and Molecules-The Bethe Theory Revisited. *Rev Mod Phys* (1971) 43:297–347. doi:10.1103/revmodphys.43.297
17. Bote D, Salvat F. Calculations of Inner-Shell Ionization by Electron Impact with the Distorted-Wave and Plane-Wave Born Approximations. *Phys Rev A* (2008) 77:042701. doi:10.1103/physreva.77.042701
18. Segui S, Dingfelder M, Salvat F. Distorted-wave Calculation of Cross Sections for Inner-Shell Ionization by Electron and Positron Impact. *Phys Rev A* (2003) 67:062710. doi:10.1103/physreva.67.062710
19. Llovet X, Powell CJ, Salvat F, Jablonski A. Cross Sections for Inner-Shell Ionization by Electron Impact. *J Phys Chem Reference Data* (2014) 43:013102. doi:10.1063/1.4832851
20. Chen MH, Crasemann B, Mark H. Relativistic Calculation of atomicM-Shell Ionization by Protons. *Phys Rev A* (1983) 27:2358–64. doi:10.1103/physreva.27.2358
21. Hsiung Chen M, Crasemann B. Relativistic Cross Sections for Atomic K- and L-Shell Ionization by Protons, Calculated from a Dirac-Hartree-Slater Model. *At Data Nucl Data Tables* (1985) 33:217–33. doi:10.1016/0092-640x(85)90002-6
22. Chen MH, Crasemann B. Atomic K-, L-, and M-Shell Cross Sections for Ionization by Protons: A Relativistic Hartree-slater Calculation. *At Data Nucl Data Tables* (1989) 41:257–85. doi:10.1016/0092-640x(89)90020-x
23. Brandt W, Lapicki G. L-shell Coulomb Ionization by Heavy Charged Particles. *Phys Rev A* (1979) 20:465–80. doi:10.1103/physreva.20.465
24. Amundsen PA. Coulomb Deflection Effects in Ion-Induced K-Shell Ionisation. *J Phys B: Mol Phys* (1977) 10:2177–87. doi:10.1088/0022-3700/10/11/018
25. Verbeek N, Wulff J, Bäumer C, Smyczek S, Timmermann B, Brualla L. Single Pencil Beam Benchmark of a Module for Monte Carlo Simulation of Proton Transport in the PENELOPE Code. *Med Phys* (2020) 48:456–76. doi:10.1002/mp.14598
26. Ishii K. PIXE and its Applications to Elemental Analysis. *QuBS* (2019) 3:12. doi:10.3390/qubs3020012
27. Perkins ST, Cullen DE, Chen MH, Hubbell JH, Rathkopf J, Scofield J. Tables and Graphs of Atomic Subshell and Relaxation Data Derived from the LLNL Evaluated Atomic Data Library (EADL), Z = 1–100. Technical Report UCRL-ID-50400. Livermore, California: Lawrence Livermore National Laboratory (1991).
28. Llovet X, Salvat F. PENEPMA: A Monte Carlo Program for the Simulation of X-Ray Emission in Electron Probe Microanalysis. *Microsc Microanal* (2017) 23:634–46. doi:10.1017/s1431927617000526
29. Ishii K, Yamazaki H, Matsuyama S, Galster W, Satoh T, Budnar M. Contribution of Atomic Bremsstrahlung in PIXE Spectra and Screening Effect in Atomic Bremsstrahlung. *X-ray Spectrom* (2005) 34:363–5. doi:10.1002/xrs.838

Conflict of Interest: The authors declare that the research was conducted in the absence of any commercial or financial relationships that could be construed as a potential conflict of interest.

frontiers in Physics

ORIGINAL RESEARCH
published: 14 December 2021
doi: 10.3389/fphy.2021.738735

The PENELOPE Physics Models and Transport Mechanics. Implementation into Geant4

Makoto Asai[1], *Miguel A. Cortés-Giraldo*[2]*, *Vicent Giménez-Alventosa*[3], *Vicent Giménez Gómez*[4] *and Francesc Salvat*[5]*

[1]SLAC National Accelerator Laboratory, Menlo Park, CA, United States, [2]Dep. de Física Atómica, Molecular y Nuclear, Universidad de Sevilla, Sevilla, Spain, [3]I3M Instituto de Instrumentación para Imagen Molecular, CSIC-Universitat Politècnica de València, València, Spain, [4]Dep. Física Teòrica and IFIC, Universitat de València-CSIC, Burjassot, Spain, [5]Facultat de Física (FQA and ICC), Universitat de Barcelona, Barcelona, Spain

A translation of the PENELOPE physics subroutines to C++, designed as an extension of the GEANT4 toolkit, is presented. The Fortran code system PENELOPE performs Monte Carlo simulation of coupled electron-photon transport in arbitrary materials for a wide energy range, nominally from 50 eV up to 1 GeV. PENELOPE implements the most reliable interaction models that are currently available, limited only by the required generality of the code. In addition, the transport of electrons and positrons is simulated by means of an elaborate class II scheme in which hard interactions (involving deflection angles or energy transfers larger than pre-defined cutoffs) are simulated from the associated restricted differential cross sections. After a brief description of the interaction models adopted for photons and electrons/positrons, we describe the details of the class-II algorithm used for tracking electrons and positrons. The C++ classes are adapted to the specific code structure of GEANT4. They provide a complete description of the interactions and transport mechanics of electrons/positrons and photons in arbitrary materials, which can be activated from the G4ProcessManager to produce simulation results equivalent to those from the original PENELOPE programs. The combined code, named PENG4, benefits from the multi-threading capabilities and advanced geometry and statistical tools of GEANT4.

Keywords: coupled electron-photon transport, Monte Carlo simulation, PENELOPE code system, random-hinge method, GEANT4 toolkit

OPEN ACCESS

Edited by:
Laurent Ottaviani,
Aix-Marseille Université, France

Reviewed by:
Matteo Duranti,
Istituto Nazionale di Fisica Nucleare di Perugia, Italy
Tuba Conka Yildiz,
Türkisch-Deutsche Universität, Turkey

****Correspondence:***
Miguel A. Cortés-Giraldo
miancortes@us.es
Francesc Salvat
francesc.salvat@ub.edu

Specialty section:
This article was submitted to Radiation Detectors and Imaging, a section of the journal Frontiers in Physics

Received: *09 July 2021*
Accepted: *18 October 2021*
Published: *14 December 2021*

Citation:
Asai M, Cortés-Giraldo MA, Giménez-Alventosa V, Giménez Gómez V and Salvat F (2021) The PENELOPE Physics Models and Transport Mechanics. Implementation into Geant4. Front. Phys. 9:738735. doi: 10.3389/fphy.2021.738735

1 INTRODUCTION

Monte Carlo simulation has become the tool of choice for describing the transport of radiation through matter. The general-purpose code system PENELOPE[1] [1, 2] provides a reliable description of the coupled transport of electrons and photons in a wide energy range, nominally, from 50 eV up to 1 GeV, which are the lower and upper limits of the interval covered by the interaction database. However, the approximations underlying the interaction models and the tracking algorithm are expected to be valid only for energies larger than about 1 keV. Therefore, the results from simulations of particles with energies less than this value should be considered as semi-quantitative. The code has been used in a variety of applications, including dosimetry, radiation metrology, radiotherapy,

[1]The name is an acronym that stands for "PENetration and Energy LOss of Positrons and Electrons."

detector characterization, electron microscopy and microanalysis, and x-ray fluorescence. After more than 25 years of development guided by user needs and physics improvements, PENELOPE has become a robust and versatile simulation tool with unique capabilities in electron transport. Direct evidence of the reliability of the code was given by a series of benchmark comparisons of simulation results with a variety of absolute measurement data from the literature [3].

The PENELOPE code is programmed in Fortran, mostly in Fortran 77 with a few extensions of Fortran 90. The original programs are readable and well documented, with abundance of comments, and are accompanied by a detailed manual [2] where the physics models, particle tracking scheme, and numerical sampling methods are described. However the Fortran programs do not allow running parallel simulations (only a manual process is provided to run independent simulations in different processing units, with a summing program to collect the results in a single set of output files). In addition, the Fortran subroutines are difficult to link to other simulation codes. The C++ code presented here is a strict translation of the original Fortran subroutines, which can be linked to GEANT4 [4–6] so as to make the PENELOPE physics available as part of the GEANT4 toolkit, and to take advantage of the multi-threading capabilities and advanced geometry and statistical tools of GEANT4.

The subroutine package PENELOPE is designed as a generator of random electron-photon showers in material media of infinite extent. In the simulations, all position and direction vectors refer to a fixed orthogonal frame, the laboratory frame, which is implicitly set through the geometry definition. Lengths and energies are given in cm and eV, respectively. Occasionally, directions (unit vectors, $\hat{\mathbf{d}}$) are specified by giving their polar and azimuthal angles, θ and ϕ, respectively. We have

$$\hat{\mathbf{d}} = (u, v, w) = (\sin\theta\ \cos\phi,\ \sin\theta\ \sin\phi,\ \cos\theta), \tag{1}$$

where u, v, w are the Cartesian components (direction cosines) of the vector $\hat{\mathbf{d}}$. The state of a transported particle is determined by its energy E, position coordinates, $\mathbf{r} = (x, y, z)$, and the unit vector $\hat{\mathbf{d}}$ in the direction of flight. The physics simulation subroutines generate each particle history as a random sequence of free flights and interactions. The length s of the free flight, the kind of interaction that occurs at the end of the flight, as well as the energy loss W and the angular deflection $\Omega = (\theta, \phi)$ caused by that interaction, are sampled randomly from appropriate probability density functions determined by the differential cross sections of the active interaction processes.

The type of particles that are transported is identified by the value of the integer label KPAR (= 1, electron; 2, photon; 3, positron). Each particle trajectory is simulated from its initial state $(\mathbf{r}, E, \hat{\mathbf{d}})$ until its energy becomes less than the corresponding absorption energy $E_{\rm abs}$(KPAR) selected by the user, where the simulation of the trajectory terminates. Secondary particles with energies larger than $E_{\rm abs}$(KPAR) may be released in interactions (other than Rayleigh scattering of photons and elastic scattering of electrons and positrons), as well as in the relaxation of atoms following inner-shell ionization (x-rays and Auger electrons). Secondary particles are initially stored in a LIFO (last-in-first-out) stack, and they are simulated after completion of the current particle trajectory.

The present article is organized as follows. The physics interaction models implemented in PENELOPE are briefly described in **Section 2**. **Section 3** deals with the generation of electron-photon showers. Photons are simulated by means of the conventional detailed (*i.e.*, interaction-by-interaction) method. The tracking of electrons and positrons is performed by means of a flexible class-II (mixed) algorithm, which is tuned by a small number of user-defined simulation parameters. The algorithm is tailored to optimize accuracy (*i.e.*, consistency with detailed simulation) and stability under variations of the simulation parameters. Since the PENELOPE approach has clear advantages in front of the condensed multiple-scattering schemes adopted in most general-purpose Monte Carlo codes, we present a detailed formulation of the class-II algorithm, which is extensible to simulate the transport of charged particles other than electrons and positrons. The C++ version of the PENELOPE classes and their linking to GEANT4 are described in **Section 4**. Sample simulation results are presented in **Section 5**, where we also verify the consistency of the integration of PENELOPE into GEANT4 with the original Fortran programs. Finally, in **Section 6** we give a few concluding comments.

2 INTERACTION MODELS

The materials where radiation propagates are assumed to be amorphous, homogeneous and isotropic. PENELOPE describes the relevant interactions of transported particles by means of the corresponding differential cross sections (DCSs). In a typical collision measurement, projectile particles with energy E moving in the direction $\hat{\mathbf{d}} = \hat{\mathbf{z}}$ impinge on the target and, after the interaction, they emerge with energy $E - W$ in the direction $\mathbf{d}'$ defined by the polar and azimuthal scattering angles θ and ϕ, respectively. The quantity W is the energy transfer in the interaction. Each interaction process (int) is defined by its "molecular" DCS per unit energy transfer and per unit solid angle,

$$\frac{\mathrm{d}\sigma_{\rm int}(E)}{\mathrm{d}W\,\mathrm{d}\Omega} = \sigma_{\rm int}(E)\ p_{\rm int}(E; W, \theta, \phi), \tag{2}$$

where $\sigma_{\rm int}(E)$ is the total cross section,

$$\sigma_{\rm int} = \int_0^E \mathrm{d}W \int \mathrm{d}\Omega\ \frac{\mathrm{d}\sigma_{\rm int}(E)}{\mathrm{d}W\,\mathrm{d}\Omega}, \tag{3}$$

and $p_{\rm int}(E;\ W,\ \theta,\ \phi)$ is the normalized joint probability density function of the energy transfer and the scattering angles θ and ϕ. Because of the assumed isotropy of the medium, the DCSs are generally independent of the azimuthal angle; the only exceptions are the DCSs for interactions of polarized photons. For simulation purposes, it is convenient to replace the polar angle θ with the variable

$$\mu = \frac{1 - \cos\theta}{2}, \tag{4}$$

which varies from 0 ($\theta = 0$) to 1 ($\theta = \pi$). Notice that the element of solid angle is $\mathrm{d}\Omega = \sin\theta\ \mathrm{d}\theta\ \mathrm{d}\phi = 2\ \mathrm{d}\mu\ \mathrm{d}\phi$. The DCS, per unit energy transfer and per unit deflection is then

$$\frac{\mathrm{d}\sigma_{\mathrm{int}}(E)}{\mathrm{d}W\mathrm{d}\mu} = 2\int_0^{2\pi}\mathrm{d}\phi\ \frac{\mathrm{d}\sigma_{\mathrm{int}}(E)}{\mathrm{d}W\mathrm{d}\Omega} = 4\pi\ \frac{\mathrm{d}\sigma_{\mathrm{int}}(E)}{\mathrm{d}W\mathrm{d}\Omega}. \quad (5)$$

The last expression is valid only when scattering is axially symmetric, in which case the azimuthal angle is a random variable uniformly distributed in $[0, 2\pi)$.

The mean free path between interactions is

$$\lambda_{\mathrm{int}}(E) = \frac{1}{\mathcal{N}\sigma_{\mathrm{int}}(E)}. \quad (6)$$

$\mathcal{N}$ is the number of molecules per unit volume, given by

$$\mathcal{N} = \frac{N_{\mathrm{A}}\rho}{A_{\mathrm{m}}}, \quad (7)$$

where $N_{\mathrm{A}} = 6.022\,141\,29 \times 10^{23}$ g/mol is Avogadro's number, ρ is the mass density (g/cm^3), and A_{m} is the molar mass (g/mol) of the material. The inverse mean free path $\lambda_{\mathrm{int}}^{-1} = \mathcal{N}\sigma_{\mathrm{int}}$ gives the interaction probability per unit path length of the projectile.

The interaction models implemented in PENELOPE combine results from first-principles calculations, semi-empirical formulas and evaluated databases. The DCS of each interaction mechanism is either defined numerically or given by an analytical formula with parameters fitted to relevant theoretical or experimental information. PENELOPE uses the most accurate physics models available that are compatible with the intended generality of the code.

Most of the physics models pertain to interactions with free atoms or with single-element materials. In the case of a compound (or mixture), the molecular DCS is obtained by means of the independent-atom approximation (*i.e.*, as the sum of DCSs of the atoms in a molecule). This approximation is expected to be valid whenever the de Broglie wave length of the radiation is much shorter than typical inter-atomic distances in the material. Inelastic collisions of charged particles are peculiar in that they are dominated by excitations of weakly bound electrons and, hence, they are strongly affected by the state of aggregation of the material. The DCS for inelastic collisions is obtained from an analytical model with parameters determined by the mass density ρ and the mean excitation energy I of the material, the central parameter in the Bethe stopping power formula [7, 8]. Empirical I values of materials [9] are used, so as to account approximately for the aggregation state of the material.

The PENELOPE code system includes an extensive database of atomic DCSs and total (integrated) cross sections, for all elements in the periodic system, from hydrogen ($Z = 1$) to einsteinium ($Z = 99$), covering the energy range from 50 eV to 1 GeV. In the following Subsections we give a brief description of the interaction models adopted for photons and electrons/positrons. Further details on the physics models, and a thorough description of sampling methods for the different interaction mechanisms, are given in the PENELOPE manual [2]. References to the underlying theory and calculations can also be found in the review article by Salvat and Fernández-Varea [10].

2.1 Photon Interactions

The considered interactions of photons and the corresponding physics models are:

- *Rayleigh scattering (Ra).* The DCS for the coherent scattering of unpolarized photons by atoms is a function of the polar angle θ of the direction of the scattered photon. It is expressed as the product of the Thomson DCS (which describes the scattering of electromagnetic waves by free electrons at rest) and the squared modulus of the atomic form factor plus angle-independent anomalous scattering factors [11]. The atomic form factors and the total (integrated) atomic cross sections are taken from the LLNL Evaluated Photon Data Library [12]. The direction of the scattered photon is sampled from the DCS in the form-factor approximation, *i.e.*, disregarding the anomalous scattering factors.
- *Compton scattering (Co).* The atomic DCS for the incoherent scattering of photons by atoms depends on the direction and energy E' of the scattered photon. It is calculated from the relativistic impulse approximation with analytical one-electron Compton profiles [13] that approach the numerical Hartree-Fock Compton profiles given by Biggs *et al.* [14]. This approximation accounts for the effect of electron binding and Doppler broadening in a consistent way. The total atomic cross section is obtained as the sum of contributions of the various electron subshells. In the case of conductors, conduction electrons are assumed to behave as a degenerate electron gas having the electron density of the conduction band. The DCS for Compton scattering is a function of the energy transfer $W = E - E'$ and the polar angle θ of the direction of the scattered photon.
- *Photoelectric absorption (ph).* The photoelectric effect is described by using total atomic cross sections, and partial cross sections for the K shell and L, M, and N subshells of neutral atoms, which were calculated by using conventional first-order perturbation theory [15]. In these calculations (as well as in those of impact ionization by electron and positron impact, *see* below), atomic wave functions are represented as single Slater determinants built with one-electron orbitals that are solutions of the Dirac equation for the Dirac-Hartree-Fock-Slater self-consistent potential [16, 17]. The cross sections in the database account only for ionization, *i.e.*, contributions from excitations of atoms to discrete bound energy levels are disregarded. Additionally, the photon energy was shifted slightly so that the shell ionization thresholds coincide with the electron binding energies recommended by Carlson [18], which were obtained from a combination of experimental data and theoretical calculations. Our cross sections practically coincide with those in the LLNL Evaluated Photon Data Library [12], although they are tabulated in a denser grid of energies to accurately describe the structure of the cross section near absorption edges. A screening normalization correction, initially proposed by Pratt [19] is included. The initial direction of photoelectrons is sampled from Sauter's K-shell hydrogenic DCS [20], which is a function of the polar angle θ of the direction of the emitted photoelectron.
- *Electron-positron pair production (pp).* The total atomic cross sections for pair (and triplet) production were obtained from the XCOM program of Berger *et al.* [21]. The initial kinetic energies of the produced particles are sampled from the Bethe-Heitler DCS for pair production,

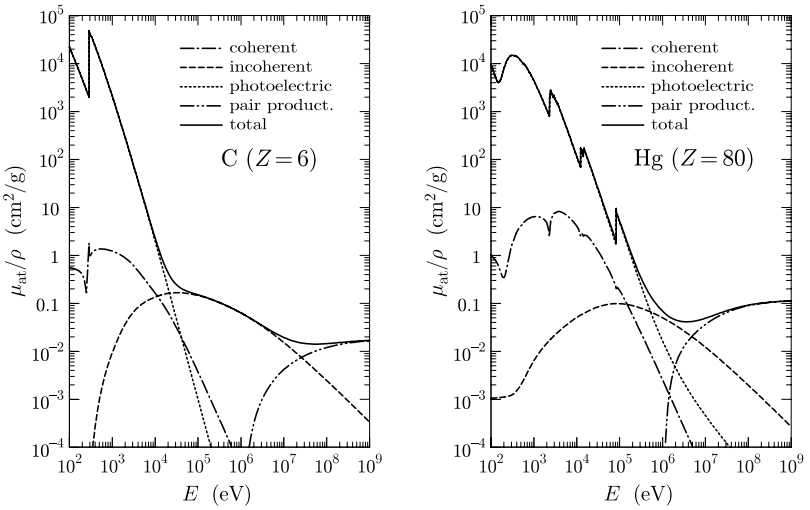

FIGURE 1 | Partial and total mass attenuation coefficients of carbon and mercury as functions of the photon energy. Notice the different low-E behavior of the incoherent-scattering contribution, $\mathcal{N}\sigma_{\mathrm{Co}}/\rho$, for insulators (carbon) and conductors (mercury).

with exponential screening and Coulomb correction, empirically modified to improve its reliability for energies near the pair-production threshold. This DCS is a function of the kinetic energy of the electron, E_{-}; the energy of the positron is determined by energy conservation.

The total cross section for each of these processes is obtained by integration of its DCS,

$$\frac{\mathrm{d}\sigma_{\mathrm{Ra}}(E)}{\mathrm{d}\mu}, \quad \frac{\mathrm{d}^2\sigma_{\mathrm{Co}}(E)}{\mathrm{d}W\mathrm{d}\mu}, \quad \frac{\mathrm{d}\sigma_{\mathrm{ph}}(E)}{\mathrm{d}\mu}, \quad \text{and} \quad \frac{\mathrm{d}\sigma_{\mathrm{pp}}(E)}{\mathrm{d}E_{-}}, \tag{8}$$

over the corresponding variables. The total molecular cross section, σ_{tot}, is the sum of contributions,

$$\sigma_{\mathrm{tot}}(E) = \sigma_{\mathrm{Ra}}(E) + \sigma_{\mathrm{Co}}(E) + \sigma_{\mathrm{ph}}(E) + \sigma_{\mathrm{pp}}(E). \tag{9}$$

The length s of each photon free flight is sampled from the familiar exponential distribution

$$p(s) = \mu_{\mathrm{at}} \ \exp\left(-\mu_{\mathrm{at}} s\right), \tag{10}$$

where

$$\mu_{\mathrm{at}}(E) = \mathcal{N}\sigma_{\mathrm{tot}}(E) \tag{11}$$

is the attenuation coefficient (*i.e.*, the inverse mean free path) for photons of energy E. Partial and total mass attenuation coefficients, μ_{at}/ρ, of carbon and mercury are displayed in **Figure 1**.

PENELOPE can also simulate Rayleigh and Compton scattering of polarized photons, with the state of polarization described by means of the Stokes parameters [2]. The polarization of photons does not alter neither the total cross sections nor the distributions of polar angles (*see*, *e.g.*, Ref. [2]), but the distribution of azimuthal angles ceases to be uniform. Characteristic x rays and bremsstrahlung photons emitted by electrons or positrons, as well as positron annihilation quanta, are assumed to be unpolarized.

2.2 Electron and Positron Interactions

The interactions of electrons and positrons considered in PENELOPE are:

- *Elastic collisions (el).* The DCSs for elastic collisions of electrons and positrons were calculated numerically by running the program ELSEPA [22, 23] which uses the relativistic Dirac partial-wave expansion method for the electrostatic potential of the target atom obtained from Dirac-Fock atomic electron densities [24, 25], with the exchange potential of Furness and McCarthy [26] for electrons. **Figure 2** displays DCSs from the ELSEPA database for elastic scattering of electrons and positrons by carbon and mercury atoms. These plots illustrate the variation of the DCS with the atomic number Z, the charge of the projectile, and the energy E.
- *Inelastic collisions (in).* Interactions involving electronic excitations of the medium are simulated on the basis of the plane-wave Born approximation with the Sternheimer-Liljequist generalized oscillator strength model [27, 28]. The model is designed to simplify the simulation of inelastic collisions and to facilitate the calculation of the density-effect correction. The excitation spectrum is modeled as a discrete set of delta oscillators. Each oscillator represents excitations of an electron subshell, its strength is set equal to the number of electrons in that subshell and its resonance energy is proportional to the subshell binding energy. The proportionality constant is the same for all subshells, and it is determined from the requirement that the generalized oscillator strength model reproduces the empirical value of the mean excitation energy I recommended in the ICRU Report 37 [9]. This procedure ensures that the stopping powers calculated from this model agree closely with the tabulated values in the ICRU Report 37. To smear out the

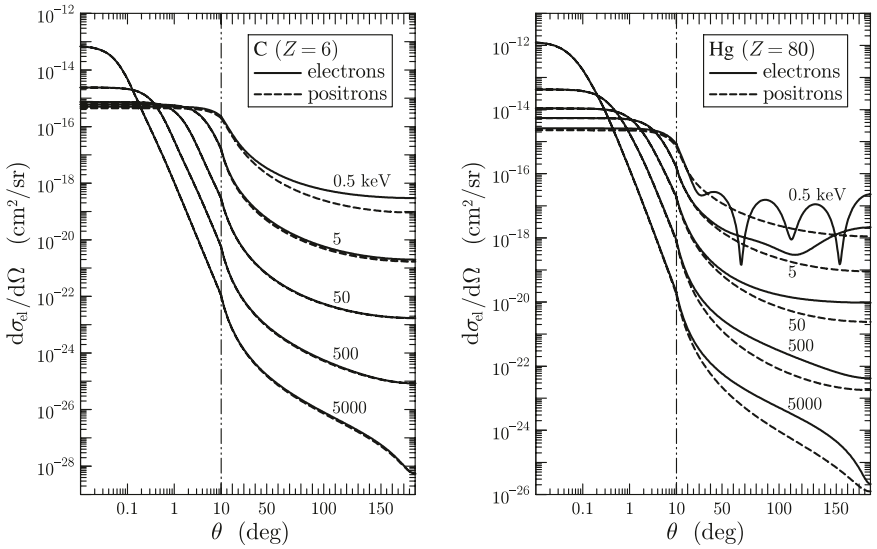

FIGURE 2 | DCS for elastic scattering of electrons and positrons by carbon and mercury atoms as a function of the polar deflection angle θ. Notice the change from logarithmic to linear scale at θ = 10 deg.

effect of discrete resonances, the energy loss in distant interactions with bound electrons is sampled from a continuous (triangular) distribution with a mean value equal to the resonance energy of the active subshell.

- *Ionization of inner shells by impact of electrons and positrons (si).* The K shell, and the L, M, and N subshells that have binding energies larger than about 50 eV are considered as inner atomic electron shells. Because the total cross sections obtained from the Sternheimer-Liljequist generalized oscillator strength model are not sufficiently accurate for describing the ionization of inner shells, PENELOPE uses numerical shell-ionization cross sections calculated by Bote and Salvat [29] by means of the distorted-wave (first) Born approximation with the Dirac-Hartree-Fock-Slater self-consistent potential (*see* also Ref. [30]), multiplied by an energy-dependent factor that accounts for the density-effect correction. The energy loss and the momentum transfer in ionizing collisions are sampled from the distribution given by the Liljequist-Sternheimer model. The total cross sections of outer subshells are renormalized to keep the value of the stopping power unaltered. This approach yields the correct number of ionizations per unit path length, without altering substantially the modeling of inelastic collisions.
- *Bremsstrahlung emission (br).* The energy W of the emitted photon is set equal to the energy loss of the projectile. It is sampled from numerical energy-loss spectra obtained from the scaled cross-section tables of Seltzer and Berger [31, 32]. The intrinsic angular distribution of emitted photons is described by an analytical expression —an admixture of two "boosted" dipole distributions— [33] with parameters determined by fitting a set of 910 angular distributions calculated with the program of Poškus [34], which extends the previously available calculation of Kissel *et al.* [35]. PENELOPE assumes that elastic collisions account for all angular deflections of the particle trajectory caused by the atomic field and, consequently, that radiative events do not modify the direction of the electron or positron.
- *Positron annihilation (an).* In the simulation of positron annihilation the target electrons are assumed to be at rest. The process is described by the Heitler DCS [36, 37] for in-flight annihilation with emission of two photons of energies E_- and E_+, with $E_- \leq E_+$, which add to $E + 2m_ec^2$, where m_e is the rest mass of the electron and $m_ec^2 \simeq 511$ keV its rest energy. The Heitler DCS is a function of the energy E_- of the less energetic photon. The directions of the two photons are determined by energy and momentum conservation. When the energy of a positron is less than its absorption energy, $E_{\rm abs}$ (3), it is assumed to annihilate with emission of two photons of energy equal to m_ec^2 with opposite directions.

The DCSs for these interaction mechanisms,

$$\frac{\mathrm{d}\sigma_{\rm el}(E)}{\mathrm{d}\mu}, \quad \frac{\mathrm{d}^2\sigma_{\rm in}(E)}{\mathrm{d}W\mathrm{d}\mu}, \quad \frac{\mathrm{d}\sigma_{\rm br}(E)}{\mathrm{d}W}, \quad \text{and} \quad \frac{\mathrm{d}\sigma_{\rm an}(E)}{\mathrm{d}E_-}, \tag{12}$$

are functions of the angular deflection $\mu = (1 - \cos\theta)/2$ and/or the energy loss W, or the photon energy E_-. The corresponding total cross sections are obtained by integration of these DCSs over the allowed intervals of the relevant variables. The mean free path λ of electrons and positrons is

$$\lambda(E) = \frac{1}{\mathcal{N}\sigma_{\rm tot}(E)}, \tag{13}$$

where

$$\sigma_{\rm tot}(E) = \sigma_{\rm el}(E) + \sigma_{\rm in}(E) + \sigma_{\rm br}(E)[+\sigma_{\rm an}(E)], \tag{14}$$

with the annihilation term present only for positrons.

Elastic scattering is characterized by the mean free path,

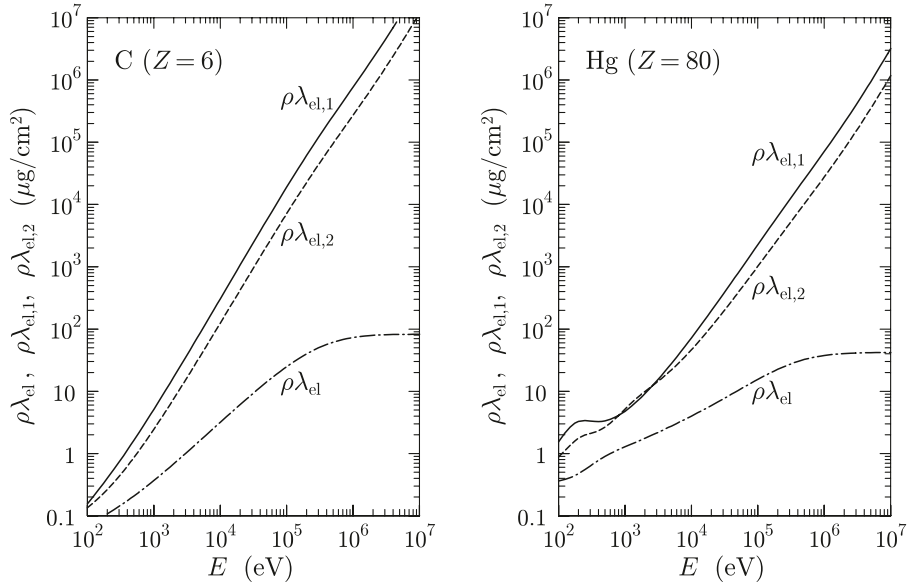

FIGURE 3 | Elastic mean free path, λ_{el}, and first and second transport mean free paths, $\lambda_{el,1}$ and $\lambda_{el,2}$, for electrons scattered in carbon and mercury as functions of the kinetic energy of the projectile.

$$\frac{1}{\lambda_{el}(E)} = \mathcal{N}\int_0^1 \frac{d\sigma_{el}(E)}{d\mu}\, d\mu, \tag{15}$$

and the transport mean free paths, $\lambda_{el,\ell}$, defined by

$$\frac{1}{\lambda_{el,\ell}(E)} = \mathcal{N}\int_0^1 [1 - P_\ell(\cos\theta)]\frac{d\sigma_{el}(E)}{d\mu}\, d\mu, \tag{16}$$

where $P_\ell(\cos\theta)$ are Legendre polynomials with the argument $\cos\theta = 1 - 2\mu$. The inverse first and second transport mean free paths can be expressed as

$$\lambda_{el,1}^{-1}(E) = \frac{\langle 1 - \cos\theta\rangle_1}{\lambda_{el}(E)} = \frac{2\langle\mu\rangle_1}{\lambda_{el}(E)} \tag{17}$$

and

$$\lambda_{el,2}^{-1}(E) = \frac{3}{2}\,\frac{\langle 1 - \cos^2\theta\rangle_1}{\lambda_{el}(E)} = 6\,\frac{\langle\mu - \mu^2\rangle_1}{\lambda_{el}(E)}, \tag{18}$$

where the notation $\langle\ldots\rangle_1$ indicates the average value in a single collision. $\lambda_{el,1}^{-1}$ gives a measure of the average angular deflection per unit path length; by analogy with the stopping power (*see* below), the quantity $2\lambda_{el,1}$ is sometimes called the *scattering power*[2]. **Figure 3** shows elastic mean free paths and transport mean free paths for electrons in carbon and mercury. For energies larger than about 10 keV, when E increases the DCS becomes strongly peaked in the forward direction. In the high-energy limit, scattering is preferentially at small angles (with $\sin\theta \simeq \theta$) and $\lambda_{el,2} \simeq \lambda_{el,1}/3$.

The mean free path λ_{in} between inelastic collisions is

$$\lambda_{in}(E) = \left[\mathcal{N}\int_0^E\left(\int_0^1 \frac{d\sigma_{in}(E)}{dW\, d\mu}\, d\mu\right)dW\right]^{-1}. \tag{19}$$

The total cross section for bremsstrahlung emission is infinite because the corresponding DCS diverges as W^{-1} at $W = 0$ (*see* Ref. [10] and references therein).

A fundamental quantity in transport studies is the stopping power S (= average energy loss per unit path length), given by

$$S(E) = \mathcal{N}\int_0^E W\left[\left(\int_0^1 \frac{d\sigma_{in}(E)}{dW\, d\mu}\, d\mu\right) + \frac{d\sigma_{br}(E)}{dW}\right]dW, \tag{20}$$

where the terms in square brackets are the energy-loss DCSs for inelastic collisions and bremsstrahlung emission, respectively. Relatively small energy transfers also occur in elastic collisions, which manifest as the recoil of the target atom or as phonon excitations, and give rise to the so-called nuclear stopping power. PENELOPE disregards the energy loss in elastic events because the nuclear stopping power is typically four orders of magnitude smaller than S. Another relevant quantity is the energy-straggling parameter (= increase of the variance of the energy distribution per unit path length) given by

$$\Omega^2(E) = \mathcal{N}\int_0^E W^2\left[\left(\int_0^1 \frac{d\sigma_{in}(E)}{dW\, d\mu}\, d\mu\right) + \frac{d\sigma_{br}(E)}{dW}\right]dW. \tag{21}$$

We notice that the contributions from inelastic collisions to the stopping power and to the energy-straggling parameter can be expressed as

$$S_{in}(E) = \frac{\langle W\rangle_1}{\lambda_{in}(E)} \qquad \text{and} \qquad \Omega_{in}^2(E) = \frac{\langle W^2\rangle_1}{\lambda_{in}(E)}, \tag{22}$$

respectively, where $\langle W^n\rangle_1$ denotes the average value of W^n in a collision. **Figure 4** displays the mean free path of inelastic

[2]When small angles dominate, $\langle\mu\rangle_1 \simeq \langle\theta^2\rangle_1/4$ and $\lambda_{el,1}^{-1} \simeq \langle\theta^2\rangle_1/(2\lambda_{el})$.

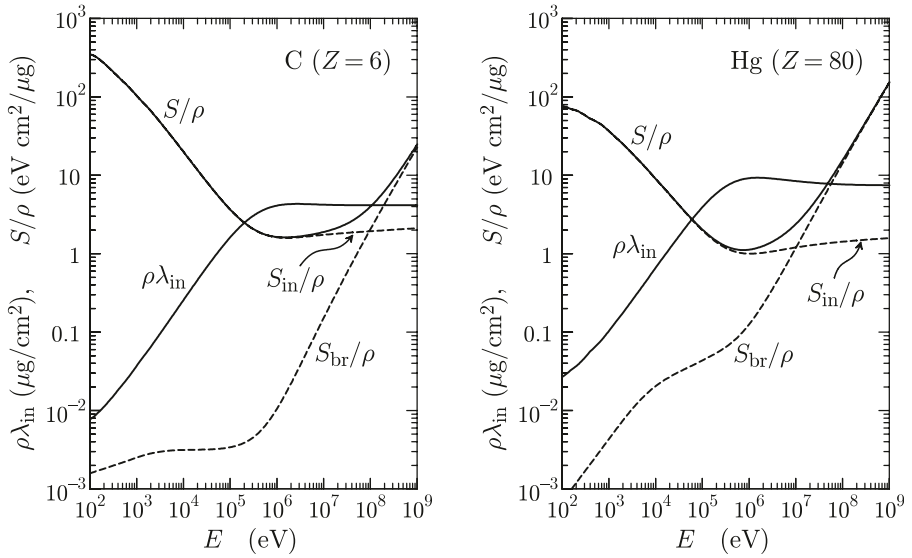

FIGURE 4 | Mean free path of inelastic collisions and stopping powers for electrons in carbon and mercury as functions of the kinetic energy E. The plotted quantities are $\rho\lambda_{\text{in}}$ and S/ρ. The dashed curves represent the contributions from inelastic collisions and from bremsstrahlung emission to the stopping power.

collisions and the stopping power for electrons in carbon and mercury, together with the collision and radiative contributions to the stopping power.

2.3 Atomic Relaxation

PENELOPE simulates the emission of characteristic x rays and Auger electrons with energies larger than E_{abs}(KPAR) that result from vacancies produced in the inner subshells of atoms by photoelectric absorption and Compton scattering of photons and by electron or positron impact. The relaxation of excited ions is simulated as a sequence of transitions in which vacancies move towards the outer subshells by emission of Auger electrons and x rays; the relaxation process is followed until all vacancies have moved to subshells with binding energies less than a certain value E_{cut}, which is determined by the absorption energies of electrons and photons. The adopted transition probabilities, as well as the energies of Auger electrons, were extracted from the LLNL Evaluated Atomic Data Library [38]. The energies of K and L x-ray lines are taken from the review of Deslattes *et al.* [39], while those of M and N lines are from Bearden's compilation [40]. X rays and electrons are emitted in random directions sampled from the isotropic distribution.

3 GENERATION OF RANDOM ELECTRON-PHOTON SHOWERS

A detailed description of the sampling algorithms used to simulate the various interactions from their associated DCSs is given in the PENELOPE manual [2]. Most continuous distributions are sampled numerically by means of the adaptive algorithm RITA (Rational Inverse Transform with Aliasing); Walker's aliasing method [41] is utilized to sample discrete distributions with large numbers of possible outcomes. The adopted sampling methods are both fast and robust.

The simulation of photons follows the usual detailed procedure, where all interaction events in a photon history are simulated in chronological succession. The physics simulation subroutines set the distance s from the current position $\mathbf{r}$ to the next interaction, assuming the medium is infinite, by random sampling from the exponential distribution defined in **Eq. 10**. The program then propagates the photon the distance s along the ray, *i.e.*, to a position $\mathbf{r} + s\hat{\mathbf{d}}$, where the next interaction takes place. In Rayleigh and Compton scattering, the photon is absorbed and a second photon is emitted with energy E' (equal to or less than E). When $E' > E_{\text{abs}}$ (2), the surviving photon is followed by repeating these steps. That is, a photon history represents the evolution of the primary photon *and its descendants* resulting from Compton and Rayleigh interactions. Photoabsorption and pair production terminate the photon history. Each photon history consists of a sequence of a relatively small number ($\lesssim 10$) of free flights and interactions, which can be simulated rapidly.

The simulation of electron and positron histories is more difficult because of the large number of interactions these particles undergo before being brought to rest. On average, an electron looses a few tens of eV at each individual interaction. Therefore, detailed simulation of electrons and positrons is feasible only in situations where the number of interactions is sufficiently small, that is, for energies up to about 50 keV, and for particles with higher energies traveling through thin material foils. To cope with this difficulty, charged particles are usually tracked by using condensed simulation schemes (class-I schemes in the terminology of Berger [42]) which consist in decomposing each particle trajectory into a number of steps (either of fixed or random lengths), and the global effect of all the interactions that occur along each step is described *approximately* by using

multiple scattering theories. Because these theories apply to homogeneous infinite media, a limitation of class-I schemes occurs when a particle is close to a material interface: the step length must then be kept smaller than the distance to the nearest interface, to prevent the particle from entering the next medium. Therefore, in class-I simulations the geometry subroutines must keep control of the proximity of interfaces.

The practical alternative are class-II schemes [42], also called mixed schemes, which take advantage of the fact that the DCSs for interactions of high-energy charged particles are rapidly decreasing functions of the energy loss W and the polar scattering angle θ. Consequently, cutoffs W_c and θ_c can be set so that the number of "hard" interactions (*i.e.*, interactions with energy loss or polar scattering angle larger than the corresponding cutoffs) that occur along each particle history is small enough to allow their individual simulation by random sampling from the corresponding *restricted* DCSs. The accumulated angular deflection caused by all soft interactions (with sub-cutoff energy transfers or angular deflections) that occur along a trajectory step between two successive hard interactions can be described by means of a multiple-scattering approach consistent with the DCSs restricted to soft events. The energy loss caused by soft interactions along the step can be obtained from a simple distribution having the exact first and second moments, as calculated from the energy-loss DCS restricted to soft interactions.

Class-II schemes are more accurate than purely condensed simulation because: *1*) hard events are simulated exactly from the corresponding restricted DCSs, and *2*) multiple scattering approximations have a milder effect when applied to soft interactions only. A further advantage of these schemes is that the tracking algorithm only requires computing intersections of particle rays (straight lines) with interfaces, instead of having to control the distances to the interfaces. In addition, class-II schemes allow verifying the stability of simulation results under variations of the cutoffs, as well as the accuracy of the multiple-scattering approximations adopted for describing the soft interactions. The only disadvantage of class-II schemes is that they require a more elaborate coding of the simulation program, and somewhat larger look-up tables.

Most general-purpose Monte Carlo codes for high-energy radiation transport (*e.g.*, ETRAN [43–45], ITS3 [46], EGS4 [37], EGSnrc [47], MCNP [48], GEANT4 [4–6], FLUKA [49], EGS5 [50] MCNP6 [51]) simulate charged particles by means of a combination of class-I and class-II schemes. By contrast, PENELOPE [1, 2], and recently the PENELOPE-based PENRED [52], make systematic use of class-II schemes for all interactions of electrons and positrons.

3.1 Simulation of Electron and Positron Trajectories

PENELOPE describes the transport of electrons and positrons by means of an elaborate class-II scheme, with fixed energy-loss cutoffs and an energy-dependent angular cutoff θ_c for elastic collisions, which is set internally by the program in terms of two user-defined simulation parameters. Particle trajectories are generated by using the random-hinge method [53], which operates similarly to detailed simulations, *i.e.*, the transported particle is moved in straight "jumps," and the energy and direction of movement change only through discrete events (hard interactions and hinges). With the appropriate set of DCSs, the method is applicable to any charged particle; class-II simulations of protons with the random-hinge method have been reported by Salvat and Quesada [54, 55].

3.1.1 Interactions With Energy Loss

Electrons and positrons lose energy through inelastic collisions and bremsstrahlung emission. These interactions are classified by the respective cutoff energy-loss values, W_{cc} and W_{cr}, which are assumed to be independent of the energy of the projectile. Interactions with energy loss W larger than the corresponding cutoff are considered as hard interactions and are simulated individually by sampling from the corresponding restricted DCSs. The slowing down caused by soft interactions is described by the *restricted* stopping power,

$$S_s(E) = \mathcal{N}\int_0^{W_{cc}} W\left(\int_0^1 \frac{d\sigma_{in}(E)}{dW\ d\mu}\ d\mu\right)dW + \mathcal{N}\int_0^{W_{cr}} W\ \frac{d\sigma_{br}(E)}{dW}\ dW, \tag{23}$$

and the *restricted* energy straggling parameter,

$$\Omega_s^2(E) = \mathcal{N}\int_0^{W_{cc}} W^2\left(\int_0^1 \frac{d\sigma_{in}(E)}{dW\ d\mu}\ d\mu\right)dW + \mathcal{N}\int_0^{W_{cr}} W^2\ \frac{d\sigma_{br}(E)}{dW}\ dW. \tag{24}$$

A difficulty of class-II algorithms arises from the fact that the energy of the particle decreases along the step between two consecutive hard interactions. Because the cutoff energies W_{cc} and W_{cr} do not change with E, we can assume that, at least for small fractional energy losses, the DCSs for soft energy-loss events vary linearly with E. Under this assumption we can calculate the first moments of the distribution of the energy loss W_s of a particle with initial energy E_0 after traveling a path length s under only the influence of soft events [2]. The mean and variance of this distribution are, respectively,

$$\langle W_s\rangle = S_s(E_0)\ s\left\{1 - \frac{1}{2}\left[\frac{d\ln S_s(E)}{dE}\right]_{E=E_0} S_s(E_0)\ s\right\} \tag{25a}$$

and

$$\mathrm{var}(W_s) = \Omega_s^2(E_0)\ s\left\{1 - \left[\frac{1}{2}\frac{d\ln\Omega_s^2(E)}{dE} + \frac{d\ln S_s(E)}{dE}\right]_{E=E_0} S_s(E_0)\ s\right\}, \tag{25b}$$

where the factors in curly braces account for the global effect of the energy dependence of the soft energy-loss DCS, within the linear approximation.

In practical simulations, the energy loss W_s due to soft interactions along a path length s is sampled from a distribution, $P(W_s)$, that has the mean and variance of the actual energy-loss distribution, as given by **Eqs. 25**. When

$\langle W_s\rangle^2 \gg \mathrm{var}(W_s)$, and the cutoff energy losses W_{cc} and W_{cr} are much smaller than $\langle W_s\rangle$, the central limit theorem implies that the actual energy-loss distribution is nearly Gaussian. Unfortunately, this is not true for small path lengths, which correspond to small W_s, and one must rely on artificial distributions. In PENELOPE the distribution $P(W_s)$ has different forms, depending on the ratio

$$X = \frac{\langle W_s\rangle}{\sigma}, \tag{26a}$$

where $\sigma = [\mathrm{var}(W_s)]^{1/2}$ is the standard deviation of W_s. Specifically, we consider the following cases.

- Case I. If $X > 3$, the energy loss is sampled from the truncated Gaussian distribution (normalisation is irrelevant here),

$$P_I(W_s) = \begin{cases} \exp\left[-\dfrac{(W_s - \langle W_s\rangle)^2}{2(1.015387\ \sigma)^2}\right] & \text{if } |W_s - \langle W_s\rangle| < 3\ \sigma, \\ 0 & \text{otherwise,} \end{cases} \tag{26b}$$

where the numerical factor 1.015387 corrects the standard deviation for the effect of the truncation. Notice that the shape of this distribution is very similar to that of the "true" energy-loss distribution.

- Case II. When $3^{1/2} < X < 3$, we use the uniform distribution[3]

$$P_{II}(W_s) = U(W_1, W_2; W_s) \tag{26c}$$

with

$$W_1 = \langle W_s\rangle - \sqrt{3}\ \sigma \tag{26d}$$

and

$$W_2 = \langle W_s\rangle + \sqrt{3}\ \sigma. \tag{26e}$$

- Case III. Finally, when $X < 3^{1/2}$, the adopted distribution is an admixture of a delta distribution and a uniform distribution,

$$P_{III}(W_s) = A\delta(W_s) + (1 - A)U(0, W_0; W_s) \tag{26f}$$

with

$$A = \frac{3\mathrm{var}(W_s) - \langle W_s\rangle^2}{3\mathrm{var}(W_s) + 3\langle W_s\rangle^2} \quad \text{and}$$
$$W_0 = \frac{3\mathrm{var}(W_s) + 3\langle W_s\rangle^2}{2\langle W_s\rangle}. \tag{26g}$$

It can be easily verified that these distributions have the required mean and variance. It is also worth noticing that they yield W_s values that are less than

$$W_{s,\max} = \begin{cases} \langle W_s\rangle + 3\sigma & \text{in case I,} \\ W_2 & \text{in case II,} \\ W_0 & \text{in case III.} \end{cases} \tag{27}$$

$W_{s,max}$ is normally much less than the kinetic energy E_0 of the transported particle. Energy losses larger than E_0 might be generated only when the step length s has a value of the order of the continuous slowing down approximation (CSDA) range, but this never happens in practical simulation. Despite the artificial shapes of the distributions given by **Eqs 26**, after a moderately large number of short steps, the distribution of the accumulated energy loss has the correct first and second moments and is similar in shape to the "true" distribution for soft interactions only, which is nearly Gaussian. Further improvements of the distribution of soft-energy losses would require considering higher order moments of the energy-loss in single interaction events.

3.1.2 Elastic collisions

Angular deflections of the particle trajectories are mostly caused by elastic collisions with the atoms of the material. To analyze the cumulative effect of multiple interactions, let us consider an electron that starts from the origin of coordinates moving in the direction of the z axis with energy E. Let θ_m and (x, y, z) denote the polar angle of the direction of motion and the position coordinates of the electron after traveling a path length s. Under the assumption that energy losses are negligible, the multiple-scattering theories of Goudsmit and Saunderson [56] and Lewis [57] provide exact expressions for the angular distribution, $p(\mu_m)$ with $\mu_m = (1 - \cos\ \theta_m)/2$, which are determined by the so-called transport mean free paths $\lambda_{el,\ell}$, **Eq. 16**. In addition, the Lewis theory for pure elastic scattering gives exact analytical expressions for the average values $\langle \cos\theta_m\rangle$, $\langle \cos^2\theta_m\rangle$, $\langle z\rangle$, $\langle z\cos\theta_m\rangle$, $\langle z^2\rangle$, and $\langle x^2 + y^2\rangle$. These quantities are completely determined by the values of the transport mean free paths $\lambda_{el,1}$ and $\lambda_{el,2}$.

In PENELOPE the cutoff deflection μ_c, which separates hard and soft elastic collisions, varies with the energy E in a way that ensures that the simulation becomes purely detailed at low energies, where elastic scattering is more intense. The cutoff deflection is determined by two energy-independent user parameters, C_1 and C_2, which typically should be given small values, between 0 and 0.1. These two parameters are used to fix the mean free path between hard elastic events (*i.e.*, the average step length between consecutive hard elastic collisions), which is defined as

$$\lambda_{el}^{(h)} = \max\left\{\lambda_{el},\ \min\left[C_1\lambda_{el,1}, C_2\frac{E}{S}\right]\right\}, \tag{28}$$

where $\lambda_{el,1}$ is the first transport mean free path, and S is the stopping power due to both inelastic collisions and bremsstrahlung emission, **Eq. 20**. The equation

$$\lambda_{el}^{(h)}(E) = \left[\mathcal{N}\int_{\mu_c}^{1}\frac{d\sigma_{el}(E)}{d\mu}\ d\mu\right]^{-1} \tag{29}$$

then fixes the cutoff μ_c as a function of the energy E of the projectile. The average angular deflection of the electron

[3]The normalized uniform distribution in the interval (a, b), with $a < b$, is

$$U(a, b; x) = \begin{cases} 1/(b-a) & \text{if } a < x \le b \\ 0 & \text{otherwise.} \end{cases}$$

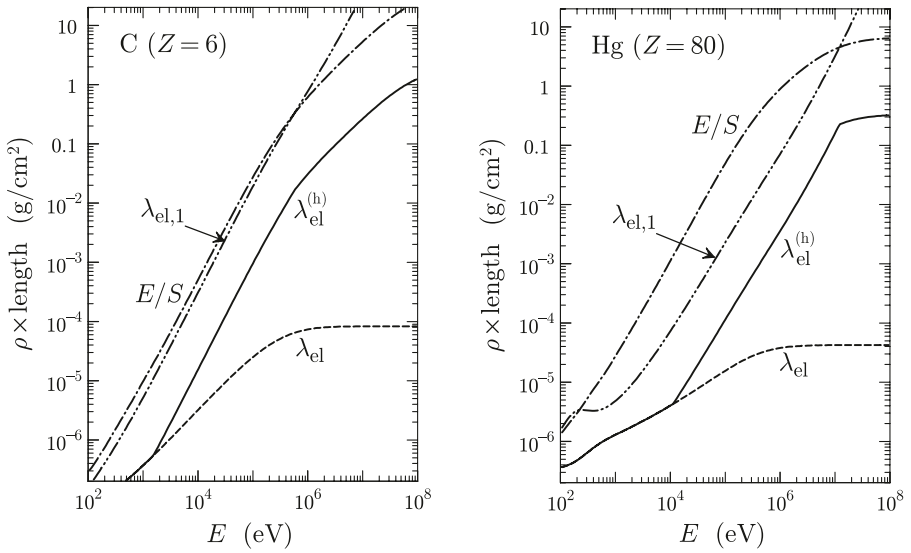

FIGURE 5 | Elastic mean free path λ_{el}, first transport mean free path $\lambda_{el,1}$ and $E/S(E)$ for electrons in carbon and mercury. The solid lines represent the mean free path between hard elastic events $\lambda_{el}^{(h)}$ obtained from **Eq. 28** with $C_1 = C_2 = 0.05$.

trajectory at the end of a step of length $\lambda_{el}^{(h)}$ can be evaluated from Lewis' theory [57] which, ignoring energy losses along the step, gives

$$1 - \langle \cos\theta_m \rangle = 1 - \exp\left(- \frac{\lambda_{el}^{(h)}}{\lambda_{el,1}} \right) \simeq \frac{\lambda_{el}^{(h)}}{\lambda_{el,1}} \lesssim C_1. \tag{30}$$

That is, C_1 defines an approximate upper limit for the cumulative average angular deflection along step. On the other hand, the average energy loss along the step is

$$\langle E - E_{final} \rangle \simeq \lambda_{el}^{(h)} S \lesssim C_2 E, \tag{31}$$

so that C_2 sets a limit to the average fractional energy loss along the step. An increase of C_1 or C_2 leads to increased values of both the mean free path between hard events, $\lambda_{el}^{(h)}$, and the cutoff deflection, μ_c, in certain energy ranges [2]. Of course, an increase of $\lambda_{el}^{(h)}$ implies a reduction in the number of hard events along a particle track with an accompanying reduction of the simulation time.

It should be noted that C_1 and C_2 act within different energy domains. This is illustrated in **Figure 5**, where the lengths λ_{el}, $\lambda_{el,1}$ and E/S for electrons in carbon and mercury are represented as functions of the kinetic energy. The mean free path $\lambda_{el}^{(h)}$ for hard elastic events, determined from the formula **(28)** with $C_1 = C_2 = 0.05$ is also plotted. For low energies, $\lambda_{el}^{(h)} = \lambda_{el}$ and the simulation is purely detailed ($\mu_c = 0$). For intermediate energies, $\lambda_{el}^{(h)} = C_1 \lambda_{el,1}$, whereas $\lambda_{el}^{(h)} = C_2 E/S$ in the high-energy domain. From **Figure 5** it is clear that increasing the value of C_2 does not have any effect on the simulation of electron tracks with initial energies that are less than about 1 and 10 MeV for carbon and mercury, respectively.

The justification for the recipe **(28)** is that it automatically forces detailed simulation ($\mu_c = 0$) at low energies, where elastic scattering dominates. In addition, when the energy increases, the portion of elastic collisions that are hard, $\propto \lambda_{el}/\lambda_{el}^{(h)}$, reduces gradually, being much less than unity at high energies, where scattering is preferentially at small-angles.

Assuming negligible energy losses, the angular distribution produced by the soft elastic collisions along a path length s is [57]

$$F_s(s;\mu_s) = \sum_{\ell=0}^{\infty} \frac{2\ell+1}{4\pi} \exp\left(-s/\lambda_{el,\ell}^{(s)}\right) P_\ell(\cos\theta_s), \tag{32}$$

where $\mu_s \equiv (1 - \cos\theta_s)/2$ is the accumulated deflection, and $\lambda_{el,\ell}^{(s)}$ are the transport mean free paths for the soft interactions,

$$\frac{1}{\lambda_{el,\ell}^{(s)}(E)} = \mathcal{N} \int_0^{\mu_c} [1 - P_\ell(\cos\theta)] \frac{d\sigma_{el}(E)}{d\mu} \, d\mu. \tag{33}$$

The DCS for soft elastic events has a discontinuity at μ_c, which implies that for small path lengths the Legendre series **(32)** does not converge with a finite number of terms. Therefore, it is impractical to sample the multiple-scattering deflection μ_s from the distribution $F_s(s; \mu_s)$.

It is important to notice that soft inelastic collisions also cause a small deflection of the projectile. The scattering effect of these interactions is accounted for by considering their contributions to the soft transport mean free paths,

$$\frac{1}{\lambda_{in,\ell}^{(s)}(E)} = \mathcal{N} \int_0^1 [1 - P_\ell(\cos\theta)] \left(\int_0^{W_{cc}} \frac{d^2\sigma_{in}(E)}{dW \, d\mu} \, dW \right) d\mu. \tag{34}$$

The combined (elastic plus inelastic) soft scattering process is then described by the transport mean free paths

$$\frac{1}{\lambda_{comb,\ell}^{(s)}(E)} = \frac{1}{\lambda_{el,\ell}^{(s)}(E)} + \frac{1}{\lambda_{in,\ell}^{(s)}(E)}. \tag{35}$$

Assuming that the energy loss is small, the first and second moments of the angular deflection after a path length s, under

the sole action of soft elastic and soft inelastic interactions, are [2, 57]

$$\langle \mu_s \rangle = \frac{1}{2}\left[1 - \exp\left(-s/\lambda^{(s)}_{\mathrm{comb},1}\right)\right] \tag{36a}$$

and

$$\langle \mu_s^2 \rangle = \langle \mu_s \rangle - \frac{1}{6}\left[1 - \exp\left(-s/\lambda^{(s)}_{\mathrm{comb},2}\right)\right]. \tag{36b}$$

In practical simulations the angular deflection μ_s after a path length s is sampled from an artificial distribution, $P(\mu_s)$, which is required to have the same moments,

$$\langle \mu_s^n \rangle = \int_0^1 \mu_s^n \; P(\mu_s)\; \mathrm{d}\mu_s, \tag{37}$$

of orders $n = 1$ and 2 as the real distribution, **Eqs 36**, but is otherwise arbitrary. In our programs we use the following

$$P(\mu_s) = A\; U(0, \mu_0; \mu_s) + (1 - A)\; U(\mu_0, 1; \mu_s), \tag{38a}$$

where $U(a, b; x)$ denotes the normalised uniform distribution in the interval (a, b). The parameters obtained by requiring the aforesaid conditions are

$$\mu_0 = \frac{2\langle \mu_s \rangle - 3\langle \mu_s^2 \rangle}{1 - 2\langle \mu_s \rangle}, \tag{38b}$$

and

$$A = 1 - 2\langle \mu_s \rangle + \mu_0. \tag{38c}$$

This simple distribution is flexible enough to reproduce the combinations of first and second moments encountered in the simulations [notice that $\langle \mu_s \rangle$, **Eq. (36a)**, is always less than 0.5] and allows fast random sampling of the deflection μ_s.

3.1.3 Random-Hinge Method

As indicated above, hard interactions are simulated individually according to their restricted DCSs. Assuming that the energy loss due to soft collisions is small, the distance s traveled by an electron with initial energy E from its current position $\mathbf{r}$ to the next hard collision can be sampled from the familiar exponential distribution, with the total mean free path $\lambda^{(h)}_T$ given by

$$\frac{1}{\lambda^{(h)}_T(E)} = \frac{1}{\lambda^{(h)}_{el}(E)} + \frac{1}{\lambda^{(h)}_{in}(E)} + \frac{1}{\lambda^{(h)}_{br}(E)} \quad \left[+\frac{1}{\lambda^{(h)}_{an}(E)}\right]. \tag{39}$$

That is, random values of s can be generated by using the sampling formula

$$s = -\lambda^{(h)}_T(E)\; \ln \xi, \tag{40}$$

where ξ is a random number uniformly distributed in (0,1).

Because of the effect of soft interactions, the kinetic energy of the transported particle varies along the step between two hard interactions. The accumulated angular deflection caused by all soft interactions that occur along a trajectory step is simulated as if it were caused by a single artificial event (a hinge), which occurs at a random position within the step. The energy loss along the step and the polar angular deflection at the hinge are sampled from approximate multiple-scattering distributions that have the correct means and variances, **Eqs 25**, **36**, which are calculated beforehand from the DCSs restricted to soft interactions [2]. Unfortunately, the multiple-scattering theories do not provide enough information to determine the spatial distribution and the correlation between the direction and the position of the electron at the end of a step. The only characteristics readily available are the low-order moments given by the theory of Lewis.

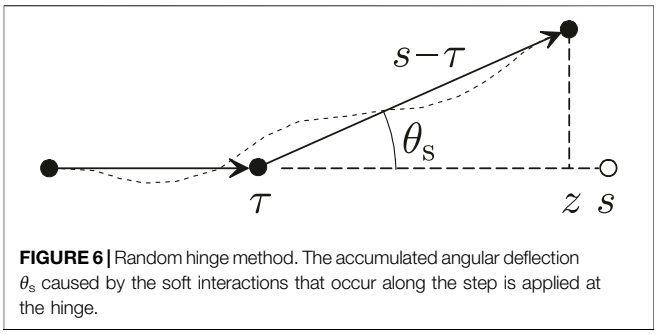

FIGURE 6 | Random hinge method. The accumulated angular deflection θ_s caused by the soft interactions that occur along the step is applied at the hinge.

The energy loss W_s and the angular deflection μ_s caused by multiple soft interactions along the step are sampled from artificial distributions, which are required to preserve the moments given by **Eqs 25** and **36**. Other details of these distributions are irrelevant, provided only that the fractional energy loss, $\langle W_s \rangle / E$, and the average soft deflection, $\langle \mu_s \rangle$, in each step are small [1, 2]. A convenient feature of the adopted energy-loss distributions, which will be helpful below, is that they permit energy transfers up to a well defined maximum value $W_{s,\max}$, **Eq. 27**, determined by the kinetic energy E of the projectile and the step length s.

In PENELOPE, the angular deflection and the space displacement due to multiple soft collisions along the path length s are described by means of the *random-hinge* method [53], which operates as follows (**Figure 6**).

1) First, the program samples the length s of the step to the next hard interaction.
2) The energy loss W_s caused by all soft interactions along the step is sampled from the distribution given by **Eqs 26**, which has the correct mean and variance, **Eqs 25**, and approaches the normal distribution for sufficiently long steps.
3) The electron then flies a random distance τ, which is sampled uniformly in the interval $(0, s)$, in the initial direction.
4) The artificial event (hinge) takes place at the end of the flight, where the electron changes its direction of movement. The polar deflection, $\mu_s = (1 - \cos\,\theta_s)/2$, is sampled from the distribution **(38)** having the mean and variance evaluated from the DCSs of soft events at an energy $E' = E - (\tau/s)W_s$. The azimuthal deflection angle ϕ_s is sampled uniformly in $(0, 2\pi)$
5) Finally, the electron flies a distance $s - \tau$ in the new direction, to the position of the next hard interaction. The energy at the end of the step is set to $E - W_s$.

Thus, each step s is simulated as a sequence of two trajectory segments.

With this tracking algorithm, the code operates as in detailed simulations, *i.e.*, the transported particle moves freely in straight trajectory segments, and the energy and direction of movement change only through discrete events (hard interactions and hinges). This strategy simplifies the simulation of transport in complex material structures consisting of homogeneous bodies with well-defined interfaces. When the electron crosses an interface, we only have to halt it at the crossing point, and resume the simulation in the new material. Because the distance τ to the hinge is distributed uniformly in $(0, s)$, the particle reaches the interface with nearly correct average energy and direction [2]. We point out that this tracking scheme only requires computing intersections of particle rays and interfaces. In the case of a generic quadric surface, this is accomplished by solving a quadratic equation. The easiness of the ray-tracing method is at variance with class-I schemes, which require calculating the distance to the nearest interface at the beginning of each step; in the case of a quadric surface the calculation of that distance involves finding a root of a polynomial of up to 6th degree [58].

In spite of its simplicity, the random-hinge method competes in accuracy and speed with other, more sophisticated transport algorithms [59, 60]. Comparison of results from detailed and class-II simulations of electrons in an infinite medium [2] shows that the randomness of the hinge position leads to correlations between the angular deflection and the displacement that are close to the actual correlations. It is also worth noting that the possible positions of the next hard interaction fill the sphere of radius s centered at **r**, the beginning of the step.

It is convenient to consider that the energy W_s is lost at a constant rate along the step, *i.e.*, as in the CSDA with an effective stopping power $S_{soft} = W_s/s$. In previous versions of PENELOPE, the energy loss W_s was deposited at the hinge. This yielded an artifact in the depth-dose distribution, which does not occur when the energy loss is distributed uniformly along the step [2]. The use of the CSDA instead of assuming a discrete loss at the hinge also reduces statistical uncertainties in the simulated distributions of fluence with respect to energy. In addition, the CSDA permits accounting for the reduced energy loss in segments that are truncated at interfaces: the energy of the electron at the intersection is $E_0 - s'S_{soft}$, where E_0 denotes the energy at the beginning of the segment and s' is the length of the segment before the interface.

A further advantage of considering that soft energy-loss interactions slow down electrons with constant stopping power is that the calculation of flight times is trivial. Consider an electron with initial energy E_0, subject to the stopping power S_{soft}. The time in which the electron moves along a trajectory segment of length s' is given by

$$t = \int \frac{\mathrm{d}s}{v} = \int_{E_0 - S_{soft}s'}^{E_0} \frac{1}{v(E)} \frac{\mathrm{d}E}{S_{soft}}.$$

Inserting the relativistic expression of the velocity,

$$v(E) = c\,\frac{\sqrt{E\,(E + 2\mathrm{m_e}c^2)}}{E + \mathrm{m_e}c^2},$$

The integral is elementary and gives

$$t = \frac{1}{cS_{soft}} \left[\sqrt{E_0\,(E_0 + 2\mathrm{m_e}c^2)} - \sqrt{(E_0 - S_{soft}s')\,(E_0 - S_{soft}s' + 2\mathrm{m_e}c^2)} \right], \tag{41}$$

where c is the speed of light in vacuum.

3.1.4 Variation of $\lambda_T^{(h)}$ With Energy

Due to soft energy-loss interactions, the energy of the transported particle decreases along the step in an essentially unpredictable way. This implies that the mean free path $\lambda_T^{(h)}(E)$ also changes along a single step. Consequently, the sampling formula **(40)** is incorrect (this formula is valid only when the energy remains constant along the step). **Figure 7** shows the inverse mean free path (interaction probability per unit path length) for hard interactions of electrons in carbon and mercury evaluated by PENELOPE for various values of the simulation parameters C_1 and C_2, all with $W_{cc} = W_{cr} = 100$ eV. Generally, when the energy increases, the inverse mean free path for hard events decreases monotonically at low energies, has a broad minimum, and then increases slowly to saturate at high energies. Note that, by varying the values of C_1 and C_2, the inverse mean free path cannot be made smaller than the contributions from hard inelastic and radiative events. Hence, at high energies, the value $\lambda^{(h)}(E)$ is determined by the cutoff energies W_{cc} and W_{cr}.

To account for the variation of $\lambda_T^{(h)}(E)$ with energy, and also to facilitate the simulation of electrons and positrons in electromagnetic fields, the user may set a maximum step length, s_{max}. By default PENELOPE uses the value $s_{max} = 4\lambda_T^{(h)}$. Let E_0 be the kinetic energy of the electron at the beginning of the step. As the adopted energy-loss distributions are such that the energy loss W_s in steps of length $s \le s_{max}$ has an upper bound $W_{s,max}$ [*see* **Eq. 27**], the energy of the particle decreases along the step from E_0 to a value that is never less than $E_0 - W_{s,max}$ at the end of the step. We can then determine the minimum value $\lambda_{T,\,min}$ of $\lambda_T^{(h)}(E)$ in the energy interval between $E_0 - W_{s,\,max}$ and E_0, and consider that the particle can undergo delta interactions (*i.e.*, fictitious events in which the energy and direction of the electron remain unchanged) with a mean free path $\lambda_\delta(E)$ such that

$$\frac{1}{\lambda_{el}^{(h)}(E)} + \frac{1}{\lambda_{in}^{(h)}(E)} + \frac{1}{\lambda_{br}^{(h)}(E)} \left[+ \frac{1}{\lambda_{an}^{(h)}(E)} \right] + \frac{1}{\lambda_\delta(E)} = \frac{1}{\lambda_{T,\,min}}. \tag{42}$$

Because this sum is constant with E, we can sample the step length s from the exponential distribution with the mean free path $\lambda_{T,min}$. When the sampled step length is larger than s_{max}, the particle is moved a length $s = s_{max}$ and a delta interaction is assumed to occur at the end of the step. The introduction of delta interactions does not affect the reliability of the simulation results because of the Markovian character of the transport process.

Once the step length is determined, the soft energy loss W_s is sampled from the distribution defined by **Eqs 26**, with the moments given by **Eqs 25**. The soft angular deflection μ_s at the hinge is sampled from the distribution **(38)** with the moments **(36)** calculated at the energy $E_{hinge} = E_0 - \tau S_{soft}$ corresponding to the hinge (within the CSDA). On average, this is equivalent

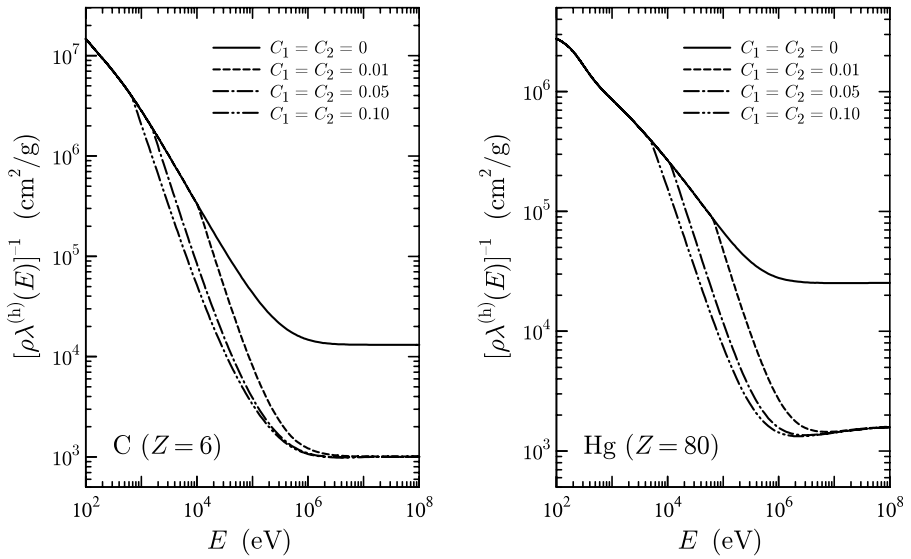

FIGURE 7 | Inverse mean free path (interaction probability per unit path length) for hard interactions of electrons in carbon and mercury for the indicated values of the simulation parameters. The plotted curves were calculated with W_{cc} = W_{cr} = 100 eV.

to assuming that the transport mean free paths $\lambda_{el,1}^{(s)}$ and $\lambda_{el,2}^{(s)}$ vary linearly with energy. When the sampled step length s is less than s_{max}, the kind of event (hard or delta interaction) that occurs at the end of the step is sampled from the corresponding partial inverse mean free paths. The angular deflection and/or the energy loss at hard interactions is sampled from the corresponding restricted DCSs. The simulation of a particle ends when either its energy becomes lower than the predefined absorption energy, E_{abs} (KPAR), or when it leaves the entire geometry.

3.2 Selecting the Simulation Parameters

The speed and accuracy of the simulation of coupled electron-photon transport is determined by the values of the simulation parameters E_{abs} (KPAR), C_1, C_2, W_{cc}, and W_{cr}, which are selected by the user for each material in the simulated structure. Here we summarize the rules for assigning "safe" values to these parameters.

The absorption energies E_{abs} (KPAR) should be estimated from either the characteristics of the experiment or the required space resolution. The quantities to be considered are the desired resolution of energy-deposition spectra and the penetration distances of particles with these energies (*i.e.*, photon mean free path and the residual ranges of electrons/positrons). PENELOPE prints tables of mean free paths and particle ranges when the initialization method PEINIT is invoked with the input parameter INFO= 3 or larger. For example, to calculate spatial dose distributions, the values E_{abs} (KPAR) should be such that the penetration distances of particles with these energies are less than the typical dimensions of the volume bins used to tally the dose map. In other cases, it is advisable to run short simulations with increasing values of E_{abs} (KPAR) (starting from 50 eV) to study the effect of these parameters on the results.

The use of different absorption energies in neighboring bodies may create visible artifacts in the space distribution of absorbed dose. For instance, if the values of E_{abs} (1) for electrons in bodies 1 and 2 are, respectively, 10 and 100 keV, electrons entering body 2 from body 1 with E less than 100 keV will be absorbed at the first interaction, giving an excess of dose at the border of body 2. When the spatial distribution of absorbed dose is important, absorption energies should be given similar values over the region of interest. If the absorption energies of *the three types of transported particles* are given the same value in all the materials present, the simulated dose distribution is continuous when there is effective equilibrium of radiation with energy less than E_{abs} (KPAR).

The random-hinge method for electrons and positrons is expected to work well when the accumulated effect (energy loss and angular deflection) of the soft interactions along a step is small. The cutoff energies W_{cc} and W_{cr} have a weak influence on the accuracy of the results provided that they are both smaller than the width of the bins used to tally energy distributions. It is worth recalling that the DCSs for inelastic collisions and bremsstrahlung emission decrease rapidly with the energy loss W (roughly as W^{-2} and W^{-1}, respectively). As a consequence, for particles with energies larger than about 100 keV, when W_{cc} and W_{cr} are increased, the simulation speed tends to a saturation value. For these high energies, the gain in speed is small when the cutoffs are made larger than about 5 keV. On the other hand, these cutoff energies have an effect on the energy-straggling distributions, which are faithfully described only when the number of hard interactions is "statistically sufficient." Therefore, the cutoff energies should not be too large. Our recommendation is to set the cutoff energies equal to one 100th of the typical energy of primary particles, or 5 keV, whichever is the smallest. Note that, for the sake of consistency, W_{cc} should be smaller than the absorption energy of electrons in

the material, $E_{abs}(1)$; otherwise, we would miss secondary electrons that have energies larger than $E_{abs}(1)$. Similarly, W_{cr} should be less than the photon absorption energy $E_{abs}(2)$.

The allowed values of the elastic-scattering parameters C_1 and C_2 are limited to the interval [0,0.2]. Because the energy dependence of the cross sections for soft interactions and of the hard mean free paths is effectively accounted for (*see* **Section 3.1**), these two parameters have a very weak influence on the results. The recommended practice is to set $C_1 = C_2 = 0.05$, which is fairly conservative. Before increasing the value of any of these parameters, it is advisable to perform short test simulations to verify that the results remain essentially unaltered when using the augmented parameter value (and that the simulation runs faster; if there is no gain in speed, keep the conservative values).

The parameter s_{max} is the maximum allowed step length. Limiting the step length is necessary to account for the variation of the mean free path for hard events, $\lambda_T^{(h)}$, with the energy of the particle. The value of s_{max} should be about, or less than one 10th of the characteristic thickness of the body where the particle is transported. This ensures that, on average, there will be more than 10 hinges along a typical electron/positron track through that body, which is enough to "wash out" the details of the artificial distributions used to sample these events. We recall that PENELOPE internally forces the step length to be less than $4\lambda_T^{(h)}$. Therefore, for thick bodies (thicker than $\sim 10\lambda_T^{(h)}$), the average number of hinges along each track is larger than about 10, and it is not necessary to limit the length of the steps. If the slowing-down of the particle due to soft events is described as a continuous stopping process, external step control is not critical.

It is interesting to observe that when the parameters C_1, C_2, and W_{cc} are set to zero, our class-II scheme becomes purely detailed (*i.e.*, nominally exact) simulation of elastic and inelastic collisions. Bremsstrahlung emission cannot be simulated detailedly because its DCS diverges at zero photon energy (and, hence, the total cross section is infinite), although the radiative stopping power is finite. When the input value of W_{cr} is negative, PENELOPE sets W_{cr} = 10 eV and disregards the emission of photons with lower energies, thus performing an almost detailed simulation of radiative events. A clear advantage of our class-II scheme is that its accuracy and stability under variations of the user parameters can be numerically verified by simply comparing the simulation results with those of a detailed simulation.

4 C++ CLASSES AND COUPLING TO GEANT4

Linking the PENELOPE physics and tracking subroutines to GEANT4 was not trivial because *1*) PENELOPE transports electrons and positrons by using a class-II algorithm which operates differently to the tracking method used by GEANT4, and *2*) PENELOPE builds its interaction models from a material database that is different from the one used by GEANT4. To ensure consistency, and to reduce the interference between the two transport modes, the PENELOPE tracking is allowed in a limited energy interval, which by default extends from E_{min} = 50 eV to E_{max} = 1 GeV. Electrons, positrons, and photons with energies higher than E_{max} are followed by GEANT4 as ordinary particles. The user defines a threshold energy E_{thr}, necessarily less than E_{max}, at which the transported electron, positron or gamma is converted into a PENELOPE-type particle by cloning its state variables, and the remaining part of the history, until its completion, is generated by the PENELOPE classes. To prevent interfering with the GEANT4 logic, electrons, positrons, and photons passed to the PENELOPE classes are considered as particles of a special type (denoted as "pe-", "pe+", and "pgamma", respectively) different from the GEANT4 "ordinary" particles. In addition, secondary electrons, positrons, and photons released with initial energies less than E_{thr} are directly tracked by the PENELOPE classes.

The C++ translation of the PENELOPE physics and transport subroutines is organized in two directories: `penG4include` and `penG4src`, which store the corresponding header and source files, respectively. The coupling of the two simulation codes is organized as follows:

- The file `penG4include/PenelopeDefines.hh` includes the definitions of all the constants, global variables and global-scope methods. Similarly, common variables and namespaces are declared in `penG4include/common-share.hh`.
- The C++ PENELOPE classes are organized into shared and thread-local sets according to the multi-thread design of GEANT4. Thus, the PENELOPE methods and data with thread-local scope are declared in `penG4include/local.h` and defined in `*.cpp` files contained in the `penG4src/localSubs` directory, whereas methods and data that are shared over threads are declared in `penG4include/share.h` and implemented in files named `*.cpp` and placed in the `penG4src/shareSubs/`directory.
- The classes `PenInterface` and `PenPhys` encapsulate the C++ PENELOPE classes. They constitute the "bridge" between PENELOPE and the classes of the GEANT4 application using them.
- The class `PenPhys` encapsulates the PENELOPE physics functions that are called during the tracking of particles, and it works with the thread-local classes mentioned above. Its public methods are issued from the `PenEMProcess` class, which dictates the physics and tracking models that are applied and proposes changes in the state variables of the particle being tracked.
- `PenInterface` is a singleton class which contains all the methods shared over threads. In the GEANT4 application, this class is used *1*) to register each material in the `DetectorConstruction` class with its corresponding transport parameters `EABS(1-3)`, `C1`, `C2`, `WCC` and `WCR` for tracking of "pe-", "pe+", and "pgamma" particles, and *2*) to define the energy range (E_{min}, E_{max}) where the PENELOPE tracking is applied. By default the code sets E_{min} = 50 eV and E_{max} = 1 GeV; these values can be set from the `PenelopeEMPhysics` constructor as indicated below. In addition, `PenInterface` is responsible for initializing the PENELOPE classes. The class design also allows the user to create user-interface commands to set the transport parameters for each material.
- The remaining classes of the code interface define the PENELOPE-type particles being tracked by the GEANT4 application and the *processes* modeling their

electromagnetic interactions with matter. The code defines three new particle types by using the `G4ParticleDefinition` constructor, which correspond to electrons, photons, and positrons that are tracked by PENELOPE and clone the static properties (rest mass, charge, etc.) of ordinary GEANT4 particles,

- `PenElectron` for a PENELOPE-type electron, "`pe-`",
- `PenGamma` for a PENELOPE-type photon, "`pgamma`",
- `PenPositron` for a PENELOPE-type positron, "`pe+`".

Thus, during the same simulation we may use either `G4Electron`, `G4Gamma` and `G4Positron` and follow particles with ordinary GEANT4 electromagnetic physics, or `PenElectron`, `PenGamma` and `PenPositron` for tracking them with the PENELOPE physics and tracking.

As mentioned above, particles with energy E higher than E_{thr} are tracked by GEANT4. When a particle (electron, photon, or positron) reaches a kinetic energy below E_{thr}, it must be converted to the corresponding PENELOPE-type particle to switch the tracking to PENELOPE. With this purpose, two classes derived from `G4VProcess` were defined:

- `PenEMProcess` is the wrapper class for the PENELOPE physics; it is only applicable to PENELOPE-type particles. All the changes of the particle state variables are proposed *via* the process `PostStepDoIt()`, *i.e.*, in the same way as for discrete interactions. In addition, the `PenInterface` singleton is initialized within `PenEMProcess::BuildPhysicsTable()`, which in multi-thread mode is invoked once the GEANT4 execution gets initialized by, for instance, issuing (blank) `run/initialize` command in a macro file.
- `PenPartConvertProcess` is the process responsible for converting a GEANT4-type particle into the equivalent PENELOPE-type particle once its kinetic energy falls below the threshold energy E_{thr}. The value of E_{thr}, which must be $\leq E_{\text{max}}$ can be set by passing it as an argument of the `PenPartConvertProcess` constructor or using the `SetThresholdEnergy()` method. The class `PenEMProcess` is derived from `G4VDiscreteProcess`, it is of type `fDecay` and is only applicable to particles of types `G4Electron`, `G4Gamma` and `G4Positron`. It works by defining a special "decay" from the GEANT4 ordinary particle to its corresponding PENELOPE particle, keeping its dynamic properties (position, energy, direction of momentum, total time of flight...).

Notice that no process is defined to do the inverse conversion, *i.e.*, we assume that once the PENELOPE mode is entered, it remains active until the end of the transported particle history. It is also important to point out that the GEANT4 production thresholds do not apply to the PENELOPE physics and tracking.

Finally, a physics constructor named `PenelopeEMPhysics` derived from the generic `G4VPhysicsConstructor`, has been written to ease the inclusion of PENELOPE physics into a GEANT4 application by using a modular physics list. The value E_{thr} = 500 keV is assumed by default; it can be modified by passing the desired value as argument of the `G4PenelopeEMPhysics` constructor. Moreover, E_{max} can be set within the `ConstructProcess()` method *via* the `PenInterface` singleton. The values E_{thr} and E_{max} can also be set by issuing commands from a macro file. The `PenelopeEMPhysics` constructor registers in the `ConstructParticles()` method the PENELOPE-type particles (`PenElectron`, `PenGamma`, and `PenPositron`). The `ConstructProcess()` method has been designed *1*) to add `PenPartConvertProcess` as a discrete process that converts the ordinary GEANT4 electrons, photons, and positrons, when their energies fall below E_{thr}, into PENELOPE-type particles, and *2*) to add `PenEMProcess` as the *only* discrete process for the PENELOPE-type particles.

In what follows, for the sake of brevity, the combination of GEANT4 and the PENELOPE C++ methods and database will be named PENG4.

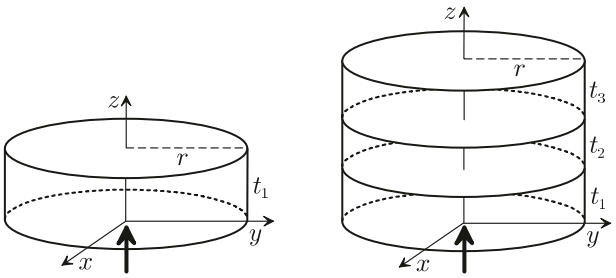

FIGURE 8 | Schematic diagram of the geometries adopted in the example simulations. In all the examples, a pencil beam of particles impinges on the lower surface of the material cylinder along the *z* axis.

5 VALIDATION OF THE PENELOPE CLASSES

To verify the correctness of the implementation of the PENELOPE physics and tracking scheme into GEANT4, a series of simulations of monoenergetic pencil beams of electrons, positrons and photons incident on simple material structures have been performed. The considered geometries (*see* **Figure 8**) are either a homogeneous cylinder of radius r and thickness t_1, or a number of stacked cylinders of the same radius and heights t_1, t_2, ... In all cases the radiation beam impinges along the z axis, which coincides with the symmetry axis of the cylinders.

Simulations were performed by running the PENELOPE Fortran code and the PENG4 C++ code under strictly equivalent conditions, *i.e.*, for the same materials and geometry parameters, the same beam characteristics, and the same set of simulation parameters. As the two codes utilize different random number generators, their results are expected to be consistent (within estimated statistical uncertainties) but not identical. The simulated arrangements were selected so as to evidence the consistency of the two simulations, and to magnify

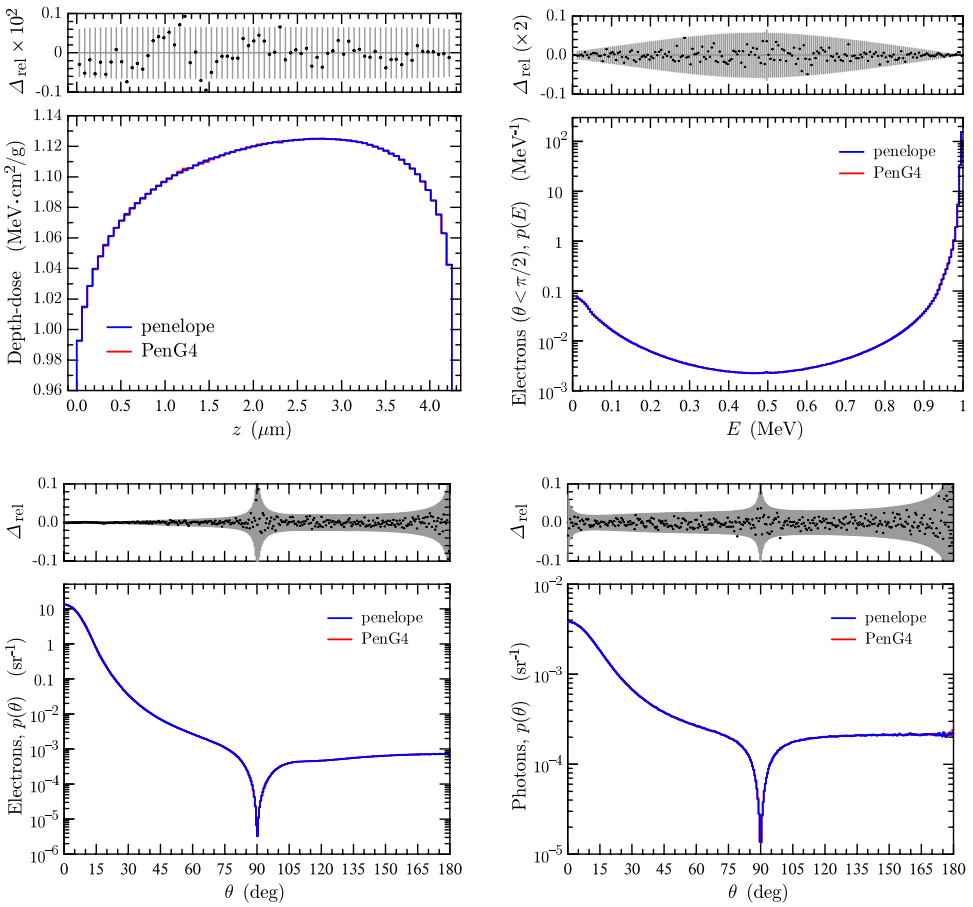

FIGURE 9 | Simulation results for 1 MeV electrons incident on a copper cylinder, as described in the text. The blue histograms are results from PENELOPE. Red histograms, practically invisible, are results from PENG4. The upper diagram in each plot displays the relative differences of the results (dots) and their associated statistical uncertainties with coverage factor = 3 (gray bars).

the effect of interfaces in thin structures, which is where the PENELOPE tracking is deemed to be superior. It is worth mentioning that the adopted values of the simulation parameters were set to magnify the relevant processes, rather than ensuring reliability of the results.

In the following paragraphs we give a brief description of the various cases considered for validation of PENG4, with plots of sample results. The provided results era expected to be helpful to users of PENG4 as a basic test to confirm that the code is being used correctly. All distributions are normalized per primary particle and thus, for instance, the integral of the depth-dose distribution $D(z)$ over depth z equals the average energy deposited into the target by each incident particle. Each plotted distribution is accompanied with a small plot of the relative difference Δ_{rel} between the PENG4 and PENELOPE values (dots) and its statistical uncertainty (gray bars). Generally, Δ_{rel} is less than its uncertainty, that is, the results from the two codes are statistically consistent.

1. Electron Beam on a Copper Cylinder

In this example a beam of 1 MeV electrons impinged on a copper cylinder (material ID = 29) having radius $r = 1$ cm and thickness $t_1 = 4.25 \times 10^{-4}$ cm, about 75 elastic mean free paths of electrons with the initial energy. The parameters used in these simulations were $E_{\text{max}} = E_{\text{thr}} = 1$ MeV (*i.e.*, all particles were of PENELOPE type), $C_1 = C_2 = 0.05$, $W_{\text{cc}} = W_{\text{cr}} = 1$ keV, $E_{\text{abs}}(1) = E_{\text{abs}}(3) = 10$ keV, $E_{\text{abs}}(2) = 1$ keV, $s_{\text{max}} = 2 \times 10^{-5}$ cm, and each simulation run involved the generation of 2.0×10^9 showers. **Figure 9** shows partial results from the simulations: the depth-dose distribution (integrated laterally), the energy distribution of transmitted (upbound) electrons, and the angular distributions of electrons and photons emerging from the material cylinder. The blue histograms are results from PENELOPE; they effectively mask the results from PENG4, represented as red histograms, which are only visible where statistical uncertainties are appreciable.

2. Electrons on a Tungsten Plate

Figure 10 shows partial results from simulations of 125 keV electrons impinging on a tungsten cylinder (material ID = 74) with radius $r = 1$ cm and thickness $t_1 = 24\,\mu$m, approximately equal to the CSDA range of incident electrons. The adopted

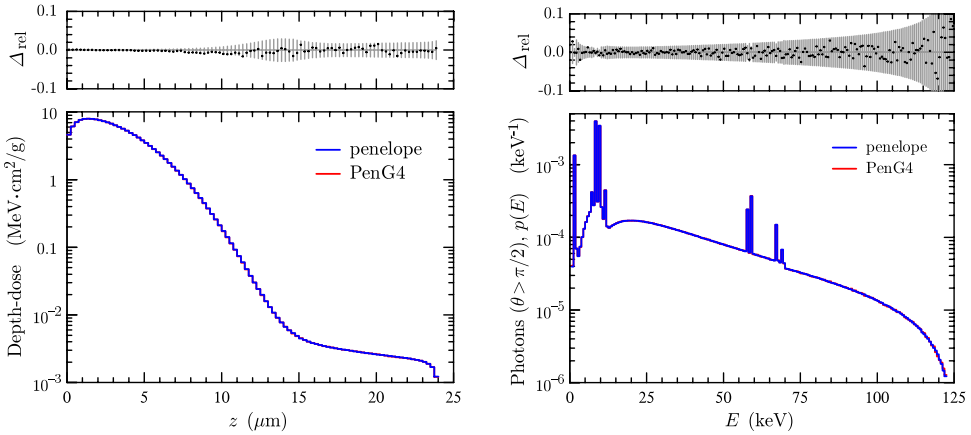

FIGURE 10 | Simulation results for 125 keV electrons incident on a tungsten cylinder. Details are the same as in **Figure 9**.

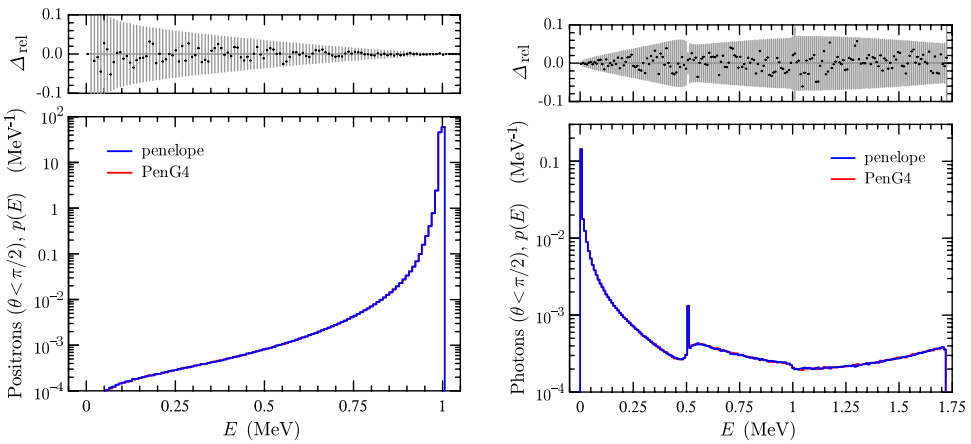

FIGURE 11 | Simulation results for 1 MeV positrons on a copper foil. Details are the same as in **Figure 9**.

simulation parameters were $E_{\rm max} = E_{\rm thr} = 125$ keV, $C_1 = C_2 = 0.05$, $W_{\rm cc} = W_{\rm cr} = 1$ keV, $E_{\rm abs}(1) = E_{\rm abs}(3) = 5$ keV, $E_{\rm abs}(2) = 1$ keV. The variance-reduction techniques of interaction forcing and bremsstrahlung and x-ray splitting were used in the PENELOPE simulation, while PENG4 did an analogue simulation. The displayed results are the depth-dose distribution (integrated laterally) and the energy distribution of photons released with polar angles $\theta > 90^\circ$ (lower hemisphere).

3. Positron Beam on a Copper Foil

Simulations were performed for 1 MeV positrons incident on a copper foil (material ID = 29) having radius $r = 1$ cm and thickness $t_1 = 4.25 \times 10^{-4}$ cm. The parameters used in these simulations were $E_{\rm max} = E_{\rm thr} = 1.82952$ MeV (*i.e.*, 1.21 times the initial total energy of positrons, including their rest mass), $C_1 = C_2 = 0.05$, $W_{\rm cc} = W_{\rm cr} = 1$ keV, $E_{\rm abs}(1) = E_{\rm abs}(3) = 10$ keV, $E_{\rm abs}(2) = 1$ keV, $s_{\rm max} = 2 \times 10^{-5}$ cm, and 2.0×10^9 showers were generated in each run. **Figure 11** shows the calculated energy distributions of transmitted positrons and photons, which are sensitive to both positron and photon transport.

4. Photons on a 1.5" NaI Detector With Aluminium Backing

In this simulation example a 1.25 MeV photon beam impinges on a NaI cylinder (material ID = 253) covered with an aluminium cylinder (material ID = 13); the two cylinders have the same radius, $r = 1.905$ cm, and the heights of the NaI and the Al cylinders are $t_1 = 3.810$ cm and $t_2 = 2.190$ cm, respectively. Simulations were run with the parameters $E_{\rm max} = E_{\rm thr} = 1.25$ MeV, $C_1 = C_2 = 0.1$, $W_{\rm cc} = W_{\rm cr} = 2$ keV, $E_{\rm abs}(1) = E_{\rm abs}(3) = 50$ keV, $E_{\rm abs}(2) = 10$ keV. **Figure 12** shows depth-dose distribution (integrated laterally) with a noteworthy interface discontinuity, and the spectrum of energy deposited in the NaI cylinder, which features scape peaks of positron-annihilation photons and a visible Compton backscattering peak around the position of the double-scape peak.

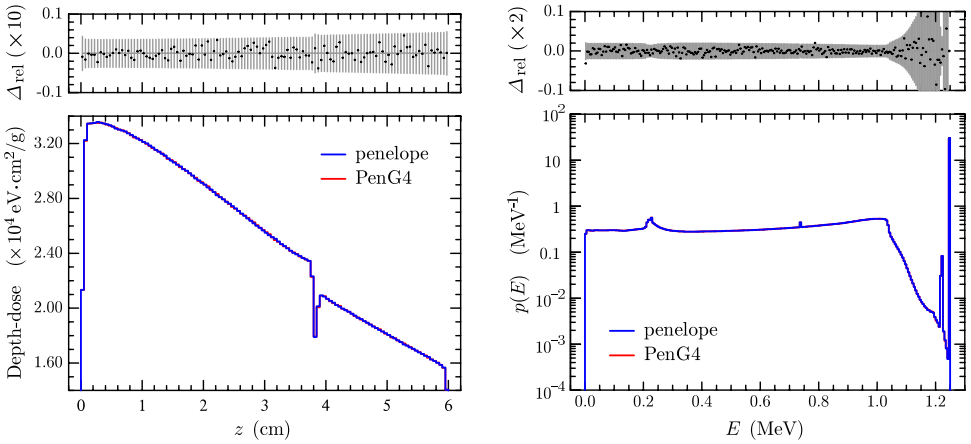

FIGURE 12 | Simulation results for 1.25 MeV photons incident on a NaI cylinder with aluminium backing. Details are the same as in **Figure 9**.

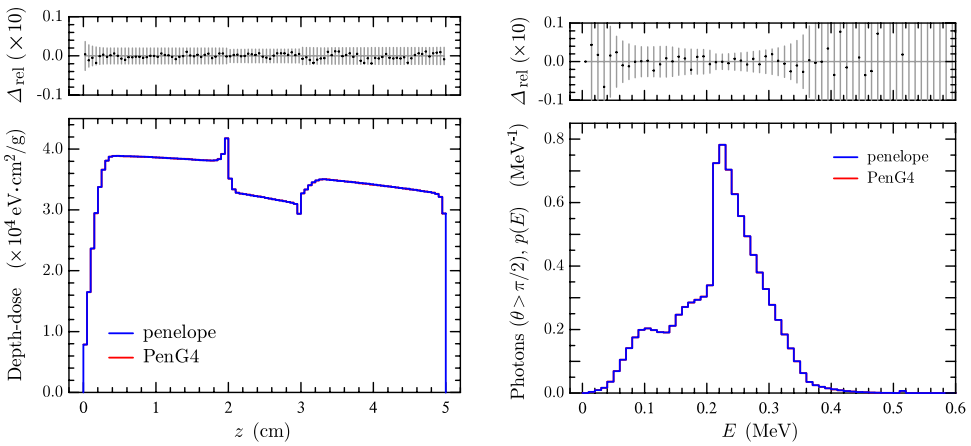

FIGURE 13 | Results for a 1.25 MeV photon beam incident on a stack of three cylinders of water, aluminium, and water. Details are the same as in **Figure 9**.

5. Photons on a Stack of Three Cylinders of Different Materials

We performed simulations of a 1.25 MeV photon beam incident on a stack of three cylinders of radius 50 cm consisting of two layers of liquid water (t_1 = 2 cm and t_3 = 2 cm, material ID = 278) separated by a layer of aluminium (t_2 = 1 cm, material ID = 13). The adopted simulation parameters were $E_{max} = E_{thr}$ = 1.25 MeV, $C_1 = C_2$ = 0.1, $W_{cc} = W_{cr}$ = 2 keV, E_{abs} (1) = E_{abs} (3) = 50 keV, E_{abs} (2) = 10 keV. **Figure 13** shows the simulated depth-dose distributions (integrated laterally) with characteristic discontinuities at the interfaces, and the energy spectra of downbound photons, *i.e.*, emerging from the irradiated object with polar angles larger than 90° (lower hemisphere).

6 CONCLUSION

The code system PENELOPE implements reliable interaction models and a robust class-II mixed scheme for tracking electrons and positrons through complex geometrical structures. In the present article we have summarized the interaction models implemented in the code, and provided a concise description of the class-II algorithm used for tracking electrons and positrons, in a way that can be readily applied to other charged particles (*see*, *e.g.*, Refs. [54, 55]).

Since there is ample evidence of the reliability of PENELOPE's simulation results for electrons/positrons and photons with energies from about 1 keV up to ~1 GeV, we have translated the PENELOPE physics and tracking subroutines to C++ and organized them to be accessible from GEANT4 as an additional physics package. The new tool, named PENG4 has been shown to couple correctly to GEANT4 and to yield results equivalent to those from the original PENELOPE code.

Using the two codes, we have performed a set of test simulations with various incident particles and material structures, which were designed to explore different aspects of the transport physics, and we obtained consistent results. Inclusion of PENG4 as part of the GEANT4 toolkit allows taking advantage of the multi-threading capabilities and advanced geometry and statistical tools of GEANT4.

The PENG4 package, including the PENELOPE C++ classes and physics database, is currently available from the authors, and it will soon be distributed through international agencies.

DATA AVAILABILITY STATEMENT

The original contributions presented in the study are included in the article, further inquiries can be directed to the corresponding authors.

AUTHOR CONTRIBUTIONS

All authors have contributed equally to the work.

ACKNOWLEDGMENTS

Financial support from the Spanish Ministerio de Ciencia, Innovación y Universidades/Agencia Estatal de Investigación/ European Regional Development Fund, European Union, (projects nos. RTI2018-098117-B-C21 and RTI2018-098117-B-C22) is gratefully aknowledged. The work of VA was supported by the program "Ayudas para la contratación de personal investigador en formación de carácter predoctoral, programa VALi+d" under grant number ACIF/2018/148 from the Conselleria d'Educació of the Generalitat Valenciana and the Fondo Social Europeo (FSE). VG acknowledges partial support from FEDER/MCIyU-AEI under grant FPA2017-84543-P, by the Severo Ochoa Excellence Program under grant SEV-2014-0398 and by Generalitat Valenciana through the project PROMETEO/2019/087.

REFERENCES

1. Baró J, Sempau J, Fernández-Varea JM, Salvat F. PENELOPE: An Algorithm for Monte Carlo Simulation of the Penetration and Energy Loss of Electrons and Positrons in Matter. *Nucl Instr Methods Phys Res Section B: Beam Interactions Mater Atoms* (1995) 100:31–46. doi:10.1016/0168-583x(95)00349-5
2. Salvat F. *penelope-2018: A Code System for Monte Carlo Simulation of Electron and Photon Transport*. Boulogne-Billancourt, France: OECD Nuclear Energy Agency, document NEA/MBDAV/R(2019)1 (2019). doi:10.1787/32da5043-en
3. Sempau J, Fernández-Varea JM, Acosta E, Salvat F. Experimental Benchmarks of the Monte Carlo Code PENELOPE. *Nucl Instr Methods Phys Res Section B: Beam Interactions Mater Atoms* (2003) 207:107–23. doi:10.1016/s0168-583x(03)00453-1
4. Agostinelli S, Allison J, Amako K, Apostolakis J, Araujo H, Arce P, et al. Geant4—A Simulation Toolkit. *Nucl Instrum Meth A* (2003) 506:250–303. doi:10.1016/S0168-9002(03)01368-8
5. Allison J, Amako K, Apostolakis J, Araujo H, Arce Dubois P, Asai M. Geant4 Developments and Applications. *IEEE Trans Nucl Sci* (2006) 53:270–8. doi:10.1109/TNS.2006.869826
6. Allison J, Amako K, Apostolakis J, Arce P, Asai M, Aso T. Recent Developments in Geant4. *Nucl Instrum Meth A* (2016) 835:186–225. doi:10.1016/j.nima.2016.06.125
7. Fano U. Penetration of Protons, Alpha Particles, and Mesons. *Annu Rev Nucl Sci* (1963) 13:1–66. doi:10.1146/annurev.ns.13.120163.000245
8. Inokuti M. Inelastic Collisions of Fast Charged Particles with Atoms and Molecules-The Bethe Theory Revisited. *Rev Mod Phys* (1971) 43:297–347. doi:10.1103/revmodphys.43.297
9. ICRU Report 37. *Stopping Powers for Electrons and Positrons*. Bethesda, MD: ICRU (1984). .
10. Salvat F, Fernández-Varea JM. Overview of Physical Interaction Models for Photon and Electron Transport Used in Monte Carlo Codes. *Metrologia* (2009) 46:S112–S138. doi:10.1088/0026-1394/46/2/s08
11. Cromer DT, Liberman D. Relativistic Calculation of Anomalous Scattering Factors for X Rays. *J Chem Phys* (1970) 53:1891–8. doi:10.1063/1.1674266
12. Cullen DE, Hubbell JH, Kissel L. EPDL97 the Evaluated Photon Data Library, '97 Version. In: *Tech. Rep. UCRL-50400*. Livermore, CA: Lawrence Livermore National Laboratory (1997).
13. Brusa D, Stutz G, Riveros JA, Fernández-Varea JM, Salvat F. Fast Sampling Algorithm for the Simulation of Photon Compton Scattering. *Nucl Instr Methods Phys Res Section A: Acc Spectrometers, Detectors Associated Equipment* (1996) 379:167–75. doi:10.1016/0168-9002(96)00652-3
14. Biggs F, Mendelsohn LB, Mann JB. Hartree-Fock Compton Profiles for the Elements. *At Data Nucl Data Tables* (1975) 16:201–309. doi:10.1016/0092-640x(75)90030-3
15. Sabbatucci L, Salvat F. Theory and Calculation of the Atomic Photoeffect. *Radiat Phys Chem* (2016) 121:122–40. doi:10.1016/j.radphyschem.2015.10.021
16. Liberman DA, Cromer DT, Waber JT. Relativistic Self-Consistent Field Program for Atoms and Ions. *Comp Phys Commun* (1971) 2:107–13. doi:10.1016/0010-4655(71)90020-8
17. Salvat F, Fernández-Varea JM. Radial: A Fortran Subroutine Package for the Solution of the Radial Schrödinger and Dirac Wave Equations. *Comp Phys Commun* (2019) 240:165–77. doi:10.1016/j.cpc.2019.02.011
18. Carlson TA. *Photoelectron and Auger Spectroscopy*. New York, NY: Plenum Press (1975).
19. Pratt RH, Tseng HK. Behavior of Electron Wave Functions Near the Atomic Nucleus and Normalization Screening Theory in the Atomic Photoeffect. *Phys Rev A* (1972) 5:1063–72. doi:10.1103/physreva.5.1063
20. Sauter F. Über den atomaren Photoeffekt in der K-Schale nach der relativistischen Wellenmechanik Diracs. *Ann Phys* (1931) 403:454–88. doi:10.1002/andp.19314030406
21. Berger MJ, Coursey JS, Zucker MA, Chang J. *Stopping-power and Range Tables for Electrons, Protons, and Helium Ions*. Gaithersburg, MD: Tech. rep., Institute of Standards and Technology (2005). Available at: www.nist.gov/pml/data/star/index.cfm.
22. Salvat F, Jablonski A, Powell CJ. Elsepa-Dirac Partial-Wave Calculation of Elastic Scattering of Electrons and Positrons by Atoms, Positive Ions and Molecules. *Comp Phys Commun* (2005) 165:157–90. doi:10.1016/j.cpc.2004.09.006
23. ICRU Report 77. *Elastic Scattering of Electrons and Positrons*. Bethesda, MD: ICRU (2007).
24. Desclaux JP. A Multiconfiguration Relativistic Dirac-Fock Program. *Comp Phys Commun* (1975) 9:31–45. doi:10.1016/0010-4655(75)90054-5
25. Desclaux JP. Erratum Notice. *Comput Phys Commun* (1977) 13:71. doi:10.1016/0010-4655(77)90029-7
26. Furness JB, McCarthy IE. Semiphenomenological Optical Model for Electron Scattering on Atoms. *J Phys B: Mol Phys* (1973) 6:2280–91. doi:10.1088/0022-3700/6/11/021
27. Liljequist D. A Simple Calculation of Inelastic Mean Free Path and Stopping Power for 50 eV-50 keV Electrons in Solids. *J Phys D: Appl Phys* (1983) 16:1567–82. doi:10.1088/0022-3727/16/8/023
28. Sternheimer RM. The Density Effect for the Ionization Loss in Various Materials. *Phys Rev* (1952) 88:851–9. doi:10.1103/physrev.88.851
29. Bote D, Salvat F. Calculations of Inner-Shell Ionization by Electron Impact with the Distorted-Wave and Plane-Wave Born Approximations. *Phys Rev A* (2008) 77:042701. doi:10.1103/physreva.77.042701
30. Llovet X, Powell CJ, Salvat F, Jablonski A. Cross Sections for Inner-Shell Ionization by Electron Impact. *J Phys Chem Reference Data* (2014) 43:013102. doi:10.1063/1.4832851
31. Seltzer SM, Berger MJ. Bremsstrahlung Spectra from Electron Interactions with Screened Atomic Nuclei and Orbital Electrons. *Nucl Instr Methods Phys Res Section B: Beam Interactions Mater Atoms* (1985) 12:95–134. doi:10.1016/0168-583x(85)90707-4
32. Seltzer SM, Berger MJ. Bremsstrahlung Energy Spectra from Electrons with Kinetic Energy 1 keV-10 GeV Incident on Screened Nuclei and Orbital

Electrons of Neutral Atoms with Z = 1-100. *At Data Nucl Data Tables* (1986) 35:345–418. doi:10.1016/0092-640x(86)90014-8
33. Acosta E, Llovet X, Salvat F. Monte Carlo Simulation of Bremsstrahlung Emission by Electrons. *Appl Phys Lett* (2002) 80:3228–30. doi:10.1063/1.1473684
34. Poškus A. BREMS: A Program for Calculating Spectra and Angular Distributions of Bremsstrahlung at Electron Energies Less Than 3 MeV. *Comput Phys Commun* (2018) 232:237–55. doi:10.17632/mvd57skzd9.1
35. Kissel L, Quarles CA, Pratt RH. Shape Functions for Atomic-Field Bremsstrahlung from Electrons of Kinetic Energy 1-500 keV on Selected Neutral Atoms $1 \leq Z \leq 92$. *At Data Nucl Data Tables* (1983) 28:381–460. doi:10.1016/0092-640x(83)90001-3
36. Heitler W. *The Quantum Theory of Radiation*. London, UK: Oxford University Press (1954).
37. Nelson WR, Hirayama H, Rogers DWO. *The EGS4 Code System*. Stanford, CA: Stanford Linear Accelerator Center (1985).
38. Perkins ST, Cullen DE, Chen MH, Hubbell JH, Rathkopf J, Scofield J. *Tables and Graphs of Atomic Subshell and Relaxation Data Derived from the LLNL Evaluated Atomic Data Library (EADL), Z = 1–100*. Livermore, CA: Lawrence Livermore National Laboratory (1991).
39. Deslattes RD, Kessler EG, Indelicato P, de Billy L, Lindroth E, Anton J. X-ray Transition Energies: New Approach to a Comprehensive Evaluation. *Rev Mod Phys* (2003) 75:36–99. doi:10.1103/revmodphys.75.35
40. Bearden JA. X-ray Wavelengths. *Rev Mod Phys* (1967) 39:78–124. doi:10.1103/revmodphys.39.78
41. Walker AJ. An Efficient Method for Generating Discrete Random Variables with General Distributions. *ACM Trans Math Softw* (1977) 3:253–6. doi:10.1145/355744.355749
42. Berger MJ. Monte Carlo Calculation of the Penetration and Diffusion of Fast Charged Particles. In: B Alder, S Fernbach, M Rotenberg, editors. *Methods in Computational Physics*. New York, NY: Academic Press (1963). 135–215.
43. Berger MJ, Seltzer SM. An Overview of ETRAN Monte Carlo Methods. In: TM Jenkins, WR Nelson, A Rindi, editors. *Monte Carlo Transport of Electrons and Photons*. New York, NY: Plenum (1988).
44. Berger MJ, Seltzer SM. Applications of ETRAN Monte Cario Codes. In: TM Jenkins, WR Nelson, A Rindi, editors. *Monte Carlo Transport of Electrons and Photons*. New York, NY: Plenum (1988).
45. Berger MJ, Seltzer SM. ETRAN — Experimental Benchmarks. In: TM Jenkins, WR Nelson, A Rindi, editors. *Monte Carlo Transport of Electrons and Photons*. New York, NY: Plenum (1988).
46. Halbleib JA, Kensek RP, Mehlhorn TA, Valdez GD, Seltzer SM, Berger MJ. ITS Version 3.0: the Integrated TIGER Series of Coupled Electron/photon Monte Carlo Transport Codes. In: *Tech. Rep. SAND91-1634*. Albuquerque, NM: Sandia National Laboratories (1992).
47. Kawrakow I, Rogers DWO. EGSnrc Code System: Monte Carlo Simulation of Electron and Photon Transport. In: *Tech. Rep. PIRS-701*. Ottawa: National Research Council of Canada (2001).
48. X-5 Monte Carlo Team. *MCNP—A General Monte Carlo N-Particle Transport Code)*. Los Alamos, NM: Los Alamos National Laboratory (2003).
49. Ferrari A, Sala PR, Fassò A, Ranft J. Fluka: A Multi-Particle Transport Code. In: *Tech. Rep. CERN-2005-00X*. Geneva: CERN (2005). doi:10.2172/877507
50. Hirayama H, Namito Y, Bielajew AF, Wilderman SJ, Nelson WR. *The EGS5 Code System. Tech. Rep. SLAC-R-730*. Menlo Park, CA: Stanford Linear Accelerator Center (2006).
51. Goorley JT, James MR, Booth TE, Brown FB, Bull JS, Cox LJ, et al.*Initial MCNP6 Release Overview - MCNP6 Version 1.0*. Los Alamos, NM: Los Alamos National Laboratory (2013).
52. Giménez-Alventosa V, Giménez Gómez V, Oliver S. PenRed: An Extensible and Parallel Monte-Carlo Framework for Radiation Transport Based on PENELOPE. *Comp Phys Commun* (2021) 267:108065. doi:10.1016/j.cpc.2021.108065
53. Fernández-Varea JM, Mayol R, Baró J, Salvat F. On the Theory and Simulation of Multiple Elastic Scattering of Electrons. *Nucl Instr Methods Phys Res Section B: Beam Interactions Mater Atoms* (1993) 73:447–73. doi:10.1016/0168-583x(93)95827-r
54. Salvat F. A Generic Algorithm for Monte Carlo Simulation of Proton Transport. *Nucl Instr Methods Phys Res Section B: Beam Interactions Mater Atoms* (2013) 316:144–59. doi:10.1016/j.nimb.2013.08.035
55. Salvat F, Quesada JM. Nuclear Effects in Proton Transport and Dose Calculations. *Nucl Instr Methods Phys Res Section B: Beam Interactions Mater Atoms* (2020) 475:49–62. doi:10.1016/j.nimb.2020.03.017
56. Goudsmit S, Saunderson JL. Multiple Scattering of Electrons. *Phys Rev* (1940) 57:24–9. doi:10.1103/physrev.57.24
57. Lewis HW. Multiple Scattering in an Infinite Medium. *Phys Rev* (1950) 78:526–9. doi:10.1103/physrev.78.526
58. Bielajew AF. HOWFAR and HOWNEAR: Geometry Modeling for Monte Carlo Particle Transport. In: *Tech. Rep. PIRS-0341*. Ottawa: National Research Council of Canada (1995).
59. Kawrakow I, Bielajew AF. On the Condensed History Technique for Electron Transport. *Nucl Instr Methods Phys Res Section B: Beam Interactions Mater Atoms* (1998) 142:253–80. doi:10.1016/s0168-583x(98)00274-2
60. Bielajew AF, Salvat F. Improved Electron Transport Mechanics in the PENELOPE Monte-Carlo Model. *Nucl Instr Methods Phys Res Section B: Beam Interactions Mater Atoms* (2001) 173:332–43. doi:10.1016/s0168-583x(00)00363-3

Conflict of Interest: The authors declare that the research was conducted in the absence of any commercial or financial relationships that could be construed as a potential conflict of interest.

Publisher's Note: All claims expressed in this article are solely those of the authors and do not necessarily represent those of their affiliated organizations, or those of the publisher, the editors and the reviewers. Any product that may be evaluated in this article, or claim that may be made by its manufacturer, is not guaranteed or endorsed by the publisher.

frontiers in Physics

ORIGINAL RESEARCH
published: 07 January 2022
doi: 10.3389/fphy.2021.797354

The Evolution of Lateral Dose Distributions of Helium Ion Beams in Air: From Measurement and Modeling to Their Impact on Treatment Planning

Judith Besuglow[1,2,3,4], *Thomas Tessonnier*[5], *Benedikt Kopp*[1,2,3], *Stewart Mein*[1,2,3] *and Andrea Mairani*[1,5,6]*

[1]Clinical Cooperation Unit Translational Radiation Oncology, German Cancer Consortium (DKTK) Core-Center Heidelberg, National Center for Tumor Diseases (NCT), Heidelberg University Hospital (UKHD) and German Cancer Research Center (DKFZ), Heidelberg, Germany, [2]Division of Molecular and Translational Radiation Oncology, Heidelberg Faculty of Medicine (MFHD) and Heidelberg University Hospital (UKHD), Heidelberg Ion-Beam Therapy Center (HIT), Heidelberg, Germany, [3]Heidelberg Faculty of Medicine (MFHD), Heidelberg Institute of Radiation Oncology (HIRO), National Center for Radiation Oncology (NCRO), Heidelberg University Hospital (UKHD), Heidelberg Ion-Beam Therapy Center (HIT), and German Cancer Research Center (DKFZ), Heidelberg, Germany, [4]Department of Physics and Astronomy, Heidelberg University, Heidelberg, Germany, [5]Heidelberg Ion-Beam Therapy Center (HIT), Department of Radiation Oncology, Heidelberg University Hospital (UKHD), Heidelberg, Germany, [6]National Centre of Oncological Hadrontherapy (CNAO), Medical Physics, Pavia, Italy

OPEN ACCESS

Edited by:
Miguel Antonio Cortés-Giraldo, Sevilla University, Spain

Reviewed by:
Alejandro Bertolet, Massachusetts General Hospital and Harvard Medical School, United States
Mauro Valente, CCT CONICET Córdoba, Argentina

***Correspondence:**
Andrea Mairani
andrea.mairani@med.uni-heidelberg.de

Specialty section:
This article was submitted to Radiation Detectors and Imaging, a section of the journal Frontiers in Physics

Received: *18 October 2021*
Accepted: *24 November 2021*
Published: *07 January 2022*

Citation:
Besuglow J, Tessonnier T, Kopp B, Mein S and Mairani A (2022) The Evolution of Lateral Dose Distributions of Helium Ion Beams in Air: From Measurement and Modeling to Their Impact on Treatment Planning. Front. Phys. 9:797354. doi: 10.3389/fphy.2021.797354

To start clinical trials with the first clinical treatment planning system supporting raster-scanned helium ion therapy, a comprehensive database of beam characteristics and parameters was required for treatment room-specific beam physics modeling at the Heidelberg Ion-Beam Therapy Center (HIT). At six different positions in the air gap along the beam axis, lateral beam profiles were systematically measured for 14 initial beam energies covering the full range of available energies at HIT. The 2D-array of liquid-filled ionization chambers OCTAVIUS from PTW was irradiated by a pencil beam focused at the central axis. With a full geometric representation of HIT's monitoring chambers and beamline elements in FLUKA, our Monte Carlo beam model matches the measured lateral beam profiles. A second set of measurements with the detector placed in a water tank was used to validate the adjustments of the initial beam parameters assumed in the FLUKA simulation. With a deviation between simulated and measured profiles below ±0.8 mm for all investigated beam energies, the simulated profiles build part of the database for the first clinical treatment planning system for helium ions. The evolution of beamwidth was also compared to similar simulations of the clinically available proton and carbon beam. This allows a choice of treatment modality based on quantitative estimates of the physical beam properties. Finally, we investigated the influence of beamwidth variation on patient treatment plans in order to estimate the relevance and necessary precision limits for lateral beam width models.

Keywords: particle therapy, Monte Carlo simulation, Helium, treatment planning system, ion beam, lateral profiles, dosimetry

1 INTRODUCTION

Lyman and Howard measured the first helium Bragg peaks to use in radiotherapy in the 1970s [1]. Between 1975 and 1992, over 2000 patients received helium ion radiotherapy at the Lawrence Berkeley National Laboratory (LBNL) [2–6]. However, the treatment with helium ions was discontinued in the early 1990s, when the Bevatron and 184-inch-synchrocyclotron were dismantled.

At the Heidelberg Ion-Beam Therapy Center (HIT), protons, helium, carbon, and oxygen ions are accelerated and delivered with active beam scanning [7] for radiotherapeutic and research purposes since 2009. To this day, only protons and carbon ions are in regular clinical use. However, with the work presented in this study the first clinical application of helium ion beams was possible this year.

The treatment planning system (TPS) previously used (syngo® PT Treatment, Siemens AG, Erlangen, Germany) had only been commissioned for carbon ion and proton treatment. Therefore, we supported the beam physics modeling within the first commercial TPS (RayStation, RaySearch Laboratories, Stockholm, Sweden [8]) supporting helium ion irradiation through the creation of a database comprising beam-specific parameters and characteristics based on measurements or simulations.

A general attempt at gathering facility-specific helium beam properties at HIT had been made by Tessonnier et al. [9–12] by establishing a Monte Carlo (MC) framework for recalculating irradiation plans with FLUKA [13, 14]. However, the agreement between measurement and simulations showed limitations for fields with high initial beam energies [10], calling for a more precise estimation of secondary particle production in medium. Since then, new charge- and mass-changing cross-sections in the energy region between 70–220 MeV/u have been determined experimentally [15] and updated in FLUKA. At HIT, attempts of measuring the secondary particles produced by helium ions have been made [16]. Additional characterization of the double differential nuclear reaction cross-section for helium in the therapeutically relevant energy range could further improve dose estimation in beam entrance and fragmentation tail [17]. The implementation of this newly available data calls for revalidation of the beam properties in our MC framework.

Helium ions exhibit physical and biological properties that are moderate between protons and carbon ions. In contrast, carbon ions feature a very sharp lateral penumbra, a sharp peak in the depth dose distribution, and a high linear energy transfer (LET) compared to helium ions and protons. However, their produced secondary particles result in a more significant fragmentation tail. Proton Bragg peaks, on the other hand, exhibit a smaller peak-to-plateau ratio than helium ions. Both, carbon ions and protons, have distinct strengths and weaknesses in the context of clinical practice, as nicely summarized in review papers [18, 19]. Thus, helium ions can bridge the gap in achievable dose conformality and LET between proton and carbon ion beams.

Similar to the HIT carbon ion commissioning [20–23], the set of data gathered for beam physics modeling in the RayStation TPS included laterally integrated depth dose curves (iDDDs), calibration of absolute dose per particle, and particle spectra [24]. However, while the collection of depth dose curves and absolute calibrations of helium ion dose was updated with respect to previous publications, lateral profiles in the air gap between the last beamline element and phantom had never been thoroughly investigated for raster-scanned helium ion beams.

Schardt et al. reported in [25] how beamline materials and the airgap affect the beam widths of proton and carbon ions. On the one hand, carbon ions are relatively heavy, and the beam broadening in air is primarily independent of the initial beam energy. The broadening of proton beams, on the other hand, is much more considerable than for carbon of any energy, and it depends heavily on the initial beam energy. The same multiple scattering processes apply to helium ions. While the resulting broadening of beamwidth could be estimated analytically via the Highland approximation [26, 27], this approach would neglect large angle scattering and the dose contribution of secondary hadron production in the beamline. Analytical calculations of beam broadening by multiple scattering via Molière-theory [28–30] would be quite time-intensive and would still neglect the beam shape specific to the HIT beamline. Moreover, no knowledge of the actual beam shape in air could be gained. Würl et al. [31] showed for protons that the beam shape in air impacts the dose distribution in the patient as well.

Therefore, precise knowledge of the profiles in the air between the vacuum exit and the patient should improve the prediction of the beam shape at the surface entrance point of a phantom or patient. As the lateral dose distribution in this airgap has not been investigated for actively scanned helium beams before, this work quantifies the evolution of the beamwidth and its impact on treatment planning.

Measured beam profiles in air provide the starting beam parameters in vacuum for our MC physical beam model. The MC model then provides particle spectra and lateral dose distributions as base data to the clinical TPS in addition to measured iDDDs. The TPS then parameterizes the beam profile at the surface entrance point of the patient and propagates the dose based on analytical dose models. Apart from clinical use of the TPS, the MC beam model with all validated beam parameters can support further experimental studies at HIT.

This work reports on the creation of the database of lateral dose profiles specific to the HIT beamline for the first commercial TPS for helium ions. The lateral profiles of single-spot pencil beams are measured in the air gap between the last element of the beamline and patient, as well as inside a water tank. As not all profiles of the 255 available beam energies can be measured, an MC beam model is created, and a database of the lateral beam profiles is simulated in FLUKA.

Furthermore, the beam profiles of helium are compared to those of carbon and proton beams. Lastly, the impact of deviations in the beam profile on dose distributions in patients is studied, and possible applications of the gained knowledge are discussed.

2 MATERIALS AND METHOD

2.1 Helium Ions at Heidelberg Ion Beam Therapy-Center

The HIT is a synchrotron-based particle therapy center with two horizontal treatment rooms and a gantry. Three ion sources

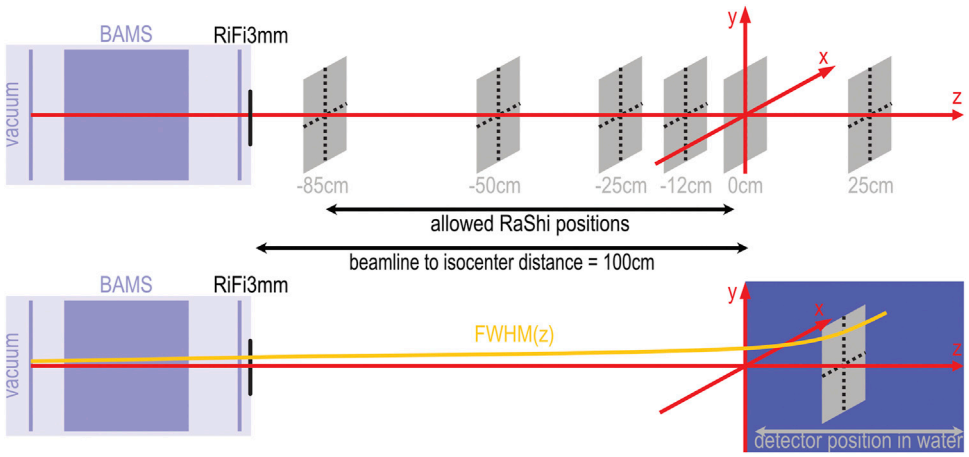

FIGURE 1 | Experimental setup schematic for measurements and simulation. The upper half shows the beamline with monitor system (BAMS) and ripple filter (RiFi3mm) and the positions at which measurements were performed with the OCTAVIUS phantom in air. The lower half of the sketch shows the position of the water tank relative to the isocenter marked by the red coordinate system. A yellow curve sketches the assumed evolution of the beamwidth. The beamline to isocenter distance is 100 cm in the horizontal treatment rooms. At the gantry, this distance is reduced to 80 cm. The allowed positions for the range shifter (RaShi) are continuous between −85 and −2 cm for the horizontal treatment room and between −38.5 and −2 cm for the gantry.

enable the acceleration of protons (1H), helium (4He), carbon (12C), and oxygen (16O) ions. Since 2009, patients have been treated daily with proton and carbon ion beams. The synchrotron accelerates helium ions to 255 discrete energies between 50.57 MeV/u and 220.51 MeV/u, corresponding to ranges of approximately 2.1 and 30.8 cm in water without any beam modifiers. Bunches of primary ions are extracted from the synchrotron by the so-called beam scraper using slow knockout extraction [32, 33] and sent to the individual treatment rooms. Scanning magnets bend the beam across the treated volume, which results in a virtual source-axis-distance of approximately 7 m in the horizontal rooms and about 43 m in the gantry.

Before entering each patient treatment room, the beam passes through a monitoring system (BAMS) consisting of three ionization chambers and two multi-wire proportional chambers, as described by Tessonnier et al. [9]. Behind the BAMS chambers, additional beam modifiers can be inserted into the beamline at positions indicated in **Figure 1**. A 3 mm ripple filter (RiFi3mm) [34] spreads out the individual Bragg peaks to about 2–3 mm and reduces the range by the same length. The insertion of the ripple filter allows a tumor volume to be irradiated faster, as homogeneity in depths can be achieved using only every third available beam energy. A PMMA range shifter of approximately 2 cm water equivalent thickness allows the irradiation of very superficial tumors. It can be placed anywhere between the beamline exit and the room's isocenter.

Each irradiation requires a control file including desired beam energies, beam positions, discrete nominal beamwidths and particle intensity chosen from the accelerator library (LIBC). This so-called irradiation plan also includes the gantry angle and detector or patient table position.

While the beam position (spot) can theoretically be any continuous position in the x,y-plane at the room's isocenter, in practice at HIT, spots are placed on a cartesian or hexagonal grid with fixed spacing to compensate for variations in beamwidth caused by the synchrotron and beamline. The nominal beamwidth is defined as the full width at half maximum (FWHM) in the treatment room's isocenter without any beam modifiers placed in the room. The methodology of creating the accelerator library has been described before [12]. The LIBC contains four discrete nominal beamwidths for each beam energy. Within each discrete configuration, the total beamwidth decreases with increasing beam energy. For treatment planning, a relatively stable spot size over the whole energy range is desired to achieve a homogeneous dose with a fixed spot spacing. Following the results of Parodi et al. [20], beamwidths at least three times larger than the spot spacing still assure homogeneity of the treatment fields. This assumption was made during the first trials for raster scanning ion beams [7, 35]. Thus, for a proposed spot spacing of approximately 2 mm, the beamwidth must be at least 6 mm to achieve a robust homogeneity against beamwidth variation. As the smallest available nominal beamwidth is smaller than this threshold for energies larger than 167 MeV/u, the second nominal beamwidth setting is used for higher energies.

2.2 Measurements with Octavius Phantom

To measure the lateral profiles in air, we positioned a 2D-ionization chamber array (OCTAVIUS 1000 SRS, SN000308, PTW Freiburg) perpendicular to the central beam axis at six positions along the beam axis. Relative to the treatment room's isocenter, the reference point of the detector was positioned at −85, −50, −25, −12, 0 and 12 cm, where "-" denotes any upstream positions. In **Figure 1**, the measurement positions relative to the isocenter are depicted by grey squares.

The OCTAVIUS 1000 SRS consists of 977 liquid-filled ionization chambers with a sensitive volume of 3 mm^3 in a cartesian grid of

2.5 mm spacing in a central area of $(5.5 \times 5.5)\,\mathrm{cm}^2$. At the outer edges the ionization chambers are spaced twice as far apart.

With a dynamic measurement range from 0.2 to 36 Gy/min, the OCTAVIUS chamber array allowed a 0.1 mGy resolution in absolute dose measurement, with a relative uncertainty of ±0.5% local dose, according to the manufacturer.

For each measurement position and tabulated beamwidth, we obtained the lateral dose distributions for 14 initial beam energies distributed over the entire available energy range by irradiating the detector with approximately 10^9 helium ions on the central beam axis. The particle intensity was adjusted for each energy to ensure dose deposition rates within the measurement range.

At the isocenter, we irradiated the same spots without the ripple filter inserted into the beam, allowing for comparison to the accelerator specifications.

Following the same protocol, we measured lateral dose distributions in the gantry at a 90° rotation angle.

2.3 Monte Carlo Simulation

Our simulation of the lateral profiles was based on the MC code FLUKA [13, 14] with the implementation of BAMS and RiFi3mm reported in previous works [9, 10, 21]. All physical interactions were simulated in FLUKA with the HADROTHERAPY defaults. We assumed that delta electrons are not transported by switching off delta ray production. Additionally, we reduced the step size for charged hadrons and muons to 0.02 of the kinetic energy. The evaporation model for heavy fragments and coalescence mechanism was activated as well. All simulations ran with the physics models of the currently available FLUKA version.

The beam was assumed to be non-divergent before leaving the vacuum window of the beamline. For each discrete beam setting of the accelerator, the simulation required three beam parameters: initial beam energy in vacuum, initial Gaussian momentum dispersion, and the Gaussian width of the beam's initial lateral fluence profile. The initial beam energy was assumed to be identical to the nominal beam energy. Following previous works [9], we manually modified the initial momentum spread until simulated depth dose curves matched the commissioning measurements in shape and peak width. With the ripple filter removed from the simulated beamline, we iteratively optimized the initial Gaussian fluence profile to reproduce the nominal beamwidth at the isocenter. Some fine-tuning of the initial parameters regarding those used in previous works [11] was necessary for the updated FLUKA version (2021.1).

Once we found the optimal initial beamwidth, the profiles at all six detector positions were simulated with the ripple filter in place as follows: The simulated geometry included a detailed representation of BAMS and additional beam modifiers. For the profiles in air, a thin disk of water ($r = 14\,\mathrm{cm}$, $\Delta z = 1\,\mathrm{mm}$), at the detector position relative to the beamline, represented the detector. Within this disk, we scored the dose profile D(r) in cylindrical coordinates summing over the azimuthal angle in increments of $\Delta r = 0.5$ mm. For each setting, the dose distribution was averaged over 10^8 primary helium ions initiated in the simulation.

2.4 Evaluation and Comparison of Profiles

From the 2D dose array of the OCTAVIUS, we extracted the central x- and y-profiles and diagonal profiles. These four profiles were fitted with a Gaussian to determine the beam center and normalization. If necessary, a shift and normalization to the maximal dose were applied to overcome lateral positioning uncertainties.

Previous simulations for protons and carbon ions assumed the lateral beamwidth $\mathrm{FWHM}_{\mathrm{tot}}(z)$ could be parametrized by the depth-dependent spread due to scattering and the inherent beamwidth in vacuum $\mathrm{FWHM}_{\mathrm{vac}}$ [22, 21, 10]. Whereas the depth-dependent width can be further split into the constant contribution of the beam modifiers (BAMS and RiFi3mm) and the contribution of the air gap:

$$\mathrm{FWHM}_{\mathrm{tot}}(z)^2 = \mathrm{FWHM}_{\mathrm{vac}}^2 + \left(\mathrm{FWHM}_{\mathrm{BAMS}}^2 + \mathrm{FWHM}_{\mathrm{RiFi3mm}}^2 + \mathrm{FWHM}_{\mathrm{air}}(z)^2\right).$$

At the isocenter ($z = 0$), the total beamwidth without ripple filter should per definition be identical to the nominal beam width $\mathrm{FWHM}_{\mathrm{nom}}$. Since the measurable beam width is subject to daily variations, a scaling factor s_{daily} is introduced for the measurements. Although the contribution of air gap and beam modifiers should be constant, we assumed that the factor equally applies to both sides of the equation. This factor scales the measured profile to the nominal $\mathrm{FWHM}_{\mathrm{nom}}$ of the accelerator library that the simulation was set up to reproduce.

$$\begin{aligned} s_{\mathrm{daily}} &= \frac{\mathrm{FWHM}_{\mathrm{nom}}}{\mathrm{FWHM}_{\mathrm{OCTAVIUS,\,noRiFi}}(z=0)} \\ &\Rightarrow \mathrm{FWHM}_{\mathrm{OCTAVIUS,RiFi3mm}}(z)^2 \cdot s_{\mathrm{daily}}^2 \\ &= s_{\mathrm{daily}}^2 \cdot \left[\mathrm{FWHM}_{\mathrm{vac,daily}}^2 + \left(\mathrm{FWHM}_{\mathrm{BAMS}}^2 \right.\right. \\ &\quad \left.\left. + \mathrm{FWHM}_{\mathrm{RiFi3mm}}^2 + \mathrm{FWHM}_{\mathrm{air}}(z)^2\right)\right] \\ &\cong \mathrm{FWHM}_{\mathrm{tot}}(z)^2 \\ &= \mathrm{FWHM}_{\mathrm{FLUKA,\,RiFi3mm}}(z)^2 \end{aligned}$$

The shape of measurable horizontal profiles is influenced by the slow knockout-extraction from the synchrotron [32]. Thus, only the beam width from the vertical y-profiles measured without ripple filter at the isocenter was considered in calculating the scaling factor.

After scaling the profiles measured with ripple filter by s_{daily}, the beamwidth of scaled, measured profiles should thus be reproduced by the simulated profiles. The simulated and scaled, measured profiles were plotted directly against each other to determine whether the beam shape was sufficiently reproduced. The absolute beam widths (FWHM) were extracted by calculating the width at half of the maximum dose. We reported the average of the four extracted profiles for measured beam widths to even out deviations from axial symmetry. The extracted widths were then analyzed and compared in dependency on the position along the beam axis and initial energy.

2.5 Impact of Beam Width Variation on Patient Treatment

We investigated the effect of the beamwidth at the surface entry point on a treatment plan optimized with RayStation 10 A. A clinical-like treatment plan for helium therapy was generated using multi-field optimization on a patient data set representative for meningioma treatment. For simplicity, we chose beam angles of 0° and 270° and placed the isocenter in the center of the treatment volume. The biological dose optimization was based on the modified

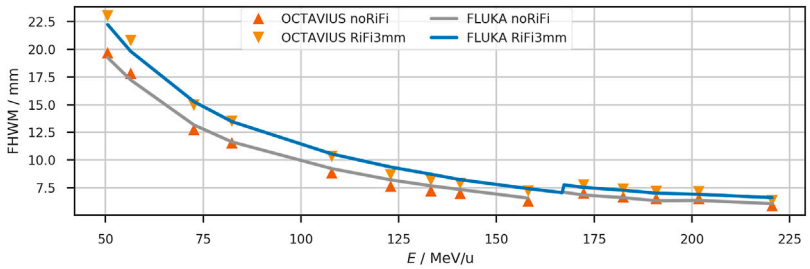

FIGURE 2 | The lateral beam width (FWHM) at the isocenter of the horizontal treatment room. Comparison between measurement (triangles) and simulation (solid lines) with and without ripple filter. For clinical application, the ripple filter is inserted into the beamline. The measurements were scaled to reproduce the nominal accelerator settings when the ripple filter is not used. Between the measured energies, the beam width is interpolated linearly. At nominal beam energy of 167 MeV/u, the beam width jumps to the next higher tabulated focus to fulfill the >6 mm requirement. The measured FWHM has a standard deviation of approximately 0.2 mm at the isocenter.

TABLE 1 | Lateral Widths (FWHM) of the lateral dose profile of a helium beam at the isocenter (z = 0 cm) without ripple filter as extracted from the simulated profiles in FLUKA and scaled profiles measured with the OCTAVIUS detector. Range (R80) and initial beam energy (E) of the unmodified beam and nominal width are also provided in addition to the absolute and relative deviation (ΔFWHM) between measured and simulated profiles.

E in MeV/u		50.57	56.44	72.65	82.33	107.93	122.93	133.21	140.71	158.08	172.28	182.43	190.85	201.71	220.51
R80 in cm		2.14	2.65	4.25	5.36	8.78	11.09	12.79	14.10	17.31	20.12	22.23	24.04	26.45	30.82
FWHM in mm	nominal	18.6	16.7	12.8	11.3	8.9	7.9	7.4	7.1	6.3	6.8	6.6	6.4	6.3	6.1
	OCTAVIUS	19.7	17.8	12.7	11.6	8.8	7.6	7.2	7.0	6.3	7.0	6.7	6.5	6.5	5.9
	FLUKA	19.3	17.2	13.2	11.6	9.2	8.2	7.7	7.3	6.6	6.8	6.6	6.3	6.3	6.0
ΔFWHM in mm		−0.5	−0.6	0.4	0.1	0.4	0.6	0.5	0.4	0.3	−0.2	−0.1	−0.2	−0.2	0.2
ΔFWHM in %		−2.3	−3.4	3.3	0.6	4.5	7.3	6.2	5.3	4.1	−2.8	−1.3	−3.4	−2.8	2.8

microdosimetric-kinetic model (mMKM) with an α/β-ratio of 2 Gy [24].

Then, we varied the beamwidth of the individual pencil beams in air close to the patient entrance point by approximately ∓10% for the same plan to investigate the impact on the irradiated field and organs at risk. The dose distributions produced with varied beam width were forward calculated in the TPS.

From the recalculated plans, we extracted lateral profiles of biological and physical dose in the entrance channel of each beam and diagonally through the clinical target volume (CTV). The profiles extracted from the patient plan were compared and analyzed for differences in the penumbra (lateral distance between 20% and 80% of maximum dose) among the three scenarios. Additionally, we analyzed the dose-volume histograms (DVH) of the target volume (CTV around meningioma) and three neighboring organs at risk (OAR), namely the left parotid gland, right optical nerve and the brain stem.

3 RESULTS

3.1 Beam Profiles

The beamwidth at FWHM at the isocenter is reproduced by the simulations as shown in **Figure 2** and **Table 1**. The nominal accelerator beamwidth is reproduced within 4% when the ripple filter is removed from the beamline. The beam widening by the ripple filter is also reproduced in the simulations, as the dark blue line in **Figure 2** shows. The scaled measurements agree well with the beamwidth extracted from simulated profiles for the beam with the ripple filter in place. The standard deviation of the scaled measured FWHM extracted from the four measured lateral profiles (horizontal, vertical and diagonal) is approximately 0.2 mm or 2% for each position and energy.

Figure 3 shows the shape of lateral profiles at all measured positions for the helium beam with an initial energy of 107.93 MeV/u (158.08 MeV/u). This energy corresponds to a range of approximately 8.8 cm (17.3 cm) in water after passing the beamline and ripple filter. Triangles depict the measured profile. The simulated profiles are scaled to their maximum and shown as a blue line. While the nominal beamwidth without ripple filter is 8.9 mm (6.3 mm) at the isocenter, the measurement yields an average width of 8.8 mm (6.3 mm). The simulation produces a width of 9.2 mm (6.5 mm). With the ripple filter, the average measured beam width is 10.3 mm (7.2 mm) after scaling, and the simulated profile has a beamwidth of 10.5 mm (7.4 mm) at the isocenter. So, the ripple filter broadens the beam of this specific energy by approximately 1.4 mm (0.9 mm). For other investigated beam energies, the extracted profiles with ripple filter are provided in **Table 2**.

3.2 Effect of Beam Width Variation on Patient Treatment

In **Figure 4**, we show the effects of beamwidth variation on the dose distribution produced by a patient treatment plan. In the top panel (A), a selected slice of the patient CT with overlaid dose

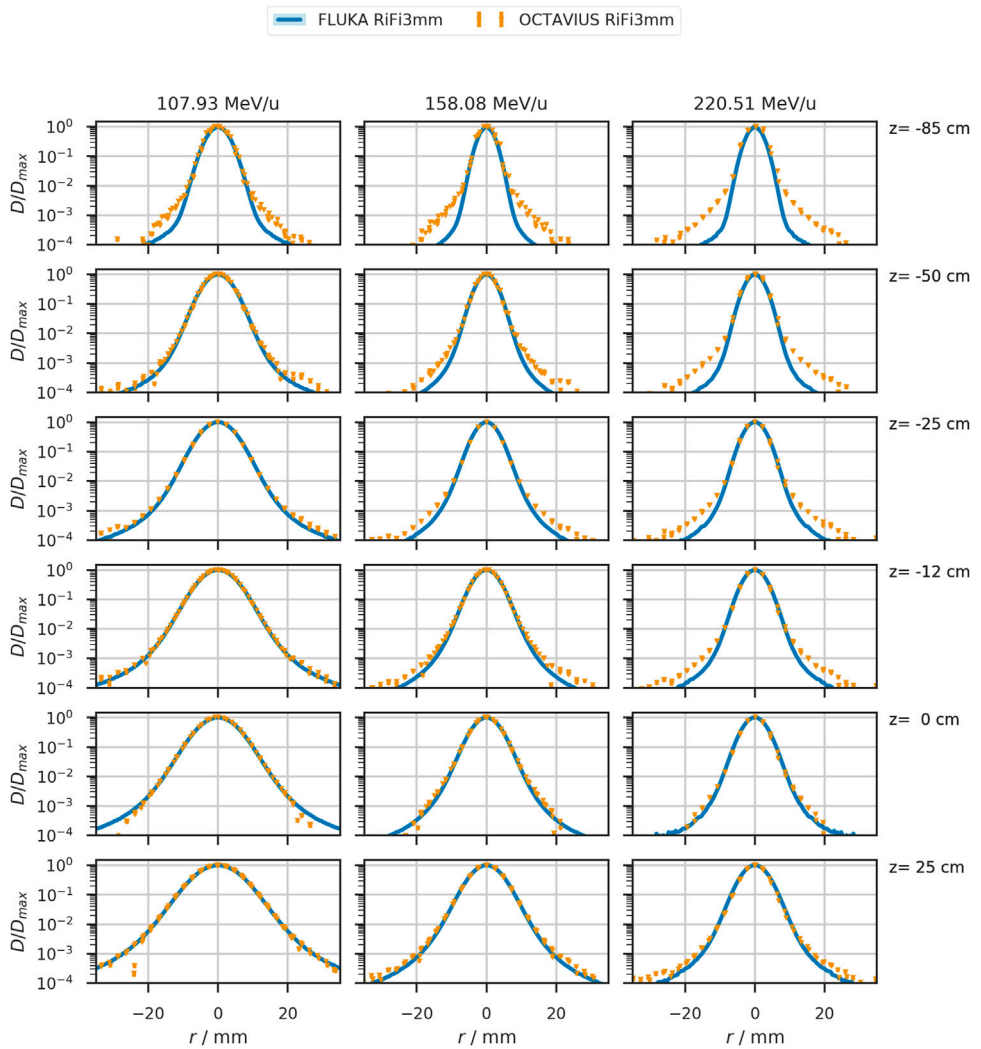

FIGURE 3 | Lateral beam profiles in air of the 107.93 MeV/u, 158.08MeV/u, and 220.51 MeV/u helium beam as simulated in FLUKA (solid blue line) and measured (orange triangles). The detector position relative to the treatment room's isocenter is indicated on the right of each row. Measured data contains datapoints from the four prominent profiles with an estimated uncertainty of at least 0.5% or 1 mGy for the local dose deposition. This uncertainty corresponds to four orders of magnitude lower than the local dose maximum in each profile.

distribution is depicted for the original case, reduced and increased beam width from left to right. Dose profiles were extracted at the entrance of each of the two treatment fields, indicated by the purple (superior field) and orange (left field) line in panel (A). These dose profiles show a variation in the penumbra (distance between 20% and 80% of local dose maximum) between $15.3^{-1.0}_{+0.9}$ mm in the lateral field impinging from the left and $11.2^{-0.8}_{+0.7}$ mm for the field superiorly impinging as plotted in panel (B). The profile extracted diagonally through the target volume is indicated as a green line; the contributions of the individual fields are plotted separately in the bottom graph of panel (B). The differences in dose distribution are non-significant, with only slight deviations even in the dose-volume-histogram (panel (C)) of **Figure 4C**. The dose received by >98% of the clinical target volume varies by + 0.8% and −1.2%. And the $D_{50\%}$ varies by +0.8% and −0.9%. Organs at risk in lateral proximity to tumor and beam path are the brainstem, left parotid gland, and the right optic nerve. The highest dose received by <2% of the brainstem is $(51.18^{+0.66}_{-0.69})$Gy (RBE), while less than 2% of the left parotid gland (delineated in bright orange) receive a high dose of $(39.52^{+0.06}_{-0.24})$Gy (RBE). In the right optic nerve, $D_{2\%}$ is $(26.04^{+0.34}_{-0.15})$Gy (RBE).

4. DISCUSSION

4.1 Beamwidth in Air

The measured lateral profiles without ripple filter showed deviations from the nominal beam width (i.e., FWHM) at the isocenter of about 5%, which agrees with the standard deviation of the four averaged profiles.

TABLE 2 | Lateral beamwidth (FWHM) of the helium beam with ripple filter (RiFi3mm) at measured positions z in the airgap behind the last beamline component. Dose profiles were either measured with the OCTAVIUS phantom and scaled by the daily deviation of the unmodified beam from nominal beam width or simulated with FLUKA as the dose to water in a thin slice at the corresponding position in the treatment room. The standard deviation of measured lateral beamwidth for each position is approximately 0.2 mm for each position and energy. The profiles corresponding to the initial beam energies E, highlighted in italics, are plotted in **Figure 3**.

E in MeV/u	Dataset	FWHM in mm with RiFi3mm at position z relative to the isocenter					
		–85 cm	–50 cm	–25 cm	–12 cm	0 cm	25 cm
50.57	OCTAVIUS	12.07	15.43	19.10	21.09	23.01	27.24
	FLUKA	12.60	15.79	18.85	20.66	22.24	26.25
56.44	OCTAVIUS	10.52	13.63	17.10	19.03	20.79	24.74
	FLUKA	11.35	14.20	16.92	18.50	19.83	23.31
72.65	OCTAVIUS	5.62	8.83	11.90	13.43	14.94	18.10
	FLUKA	8.45	10.79	12.89	14.08	15.27	17.92
82.33	OCTAVIUS	5.59	8.33	10.86	12.25	13.51	16.27
	FLUKA	7.48	9.55	11.32	12.44	13.47	15.77
107.93	*OCTAVIUS*	*6.17*	*7.17*	*8.58*	*9.39*	*10.32*	*12.18*
	FLUKA	*6.00*	*7.63*	*9.00*	*9.77*	*10.54*	*12.28*
122.93	OCTAVIUS	5.82	6.46	7.45	8.04	8.67	10.23
	FLUKA	5.31	6.81	7.98	8.68	9.36	10.83
133.21	OCTAVIUS	5.54	6.07	7.04	7.60	8.17	9.61
	FLUKA	5.03	6.37	7.46	8.11	8.72	10.07
140.71	OCTAVIUS	5.42	5.88	6.82	7.33	7.88	9.25
	FLUKA	4.89	6.13	7.02	7.63	8.22	9.50
158.08	*OCTAVIUS*	*4.75*	*5.21*	*6.16*	*6.66*	*7.17*	*8.30*
	FLUKA	*4.37*	*5.46*	*6.38*	*6.92*	*7.41*	*8.62*
172.28	OCTAVIUS	6.79	6.70	7.02	7.35	7.72	8.64
	FLUKA	4.93	5.87	6.64	7.03	7.52	8.51
182.43	OCTAVIUS	6.64	6.50	6.75	7.01	7.35	8.20
	FLUKA	4.86	5.79	6.48	6.90	7.26	8.19
190.85	OCTAVIUS	6.65	6.41	6.63	6.84	7.16	7.94
	FLUKA	4.67	5.53	6.18	6.57	7.00	7.86
201.71	OCTAVIUS	6.86	6.55	6.67	6.88	7.13	7.83
	FLUKA	4.79	5.56	6.18	6.52	6.90	7.77
220.51	*OCTAVIUS*	*6.41*	*6.14*	*6.07*	*6.17*	*6.31*	*6.72*
	FLUKA	*4.69*	*5.35*	*5.95*	*6.26*	*6.60*	*7.33*

Scaling the measured profiles with the daily deviation factor to nominal settings resulted in an agreement within ±0.8 mm between simulation and measurement in air.

For positions close to the beamline, the deviation between measured and simulated profiles was the largest. Scaling the measured data with the nominal beam width at the isocenter, as described in **Section 2.4**, improved the match between simulation and measurement for all positions.

As a variation of the beamwidth at the isocentre between ±15% is occasionally observed in daily quality assurance measurements, the reproduction of nominal settings and measured beam widths by the simulation is very well achieved. Thus, the simulated profiles are validated to become a critical component of the base data for the clinical TPS.

The enlarged deviation close to the beamline could originate from secondaries produced by high Z components in the beamline, as interaction cross-sections for these might not be known accurately enough in FLUKA for these materials [17]. Another contribution could originate from beam optics that were not considered in the FLUKA simulation. Further investigations have been made regarding deviations in shape.

4.2 Beam Shape

A systematic deviation in the order of $10^{-3}D_{max}$ is well visible in the profiles obtained at position "-85 cm". The measured profiles seem to have a second Gaussian envelope, which the simulation does not fully reproduce. Two solutions would be possible: An improvement in the geometric representation of the high Z material in the beamline in FLUKA or the correction of the initial beam shape in vacuum. Introducing a double Gaussian (DG) beam shape in vacuum instead of the single Gaussian (SG) approach used for the database improved the match between simulated and measured lateral beam profiles. The estimated parameters for the double Gaussian were approximately equal to the weighted sum of the original single Gaussian with a 6.5-8.0% contribution of a second Gaussian. The second Gaussian had an FWHM between 2 and 4 times the FWHM of the first Gaussian. With the double Gaussian approach matched to isocentric measurement, the shape deviations at other measurement positions in air were reduced, as shown for the same three energies in **Figure 5**. For further investigation in water, we used a dedicated water tank provided by PTB (Physikalisch-Technische Bundesanstalt, Braunschweig, Germany). This water tank includes a

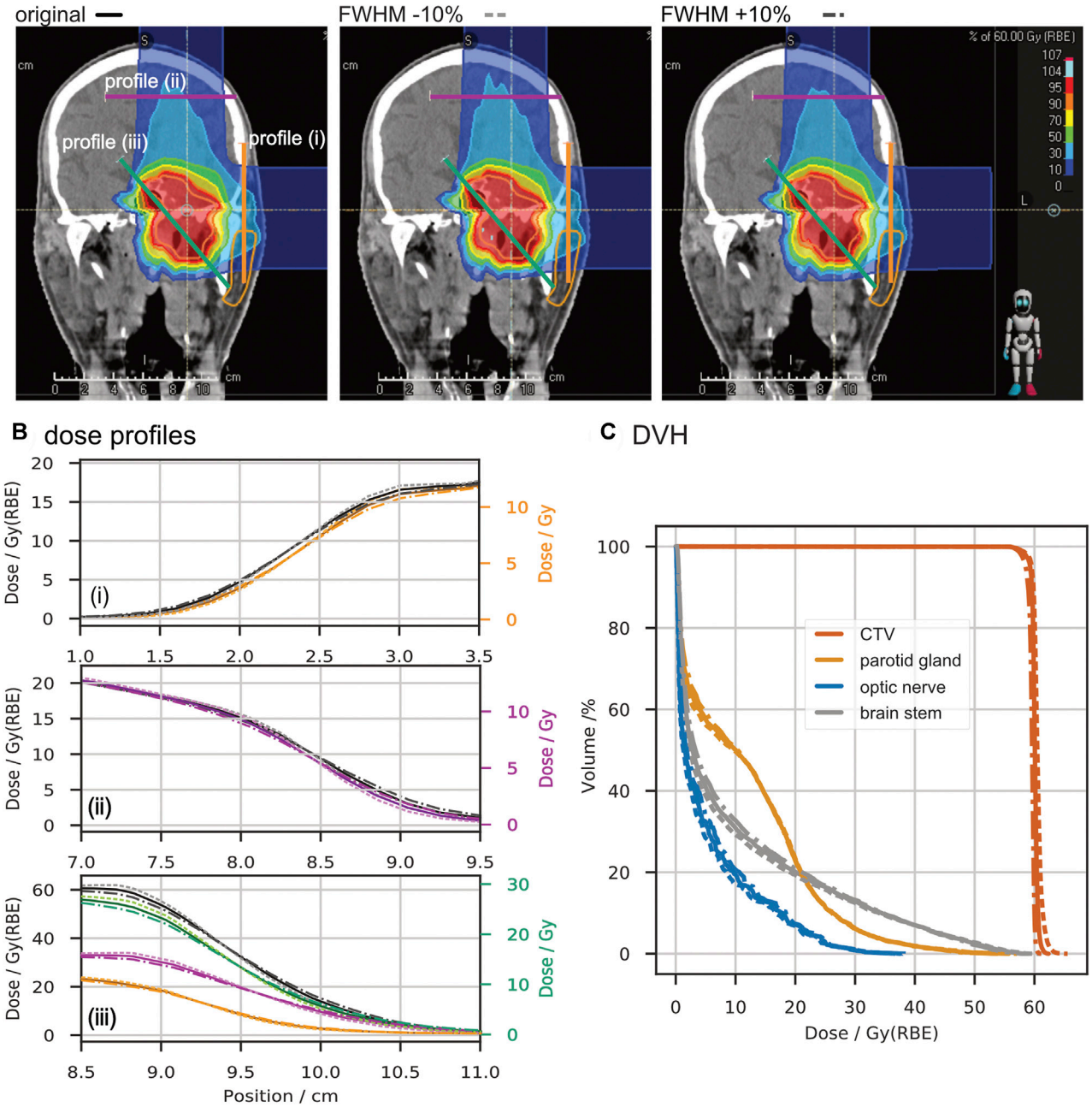

FIGURE 4 | Comparison of a patient treatment plan with a change of ∓10% in beamwidth. Panel **(A)** shows screenshots of the dose distribution in the TPS with lines marked for profile extraction. Panel **(B)** depicts the extracted profiles in units of biologically equivalent dose (Gy (RBE)) and absorbed dose (Gy). From top to bottom, the entrance profile of the superior treatment field (i), the entrance profile of the lateral treatment field (ii), and a profile through the target volume (iii) are drawn. Panel **(C)** shows the dose-volume histograms for the clinical target volume (CTV) and critical organs (parotid gland, optic nerve, and brain stem) obtained from the three scenarios. In panels **(B)** and **(C)**, solid lines represent data of the original plan, dotted lines depict the data with reduced beamwidth, and dash-dotted lines represent the increased beamwidth.

motorized PMMA-sleeve for detector accommodation. With the entrance window placed at the isocenter of the treatment room, profiles at about five positions around the maximum dose of each investigated energy were measured for each investigated beam. MC scoring of the lateral dose distribution in water was obtained in a water cylinder ($r = 14\,\text{cm}, z = 32\,\text{cm}$, $\Delta z = 0.1\,\text{mm}$ and $\Delta r = 0.5\,\text{mm}$) behind the isocenter summing over the azimuthal angle. **Figure 6**

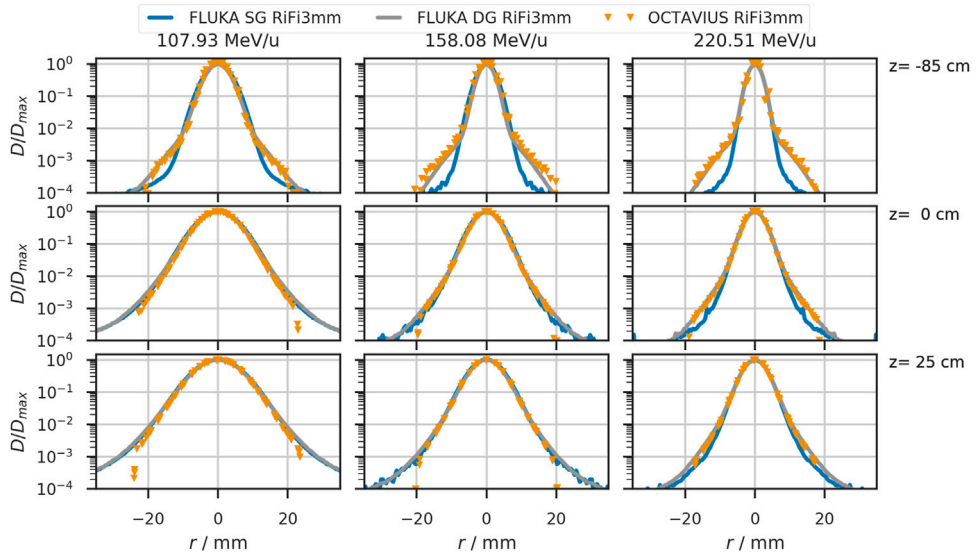

FIGURE 5 | Lateral beam profiles in air for helium beams with initial beam energies of 107.93 MeV/u, 158.08 MeV/u, and 220.51 MeV/u. The solid blue line shows the simulated profiles with a single Gaussian (SG) in vacuum. Orange triangles depict profiles obtained from the OCTAVIUS chamber array at indicated depth z. The grey line shows the profiles obtained from simulation with a double Gaussian (DG) beam profile in vacuum. Positions at which the detector was placed relative to the treatment room's isocenter are indicated on the right of each row.

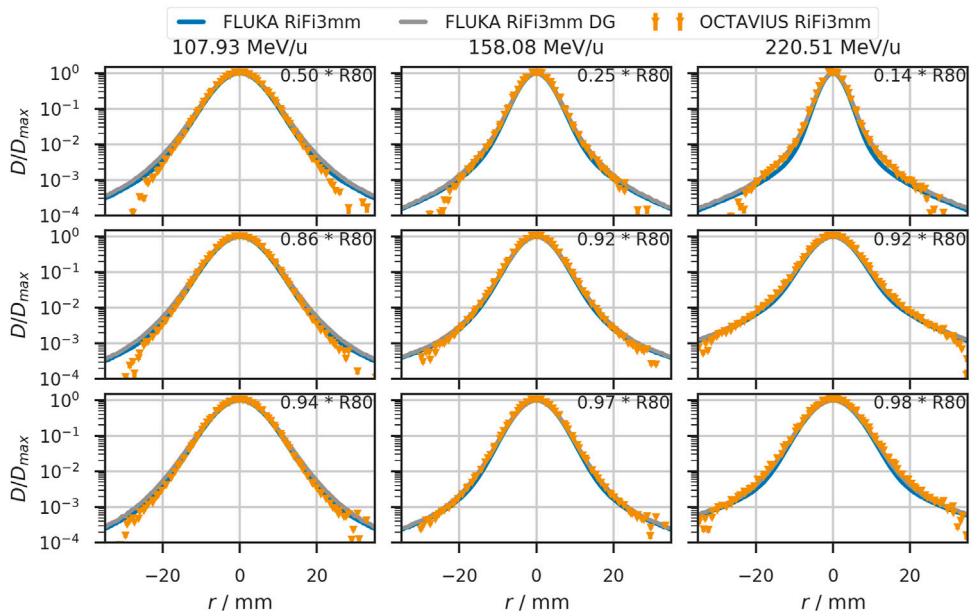

FIGURE 6 | Lateral beam profiles in water for helium beams with initial beam energies of 107.93 MeV/u, 158.08 MeV/u, and 220.51 MeV/u. The solid blue line shows the simulated profiles with a single Gaussian (SG) in vacuum. Orange triangles depict profiles obtained from the OCTAVIUS chamber array at indicated depth z. The grey line shows the profiles obtained from simulation with a double Gaussian (DG) beam profile in vacuum. Detector positions are given relative to the distal 80% range of the depicted beam.

shows that the double gaussian approach improves the agreement between simulations and measurements even in water.

4.3 Comparison to Other Ions

To compare the width evolution of the three available ions, the beamwidth is plotted against the detector positions for three beam energies of comparables ranges (approx. 8.8 cm in water) in **Figure 7**. The beam is simulated as a single Gaussian profile in vacuum, with the FWHM being 5.55 mm (6.17 mm, 4.95 mm) for helium (protons and carbon ions), corresponding to the smallest clinical beamwidth.

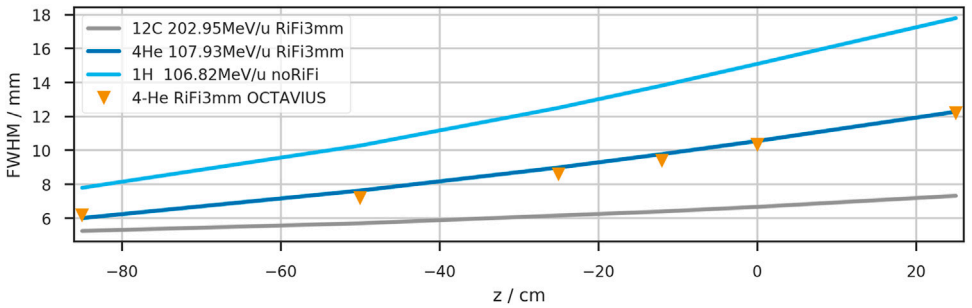

FIGURE 7 | Depth dependency of the beam width (FWHM) in air for three therapeutically available ions. The initial beamwidth in vacuum was chosen to reproduce the nominal accelerator settings at z = 0 cm when the RiFi is not inserted.

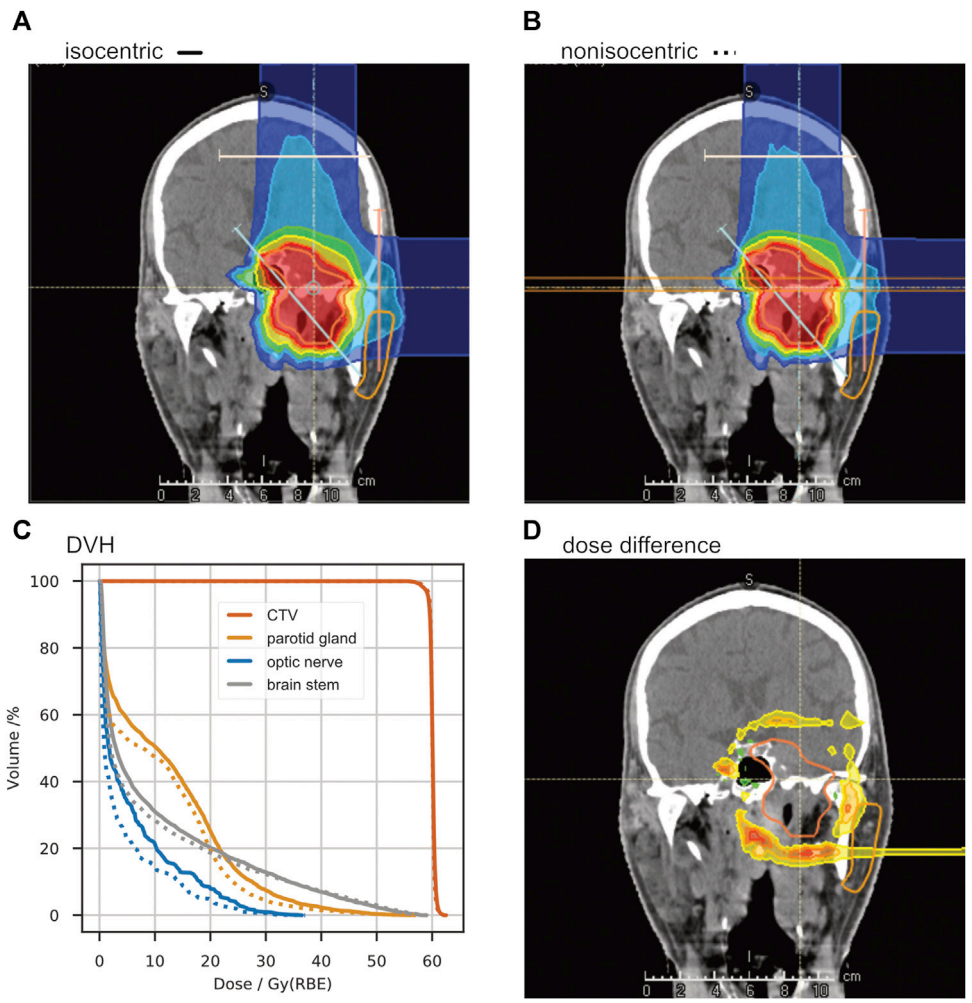

FIGURE 8 | A study of non-isocentric treatment planning. Panel **(A)** shows the dose distribution of a "standard" treatment plan with the room's isocenter in the target volume. With the same beam angles, another treatment plan was optimized with the patient placed as close as possible to the treatment nozzle, reducing the air gap to about 20 cm **(B)**. The dose-volume-histogram in panel **(C)** shows a significant dose reduction in the organs at risk (ipsilateral parotid gland, contralateral optic nerve, and brainstem). The absolute dose difference is shown in panel **(D)**.

While the carbon beam shows minor widening in the air gap (39% increase from −85 cm to +25 cm), the proton width increases by 228%. The helium beamwidth increases by 204% in the same air distance. Between vacuum and isocenter, the beamwidth increases by 29% for carbon ions, 90% for helium ions, and 144% for protons.

4.4 Patient Case

With the variation of the beamwidth by ∓10% FWHM, the differences in field profiles and DVH are minor, as depicted in **Figure 4**. This observation is in line with the clinical intervention limits of +25% and −15% deviation from tabulated widths. Thus, we have shown for this specific case that variations up to approximately 10% in the beamwidths do not critically impact dose conformity and lateral organs at risk.

To further exploit the fact that the beamwidth is much smaller with reduced air gap and the lateral profiles' implementation into the TPS, we performed a second patient plan investigation positioning the patient much closer to the beam exit and reducing the air gap. At MedAustron in Wiener Neustadt, Austria, a similar approach of non-isocentric treatment planning has already been commissioned for protons [36, 37].

This approach enables a dose reduction – in the organs at risk lateral to the treatment field – by decreasing the beamwidth at the patient entrance point. **Figure 8** shows the differences in dose distribution for the same slice as **Figure 4**. In the right (contralateral) optic nerve, a reduction of $D_{50\%}$ from 1.71 to 0.89 Gy (RBE) is achieved and the $D_{50\%}$ in the left (ipsilateral) parotid gland can be reduced from 10.34 to 7.71Gy (RBE). In the brain stem the $D_{50\%}$ could be reduced by 31% from 2.94 to 2.04 Gy (RBE), whereas the target coverage remains the same. The maximum dose received by the three OARs remains approximately unchanged. There is no visible change in the DVH for the CTV in panel (C), which is expected since the plan was reoptimized for the reduced air gap.

5 CONCLUSION AND OUTLOOK

In summary, our accurate simulation and measurement of beam profiles in air along the beam path led to a more precise TPS beam model which has been applied for the first patient irradiation with helium ions at HIT.

While other groups have investigated the effect of airgaps in a phantom [16], we can now provide a precise representation of the beam characteristics between beamline exit and entering any patient or phantom. The commercial TPS and any experimental investigations rely on energy and setting-specific MC beam model to calculate dose and particle distributions in phantoms placed downstream of the beamline exit.

In principle, the gained knowledge affords greater freedom in patient positioning along the beam axis. Since the helium beam broadens in air, not as much as protons but significantly more than the carbon beam, a reduced air gap would be favorable if critical organs are in lateral proximity to the beam axis. However, routine non-isocentric treatment planning would require a patient positioning and alignment system that is as precise close to the beam exit as it is in the treatment room's isocenter.

As expected, the broadening of the helium ion beam is intermediate between that of protons and carbon ions. With a complete representation of all available beam energies in the FLUKA simulation framework, we were able to quantify the broadening and directly compare available beamwidths for specific ranges and positions along the beam axis.

Regarding the good results while looking at the scenario of beamwidth variation in **Section 3.2**, the clinical approach to ensure a good field homogeneity with a spot spacing smaller than 1/3 width of the unmodified beam seems sufficient for helium ions and agrees with previous studies for protons and carbon ions [20].

For even better accuracy of the TPS, non-Gaussian beam shapes in vacuum could be investigated further. Then, the asymmetric shapes created by the particle extraction from the accelerator could be accounted for. With the observed agreements between measurement and simulation in the setup at HIT, airgaps smaller than about 50 cm would most likely benefit from such a further investigation.

The beamwidth of the helium ion beam would reduce further if the ripple filter had been removed from the beamline. This would, however, require the measurement and simulation of an entire additional database with depth dose curves, lateral profiles, absolute dosimetry, and secondary particle spectra. The treatment time for each patient field would also increase.

Together with measured depth dose curves, the lateral dose distributions reported in this paper add another milestone in the development of the physical beam model for raster-scanned helium ions. With the MC model verified against measurements and particle spectra for biological equivalent dose calculation [24] simulated, the first clinical TPS for helium ions is finished. So, after the first clinical trials with helium ion beams at the LBNL observed positive outcomes, especially for patients with small tumors, such as uveal melanoma [2], we now have the means to restart helium ion therapy with raster scanning beam technology.

DATA AVAILABILITY STATEMENT

The raw data supporting the conclusions of this article will be made available by the authors, without undue reservation.

AUTHOR CONTRIBUTIONS

TT gave substantial scientific advice and created the patient treatment plans. AM contributed to the conception and design of the study and pre-optimized the initial beamwidths for helium. SM pre-optimized the initial beamwidths for carbon. BK pre-optimized the lateral profiles for the proton beam. JB performed the analysis and most measurements, simulated the

last version of the helium base data, recalculated the proton and carbon profiles, and wrote the manuscript. All authors contributed to manuscript revision, read, and approved the submitted version.

FUNDING

JB's position is funded via grant NCT3.0-2015.22 BioDose.

ACKNOWLEDGMENTS

Thanks to Stephan Brons from the HIT medical physics team for performing additional measurements with all available beam foci of the helium beam; Amir Abdollahi for providing the research position in his group and Jürgen Debus for being the principal scientific advisor to the Ph.D. project of JB.

REFERENCES

1. Lyman JT, Howard J. Dosimetry and Instrumentation for Helium and Heavy Ions. *Int J Radiat Oncol Biol Phys* (1977) 3:81–5. doi:10.1016/0360-3016(77)90231-0
2. Castro JR, Char DH, Petti PL, Daftari IK, Quivey JM, Singh RP, et al. 15 Years Experience with Helium Ion Radiotherapy for Uveal Melanoma. *Int J Radiat Oncol Biol Phys* (1997) 39(5):989–96. doi:10.1016/s0360-3016(97)00494-x
3. Castro JR. Results of Heavy Ion Radiotherapy. *Radiat Environ Biophys* (1995) 34:45–8. doi:10.1007/BF01210545
4. Jermann M. Particle Therapy Statistics in 2014. *Int J Part Ther* (2015) 2(1):50–4. doi:10.14338/ijpt-15-00013
5. Saunders W, Castro JR, Chen GTY, Collier JM, Zink SR, Pitluck S, et al. Helium-Ion Radiation Therapy at the Lawrence Berkeley Laboratory: Recent Results of a Northern California Oncology Group Clinical Trial. *Radiat Res* (1985) 104:S227–34. doi:10.2307/3576652
6. Saunders WM, Char DH, Quivey JM, Castro JR, Chen GT, Collier JM, et al. Precision, High Dose Radiotherapy: Helium Ion Treatment of Uveal Melanoma. *Int J Radiat Oncol Biol Phys* (1985) 11(2):227–33. doi:10.1016/0360-3016(85)90143-9
7. Haberer T, Becher W, Schardt D, Kraft G. Magnetic Scanning System for Heavy Ion Therapy. *Nucl Instr Methods Phys Res Section A: Acc Spectrometers, Detectors Associated Equipment* (1993) 330(1-2):296–305. doi:10.1016/0168-9002(93)91335-k
8. Germany's Heidelberg University Hospital will become the world's first cancer center to use RayStation for helium ion therapy planning (2021). URL: https://www.raysearchlabs.com/media/press-releases/2020/germanys-heidelberg-university-hospital-will-become-the-worlds-first-cancer-center-to-use-raystation-for-helium-ion-therapy-planning/. (Accessed December 2, 2021).
9. Tessonnier T, Böhlen TT, Ceruti F, Ferrari A, Sala P, Brons S, et al. Dosimetric Verification in Water of a Monte Carlo Treatment Planning Tool for Proton, Helium, Carbon and Oxygen Ion Beams at the Heidelberg Ion Beam Therapy center. *Phys Med Biol* (2017) 62:6579–94. doi:10.1088/1361-6560/aa7be4
10. Tessonnier T, Mairani A, Brons S, Sala P, Cerutti F, Ferrari A, et al. Helium Ions at the Heidelberg Ion Beam Therapy center: Comparisons between FLUKA Monte Carlo Code Predictions and Dosimetric Measurements. *Phys Med Biol* (2017) 62:6784–803. doi:10.1088/1361-6560/aa7b12
11. Tessonnier T, Mairani A, Brons S, Haberer T, Debus J, Parodi K. Experimental Dosimetric Comparison of 1H, 4H, 12C and 16O Scanned Ion Beams. *Phys Med Biol* (2017) 62:3958–82. doi:10.1088/1361-6560/aa6516
12. Parodi K, Mairani A, Brons S, Hasch BG, Sommerer F, Naumann J, et al. Monte Carlo Simulations to Support Start-Up and Treatment Planning of Scanned Proton and Carbon Ion Therapy at a Synchrotron-Based Facility. *Phys Med Biol* (2012) 57:3759–84. doi:10.1088/0031-9155/57/12/3759
13. Böhlen TT, Cerutti F, Chin MPW, Fassò A, Ferrari A, Ortega PG, et al. The FLUKA Code: Developments and Challenges for High Energy and Medical Applications. *Nucl Data Sheets* (2014) 120:211–4. doi:10.1016/j.nds.2014.07.049
14. Ferrari A, Sala PR, Fassó A, Ranft J. FLUKA: a Multi-Particle Transport Code (2005). Available From: http://www.slac.stanford.edu/pubs/slacreports/reports16/slac-r-773.pdf. doi:10.2172/877507
15. Horst F, Aricò G, Brinkmann K-T, Brons S, Ferrari A, Haberer T, et al. Measurement of He4 Charge- and Mass-Changing Cross Sections on H, C, O, and Si Targets in the Energy Range 70-220 MeV/u for Radiation Transport Calculations in Ion-Beam Therapy. *Phys Rev C* (2019) 99:1. doi:10.1103/physrevc.99.014603
16. Gallas RR, Arico G, Burigo LN, Gehrke T, Jakůbek J, Granja C, et al. A Novel Method for Assessment of Fragmentation and Beam-Material Interactions in Helium Ion Radiotherapy with a Miniaturized Setup. *Physica Med* (2017) 42:116–26. doi:10.1016/j.ejmp.2017.09.126
17. Norbury JW, Battistoni G, Besuglow J, Bocchini L, Boscolo D, Botvina A, et al. Are Further Cross Section Measurements Necessary for Space Radiation Protection or Ion Therapy Applications? Helium Projectiles. *Front Phys* (2020) 8:409. doi:10.3389/fphy.2020.565954
18. Weber U, Kraft G. Comparison of Carbon Ions versus Protons. *Cancer J* (2009) 15(4):325–32. doi:10.1097/ppo.0b013e3181b01935
19. Uhl M, Herfarth K, Debus J. Comparing the Use of Protons and Carbon Ions for Treatment. *Cancer J* (2014) 20(6):433–9. doi:10.1097/ppo.0000000000000078
20. Parodi K, Mairani A, Brons S, Naumann J, Krämer M, Sommerer F, et al. The Influence of Lateral Beam Profile Modifications in Scanned Proton and Carbon Ion Therapy: a Monte Carlo Study. *Phys Med Biol* (2010) 55:5169–87. doi:10.1088/0031-9155/55/17/018
21. Parodi K, Mairani A, Sommerer F. Monte Carlo-Based Parametrization of the Lateral Dose Spread for Clinical Treatment Planning of Scanned Proton and Carbon Ion Beams. *J Radiat Res* (2013) 54(suppl_1):i91–i96. doi:10.1093/jrr/rrt051
22. Schwaab J, Brons S, Fieres J, Parodi K. Experimental Characterization of Lateral Profiles of Scanned Proton and Carbon Ion Pencil Beams for Improved Beam Models in Ion Therapy Treatment Planning. *Phys Med Biol* (2011) 56:7813–27. doi:10.1088/0031-9155/56/24/009
23. Krämer M, Jäkel O, Haberer T, Kraft G, Schardt D, Weber U. Treatment Planning for Heavy-Ion Radiotherapy: Physical Beam Model and Dose Optimization. *Phys Med Biol* (2000) 45:3299–317. doi:10.1088/0031-9155/45/11/313
24. Kopp B, Mein S, Tessonnier T, Besuglow J, Harrabi S, Heim E, et al. Rapid Effective Dose Calculation for Raster-Scanning 4He Ion Therapy with the Modified Microdosimetric Kinetic Model (mMKM). *Physica Med* (2021) 81:273–84. doi:10.1016/j.ejmp.2020.11.028
25. Schardt D, Elsässer T, Schulz-Ertner D. Heavy-ion Tumor Therapy: Physical and Radiobiological Benefits. *Rev Mod Phys* (2010) 82(1):383–425. doi:10.1103/revmodphys.82.383
26. Highland VL. Some Practical Remarks on Multiple Scattering. *Nucl Instr Methods* (1975) 129(2):497–9. doi:10.1016/0029-554x(75)90743-0
27. Highland VL. Erratum: Some Practical Remarks on Multiple Scattering. *Nucl Instr Methods* (1979) 161(1):171. doi:10.1016/0029-554x(79)90379-3
28. Scott WT. The Theory of Small-Angle Multiple Scattering of Fast Charged Particles. *Rev Mod Phys* (1963) 35(2):231–313. doi:10.1103/RevModPhys.35.231
29. Molière G. Theorie der Streuung schneller geladener Teilchen. III Die Vielfachstreuung von Bahnspuren unter Berücksichtigung der statistischen Kopplung. *Z für Naturforschung A* (1955) 10(3):177–211. doi:10.1515/zna-1955-0301
30. Hollmark M, Gudowska I, Belkić D, Brahme A, Sobolevsky N. An Analytical Model for Light Ion Pencil Beam Dose Distributions: Multiple Scattering of Primary and Secondary Ions. *Phys Med Biol* (2008) 53:3477–91. doi:10.1088/0031-9155/53/13/005
31. Würl M, Englbrecht F, Parodi K, Hillbrand M. Dosimetric Impact of the Low-Dose Envelope of Scanned Proton Beams at a ProBeam Facility: Comparison of Measurements with TPS and MC Calculations. *Phys Med Biol* (2016) 61:958–973. doi:10.1088/0031-9155/61/2/958

32. Ondreka D, Weinrich U. The Heidelberg Ion Therapy (HIT) Accelerator Coming into Operation. *Conf Proc C* (2008):0806233. Available from: https://accelconf.web.cern.ch/e08/papers/tuocg01.pdf (Accessed December 2, 2021).
33. Schoemers C, Feldmeier E, Naumann J, Panse R, Peters A, Haberer T. The Intensity Feedback System at Heidelberg Ion-Beam Therapy Centre. *Nucl Instr Methods Phys Res Section A: Acc Spectrometers, Detectors Associated Equipment* (2015) 795:92–9. doi:10.1016/j.nima.2015.05.054
34. Weber U, Kraft G. Design and Construction of a Ripple Filter for a Smoothed Depth Dose Distribution in Conformal Particle Therapy. *Phys Med Biol* (1999) 44 (11):2765–75. doi:10.1088/0031-9155/44/11/306
35. Krämer M, Scholz M. Treatment Planning for Heavy-Ion Radiotherapy: Calculation and Optimization of Biologically Effective Dose. *Phys Med Biol* (2000) 45 (11):3319–30. doi:10.1088/0031-9155/45/11/314
36. Elia A, Resch AF, Carlino A, Böhlen TT, Fuchs H, Palmans H, et al. A GATE/Geant4 Beam Model for the MedAustron Non-isocentric Proton Treatment Plans Quality Assurance. *Physica Med* (2020) 71:115–23. doi:10.1016/j.ejmp.2020.02.006
37. Carlino A, Böhlen T, Vatnitsky S, Grevillot L, Osorio J, Dreindl R, et al. Commissioning of Pencil Beam and Monte Carlo Dose Engines for Non-isocentric Treatments in Scanned Proton Beam Therapy. *Phys Med Biol* (2019) 64:17NT01. doi:10.1088/1361-6560/ab3557

Conflict of Interest: The authors declare that the research was conducted in the absence of any commercial or financial relationships that could be construed as a potential conflict of interest.

Publisher's Note: All claims expressed in this article are solely those of the authors and do not necessarily represent those of their affiliated organizations, or those of the publisher, the editors and the reviewers. Any product that may be evaluated in this article, or claim that may be made by its manufacturer, is not guaranteed or endorsed by the publisher.

NOMENCLATURE

BAMS active beam monitoring system consisting of three transmission ionization chambers and two multi-wire proportional chambers in the beamline downstream of the vacuum pipe

CTV clinical target volume

contralateral on the opposite side of a person's body

$D_{xx\%}$ dose received by at least xx% of the volume

DVH dose volume histogram

FLUKA an MC code to simulate particle propagation through material

FWHM full width half maximum

iDDD laterally integrated depth dose distribution, typically integrated over radii matching the sensitive region of the used detector, or infinity.

ipsilateral on the same side of a person's body

irradiation or treatment plan a set of beam angles and energy-specific particle intensity maps necessary to achieve the desired dose distribution in a patient or phantom

LIBC accelerator library containing nominal beam energies, beamwidths and intensity settings

MC Monte Carlo

mMKM modified microdosimetric-kinetic model

noRiFi no ripple filter in the beamline

OAR organ at risk

patient entrance point the point of the patient that is closest to the beamline at a given patient position

penumbra lateral fall-off in the dose distribution accumulated by all irradiated spots of an irradiated field, typically defined as the distance between 80 and 20% isodose line perpendicular to the beam direction.

PMMA Polymethylmethacrylate

PTB Physikalisch Technische Bundesanstalt

range (R80) distal point along the depth dose curve at which 80% of the maximal dose is reached

RaShi range shifter

RiFi3mm ripple filter

spot one point in the plane perpendicular to the beam axis aimed at by a single pencil beam of the raster scanning system

slice a slice in a CT scan refers to a two-dimensional plane extracted from a three-dimensional image volume

TPS treatment planning system

width FHWM of the lateral beam profile at any given point along the beam

frontiers in Physics

BRIEF RESEARCH REPORT
published: 13 January 2022
doi: 10.3389/fphy.2021.711317

Status and Extension of the Geant4-DNA Dielectric Models for Application to Electron Transport

Ioanna Kyriakou[1]*, *Dimitris Emfietzoglou*[1] *and Sebastien Incerti*[2]

[1]*Medical Physics Laboratory, Department of Medicine, University of Ioannina, Ioannina, Greece,* [2]*Univ. Bordeaux, CNRS, CENBG, UMR 5797, Gradignan, France*

The development of accurate physics models that enable track structure simulations of electrons in liquid water medium over a wide energy range, from the eV to the MeV scale, is a subject of continuous efforts due to its importance (among other things) in theoretical studies of radiation quality for application in radiotherapy and radiation protection. A few years ago, the Geant4-DNA very low-energy extension of the Geant4 Monte Carlo code had offered to users an improved set of physics models for discrete electron transport below 10 keV. In this work we present refinements to this model set and its extension to energies up to 1 MeV. Preliminary comparisons against the existing Geant4-DNA physics models with respect to total and differential ionization cross sections of electrons in liquid water are reported and discussed.

Keywords: Geant4-DNA, Monte Carlo, track structure, dielectric function, cross sections

OPEN ACCESS

Edited by:
Vasilis Vlachoudis, European Organization for Nuclear Research (CERN), Switzerland

Reviewed by:
Tuba Conka Yildiz, Türkisch-Deutsche Universität, Turkey
Emanuele Scifoni, Ministry of Education, Universities and Research, Italy

***Correspondence:**
Ioanna Kyriakou
ikyriak@uoi.gr

Specialty section:
This article was submitted to Radiation Detectors and Imaging, a section of the journal Frontiers in Physics

Received: *18 May 2021*
Accepted: *07 December 2021*
Published: *13 January 2022*

Citation:
Kyriakou I, Emfietzoglou D and Incerti S (2022) Status and Extension of the Geant4-DNA Dielectric Models for Application to Electron Transport. Front. Phys. 9:711317. doi: 10.3389/fphy.2021.711317

1 INTRODUCTION

Theoretical studies of the effects of ionizing radiation in biological cells usually rely on Monte Carlo track-structure (MCTS) simulation codes [1]. The core input in these codes consists of a variety of discrete physics models that permit simulation of each and every interaction of radiation with the transport medium. Thus, MCTS codes may offer molecular resolution at the nanometer scale which is important for investigating radiation action at the cellular and sub-cellular level [2, 3]. This is in contrast to conventional macroscopic MC codes that are based on the condensed-history approach whereby interactions are grouped together and treated by multiple scattering models [4, 5]. In such MC simulations, the spatial resolution is usually at the micro-to milli-meter scale [6].

In medical physics applications, the transport medium is usually represented by liquid water which, to a good approximation, resembles soft tissue in terms of its radiation interaction properties. Although liquid water may be a poor approximation for other body tissues (like bone) or less accurate for specific biomolecules (like DNA), it is still the medium of choice since about 70–80% of the cellular material is composed of water [7]. For MCTS studies at the DNA level, many investigators have developed interaction cross sections specific to DNA bases or constituents to replace those of liquid water (e.g., [8–10]). These efforts rely on well-established atomic models that have been proved reliable for gas-phase molecular targets over a wide energy range and have the added value of being computationally tractable (e.g., [11]). DNA-specific cross sections in the condensed-phase have also been presented based on the dielectric approach [12–14].

MCTS codes are historically considered an important theoretical tool in understanding radiation quality aspects. This connection stems from the recognition that radiation quality originates from the spatial distribution of the discrete energy deposition events in the irradiated medium at the molecular scale [15]. Thus, MCTS codes have been widely used for RBE (relative biological effectiveness)

studies in radiotherapy and radiation protection practice [16–21]. Since electrons form the main product of all types of ionizing radiation with significant contribution to absorbed dose and biological damage, the details of their interactions with matter consist a priority of every MCTS code [22]. Thus, discrete electron models of elastic and inelastic scattering is a prerequisite for MCTS simulations, and several such models have been developed [23–25]. Towards this goal, a major obstacle is handling electron interactions down to very low energies (eV scale) given that the physics of electron interactions becomes increasingly complicated [26]. This is especially true for condensed media (liquids and solids) due to long-range screening effects which represent a particularly difficult theoretical problem.

The Geant4 MC code, through its Geant4-DNA very low-energy extension, offers MCTS capabilities down to a few eV [27–30]. For the simulation of low energy electron interactions in liquid water, Geant4-DNA offers three sets of alternative discrete electron models that correspond to different sets of elastic and inelastic scattering cross sections [30]. These sets of models, formally called constructors, are the default "G4EmDNAPhysics_option2" constructor (which will be referred to as Opt2) [28], the "G4EmDNAPhysics_option4" constructor (which will be referred to as Opt4) [31] and the "G4EmDNAPhysics_option6" constructor (which will be referred to as Opt6) [32]. Ionization and excitation cross sections in both Opt2 and Opt4 are based on the dielectric theory of inelastic scattering [7, 25]. This is a key difference against Opt6 which employs analytical atomic models. A benefit of the dielectric approach is that condensed-phase effects are in-built into the methodology through the use of the dielectric response function (DRF) of the medium. The DRF of liquid water medium in both Opt2 and Opt4 is obtained from optical data models that allow, in the framework of the plane wave Born approximation (PWBA), to calculate with only moderate effort, inelastic cross-sections. Opt4 has proved to be more accurate than Opt2 at low electron energies due to the implementation of an improved parameterization algorithm [31]. However, contrary to Opt2 which extends up to 1 MeV, the upper energy of Opt4 is limited to 10 keV [33]. In the present work we report the relativistic extension of Opt4 (hereafter called Opt4Rel) up to 1 MeV along with an improved DRF parameterization that further reduces the sum-rule errors compared to the existing Opt4.

2 METHODS

2.1 The Energy Loss Function

In both the existing (Opt2 and Opt4) and new (Opt4Rel) electron models of Geant4-DNA, the DRF is used to determine the energy-loss function (ELF) of liquid water through the standard expression for bulk media [34, 35]:

$$\mathrm{ELF} \equiv \mathrm{Im}\left[-\frac{1}{\varepsilon(E,q)}\right] = \frac{\varepsilon_2(E,q)}{\left|\varepsilon(E,q)\right|^2} \tag{1}$$

where E and q are the energy- and momentum-transfer, respectively, and $\varepsilon(E,q) = \varepsilon_1(E,q) + i\,\varepsilon_2(E,q)$ is the complex-valued DRF with the real and imaginary part being related through the Kramers-Kronig relations. The numerator in **Eq. 1** describes the absorption spectrum of the medium and it is partitioned to the individual excitation levels (k) and ionization shells (n) as:

$$\varepsilon_2(E,q) = \sum_n^{ioniz.} \varepsilon_2^{(n)}(E,q) + \sum_k^{excit.} \varepsilon_2^{(k)}(E,q) \tag{2}$$

In both the existing (Opt2 and Opt4) and new (Opt4Rel) models, five excitation levels (A^1B_1, B^1A_1, Ryd A + B, Ryd C + D, db) and four outer shells (1b1, 3a1, 1b2, 2a1) are used and they are analytically represented by a sum of Drude-type functions. The details of the parameterization, however, differ among the models. Specifically, in Opt2 the imaginary part of DRF at the optical limit (q = 0) is represented by:

$$\begin{aligned}\varepsilon_2(E,q=0) = &\sum_{n=1}^{4}\left[D_n(E;E_n)\,\Theta(E-B_n)\right] \\ &+\sum_{k=1}^{5}\left[D_k^*(E;E_k)\,\Theta(E-B_k)\right]\end{aligned} \tag{3}$$

where $D_n(E;E_n)$ and $D_k^*(E;E_k)$ are the ordinary and derivative Drude functions, $E_{n,k}$ are the Drude coefficients for the transition energies, $B_{n,k}$ are the threshold energies, i.e., shell binding energies and band gap excitation energies, and $\Theta(\ldots)$ is the Heaviside function. The step-functions $\Theta(E-B_k)$ eliminate the non-physical contribution of the Drude functions below $B_{n,k}$. As discussed elsewhere [31], an important shortcoming of **Eq. 3** is the partial violation of sum rules and the non-analyticity of $\varepsilon_1(E,0)$. To overcome these shortcomings, both Opt4 and Opt4Rel make use of the Emfietzoglou-Kyriakou partitioning algorithm by replacing **Eq. 3** with:

$$\begin{aligned}\varepsilon_2(E,q=0) = &\sum_{n=1}^{4}\left\{\left[D(E;E_n) - D(E;B_n)\exp(B_n-E)\right.\right. \\ &\left.\left.+F_n(E)\right]\Theta(E-B_n)\right\} \\ &+\sum_{k=1}^{5}\left\{\left[D_k^*(E;E_k)+F_k(E)\right]\Theta(E-B_k)\right\}\end{aligned} \tag{4}$$

with $D(E;B_n)\exp(B_n-E)$ being an exponential smoothing function for ionizations, and $F_{n,k}(E)$ are contributions from higher energy-levels, as determined by the Emfietzoglou-Kyriakou algorithms. The Drude coefficients in both **Eqs 3**, **4** are obtained through a fit to the experimental optical data [36]. Then, from **Eqs 2–4** the ELF of **Eq. 1** can be partitioned to the individual excitation levels and ionization shells according to the expression:

$$\mathrm{ELF} = \mathrm{ELF}_{\mathrm{excit.}} + \mathrm{ELF}_{\mathrm{ioniz.}} = \sum_n^{ioniz.} \frac{\varepsilon_2^{(n)}(E,q)}{\left|\varepsilon(E,q)\right|^2} + \sum_k^{excit.} \frac{\varepsilon_2^{(k)}(E,q)}{\left|\varepsilon(E,q)\right|^2} \tag{5}$$

It is noteworthy that for each excitation level (k) or ionization shell (n) contribution to the ELF, the denominator of **Eq. 5**

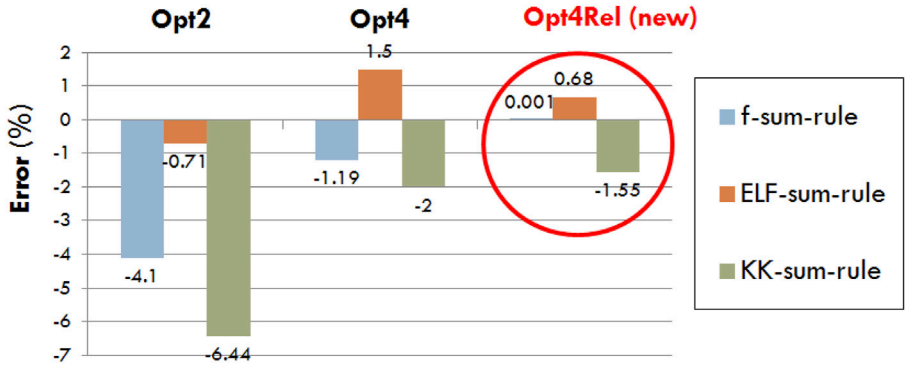

FIGURE 1 | Percentage error in the f-, ELF-, and KK-sum-rules for the existing (Opt2 and Opt4) and new (Opt4Rel) Geant4-DNA physics models.

represents the screening of the entire (outershell) electronic subsystem, i.e., represents the contribution of all k and n. The real part of the DRF, $\varepsilon_1(E,q)$, that enters in the denominator of **Eq. 5**, is formally obtained by the Kramers-Kronig (KK) relation [35]. In the case of Opt2 (**Eq. 3**), the KK pair of $\varepsilon_2(E,0)$ is non-analytic. In contrast, in Opt4 (and Opt4Rel) the real part of the DRF at the optical limit (q = 0) may still be obtained analytically from:

$$\varepsilon_1(E,q=0) = 1 + \sum_n^{ioniz.} D_n^{KK}(E;E_n) + \sum_k^{excit.} D_k^{KK}(E;E_k) \quad (6)$$

where $D_n^{KK}(E;E_n)$ and $D_k^{KK}(E;E_k)$ represent the KK pairs of $D_n(E;E_n)$ and $D_k^*(E;E_k)$, respectively [33].

To obtain the ELF for arbitrary values of q, analytic dispersion relations are introduced into the Drude coefficients [33]. These dispersion relations ensure that the ELF has the proper limiting behavior at q = 0 and q = ∞. The dispersion relations used in Geant4-DNA are common to all models (Opt2, Opt4, Opt4Rel).

An important aspect of the dielectric approach is that the fitting of ELF to the experimental data can be tested for internal consistency. In Geant4-DNA models, the following sum-rule constraints have been considered:

f sum-rule:

$$\frac{2}{\pi E_p^2}\int_0^\infty E\,\mathrm{Im}[\varepsilon(E,0)]dE = 1 \quad (7)$$

ELF sum-rule:

$$\frac{2}{\pi E_p^2}\int_0^\infty E\,\mathrm{Im}[-1/\varepsilon(E,0)]dE = 1 \quad (8)$$

KK sum-rule:

$$\frac{2}{\pi}\int_0^\infty \frac{1}{E}\mathrm{Im}[-1/\varepsilon(E,0)dE + \mathrm{Re}[1/\varepsilon(0,0)]] = 1 \quad (9)$$

where E_p =21.4 eV for liquid water. In the new Opt4Rel model, the contribution of the 2a1 shell to the ELF is modified in order to better fulfill the sum rules of **Eqs 7–9**. This is possible since the 2a1 shell with binding energy at ~32 eV is not within the range of the particular experimental data set used [36], so the Drude coefficients of that shell are at our disposal to improve the fulfillment of the sum rules. This adjustment was deemed necessary to also bring **Eq. 4** in better agreement with a more recent experimental data set [37] that extends well beyond the 2a1 energy threshold (not shown here).

In all dielectric models of Geant4-DNA (Opt2, Opt4, Opt4Rel), the ELF is used to describe the excitation and ionization of the outer-shell electrons (8 in number) of the water molecule which have condensed-phase properties, while the ionization of the innermost (K-shell) electrons is described by the BEAX model. Although the latter is of an atomic origin and disregards aggregation effects, it is generally considered a reasonable approximation for inner-shell electrons which are minimally perturbed by the phase of the medium.

2.2 Non-relativistic Born approximation

In the framework of the PWBA, ELF is the only non-trivial material input to calculate inelastic cross sections due to the proportionality relation:

$$\frac{d^2\sigma_{PWBA}}{dEdQ} \propto \mathrm{Im}\left[-\frac{1}{\varepsilon(E,Q)}\right] \quad (10)$$

where Q is the free-recoil energy, $Q(q) = q^2/2m$, with m the electron rest mass. By integrating **Eq. 10** over Q and E one obtains the differential and total inelastic cross section, respectively. Importantly, by entering **Eq. 5** into **Eq. 10**, one may calculate differential and total inelastic cross sections specific to each excitation level and ionization shell. For example, the singly differential ionization cross section (DICS) which will be presented below is calculated from:

$$\frac{d\sigma_{PWBA}}{dE} = \frac{1}{\pi\alpha_0 NT}\sum_n^{ioniz.}\int_{Q_{n,-}}^{Q_{n,+}} \frac{\varepsilon_2^{(n)}(W+B_n,Q)}{|\varepsilon(E,Q)|^2}\frac{dQ}{Q} \quad (11)$$

where α_0 is the Bohr radius, N is the density of water molecules (=3.343 10^{22} molecules/cm^3 in unit density water), T is the non-relativistic incident electron energy and $W = E - B_n$ is the kinetic energy of the secondary electron. The limits of integration in **Eq. 11** are based on energy-momentum conservation:

$$Q_{n,\pm} = \left[T^{1/2} \pm (T - W - B_n)^{1/2}\right]^2 \quad (12)$$

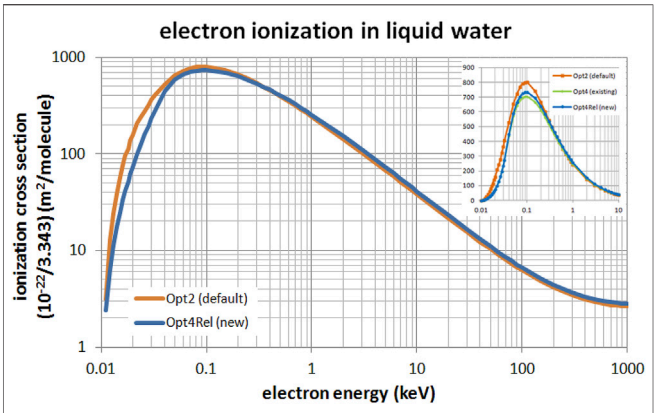

FIGURE 2 | Total ionization cross section of electrons in liquid water in the energy range from 10 eV to 1 MeV. Comparison between the default Opt2 and new Opt4Rel Geant4-DNA physics models is shown. The inset focuses on the low-energy range (up to 10 keV) with the addition of the non-relativistic Opt4.

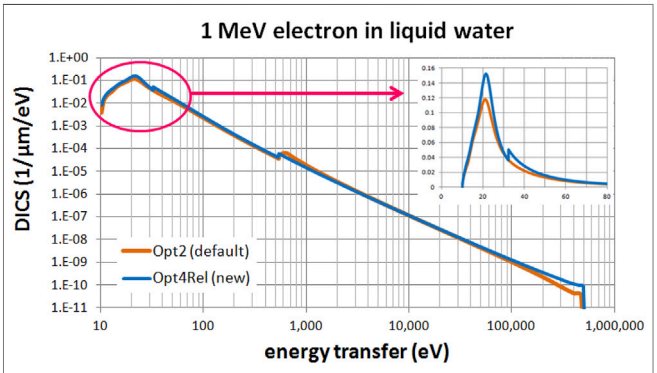

FIGURE 3 | Differential ionization cross section (DICS) for 1 MeV electron in liquid water. Comparison between the default Opt2 and new Opt4Rel Geant4-DNA physics models. The inset focuses on the low energy-transfer part (up to 80 eV).

To calculate inelastic cross sections via **Eq. 11**, it is necessary to have defined the ELF for arbitrary values of q, i.e., within the limits imposed by **Eq. 12**. For ionizations, the non-relativistic quadratic (in q) dispersion relation is used and implemented within the Drude functions:

$$E_n(q) = E_n + Q(q) \tag{13}$$

2.3 Relativistic Born Approximation

In the framework of the relativistic PWBA (RPWBA), the DICS is obtained as a sum of two terms:

$$\frac{d\sigma_{RPWBA}}{dE} = \frac{d\sigma_L}{dE} + \frac{d\sigma_T}{dE} \tag{14}$$

where the subscripts "L" and "T" denote the longitudinal and transverse terms, respectively [38]. The longitudinal DICS reads:

$$\frac{d\sigma_L}{dE} = \frac{1}{\pi\alpha_0 N mc^2\beta^2}\sum_n^{ioniz.} \times \int_{Q_{n,-}}^{Q_{n,+}} \left[\frac{\varepsilon_2^{(n)}(W+B_n,Q)}{|\varepsilon(E,Q)|^2}\right]\frac{1+Q/mc^2}{Q(1+Q/2mc^2)}dQ \tag{15}$$

where and $\beta = \upsilon/c$ with υ the incident electron velocity and c the speed of light, and the relativistic form of the free-recoil energy is $Q(Q+2mc^2) = (cq)^2$. The limits of integration in **Eq. 14** are:

$$Q_{\pm,n} = \left\{\left[\sqrt{T(T+2mc^2)} \pm \sqrt{(T-W-B_n)(T-W-B_n+2mc^2)}\right]^2 + (mc^2)^2\right\}^{1/2} - mc^2 \tag{16}$$

In Opt4Rel, the following relativistic dispersion relation is used:

$$E_n(q) = E_n + (mc^2)^{1/2}(q^2/m + mc^2)^{1/2} - mc^2 \tag{17}$$

The transverse DICS term is calculated from:

$$\frac{d\sigma_T}{dE} = \frac{1}{\pi\alpha_0 N mc^2\beta^2}\left[\sum_n^{ioniz.}\frac{\varepsilon_2^{(n)}(W+B_n,0)}{|\varepsilon(E,0)|^2}\right]\left[\ln\left(\frac{1}{1-\beta^2}\right) - \beta^2\right] \tag{18}$$

Note that only collisions with zero momentum transfer ($q = 0$ or $Q = 0$) contribute to **Eq. 18** according to the small-angle approximation [38].

2.4 Low-Energy Born Corrections

The low-energy corrections implemented in Opt2 and Opt4 are of two kinds, namely, corrections for exchange (EX) in electron-electron interactions and Coulomb (CB) corrections to account for deviations from first-order perturbation theory [39, 40]. As discussed elsewhere, the existing version of Opt4 includes a more consistent implementation of the low-energy (EX and CB) corrections terms [31, 33]. These improvements are also passed onto Opt4Rel. However, all low-energy (EX and CB) correction terms had to be re-evaluated in Opt4Rel using the new Drude coefficients that enter into the ELF.

2.5 Calculation Scheme

The application of low-energy and relativistic corrections implemented in Opt4Rel increase the complexity of the calculations. Therefore, corrections are applied only within the energy regime that have a sizeable effect. In the present work, corrections to PWBA are applied only if they change the total electronic stopping power by at least 0.5–1%. Based on this criterion we distinguish between the following three regimes: 1) in the energy range 0.01–1 keV, we use the PWBA expression, **Eq. 8**, together with EX and CB corrections; 2) in the energy range 1–100 keV, we use the RPWBA expression, **Eq. 10** (but setting the transverse term equal to zero), together with EX and CB corrections; and 3) in the energy range 100–1,000 keV, we use the complete RPWBA expression, **Eq. 10**.

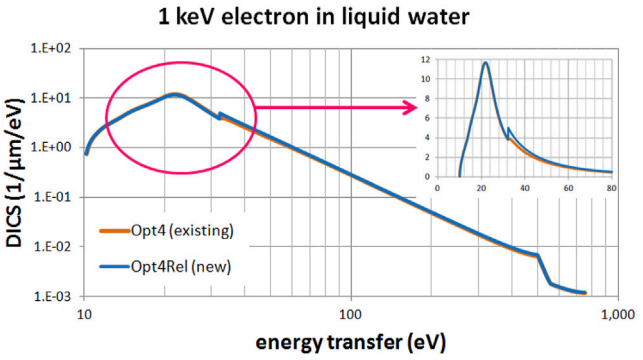

FIGURE 4 | Differential ionization cross section (DICS) for 1 keV electron in liquid water. Comparison between the existing Opt4 and new Opt4Rel Geant4-DNA physics models. The inset focuses on the low energy-transfer part (up to 80 eV).

3 RESULTS AND DISCUSSION

In this section we report upon the internal consistency of the new ELF model implemented into Opt4Rel based on the estimated sum-rule errors. We also report results on the total and differential ionization cross section and compare the new Opt4Rel model against the default Opt2 and the existing (non-relativistic) Opt4 models. Since the excitation part of the ELF is similar between the new Opt4Rel and the existing (non-relativistic) Opt4, the difference in the corresponding cross section is negligible. Likewise, differences in the excitation cross sections between the new Opt4Rel and the default Opt2 can be inferred from earlier comparisons between Opt4 and Opt2 reported in previous publications [33].

In **Figure 1** we compare the sum-rule errors of Opt2, Opt4, and Opt4Rel, which is defined as the deviation of **Eqs 7–9** from unity. In all cases a reduction of the sum-rule error is achieved by Opt4Rel (compared to both Opt2 and Opt4), with the error in the f sum-rule being nearly zero, the error in the ELF sum-rule being below 1% and the error in the KK sum-rule being below 2%. The very small errors in the sum rules offer an extra degree of confidence about the internal consistency of our semi-empirical DRF and ELF of the liquid water medium.

Figure 2 presents a comparison of the total ionization cross section of the default Opt2, the existing non-relativistic Opt4, and the new Opt4Rel models. The comparison between Opt2 and Opt4Rel extends from 10 eV up to 1 MeV (main panel) whereas the comparison against Opt4 (inset) is limited up to 10 keV since this model is not available beyond this energy. It may be seen from **Figure 2** that differences between models are most evident at sub-keV energies. Specifically, compared to the default Opt2 model, the ionization cross section of the new Opt4Rel is slightly enhanced (by 5–10%) at high energies (>1 keV) whereas it is significantly lower (up to 50%) at sub-keV energies. These differences are mostly due to the different ELF parameterization that results from the implementation of the Emfietzoglou-Kyriakou algorithm in the new model. Compared to the existing Opt4, the new Opt4Rel is constantly higher (not visible) by about 5% above 32 eV due to the enhanced contribution of the 2a1 shell in the new model. Below the onset of the 2a1 shell, Opt4 and Opt4Rel are nearly identical. Note that Opt4Rel is still much lower than Opt2 at sub-keV energies, so the reported differences between Opt4 and Opt2 in low-energy electron transport should persist with Opt4Rel.

Figures 3, **4** present a comparison of the differential ionization cross section (DICS) between the models. In **Figure 3** we compare the new Opt4Rel model against the default Opt2 model at 1 MeV electron energy. Sizeable difference is observed at both the region of the peak (around 20 eV) and at the onset of the 2a1 ionization shell (32 eV). These differences stem (mainly) from the different ELF parameterization in these two models as discussed also above. As the energy-transfer is increased well beyond the 2a1 binding energy (>32 eV) differences gradually diminish. In **Figure 4** we compare the new Opt4Rel model against the existing non-relativistic Opt4 model at 1 keV electron energy. As expected, the difference between these two models is restricted around the onset of the 2a1 ionization shell, due to the different Drude coefficients being used for the contribution of this shell. Contrary to **Figure 3**, no difference around the peak region (20 eV) is observed in **Figure 4**, due to the similarities of the ELF models of Opt4 and of Opt4Rel in the sub-32 eV energy range. It must be emphasized that the observed differences between the models depicted in **Figures 3**, **4** persist at almost all electron energies because the DICS is (roughly) proportional to the ELF.

In conclusion, a relativistic extension and improvement of the inelastic model of Opt4 has been developed, offering improved electron transport capabilities from 10 eV up to 1 MeV. The new developments are based on the relativistic plane wave Born approximation and the ELF of the medium which is a slightly improved version of the existing (non-relativistic) Opt4. Work is in progress to further extend the new model up to 10 MeV. Once the complete relativistic extension is validated and benchmarked, the methodology can be extended to other condensed biologica media for which the needed DRF data are available.

DATA AVAILABILITY STATEMENT

The raw data supporting the conclusion of this article will be made available by the authors, without undue reservation.

AUTHOR CONTRIBUTIONS

IK and DE have developed the physics models used in the study, performed simulations and written the manuscript. SI has performed benchmarking simulations. All authors contributed in reading, revising and approving the submitted version.

FUNDING

We would like to acknowledge financial support from the France-Greece "Projet International de Cooperation Scientifique (PICS)" #8235. IK and DE acknowledge financial support from European Space Agency (ESA Contract No. 4000126645/19/NL/BW).

REFERENCES

1. Nikjoo H, Uehara S, Emfietzoglou D, Cucinotta FA. Track-structure Codes in Radiation Research. *Radiat Measurements* (2006) 41:1052–74. doi:10.1016/j.radmeas.2006.02.001
2. Friedland W, Dingfelder M, Kundrát P, Jacob P. Track Structures, DNA Targets and Radiation Effects in the Biophysical Monte Carlo Simulation Code PARTRAC. *Mutat Research/Fundamental Mol Mech Mutagenesis* (2011) 711: 28–40. doi:10.1016/j.mrfmmm.2011.01.003
3. Nikjoo H, Taleei R, Liamsuwan T, Liljequist D, Emfietzoglou D. Perspectives in Radiation Biophysics: From Radiation Track Structure Simulation to Mechanistic Models of DNA Damage and Repair. *Radiat Phys Chem* (2016) 128:3–10. doi:10.1016/j.radphyschem.2016.05.005
4. Andreo P. Monte Carlo Techniques in Medical Radiation Physics. *Phys Med Biol* (1991) 36:861–920. doi:10.1088/0031-9155/36/7/001
5. Rogers DW. Fifty Years of Monte Carlo Simulations for Medical Physics. *Phys Med Biol* (2006) 51:R287–301. doi:10.1088/0031-9155/51/13/R17
6. Dingfelder M. Track Structure: Time Evolution from Physics to Chemistry. *Radiat Prot Dosim* (2006) 122:16–21. doi:10.1093/rpd/ncl494
7. Dingfelder M. Track-structure Simulations for Charged Particles. *Health Phys* (2012) 103:590–5. doi:10.1097/hp.0b013e3182621292
8. LaVerne JA, Pimblott SM. Electron Energy-Loss Distributions in Solid, Dry DNA. *Radiat Res* (1995) 141:208–15. doi:10.2307/3579049
9. Bug MU, Yong Baek W, Rabus H, Villagrasa C, Meylan S, Rosenfeld AB. An Electron-Impact Cross Section Data Set (10 eV-1 keV) of DNA Constituents Based on Consistent Experimental Data: A Requisite for Monte Carlo Simulations. *Radiat Phys Chem* (2017) 130:459–79. doi:10.1016/j.radphyschem.2016.09.027
10. Zein SA, Bordage MC, Francis Z, Macetti G, Genoni A, Cappello CD, et al. Electron Transport in DNA Bases: An Extension of the Geant4-DNA Monte Carlo Toolkit. *Nucl Instrum Meth B* (2012) 488:70–82. doi:10.1016/j.nimb.2020.11.021
11. Kim Y-K, Rudd ME. Binary-encounter-dipole Model for Electron-Impact Ionization. *Phys Rev A* (1994) 50:3954–67. doi:10.1103/physreva.50.3954
12. Abril I, Garcia-Molina R, Denton CD, Kyriakou I, Emfietzoglou D. Energy Loss of Hydrogen- and Helium-Ion Beams in DNA: Calculations Based on a Realistic Energy-Loss Function of the Target. *Radiat Res* (2011) 175:247–55. doi:10.1667/rr2142.1
13. Abril I, Garcia-Molina R, de Vera P, Kyriakou I, Emfietzoglou D. Inelastic Collisions of Energetic Protons in Biological media. *Adv Quan Chem.* (2013) 65:129–64. doi:10.1016/b978-0-12-396455-7.00006-6
14. Garcia-Molina R, Abril I, Kyriakou I, Emfietzoglou D. Inelastic Scattering and Energy Loss of swift Electron Beams in Biologically Relevant Materials. *Surf Interf Anal.* (2017) 49:11–7. doi:10.1002/sia.5947
15. ICRU, 36. Microdosimetry. *Int J Comm Radiat Units Meas* (1983) 19:1–119.
16. Lindborg L, Hultqvist M, Carlsson Tedgren Å, Nikjoo H. Lineal Energy and Radiation Quality in Radiation Therapy: Model Calculations and Comparison with experiment. *Phys Med Biol* (2013) 58:3089–105. doi:10.1088/0031-9155/58/10/3089
17. Friedland W, Schmitt E, Kundrát P, Dingfelder M, Baiocco G, Barbieri S, et al. Comprehensive Track-Structure Based Evaluation of DNA Damage by Light Ions from Radiotherapy-Relevant Energies Down to Stopping. *Sci Rep* (2017) 7:45161. doi:10.1038/srep45161
18. Tang N, Bueno M, Meylan S, Perrot Y, Tran HN, Freneau A, et al. Assessment of Radio-Induced Damage in Endothelial Cells Irradiated with 40 kVp, 220 kVp, and 4 MV X-Rays by Means of Micro and Nanodosimetric Calculations. *Ijms* (2019) 20:6204. doi:10.3390/ijms20246204
19. Matsuya Y, Kai T, Yoshii Y, Yachi Y, Naijo S, Date H, et al. Modeling of Yield Estimation for DNA Strand Breaks Based on Monte Carlo Simulations of Electron Track Structure in Liquid Water. *J Appl Phys* (2019) 126:124701. doi:10.1063/1.5115519
20. Margis S, Magouni M, Kyriakou I, Georgakilas AG, Incerti S, Emfietzoglou D. Microdosimetric Calculations of the Direct DNA Damage Induced by Low Energy Electrons Using the Geant4-DNA Monte Carlo Code. *Phys Med Biol* (2020) 65:045007. doi:10.1088/1361-6560/ab6b47
21. Kyriakou I, Tremi I, Georgakilas AG, Emfietzoglou D. Microdosimetric Investigation of the Radiation Quality of Low-Medium Energy Electrons Using Geant4-DNA. *Appl Radiat Isot* (2021) 172:109654. doi:10.1016/j.apradiso.2021.109654
22. Emfietzoglou D, Nikjoo H. The Effect of Model Approximations on Single-Collision Distributions of Low-Energy Electrons in Liquid Water. *Radiat Res* (2005) 163:98–111. doi:10.1667/rr3281
23. Dingfelder M, Inokuti M. The Bethe Surface of Liquid Water. *Radiat Environ Biophys* (1999) 38:93–6. doi:10.1007/s004110050143
24. Emfietzoglou D, Papamichael G, Nikjoo H. Monte Carlo Electron Track Structure Calculations in Liquid Water Using a New Model Dielectric Response Function. *Radiat Res* (2017) 188:355–68. doi:10.1667/rr14705.1
25. Nikjoo H, Emfietzoglou D, Liamsuwan T, Taleei R, Liljequist D, Uehara S. Radiation Track, DNA Damage and Response-A Review. *Rep Prog Phys* (2016) 79:116601. doi:10.1088/0034-4885/79/11/116601
26. Emfietzoglou D, Kyriakou I, Garcia-Molina R, Abril I. Inelastic Mean Free Path of Low-Energy Electrons in Condensed media: beyond the Standard Models. *Surf Interf Anal.* (2017) 49:4–10. doi:10.1002/sia.5878
27. Incerti S, Baldacchino G, Bernal M, Capra R, Champion C, Francis Z, et al. The Geant4-DNA Project. *Int J Model Simul Sci Comput* (2010) 01:157–78. doi:10.1142/s1793962310000122
28. Incerti S, Ivanchenko A, Karamitros M, Mantero A, Moretto P, Tran HN, et al. Comparison ofGEANT4very Low Energy Cross Section Models with Experimental Data in Water. *Med Phys* (2010) 37:4692–708. doi:10.1118/1.3476457
29. Bernal MA, Bordage MC, Brown JMC, Davídková M, Delage E, El Bitar Z, et al. Track Structure Modeling in Liquid Water: A Review of the Geant4-DNA Very Low Energy Extension of the Geant4 Monte Carlo Simulation Toolkit. *Physica Med* (2015) 31:861–74. doi:10.1016/j.ejmp.2015.10.087
30. Incerti S, Kyriakou I, Bernal MA, Bordage MC, Francis Z, Guatelli S, et al. Geant4-DNA Example Applications for Track Structure Simulations in Liquid Water: A Report from the Geant4-DNA Project. *Med Phys* (2018) 45:722–39. doi:10.1002/mp.13048
31. Kyriakou I, Incerti S, Francis Z. Technical Note: Improvements in Geant 4 Energy-Loss Model and the Effect on Low-Energy Electron Transport in Liquid Water. *Med Phys* (2015) 42:3870–6. doi:10.1118/1.4921613
32. Bordage MC, Bordes J, Edel S, Terrissol M, Franceries X, Bardiès M, et al. Implementation of New Physics Models for Low Energy Electrons in Liquid Water in Geant4-DNA. *Physica Med* (2016) 32:1833–40. doi:10.1016/j.ejmp.2016.10.006
33. Kyriakou I, Šefl M, Nourry V, Incerti S. The Impact of New Geant4-DNA Cross Section Models on Electron Track Structure Simulations in Liquid Water. *J Appl Phys* (2016) 119:194902. doi:10.1063/1.4950808
34. Kyriakou I, Emfietzoglou D, Garcia-Molina R, Abril I, Kostarelos K. Simple Model of Bulk and Surface Excitation Effects to Inelastic Scattering in Low-Energy Electron Beam Irradiation of Multi-Walled Carbon Nanotubes. *J Appl Phys* (2011) 110:054304. doi:10.1063/1.3626460
35. Nikjoo H, Uehara S, Emfietzoglou D. *Interaction of Radiation with Matter*. Boca Raton, FL: CRC Press (2012). p. 348.

36. Heller JM, Hamm RN, Birkhoff RD, Painter LR. Collective Oscillation in Liquid Water. *J Chem Phys* (1974) 60:3483–6. doi:10.1063/1.1681563
37. Hayashi H, Watanabe N, Udagawa Y, Kao C-C. The Complete Optical Spectrum of Liquid Water Measured by Inelastic X-ray Scattering. *Proc Natl Acad Sci* (2000) 97:6264–6. doi:10.1073/pnas.110572097
38. Fernández-Varea JM, Llovet X, Salvat F. Cross Sections for Electron Interactions in Condensed Matter. *Surf Interf Anal.* (2005) 37:824–32. doi:10.1002/sia.2101
39. Emfietzoglou D, Kyriakou I, Garcia-Molina R, Abril I, Nikjoo H. Inelastic Cross Sections for Low-Energy Electrons in Liquid Water: Exchange and Correlation Effects. *Radiat Res* (2013) 180:499–513. doi:10.1667/rr13362.1
40. Fernandez-Varea JM, Mayol R, Liljequist D, Salvat F. Inelastic Scattering of Electrons in Solids from a Generalized Oscillator Strength Model Using Optical and Photoelectric Data. *J Phys Condens Matter* (1993) 5:3593–610. doi:10.1088/0953-8984/5/22/011

Conflict of Interest: The authors declare that the research was conducted in the absence of any commercial or financial relationships that could be construed as a potential conflict of interest.

frontiers in Physics

ORIGINAL RESEARCH
published: 27 January 2022
doi: 10.3389/fphy.2021.788253

New Capabilities of the FLUKA Multi-Purpose Code

C. Ahdida[1], D. Bozzato[1,2], D. Calzolari[1], F. Cerutti[1], N. Charitonidis[1], A. Cimmino[3], A. Coronetti[1,4], G. L. D'Alessandro[1], A. Donadon Servelle[1,5], L. S. Esposito[1], R. Froeschl[1], R. García Alía[1], A. Gerbershagen[1], S. Gilardoni[1], D. Horváth[3], G. Hugo[1], A. Infantino[1], V. Kouskoura[1], A. Lechner[1], B. Lefebvre[3], G. Lerner[1], M. Magistris[1], A. Manousos[1,6], G. Moryc[1], F. Ogallar Ruiz[1,7], F. Pozzi[1], D. Prelipcean[1,8], S. Roesler[1], R. Rossi[1], M. Sabaté Gilarte[1], F. Salvat Pujol[1], P. Schoofs[1], V. Stránský[3], C. Theis[1], A. Tsinganis[9], R. Versaci[3], V. Vlachoudis[1], A. Waets[1] and M. Widorski[1]*

[1]European Organization for Nuclear Research (CERN), Geneva, Switzerland, [2]Karlsruhe Institute for Technology (KIT), Karlsruhe, Germany, [3]ELI Beamlines Centre, Institute of Physics, Czech Academy of Sciences, Dolní Břežany, Czech Republic, [4]Department of Physics, University of Jyväskylä, Jyväskylä, Finland, [5]Ecole Polytechnique Fédérale de Lausanne, Institute of Physics, Lausanne, Switzerland, [6]Department of Physics, Aristotle University of Thessaloniki, Thessaloniki, Greece, [7]Department of Atomic, Molecular and Nuclear Physics, University of Granada, Granada, Spain, [8]Department of Physics, Technical University of Munich (TUM), Munich, Germany, [9]European Commission, Joint Research Centre (JRC), Geel, Belgium

OPEN ACCESS

Edited by:
Peter R. Hobson, Queen Mary University of London, United Kingdom

Reviewed by:
Fabrizio Ambrosino, University of Campania Luigi Vanvitelli, Italy
Francesco Nozzoli, University of Trento, Italy

***Correspondence:**
F. Cerutti
francesco.cerutti@cern.ch

Specialty section:
This article was submitted to Radiation Detectors and Imaging, a section of the journal Frontiers in Physics

Received: *01 October 2021*
Accepted: *08 November 2021*
Published: *27 January 2022*

Citation:
Ahdida C, Bozzato D, Calzolari D, Cerutti F, Charitonidis N, Cimmino A, Coronetti A, D'Alessandro GL, Donadon Servelle A, Esposito LS, Froeschl R, García Alía R, Gerbershagen A, Gilardoni S, Horváth D, Hugo G, Infantino A, Kouskoura V, Lechner A, Lefebvre B, Lerner G, Magistris M, Manousos A, Moryc G, Ogallar Ruiz F, Pozzi F, Prelipcean D, Roesler S, Rossi R, Sabaté Gilarte M, Salvat Pujol F, Schoofs P, Stránský V, Theis C, Tsinganis A, Versaci R, Vlachoudis V, Waets A and Widorski M (2022) New Capabilities of the FLUKA Multi-Purpose Code. Front. Phys. 9:788253. doi: 10.3389/fphy.2021.788253

FLUKA is a general purpose Monte Carlo code able to describe the transport and interaction of any particle and nucleus type in complex geometries over an energy range extending from thermal neutrons to ultrarelativistic hadron collisions. It has many different applications in accelerator design, detector studies, dosimetry, radiation protection, medical physics, and space research. In 2019, CERN and INFN, as FLUKA copyright holders, together decided to end their formal collaboration framework, allowing them henceforth to pursue different pathways aimed at meeting the evolving requirements of the FLUKA user community, and at ensuring the long term sustainability of the code. To this end, CERN set up the FLUKA.CERN Collaboration[1]. This paper illustrates the physics processes that have been newly released or are currently implemented in the code distributed by the FLUKA.CERN Collaboration[2] under new licensing conditions that are meant to further facilitate access to the code, as well as intercomparisons. The description of coherent effects experienced by high energy hadron beams in crystal devices, relevant to promising beam manipulation techniques, and the charged particle tracking in vacuum regions subject to an electric field, overcoming a former lack, have already been made available to the users. Other features, namely the different kinds of low energy deuteron interactions as well as the synchrotron radiation emission in the course of charged particle transport in vacuum regions subject to magnetic fields, are currently undergoing systematic testing and benchmarking prior to release. FLUKA is widely used to evaluate radiobiological effects, with the powerful support of the Flair graphical interface, whose new generation (Available at http://flair.cern) offers now additional capabilities, e.g., advanced 3D visualization with photorealistic rendering and support

[1]In this paper, depending on the context, references to FLUKA are to code developed jointly by INFN and CERN until 31 August 2019, or to further code developments performed after this date in the framework of the FLUKA.CERN Collaboration
[2]At https://fluka.cern.

for industry-standard volume visualization of medical phantoms. FLUKA has also been playing an extensive role in the characterization of radiation environments in which electronics operate. In parallel, it has been used to evaluate the response of electronics to a variety of conditions not included in radiation testing guidelines and standards for space and accelerators, and not accessible through conventional ground level testing. Instructive results have been obtained from Single Event Effects (SEE) simulations and benchmarks, when possible, for various radiation types and energies. The code has reached a high level of maturity, from which the FLUKA.CERN Collaboration is planning a substantial evolution of its present architecture. Moving towards a modern programming language allows to overcome fundamental constraints that limited development options. Our long term goal, in addition to improving and extending its physics performances with even more rigorous scientific oversight, is to modernize its structure to integrate independent contributions more easily and to formalize quality assurance through state-of-the-art software deployment techniques. This includes a continuous integration pipeline to automatically validate the codebase as well as automatic processing and analysis of a tailored physics-case test suite. With regard to the aforementioned objectives, several paths are currently envisaged, like finding synergies with Geant4, both at the core structure and interface level, this way offering the user the possibility to run with the same input different Monte Carlo codes and crosscheck the results.

Keywords: FLUKA, Monte Carlo transport, beam-matter interaction, high energy physics, crystal channeling, medical physics, single event effects (SEE)

1 INTRODUCTION

The FLUKA (FLUktuierende KAskade in German, i.e., fluctuating cascade) code was born at the European Organisation for Nuclear Research (CERN) from the work of J. Ranft, who in the mid nineteen-sixties developed several Monte Carlo programs for the determination of shielding thicknesses, estimation of induced radioactivity levels and prediction of dose absorption in critical components at high energy proton accelerators. As one of them, FLUKA was a purely analogue code simulating the particle cascade in a cylindrical block of a specified elemental material and calculating the spatial distribution of nuclear reaction ("star") and energy deposition densities per incoming primary proton or charged pion. The user input was to be provided by means of formatted control and data cards, representing a lasting legacy.

Building on that ground, the first generation of FLUKA versions spanned until the late seventies, relying again on the work of J. Ranft (then affiliated with the Karl Marx University of Leipzig) and his collaboration with J. Routti of Helsinki University of Technology (HUT). A second generation, addressing the reformulation of the hadron interaction model among other significant advances, can be identified across the eighties with the joint effort of CERN (G.R. Stevenson and A. Fassò), HUT (J. Sandberg and P. Aarnio) and the Leipzig University group (J. Ranft and H.-J. Moehring).

The modern (third generation) FLUKA moved from a plan by A. Ferrari (initially INFN, then CERN) and A. Fassò to transform the code into a multi-purpose multi-particle tool and featured a substantial restructuring, improvement and extension, eventually increasing by one order of magnitude the Fortran source size, with the contribution of P. Sala (INFN). In 2000, dedicated support was provided by NASA to enable the treatment of heavy ion interactions, including the interface to external event generators. In 2003, a collaboration agreement between CERN and INFN was set up in order to develop, maintain and release FLUKA, integrating through the years the work of several other collaborators (see for instance [1] and references therein).

In 2019, more than 15 years on, the formal collaborative framework between the two copyright holders was succeded by an arrangement aimed at ensuring FLUKA's long-term sustainability and capability to meet the evolving requirements of its user community. This offered the opportunity to leverage lessons learned and current standards in the organization of software collaborations, while fostering the active involvement of both established FLUKA contributors as well as new partners. As a result, CERN recently put in place a multilateral collaboration framework, already joined by ELI Beamlines, and a new licensing scheme expanding the access to the source code and allowing for its customization as well as result intercomparison and physics model benchmarking. In parallel, a modern user support platform has been adopted[3] and a significantly higher distribution pace has materialized, with

[3]https://fluka-forum.web.cern.ch/

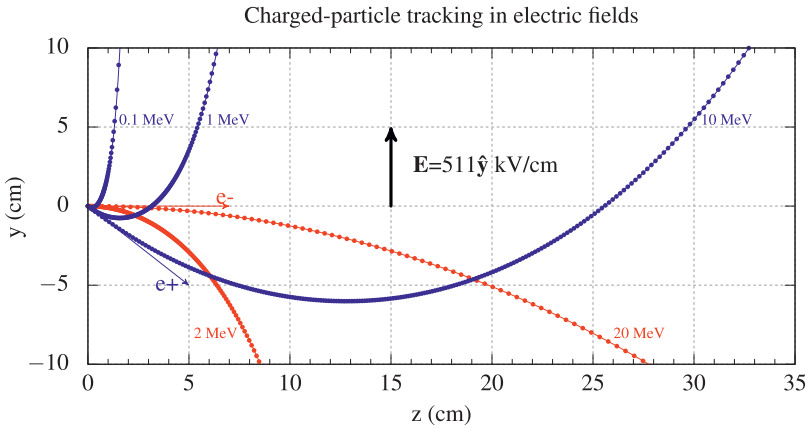

FIGURE 1 | Comparison between FLUKA (dots) and analytical (solid curves) electron (red) and positron (blue) trajectories starting at the origin of coordinates along the direction indicated by the respective arrows, in a 511 kV/cm electric field along the *y* axis for energies ranging from 0.1 to 20 MeV as per the figure labels.

two major releases in 2020 and a third one planned to take place before the end of 2021.

Selected physics developments that provide FLUKA with new capabilities are detailed in **section 2**. They are the description of coherent effects experienced by charged particles traversing crystals, the transport of charged particles in electric fields, the simulation of nuclear reactions by deuterons below 300 MeV, and the synchrotron radiation emission by charged particles in magnetic fields.

Section 3 reports on advances of the FLUKA Advanced InteRface (Flair), whose restructuring in Python v3 integrated a new medical visualization module highly improving the volumetric rendering of voxelized phantoms and dose distributions. **Section 4** focuses on another field of FLUKA applications, namely radiation to electronics, and, after reviewing relevant achievements of the last decade, includes new results regarding photon-induced Single Event Effects (SEE).

Section 5 discusses the main quality assurance measures featuring the development, testing and benchmarking framework put in place for FLUKA v4 (that is currently distributed by the FLUKA.CERN Collaboration as fourth FLUKA generation) in order to properly validate the code evolution prior to release and indicate the improvement needs. Finally, **section 6** introduces the long term perspective and the associated project stages towards a fifth FLUKA generation, the first of which already started in parallel with the steady investment on FLUKA v4.

2 NEW PHYSICS DEVELOPMENTS

2.1 Transport of Charged Particles in Electric Fields

FLUKA has been able to track charged particles in magnetic fields since the late 1980s, thus allowing users from a relatively early stage on to model charged particle transport e.g. in complex particle accelerator components, such as dipole or quadrupole magnets and beam kickers. The availability of user routines provides full customization capabilities to tackle the transport of charged particles in arbitrary user-defined magnetic fields.

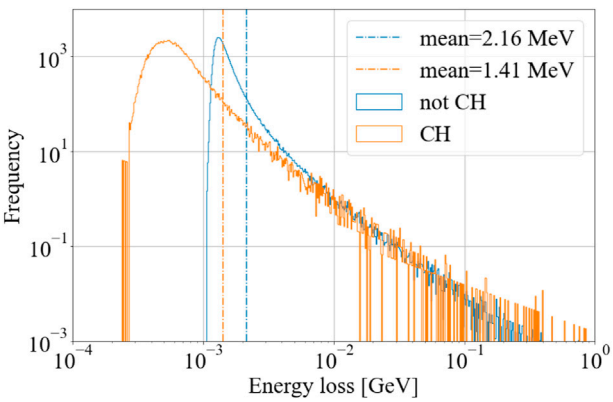

FIGURE 2 | Energy loss distribution for 180 GeV protons on a 4 mm-long crystal in channeling regime (orange) and in amorphous regime (blue).

Instead, the transport of charged particles in electric fields [2] was a longstanding pending ingredient in FLUKA's transport algorithm. This lack prevented users from modelling electrostatic septa in particle accelerator extraction studies, for example. Users were forced to resort to a proxy magnetic field effectively providing the desired force (permissible whenever the change of the charged particle energy is negligible). To overcome this shortcoming, a dedicated module for charged particle transport in electric fields in vacuum has been recently included in FLUKA.

The transport of charged particles in both magnetic and electric (static) fields relies on the same adaptive stepping algorithm to solve the resulting equation of motion, offering users an accurate control of both the particle step size and the tolerance with which boundaries to nearby regions can be intercepted by the (effectively curved) particle steps. FLUKA's module for charged particle tracking in electric fields accounts for

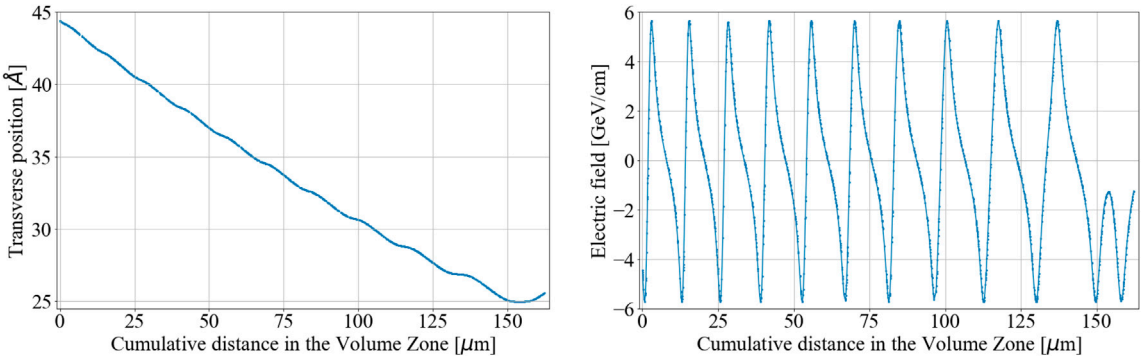

FIGURE 3 | Left: Quasi-channeled particle trajectory through a crystal close to the tangency point as a function of the cumulative longitudinal coordinate. Oscillations are due to the Molière potential and volume reflection can be seen at the right-hand side of the chart. **Right:** Corresponding electric field along the particle trajectory.

the variation (decrease or increase) of the particle's kinetic energy, and it includes an algorithm which treats situations where the electrostatic force opposes the direction of motion, accurately resolving the trajectory turning point where relevant.

Following the example proposed by A. Bielajew [3], **Figure 1** displays the excellent agreement between the analytical (solid curves) and FLUKA (symbols) electron (red) and positron (blue) trajectories starting at the origin of coordinates along the direction indicated by the respective arrows in the yz plane, in an electric field of 511 kV/cm along the y axis.

2.2 Coherent Effects in Crystals

Coherent interactions of charged particles in bent crystals can be used for beam collimation or extraction purposes. Crystals have long been under study at CERN and in other research centers [4, 5] leading to very promising results for the Large Hadron Collider (LHC) collimation [6, 7]. In this context, crystals are planned to be part of the collimation system for High Luminosity LHC Ion runs [8]. In parallel with this activity, a module able to reproduce the various coherent effects such as channeling, volume capture and volume reflection was added to FLUKA [9]. This module also accounts for the change in both interaction and energy loss rate in these regimes. In the following, relevant aspects of the model are introduced and the most recent developments are detailed.

In a FLUKA geometry, a crystal is a region for which several characteristics such as torsion, temperature, radius of curvature and channel orientation are specified. These are set up independently and it is therefore the user's responsibility to ensure that microscopic features of the device are consistent with its geometry. However, this decoupling offers an additional degree of freedom, for instance the possibility to introduce a deliberate mismatch between crystal edges and plane orientation to reproduce miscut[4].

[4]Miscut is a crystal manufacturing defect causing crystal edges to not be perfectly parallel to the channel planes. More information on miscut and its effects on channeling can be found in e.g., [11].

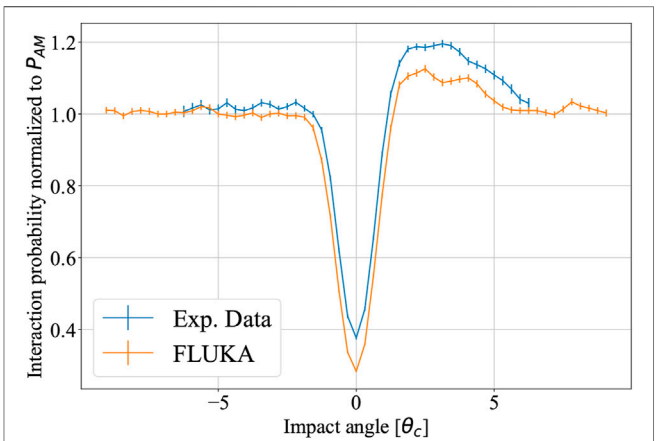

FIGURE 4 | Nuclear interaction rate as a function of the particle incoming angle, normalized to the interaction rate in amorphous mode. The dip corresponds to channeled particles, experiencing low interaction rate in the channel. The excess observed for small positive angles corresponds to the increased rate experienced by quasi-channeled particles when crossing multiple channels. Experimental data from [13].

As the crystal channel direction is defined, the incoming angle of each entering particle can be calculated. When the angle is small enough, the particle becomes trapped in between the transverse Molière potential barriers sitting at each atomic center. The particle enters the channeling regime and is transported along the channel. For a bent crystal, this implies tracking along an arc which is implemented through the use of a proxy magnetic field. In addition, the channeled particle oscillates transversally between the channeling planes with an amplitude depending on its transverse momentum.

This oscillation is important for the computation of reduced interaction rate in channeling. Firstly, the electronic stopping power for channeled projectiles is reduced compared with the one of an amorphous medium. The FLUKA algorithm uses a prescription similar to that of Esbensen et al. [10], maintaining the contribution of distant

collisions to the stopping power unaltered and scaling that of close collisions[5] by the fraction of the channel electron density subtended by the oscillating trajectory of the particle. The reduction factor is typically of the order of 2, as shown in **Figure 2** for the case of 180 GeV protons through a 4 mm-long Si crystal.

Secondly, Coulomb scattering of channeled particles on the screened potential of target atoms is computed on a single event basis rather than in multiple scattering. Contributions from small impact parameter collisions are suppressed, with a cutoff corresponding to the minimum distance between the particle oscillatory path and the atomic centers.

Thirdly, nuclear interactions are scaled to the average nuclear density along the particle oscillatory path. This leads to a substantial reduction of the nuclear interaction rate [11] for the channeled population at large.

Coherent effects are not limited to channeling. Some particles can experience volume effects inside the crystal: a reflection on the crystal planes or a capture in their current channel after interaction. Both take place when the particle trajectory is almost tangent with the planes, which can only happen when their incoming angle has the same sign as the crystal bending. In order to reproduce these mechanisms, the equations of motion of the particle are solved in the potential of interest, in this case an electrostatic Molière potential to which a centrifugal term is added due to bending.

The volume reflection naturally results from this tracking: on **Figure 3** the trajectory of a quasi-channeled particle is displayed close to its tangency point with the planes, as a function of the longitudinal coordinate. After crossing several planes, the particle acquires a small angular deflection in the direction opposite to bending. While progressing through this region, quasi-channeled particles can undergo a disrupting scattering event, which can lead to the capture of the particle if its transverse momentum drops below the Molière potential energy. A captured particle becomes channeled from that point on until it is dechanneled or reaches the end of the crystal.

Microscopic treatment of the coherent effects of quasi-channeled particles is an important recent development of the model. The nuclear interaction rate is altered for quasi-channeled particles, akin to what is implemented for channeled ones. However, quasi-channeled particles cross atomic planes and the resulting interaction rate is higher than in amorphous mode. This increase is apparent on **Figure 4** displaying the nuclear interaction rate as a function of the incoming angle of the particle for a crystal bent towards positive angles. The main dip reflects the suppression of nuclear interactions for channeled particles. Next to it, the interaction rate comes back to amorphous regime values, with the excess on the right reflecting the increased interaction probability of quasi-channeled particles, in accordance with experimental data. The extent of the excess, however, remains slightly lower than the data shows and will be the focus of upcoming developments.

2.3 Low-Energy-Deuteron Nuclear Interactions

Another longstanding shortcoming of FLUKA's transport algorithm concerned the lack of a dedicated model for nuclear reactions of low energy deuterons (below 150 MeV/n). Up to version 4.1, FLUKA included a coarse tentative model to effectively split the deuteron into its constituent neutron and proton, each taking ~50% of the kinetic energy of the deuteron. FLUKA was therefore not recommended for deuteron-beam applications.

Recently, deuteron transport has gained increased attention, for applications as diverse as the production of radioisotopes for medical applications using deuteron beams [12, 13], their radiobiological effects and associated radiation protection aspects [14], as well as for nuclear fusion studies [15]. Furthermore, deuteron production from hadron- and nucleus-nucleus inelastic interactions is often far from negligible; an accurate description of their subsequent nuclear interactions is necessary. Consequently, a dedicated model for low energy deuteron nuclear reactions has been developed and will be included in FLUKA 4.2.

The model consists of the following main components: deuteron stripping to the continuum is modelled on the basis of the Serber model [16] for the (uncorrelated) energy and angle distribution of the stripped nucleon, coupled to FLUKA's hadron-nucleus interaction model PEANUT (Pre-Equilibrium Approach to NUclear Thermalization) [17] in order to properly describe the nuclear inelastic interaction of the remaining nucleon with the target nucleus; deuteron elastic break-up is described within the zero-range distorted wave Born approximation (DWBA) for nuclei with atomic number $Z \geq 3$ [18]; deuteron stripping to discrete levels is also accounted for within the DWBA [19] for the (d,p) and (d,n) reaction channels on a selection of light isotopes for which this interaction mechanism is relevant, including ^{6,7}Li, ^{9}Be, and ^{12}C. More details and benchmarking of this model will be provided in an upcoming dedicated publication.

Furthermore, a complete-fusion channel is included via the Boltzmann Master Equation (BME) event generator, already employed in FLUKA to describe nucleus-nucleus inelastic interactions up to 150 MeV/n [20]. Whereas the three model components described above imply at most one nucleon penetrating the nucleus, the complete-fusion channel effectively permits both nucleons to penetrate the target nucleus, thus providing a larger excitation energy and accounting for the experimentally observed emission of light nuclear fragments beyond a neutron or proton (d, t, ^{3}He, ^{4}He, etc.).

As an example showcasing the performance of the new low-energy deuteron nuclear interaction model in FLUKA, **Figure 5** displays the double-differential (energy and angle) cross section for the emission of protons from ^{58}Ni under

[5]giving an otherwise equal contribution to the stopping power as per [12].

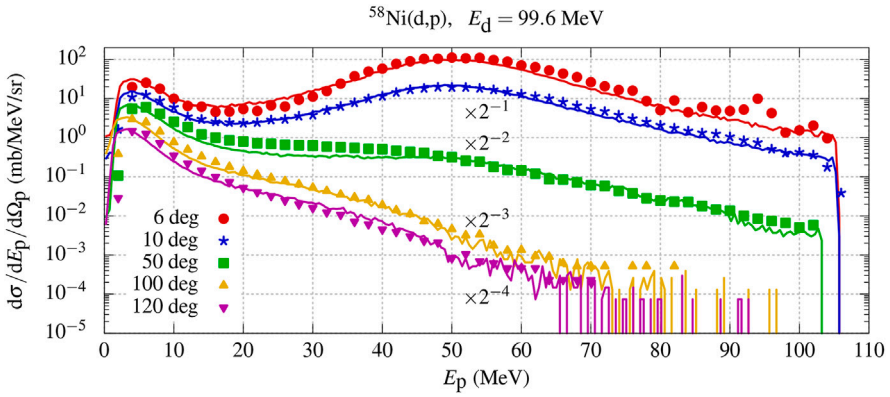

FIGURE 5 | Comparison in absolute units between FLUKA (solid curve) vs experimental (symbols) [21] double-differential (energy and angle) proton emission cross section from ^{58}Ni under bombardment with 99.6 MeV deuterons, resolved as a function of the proton energy E_p for the various indicated emission angles in the lab frame. The curve for 6 deg emission is in absolute units; subsequent curves have been scaled down respectively by the indicated factors for clarity.

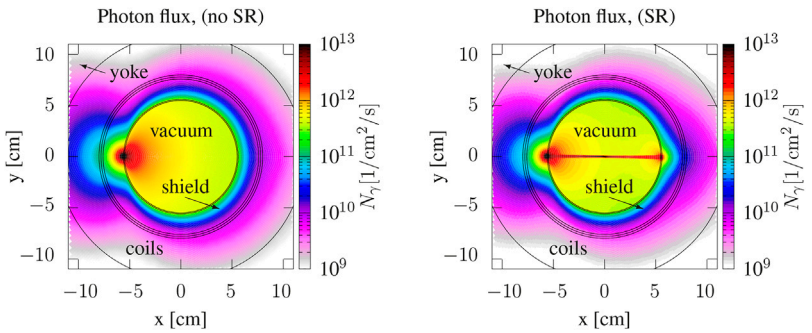

FIGURE 6 | Photon flux distribution in the 10.2 T bending dipole of a 4.5 km ring accomodating a 1.5 TeV negative muon beam with a bunch intensity of 2×10^{12} particles (transverse section). Bunches are injected with a 12 Hz frequency. Sychrotron radiation emitted by high energy electrons generated by muon decay is neglected on the left and accounted for on the right.

99.6 MeV deuteron bombardment at various emission angles, resolved as a function of the proton energy, comparing in absolute units the FLUKA simulation results (solid curves) with available experimental data [21] (in symbols). The simulated proton energy spectra exhibit a remarkably good agreement with the experimental data, reproducing their essential features: a peak at half the deuteron kinetic energy, particularly intense for forward emission angles and due to deuteron stripping to the continuum, as well as a peak at low proton energies from the evaporation stage of the conjugate neutron-nucleus inelastic interaction. **Figure 5** shows that good agreement is preserved throughout the angular domain covered by the experimental data.

2.4 Synchrotron Radiation Emission During Charged Particle Tracking

The emission of synchrotron radiation (SR) photons is possible in FLUKA by means of a special source term. This allows the user to define up to two arcs of a charged particle trajectory in a dipole field, along which SR photons are sampled as source particles for the simulation. The radiating charged particle itself is not explicitly tracked. Such a scheme is useful for applications where SR emission is dominated by beam particles, for example when modelling arcs of electron storage rings. This approach is however not suitable for cases where secondary and higher-generation particles lose a significant fraction of their energy through SR emission. This is for instance the case for high energy muon storage rings and colliders, where SR emission by decay electrons and positrons cannot be neglected when assessing the heat load distribution in magnets or the beam-induced background in detectors.

To overcome this drawback, the FLUKA tracking algorithm for charged particles in a magnetic field in vacuum has been enhanced by including the emission of SR photons as a supplementary discrete process during tracking.

SR photons are explicitly generated and the corresponding energy loss of the radiating charged particle is taken into account. The user can control the SR emission mechanism via dedicated production thresholds.

The new feature is illustrated in **Figure 6**, showing the photon flux in a bending magnet of a 1.5 TeV muon storage ring. The two plots compare different FLUKA simulations with and without SR emission by decay electrons. In the latter case, without the new

emission model, the photon flux in the vacuum chamber, shielding and magnet is exclusively due to the impact of decay electrons on the machine aperture. The dipole field bends all decay electrons towards the center of the ring, which leads to a localized energy deposition hot spot on one side of the magnet. In the other case, SR photons are generated along the electron trajectories and can impact either on the inner or outer side of the vacuum chamber, resulting in a larger spread of the energy released in the decay of beam particles. At such or even higher energies, neglecting this phenomenon may lead to a non-faithful representation of the secondary particle distribution in the magnets, energy deposition and background to experiments.

3 FLAIR, THE FLUKA USER INTERFACE

3.1 Flair Version 3 Upgrade

The FLUKA advanced graphical interface Flair[6] [22] made its first appearance in 2007. It is a fully integrated working environment that assists the user in all stages of a Monte Carlo simulation, from constructing the input and the geometry to running the simulation, processing the output files and plotting the results. Thanks to its advanced capabilities and intuitive use, it quickly became the most popular way of working with FLUKA. Flair is in constant evolution, continuously expanding its features.

Up to version 2, Flair was based on Python v2, which the Python community decided to phase out in 2020[7]. Profiting from this opportunity, it was decided not only to migrate to v3, but also to restructure the code so as to facilitate its further cooperative development. The most notable improvement concerns the decoupling of the graphical interface from the underlying functionality, which was achieved by the introduction of an intermediate abstract layer allowing Flair to support other simulation packages besides FLUKA. While support for MCNP inputs [23] is partial, in the case of Geant4 it is in a quite advanced state, thanks to a dedicated Geant4 application called *Moira* (see **Section 6**).

Particular attention has been paid to computational performance, to further optimize Flair both in terms of CPU-time and numerical precision. A considerable speedup (up to a factor 10) has been attained during the loading and displaying of large input files, thanks to the use of a tk:Text module replacing the previous use of a tk:Canvas[8]. Likewise, the performance and the numerical precision of the geometry editor has been greatly optimized. This has been achieved through the use of z-buffers for 3D rendering, the implementation of an adaptive anti-aliasing algorithm, and the storage of quadratic surfaces also in reduced form, in order to minimize numerical rounding errors introduced by geometric transformations, to name but a few.

Among the new features of Flair v3, we highlight the graphical tool for planning radiation protection interventions: starting from a FLUKA Cartesian 3D dose map, the user can define a path which an operator will follow in space and time by means of a spline to obtain a report detailing the dose acquired along the path. In addition, short animated movies can be created displaying the 3D geometry (and the simulation results) by means of a camera object moving along a user-defined 3D spline. To reinforce the consistency of the input interpretation by FLUKA and Flair, the Flair input file now persistently embeds all the FLUKA input information, which can still be directly manipulated in the FLUKA input file.

3.2 Flair Developments for Medical Applications

As high-throughput computational power is getting more accessible, the use of Monte Carlo-based treatment planning systems (TPS) becomes a viable option for clinical applications of radiation therapy. Codes like FLUKA have important advantages over classical treatment planning systems as they can take a wide range of physical effects (e.g., full secondary particle generation due to implants) accurately into account. Yet, the best physics results cannot be fully exploited if they are not put into an anatomic context which speaks to the medical practitioner.

A dedicated effort has been invested in making Flair v3 a self-contained working environment for the use of FLUKA in medical physics applications. Recent developments include an improved DICOM handling[9], facilitating the generation of voxel geometries with built-in automatic conversion from Hounsfield units to material composition. For instance, boolean operations can now be applied on predefined regions of interest (ROI) to customize the material assignment in the simulation. Moreover, Flair now includes a DICOM editor to perform common tasks like anonymizing patient information and, in general, the editing of DICOM tags. The embedded *RTViewer* helps the user to compare the planned dose calculated by a treatment planning system with the dose simulated by FLUKA. An automatic dose-volume-histogram generator (DVH) is included. RTPLAN-modality DICOM files can be imported to generate the corresponding primary-source cards for FLUKA. Furthermore, RTDOSE-modality DICOM files can be converted to FLUKA's standard 3D mesh scoring (USRBIN), which can not only be readily visualized in 2D and 3D in Flair, but also be used as a volumetric primary source for further simulations. The opposite conversion from USRBIN to RTDOSE is also implemented.

While support for 3D visualization is becoming increasingly available in the domain of Monte Carlo transport codes, visual quality often trails behind current industry standards. In addition, common surface rendering techniques are not suitable for medical visualization due to the loss of contextual information in one dimension. This stems from the fact that there is no well-defined geometry but the input is a discrete cloud of density values obtained

[6]https://flair.cern

[7]See https://www.python.org/doc/sunset-python-2/

[8]https://www.tcl.tk

[9]Details concerning the current version of the DICOM standard are available at https://www.dicomstandard.org/current.

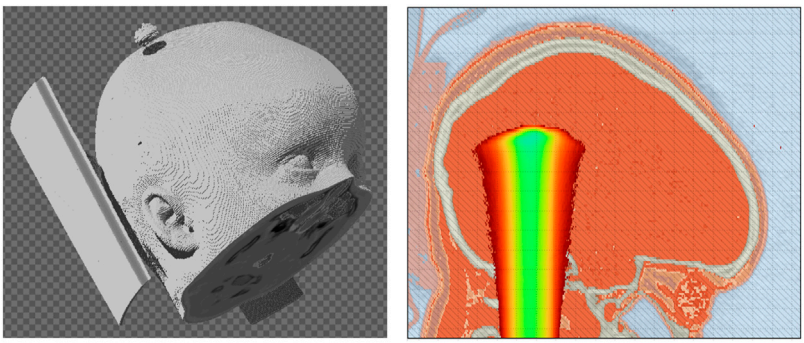

FIGURE 7 | Classic surface-based visualization of a voxelized phantom and dose distribution from an exemplary photon beam irradiation.

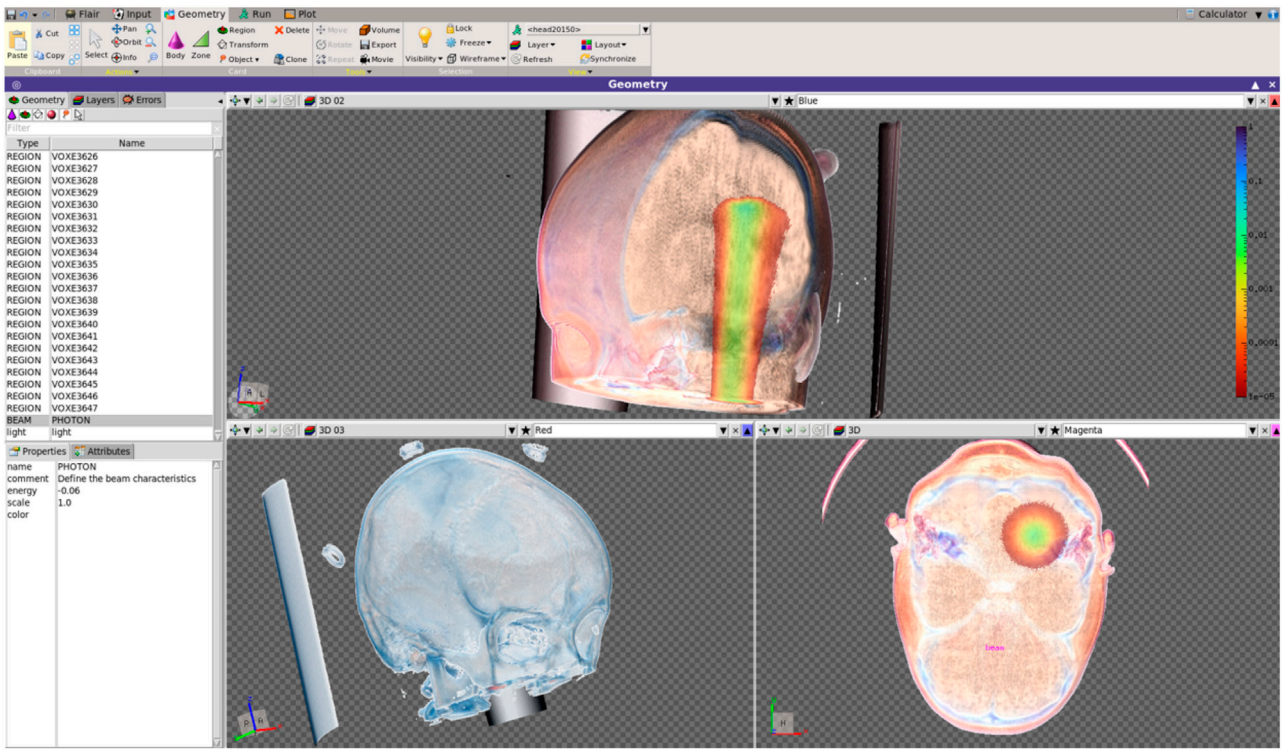

FIGURE 8 | Volumetric visualization of a voxelized phantom and dose distribution from a photon beam irradiation with the new renderer available in Flair v3.

from CT or MRI scans. Consequently, there is no defined geometric surface that one can work with nor are the data continuous in space due to the discretization originating from the data acquisition. The most common way is to assign each point a proxy geometry, e.g. a small cube, and render these with standard techniques. However, this leads to the loss of crucial information as intricate 3D anatomic relationships are not presented anymore to the attending physician. To overcome this drawback, the completely new visualization module in Flair v3 now includes a number of volume rendering techniques for medical applications. These methods allow for proper reconstruction of a 3D function from the discrete dataset via ray-marching based algorithms. Texture-based slicing methods would offer performance advantages due to the possibility of GPU implementation. Nonetheless, for large data sets one quickly reaches the limits of standard consumer hardware and, in addition, ray-casting methods seamlessly integrate with Flair's new photorealistic, interactive ray tracer for standard geometries. **Figures 7** and **8** illustrate the use of standard surface visualization methods versus Flair v3's new medical visualization module using the same dataset. As can be seen, volumetric rendering retains 3D anatomic structures from the scans even on a very fine level and permits a superior evaluation of the dose distribution in a voxel geometry by the medical physicist or physician. Visualization of the geometry is immediate with progressive refinement based on so-called space

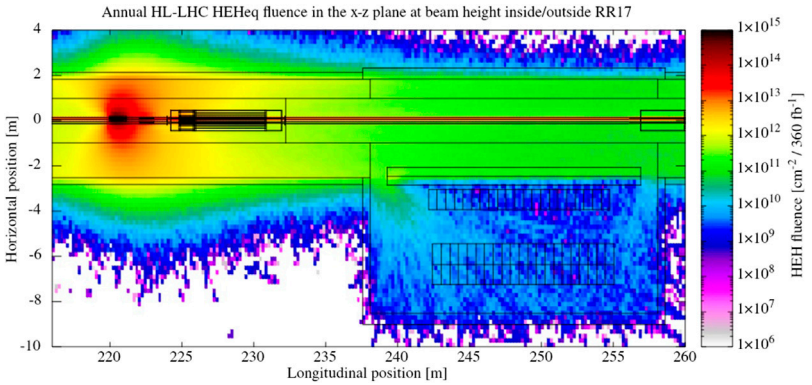

FIGURE 9 | Top view of the annual High Energy Hadron-equivalent fluence at beam height in a portion of the LHC Long Straight Section at Point 1, showing the main tunnel and the nearby RR17 alcove where electronic equipment is hosted.

filling curves opening up real-time user feedback while profiting from optimized use of CPU cache lines.

4 RADIATION TO ELECTRONICS

Radiation effects in electronic components and systems are a well-known threat for the reliable operation of electronics in space and can also be a risk for the successful operation of high energy accelerators [24]. In fact, during the LHC Run 1 (2010–2013), Radiation to Electronics (R2E) issues were one of the main causes of unavailability and downtime of the machine [25]. Monte Carlo transport codes constitute a powerful tool to predict and mitigate such effects, both with regards to the simulation of the radiation environment as well as to its effects on electronics. As will be shown, FLUKA is critical in the context of the R2E activities, where it is used for a variety of purposes and applications.

4.1 High Energy Accelerator Radiation Environment

A key task carried out with FLUKA is the simulation of the radiation field in the CERN accelerator complex, as well as in experimental and test facilities. To this end, FLUKA is used to calculate 3D space distributions of the key radiation level quantities that are needed to assess radiation impact on electronic equipment, both in terms of lifetime degradation and stochastic SEEs.

Lifetime effects are quantified with Total Ionising Dose (TID), i.e., the energy loss due to ionising radiation per unit mass, and the equivalent fluence of 1 MeV neutrons in Silicon, which is used to express Displacement Damage effects in material lattices. On the other hand, FLUKA provides the High Energy Hadron-equivalent (HEH-eq) fluence, i.e., the fluence of all hadrons with $E > 20$ MeV plus the neutrons in the 0.2–20 MeV range with energy-dependent Weibull weights, and the thermal neutron equivalent fluence, where neutrons are weighted proportionally to the inverse of their velocity. These quantities are directly linked to the SEE evaluation.

Figure 9 shows a representative example of radiation environment characterization. It displays the HEH-eq fluence in a portion of LHC tunnel located between 216 and 260 m from Interaction Point (IP) 1, where beam collisions take place. In this case, FLUKA is employed to generate and transport products of inelastic proton-proton interactions from IP1, inducing radiation showers through machine elements, the LHC tunnel infrastructure and nearby underground areas. This way the space distribution of HEH-eq fluence can be obtained and 1D and 2D projections can be extracted for an area of interest (as shown in **Figure 9**), which in this case consists of the highlighted tunnel section and the nearby RR17 alcove hosting electronic equipment. The simulation is scaled to an integrated luminosity of 360 fb^{-1}, so as to represent annual radiation levels in the final years of LHC operation after the High-Luminosity LHC upgrade. These results, along with similar calculations in other LHC areas, serve as basis for the definition of radiation level specifications for electronics. They are essential to define qualification requirements in accordance with a standard Radiation Hardness Assurance procedure [26].

4.2 Monte Carlo Simulation of Single Event Effects

As introduced above, radiation effects can be classified as either cumulative or stochastic. Monte Carlo codes are particularly suited to the prediction and better understanding of the latter which are of random and single-event-like nature. This capability is especially relevant for high energy accelerator applications in which the related response to the passage of a broad range of particles and energies [27] needs to be derived from a relatively limited data set, typically consisting of experimental results from 200 MeV protons.

In particular, codes like FLUKA can accurately simulate energy deposition distributions from single-particle events in sensitive volumes (SV) of microelectronic components. After the energy deposition step, additional dedicated simulations are performed to determine charge collection and related circuit response, which in turn are used to predict the SEE

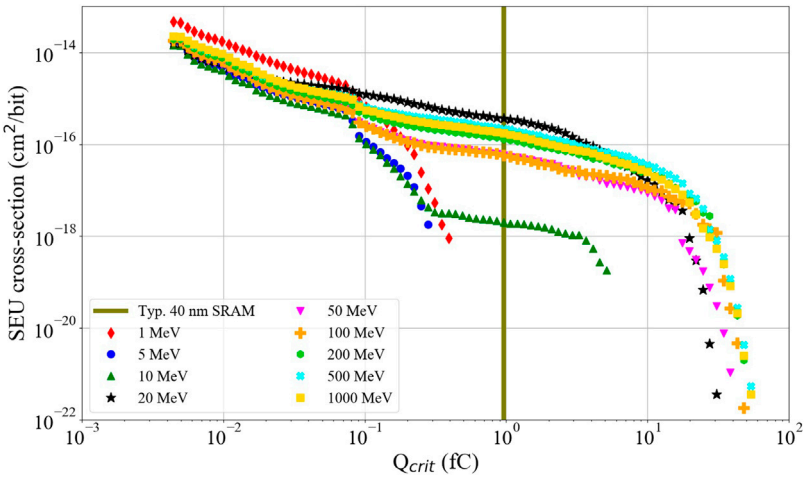

FIGURE 10 | FLUKA simulation of SEU cross section obtained from the integral of the energy deposition distribution by mono-energetic photons above Q_{crit} in the RPP model representing an SRAM sensitive volume for SEU, plotted as a function of Q_{crit}. The vertical line represents a typical value of the critical charge for 40 nm devices.

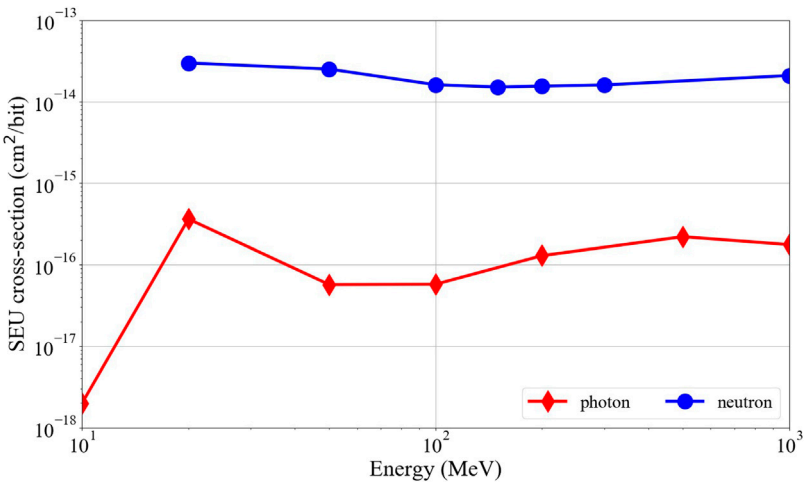

FIGURE 11 | Simulated photon and neutron SEU cross section for 40 nm commercial SRAM.

cross section of the device. In first approximation however, FLUKA can be used for this purpose as well, modelling the SV of the device as a Rectangular Parallelepiped (RPP) [28] or Integral RPP (IRPP)[29], assuming the energy deposited in this volume directly translates to ionization charge collected by the circuit with 100% efficiency. Under this assumption, an SEE will occur if the collected charge is above a certain critical charge value (Q_{crit}) in the RPP case or typically determined experimentally through heavy ion SEE testing, in the IRPP case.

This method has been applied to demonstrate that all hadrons have an approximately equal SEE cross section above 20 MeV [30] in a mixed-field environment. For highly sensitive devices (i.e., low Q_{crit} with small SVs, this finding has been validated within a factor 2 up to hundreds of GeV [31]. The resulting SEE rate prediction is typically estimated within ±50%, which is considered acceptable for mixed radiation field applications. Moreover, the related predictions were successfully benchmarked against experimental measurements, [30].

Various exceptions to the above formalism were studied with FLUKA. This includes for example differences between pion- and nucleon-induced SEE cross section [32], the enhanced SEE cross section of low-sensitivity devices (i.e. high Q_{crit} with high-Z material near the SV in the hadron energy range from 200 MeV to 3 GeV due to fission reactions [33] and the impact of directly ionizing light charged particles such as protons [34] and muons [35]. Additional studies investigated SEEs induced by electro-and photonuclear reactions [36] and, via a Geant4-based extension, by neutrons in the 0.1–10 MeV neutron range [37].

Beyond accelerator applications, similar FLUKA models were used to predict the dominance of protons versus heavy ions for

nuclear induced events in space [38], as well as to use experimental SEE results obtained in hadron environments to predict or bound the error rate induced by heavy ions [39]. Likewise, FLUKA was used to study fragmentation and indirect energy deposition from high-energy heavy ions [40].

As a final illustration of the FLUKA capabilities to gauge radiation effects on electronics, the following lines present results of the simulation of SEEs induced by mono-energetic photons in the 1 MeV-1 GeV range in an RPP model of a 40 nm commercial SRAM[10]. The SEE cross section is obtained from the integral of the distribution of the energy deposited by the photons in the SV above a fixed threshold referred to as Q_{crit}, assuming Q [fC] = E_{dep} [GeV] × 10^6/22.5 in Silicon. Its simulated value is shown in **Figure 10** as a function of Q_{crit}. Considering a critical charge of 1 fC, **Figure 10** shows that photons below 10 MeV are not capable of inducing SEUs. Indeed, they interact mostly through Compton scattering which deposits low energy in the SV.

Over 10 MeV, photo-nuclear reactions lead to higher energy deposition values which can trigger SEUs. The photon-induced SEU cross section is represented in **Figure 11** as a function of the photon energy and compared to the neutron-induced one, in both cases for Q_{crit} = 1 fC. This shows, as expected, that the latter is higher by roughly two orders of magnitude. Still, for specific radiation environments such as those generated by high energy electrons (e.g., downstream the CLEAR beam dump [41], absorbing a beam of 200 MeV electrons) the relative proportion of high energy photons can be prevalent, hence potentially having a significant or even dominant contribution to the overall SEU rate.

5 CODE TESTING AND BENCHMARKING

Ensuring the integrity and quality of FLUKA throughout its full software lifecycle is of utmost importance. A software quality assurance plan is being redefined and put in place accordingly. It implements best practices in software development tailored to the specific needs of a Monte Carlo radiation transport simulations code. The quality assurance plan now includes modern source code management, a dedicated testing framework and initiatives to produce experimental data for benchmarks. This is complemented by a feedback reporting mechanism via the user forum[11] that generates input for the development process.

5.1 Source Code Management and Continuous Integration

The FLUKA source code lifecycle is managed using the CERN GitLab instance[12]. The latter offers a state-of-the-art infrastructure for full version control based on the git version control system [42] as well as Continuous Integration (CI). A continually growing number of test cases is included in the CI framework, aimed both at probing new development features and ensuring the consistency with respect to the established FLUKA version. These test cases run automatically for every pushed commit. A further in-depth validation at the model level and for full-scale test cases is performed within the FLUKAVAL framework (see next subsection). As an additional quality assurance check prior to public releases, the code is deployed and intensively tested in the respective computing clusters of the collaborating institutes, monitoring its performance and stability in real-world applications.

5.2 FLUKAVAL Framework

The FLUKAVAL framework is a Python-based command line application that enables semi-automatic batch submission, processing, validation and reporting of test cases. Any FLUKA input and even model-level based tests can be adapted and integrated in a few steps into the framework. FLUKAVAL makes extensive use of the git version control system to store simulation and reference data sets on the CERN GitLab instance. In its current version, FLUKAVAL is optimised for the submission of a large number of test cases to the CERN Batch Service (LXBATCH), which provides distributed computing power with over 220,000 CPU cores.

FLUKA output data are stored in standardised JSON format, which is compatible with the Geant Validation Portal[13], to simplify future direct comparisons of identical test cases with Geant4.

The results are processed, validated and compiled in a comprehensive evaluated report, which allows the direct comparison of results from the FLUKA version under validation with results obtained with previous FLUKA versions, other radiation transport codes and/or experimental data. A quantitative analysis is performed in addition to a qualitative comparison whenever possible. The resulting report is stored in the CERN document management system once the proper approval process is positively completed.

5.3 Validation Procedure

One of the ways to validate a FLUKA version and achieve quality assurance is to directly and quantitatively compare results from the version under development to results obtained with previous released versions of the code. A growing number of test cases is available within the FLUKAVAL framework, each of them aiming to investigate selected features of the code. Specific acceptance criteria are chosen for each of the test cases based on the observable/physics quantity to validate.

Two kinds of test cases are available at present in order to validate the different features of the code, namely on the model/interaction level and full-scale test cases. The first kind of test cases aims to validate a FLUKA version at the

[10]detailed in [34].

[11]https://fluka-forum.web.cern.ch/

[12]https://gitlab.cern.ch

[13]https://geant-val.cern.ch/

model/interaction level by running specific drivers that have access to internal functionalities of the code. Among others, these drivers allow to estimate reaction cross sections, double differential cross sections and yields as a function of energy for any kind of projectile and known target element either as a single isotope or in its natural isotopic composition. These tailored test cases provide a fine control over the changes and improvements of the implemented physics model. Full-scale test cases, instead, aim to validate the code with FLUKA simulations based on real case applications. These test cases provide a coverage of different fields of application and FLUKA functionalities. They can test several observables such as energy deposition, energy and/or spatial particle fluence distributions, radionuclide inventory and residual dose in a more elaborate case. That can include, for example, complex geometries and material definitions, tracking in magnetic fields, special sources and custom user routines.

Comparisons to other codes also provide useful input for the development process. The FLUKAVAL framework can include simulation results of other Monte Carlo radiation transport simulations codes and compare them quantitatively to FLUKA results. In addition, the FLUKA code is regularly included in international Monte Carlo code inter-comparisons, for example the particle production inter-comparison at the SATIF workshop series [43, 44].

Comparisons to experimental data are vital for the quality assurance of FLUKA. The FLUKAVAL framework can embed experimental data and allows for a quantitative comparison with FLUKA results. The experimental data in the FLUKAVAL framework ranges from the single interaction level data, e.g., radionuclide production cross-sections from the EXFOR database, up to measurements in large experiments.

All the above is complemented by a long-standing initiative to generate new experimental data for benchmarks of radiation transport simulation codes with a focus on the relevance to real-world applications. Examples are neutron spectra at the CERN-EU High-Energy Fields (CERF) facility [45–47], neutron spectra and activation at the CERN Shielding Benchmark Facility (CSBF) [48, 49], activation at the CERN High-energy AcceleRator (CHARM) test facility [50] and activation due to stray radiation from the annihilation of low-energy antiprotons in steel [51].

6 OUTLOOK

The present code has reached a high level of maturity, but its rigid structure and procedural programming paradigm pose an intrinsic limitation for future contributions and developments. While improving and extending the physics performance of FLUKA remains a key objective, a concurrent development activity has been started, aiming at a substantial evolution of the code architecture. Modernizing the codebase, increasing its modularity, and reinforcing a collaborative environment is an essential path for assuring the long-term sustainability of FLUKA. The new code will be based on C++, profiting from the advantages of an object-oriented design. At the same time, key objectives are to improve the user friendliness and to offer a rich set of built-in options beyond the existing functionality of present FLUKA releases.

6.1 Moira

The first stage of the development project, which is named Moira, is presently in an exploratory phase. To foster synergies with other Monte Carlo codes and benefit from existing development efforts, the new code will be based on the Geant4 framework [52–54]. The technical functionalities of FLUKA are translated into a Geant4-based application, incorporating a wide spectrum of existing FLUKA capabilities (e.g., scoring, biasing, radioactive decay calculations). Where available, existing features of Geant4 will be utilized.

The new code will continue to support combinatorial geometries based on the present FLUKA input format, using Flair as an external geometry navigator. At the same time, it will offer access to Geant4-compatible geometry descriptions, for example in the GDML format. A versatile set of built-in scoring options will be provided, which can be used with any type of geometry description. Moira will be closely integrated with Flair in order to preserve an intuitive visual user experience through a graphical user interface and an advanced geometry viewer.

6.2 A Fifth FLUKA Generation

In a second stage, the FLUKA physics models will be migrated. When the Moira program reaches a sufficient level of maturity, it will be distributed as a new FLUKA generation. The goal is to provide a fully integrated package to the user with a fixed set of physics models that have undergone strict quality assurance processes and thus will deliver well identifiable physics results, being consistent with the ones of FLUKA v4 at that time. The development effort until the first release is expected to expand over several years. Nevertheless, in the interest of the Monte Carlo user community, it is planned to distribute intermediate Moira versions at earlier stages, enabling the use of the FLUKA input files also for Geant4 calculations. The modernization and modularization of the program, profiting in particular from existing interfaces in Geant4, will facilitate contributions from a wider community.

DATA AVAILABILITY STATEMENT

The raw data supporting the conclusions of this article will be made available by the authors, without undue reservation.

AUTHOR CONTRIBUTIONS

The authors of this manuscript are participants in the FLUKA.CERN Collaboration. Section 1 was written by FC.

DC, LE, AL, FSP, and PS elaborated section 2. CT and VV composed section 3. ACo, RGA and GL produced section 4. CA, DB, RF, AI, and MW wrote section 5, while GH and AL provided section 6. NC, DH, FOR, SR, AT, RV, AW have revised the manuscript. All authors contributed to the work and approved the submitted version.

ACKNOWLEDGMENTS

We would like to deeply thank the CERN Knowledge Transfer and Legal Service teams for their essential and extended support. Our appreciation also goes to the FLUKA.CERN Collaboration Board members for their strong commitment.

REFERENCES

1. Battistoni G, Boehlen T, Cerutti F, Chin PW, Esposito LS, Fassò A, et al. (2015). Overview of the FLUKA Code. *Ann Nucl Energ* 82:10–8. doi:10.1016/j.anucene.2014.11.007
2. Ambrosino F, Roca V, Buompane R, Sabbarese C (2020). Development and Calibration of a Method for Direct Measurement of 220rn (Thoron) Activity Concentration. *Appl Radiat Isot* 166:109310. doi:10.1016/j.apradiso.2020.109310
3. Bielajew A (1987). Electron Transport in E and B fields. In: *Monte Carlo Transport of Electrons and Photons*. New York, NY: Plenum Press. p. 421–34.
4. Afonin AG, Baranov VT, Biryukov VM, Breese MBH, Chepegin VN, Chesnokov YA, et al. (2001). High-efficiency Beam Extraction and Collimation Using Channeling in Very Short Bent Crystals. *Phys Rev Lett* 87:94802. doi:10.1103/physrevlett.87.094802
5. Scandale W, Arduini G, Butcher M, Cerutti F, Gilardoni S, Lechner A, et al. (2014). Observation of Focusing of 400 GeV/c Proton Beam with the Help of Bent Crystals. *Phys Lett B* 733:366–72. doi:10.1016/j.physletb.2014.05.010
6. Rossi RThe UA9 collaboration (2016). Observation of Channeling in Bent Crystals at the CERN LHC. In: 38th International Conference on High Energy. PoS ICHEP2016, Chicago. p. 867. doi:10.22323/1.282.0867
7. Rossi R (2017). *Experimental Assessment of Crystal Collimation at the Large Hadron Collider*. Ph.D. Thesis. Presented 26 Jan 2018.
8. Redaelli S, Butcher M, Barreto C, Losito R, Masi A, Mirarchi D, et al. (2021). First Observation of Ion Beam Channeling in Bent Crystals at Multi-Tev Energies. *Eur Phys J C* 81:1–7. doi:10.1140/epjc/s10052-021-08927-x
9. Schoofs P, Cerutti F, Ferrari A, Smirnov G (2015). Benchmark of the FLUKA Model of crystal Channeling against the UA9-H8 experiment. *Nucl Instr Methods Phys Res Section B: Beam Interactions Mater Atoms* 355:374–7. doi:10.1016/j.nimb.2015.03.074
10. Esbensen H, Fich O, Golovchenko JA, Madsen S, Nielsen H, Schiøtt HE, et al. (1978). Random and Channeled Energy Loss in Thin Germanium and Silicon Crystals for Positive and Negative 2-15-GeV/cpions, Kaons, and Protons. *Phys Rev B* 18:1039–54. doi:10.1103/PhysRevB.18.1039
11. Schoofs P (2014). *Monte Carlo Modeling of Crystal Channeling at High Energies*. Ph.D. Thesis. CERN-THESIS-2014-131.
12. Alliot C, Audouin N, Barbet J, Bonraisin AC, Bosse VR, Bourdeau CC, et al. (2015). Is There an Interest to Use Deuteron Beams to Produce Non-conventional Radionuclides? *Front Med* 2:31. doi:10.3389/fmed.2015.00031
13. Sitarz M, Szkliniarz K, Jastrzębski J, Choiński J, Guertin A, Haddad F, et al. (2018). Production of Sc Medical Radioisotopes with Proton and Deuteron Beams. *Appl Radiat Isot* 142:104–12. doi:10.1016/j.apradiso.2018.09.025
14. Takada M, Mihara E, Sasaki M, Nakamura T, Honma T, Kono K, et al. (2004). Neutron Field Produced by 25 MeV Deuteron on Thick Beryllium for Radiobiological Study; Energy Spectrum. *Radiat Prot Dosimetry* 110:601–6. doi:10.1093/rpd/nch142
15. Chauvin N, Akagi T, Bellan L, Beauvais P-Y, Bolzon B, Cara P, et al. (2019). Deuteron Beam Commissioning of the Linear IFMIF Prototype Accelerator Ion Source and Low Energy Beam Transport. *Nucl Fusion* 59:106001. doi:10.1088/1741-4326/ab1c88
16. Serber R (1947). The Production of High Energy Neutrons by Stripping. *Phys Rev* 72:1008–16. doi:10.1103/physrev.72.1008
17. Ferrari A, Sala P (1998). The Physics of High Energy Reactions. In: Proceeding: Workshop on Nuclear Reaction Data and Nuclear Reactor. Physics, Design and Safety, Trieste (Italy). World Scientific. 424.
18. Baur G, Rösel F, Trautmann D (1976). Investigations of the Deuteron Break-Up on Heavy Nuclei above the Coulomb Barrier. *Nucl Phys A* 265:101–12. doi:10.1016/0375-9474(76)90118-4
19. Titus L (2016). *Effects of Non-locality on Transfer Reactions*. Ph.D. Thesis. East Lansing, MI: Michigan State University. arXiv:1604.00094v1.
20. Cerutti F, Battistoni G, Capezzali G, Colleoni P, Ferrari A, Gadioli E, et al. (2006). Low Energy Nucleus-Nucleus Reactions: the BME Approach and its Interface with FLUKA. In: Proceedings of the 11th International Conference on Nuclear Reaction Mechanisms, Varenna.
21. Ridikas D, Mittig W, Savajols H, Roussel-Chomaz P, Foertsch S, Lawrie J, et al. (2000). Inclusive Proton Production Cross Sections in (D,xp) Reactions Induced by 100 MeV Deuterons. *Phys Rev C* 63:014610. doi:10.1103/physrevc.63.014610
22. Vlachoudis V (2009). FLAIR: A Powerful but User Friendly Graphical Interface for FLUKA. In: Proceedings: International Conference on Mathematics, Computational Methods and Reactor Physics, Saratoga Springs, NY.
23. Werner CJ (2017). *MCNP Users Manual-Code Version 6.2*. Los Alamos, NM: Los Alamos National Security LLC.
24. García Alía R, Brugger M, Danzeca S, Cerutti F, de Carvalho Saraiva JP, Denz R, et al. (2017). Single Event Effects in High-Energy Accelerators. *Semiconductor Sci Techn* 32:034003. doi:10.1088/1361-6641/aa5695
25. Apollonio A, Brugger M, Rossi L, Schmidt R, Todd B, Wollmann D, et al. (2015). Roadmap towards High Accelerator Availability for the CERN HL-LHC Era. In: Proceedings, 6th International Particle Accelerator Conference (IPAC 2015). Richmond, Virginia, USA.
26. Aberle O, Béjar Alonso I, Brüning O, Fessia P, Rossi L, Tavian L, et al. (2020). High-Luminosity Large Hadron Collider (HL-LHC): Technical Design Report. CERN Yellow Reports: Monographs. Geneva: CERN. doi:10.23731/CYRM-2020-0010
27. Alia RG, Tali M, Brugger M, Cecchetto M, Cerutti F, Cononetti A, et al. (2020). Direct Ionization Impact on Accelerator Mixed-Field Soft-Error Rate. *IEEE Trans Nucl Sci* 67:345–52. doi:10.1109/TNS.2019.2951307
28. Weller RA, Reed RA, Warren KM, Mendenhall MH, Sierawski BD, Schrimpf RD, et al. (2009). General Framework for Single Event Effects Rate Prediction in Microelectronics. *IEEE Trans Nucl Sci* 56:3098–108. doi:10.1109/tns.2009.2033916
29. Petersen EL, Pouget V, Massengill LW, Buchner SP, McMorrow D (2005). Rate Predictions for Single-Event Effects - Critique II. *IEEE Trans Nucl Sci* 52:2158–67. doi:10.1109/TNS.2005.860687
30. García Alía R, Biskup B, Brugger M, Calviani M, Poivey C, Roed K, et al. (2013). SEU Measurements and Simulations in a Mixed Field Environment. *IEEE Trans Nucl Sci* 60:2469–76. doi:10.1109/TNS.2013.2249096
31. García Alía R, Brugger M, Danzeca S, Ferlet-Cavrois V, Poivey C, Roed K, et al. (2013). SEE Measurements and Simulations Using Mono-Energetic GeV-Energy Hadron Beams. *IEEE Trans Nucl Sci* 60:4142–9. doi:10.1109/TNS.2013.2279690
32. Coronetti A, García Alía R, Cerutti F, Hajdas W, Soderstrom D, Javanainen A, et al. (2021). The Pion Single-Event Latch-Up Cross Section Enhancement: Mechanisms and Consequences for Accelerator Hardness Assurance. *IEEE Trans Nucl Sci* 68:1613–22. doi:10.1109/TNS.2021.3070216
33. García Alía R, Brugger M, Cecchetto M, Cerutti F, Danzeca S, Delrieux M, et al. (2018). SEE Testing in the 24-GeV Proton Beam at the CHARM Facility. *IEEE Trans Nucl Sci* 65:1750–8. doi:10.1109/TNS.2018.2829916
34. Coronetti A, García Alía R, Wang J, Tali M, Cecchetto M, Cazzaniga C, et al. (2021). Assessment of Proton Direct Ionization for the Radiation Hardness Assurance of Deep Submicron Srams Used in Space Applications. *IEEE Trans Nucl Sci* 68:937–48. doi:10.1109/TNS.2021.3061209
35. Infantino A, García Alía R, Brugger M (2017). Monte Carlo Evaluation of Single Event Effects in a Deep-Submicron Bulk Technology: Comparison

between Atmospheric and Accelerator Environment. *IEEE Trans Nucl Sci* 64: 596–604. doi:10.1109/TNS.2016.2621238
36. Tali M, García Alía R, Brugger M, Ferlet-Cavrois V, Corsini R, Farabolini W, et al. (2019). Mechanisms of Electron-Induced Single-Event Latchup. *IEEE Trans Nucl Sci* 66:437–43. doi:10.1109/TNS.2018.2884537
37. Cecchetto M, García Alía R, Wrobel F, Coronetti A, Bilko K, Lucsanyi D, et al. (2021). 0.1-10 MeV Neutron Soft Error Rate in Accelerator and Atmospheric Environments. *IEEE Trans Nucl Sci* 68:873–83. doi:10.1109/TNS.2021.3064666
38. García Alía R, Brugger M, Ferlet-Cavrois V, Brandenburg S, Calcutt J, Cerutti F, et al. (2017). Proton Dominance of Sub-LET Threshold GCR SEE Rate. *IEEE Trans Nucl Sci* 64:388–97. doi:10.1109/TNS.2016.2628363
39. García Alía R, Brugger M, Daly E, Danzeca S, Ferlet-Cavrois V, Gaillard R, et al. (2017). Simplified SEE Sensitivity Screening for COTS Components in Space. *IEEE Trans Nucl Sci* 64:882–90. doi:10.1109/TNS.2017.2653863
40. Kastriotou M, Fernandez-Martinez P, García Alía R, Cazzaniga C, Cecchetto M, Coronetti A, et al. (2020). Single Event Effect Testing with Ultrahigh Energy Heavy Ion Beams. *IEEE Trans Nucl Sci* 67:63–70. doi:10.1109/TNS.2019.2961801
41. Sjobak K, Adli E, Bergamaschi M, Burger S, Corsini R, Curcio A, et al. (2019). Status of the clear Electron Beam User Facility at Cern. In: Proceedings of the 10th International Particle Accelerator Conference, Melbourne, Australia.
42. Chacon S, Straub B (2014). Pro Git. Apress.
43. Hirayama H, Sanami T (2014). Inter-Comparison of Particle Production. In: Shielding Aspects of Accelerators, Targets and Irradiation Facilities (SATIF-12); 28-30 April, 2014; Batavia, Illinois, USA. 242–51. OECD/NEA/NSA/R(2015)3.
44. Hirayama H, Sanami T (2018). Inter-Comparison of Particle Production. In: Shielding Aspects of Accelerators, Targets and Irradiation Facilities (SATIF-14); 30 October-2 November, 2018; Gyeonju, South Korea.
45. Nakao N, Rokni SH, Brugger M, Roesler S, Vincke H, Kosako K (2006). Calculation of High-Energy Neutron Spectra with Different Monte Carlo Transport Codes and Comparison to Experimental Data Obtained at the CERF Facility. In: Shielding Aspects of Accelerators, Targets and Irradiation Facilities - SATIF 8, Proceedings of the 8th Meeting, Nam-Gu Pohang, Republic of Korea, 2006.
46. Pozzi F, Silari M (2020). The CERN-EU High-Energy Reference Field (CERF) Facility: New FLUKA Reference Values of Spectral Fluences, Present and Newly Proposed Operational Quantities. *Nucl Instr Methods Phys Res Section A: Acc Spectrometers Detectors Associated Equipment* 979:164477. doi:10.1016/j.nima.2020.164477
47. Nakao N, Taniguchi S, Roesler S, Brugger M, Hagiwara M, Vincke H, et al. (2008). Measurement and Calculation of High-Energy Neutron Spectra behind Shielding at the CERF 120GeV/c Hadron Beam Facility. *Nucl Instr Methods Phys Res Section B: Beam Interactions Mater Atoms* 266:93–106. doi:10.1016/j.nimb.2007.09.043
48. Iliopoulou E, Bamidis P, Brugger M, Froeschl R, Infantino A, Kajimoto T, et al. (2018). Measurements and FLUKA Simulations of Bismuth and Aluminium Activation at the CERN Shielding Benchmark Facility (CSBF). *Nucl Instr Methods Phys Res Section A: Acc Spectrometers Detectors Associated Equipment* 885:79–85. doi:10.1016/j.nima.2017.12.058
49. Iliopoulou E, Bamidis P, Brugger M, Froeschl R, Infantino A, Kajimoto T, et al. (2018). Measurements and FLUKA Simulations of Bismuth, Aluminium and Indium Activation at the Upgraded CERN Shielding Benchmark Facility (CSBF). *J Phys Conf Ser* 1046:012004. doi:10.1088/1742-6596/1046/1/012004
50. Nakao N, Kajimoto T, Sanami T, Froeschl R, Iliopoulou E, Infantino A, et al. (2021). Measurements and Monte Carlo Simulations of High-Energy Neutron Streaming through the Access Maze Using Activation Detectors at 24 Gev/c Proton Beam Facility of Cern/charm. *J Nucl Sci Techn* 58:899–907. doi:10.1080/00223131.2021.1887003
51. Ahdida C, Froeschl R, Iliopoulou E, Infantino A, Jensen S (2020). Measurements and FLUKA Simulations of Aluminium, Bismuth and Indium Activation by Stray Radiation from the Annihilation of Low Energy Antiprotons. *Nucl Instr Methods Phys Res Section A: Acc Spectrometers Detectors Associated Equipment* 950:162972. doi:10.1016/j.nima.2019.162972
52. Agostinelli S, Allison J, Amako K, Apostolakis J, Araujo H, Arce P, et al. (2003). Geant4-a Simulation Toolkit. *Nucl Inst Meth A* 506:250–303. doi:10.1016/S0168-9002(03).01368-8
53. Allison J, Amako K, Apostolakis J, Araujo HM, Arce Dubois P, Asai M, et al. (2006). Geant4 Developments and Applications. *IEEE Trans Nucl Sci* 53: 270–8. doi:10.1109/TNS.2006.869826
54. Allison J, Amako K, Apostolakis J, Arce P, Asai M, Aso T, et al. (2016). Recent Developments in Geant4. *Nucl Inst Meth A* 835:186–225. doi:10.1016/j.nima.2016.06.125

Conflict of Interest: The authors declare that the research was conducted in the absence of any commercial or financial relationships that could be construed as a potential conflict of interest.

Publisher's Note: All claims expressed in this article are solely those of the authors and do not necessarily represent those of their affiliated organizations or those of the publisher, the editors, and the reviewers. Any product that may be evaluated in this article, or claim that may be made by its manufacturer, is not guaranteed or endorsed by the publisher.

Advantages of publishing in Frontiers

OPEN ACCESS
Articles are free to read for greatest visibility and readership

FAST PUBLICATION
Around 90 days from submission to decision

HIGH QUALITY PEER-REVIEW
Rigorous, collaborative, and constructive peer-review

TRANSPARENT PEER-REVIEW
Editors and reviewers acknowledged by name on published articles

Frontiers
Avenue du Tribunal-Fédéral 34
1005 Lausanne | Switzerland

Visit us: www.frontiersin.org
Contact us: frontiersin.org/about/contact

REPRODUCIBILITY OF RESEARCH
Support open data and methods to enhance research reproducibility

DIGITAL PUBLISHING
Articles designed for optimal readership across devices

FOLLOW US
@frontiersin

IMPACT METRICS
Advanced article metrics track visibility across digital media

EXTENSIVE PROMOTION
Marketing and promotion of impactful research

LOOP RESEARCH NETWORK
Our network increases your article's readership